

AD A068808

DDC FILE COPY

AGARD-LS-98

# AGARD

ADVISORY GROUP FOR AEROSPACE RESEARCH & DEVELOPMENT

7 RUE ANCELLE 92200 NEUILLY SUR SEINE FRANCE

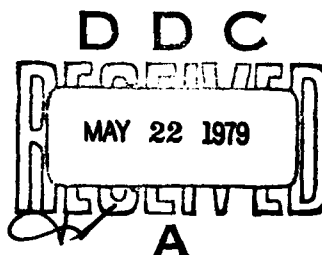
## LEVEL

AGARD LECTURE SERIES No. 98

## Missile Aerodynamics

**DISTRIBUTION STATEMENT A**

Approved for public release;  
Distribution Unlimited

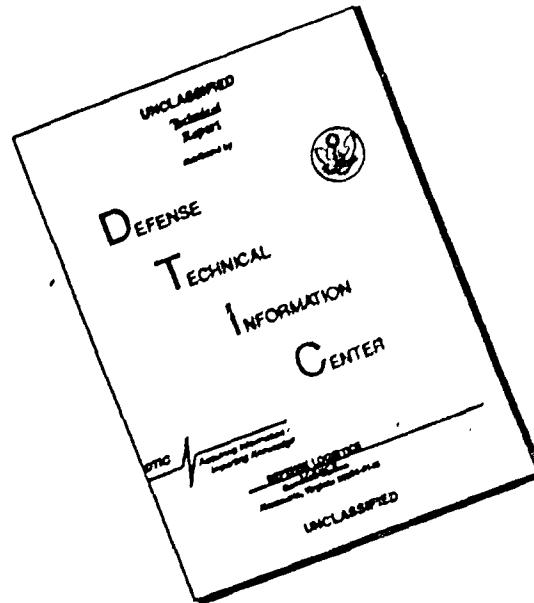


NORTH ATLANTIC TREATY ORGANIZATION



DISTRIBUTION AND AVAILABILITY  
ON BACK COVER

# DISCLAIMER NOTICE



THIS DOCUMENT IS BEST QUALITY AVAILABLE. THE COPY FURNISHED TO DTIC CONTAINED A SIGNIFICANT NUMBER OF PAGES WHICH DO NOT REPRODUCE LEGIBLY.

NORTH ATLANTIC TREATY ORGANIZATION  
 ADVISORY GROUP FOR AEROSPACE RESEARCH AND DEVELOPMENT ✓  
 (ORGANISATION DU TRAITE DE L'ATLANTIQUE NORD)

9 AGARD Lecture Series No. 98 ✓

1 MISSILE AERODYNAMICS.

11 F. 111

1237141

ADDITION BY	
DTIC	Write Section <input checked="" type="checkbox"/>
DOC	Self Section <input type="checkbox"/>
UNANNOUNCED	<input type="checkbox"/>
JUSTIFICATION	
BY	
DISTRIBUTION/AVAILABILITY NOTES	
Date	
A	

The material in this publication was assembled to support a Lecture Series under the sponsorship of the Fluid Dynamics Panel, the Consultant and Exchange Programme of AGARD and the von Kármán Institute for Fluid Dynamics presented on: 5-6 March in Ankara, Turkey; 8-9 March in Rome, Italy and 12-16 March at the von Kármán Institute, Rhode-Saint-Genèse, Belgium.

## THE MISSION OF AGARD

The mission of AGARD is to bring together the leading personalities of the NATO nations in the fields of science and technology relating to aerospace for the following purposes:

- Exchanging of scientific and technical information;
- Continuously stimulating advances in the aerospace sciences relevant to strengthening the common defence posture;
- Improving the co-operation among member nations in aerospace research and development;
- Providing scientific and technical advice and assistance to the North Atlantic Military Committee in the field of aerospace research and development;
- Rendering scientific and technical assistance, as requested, to other NATO bodies and to member nations in connection with research and development problems in the aerospace field;
- Providing assistance to member nations for the purpose of increasing their scientific and technical potential;
- Recommending effective ways for the member nations to use their research and development capabilities for the common benefit of the NATO community.

The highest authority within AGARD is the National Delegates Board consisting of officially appointed senior representatives from each member nation. The mission of AGARD is carried out through the Panels which are composed of experts appointed by the National Delegates, the Consultant and Exchange Programme and the Aerospace Applications Studies Programme. The results of AGARD work are reported to the member nations and the NATO Authorities through the AGARD series of publications of which this is one.

Participation in AGARD activities is by invitation only and is normally limited to citizens of the NATO nations.

The content of this publication has been reproduced  
directly from material supplied by AGARD or the authors.

Published February 1979

Copyright © AGARD 1979  
All Rights Reserved

ISBN 92-835-0234-5



*Printed by Technical Editing and Reproduction Ltd  
Harford House, 7-9 Charlotte St, London, W1P 1HD*



## PREFACE

The differences in flight conditions and geometric configurations between aircraft and missiles mean that aerodynamic techniques for missile applications frequently differ from those used for aircraft. This lecture series aimed to emphasize these differences in the aerodynamic design features of both guided and unguided weapons. In addition to treating the component parts of the weapons themselves (e.g., wings, bodies, controls, propulsion units) and particular aspects of complete weapons (e.g., kinetic heating, high incidence effects), the course also dealt with the effects of air-breathing engines on the aerodynamics and vice versa, the interactions between aircraft and the weapons they carry, stores separation, and model test techniques.

The course was aimed at staff (junior aerodynamicists and senior non-aerodynamicists) at firms, research establishments, the military and engineering teaching institutions who could profit from a wide-ranging survey of the subject. Lectures generally started with a review of fundamentals and paid particular attention to practical methods of estimation and design and to comparison of these with experimental results.

This Lecture Series conceived and supported by the AGARD Fluid Dynamics Panel and the von Kármán Institute has been developed from two similar previous events organized at VKI in 1974 (VKI LS 67) and 1976 (VKI LS 88). Some of the articles are in a similar, but updated form, however, new articles especially in the field of weapon aircraft interactions and stores separation and air-breathing propulsion units have been included.

Les différences de conditions de vol et de configurations géométriques qui distinguent les aéronefs des missiles font que les techniques aérodynamiques qui leur sont appliquées diffèrent aussi fréquemment. Le cycle de conférences dont il est rendu compte ici avait pour objectif de souligner ces différences, telles qu'elles apparaissent dans les caractéristiques conceptuelles aérodynamiques des armes guidées et non guidées. Outre les éléments composants des armes proprement dites (ex: ailes, corps, gouvernes, groupes propulseurs) et certains aspects particuliers de ces armes considérées dans leur intégralité (ex: échauffement cinétique, effets des incidences élevées), les questions traitées au cours des conférences englobaient les effets des moteurs aérobies sur l'aérodynamique, et vice-versa, les interactions entre les avions et les armes qu'ils transportent, la séparation des éléments largables, et les techniques d'essais de maquettes.

Ce cours était destiné au personnel de l'industrie privée (jeunes aérodynamiciens et cadres non aérodynamiciens), aux établissements de recherche, aux militaires et aux écoles de formation d'ingénieurs, bref, à tous ceux qui étaient à même de bénéficier d'une étude de grande envergure sur ce sujet. Les conférences débutèrent en général par un rappel des principes fondamentaux, et s'attachèrent en particulier à l'examen des méthodes pratiques d'évaluation et de conception, ainsi qu'à la comparaison de ces dernières avec les résultats expérimentaux.

Ce cycle de conférences, conçu et réalisé sous l'égide du Panel de Dynamique des Fluides de l'AGARD et de l'Institut von Kármán (VKI), constituait le développement de deux expériences similaires organisées précédemment au VKI: en 1974 (VKI LS 67) et en 1976 (VKI LS 88). Certains des articles de cet ouvrage se présentent sous une forme semblable mais ont fait l'objet d'une remise à jour: toutefois, de nouveaux articles ont été ajoutés, en particulier en ce qui concerne les interactions entre aéronefs et armement, la séparation des éléments largables, et les groupes propulseurs aérobies.

### Editors:

G.G.BREBNER,  
RAE-Farnborough, UK

B.E.RICHARDS,  
VKI, Belgium

W.STAHL  
DFVLR/AVA Göttingen, Germany

*B. Richards*

B.E.RICHARDS  
Lecture Series Director

## LIST OF SPEAKERS AND CONTRIBUTORS

Lecture Series Director: Professor B.E.Richards  
von Kármán Institute for Fluid Dynamics  
72 Chaussee de Waterloo  
1640 Rhode-Saint-Genèse  
Belgium

Mr G.G.Brebner  
Ministry of Defence  
Procurement Executive  
Royal Aircraft Establishment  
Farnborough, Hants  
UK

Mr J.Delery and Mr M.Sirieux  
ONERA  
29 Avenue de la Division Leclerc  
92320 Châtillon sous Bagneux  
France

Mr H.Esch  
DFVLR (Porz-Wahn)  
Institut für Angewandte Gasdynamik  
Postfach 90 6058  
5000 Cologne 90  
Germany (GFR)

Mr C.Mathews  
Air Force Armaments Laboratory/DLJC  
Eglin Air Force Base  
3252 Florida  
USA

Dr W.Stahl  
DFVLR/AVA  
Institut für Stromungsmechanik  
Bunsenstrasse 10  
D 3400 Göttingen  
Germany (GFR)

Dr A.B.Wardlaw, Jr  
Naval Surface Weapons Center  
White Oak  
Maryland 20910  
USA

## CONTENTS

	Page
<b>PREFACE</b> by B.E.Richards	iii
<b>LIST OF SPEAKERS AND CONTRIBUTORS</b>	iv
	Reference
<b>A BRIEF REVIEW OF AIR FLIGHT WEAPONS</b> by G.G.Brebner	1
<b>GENERAL MISSILE AERODYNAMICS</b> by G.G.Brebner	2
<b>AERODYNAMICS OF LOW ASPECT RATIO WINGS</b> by W.H.Stahl	3
<b>BODIES</b> by H.Esch	4
<b>HIGH-ANGLE-OF-ATTACK MISSILE AERODYNAMICS</b> by A.B.Wardlaw, Jr	5
<b>ECOULEMENTS DE CULOT</b> par J.Delery et M.Sirieix	6
<b>THE CONTROL OF GUIDED WEAPONS</b> by G.G.Brebner	7
<b>STORE SEPARATION</b> by C.B.Mathews	8
<b>KINETIC HEATING OF HIGH SPEED MISSILES</b> by B.E.Richards	9

## A BRIEF REVIEW OF AIR FLIGHT WEAPONS

by

George G Brebner  
Aerodynamics Department  
Royal Aircraft Establishment  
Farnborough, Hants, GU14 6TD, UK

## SUMMARY

The differences in design objectives and consequently in geometry between aircraft and weapons, and the aerodynamic repercussions, are described. Various general categories of air flight weapons are listed - propelled and unpropelled, guided and unguided - and in the particular category of propelled guided weapons different classes are identified. The following components of a guided weapon are described briefly: warhead, propulsive unit, safety and arming mechanism, fuze, guidance system and control system. Their functions and their effects on the aerodynamic design are described. Finally, the place of the aerodynamicist in the design of a guided weapon is discussed, and related to the various stages of the design and development process.

## 1 INTRODUCTION

The history of air-flight weapons probably began with the sling-shot, the spear, the arrow and perhaps the boomerang. The invention of gunpowder brought about a huge increase in range, but prior to the 20th century gun-fired projectiles were purely ballistic in their flight - they had no built-in propulsion, no built-in guidance, no built-in control. The science of ballistics pre-dated the science of aerodynamics and the first studies of supersonic flight were prompted by the behaviour of artillery projectiles. During the 20th century, however, and particularly since the second world war there has been a great increase in the number of weapons which are self-propelled or guided or both, and the science of aerodynamics, which has been so extensively developed in the study of aircraft flight, now contributes more than ballistics to the design of modern air-flight weapons.

Let us start by considering why the title of this Lecture Series is "Missile Aerodynamics". We might infer from this that the science of aerodynamics and its laws are different when applied to the design of weapons than they are when applied to the design of aircraft. This, of course, would be wrong. The scientific laws are the same, but it is sensible to differentiate between weapon aerodynamics and aircraft aerodynamics on three grounds:

- 1 The objectives of the design of the flying vehicles are usually quite different.
- 2 The range of attitudes and flight conditions are usually quite different.
- 3 The shapes which are appropriate to achieve the design objectives in the required flight conditions can be very different, and since applied aerodynamics usually requires a number of assumptions and approximations to be made in order to obtain practically useful results, the assumptions and approximations appropriate for typical weapons may not be appropriate for aircraft shapes.

The difference in design objectives between civil aircraft and weapons can be seen from Figure 1. The aircraft is designed for efficient and economical cruising flight, which implies a high value of lift/drag ratio: by the use of variable geometry devices it adapts its flying characteristics to make it suitable for landing and take-off: its manoeuvres and acceleration must be tolerable by ordinary people wearing ordinary clothes who comprise the payload. A typical weapon, on the other hand does not have the same emphasis on economical operations. It is required to deliver a payload to a prescribed point in space as effectively as possible. The lateral and longitudinal accelerations necessary to do this may well be beyond the range acceptable to human beings. The weapon is controlled, if at all, by an autopilot which does not have the same flexibility of response as a human being but which will be much faster. On grounds of cost and reliability, control systems including aerodynamic controls must be as simple as possible so that varying the geometry during flight, as with variable-sweep wings and complicated flap systems, is not usually a practical proposition.

Military aircraft lie between civil aircraft and weapons in this comparison since the aircrew can be asked to tolerate an environment that would be unacceptable to civilian passengers, and because there is not the same emphasis on the economics of the flight. In recent years, remotely piloted vehicles (RPV), hitherto used primarily as target aircraft, have been considered for operational roles in order to avoid the expenditure of the lives of human aircrew, so the distinction between military aircraft and weapons is becoming less clearly defined. Moreover, manned military aircraft are now beginning to venture into flight conditions hitherto explored only by guided missiles, such as extreme agility of manoeuvre and stability augmentation by electronic or electro-mechanical means. Some of the earlier guided weapons, such as Mace, Bomarc and Styx, had monoplane configurations similar to aircraft, but improved performance required designs more appropriate for the function.

How then, do we define the field of interest of the weapon aerodynamicist. I suggest that our field is the aerodynamics of narrow, low-aspect-ratio, slender wing-body-control combinations. Not all these descriptions necessarily apply to a given shape, - for example, low aspect ratio does not necessarily imply aerodynamic slenderness, - and not all weapons have these three component parts. The aerodynamics of aircraft would not generally be regarded as a narrow specialisation because the subject has so many facets. Yet the corresponding field of weapon aerodynamics is regarded as a specialised activity. The fact is,

however, that the weapon aerodynamicist has to have a wide knowledge of many areas within the subject: the flow around inclined bodies; the characteristics of wings (usually very different in geometry from aircraft wings) and the interference effects between wings and bodies; the behaviour of several types of controls; the effect of the complete range of roll angle on monoplane and cruciform configurations; boundary layers, especially on bodies; base pressure and base drag with a very hot jet efflux present; the effects of vortices on downstream components; the effect of nose shape on drag and the drag due to excrescences and protuberances; kinetic heating effects; an incidence range from  $0^\circ$  to  $180^\circ$ ; a Mach number range from moderate subsonic to high supersonic; static and dynamic aerodynamic derivatives. All this has to be applied to shapes which may be by no means ideal for aerodynamic efficiency and which may not be amenable to accurate aerodynamic calculation, such as bodies with square cut noses (Figure 2), or wings which look like those in Figure 3, or the bomblet shown in Figure 4. It must be conceded that the weapon aerodynamicist does not usually have to concern himself with the fine details of the flow around a configuration, such as the effect of the three-dimensional boundary layer on a swept wing, but this is at least partly offset by the need to consider a wide range of incidence angle and roll angle.

## 2 CATEGORIES OF WEAPONS

The family of air flight weapons can be conveniently divided into the four categories shown in Figure 5:

- 1 Unguided and unpropelled.
- 2 Unguided and propelled.
- 3 Guided and unpropelled.
- 4 Guided and propelled.

The first category includes the only true ballistic weapons such as air-flight bombs and artillery shells including high-velocity, flat-trajectory projectiles. Artillery shells are of course propelled by the charge in the gun, but I here use the term "propelled" to mean that the weapon has a propulsion unit contained in itself. The second category, unguided and propelled weapons, contains for example rocket-powered projectiles fired from aircraft and from the ground, and gun-fired rocket-assisted projectiles. The third category contains glide bombs and those weapons which are nowadays called "smart bombs". The fourth category is the one which people usually mean when they refer to guided weapons. The long range strategic ballistic missile, such as Polaris or Minuteman, comes in Category 4, that is guided and propelled for at least part of the flight, and is therefore not a true ballistic weapon. The guidance however consists of corrections to follow a path determined before launch and monitored by an inertial system on board the weapon. Such missiles have aerodynamic problems which are peculiar to themselves and may have little relevance to other weapons - for example, hypersonic speeds and flight through a rarefied atmosphere. This course therefore excludes consideration of these strategic weapons.

In Category 1 a significant difference between bombs dropped from aircraft and shells fired from guns is that the former are usually stabilised by means of tail fins (Figure 6) whereas shells have usually been stabilised by spinning them at a high rate by means of "rifling" in the gun barrel and a "driving band" on the projectile which transmits the spin torque of the rifling to the shell. Nowadays fin-stabilised weapons can be fired from smooth-bored guns either by using "flip-out fins" which are erected after leaving the gun barrel as on the American Copperhead projectile, or by using fins whose span does not exceed the diameter of the gun barrel, thereby stabilising the projectile both inside the barrel and in free flight. Alternatively a "ring-tail" or "drum-tail" enclosing supporting struts can be used, (Figure 6). Projectiles which spin at a high rate introduce a branch of aerodynamics called Magnus effects which I shall refer to briefly in my second introductory lecture. Aerial bombs in recent years have developed a new sub-division, namely "cluster weapons". The "bomb case" is actually a container for a large number of much smaller projectiles which are released in the air and fall in what is hoped will be a pre-determined area.

In Category 2, the weapons which come to mind are air-launched and ground-launched rockets, usually fired in salvos at targets on the ground. Each rocket propels itself from its individual tube, and is stabilised by a set of tail fins which are folded before launch and are erected when clear of the launcher, (Figure 7). Recent developments in artillery include gun-launched projectiles which have a rocket motor to increase the range.

The examples in Category 3 have arrived there by two routes. In one case, guidance and control packs have been added to basic ballistic bombs to enhance their effectiveness. In the other case, new vehicles have been designed as controlled gliders incorporating guidance equipment. For the latter, television is a common form of guidance, as on Walleye, and the guided bombs have tended to use laser systems.

Finally we come to Category 4, weapons which are both propelled and guided, and these are the weapons which are usually meant by the terms "guided weapons" or "guided missiles". They form a much more extensive and varied group than the other 3 categories and are much more complex and challenging pieces of engineering. It is worth while considering the natural sub-divisions of this category, but before doing so I would emphasise that the study of weapon aerodynamics as defined here is relevant to all 4 categories.

## 3 CLASSES OF GUIDED WEAPONS

### 3.1 Surface-to-Surface Guided Weapons (SSGW)

Apart from long-range ballistic weapons, this class consists of:

- a. Weapons used by land forces against other forces some distance away. These are a form of artillery, for example Sergeant and Lance, and they usually have inertial guidance. A recent development using terrain comparison guidance is the ground launched cruise missile, such as Tomahawk.

b. Ground-launched anti-tank weapons. These are of comparatively short range and are among the less complex guided weapons, for example Swingfire, Milan and TOW.

c. Ship-to-Surface Weapons. These are usually designed to attack other surface shipping, although they could in principle be directed against land targets. Current examples are Exocet and Styx.

### 3.2 Surface-to-Air Guided Weapons (SAGW)

This class consists of missiles launched from ground launchers or from ships against airborne targets. They cover a wide range of size and maximum altitudes, depending on the type of target to be attacked. Current ground-launched weapons are Rapier, Hawk and Crotale; and among ship-launched weapons are Seaslug 2, Sea Dart and Tartar.

### 3.3 Air-to-Surface Guided Weapons (ASGW)

These are launched from aircraft, including helicopters, against targets on the ground or on the surface of the sea. Current examples include Martel, Maverick and, under development, the air launched cruise missiles.

### 3.4 Air-to-Air Guided Weapons (AAGW)

This class is launched from aircraft against airborne targets. Current missiles in this class are Red Top, Sparrow and Magic.

### 3.5 Surface-to-Sub-Surface Weapons (S Sub GW)

There are few weapons in this category. They are ship-launched and are aimed against submarines. They include the Australian Ikara and the French Malafon.

### 3.6 Submarine-to-Surface and Submarine-to-Sub-Surface Guided Weapons (Sub S GW)

It is possible to fire guided weapons from submarine torpedo tubes. The American Subroc was one of these, aimed at submarine targets. Other weapons under development are aimed at surface shipping targets.

It should be remembered that a single design of guided weapon may be adapted to fill several roles. This obviously has economic advantages. The American Harpoon missile can be launched against shipping targets from aircraft, ships or submarines. The British anti-aircraft missile, Seacat, launched from a ship, has been adapted for ground launch. It is usually more feasible to adapt the method of launching than to adapt a missile to attack different kinds of target, since the guidance system will be designed to cope with targets having a certain range of speed and manoeuvrability. It is possible however to fit alternative guidance systems. Martel is an example of this.

## 4 COMPONENTS OF MISSILE DESIGN

Having defined these classes of guided weapons, let us now look at the component parts of a guided weapon as shown schematically in Figure 8, and consider their relationship to the aerodynamic design.

### 4.1 Warhead

This is the reason for the existence of a guided weapon, the purpose of which is to deliver the warhead to a particular point in space. Sometimes the warhead has to be oriented in a particular manner at impact or at detonation. For example, the "shaped charge" warhead has brought about a substantial improvement in the armour-piercing capability of anti-tank weapons. Warheads may be described as armour-piercing or semi-armour-piercing which implies that a direct hit on the target is necessary. Other types of warhead are blast, fragmentation, continuous rods, and, of course, nuclear. Most warheads are axisymmetric with a fineness ratio between 1 and 2, and to maximise their effectiveness it is sometimes necessary for the weapon body around them to have a regular circular form, without attachments such as wings or strakes to interfere with the pattern of the explosion. Although I have said that the warhead is the essential part and *raison d'être* of a missile, it is true that even without one a weapon can do considerable damage to the target by virtue of its kinetic energy provided it hits the target. However, not all weapons are designed to achieve direct hits every time.

### 4.2 Propulsive Unit

This can be either a rocket motor carrying both fuel and oxidant internally or an air-breathing engine which carries only the fuel internally.

Rocket motors can have either a solid fuel-cum-oxidant or a liquid fuel with separate liquid oxidant. Most rockets used in guided weapons use solid fuel as this is convenient for storage, but modern "packaged-liquid" motors, which are self-contained sealed units, may well find applications in this field. Solid fuel rockets have a charge of cylindrical shape and the motor case containing it is frequently used as part of the missile body to which wings, for example, can be attached directly. In liquid fuel motors combustion takes place in a combustion chamber which can be separate from the fuels and oxidant containers, thus conferring more flexibility in the design than with a solid fuel motor.

For longer range missiles, the penalty of carrying oxidant as well as fuel becomes excessive and air-breathing engines become more attractive. These may be either turbo-jets or ram-jets, the former being more appropriate for subsonic and low supersonic speeds, the latter more appropriate for speeds in excess of, say, Mach 2. The range at which the air-breathers begin to show an advantage over rockets is round about 30 km but this depends on the missile's weight and altitude. If a ram-jet is used it is necessary to boost the missile to a suitable speed before the ram-jet can operate and this is done by means of a separate rocket boost motor which may or may not be jettisoned after it has burnt out. Indeed combinations of two or more

power units are quite usual even when only rocket motors are employed. A common arrangement is for a rocket of high thrust and short duration to boost a missile quickly to its cruise speed, at which it is sustained by a second motor of lower thrust and longer duration. In many cases the coasting phase after motor burn-out can provide an effective phase of the controlled trajectory.

Nowadays, sophisticated hybrid power units have been designed and manufactured which combine two kinds of propulsion in a single integrated package. For example a ram-jet can be designed which contains solid rocket fuel. The rocket motor boosts the missile to its cruising speed and the empty combustion chamber then functions as a ram-jet using the same propulsive nozzle.

The aerodynamic contribution to the propulsive unit consists of the design of the nozzle and, in the case of air-breathing engines, the design of the air intakes. These can usually be much simpler than those necessary for jet aircraft, but have to be arranged so that a usable air supply is available to the engine over the whole range of attitude and speed appropriate to the weapon without the use of complicated variable geometry. As regards external aerodynamics, the component of force most significant to the power unit is the drag, since the thrust and drag must be in balance during constant speed flight. An important contribution to the missile drag is base drag and afterbody drag, which may be affected by the geometry of the nozzle and the jet efflux characteristics.

#### 4.3 Safety and Arming Mechanism

This is usually electro-mechanical in nature. It prevents premature detonation of the warhead, thus ensuring safety in the neighbourhood of the launcher, and it usually has no effect on the aerodynamic design.

#### 4.4 Fuze

The fuze controls the moment at which the warhead is exploded at or near the target. It is a sensing device which determines how close the missile is to the target or how far it has penetrated the target. The former, the proximity fuze, is of an electrical or electronic nature, and may affect the aerodynamic configuration by requiring airdials to be placed at a suitable position on the body, usually near the front.

#### 4.5 Guidance System

This unit is naturally of the utmost importance in a guided weapon, and is one of the most expensive parts of such a weapon. Its purpose is to detect a target, to compare its position with that of the weapon and to pass instructions to the control system such that the two positions eventually coincide. The design of most guided missiles begins with the guidance system, and the rest of the design has to be compatible with it. However, in later developments of a missile, substantial changes may be made in the guidance system, and a recent example is the use of the American Sparrow airframe with a new British guidance system to form the new air-to-air missile, Skyflash.

Guidance systems may initially be divided into four categories, homing systems, beam-riding systems, command systems, and inertial systems, (Figure 9). The homing, beam-riding and inertial systems require some guidance equipment in the missile, the command system does not. Homing systems can be divided into three classes - active, semi-active and passive. In an active system a signal is transmitted from the missile, reflected from the target and received back in the missile. The direction and sometimes the distance of the target can thus be determined. A semi-active system works on the same principle but in this case the transmitter is located externally to the weapon, usually close to the launch point. The transmitted signal is usually a pulsed radar beam or a continuous-wave radio transmission, but laser beams are coming into use for shorter range weapons. This applies to both active and semi-active systems. A passive weapon is dependent on receiving a signal emanating spontaneously from the target. Passive systems may home on a radar transmission from the target, on a heat source by means of the associated infrared radiation, or on the image of the target received by a television camera. In a beam-riding system, the missile senses its position relative to a narrow beam of electro-magnetic radiation pointed at a target from a transmitter external to the missile. The error signal is used to correct the missile flight path. In a command system, the equipment external to the missile locates the target, compares the relative positions of target and missile, and sends instructions to the missile to change its course accordingly. In an inertial system the information about the target position is obtained externally to the missile and fed continuously into the missile prior to launch. After launch, the missile is guided inertially to the last target position fed to it, and such a system is therefore only useful against stationary or relatively slow targets.

There are very many variations on these basic systems, and some guided weapons may employ different systems for different parts of their trajectory. For example, a missile may be guided inertially until it gets near the target, at which point an active homing system takes over until the target is reached. In Figure 10 there are listed a few examples of the guidance systems used in guided weapons at present in service or in development.

The guidance system has not only to locate a target but also to pass instructions to the control system so that the appropriate manoeuvres are executed to bring the missile to the target. These instructions are based on a Navigation Law, which relates the information supplied by the guidance system to the demanded manoeuvre.

The most common navigation law is called Proportional Navigation, or PN for short. This is a very simple law, which states that the rate of turn of the missile's flight path,  $\dot{\gamma}$ , is proportional to the "sight-line spin", that is to the rate of rotation of the line joining the missile to the target,  $\dot{\phi}$ . Thus the law is simply expressed as:

$$\dot{\gamma} = k \dot{\phi}$$

where  $k$  is called the Navigation Constant. There are a number of other Navigation Laws in use, but

Proportional Navigation, in one or other of its developments is the most common. The translation of  $\dot{Y}$  into an acceleration perpendicular to the missile axis is the function of the next component on our list, the control system.

The link between guidance and control systems is so close that it is easy to think of them together, especially in their effects on the aerodynamic design. The guidance law chosen certainly can have some effect on the required aerodynamic characteristics, but most of the interaction stems from the control system, which will be discussed in the next section. There is one aspect of the guidance system, however, which has a direct effect on the aerodynamic shape, and that is the shape of the nose when the forebody contains a radar transmitter and/or receiver, a television camera or a passive infrared sensor. In the case of radar and infrared systems the problem is to avoid or minimise aberrations of the direction of the signals as they are refracted on passing through the dielectric material of the radome or the optical material of the infrared "window". In each case the shape preferred by the guidance designer is a hemisphere which, in a simplified analysis, can reduce the aberration to zero. The high drag of a hemispherical nose at transonic and supersonic speeds may, however, make the use of such a shape impracticable and an elliptical or ogival shape with higher drag rise Mach number and lower wave drag has to be used, at the expense of a certain amount of aberration. Similarly, the ideal shape for a television "window" would be a plane surface, but again this may have to be compromised in order to reduce the drag. A well-known example of the latter is the TV version of Martel shown in Figure 11. The temperature rise due to kinetic heating effects is likely to be greatest at the nose, and at high supersonic Mach numbers special attention may have to be paid to the survival of the radome or "window" and the internal equipment.

#### 4.6 The Control System

The control system is really the heart of the aerodynamic design of a guided missile. In the past, remarks have been made along the lines of "We don't care what the aerodynamic characteristics are as long as we know what they are". Or, more concisely, "We can fly an elephant". These remarks imply that the presence of an autopilot in a guided weapon makes it possible to achieve a satisfactory flight path whatever the aerodynamic characteristics may be. It must be admitted that there is a small element of truth in such a statement since the autopilot can certainly smooth over some irregularities in the aerodynamics and some lack of inherent stability. But this attitude ignores the fact that the autopilot can only affect the flight path through a set of controls which are usually aerodynamic in their nature, and which must have the required effectiveness in airborne flight. It will be seen in a later lecture that under certain circumstances the result of moving a control in a certain direction can be substantially affected, even reversed, by different flight conditions.

The autopilot receives "instructions" from the guidance equipment as to the flight path the missile should take to reach the target, and it translates these instructions into the appropriate movement of the missile control. Autopilots can be divided into "open loop" and "closed loop" systems. In the former, the control movement is affected only by the direction of the sight line between the missile and the target or whatever other observation is being used to define the required motion. In the latter, there is a feedback to the autopilot from the missile's motion so that, as the missile turns towards the demanded flight path, the control deflection is reduced and any "overshoot" is thereby minimised. The open-loop system may be quite suitable for simpler guided weapons, and, being less complex, it is cheaper than a closed loop design.

The most common type of control is the deflected aerodynamic surface in one of the forms illustrated diagrammatically in Figure 12. On guided weapons the whole control surface is usually deflected, but sometimes hinged flaps at the rear of fixed surfaces are used, as on aircraft wings and tailplanes. On most weapons the control surfaces are at the tail, but it is not uncommon to find the "canard" arrangement where the controls are placed near the nose of the body. Rather less common nowadays is the "moving-wing" system, where the control surface is placed close to the centre of gravity of the aircraft, so that the force on the control surface acts directly to provide a lateral acceleration, instead of changing the angle of incidence of the complete missile. In the aerodynamic design of control surfaces, one is interested in knowing the change in the overall forces and moments and also the forces on the control panels, over the range of deflection, incidence angle and roll angle considered appropriate. In addition, the moments of the panel forces about the hinge line are important, since the control actuation mechanism is invariably required to be as light and compact as possible. When one considers the wide range of missile attitudes over which control may have to be maintained, and the possible interference effects from the body and other surfaces, it is clear that the design of effective controls can be full of problems. A more complete survey of this subject will be given in a later lecture.

Although deflected surfaces are the most common form of control, other kinds of control can be considered where their particular characteristics are appropriate. Among these are mechanical spoilers, jet reaction controls and thrust vector controls.

Mechanical spoilers are used on aircraft either as drag devices, such as air brakes, or as an alternative to a flap type of control. In the latter case the objective is usually to produce the control force further forward on the wing, thereby reducing or eliminating the torsional distortion and other aeroelastic effects that a hinged flap might cause, particularly on a swept wing. The spoiler is usually used as an aileron control rather than a pitch control, and acts as its name implies by reducing the lift on a wing rather than by increasing it. Not many applications to missiles appear in the literature.

With a jet reaction control a gas jet is exhausted from a surface, and the reaction force or thrust on the surface provides the control force. A control force is thus produced in the absence of an external stream, and the jet reaction control is therefore useful at very high altitudes where the density is low and at times when the missile velocity is very low. When the jet exhausts into an external stream, rather than into a vacuum, there are interaction effects between the two flows and this may result in a control force greater or less than the reaction force alone. The "augmentation factor" depends on the longitudinal position of the jets on the body and on the ratio of jet pressure to the static pressure of the free stream, and in unfavourable circumstances may be less than unity. The jets may exhaust through slots or holes and from the body or from wing or tail surfaces. One disadvantage of this form of control is that a source of



gas must be carried in the weapon, at the expense of an increase in weight and volume. This source can be either stored gas in a container or a gas generator (for example, an isopropyl nitrate generator). Alternatively ram air, introduced through inlets, can be modulated to provide a control force of this type.

Thrust vector control systems operate by deflecting the jet efflux from the propulsion unit. A turning moment is therefore applied directly to the body. There are numerous ways of deflecting the thrust, including:

- a. Using a mechanical spoiler or transverse gas jet in the nozzle.
- b. Pivoting the nozzle on a flexible mounting.
- c. Placing in the efflux an aerofoil which can be deflected.
- d. "Semaphore" arms pivoted on the base plate of the body and moving into the jet efflux.

As with jet reaction controls, thrust vector controls provide an effective control force when either the free stream velocity or ambient density are low (that is, a low dynamic pressure). However, thrust vector control is only available while the motor is thrusting, whereas jet reaction controls may operate as long as the gas supply lasts.

Finally in this summary of control systems let us return to the autopilot. There are two ways in which the missile is manoeuvred. In one, called a "Cartesian" system, it is necessary to have a cruciform design rather than a monoplane layout. As shown in Figure 13 if the missile is required to move in the direction AB, each pair of controls is deflected in such a way that the resultant motion is in the required direction. In the other method called a "Twist and Steer" system, the missile is manoeuvred like an aircraft and is therefore suitable for a monoplane configuration. The missile is rolled until the "demand vector" is at right angles to the plane of the elevator controls, which are then deflected until the appropriate lateral acceleration is generated. In practice the "Twist" and the "Steer" may overlap, instead of taking place successively. The twist and steer system is generally felt to be slower in response than the cartesian system, though under certain circumstances it may be preferable. The characteristics of the guidance system may make it necessary to "roll position stabilise" the missile (as with TV guidance) or "roll rate stabilise" the missile (as with laser guidance).

## 5 THE PROCESS OF AERODYNAMIC DESIGN OF A WEAPON

Even at this early stage in the series of lectures it is worth while considering the place of the aerodynamicist in the process of designing and developing a guided weapon. One reason is that it is important to appreciate how the aerodynamic design may be constrained by the requirements of other design features. Another reason is that the level of aerodynamic activity varies during the development and it is important to appreciate the time scales with which the aerodynamicist has to comply. A third reason is that the accuracy of aerodynamic estimates and measurements is determined by the uses to which they are put. I hope, therefore, that this summary will put the later lectures on various aspects of aerodynamics into the context of the situations in which they will be applied.

The aerodynamicist involved in weapon design does not enjoy the same elevated status relative to his colleagues in other disciplines as does the aircraft aerodynamicist. In the design of an aircraft, the critical performance parameters, such as lift/drag ratio, are achieved mainly through the aerodynamic design, and though the structural and propulsive designers are of the utmost importance, they seldom influence the configuration of an aircraft as vitally as does the aerodynamicist. In the design of a weapon, however, other specialists may be of at least equal importance to the aerodynamicist. This is particularly true of guided missiles, when the initial exercises and studies of the possibilities of developing a missile to do a particular task will be based on the size of the warhead, the propulsion unit and the guidance and control systems. These define the destructive effect of the weapon, and the kinematics of the air flight. Whether the dynamic and aerodynamic characteristics of the weapon will permit these kinematic conditions to be achieved may be ignored initially - but not for long.

The procedures involved in designing and developing a guided weapon naturally vary from one firm to another. They also vary from one country to another, because almost all such weapons are developed in response to Government requirements and the details of the development phase depend on the philosophy of the Government concerned. I am therefore only able to speak about the systems I have been associated with in Britain and involving British firms.

In Britain it is always possible for one of the weapon firms to initiate a proposal for the development of a particular missile, as a result of its own studies. This proposal will be compared with the views of the Armed Services about the nature of their future requirements. On the other hand, the initial stimulus for the development of a new weapon may come from the Armed Services themselves.

The main stages in the evolution of a weapon can be listed as in Figure 14. The Staff Target or Staff Requirement will be written by the branch of the Armed Services concerned. A Staff Target sets out, without very much detail, the kind of performance envisaged for a new weapon. This is followed by the Feasibility Study, in which all aspects of the design of such a weapon are studied theoretically to determine whether the required performance is likely to be achieved, and to reveal the problems which must be solved before success can be reached. It is unusual for much experimental work to be done during the Feasibility Study and the end product at this stage is paper - a review of the study, the problems, the proposed solutions, etc. If, as a result of the initial Feasibility Study, the prospects of success look good, a Staff Requirement will be written which is much more comprehensive and precise than the Staff Target, and the weapon goes into the Project Definition Stage and the Development Stage. Towards the end of Development it is offered to the customer, namely the Armed Services, for acceptance, and if it is accepted it goes into production.

The aerodynamicist will become involved at the time of the Feasibility Study. One of the first decisions at this point is likely to be the choice of guidance system. This decision will probably have nothing to do with aerodynamics, and will be made as a result of performance calculations based on guidance system parameters and a simple kinematic description of the flight characteristics. The propulsion units will also be defined broadly by the range, speed and altitude set out in the Staff Target, using a necessarily very approximate figure for the drag of the weapon. At this stage, naturally, there is considerable iteration in attempts to find designs which are self-consistent in all the various aspects and components which make up a guided missile. Ideally the aerodynamicist would wish to start with a clean sheet of paper and freedom to study all possible configurations, but in practice this would be a time-consuming and relatively expensive exercise. Instead he will probably have to use his accumulated experience to restrict the possible configurations to those which he feels to be practicable. One of the most important inputs to his choice will be the physical and geometric constraints imposed by the environment in which the weapon is stored and used. For example, a ship-to-air or ship-to-surface weapon may have to be stored vertically between decks, so that its overall length will be limited, unless the Staff Target indicates that the weapon may be divided into two parts for stowage. Again, the demands of storage space, or a requirement to be carried in and fired from a sealed box, may restrict the maximum span or else make it necessary to fold the wings and/or control surfaces. It is important that such constraints should be made known as early as possible to avoid wasting time and money on configuration studies which later turn out to be unsuitable.

One of the main parts of the weapon affecting guided missile design is the guidance and control system. For example, if the missile has to be stabilised in roll because of the guidance characteristics, it is unlikely that a canard configuration will be suitable, because of the poor roll control effectiveness generally found with this layout. Again, if a cartesian control system is to be used, a cruciform configuration will be necessary, whereas if a twist and steer system is to be used, either a monoplane or a cruciform layout may be suitable. If a homing system is chosen, the nose shape of the missile body may be partly determined by the transmission or reception requirements of the homing equipment, whereas with command or inertial systems the nose shape can probably be determined from considerations of aerodynamic drag alone. It is during the Feasibility Study that the accuracy of aerodynamic estimation methods first assume importance, because the choice of the weapon configuration may depend on the answers, and a change in the configuration at a later date may be costly in terms of time and money. One should aim for a situation where an error of, say, 10% in estimating an aerodynamic coefficient or derivative does not have such a serious effect that the concept of the weapon is invalidated or the physical constraints on the weapon geometry violated. If the success of the weapon does appear to be very sensitive to aerodynamic prediction accuracy, it might be better to revise the concept in some way. Also during the Feasibility Study the aerodynamicist should be looking for possible sources of trouble that his experience tells him may occur, even though these are not predictable by standard methods. For example there may be difficulties in achieving a reliable separation of a tandem boost motor after it has burnt out. At this stage the first performance calculations will be done on the basis of the predicted aerodynamics.

If the Feasibility Study conclusions are favourable, and a Staff Requirement is issued, the weapon goes into Development. This may be preceded by an additional stage called "Project Definition" in which the concept of the weapon is refined and steps taken to study the major sources of uncertainty. In many cases a set of "design aims" will be defined in each of the specialist areas, in which the overall performance specification is translated into technical requirements in each area. For example, aerodynamic design aims are determined by interpreting the dynamic and kinematic performance of the proposed weapon in aerodynamic terms, such as the required lateral acceleration at a given angle of body incidence, the drag at given speeds, the control size and the maximum control deflections, the stability margins. These design aims may be relaxed or made more severe as the iterative process of the design continues.

During the Development stage a comprehensive programme of wind tunnel testing is carried out. This has two objectives:

- 1 To confirm the aerodynamic estimates made in the Feasibility Study.
- 2 To provide the aerodynamic raw material for constructing a computer program to predict all aspects of the weapon's performance.

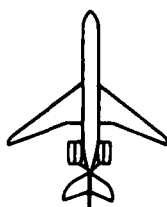
The first objective would require a comparatively simple wind tunnel programme since the estimates would almost certainly have been limited in extent - say  $0^\circ$  and  $45^\circ$  roll angle and a restricted number of speeds. The second objective however requires a much larger programme in order that the functional dependence of the aerodynamic characteristics on the independent variables may be sufficiently well defined. For example, roll angles at  $11\frac{1}{2}^\circ$  intervals and Mach numbers at intervals of 0.05 or 0.1 may be justified, along with a range of total incidence which will cover all the expected values.

Although the aerodynamicist naturally hopes that the configuration tested will be the final one, it may be necessary to change it, either because the experimental results do not agree very well with the estimates or because other design features change in some way. For example, it is quite common for the position of the centre of gravity to wander backwards and forwards as the engineering design proceeds, thereby affecting the stability. It is therefore often prudent to test some variants of the basic configuration so that the effects of such changes can be readily assessed - for example, three different longitudinal wing positions and two control sizes. It is naturally helpful if the wind tunnel model is constructed so that such modifications are easily made.

The results of wind tunnel tests are converted into inputs to performance calculations, either by constructing tables of forces and moments, or their coefficients, as functions of variables such as incidence angle, roll angle, speed and altitude, and interpolating as necessary between these tabulated values; or by fitting mathematical functions of the independent variables - for example, polynomials - to the experimental results. The former method requires a very large computer store, and in most cases the curve-fitting method is employed. The necessary degree of accuracy of the curve-fit is a matter of judgement and experience.

There may now be an interval in aerodynamic activity until flight trials begin. The extent of the flight trials programme depends on the philosophy of the country concerned and on the amount of money available, since such trials are comparatively expensive. In Britain the usual view is that the early flight trials rounds should test missiles of gradually increasing complexity so that the cause of faults, if they occur, can be more readily identified. The first one or two rounds may be fired simply to prove the operation of the launching gear and the propulsive units. Such rounds can be used to give information on aerodynamic drag by measuring longitudinal acceleration, combustion chamber pressure (to give the thrust), and the trajectory. By setting the controls in suitable fixed positions, other trials rounds can be made to follow a fixed barrel-rolling path, and by means of lateral accelerometers in the body the normal force and centre of pressure can be derived. On later rounds the controls can be operated in a programmed sequence by telemetered ground signals and by comparing the trajectories with performance calculations the aerodynamic control power can be checked. This is about all that can be done to acquire aerodynamic data from flight trials, and the main trials programme which follows afterwards will be concentrated on the performance of the guidance and control systems against various targets.

It will be clear from what I have said that the aerodynamics activities in guided weapon development are generally concentrated in the first stages of both feasibility studies and development programmes. This is in contrast to some of the other technical areas, such as the fuze and the safety and arming equipment, which may not be developed until quite late in the total programme. If the estimation methods used in feasibility studies are as complete and sophisticated as possible and if the wind tunnel test programme has been well planned, there should be few aerodynamic problems in the later stages because, unlike the guidance and control designers, for example, the aerodynamicist is not at the mercy of the reliability of equipment in the missile. Any substantial revision of the aerodynamic characteristics of the missile is likely to be due to changes introduced in other aspects of the missile design, but if there is an aerodynamic problem it is likely to be because of characteristics which cannot be readily calculated or represented in wind tunnel tests, such as the separation of boost motors.



1. Economical cruise at one speed
2. High aspect ratio monoplane, producing vertical lift force efficiently (low induced drag)
3. Very accurate aerodynamic data required over limited range of conditions
4. Max  $g \sim 2$

1. Highly manoeuvrable over a wide speed range
2. Cruciform low aspect ratio wing-body-control combination able to develop lateral force in any direction
3. Aerodynamic data required over a wide range of incidence, roll angle and Mach number
4. Max  $g \sim 5-50$

FIG.1 AERODYNAMIC DIFFERENCES BETWEEN CIVIL AIRCRAFT AND GUIDED WEAPONS

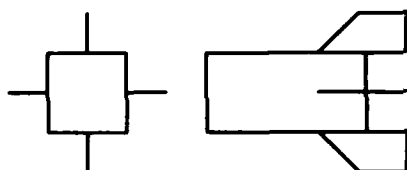


FIG.2 'CONFORMAL' STORE

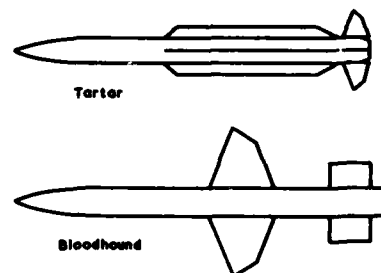


FIG.3 GUIDED MISSILE WING SHAPES

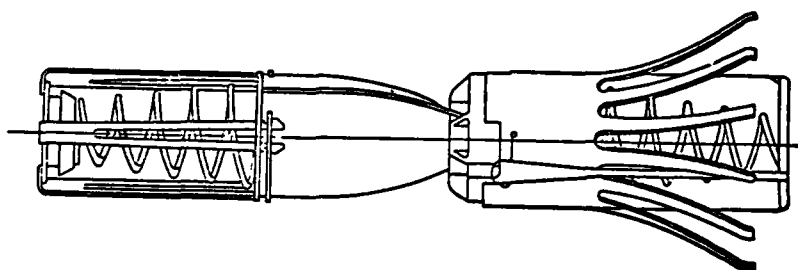


FIG.4. CLUSTER BOMBLET

<b>UNGUIDED UNPROPELLED</b> Air-flight bombs Artillery shells	<b>UNGUIDED PROPELLED</b> Aircraft rockets Artillery rockets Rocket-assisted projectiles (rap)
<b>GUIDED UNPROPELLED</b> 'Smart' bombs 'Walleye'	<b>GUIDED PROPELLED</b> 'Martel' 'Rapier' 'Exocet' 'Red top'

FIG.5 CATEGORIES OF WEAPONS

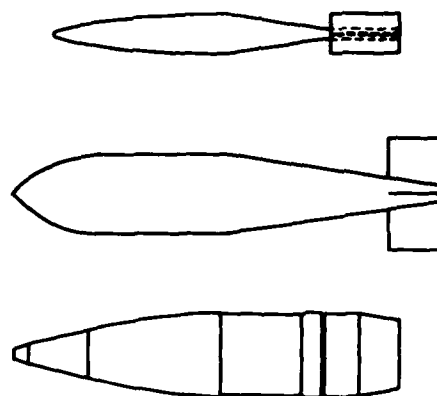


FIG.6 UNGUIDED, UNPROPELLED MISSILES

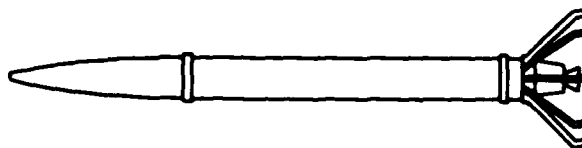


FIG.7 AIR - LAUNCHED ROCKET

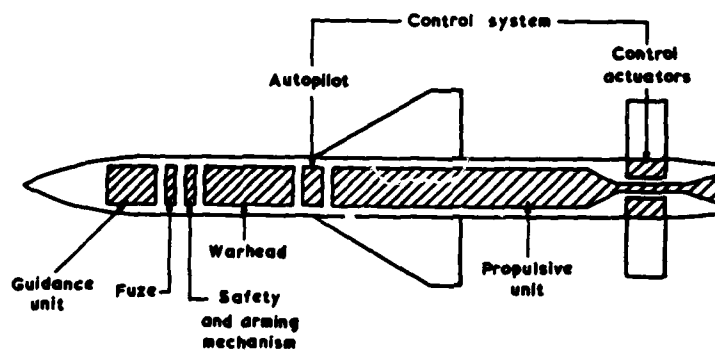


FIG.8 LAYOUT OF A TYPICAL GUIDED WEAPON

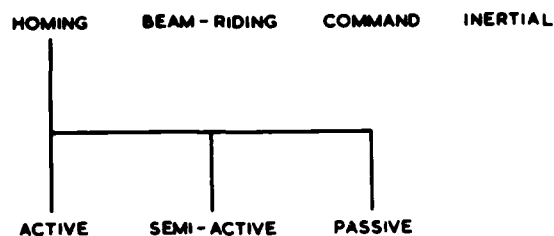


FIG. 9 TYPES OF GUIDANCE SYSTEMS

WEAPON	GUIDANCE SYSTEM
Sea Dart	Semi-active radar homing
Sidewinder (AIM-9b)	Passive infra-red homing
Martel	Passive TV or radar homing
Otomat	Inertial during cruise, active radar homing in terminal phase
Sergeant	Inertial
Dragon (XM-47)	Command to line of sight, wire link
AS-30	Visual, radio command
Seaslug 2	Beam-riding

FIG. 10 EXAMPLES OF GUIDANCE SYSTEMS

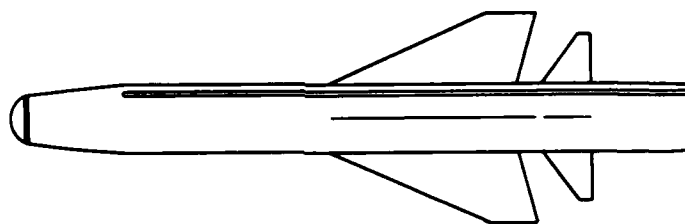
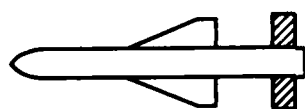
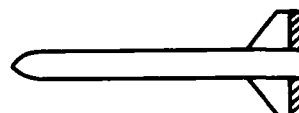


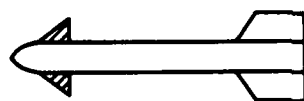
FIG. 11 MARTEL, TV-GUIDED VERSION



TAIL CONTROLS



TRAILING EDGE FLAP CONTROLS



CANARD CONTROLS



MOVING WING CONTROLS

FIG. 12 DEFLECTED AERODYNAMIC SURFACE CONTROLS

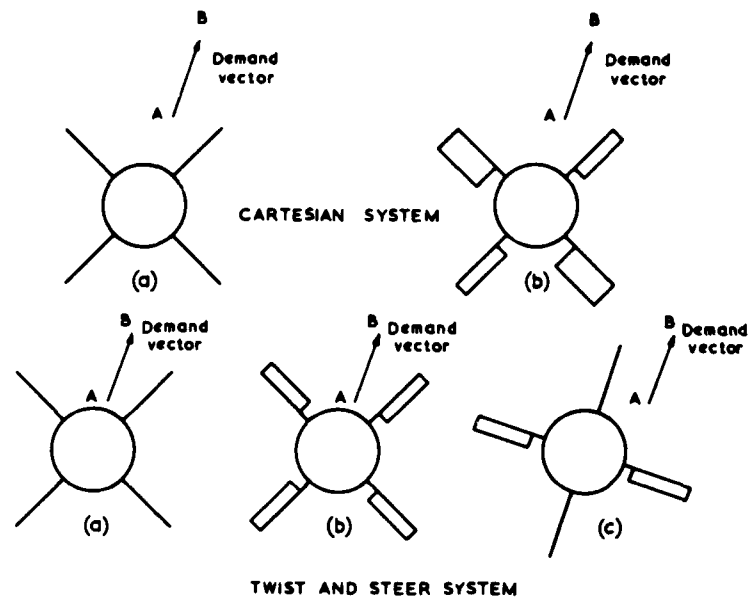


FIG.13 SYSTEMS OF AERODYNAMIC CONTROL

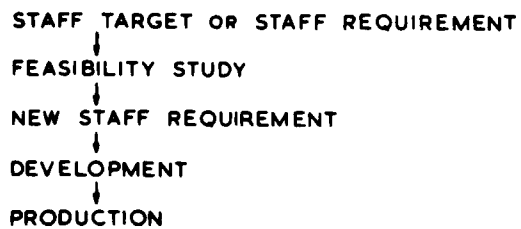


FIG.14 STAGES IN MAKING A NEW WEAPON

## GENERAL MISSILE AERODYNAMICS

George G Brebner  
Aerodynamics Department  
Royal Aircraft Establishment  
Farnborough, Hants, GU14 6TD, UK

## SUMMARY

The differences in design objectives and therefore in geometric proportions between aircraft and guided weapons mean that different aerodynamic calculation methods may often be required for the two applications. Typical weapon shapes are less amenable than typical aircraft to precise theoretical treatment, and experimental results should therefore be analysed to validate and augment theoretical methods.

The six components of aerodynamic force and moment acting on an air flight missile are taken in turn, their importance discussed and their various characteristics described, along with some comments on methods of estimating them.

The non-dimensional forms of these forces and moments are functions of the components of linear and angular velocities, and their derivatives with respect to these velocities are listed and the more important ones defined.

Brief descriptions are given of the origins and significance of Magnus effects and cross-coupling effects.

## NOTATION

A	aspect ratio
$C_x$	coefficient of axial force
$C_y$	coefficient of side force
$C_z$	coefficient of normal force
$C_\ell$	coefficient of rolling moment
$C_m$	coefficient of pitching moment
$C_n$	coefficient of yawing moment
$C_N$	coefficient of normal force (usually = $-C_z$ )
$C_L$	coefficient of lift
d	characteristic length or reference length
$K_\phi$	roll interference factor
$\ell$	body length
L, M, N	aerodynamic moment components about the x, y and z axes
M	Mach number
$M_D$	Drag rise Mach number
p	angular velocity about Ox
q	angular velocity about Oy, or $\partial\theta/\partial t$
r	angular velocity about Oz
R	Reynolds number
S	characteristic area or reference area
t	time
u	velocity along Ox
v	velocity along Oy
w	velocity along Oz
V	free stream velocity



$x, y, z$	cartesian coordinates in a system of axes $Ox, Oy, Oz$
$X, Y, Z$	aerodynamic force components along the $x, y$ and $z$ axes
$\alpha$	incidence angle
$\beta$	sideslip angle, or $\sqrt{M^2 - 1}$
$\lambda$	roll angle
$\phi$	roll angle
$\theta$	total incidence angle, or angle between longitudinal axis and a direction fixed in space
$\rho$	air density
$\sigma$	total incidence angle
$\omega$	frequency

## 1 INTRODUCTION

In this second introductory lecture I propose to consider the main aerodynamic effects, coefficients and derivatives which are of importance in the design of weapons, and to indicate in broad terms some of the methods that may be used to estimate their values. It is not my intention to treat any specific aspect in depth, or to give a comprehensive set of equations that may be used, but rather to set the scene for the detailed expositions by the other lecturers on their particular subjects.

As I have said in my first lecture, the job that a guided weapon is required to do usually dictates that its configuration is very different from that of an aircraft, particularly a commercial aircraft. It may be that, for a comparatively long-range weapon with a substantial period of cruising flight, a configuration like that of an aircraft is very suitable, and in that case aerodynamic design methods appropriate for aircraft may be used. In particular, it may be worthwhile to consider the design of suitable aerofoil sections for efficient flight. It must always be remembered however, that there is usually a strong incentive to keep the production costs of weapons as low as possible, so that a shape which requires many man-hours to produce will be unpopular with the project managers. For the great majority of weapons, the configuration will be of lower aspect ratio than for aircraft, and the shapes will be as simple as possible to permit ease and cheapness of production. For example, wings may have simple double-wedge or hexagonal sections, probably with a specified non-zero thickness at leading and trailing edges.

It is clear therefore that we will probably not be concerned with the fine details of aerodynamic behaviour, such as the three-dimensional boundary layer over the wings. The accuracy required in the estimation - and measurement - of the aerodynamic characteristics of weapons cannot be defined in general terms. It will be determined as a result of performance calculations, when the sensitivity of the performance to various changes to the aerodynamic coefficients and derivatives can be studied.

In the great body of experimental and theoretical work that has been built up over many years for application to aircraft design, two of the most useful simplifications have been the assumption of two-dimensional flow in the design of lifting surfaces, and the restriction of angular attitudes to small values so that the assumption of linear perturbations may be justifiable. In the case of weapons, the great majority of designs are of small aspect ratio so that the usual two-dimensional assumptions are invalid. Also weapons usually attain angles of incidence, yaw and roll which are large enough to introduce non-linear variations of the aerodynamic characteristics. For example, one of the lecturers in this course will be dealing with forces and moments at incidence angles up to  $90^\circ$  or beyond.

Because of the characteristic shape of weapons, however, a variant of two-dimensional theory, namely slender-body theory, does have considerable value in two respects: firstly, to provide a quick first estimate of some of the main aerodynamic characteristics such as normal force and pitching moment; and secondly, to provide a practicable theoretical approach to some of the more complex characteristics - for example, the forces and moments in non-uniform flow. The textbook "Missile Aerodynamics" by Nielsen<sup>1</sup> gives a detailed exposition of slender-body theory and many of its applications. Slender-body theory is essentially an inviscid theory and so does not cover the effects of flow separation which, on low aspect ratio shapes at large incidence angles, can be very significant. The theory is usually developed and applied with the further assumption of linear characteristics, but even within the bounds of potential flow this is not essential, and higher-order effects also can be calculated. Non-linear effects due to viscosity, which are much more important than higher-order potential flow effects, cannot of course be calculated by slender-body theory, and have to be allowed for separately. A useful complementary volume to Ref 1 is "Missile Configuration Design"<sup>2</sup>, by Chin, which deals with aerodynamics in a less rigorous fashion but includes other topics such as propulsion and structural design.

The importance of non-linear characteristics in weapon aerodynamics means that estimation methods for practical application should be checked by comparison with experimental results, and the latter analysed to provide empirical or semi-empirical modifications to theory. Wind-tunnel test results on models of missile projects are usually restricted in their distribution because of their security classification. Moreover practical weapons may have features such as launcher lugs and aeriels, which make generalised analysis suspect. There are however many sources of test results on generalised models, some of which are listed as Refs 3-24. Unfortunately this mass of useful experimental data has seldom been subjected to thorough analysis, and one feels that there is a rich mine of information waiting to be exploited. This

is probably because the number of aerodynamicists working in the weapons field is comparatively small, and the demands of project design and development take priority over analytical research.

In most of the lecture, I shall take different aerodynamic coefficients and derivatives in turn, and consider their importance and methods of estimating their value. In performance calculations of missiles it is usually necessary to use a set of reference axes fixed in space, but in studying the aerodynamics of missiles it is customary to use a system of axes fixed with respect to the body. This may have two forms - a set in which the axes roll with the body and a set in which they do not. The x-axis in both systems coincides with the body axis. In the non-rolling system the z-axis is always in the incidence plane (incidence angle =  $\sigma$  or  $\theta$ ) and the roll angle ( $\lambda$  or  $\phi$ ) is specified with reference to this plane. In the rolling axis system, the incidence and yaw planes are fixed in the body, so that the total incidence angle,  $\sigma$  or  $\theta$ , is resolved into an incidence angle  $\alpha$  and a sideslip angle  $\beta$ . A system of body axes is shown in Figure 1. The components of force and moment are the axial force, the normal force (at right angles to the body axis in the incidence plane), the side force, the pitching, yawing and rolling moments. This system of forces and moments differs from that usually used in aircraft aerodynamics, in which the forces are resolved in and perpendicular to the wind direction - for example, drag and lift instead of axial force and normal force.

The aerodynamic force on a missile, and consequently the three components of this force, are proportional to the air density, to the square of the velocity and to the square of the linear dimensions of the body, that is, to a characteristic area. The aerodynamic moment and its three components are proportional to the cube, not the square, of the linear dimensions, that is to the product of the characteristic area and a characteristic length. In missile aerodynamics it is customary to choose the body cross-section area and the body diameter as the characteristic area and length. The force and moment components may therefore be generalised in the form of non-dimensional coefficients by dividing by  $\frac{1}{2}\rho V^2 S$  or  $\frac{1}{2}\rho V^2 S d$  as appropriate:

$$\begin{aligned} C_x &= \frac{X}{\frac{1}{2}\rho V^2 S} & C_\ell &= \frac{L}{\frac{1}{2}\rho V^2 S d} \\ C_y &= \frac{Y}{\frac{1}{2}\rho V^2 S} & C_m &= \frac{M}{\frac{1}{2}\rho V^2 S d} \\ C_z &= \frac{Z}{\frac{1}{2}\rho V^2 S} & C_n &= \frac{N}{\frac{1}{2}\rho V^2 S d} \end{aligned}$$

where X, Y and Z are the components of force along the x, y and z axes,

L, M and N are the components of moment about the x, y and z axes,

$\rho$  = air density

V = free stream velocity

S = characteristic area or reference area

d = characteristic length or reference length.

## 2 COEFFICIENTS OF STATIC FORCE AND MOMENT

### 2.1 Normal Force

The majority of weapons have bodies which are essentially axisymmetric. This is a suitable shape for rocket or air-breathing propulsion units and for cheapness of manufacture. To this body are attached whatever lifting surfaces and control surfaces may be appropriate. In calculating the normal force coefficient of such a combination, it is customary to calculate the normal force on body, wings, controls, etc, separately and to add them together with appropriate factors to allow for interference between the components.

In general the body will have a nose section, a cylindrical section and a rear section in the shape of a boat-tail or flare (Figure 2). The shape of the nose may be a cone, a circular arc ogive, a parabola, an ellipse, a hemisphere, or one of a number of other shapes derived for a specific purpose. Slender-body theory predicts that the lift on an inclined body is distributed only over those parts where the cross-section area is changing, that is, the nose and the boat-tail or flare, (Figure 2). At subsonic and transonic speeds the slender body values for the positive lift on the nose and flare and the negative lift on the boat-tail are quite good approximations if suitable factors are applied to account for boundary layer effects. It is implicit in this theory that no variation with Mach number is predicted. Variation of the normal force with Mach number in the supersonic speed range can be calculated by linearised and second-order supersonic theories for bodies with pointed noses and for boat-tails, and charts of empirical results are available in Ref 25.

These theoretical results do not allow for the effects of viscous separation of the flow around the body, which becomes evident once the incidence angle exceeds a few degrees. The flow starts to separate about 2 or 3 calibres behind the point of the nose and forms two coiled vortex sheets above the upper surface of the body. Above about 20° incidence, depending on the nose shape, the vortices take up asymmetric positions relative to the vertical plane of symmetry<sup>26</sup>, but this is probably not very significant in calculating the component of normal force arising from flow separation. Qualitatively, it is convenient to regard this normal force contribution as arising from the component of the free stream perpendicular to the cylindrical body, and the flow of this component around the body in the manner of two-dimensional flow about a cylinder. The "cross-flow component" can be calculated on the basis of the

analogous "cross-flow drag coefficient", but it is important not to stretch this analogy too far. In particular, the value of "cross-flow drag coefficient" should not be derived from two-dimensional experiments but by analysis of normal force measurements on a true inclined body, where the cross-flow is more likely to be characteristic of the flow around elliptical cylinders, whose drag coefficients are given by Hoerner in Ref 27. Figure 3 shows how the total lift on an ogive-cylinder varies with Mach number. It is clear that there are no severe changes in the transonic region. The normal force and other aerodynamic characteristics of bodies will be dealt with in the lecture by Herr Esch, part of the initial overview at the beginning of this course.

The lift or normal force on thin plane wings at subsonic, transonic and supersonic speeds is fully covered by the appropriate linearised theories. These only apply at small incidence angles, at which there is no significant difference between lift and normal force. At low subsonic speeds, incompressible flow theory can be used and by applying the Prandtl-Glauert transformation the effect of compressibility can be allowed for almost up to Mach 1. Near Mach 1, slender body theory can be used for pointed wings, and above Mach 1 linearised supersonic theory takes over. Results of these calculations are available in chart form, for example in Ref 25. Figure 4 shows the linearised supersonic curves for the slope of the normal force coefficient against incidence angle for triangular and rectangular wings, as functions of the Mach number ( $\beta = \sqrt{M^2 - 1}$ ) and aspect ratio A.

At incidence angles higher than a few degrees, the influence of viscosity may give rise to an additional component of normal force which is non-linear with incidence. The nature and magnitude of the viscous non-linear normal force depends on the planform and Mach number. Pointed slender wings, particularly if they have sharp edges, have a flow separation at the leading edge, starting at quite low incidence angles, which is most pronounced at subsonic speeds and which effectively disappears by the time that the free stream component normal to the leading edge has reached Mach 1. The coiled vortices formed above the upper surface give rise to non-linear lift increases above the linear values. The features of this non-linear lift have been thoroughly explored in the research work aimed at supersonic transport aircraft, such as Concorde. Even sophisticated theoretical studies, however, have so far failed to provide a wholly satisfactory method of calculating this lift, and recourse has to be made to empirical or semi-empirical methods. On wings which are essentially unswept, with comparatively large wing tips, a non-linear lift increase arises from the "endplate effect" of the tip vortex sheet. On some missiles where the span is very limited because of external constraints the wings may be little more than strakes and the separated flow from the tips may contribute most of the lift.

Since missiles may be required to generate a large lateral acceleration and therefore reach high angles of incidence, it may be important to know the value of the maximum coefficient of lift or normal force and the incidence angle at which this occurs. Figure 5, which was compiled from Refs 28-30, shows that for a  $65^\circ$  delta wing at low subsonic speed both coefficients have a distinct maximum value between  $35^\circ$  and  $40^\circ$ . In contrast, at a supersonic Mach number the lift coefficient reaches a maximum value between  $40^\circ$  and  $50^\circ$  whereas the normal force coefficient continues monotonically to its maximum value at  $90^\circ$  incidence.

Most weapons employ cruciform arrangements of lifting surfaces and it is necessary to know the lift developed at any roll angle. There are two roll angles which give symmetry about the incidence plane,  $0^\circ$  and  $45^\circ$  (Figure 6). Linear theory predicts that for a given total incidence the normal force in the total incidence plane on a pair of horizontal wing panels at  $0^\circ$  roll angle is equal to that developed on 4 cruciform surfaces at any roll angle. At roll angles other than zero, the distribution of lift between two panels of an opposite pair is not equal. Linear theory and experiment both show that the lower panel carries more lift than the higher one, though the theory indicates that the total normal force on the cruciform arrangement is unaffected by this redistribution.

The difference which is observed in practice between the normal force at  $0^\circ$  and  $45^\circ$  roll angles arises because of the non-linear lift components. To a first approximation, the magnitude of the non-linear components at non-zero roll angles can be estimated by using the component of total incidence angle perpendicular to each pair of surfaces. In addition, except at small total incidence angles, the two lower panels at  $45^\circ$  roll angle have a shielding effect on the upper pair. Figure 7 shows the load on a single panel as the roll angle varies through  $180^\circ$ , from leeward to windward, for the combination of axisymmetric body and slender cruciform delta wings illustrated<sup>10</sup>.

When wings are mounted on a body, the total lift on the combination is not necessarily equal to the sum of the lift on the wings and body in isolation. A lift force due to interference between wings and bodies is developed on both components. If the body is at incidence, the effect of the upwash around the body is to increase the angle of incidence of the wings (which will usually be aligned parallel to the body axis). Moreover the lift developed on the wings gives rise to a "carry-over" lift on the body itself. A detailed treatment of missile wings and wing-body combinations will be given in the lectures by Professor Stahl and Dr Gregoriou in the overview section of the course.

Aerodynamic surfaces used as controls can be treated in the same way as wings, except for two additional features. Since there is a gap between the control surface and the body, it is possible for some of the control panel lift to be lost because the pressure difference at the root will be reduced by flow from the lower surface to the upper. Secondly, the control will not generally be aligned parallel to the body axis, and the wing-body interference factors for the lift due to control deflection are different from the factors for the lift due to the inclined body and the undeflected control. This will be discussed in my later lecture on controls.

When a configuration has two or more sets of surfaces spaced along a longitudinal direction, each set is subject to the interference effects of vortices shed from any of the other surfaces which lie upstream, as well as those from the inclined body. These effects can be very complex, and they too will be discussed in the lectures by Dr Gregoriou and myself.

## 2.2 Pitching Moment

Accurate prediction of the pitching moment is of considerable importance in determining the stability and controllability of a missile. However, accurate prediction is usually handicapped by the difficulty of estimating the interference effects, or "downwash", of the trailing vortices already mentioned. In practice the pitching moment is calculated by determining the aerodynamic centre and centre of pressure for the individual components - such as body, wing, controls - multiplying them by the appropriate components of the normal force, and dividing the sum by the total normal force. It is customary in a guided weapon to design for a small positive amount of static longitudinal stability, but in some circumstances neutral stability or a small amount of instability may be preferable - for example, in the period just after ground launch in the presence of a crosswind. In this situation, the missile speed is comparatively low and positive stability would tend to turn the missile into the crosswind. The stability requirement depends on the autopilot characteristics, and it is usually necessary to use performance calculations to indicate the best combination of autopilot characteristics and aerodynamic stability. Stability, of course, depends on the centre of gravity as well as the aerodynamic centre, and can therefore change with time as the fuel of the propulsion unit is burned.

It is worth remarking that, because of the non-linear aerodynamic characteristics commonly found in weapon design, it is sometimes possible for a weapon to take up a stable trimmed attitude at a non-zero angle of incidence, even without control deflection or other asymmetry about the median plane. This can occur, for example, if the aerodynamic centre moves to the rear as the incidence is increased until it coincides with the centre of gravity as shown in Figure 8. This feature can be used in the aerodynamic dispersion of bomblets.

For a guided weapon, the centre of gravity must not only be in the appropriate position relative to the aerodynamic centre for the required stability, but must also be in such a position that the missile can be trimmed to give the required value of lateral acceleration by deflecting the controls within their effective range.

The aerodynamic centre of wings - and control surfaces - can be determined by linear theory if applicable, using the various charts available. The non-linear lift due to a tip vortex can be assumed to act at about three-quarters of the tip chord. For slender sharp-edged pointed wings at supersonic speeds the aerodynamic centre is near the centroid of the planform, (for both linear and non-linear components) and at subsonic speeds it is further forward by some 5-10% of the root chord.

For the potential lift on the nose, boat-tail and flare of a body, the aerodynamic centre can be calculated by the appropriate theory. The viscous lift can be assumed to act on the whole of the body behind a point about 2 calibres from the nose except possibly for very short or very long bodies. At subsonic speeds it is probably good enough to assume that its distribution is constant over the whole of this length, but at supersonic speed this simple distribution is not adequate (see Figures 9 and 10, taken from Ref 31).

An important aspect of pitching moment is the hinge moment of a control surface. In order to keep the control actuation mechanism as small and light as possible the axis of the control should be placed at or near the control centre of pressure. This will in general vary with Mach number, incidence and control deflection, and it is usually necessary to choose a compromise position for the hinge line. This is one design feature which can not always be estimated with sufficient accuracy, and it is best to place the hinge line after analysing results of appropriate wind-tunnel tests.

## 2.3 Side Force

If a missile has an angle of yaw to the direction of flight, it will have a side force which is directly analogous to the normal force generated by the missile at an angle of incidence. This component of side force can therefore be treated in exactly the same way as the normal force in Section 2.1.

Up to moderate values of incidence angle, say about  $20^\circ$ , there is no side force when the roll angle is  $0^\circ$  and  $90^\circ$  for a monoplane arrangement or  $0^\circ$  and  $45^\circ$  for a cruciform arrangement, that is when there is symmetry about the incidence plane. At other roll angles, a non-zero side force exists. One can of course regard the combination of total incidence angle and roll angle as a combination of incidence angle and yaw angle relative to one of the wing planes, (see Figure 6). The side force is cyclic in nature, being zero at  $0^\circ$  and  $45^\circ$  roll angle, as shown in Figure 11 for a cruciform wing-body combination<sup>10</sup>. The corresponding variation of side force for a monoplane is also shown. The importance of this side force is that, if a demand vector lies between the symmetrical roll directions, and the missile moves in that direction, then the roll angle relative to the total incidence plane is asymmetric and the missile experiences a side force as well as a force in the direction of the demand vector. This can complicate the guidance and control process.

To calculate approximately the side force arising from asymmetric roll angle, one can revert to the incidence angles  $\alpha$  and  $\beta$  perpendicular to the planes of the two sets of surfaces (see Figure 6), calculate the force normal to these planes as described in Section 2.1, and take the component at right angles to the plane of total incidence.

Above moderate incidence angles, a side force can exist even at  $0^\circ$  and  $45^\circ$  roll angle, due to vortices shed from the forebody ahead of the lifting surfaces taking up stable asymmetric positions relative to the body. This is believed to be started by a very small asymmetry at the body nose which "triggers" the asymmetric formation. The direction of the vortex asymmetry and hence of the side force can change from side to side as the angle of incidence increases. Dr Wardlaw will deal with this subject which has become increasingly important in recent years.

## 2.4 Yawing Moment

This component is associated with the side force and arises from the same causes, as summarised in the previous section. When the side force is generated by a yaw angle, or from a roll angle other than  $0^\circ$  and  $45^\circ$ , the centre of pressure of the side force is likely to be near that of the normal force, and therefore the yaw stability will be similar to the pitch stability. However, when the side force is due to asymmetric body vortices, the centre of pressure of the side force has no direct relationship with that of the normal force. Like the side force, the yawing moment arising from asymmetric vortices can change direction as incidence angle increases.

## 2.5 Drag

The importance of drag and accurate estimation of drag in the design of a missile depends very much on the particular flight characteristics of the missile, and even for a single missile the importance of drag can vary between one part of the flight and another. For example, during a boost phase when the missile is accelerated quickly to a much higher speed, the thrust will be several times, perhaps many times, higher than the drag. It is therefore hardly worthwhile to strive for very high accuracy in predicting the drag in this phase, or to strive to reduce this drag. A 10% reduction in drag might mean only about 1% increase in the "thrust minus drag" or nett axial force. When a missile is travelling at constant speed, on the other hand, the drag is a much more important characteristic. Any increase in drag implies a corresponding increase in thrust for a given range or speed, or a decrease in range or speed if the motor thrust is kept the same.

As is the case with aircraft, drag is very difficult to estimate accurately and also very difficult to measure accurately in wind-tunnel tests. This is because of the predominating influence of viscosity, the effects of which are much less amenable to calculation than those effects which can be reasonably well predicted by potential flow assumptions. Experimentally, the Reynolds number in wind-tunnel tests is usually less than that of the missile in flight, though the defect is not nearly as great as is the case with aircraft models. When a model is supported by a sting, as is usually preferable in tests at transonic and supersonic speeds, the presence of the sting affects the base pressure of the missile which is frequently a very important contribution to the drag.

It is customary to estimate the "zero lift drag" of a weapon, which, with the symmetry characteristic of most missiles, is usually the same as the zero incidence drag. When the missile is flying, the body axis will usually be at an angle to the flight direction, and the drag, in the direction opposite to that of flight, is made up of the components in the free stream direction of the axial force and the normal force. The latter corresponds approximately to "induced drag", and an extra component of this kind occurs when surfaces are deflected.

At subsonic speeds below the onset of compressibility effects, the main drag contributions at zero incidence are skin friction, form drag, base drag and the drag of excrescences and surface irregularities. Many approximate methods are available for estimating skin friction, which for most of a missile surface is more likely to be due to a turbulent boundary layer than to a laminar boundary layer. Refs 32 and 33 contain comprehensive comparisons of various methods for twodimensional, incompressible flow and compressible flow respectively. The emphasis is on twodimensional cases but suitable factors can be used to apply the skin friction results to other shapes such as cylinders and conical noses, and other factors give the mean skin friction drag on a body in terms of the local coefficient. Wing and control surfaces, though thin, will usually have simple cross-section shapes like a double wedge. However it is usually good enough to treat them as though they were flat plates, and to assume that the boundary layer is turbulent. If it is believed that a substantial region of laminar flow exists, a simple approximation to the position of boundary layer transition is usually sufficient.

The base drag, which can amount to 25-30% of the total drag, is the most complex drag component, since its value depends on so many variables. For example, the length of the body, the shape of the rear end, the Mach number, the Reynolds number, all affect the value of the base drag when no motor or engine is exhausting from the base. In the presence of a motor efflux, the estimation of the base drag is even more difficult, being dependent on variables such as nozzle exit angle, nozzle exit area, jet temperature, and jet pressure ratio. No satisfactory comprehensive method of estimating base drag over the wide range of practical variables has yet been developed, but M. Delery and M. Sirieix will present a comprehensive review of the present state of the art.

The pressure drag on bodies, wings and the controls at subsonic speeds is seldom a very significant contribution, unless the body is very short, but at transonic and supersonic speeds the wave drag is important. The wave drag of wings and control surfaces can be calculated, for simple planforms and simple sharp-edged cross-section shapes, by linearised supersonic theory. Values have been presented in chart form<sup>25</sup>, with factors to take account of more complicated cross-section shapes. If the wings are highly swept, the drag rise Mach number,  $M_D$ , is quite high, and for the missile as a whole  $M_D$  may then be dependent on the body characteristics.

For a body, there are wave drag contributions from any portions where the cross-section is increasing or decreasing. Most commonly these will be at the nose and tail. Linear theory charts are available<sup>25</sup> for the drag of open conical frusta, both expanding (as for noses) and contracting (as for boat-tails). They also cover sharp-pointed closed nose shapes of specific form such as cones and circular arc ogives. However, for reasons of safety in handling, sharp-nosed missiles are rare - some degree of blunting is common. If the weapon is a homing missile with guidance equipment in the nose, the shape of the nose may have to be a compromise between aerodynamic and guidance requirements. For example, a radar antenna in the nose will require a nose shape which will keep the aberration to a low level, preferably a hemisphere but certainly with a certain amount of blunting. Infra-red detectors also require plane or spherical surfaces for their "windows". Such shapes can increase the wave drag contribution to a very high, perhaps unacceptable level, not only at supersonic speeds, but also at high subsonic speeds where so many present-day missiles operate. This is shown in Figure 12, where the drag characteristics of various nose shapes

are shown at high subsonic and supersonic speeds. It has been known for some 30 years that drag at supersonic speeds can be reduced by a certain amount of nose blunting, provided the nose fineness ratio is kept constant, and recent results by Ward at RAE Bedford indicate that such blunting can also be beneficial at transonic speeds. These results give some hope of being able to placate guidance engineers without sacrificing aerodynamic drag requirements.

The remaining major contribution to the drag of a missile is that due to excrescences and roughness. Because of the need to minimise production costs, it is usual for the surface finish of missiles to be less than perfect, with small steps at the joins between different parts of the structure, protruding rivets, etc. The excrescences are in the form of launcher lugs, aerials, cable ducts, tracking flares, etc, and can be quite large. When the design of the missile has progressed far enough, it is possible to calculate approximately the drag of the various excrescences, though it is still prudent to include a factor for small irregularities and roughness. In the early stages of design, before the shapes of the excrescences are known, an overall factor to the drag of the "clean" configuration is usually applied to allow for unknown contributions from this source. This factor is usually between 1.1 and 1.2, depending on the experience of the aerodynamicist and the expected size and number of the excrescences.

## 2.6 Rolling Moment

A missile with a single pair of wing panels will normally be in a stable roll attitude when the wings are horizontal. This is because a panel deflected slightly below the horizontal generates more lift than one deflected slightly above (see Figure 7). With the cruciform configuration more common on missiles, there are two basic roll orientations where the rolling moment is zero, namely at  $0^\circ$  (with the surfaces in and at right angles to the incidence plane) and at  $45^\circ$ . It is unlikely that the missile will be stable in roll at both these angles, but the stable orientation will depend on Mach number and wing shape, as shown in Figure 13.

At roll angles other than  $0^\circ$  and  $45^\circ$  the rolling moment is small at low angles of incidence but increases quickly as the incidence increases. This rolling moment comes about because of the normal force component on the surfaces due to roll angle, because of shielding of upper surfaces by lower surfaces, and by the velocities induced on the panels by vortices shed from the body ahead of the surfaces. Rolling moments at different Mach numbers and incidence angles are shown in Figure 14 for a slender wing-body-control combination. The cyclic nature of the rolling moment is evident and it is clear that in some conditions the configuration is stable at  $0^\circ$  roll angle and in other conditions at  $45^\circ$  roll angle. One can see also that the amplitude of the rolling moment does not necessarily increase continuously as incidence increases. Rolling moments arising in this manner are called "induced rolling moments".

The importance of induced rolling moments in missile design, along with rolling moments due to constructional misalignments, is that the operation of the guidance equipment may be affected by them, one way or another. If the missile is allowed to roll freely, the guidance equipment will probably not operate effectively if the roll rate exceeds a certain value. On the other hand the guidance equipment may make it necessary to stabilise the missile in roll, which therefore makes demands on the control power available. Apart from the interactions with the guidance system, both guided and unguided missiles can suffer from coupling between roll rate and pitch rate which can lead to catastrophic instabilities. For example, if the aerodynamic centre moves forward as the roll angle changes from  $0^\circ$  to  $45^\circ$ , and the missile rolls freely, a pitch oscillation linked to the roll rate can develop and lead to instability.

Accurate measurements of rolling moment in wind-tunnel tests require a high quality of tunnel flow and an accurate model to avoid contributions to the rolling moment due to misalignments. So far, no general methods for predicting induced rolling moment have been devised. The complexities introduced by viscosity and the effects of shielding are forbidding in a situation where the nett rolling moment is evaluated as the comparatively small sum of comparatively large contributions from each wing and control panel. At subsonic speeds Ogle has analysed the results on slender wing-body combinations to give the empirical values of the roll interference factor,  $K_\phi$ , shown in Figure 15. The extent to which this can be applied to other, less slender, configurations, such as a rectangular wing on a body, has not yet been assessed.

## 3 STABILITY DERIVATIVES

The static aerodynamic characteristics dealt with so far make up a set of six non-dimensional forces and moments,  $C_x, C_y, C_z, C_\ell, C_m, C_n$ , the notation being derived from the symbols of the axis system (Figure 1). There are also six components of linear and angular velocity,  $u, v, w, p, q$  and  $r$ . If the missile motions are slow enough, the forces and moments acting on it are functions only of these velocities. If we restrict ourselves to linear functions of these velocities, we have 36 partial derivatives of the six forces and moments with respect to the velocities (Figure 16). These are called velocity derivatives, those with respect to the linear velocities being called static stability derivatives and those with respect to the angular velocities being called rotary derivatives. By including terms of higher degree an unlimited number of higher order derivatives can be defined. The coefficients themselves, for example,  $C_z$ , are non-dimensional, so, if the derivative is also to be non-dimensional, the velocities must be made non-dimensional. For linear velocities this is done by dividing by the free stream velocity  $V$ , and for angular velocities by dividing by  $2V/d$  where  $d$  is a characteristic length. Provided  $w$  and  $v$  are small compared with  $V$ , the velocities  $w/V$  and  $v/V$  are the same as the incidence,  $\alpha$ , and sideslip,  $\beta$ , in an axis system which rotates with the body.

In the same way the derivatives of the force and moment coefficients can be obtained with respect to the linear and angular accelerations. These are called acceleration derivatives.

Of this total of 72 linear derivatives, only a few are of practical significance in weapon design (see Figure 17). Some second-order derivatives can also be important, for example the ones shown in Figure 17.

Some confusion can be caused by the fact that the pitch (and yaw) damping is the sum of two derivatives  $C_{mq} + C_{m\dot{q}}$ , and it is instructive to consider how this arises.  $\theta$  is defined as the angle between the missile longitudinal axis and a direction fixed in space.  $\dot{\theta} = q$  and is therefore a pitch rate about the missile centre of gravity referred to the space axis system.  $\alpha$  is defined as the angle between the missile longitudinal axis and the line of flight, and the rate of change of  $\alpha$ ,  $\dot{\alpha}$ , can be considered as arising from a "heaving" motion at right angles to a uniform stream. Three diagrams in Figure 18 show various combinations of  $q$  and  $\dot{\alpha}$ . Figure 18 (i) shows a missile whose centre of gravity describes a sinusoidal flight path while the missile axis maintains a constant angle to the flight path. Figure 18 (ii) illustrates the same sinusoidal flight path with the missile axis remaining horizontal. In Figure 18 (iii), the flight path is a straight line and the missile pitches about the centre of gravity as it moves. The characteristics of  $\dot{\alpha}$  and  $q$  in these three cases are as follows:

- (i)  $\alpha = \text{constant}$ ,  $\dot{\alpha} = 0$  and  $q$  is sinusoidal
- (ii)  $q = 0$ ,  $\alpha$  and  $\dot{\alpha}$  are sinusoidal
- (iii)  $\dot{\alpha} = q$ , and both are sinusoidal

Case (iii) is the situation if a wind-tunnel model in a uniform stream is oscillated about the pitch axis.

The evaluation of stability derivatives can be simplified by the broad symmetries which are usually apparent in missile designs. The assumptions of slenderness enable mathematical methods to be applied to their calculation. The derivation is covered fully by Nielsen<sup>1</sup> who uses a method due to Bryson which is based on considerations of apparent mass.

The geometric simplifications implicit in these mathematical methods, and their inability to treat viscous effects, mean that experimental determination of the stability derivatives is of practical importance. Measurement of the aerodynamic coefficients by conventional wind-tunnel test techniques gives derivatives with respect to attitude parameters such as incidence angle, yaw angle and roll angle. Of the rotary derivatives, damping in pitch and damping in yaw can be deduced by analysis of the static pitching moments and yawing moments<sup>2</sup>. Other wind-tunnel methods require an oscillatory support mechanism which will impart a cyclic pitching or yawing motion to the model. This oscillatory motion can be either forced or unforced. Techniques and results relevant to low aspect ratio wings are described in Refs 34-36. Damping in roll can be measured by inducing a continuous rolling motion.

Although missiles in flight generally follow a constantly changing flight path, the values of the damping derivatives are not always of major importance.

#### 4 MAGNUS EFFECTS

Instead of being stabilised by means of tail fins, projectiles can be stabilised by being spun at high speed about their longitudinal axis. This is particularly popular for projectiles fired from cylindrical guns. Spin stabilisation works because of its gyroscopic effect on the projectile and not for aerodynamic reasons. There is, however, an aerodynamic effect called the Magnus effect, which is associated with spinning bodies, and in the case of spin-stabilised projectiles Magnus effects can lead to instability and dispersion.

The simplest demonstration of Magnus effect is provided by an infinite cylinder at right angles to a uniform stream. If the cylinder is at rest there is no steady force at right angles to the free stream direction, but if the cylinder is spinning about its axis a force is generated. This force is proportional to the density and velocity of the airstream and to the circulation about the cylinder. As in the case of a conventional aerofoil at an angle of incidence this circulation could not exist in an inviscid fluid, and therefore the Magnus effect can be expected to depend on the state of the boundary layer around the cylinder.

If we now consider a spinning cylinder with its axis making an angle not equal to  $90^\circ$  with the stream direction, a similar Magnus force is obtained at right angles to the incidence plane. In addition to causing a side force, the Magnus effect also gives rise to a yawing moment, which may be unstable. It is convenient to associate this Magnus force and moment with the cross-flow component of the flow past the inclined body on the analogy of the two-dimensional cylinder, but the development of the boundary layer separation in the two cases may be quite different. If the incidence exceeds some moderate value, the spinning of the cylinder causes the separated body vortices to take up asymmetric positions, giving rise to a side force and yawing moment which is not due to the same flow mechanism as Magnus effects.

Since Magnus effects depend on boundary layer characteristics, the experimental measurement of their magnitude is very sensitive to the flow characteristics in the wind tunnel or ballistic range being used. It is therefore not surprising that, in the past, experimental results have shown considerable scatter, but the realisation of the importance of the boundary layer may lead to more reliable data. Theoretical estimation methods have so far not yielded satisfactory comparison with experiment, and are probably oversimplified. A recent review of the subject of Magnus effects has been written by Jacobson<sup>37</sup>. Finned bodies are sometimes spun to comparatively high angular rates in order to reduce the likelihood of roll-yaw coupling, and spin effects on such configurations are sometimes loosely referred to as "Magnus effects" though their origin does not lie in the flow mechanism associated with spinning cylinders.

As has already been remarked, bodies at high incidence angles and with no rolling motion may have an asymmetric separated vortex pattern. In such circumstances if the body is spun rapidly it would be difficult to separate Magnus force and moment from that due to the high incidence angle.

#### 5 CROSS-COUPLING

This term applies to missile behaviour arising either from the relative magnitudes of the moments of inertia of the missile about the 3 principal axes, called inertia cross-coupling, or from the fact that a change in one independent variable can affect more than one component of force or moment. This is called

aerodynamic cross-coupling. For example, at a given total incidence angle a change in roll angle can in practice change not only the rolling moment but also the forces in and at right angles to the total incidence plane. Simple linearised inviscid theory would predict no change in these forces. The low aspect ratio configurations typical of weapons lend themselves to inertia cross-coupling as well as aerodynamic cross-coupling, and the number of possible coupled motions is large. The need for a full understanding of the aerodynamic characteristics of a weapon is therefore obvious, and this must include non-linear effects as well as linear effects, viscous effects as well as inviscid effects. It follows that linearised, inviscid calculations of the aerodynamic coefficients and derivatives are likely to miss characteristics which have an important bearing on the dynamic behaviour. The value of experimental wind-tunnel data is thus evident.

In the case of a guided weapon the autopilot may be able to compensate adequately for any undesirable flight behaviour arising from cross-coupling effects, but these effects may have more serious results on the trajectory of an unguided weapon, such as a free fall bomb. Severe instabilities can occur which cause the bomb to fall far away from the target. Among these instabilities are:

- (i) Roll-yaw resonance instability. This can be predicted by linear theory to arise from the presence of small configuration asymmetries, together with an acceleration in roll leading to roll frequencies which resonate with the pitching frequency. The magnitude of the resulting instability depends upon the rate with which the resonant region is traversed.
- (ii) Catastrophic yaw may occur in missiles with low roll rates and is caused by rolling moments and yawing moments which depend on both yaw angle and roll attitude. It is essentially non-linear.
- (iii) Magnus instability, which occurs at high roll rates, with destabilising moments which are dependent on both spin rate and yaw angle.

In Ref 38, Regan et al discuss these problems and some measures which have been taken to study them and tackle them.

In the case of guided weapons, cross-coupling effects can affect the response to control deflection. For example, we have already observed that with a cruciform combination at an asymmetric roll angle there will in general be a rolling moment. If one of these pairs of surfaces is an all-moving control which is then deflected symmetrically, there will be a resultant change in rolling moment as well as a force increment perpendicular to the plane of the control. Once again, the need for comprehensive wind-tunnel tests to determine the magnitude of such effects is emphasised.

Copyright (C) Controller, HMSO, London, 1979

#### REFERENCES

1. J.N. Nielsen      Missile Aerodynamics, McGraw-Hill, 1960
2. S.S. Chin        Missile Configuration Design, McGraw-Hill, 1961
3. J.B. Ogle        Force tests on four slender delta wing-bodies at Mach numbers from 0.6 to 2.8, and a method of predicting the longitudinal characteristics.  
RAE Technical Report 66307, 1966
4. W.K. Osborne    Tests on a body alone, and in combination with delta wings of aspect ratios 0.83, 1.03 and 1.24 at Mach numbers up to 2.8.  
RAE Technical Report 65109, 1965
5. W.K. Osborne    Force and moment measurements on one delta and two gothic planform wing-body combinations of span-to-length ratio 5/13 at Mach numbers from 0.6 to 2.8.  
RAE Technical Report 66358, 1966
6. K.G. Winter  
S.M. Mills        Characteristics of aft mounted all-moving rectangular control surfaces on a slender cruciform missile at Mach numbers from 0.6 to 2.8.  
RAE Technical Report 66326, 1966
7. P.L. Roe        Force and moment measurements on some monoplane and cruciform slender wing-body combinations at  $M = 4.0$ .  
RAE Technical Report 66342, 1966
8. D. Treadgold  
D. Pierce        Aerodynamic characteristics at  $M = 4.3$  of monoplane, triform and cruciform slender delta wing-bodies with all-moving tail control surfaces.  
RAE Technical Report 66343, 1966
9. E.F. Lawlor     The effect of forebody length on the longitudinal characteristics of two delta wing-body combinations of wing aspect ratio 1.03 and 0.31 at Mach numbers up to 2.8.  
RAE Technical Report 66327, 1966
10. J.B. Ogle       Preliminary analysis of the effect of roll angle on the characteristics of three cruciform slender delta wing-bodies at Mach numbers from 0.6 to 2.8.  
RAE Technical Memorandum Aero 961, 1966
11. A.J. Sadler     Preliminary analysis of the characteristics of wing tip, trailing edge and aft mounted control surfaces on a monoplane delta wing-body combination of aspect ratio 0.83 at Mach numbers from 0.6 to 2.8.  
RAE Technical Memorandum Aero 962, 1966



12. W. Stahl  
K. Hartmann  
W. Schneider Force and pressure measurements on a slender delta wing at transonic speeds and varying Reynolds numbers.  
AVA Göttingen 71 A 01, 1971. (Paper presented at AGARD specialists' meeting on "Facilities and techniques for aerodynamic testing at transonic speeds and high Reynolds numbers".)
13. W. Stahl  
K. Hartmann  
W. Schneider Kraft und Druckverteilungsmessungen an einer Flügel-Kanalf-Kombination mit Flügel kleiner Streckung in kompressibler Strömung.  
DLR FB 72-08, 1972
14. W. Stahl  
K. Hartmann  
W. Schneider Experimental investigations of separated flow on slender wings with very slender wings at Mach numbers  $M_{\infty} = 0.8$  to  $1.2$ .  
AVA Göttingen IB 062-72 A 11, 1972. (Paper presented at AIAA 11th Aerodynamics Conference, 1972.)
15. K. Hartmann Aerodynamic investigations on bodies of revolution in the transonic speed range. Part I, Systematic three-component measurements.  
DLR FB 70-67, 1970
16. W.A. Corlett  
D.T. Howell Aerodynamic characteristics at Mach 0.8 to 1.2 of two cruciform missile models, one having trapezoidal wings with canard controls and the other having delta wings with tail controls.  
NASA TM X-2780, 1973
17. C.D. Trescott  
G.V. Foster Effect of fin planform on the aerodynamic characteristics of a cruciform missile with aft cruciform controls at Mach 1.6, 2.36 and 3.56.  
NASA TM X-2774, 1973
18. M.L. Spearman  
C.D. Trescott Effects of wing planform on the static aerodynamics of a cruciform wing-body missile for Mach numbers up to 3.53.  
NASA TM X-1839, 1969
19. E.B. Graves Supersonic aerodynamic characteristics of a low aspect ratio missile model with wing and tail controls and with tails in line and interdigitated.  
NASA TM X-2531, 1972
20. M.L. Spearman  
R.B. Robinson Aerodynamic characteristics of a cruciform-wing missile with canard control surfaces and of some very small span wing-body missiles at a Mach number of 1.41.  
NACA RM L54B11, 1954
21. R.B. Robinson  
M.L. Spearman Aerodynamic characteristics for combined angles of attack and sideslip of a low-aspect-ratio cruciform wing missile configuration employing various canard and trailing-edge flap controls at a Mach number of 2.01.  
NASA Memorandum 10-2-58L, 1958
22. E.R.A. Landers An experimental investigation of interference between wings and body on three planar and cruciform wing and body combinations at Mach numbers of 2.00 and 2.58.  
WRE Report HSA 17, 1964, Weapons Research Establishment, Australia
23. S.E. Gudmundson  
L. Torngren Supersonic and transonic wind tunnel tests on a slender ogive-cylinder body single and in combination with cruciform wings and tails of different sizes.  
FFA Report AU-772, 1972, Flygtekniska Försöksanstalten, Sweden
24. S.E. Gudmundson  
L. Torngren Transonic and supersonic wind tunnel tests on slender cruciform wing-body-tail configurations in different pitch and roll positions.  
FFA Technical Note AU-988, 1975, Flygtekniska Försöksanstalten, Sweden
25. Engineering Sciences Data. Engineering Sciences Data Unit, London
26. K.D. Thomson  
D.F. Morrison On the asymmetric shedding of vortices from slender cylindrical bodies at large angles of yaw.  
WRE Technical Note HSA 106, 1965, Weapons Research Establishment, Australia
27. S.F. Hoerner Fluid-dynamic Drag. Published by the author, 1958
28. P.B. Earnshaw  
J.A. Lawford Low speed wind tunnel experiments on a series of sharp-edged delta wings, Part I. Forces, moments, normal force fluctuations and positions of vortex breakdown.  
RAE Technical Note Aero 2780, 1961
29. J.J. Gallagher  
J.N. Mueller An investigation of the maximum lift of wings at supersonic speeds.  
NACA Report 1227, 1955
30. F.M. Smith  
F.H. Nichols A wind tunnel investigation of the aerodynamic characteristics of a generalised series of winged re-entry configurations at angles of attack to  $180^\circ$  at Mach numbers of 2.38, 2.99 and 4.00.  
NASA TM X-512, 1961
31. B.E. Tinling  
C.Q. Allen An investigation of the normal force and vortex wake characteristics of an ogive cylinder body at subsonic speeds.  
NASA TN D-1297, 1962

32. ed. Kline et al      Computation of turbulent boundary layers  
AFOSR-IFP Stanford Conference Proceedings, 1968
33. H.H. Fernholz      A critical compilation of compressible, turbulent boundary layer data.  
P.J. Finley      Agardograph AG 223, 1977
34. J.S. Thompson      Oscillatory derivative measurements on sting-mounted wind tunnel models:  
R.A. Fail      method of test and results for pitch and yaw on a cambered ogee wing at Mach  
numbers up to 2.6.  
R and M 3355, July 1962, Aeronautical Research Council, Teddington, England
35. J.S. Thompson      Low speed wind tunnel measurements of the oscillatory lateral stability  
R.A. Fail      derivatives for a model of a slender aircraft (HP 115) including the effects of  
J.V. Inglesby      frequency parameter.  
Current Paper 1097, 1969, Aeronautical Research Council, Teddington, England
36. C.O. O'Leary      Low speed wind tunnel measurements of the oscillatory lateral aerodynamic  
derivatives of a BAC 221 model and comparison of results with similar Concorde  
and HP 115 data.  
RAE Technical Report 70095, 1970
37. I.D. Jacobson      Magnus characteristics of arbitrary rotating bodies.  
Agardograph AG-171, 1973
38. F.J. Regan      Free-fall vehicle dynamics observation and prediction.  
F.J. Tanner      Journal of Aircraft, Vol. 7, No. 2, March-April 1970, pp. 141-144  
J.H.W. Shannon

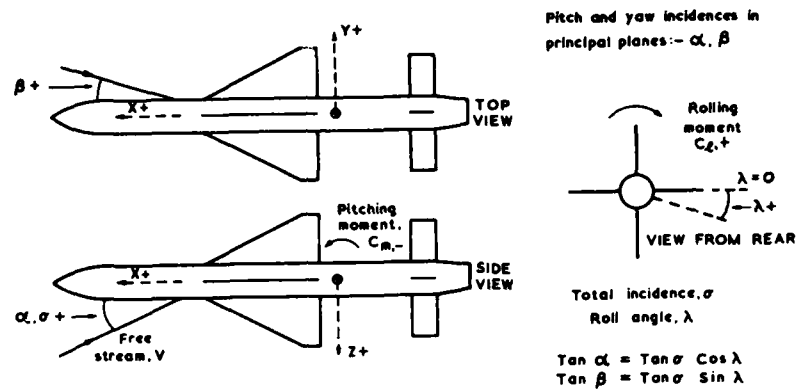


FIG. 1 A TYPICAL AXIS SYSTEM

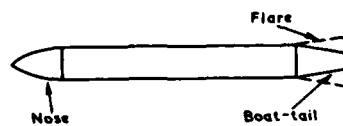


FIG. 2 BODY GEOMETRY

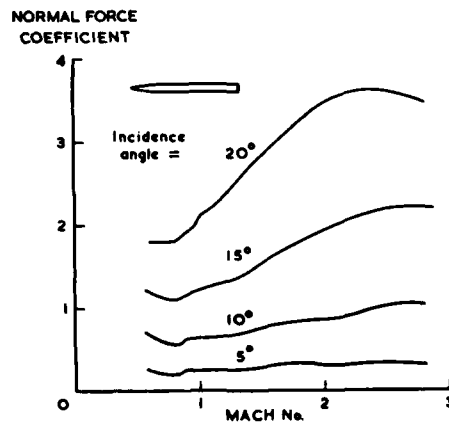


FIG. 3 NORMAL FORCE ON OGIVE-CYLINDER BODY

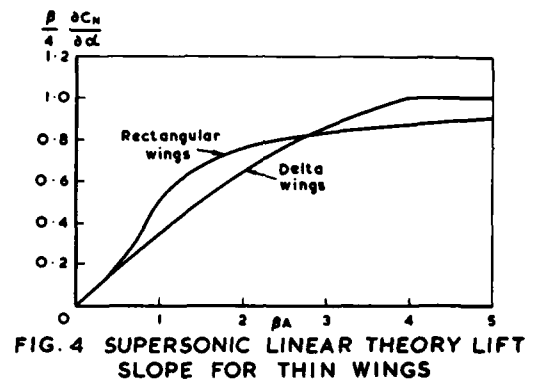


FIG. 4 SUPERSONIC LINEAR THEORY LIFT SLOPE FOR THIN WINGS

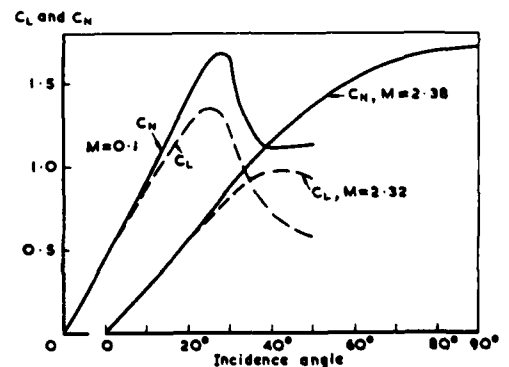


FIG. 5 HIGH INCIDENCE CHARACTERISTICS OF A 65° DELTA WING

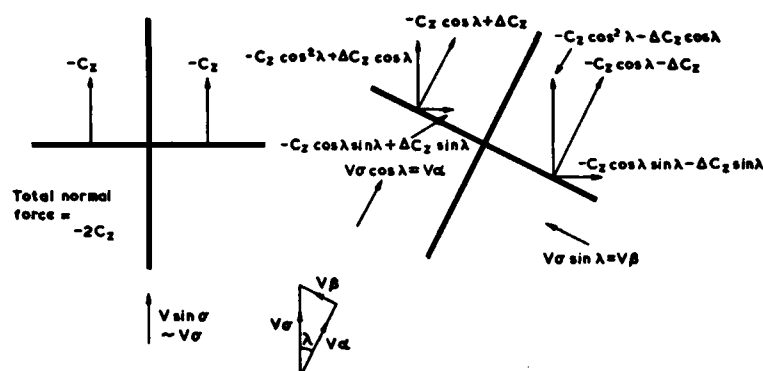


FIG.6 LINEAR NORMAL FORCE ON CRUCIFORM WINGS

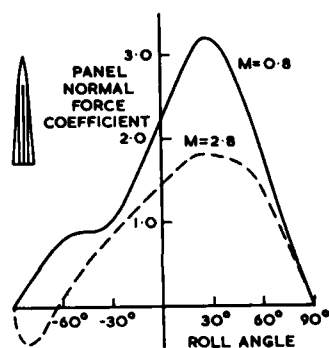


FIG.7 VARIATION OF PANEL NORMAL FORCE WITH ROLL ANGLE

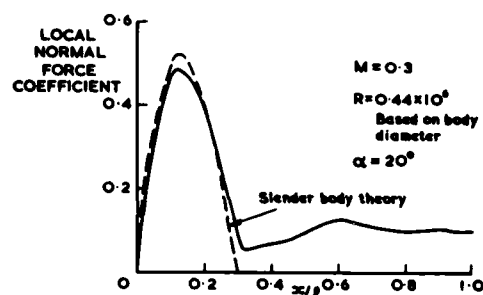


FIG.9 BODY LIFT DISTRIBUTION SUBSONIC

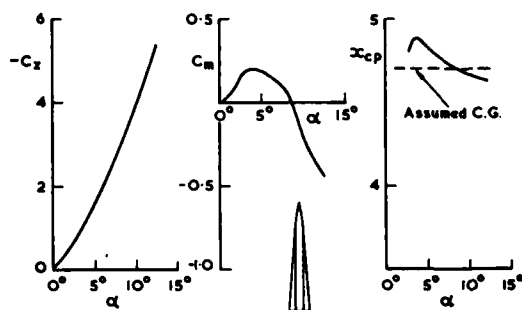


FIG.8 NON-LINEAR CHARACTERISTICS OF SLENDER WING-BODY COMBINATION

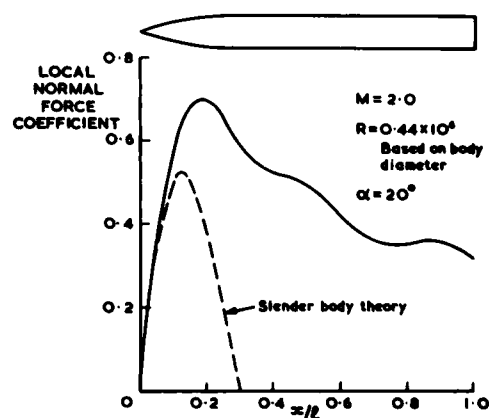


FIG.10 BODY LIFT DISTRIBUTION SUPersonic

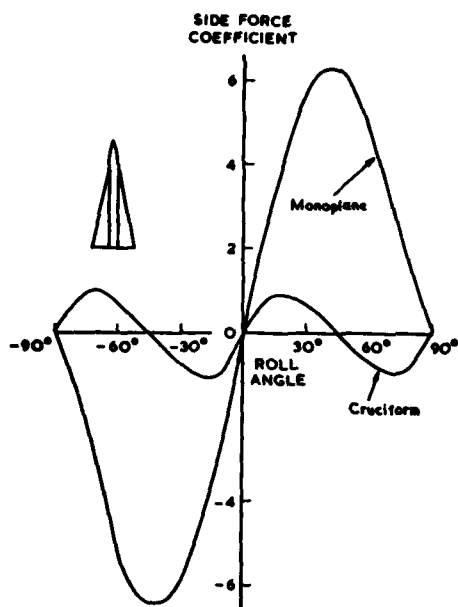


FIG. 11 SIDE FORCE ON MONOPLANE AND CRUCIFORM WING-BODY COMBINATIONS

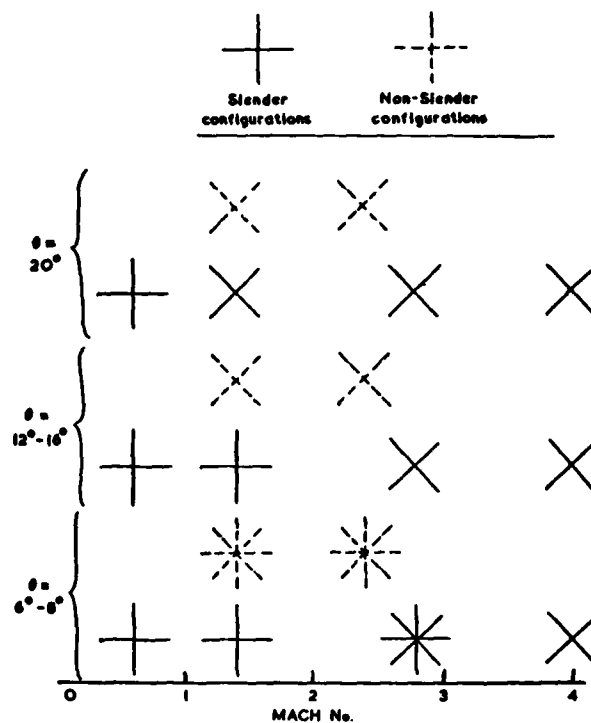


FIG. 13 STABLE POSITIONS IN ROLL

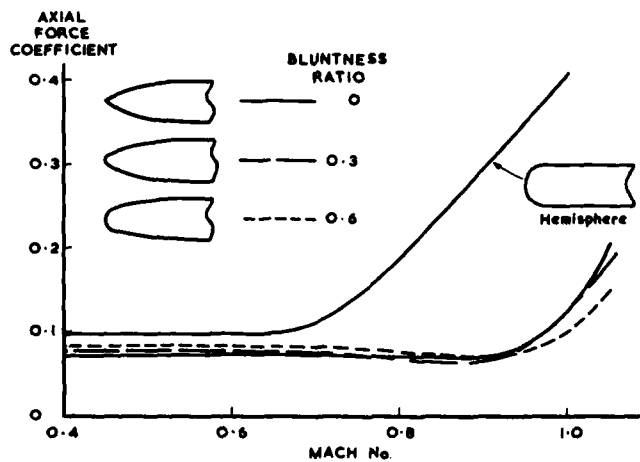


FIG. 12 EFFECT OF NOSE BLUNTNESS ON AXIAL FORCE

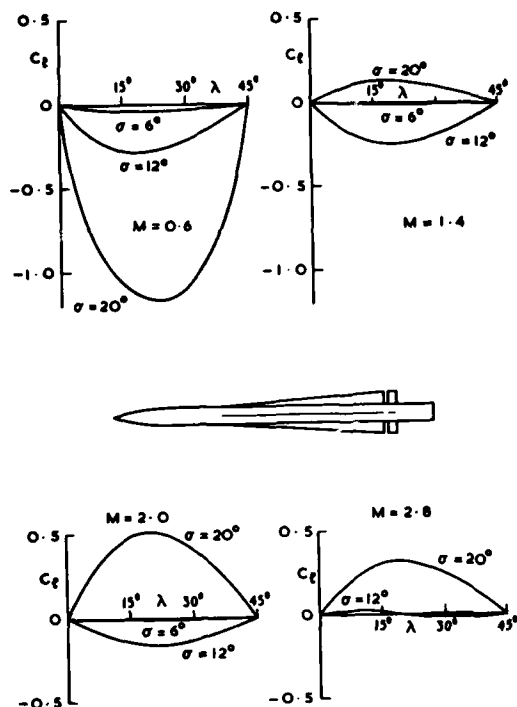
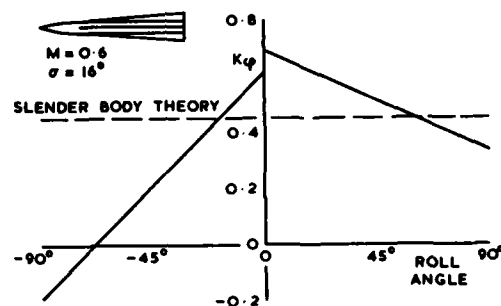


FIG.14 INDUCED ROLLING MOMENTS

FIG.15 EXPERIMENTAL VALUES OF FACTOR  $K_\phi$ 

$C_{x_u} = \frac{\delta C_x}{\delta (u/v)}$	$C_{x_v} = C_{x_\beta} = \frac{\delta C_x}{\delta \beta}$	$C_{x_w} = C_{x_\alpha} = \frac{\delta C_x}{\delta \alpha}$	$C_{x_p} = \frac{\delta C_x}{\delta (pd/2v)}$	$C_{x_q} = \frac{\delta C_x}{\delta (qd/2v)}$	$C_{x_r} = \frac{\delta C_x}{\delta (rd/2v)}$
$C_{y_u} = \frac{\delta C_y}{\delta (u/v)}$	$C_{y_v} = C_{y_\beta} = \frac{\delta C_y}{\delta \beta}$	$C_{y_w} = C_{y_\alpha} = \frac{\delta C_y}{\delta \alpha}$	$C_{y_p} = \frac{\delta C_y}{\delta (pd/2v)}$	$C_{y_q} = \frac{\delta C_y}{\delta (qd/2v)}$	$C_{y_r} = \frac{\delta C_y}{\delta (rd/2v)}$
$C_{z_u} = \frac{\delta C_z}{\delta (u/v)}$	$C_{z_v} = C_{z_\beta} = \frac{\delta C_z}{\delta \beta}$	$C_{z_w} = C_{z_\alpha} = \frac{\delta C_z}{\delta \alpha}$	$C_{z_p} = \frac{\delta C_z}{\delta (pd/2v)}$	$C_{z_q} = \frac{\delta C_z}{\delta (qd/2v)}$	$C_{z_r} = \frac{\delta C_z}{\delta (rd/2v)}$
$C_{l_u} = \frac{\delta C_l}{\delta (u/v)}$	$C_{l_v} = C_{l_\beta} = \frac{\delta C_l}{\delta \beta}$	$C_{l_w} = C_{l_\alpha} = \frac{\delta C_l}{\delta \alpha}$	$C_{l_p} = \frac{\delta C_l}{\delta (pd/2v)}$	$C_{l_q} = \frac{\delta C_l}{\delta (qd/2v)}$	$C_{l_r} = \frac{\delta C_l}{\delta (rd/2v)}$
$C_{m_u} = \frac{\delta C_m}{\delta (u/v)}$	$C_{m_v} = C_{m_\beta} = \frac{\delta C_m}{\delta \beta}$	$C_{m_w} = C_{m_\alpha} = \frac{\delta C_m}{\delta \alpha}$	$C_{m_p} = \frac{\delta C_m}{\delta (pd/2v)}$	$C_{m_q} = \frac{\delta C_m}{\delta (qd/2v)}$	$C_{m_r} = \frac{\delta C_m}{\delta (rd/2v)}$
$C_{n_u} = \frac{\delta C_n}{\delta (u/v)}$	$C_{n_v} = C_{n_\beta} = \frac{\delta C_n}{\delta \beta}$	$C_{n_w} = C_{n_\alpha} = \frac{\delta C_n}{\delta \alpha}$	$C_{n_p} = \frac{\delta C_n}{\delta (pd/2v)}$	$C_{n_q} = \frac{\delta C_n}{\delta (qd/2v)}$	$C_{n_r} = \frac{\delta C_n}{\delta (rd/2v)}$
STATIC STABILITY DERIVATIVES			ROTARY DERIVATIVES		

FIG.16 VELOCITY STABILITY DERIVATIVES

FIRST ORDER DERIVATIVES

$C_{m_\alpha}$ OR $C_{m_\sigma}$	STATIC LONGITUDINAL STABILITY
$C_{n_\beta}$	DIRECTIONAL STABILITY OR WEATHERCOCK STABILITY
$C_{m_q}, C_{m_{\dot{\alpha}}}$	DAMPING IN PITCH
$C_{n_r}, C_{n_{\dot{\beta}}}$	DAMPING IN YAW
$C_{l_p}$	DAMPING IN ROLL

SECOND ORDER DERIVATIVES

$$C_{l_{\alpha\beta}}, C_{l_{\alpha\dot{\beta}}}, C_{n_{\alpha\dot{\beta}}}$$

FIG.17 SOME SIGNIFICANT STABILITY DERIVATIVES

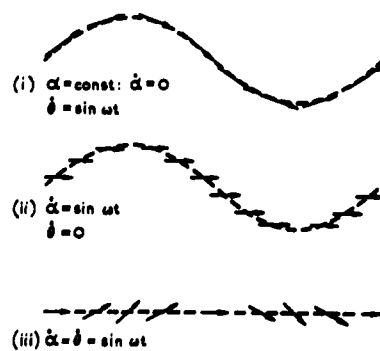


FIG.18 FORMS OF PITCHING MOTION

## AERODYNAMICS OF LOW ASPECT RATIO WINGS

W. H. Stahl

Deutsche Forschungs- und Versuchsanstalt für Luft- und Raumfahrt E.V.

Institut für Theoretische Strömungsmechanik

Bunsenstr. 10

D-3400 Goettingen, FRG

## SUMMARY

The lecture deals with the types of wings, which generally find application on missiles, that is with wings having delta, rectangular, trapezoidal, or other, planform, of more or less small aspect ratio. An overview over the available experimental evidence for the flow - fields of such wings is given, as well as a discussion of measured pressure distributions, forces, and moments at low and high speeds; also the influence of Reynolds number is considered. Various methods to predict the aerodynamic characteristics of such wings are reviewed and comparisons are made between theoretical and experimental results. An extensive list of references is provided.

## NOTATION (see Fig. 1)

A	wing aspect ratio, $= \frac{b^2}{S}$	x, y, z	coordinate system fixed in the wing
b	wing span	Z	normal force
c	wing chord	$\alpha, \beta$	angle of incidence, of yaw
$c_o$	wing inner chord	$\epsilon$	angle of trailing vortices
c	aerodynamic mean chord, $= \frac{1}{S} \int_{-b/2}^{b/2} c^2(y) dy$	$\nu_\infty$	free-stream kinematic viscosity of air
$c_L$	lift coefficient, $= \frac{L}{q_\infty S}$	$\rho_\infty$	free-stream density of air
$c_{L_{max}}$	maximum lift coefficient	$\phi$	leading-edge sweep angle
$c_M$	pitching moment coefficient, $= \frac{M}{q_\infty S c}$	$\Omega$	roll velocity
$c_p$	pressure coefficient, $= \frac{p - p_\infty}{q_\infty}$		
$c_Z$	normal force coefficient, $= \frac{Z}{q_\infty S}$		
$k_1, k_2$	coefficients		
M	pitching moment, or Mach number		
$M_\infty$	free-stream Mach number		
n	exponent		
p	static pressure		
$p_\infty$	free-stream static pressure		
$q_\infty$	free-stream dynamic pressure, $= \frac{1}{2} \rho_\infty U_\infty^2$		
Re	Reynolds number, $= \frac{U_\infty c}{\nu_\infty}$		
s	wing semi span		
S	wing planform area		
$U_\infty$	free-stream velocity		



## 1. INTRODUCTION

Missiles typically have wings which are rather long and narrow, i.e., slender, with aspect ratios being around  $A = 1 + 2$ . Often a delta or near delta planform is used; but others, like rectangular, trapezoidal, arrow, etc., have found applications, too. We shall rarely encounter an aerodynamically sophisticated profile, often the wing or fin is simply a more or less thin, flat plate which has aerodynamically sharp edges everywhere. In general, missiles have their wings in a cruciform arrangement. To provide an example, Fig. 2 shows the air-ground guided missile "Jumbo", with its more or less delta wings and trapezoidal fins in cruciform arrangements.

These low aspect ratio wings, used on missiles, are in various respects quite different to those used on airplanes, which generally have more or less large aspect ratios. In Fig. 3 some of the essential aspects of each type of wing are shown schematically and compared to each other. On one side, there is the large span wing of an airplane; it has a carefully designed profile with a rounded nose, exhibiting a flow which, over a certain range of incidences and flight speeds, stays attached on the major portion of the wing surface. A vortex sheet leaves the trailing edge, rolling up downstream from its edges in the well known manner. The high aspect ratio wing experiences a lift force which, in a certain range, depends linearly on the angle of incidence and, correspondingly, is dealt with by the so-called "linear" theories, as will be treated later on.

On the other side, there is the low aspect ratio wing. In the case of the delta wing depicted in the figure, we may consider simply a more or less thin plate with aerodynamically sharp leading edges. Its flow field is characterized by the fact that the flow separates not only at the trailing edge but also at the leading edges; the vortex sheets leaving there are coiling up to form the familiar leading-edge vortices above the wing. Such a flow field leads to a nonlinear dependence of the lift force on the angle of incidence, as is shown on the lower right-hand side of the figure. The study of these wings, with such vortex flows, led to the nonlinear theories, which became necessary in order to describe the physical facts more correctly than the linear theories can.

The material to be presented in the following on such low aspect ratio wings with various planforms is to a great part intended to provide an insight into the flow field generated by the wings and to discuss some of the effects of the flow on the wings. This should, in the end, be of help in the design of a wing with some desired properties. To this end, we shall make use of experimental evidence, as obtained in wind or water tunnels by various flow visualization techniques and from pressure measurements made on the model surfaces or in the outer flow. Some results of force measurements will then be presented to give an idea of the aerodynamic characteristics of such wings. It has to be kept in mind, however, that the wings or fins, in the end, will be used in the presence of the missile body, which may influence the flow about the wing considerably.

In a second part, a survey will be given on various theoretical methods for the prediction of the aerodynamic characteristics of low aspect ratio wings with different planforms. Results obtained from some of the theories will be compared to the results from experiments.

## 2. EXPERIMENTAL EVIDENCE

### 2.1 Delta Wings

We shall at first deal with wings, which have a delta planform or nearly so, and which are often just flat plates, with sharp leading edges. The wings, we are interested in here, are often thin and quite narrow, compared to their length, i.e., their leading edges are swept back pronouncedly. As we have already seen in Fig. 2 the "Jumbo" missile is, for example, equipped with such wings.

When such a slender delta wing with sharp leading edges is placed in an uniform flow, which is incompressible to start with, at some angle of incidence, it produces a flow field which is shown schematically with its principal features in Fig. 4. At the leading edges the flow, approaching them on the lower and upper surface, separates. A stream surface leaves from each edge, across it the velocity vector jumps in direction, therefore constituting a vortex sheet. The magnitude of the velocity vector, on the other hand, must not change discontinuously through the vortex sheet, as the sheet cannot sustain a pressure jump from one side to the other. Each sheet rolls up into a so-called vortex core above the suction side. These leading-edge vortices are characteristic for the flow field past such a slender delta wing at incidence and they are found in a wide Mach number range.

In a real flow, there are always at least small effects of the viscosity of the fluid present. The changes in velocity are actually continuous, although they occur across a small distance. The concept of a discontinuity is an idealization which, however, has proved to be very useful for theoretical analysis, an example being the treatment of the trailing vortex sheet for large aspect ratio wings. Such types of flow with vortex sheets have been treated extensively by D. Küchemann and D. Küchemann and J. Weber in Ref. 1 and Ref. 2, respectively, and the reader is referred to these papers for a very detailed treatment of vortex motions.

By means of an adequate flow visualization technique, one can readily demonstrate the presence of such a pair of leading-edge vortices above the wing in a flow at incidence. Figure 5 shows the development of the flow with incidence for a low aspect ratio, sharp-edged delta wing at a high subsonic Mach number up to high angles of attack. It is evident from the flow pictures that on such a wing the same type of flow is preserved up to large incidences, and that it develops in a regular manner, at least as far as one can tell from the pictures.

A limit to this orderly vortex flow pattern on a slender delta wing is set at higher angles of attack by what is called "vortex breakdown" or "vortex bursting". It is observed that the vortex cores above the wing undergo, at some sufficiently high incidence, an abrupt change. In smoke flow visualization or in Schlieren pictures one can see that the vortex cores increase their diameters suddenly at a certain point, the so-called "breakdown" point. Measurements in the region downstream of this point have shown that the velocities are decreased considerably here, the flow being diffuse and of turbulent nature. The phenomenon is actually first observed downstream of the trailing edge of the wing, moving upstream with increasing angles of incidence, then crossing the trailing edge, and progressing forward on the upper side of the wing. Here the influence on the aerodynamic characteristics can become noticeable and, as in the case of the lift, quite unfavorable. In Fig. 6, we can observe how the vortex flow on wings of various aspect ratios breaks down near the trailing edge, spreading over the wing. We shall discuss another example of flow with vortex breakdown later (Fig. 34); there the phenomenon is observed by means of the Schlieren method.

The angle of attack at which vortex breakdown occurs on the wing, say, at the trailing edge, depends strongly on the aspect ratio, that is, on the leading-edge sweep. This is clearly demonstrated in the flow visualizations shown in Fig. 6. It can be seen, that with decreasing leading-edge sweep the (critical) angle of attack is decreasing, for which breakdown is observed on the rear part of the wing. This dependence of the critical incidence on the leading-edge sweep is plotted in Fig. 7, based on the results of number of tests carried out in a water and various wind tunnels, as reported by H. Werlé in Ref. 3.

Vortex breakdown is found under various circumstances in different forms; it is not restricted to the flow above slender delta wings. It usually occurs, when a vortex flow penetrates into a region with an adverse pressure gradient in the outer flow, it is connected with an abrupt change in the velocity distribution of the vortex flow. A number of theories or proposals have been brought forward, to explain why this sudden change in the flow structure takes place, under what circumstances it appears and what form it takes. These attempts have taken two different directions, either relating the phenomenon to flow instability or to other causes. It is believed, that there is not necessarily only one theory which would be applicable to all the various forms of vortex breakdown. The various approaches have been discussed, e.g., by H. Ludwig in Ref. 4 and by M.G. Hall in Ref. 5. More recently a contribution to this subject has been given by Y. Hayashi and T. Nakaya, Ref. 6.

The same type of regular vortex flow above the wing is found for a wide range of Mach numbers. It exists also at supersonic speeds, as long as the leading edges are subsonic, i.e., as long as they are swept back behind the Mach cone originating in the apex of the wing. As the component of the free-stream Mach number in a plane normal to the leading edge,  $M_n$ , approaches unity, the leading-edge vortices vanish. There is then a change to a supersonic expansion of the flow around the edges. Shocks and, eventually, shock induced separations may occur inboard on the suction side. On the pressure side, with increasing Mach number,  $M_n$ , an initially detached shock moves closer to the wing and subsequently attaches at the leading edges. These types of flow, for a thin delta wing at supersonic speeds, are depicted schematically in Fig. 8, as reported by L.C. Squire in Ref. 7. On the right hand side the flow regions are indicated for three wings having different leading-edge sweep,  $\phi$ , for actual flight conditions; i.e. flight Mach number,  $M_\infty$ , and angle of attack,  $\alpha$ . Further studies to obtain information about the lee-side flow over delta wings in a range of supersonic Mach numbers and angles of attack have been performed by J. Szodrich and U. Ganzer, their results have been reported in Ref. 8.

The flow regime, in which the free-stream velocity component normal to the leading edges is sonic or near sonic has been investigated experimentally (and theoretically) by various authors, e.g. D. Küchemann, see Ref. 9. H. Esch studied the behaviour of the bow shock wave of a thick delta wing with sharp leading edges in supersonic flow at zero incidence, when the leading edges pass from being subsonic to supersonic (Ref. 10.). Fig. 9 shows, how the bow shock wave is displaced outwards more and more, relative to the Mach cone, when the edges go from subsonic to supersonic. Even in the case of a supersonic leading edge the bow shock wave may be detached.

We now turn to a more detailed description of the structure of the flow past a low aspect ratio delta wing. In Fig. 10 is given an interpretation of a visualization of the flow at the wing surface, which was obtained at an angle of incidence,  $\alpha \approx 17^\circ$ , at a transonic Mach number by W.J. Rainbird et al. in Ref. 11. One can find there, in spanwise direction, a sequence of attachments of the flow to the wing surface and separations of the boundary layer flow. We observe also on the suction side of the wing that there is not only a leading-edge, or primary, vortex present, but also a secondary and even a very small tertiary vortex is found inboard of the edge.

The boundary layer on the wing's suction side is now considered more closely for the flow directed outwards after attachment has occurred inboard. The initially laminar boundary layer has on the forward part of the wing relatively short running lengths, it stays laminar outwards to the line, where it separates in the adverse pressure field of the leading-edge vortex. The boundary layer flow far enough rearwards on the wing has running lengths which are long enough to allow transition to a turbulent boundary layer flow. This flow will also separate near the leading edge, but farther outboard, as the turbulent boundary layer is now able to penetrate farther into the adverse pressure field. Figure 11, on the left hand side, depicts schematically the different boundary layer flow regions, together with the separation lines on a slender delta wing. On the right hand side of the figure is plotted the Reynolds number,  $Re_{lr}$ , formed with the distance from the apex to the kink in the boundary layer separation lines, which marks the first transition from laminar to turbulent boundary layer flow. The diagram shows (for constant free-stream velocity), how the region of turbulent boundary layer flow spreads forward on the wing with increasing angles of incidence. These results of investigations, made by D. Hummel, were reported in Ref. 12 by H. Schlichting.

Turning now to the pressure field of the wing, we shall see how this can be brought into connection to the observed flow phenomena. In Fig. 12 is given, in a schematic presentation, how the wall pressures, on the pressure and suction sides of a slender delta wing are distributed in spanwise direction. There are distinct suction peaks in the pressure distribution on the upper surface which can be related immediately to the vortex flows above the wing. The primary and secondary vortices induce velocities with a corresponding pressure distribution on the wall, as shown in the upper part of Fig. 12. Right underneath a vortex, there are high induced velocities and the low pressures showing up as suction peaks. Some results of pressure measurements on a slender delta wing in incompressible flow, obtained by D. Hummel in Ref. 13, are depicted in Fig. 13. We have the distribution of pressures in spanwise direction on pressure and suction side, at various chordwise stations. Also given are curves obtained from the theories of J.H.B. Smith and R.T. Jones, respectively, which will be discussed later. The experimental results obtained on the suction side show over the greater part of the wing, except for the rearward section, several suction peaks in the spanwise pressure distributions, which can be attributed to the various vortices above the wing: the leading-edge vortex, the secondary and even a tertiary vortex in this case. On the lower surface, we find that the overpressures, nearly constant about the axis, are varying smoothly towards the leading edge.

The flow on such a low aspect ratio delta wing, at an angle of incidence of  $\alpha = 20.5^\circ$  has been studied in detail by D. Hummel, for laminar and turbulent boundary layers, see Ref. 14. In both cases it turned out that the flow field was non-conical. The presence of a secondary vortex has two main effects on the flow field: There exists a displacement effect by which the leading-edge vortex is shifted inwards and upwards, leading to an inboard movement and a reduction of the suction peak of the pressure distribution. Furthermore, there exists a vorticity effect, which increases the suction in the region of the secondary vortex. For turbulent boundary layers the effects are small, they are large for laminar boundary layers. This is due to the fact, that turbulent boundary layers stay longer attached and form a small secondary vortex, whereas the laminar boundary layers separate early and lead to a large secondary vortex.

Hummel also determined, from his experiments, the bound vortex lines in the wing, both for laminar and turbulent boundary layers. It was found, that free vortices are shed from the trailing-edge, with rotation opposite to that of the leading-edge vortex. This trailing vorticity is larger for laminar than for turbulent boundary layers at the trailing-edge.

Also, extensive pressure measurements were carried out downstream of the wing trailing-edge in planes perpendicular to the free stream for the case of turbulent boundary layers at the edge. The formation of a concentrated trailing vortex has been observed, with rotation opposite to that of the leading-edge vortex. This trailing vortex starts at about 70% of semispan and travels downstream on a helical path around the leading-edge vortex. At the center of this trailing vortex high velocities, as well as total and static pressure minima were found. Fig. 14 shows the plot of such a total pressure distribution in a plane downstream of the wing, taken from Ref. 14. The secondary vortex decays rapidly downstream of the trailing edge, its remains are rolled up into the trailing vortex.

We now consider results of such pressure measurements carried out on a slender delta wing in compressible flow as reported by W. Stahl et al. in Ref. 15. The spanwise pressure distributions on the suction side at various sections in the Mach number range from  $M_\infty = 0.7$  to 1.2 are shown in Fig. 15. Curves have been drawn only through the points of the front section II and the rear section IV. The variation of the pressure coefficient again is, essentially, what would be expected for such a slender wing. There is, however, a pronounced difference between the fore and aft sections around the suction peaks and farther outboard. In the forward part of the wing, the suction peak is much lower and farther inboard; this feature is observed in the whole Mach number range and at all incidences. A plausible explanation can be given, realizing the large differences in running lengths of the boundary layer of the outward flow, underneath the leading-edge vortex. Oil flow pictures provided some insight into the flow field in question. Thus it can be expected on the front portion of the wing, where only short running lengths are possible, that a laminar layer separates early in the adverse pressure field between the leading-edge vortex core and the edge. Farther back on

the wing the running lengths become sufficiently long, so that transition is possible and a turbulent boundary layer is able to penetrate closer to the leading edge.

The fact, that the state of the boundary layer on the suction side of the wing has such a strong effect on the pressure distribution led to the investigation of the influence of the free-stream Reynolds number for

$$Re = \frac{U_{\infty} \frac{2}{3} c_o}{\nu_{\infty}} = 1.3 \cdot 10^6 \text{ to } 6.5 \cdot 10^6$$

and of the influence of a transition strip.

The spanwise pressure distributions on the suction side as shown in Fig. 16 for  $M_{\infty} = 1$ , depend on Reynolds number especially near the suction peak. The pressure distributions suggest that for the high Reynolds numbers  $Re \gtrsim 3.8 \cdot 10^6$ , a turbulent boundary layer separates close to the leading edge; this view is also supported by oil flow pictures. At low Reynolds numbers, there is probably a laminar boundary layer flow, with a secondary separation farther inboard. The influence of Reynolds number on the pressure distribution of the pressure side is not very marked.

Furthermore, attempts were made to get artificial transition by means of a carborundum band, extending from the apex back to the trailing edge at 40 % semi-span. The pressure distribution at low Reynolds numbers with the transition strip becomes similar to that at high Reynolds numbers, though not attaining as high suction peaks, see Fig. 17. In this connection, attention is drawn also to the pressure measurements on a slender rhombic cone, which were carried out by J.H.B. Smith and A.G. Kurn and reported in Ref. 16.

The influence of Mach number on the spanwise pressure distribution, at the middle section, on the suction and pressure sides, is shown in Fig. 18. The pressure coefficient,  $c_p$ , increases on both sides of the wing with increasing Mach number; the tendency is reversed at  $M_{\infty} = 1.1$  on the pressure side and in the inner part of the suction side. It is also evident, that the suction peak becomes less and less pronounced. The losses on the suction side with Mach number are largely compensated by gains on the pressure side, but there is still some decrease in load with increasing Mach number at the section discussed.

We have so far considered the pressures acting on the wing. Of course, we must take account of the viscous effects, too, which are present in any real flow. There are the boundary layers, developing at the wall in the usual manner, and corresponding wall shear stresses are exerted on the wing tangentially. The forces, due to these pressures and shear stresses are adding up to the total force, exerted by the fluid on the wing. We shall have a look at some experimental evidence obtained for the various force components. Fig. 19 gives the results of three-component measurements on three delta wings of aspect ratio  $A = 1.0, 1.6$  and  $2.3$  in low speed flow, as reported in Ref. 17. We see, that the lift varies in a nonlinear way over a large range of angles of attack. This nonlinearity of the lift curve, with increasing slopes, is characteristic for such slender wings with leading-edge vortices, as was mentioned already in the beginning. We remember, that wings of large aspect ratios ( $A \gtrsim 5$ ), with their rounded leading edges and with only little or moderate sweepback, have a flow field which is characterized by an attached flow round their leading edges and on most parts of the wing, and that the lift of such wings varies linearly with incidence.

The diagrams show also the effects on lift and pitching moment, due to the breakdown of the leading-edge vortices, which has been discussed above. The loss in lift at high incidences is actually due to two phenomena, one is that the axes of the leading-edge vortices are bending back into the free-stream direction, and the other is the actual vortex breakdown occurring on the wing. The separation of these two effects was reported by D. Hummel in Ref. 13.

Furthermore, some results of force measurements are presented, which were obtained in high subsonic, transonic, and supersonic flow at constant Reynolds number; the data were reported in Refs. 15 and 18. The normal force coefficient,  $c_z$ , is shown in Fig. 20 as a function of angle of incidence for Mach number  $M_{\infty} = 0.5$  to  $1.2$ . All curves are strongly nonlinear, as is characteristic of such a slender wing. The dependence of the normal force coefficients on Mach number for the wing at various angles of incidence is shown in Fig. 21. It is seen, that  $c_z$  changes little with Mach number in the high subsonic and transonic speed range. On the other hand, we have noted the dependence on Mach number of the pressure coefficients on the wing pressure and suction sides in Fig. 18, for this speed range. Also given is the pitching moment about the axis through the center of area (at  $2/3 c_o$  from the apex) in Fig. 20. The variation of the position of the center of pressure on the wing with Mach number for various angles of incidence is shown in Fig. 22. Such a delta wing, being a conical body, should generate a conical flow field, especially in supersonic flow, where the upstream influence of the trailing edge is essentially negligible. In a conical flow field, with the flow properties constant along rays through the apex of the wing as the center of symmetry, the center of pressure coincides with the center of the wing area. One can see that this is fulfilled quite well in supersonic flow, at least for the angles of incidence  $\alpha > 5^\circ$ .

Let us now turn to the question of what importance the shape of the leading edge is, which we had up to now taken to be sharp, in general. Fig. 23 depicts experimental results, obtained on a slender delta wing with sharp and round edges, respectively, as reported in Ref. 19. It is seen, from the upper part of the figure, that with the round edges, the lift coefficient of the wing is reduced considerably. The flow from the pressure side to the suction side is now able to remain attached to the surface around these edges. The flow will then separate somewhat inboard on the upper surface and again the familiar type of vortex flow is observed above the wing. The nonlinear part of the lift, which is due to the vortices, is seen to be reduced in the case of the round edges. At the bottom of Fig. 23 is depicted the corresponding influence of the leading-edge shape on the moment coefficient about an axis in the apex. The effect of wing leading-edge radius on the longitudinal aerodynamic characteristics of highly swept wing-body configurations has been investigated by W. P. Henderson, Ref. 20. In this connection, also the work of G. E. Bartlett and R. J. Vidal, Ref. 21, has to be mentioned.

A short discussion will now be given here as to what is called ground effect. When the wing moves near the ground, the flow about the wing is influenced by the proximity of the ground, and consequently, there are certain ground effects on the aerodynamic characteristics. For slender wings, this ground effect is much more pronounced than for wings of large aspect ratio; the ground effect gives rise to an additional nonlinearity of the lift curve, as was shown by K. Gersten and J. v. d. Decken in Ref. 22. The wing near the ground has a nonlinear lift curve, even when the leading-edge vortices are neglected. Experimental, as well as theoretical results, are given in Fig. 24 for a slender delta wing at a small incidence,  $\alpha = 5^\circ$ . There is plotted the lift coefficient near the ground, related to the lift coefficient far from the ground, as a function of the distance from the ground. The lift coefficient is seen to be increased in ground proximity, though the influence is noticeable only for flight at close distance to the ground. For example, at a distance of one trailing-edge span, the increase in lift is only some percent. It has been pointed out in Ref. 23 by J. v. d. Decken, that the wing thickness also makes itself increasingly felt when the wing comes closer to the ground. The aerodynamic characteristics of delta wings, which are moving close to the ground have also been studied e.g. by S. D. Ermolenko et al., Ref. 24, and C. H. Fox, Ref. 25. Low-speed normal force and pitching moment data of slender wings in ground effect can also be found in Ref. 26.

The influence of an angle of yaw on the flow field of a slender delta wing at incidence should also be mentioned. It was found in experimental investigations, that the following changes occur. Increasing yaw angles,  $\beta$ , lead to a strengthening of the vortex core on the windward side of the wing, and it is moving inboard and downwards; the vortex core on the leeward side, on the other hand, is weakened and it moves outboard and upwards. The pressure distributions on the suction side of the wing show corresponding changes in position and strength of the suction peaks. The spanwise variation of static pressures on a slender delta wing at incidence for various yaw angles is shown in Fig. 25; the results were obtained by J. K. Harvey in Ref. 27. D. Hummel and G. Redeker reported in Ref. 28 on the influence of vortex breakdown on the aerodynamic characteristics of slender delta wings at yaw.

We shall turn now to the rolling motion of slender delta wings in low speed flow, as has been studied, e.g. by F. Schlottmann, Ref. 29. The rolling moments were measured as a function of the roll (angular) velocity and its time derivative, for various angles of attack. The flow field of the rolling wings was studied by means of a surface flow visualization technique and smoke. When the wing is rolling with zero angle of incidence, then one leading-edge vortex is formed on each side of the wing, as is shown schematically as case A in Fig. 26. This vortex configuration results from the antisymmetric spanwise distribution of the incidence, due to the rolling motion. The corresponding rolling moment curve is nonlinearly increasing with the roll velocity. When the angle of incidence is increased, at constant angular velocity, the vortex becomes stronger on the side of the wing, with the higher effective angles of incidence, resulting from the wing incidence and the roll induced incidence distribution; on the other side of the wing a weakening of the vortex results. With increasing incidence this may lead to a flow pattern, for which the leading-edge vortex has disappeared on one side, while the other one has further increased its strength. This situation is depicted schematically as case B in Fig. 26. For even higher incidences, at constant angular velocity, the angle of incidence of the wing outweighs the roll-motion induced incidence distribution, and a flow field results, with both vortices lying now on the same side of the wing, but having different strengths. This is case C in the figure. The rolling moment, which corresponds to this flow, varies linearly with angular velocity.

There are other aerodynamic aspects of low aspect ratio delta wings, which will not be dealt with in any detail, but for which a few indications to references will be given. Measurements on a low aspect ratio delta wing ( $A = 2$ ) in unsteady, incompressible flow were reported by A. G. Parker in Ref. 30. He determined the vortex location, vortex burst location, and upper surface pressure distributions in an oscillatory airstream. Investigations of the flow field of delta wings at hypersonic speeds have been performed by E. J. Cross, Ref. 31, by D. M. Rao and A. H. Whitehead, Ref. 32, among others. The latter work was performed with regard to the problem of intense heating observed on the leeward side of wings. It is this heating problem in connection with the vortex flows that becomes of greater importance there, as the surface pressures on the lee contribute only little to the aerodynamic loading at high supersonic Mach numbers.

This type of flow past low aspect ratio delta wings at incidence, has found the interest of many research workers in the past, not only in connection with the application to missiles, but also in connection with the development of the "Concorde" supersonic transport. Some of the early work should be mentioned here; it is due to, e.g. L.P. Tosti, Ref. 33; M. Roy, Ref. 34; T. Örnberg, Ref. 35; P.T. Fink, Ref. 36; D.J. Marsden et al, Ref. 37; H.F. Emerson, Ref. 38, to cite only some.

## 2.2 Rectangular Wings

We have up to now dealt with low aspect ratio wings of delta planform, because they are used quite often. Let us continue with rectangular planforms, which have applications on missiles, too. The dimensions of the rectangular wings of interest to us are such that span and chord are of about the same magnitude; i.e., the wings are, more or less, of low aspect ratio again. Another possible shape includes the trapezoidal wing; which may, in some cases, differ only little from the rectangular wing. If this is the case, one may expect, that their flow fields will not differ in essence. These wings now have a leading edge, as well as a more or less pronounced side edge. We shall try first to get some insight into the flow which passes over the leading edge, and then investigate what kind of flow occurs at the side edges.

We consider the rectangular wing, having a thin profile with a more or less rounded nose, and we assume that there is a region in the center part, where the flow is not influenced too much by the flow over the side edges, and can be treated as being more or less two-dimensional. These thin profiles, in a flow at incidence, often do not have the desired flow field and pressure distribution, as is shown schematically in Fig. 27 on the left hand side. Instead, we observe the type of flow depicted on the right hand side of the figure. It is characterized by a separation bubble from the leading edge. In this case, the boundary layer flow around the leading edge is still laminar when it separates in the adverse pressure gradient region. Further downstream, as a free shear layer, it becomes turbulent and the flow is then able to reattach to the wall. The separation bubble develops with increasing incidence from an initially short bubble to one, which, at higher angles of incidence, extends over most of the profile and finally into the wake. The pressure distribution on a thin profile with a flow, exhibiting such a "long bubble", is also given schematically in Fig. 27. Compared with the profile on the left hand side, with attached flow, one notices the reduced suction peaks, followed by a constant pressure region underneath a large part of the bubble.

In the case, in which the wing is a thin flat plate, with a sharp leading edge, we have a flow which is similar to that dealt with before. The flow, which is attaching underneath, will not be able to go around the sharp edge; instead it will separate there and reattach on the upper surface of the wing somewhat downstream. The flow pattern is then again characterized by a leading-edge bubble. Inside the bubble we have a rotating flow. Results of research work concerning the topic of separation bubbles have been presented by A.D. Young in Ref. 39.

We are turning now to the flow around the side edges of a wing at incidence. We consider again wings of rectangular shape, flat plates with sharp edges, as were investigated by H. Winter in Ref. 40. The flow from the pressure side around the side edge to the upper side separates at the sharp edge. A vortex sheet is formed by the separating stream surfaces from the lower and upper wing surface. The vortex sheet rolls up into a vortex core, which is lying above the wing. This vortex flow is shown schematically in Fig. 28. It interferes with the flow passing around the leading edge, which we have discussed already above.

In Fig. 29 a-b are given the pressure distributions on the suction side of a rectangular plate in a flow at angles of incidence  $\alpha = 8^\circ$  and  $\alpha = 30^\circ$ , respectively. In the case of the flow at the lower angle of incidence, we observe in the spanwise pressure distributions near the side edges suction peaks, as we would expect them underneath a side-edge vortex. At the high angle of incidence, the flow in the center part of the wing is dominated by flow separations, while we again observe, near the side edges, the suction peaks which are due to the vortices. The results of force measurements, carried out by H. Winter on a number of rectangular plates for a wide range of aspect ratios are presented in the following diagrams. Fig. 30 presents the normal force coefficients as obtained up to high angles of incidence. We notice immediately how the nonlinearity of the curves which is due to the vortices above the wing, increases as the aspect ratio of the wings decreases. The vortex flow is then influencing the flow field on the suction side to a larger and larger proportion. In Fig. 31 the moment coefficients (related to the chord) are given for these wings.

The work of H. Winter, on which was reported here, also contains the results of investigations on flat plates of other planforms, as elliptical, semi-elliptical and delta.

There are also results available from the investigations of N. Scholz, Ref. 41, who carried out force and pressure measurements on low aspect ratio wings, too. Furthermore, in Ref. 42, there are given results by K. Gersten of lift measurements on a series of rectangular wings of various aspect ratios. Some of the material is also discussed in the book by H. Schlichting and E. Truckenbrodt, Ref. 43. R.H. Wickens, in Ref. 44, investigated the vortex wake, as well as the distribution of the aerodynamic load of low aspect ratio rectangular plates. There should also

be mentioned the very early work on such wings by F. Ahlborn in Refs. 45 and 46.

### 2.3 Wings with Strakes

It has been shown, that on highly swept back wings in a flow at angle of incidence the flow separates from the leading edges, forming the well known rolled-up vortex sheets above the wing. On the other hand, on wings with moderate sweep, leading-edge separation occurs in an erratic and unsteady manner. While the steady vortex separation on slender wings generates large lift increments, the unsteady erratic separation on large aspect ratio wings provides undesired effects such as lift decay and force fluctuations, see e.g. D.G. Mabey, Ref. 48. Techniques have been developed successfully, to enhance the formation of stable leading-edge vortices by means of strakes or by blowing a discrete jet in spanwise direction, but the underlying flow mechanisms are not well understood. It is not intended here, to deal with the technique of spanwise blowing. A few references must suffice as a possible introduction to the subject: The work of J.J. Cornish, Ref. 49; C.J. Dixon, Ref. 50; H. Werlé and M. Gallon, Ref. 51 and R.G. Bradley et al, Ref. 52, to give only a few names. We shall give some consideration to wings with strakes in the following, since they may find application on missiles, as they have found already on airplanes.

In recent years, wing planforms have come into use with aircrafts, which are characterized by a so called "strake" ahead of the main wing. The strake has the shape of a slender delta wing, or nearly so. Examples are the SAAB-35 "Draken" with a double delta wing and the Northrop F-5 "Tiger II", having a trapezoidal wing with strake; others are the YF-16 of General Dynamics and YF-17 of Northrop. Such wings with strakes have now also found interest for application on missiles; thus it seems justified to report here on some of the results which have so far been obtained in connection with the use on airplanes.

The area of such an additional delta wing in front is usually only about 10 % of that of the main wing. Because of the large sweepback of the relatively sharp leading edges of the strake one has a strong vortex flow on the suction side, which influences the flow towards and above the main wing and which might be felt even on the controls in the rear.

There are two different cases to be dealt with; these are shown schematically in Fig. 32. On wings which have no or only moderate leading-edge sweepback and rounded noses at small angles of attack (and as long as shocks are of no importance), the vortex flow of the strake will interfere with an essentially attached flow on the main wing. The influence of the strake vortices becomes of importance at higher incidence, when the main wing would - without strake - exhibit flow separations of one or the other type (trailing-edge separation, separation bubbles at the leading edge), but also in transonic flow, when there would be shock induced separations. Secondly, there is the case, where the main wing, too, has a leading edge which is sufficiently swept back and sharp. Then, we have in a considerable range of incidences and Mach numbers, the strake vortex flow interfering with the main wing's vortex flow, as is the case for the double delta wing.

Results of experimental investigations on double delta wings at low speeds have been presented by V. Holmboe, Ref. 53; W.H. Wentz and M.C. McMahon, Refs. 54 and 55; and by P. Krogmann, Ref. 56; for high subsonic and supersonic speeds, there are results, e.g. by E.J. Hopkins et al., Ref. 57; V.R. Corsiglia et al., Ref. 58 and W. Stahl, Ref. 59.

As to the effect of such strakes on wings with essentially low sweep, we have the results by W.P. Henderson and J.K. Huffman in Ref. 60. W. Staudacher gives the results of tests undertaken on an aircraft model having trapezoidal and swept wings with various strakes at subsonic, transonic and supersonic speeds in Refs. 61 and 62. W. Schröder, in Refs. 63 and 64, reports on flow investigations on wings with cranked leading edges and unswept and swept outer wings at low speeds. W. Baumert, in his investigation of a wing-body combination with a trapezoidal wing, made velocity measurements in the outer flow above the model, as well as pressure measurements on the wall, see Refs. 65 and 66.

In Fig. 33 results are presented for a delta wing without and with strake in subsonic, transonic and supersonic flow, as reported in Ref. 59. The lift coefficient curves of the basic wing without strake show an abrupt decrease at high angles of attack for subsonic and transonic Mach numbers; they do not show these jumps for the supersonic Mach numbers; at least not in the incidence range investigated. The addition of the strake has a pronounced effect on the lift coefficients at high incidence in subsonic and transonic flow; they now further increase continuously, and it is seen that the abrupt decrease in the lift coefficient in the transonic case is displaced now to a larger incidence. There are now much higher lift coefficients available at high incidences.

An explanation is found for the discontinuities in the lift curves of the basic wing in the changes occurring in the flow field above the wing. The leading-edge vortices at first develop regularly with increasing incidence; at large enough incidences there is vortex breakdown, observed first somewhat downstream of the trailing edge. With increasing incidence the breakdown region moves forward, crossing the trailing edge and progressing upstream on the wing. Flow observations showed that at a certain incidence, this region of rather unorganized vortex flow was jumping forward, from behind the trailing edge, to the suction side of the wing, with only a very little increase in incidence;

(subsequently it was moving forward on the wing relatively slowly with incidence). This leads to a corresponding abrupt increase in pressure on the upper side and to the observed sudden decrease in lift. As this does not occur for both vortices at the same incidence, the lift curves show two discontinuities. When we add the strake to the basic wing, we have vortices from the main wing and the forward panels. Fig. 34 is showing schlieren pictures of the flow for both the basic wing and the wing with strake, at a Mach number  $M_\infty = 0.9$  for an angle of incidence  $\alpha = 18^\circ$ . One can immediately observe the effect of the addition of the strake: On the suction side of the basic wing the breakdown region reaches far forward on the wing (upper picture); on the wing with strake, however, this region is still downstream of the trailing edge (outside of the picture).

We turn now to the case where a trapezoidal wing is fitted with a strake. The results given in Fig. 35, as obtained by W. Staudacher in Ref. 62, show the influence on the lift coefficient when adding a strake to a trapezoidal wing on a fuselage at a Mach number of  $M_\infty = 0.5$ . At moderate angles of incidence, there begins a gain over the wing without strake, which becomes very considerable at high incidences. The increase of maximum lift coefficient for the wing with strakes in the regime of low subsonic to transonic velocities, is shown in Fig. 36; the gain being considerable up to the transonic Mach numbers. Detailed investigations of the effect of the strake vortex flow on the flow above the main wing at low speeds were carried out by W. Baumert; Refs. 65 and 66, on a trapezoidal wing with aspect ratio  $A = 3.2$  on a cylindrical body, the strake having a leading-edge sweep,  $\phi = 75^\circ$ . He found that the suction on the main wing is reduced inboard of the vortices, the gain in lift is effected on the wing outboard of the vortices.

On grounds of the knowledge obtained with aircrafts about the advantageous aerodynamic characteristics of wings with strakes, their application on missiles may be envisaged. Here, the situation is somewhat different, as we have seen, that missile wings are often just sharp-edged plates of small aspect ratio. Their semispans, as well as those of the strakes are small compared to the body radius. Furthermore, wing and strake may have to operate in the presence of a long forebody. Experimental investigations on such a typical missile configuration were performed by M. Akcay et al, see Ref. 67. The results obtained showed, that the addition of strakes, in subsonic and transonic flows, leads to considerable gains in normal force for higher angles of incidence, see Fig. 37. Pressure measurements on the wing's upper surface, at Mach number  $M_\infty = 0.83$ , revealed that with strake there is considerably increased suction on the forward part of the wing, as is shown in Fig. 38.

Attempts have been made to more fully understand the underlying mechanisms in the interaction of strake and main wing. S.P. Fiddes and J.H.B. Smith, Ref. 68, showed in a theoretical investigation, that the strake vortices induce a velocity field, which causes an increased effective sweep of the leading edge of the main wing near the kink section as well as an increased effective incidence of the outboard region of the main wing. Some of their results are given in Fig. 39. They suggested that the outflows induced by the strake vortices may be instrumental in delaying the low-speed stall of the wing.

E. Wedemeyer in Ref. 69 presented a theoretical study of the stability of leading-edge separation on delta wings, which is of pertinence in connection with the subject of strake effects. This investigation is an attempt to explain, why there are two distinct types of leading-edge separation. The theory follows previous results regarding the internal structure of leading-edge vortices by M.G. Hall and H. Ludwig and their stability by H. Ludwig, see Refs. 4 and 5.

In the course of his fundamental investigations on the stability of helical flows, Ludwig has shown that a stable leading-edge vortex, entering a region of increasing static pressure eventually transforms into a highly unstable structure. This finding was offered by Ludwig as an explanation for the vortex breakdown phenomenon. Extending Ludwig's hypothesis it is supposed that the two distinct types of leading-edge separation can be attributed to the existence or non-existence of a stable separated vortex.

For slender delta wings computational methods have been developed, e.g. by C.E. Brown and W.H. Michael, or J.H.B. Smith, discussed later, which permit approximate solutions for the separated flow disregarding the internal vortex structure. To these solutions are fitted Hall's solutions for the vortex core. In this way, complete - though approximate - solutions are constructed which relate the "external" parameters angle of sweep and angle of incidence to the "internal" parameters which characterize the structure of the vortex core, i.e. the velocity distributions within the core. Considerations of the stability of the corresponding vortex cores lead to the following results: For highly swept delta wings at angles of incidence below a critical value stable vortices exist; furthermore, the critical angle of incidence beyond which no stable vortex exists, decreases with decreasing angle of sweep, and for sweep angles below a limiting value unstable vortices are found for any angle of incidence. The calculated results are confirmed by experimental findings, see Fig. 40. It is supposed that the theory outlined above accounts for the performance of a strake on wings with moderate sweep angle.

Fig. 41 shows schematically the effect of the strake on the main wing. The strake vortices induce an outflow on the main wing, especially near the kink in the leading edge, as was shown also by S.P. Fiddes and J.H.B. Smith and mentioned earlier. The induced flow velocity changes



the initial flow direction thus increasing the effective sweep of the leading edge. If at higher angles of attack the flow separates from the leading edge of the main wing the inboard flow is stabilized due to the higher effective sweep there. This stable separation generates large lift increments, while without strake an unstable separation would lead to lift decay and force fluctuations. Wedemeyer quotes experimental results which lend support to his flow model.

### 3. THEORETICAL PREDICTIONS

Having a wing in a flow at a certain velocity and incidence, one would, of course, like to be able to predict its aerodynamic characteristics in a sound theoretical way and to obtain results which afterwards would be in reasonable agreement with reality. One would like to get, at least, the overall forces and moments acting on the wing, more preferable would be, if a prediction of the pressure distributions was possible, which would, of course, give much more information as to the origin of the various force components. What one has to do is to obtain first an insight into the relevant features of the flow, something we have tried to do in the previous considerations. We wish to describe this flow as accurately as is necessary and keep our description as simple as possible. For this reason, we try to devise a flow model, which we think represents the physical reality in its essential features, but is still mathematically treatable.

In Fig. 42 we recall the classical model, as was devised by Prandtl. It consists of one or more horseshoe vortices, with the bound vortices in place of the wing and with the free vortices trailing rearward in the plane of the wing. This vortex system makes possible a satisfactory description of the real conditions in the case of wings, having moderate and large aspect ratios, say  $A \gtrsim 3$ ; it is the basic underlying idea of the classical wing theory, which gives a linear dependence of the lift on incidence:

$$(1) \quad c_L = k_1 \alpha.$$

In the case of wings with small aspect ratio at incidence having a flow field, characterized by vortices above the wing, the vortex model of above has to be changed. It should now allow for the free vortices to lay above the wing, in planes inclined to the plane of the wing under some angle  $\epsilon$ , which itself is a function of the angle of incidence,  $\epsilon = \epsilon(\alpha)$ . Such a vortex system is shown in the lower part of Fig. 42, and it provides, indeed, a nonlinear dependence of the lift on the angle of incidence, of the form

$$(2) \quad c_L = k_1 \alpha + k_2 \alpha^n.$$

Thus, the lift can be considered to be composed of a linear and a nonlinear part, as was already shown in Fig. 3:

$$(3) \quad c_L = c_{L, \text{lin}} + \Delta c_L.$$

A first attempt to leave the simple vortex model of linear theory, was made by W. Bollay in Ref. 70. He presented, for the case of a rectangular wing, a vortex model, in which the free vortices leave from the side edges, trailing at an angle to the plane of the wing of  $\epsilon = \alpha/2$ , the bound vortices are assumed to be constant in spanwise direction. K. Gersten, in Ref. 42, has refined this model by using a circulation distribution which varies in spanwise direction. This theory was extended later on by him to calculate the aerodynamic forces and moments for wings of arbitrary planforms, see Ref. 71.

We shall now consider the slender delta wing, assumed to be thin and flat, in a flow at incidence. The flow about the wing was seen to be characterized by the leading-edge vortices above the wing, which give rise to an additional nonlinear lift contribution. The first attempt to calculate this flow field was made by R. Legendre in Ref. 72, by using a simplified vortex configuration and R.T. Jones' slender body theory, Ref. 73. He proposed a flow model in which each leading edge vortex is replaced by a concentrated line vortex, and where the flow is considered to be inviscid and conical, fulfilling the Kutta condition at the leading edges. M.C. Adams, in Ref. 74, proposed a theoretical approach, proceeding in the same manner. This theory does not, however, produce a unique solution for the lift. In this approach the condition was imposed that no resultant force was to be acting on the concentrated vortex. R.H. Edwards, Ref. 75, used the same simple flow model; but he introduced now a vortex sheet from the leading edge to the vortex, with the condition that there should be no resultant force on the vortex and the vortex sheet. The lift coefficient comes out to be

$$(4) \quad c_L = \frac{\pi}{2} A \alpha + \pi A^{1/3} \alpha^{5/3}.$$

C.E. Brown and W.H. Michael, in Ref. 76, used again the flow model with a concentrated vortex and a connecting plane vortex sheet to the leading edge, with the same condition as was used by R.H. Edwards, Fig. 43 depicts their flow model. The results for the lift agree, to a first approximation, with those of R.H. Edwards of eq. 4. K.W. Mangler and J.H.B. Smith in Ref. 77, represented each leading-edge vortex by a curved vortex sheet, the inner part is taken to be a potential vortex, the outer vortex sheet lies on an analytic curve; see Fig. 43. The numerical results

for the lift coefficient can be well approximated by the following expression:

$$(5) \quad c_L = \frac{\pi}{2} A \alpha + 4 \alpha^2.$$

This result contains a dependence of the lift coefficient on aspect ratio only in the linear part. J.H.B. Smith, in Ref. 78, gave for the same flow model as above, an improved iterative calculation procedure, which leads to

$$(6) \quad c_L = \frac{\pi}{2} A \alpha + 3.2 A^{0.3} \alpha^{1.7}.$$

All the authors calculated the lift of the flat, slender delta wing making use of the slender body theory. The lift coefficients obtained are all independent of the Mach number. The linear part has, in all cases, the value which is given by the slender body theory of R. T. Jones :

$$(7) \quad c_{L, \text{lin}} = \frac{\pi}{2} A \alpha.$$

The application of such inviscid models of flow separation using the vortex sheet model and the assumptions of slender-body theory, as was done by K.W. Mangler and J.H.B. Smith, has been extended to various more special cases. J.E. Barsby calculated the flow past conically - cambered slender delta wings with leading-edge separation in Ref. 104. D.I. Pullin treated the flow past a slender delta wing at yaw in Ref. 105, and the flow separation from yawed delta wings was also investigated by I.P. Jones, see Ref. 106. Oscillatory slender wings were dealt with by R.K. Cooper, Ref. 107. Non-conical flows past a slender plane wing with curved leading edges and a delta wing with lengthwise camber have been studied by R.W. Clark, Ref. 108.

We have so far presented some of the more essential contributions to calculating the non-linear lift of slender wings in incompressible flow at incidence. A survey of the authors of the better know methods, together with the underlying flow models is given in Fig. 44. The material was compiled by W. Sonnleitner and W. Kraus in Ref. 79, and they have given a very detailed analysis of these various contributions there.

A short description will now be given of an attempt to extend the initially discussed theories to supersonic velocities. All the authors mentioned earlier (Adams, Edwards, Brown-Michael, Mangler-Smith and Smith) give the lift coefficient as the sum of a linear term and a nonlinear term. The linear contribution is the solution of the slender-body theory. To this is added a nonlinear contribution which is provided by the various vortex models. In each case, therefore, one adds to the solution obtained for the incompressible cross-flow about a slender wing - with attached flow around the leading edges - the solution for the flow field due to the vortex model under consideration. It seems obvious to try to improve the linear contribution,  $c_{L, \text{lin}}$ , in order to get better predictions in supersonic flow than were hitherto obtained. Instead of the linear term of the slender-body theory, one introduces now the linear solution obtained for a delta wing, (with attached flow around the subsonic leading edges), by the well known methods, using source distributions or conical supersonic flow theory. These methods are discussed, for example, in the book of H. Schlichting and E. Truckenbrodt, Ref. 43. The result for the lift coefficient, including the nonlinear part, is now as follows:

$$(8) \quad c_L = \frac{m}{E'(m)} \frac{2\pi}{\sqrt{M_\infty^2 - 1}} \alpha + k_2 \alpha^n$$

In this equation,  $m$  is the leading-edge parameter with  $m < 1$  for subsonic leading edges, and  $E'$  being an elliptical integral. In this manner, the solutions are now, in their linear part, dependent on the Mach number. This method of extending some of the theories discussed above, has been proposed, independently, by R. Hürliemann in Ref. 94 and by W. Stahl in Ref. 95.

The rectangular wing of small aspect ratio was again treated by S.D. Ermolenko in Ref. 89 in a way similar to W. Bollay's approach. The lifting surface in subsonic flow is replaced by a system of discrete bound vortices of constant spanwise circulation, which can, however, vary for each vortex line along the chord. The free vortices are trailing from each side edge in a vertical plane, at a certain angle to the wing chord, which varies with incidence, aspect ratio and Mach number. A more realistic modeling of the side-edge vortices was achieved by S.M. Belotserkovskii, Ref. 96 developing further Ermolenko's method. He employs a finite number of discrete vortex lines, which are formed by small straight elements, each of which is aligned with the local flow in an iterative procedure.

C. Rehbach in Ref. 97 and 98 as well as O.A. Kandil in Ref. 99, O.A. Kandil et al in Ref. 100 developed inviscid discrete vortex methods, with which it is possible to calculate the flow about wings of various shapes. In the following a somewhat more detailed treatment of such a discrete-vortex approach is presented, which approximates the continuous bound and free vortex sheets, including the vortex wake springing from the side or leading edges. As an example, we follow here the approach as forwarded by O.A. Kandil in Ref. 99, and consider the cases of thin wings, having a parallelogram and delta planform, respectively, set at incidence, and with the flow assumed to be incompressible. The representation of the lifting surface by a bound-vortex sheet, is approximated

here by discrete vortex lines, arranged in such a way as to form a lattice. The free-vortex sheets leaving from the sharp edges, like the trailing edge, side edges, leading edges, are modelled by vortex lines, which do not intersect, and which are made up of short, straight vortex segments, except for the last segment, which is semi-infinite. The direction of each of the short segments is determined as part of the solution, the last segment is in the direction of the free stream. The arrangement of the discrete vortices is shown in Fig. 45 for both the parallelogram and the delta wing. At the tip of the parallelogram wing, a vortex line originates from the end of each row, so that a number of them are shown coincident in chordwise direction. In the iterative procedure to obtain the solution, these lines lift off the wing and align themselves with the flow. In the case of the delta wing, the bound-vortex lattice has extensions reaching out of the wing region, at the end of which the free-vortex lines are originating. Again, these vortex lines, in the course of the iterative computation, align themselves with the flow.

The figure shows how the lattice divides the wing region into, not necessarily planar, elements, each containing a control point, where the boundary condition of tangential flow, is fulfilled. Each element has a bound-vortex segment on the upstream spanwise edge and along the outboard chordwise edge. The Kutta condition at those edges, where it is to be prescribed, is satisfied by omitting vortex lines between the edge under consideration and the nearest control points.

Two convergence criteria must be satisfied, namely for the chosen number of elements the shape of the computed wake must converge, and subsequently the aerodynamic coefficients must converge as the number of elements is increased.

In his approach to the calculation of the flow past a delta wing, C. Rehbach, Ref. 98 starts out with the discrete vortex model for a rectangular wing. He then progressively deforms the planform by holding the trailing-edge span constant and reducing the original leading edge to zero. This procedure is sketched in Fig. 46. The application of this discrete vortex method is not restricted to specific planforms, very large or very small aspect ratios, thin wings or small angles of attack. Furthermore, the method can be used to handle the problem of interacting lifting surfaces, because of its capability to adequately provide the shape of the wake; an example is given in the cited reference. Examples of canard-wing configurations have also been treated by O.A. Kandil, D.T. Mook and A.H. Nayfeh in Ref. 101.

The method has been extended to be used for compressible flows by applying a modified Prandtl-Glauert transformation; it is however restricted to wings either with high local angles of attack and moderate subsonic Mach numbers or with moderate local incidence and high subsonic Mach number. For the effect of compressibility on the predicted nonlinear loads see also the work of O.A. Kandil, D.T. Mook, and A.H. Nayfeh in Ref. 102. For the sake of completeness it should be mentioned here, that the prediction of the unsteady, nonlinear aerodynamic characteristics of rectangular and delta wings has been dealt with by E.H. Atta, O.A. Kandil, D.T. Mook, and A.H. Nayfeh in Ref. 103. On the numerical calculation of three-dimensional unsteady flows with vortex sheets has been reported by C. Rehbach in Ref. 109. Such discrete vortex methods have been developed also by other authors, e.g. by W. Schröder, Ref. 110.

A quite different method for the prediction of the aerodynamic characteristics of wings with flow separation from the swept leading edges or from side edges has been given by Polhamus in Ref. 111. The underlying idea is that the leading-edge suction developed in flow attached around the edge cannot be realized at a sharp edge, where the flow separates in the well known way. Instead, it is the vortices above the wing to which an equivalent normal force is attributed, as sketched schematically in Fig. 47, a hypothesis which was found to work. Polhamus provided charts for the prediction of the subsonic vortex lift characteristics of wings of various planforms in Ref. 112. It has been found that with this approach one is able to predict remarkably well the lift and drag forces, as well as pitching moments and roll damping of plane wings; but it cannot give flow-field details or detailed surface pressure distributions. For various applications of the leading-edge suction analogy see also J. E. Lamar and J.M. Luckring, Ref. 113.

The application of a general computational technique to the solution of the subsonic, three-dimensional flow over wings with leading-edge vortex separation has been presented by J.A. Weber et al in Ref. 114. The method is capable of predicting forces, moments, and detailed surface pressures on thin, sharp-edged wings of rather arbitrary planform.

The essential elements of the inviscid and incompressible flow model are the wing, the trailing sheet (wake), the sheet emerging from the wing leading edge and tip (free sheet), and the rolled-up core or spiral region (fed sheet) fed by the leading-edge and tip vortex sheets, see Fig. 48. The boundary conditions imposed on these elements are, that the flow must be everywhere parallel to the wing surface, and that the free sheet and wake cannot support a pressure differential  $\Delta c_p$  and must be aligned with the local flow. The fed sheet is an entirely kinematic extension of the free sheet, and no boundary conditions are applied to the fed sheet. This is a simplified model of the true physical vortex-core region. The size of the fed sheet is taken from the conical-flow results of Smith, Ref. 78. Kutta conditions are imposed along the leading, side, and trailing edges of the wing in the presence of free sheets emanating from these edges.

The geometric description is that of a general three-dimensional (not conical) configuration consisting of a thin wing, free sheet, wake, and fed sheet (Fig. 48). The wing geometry is arbitrary in the sense that leading and trailing edges may be curved or kinked and the lifting surface may have arbitrary camber and twist. The configuration is subdivided into a network of quadrilateral panels whose corner points are defined by coordinates in transverse cutting planes. The trace of the kinematic fed sheet in a transverse cutting plane is either a circular arc extending over  $180^\circ$  or a single planar panel locally perpendicular to the free sheet.

Briefly, the main features of the numerical representation are the following. The wing and free sheet are represented by network distributions of doublets which vary as piecewise continuous quadratic functions in each of two coordinate directions over each panel of the network. An analysis type of network is employed on the wing (geometry of the wing is specified), and a design type network of doublets simulates the free sheet (unknown free-sheet geometry, zero pressure jump specified). Network types used for the wake and fed sheet are specializations of the design type network.

Let us turn now to a time-dependent discrete-vortex method for the prediction of the flow field and the aerodynamic characteristics of wings, forwarded by S.M. Belotserkovskii. The problem is no longer treated as a stationary one, one rather looks now at the time-dependent formation of the flow field in the following way: The body under consideration is regarded initially (at time  $t < 0$ ) to be at rest; it is then suddenly accelerated to its flight velocity  $U_\infty$  (at time  $t = 0$ ) and subsequently moving uniformly. The flow field which develops around the body and behind it, is computed numerically in discrete time steps. The computation is carried out until a limiting flow pattern is obtained at time  $t \rightarrow \infty$ , provided it exists. Results have been reported by S.M. Belotserkovskii in Ref. 115 for the case of a thin, plane rectangular wing of aspect ratio  $A = 1$ , in an incompressible flow at angle of attack  $\alpha = 30^\circ$ . The computed flow field is shown in Fig. 49 at a time  $t$  during the formation of the flow and for the limit of the formation process ( $t \rightarrow \infty$ ). The latter results are in agreement with those obtained with stationary theories. In the calculations the Kutta condition was not enforced at the leading edge, i.e. flow separation was not taken into account there. The specific problem of the bow shock wave of a pointed wing has been investigated by Y.C. Sun in Ref. 116 and 117. He has treated the case of a delta wing with sharp leading edges in stationary supersonic flow at zero incidence. By means of the analytical method of characteristics he determined the properties of the bow shock wave, as its shape and strength, when the leading edges pass from subsonic to supersonic. Fig. 50 shows, for a wing with rhombic cross-section of a given thickness ratio, the relative bow shock wave slope in dependence of the relative leading-edge slope. The bow shock wave is displaced outwards more and more relative to the Mach cone, when the edges pass from subsonic to supersonic; even in the case of a supersonic leading edge the bow shock wave may be detached from the leading edge.

Also, experimental results have been obtained for this wing by H. Esch, Ref. 10, which, as can be seen from the same figure confirm the theoretical results satisfactorily, the latter not taking into account the displacement effect of the boundary layer.

Having given a short survey of various of the more important theoretical methods for the prediction of aerodynamic characteristics of low aspect ratio wings, results of these methods are presented and compared with experimental results.

In Fig. 51 the predictions due to the theories of C.E. Brown and W.H. Michael, Ref. 80, R.H. Edwards, Ref. 75, K.W. Mangler and J.H.B. Smith, Ref. 77, J.H.B. Smith, Ref. 78, as well as those due to the linear theory of R.T. Jones, Ref. 73, are compared with the results of wind-tunnel tests of P.T. Fink, Ref. 36, which he obtained for a slender delta wing in incompressible flow up to high incidences. The comparison shows that all the nonlinear theories predict higher lift coefficients than are obtained experimentally, the differences are considerable in the case of the theory of Brown and Michael.

The spanwise pressure distribution on suction and pressure sides, as predicted by the theory of J.H.B. Smith is compared to the results of measurements obtained by D. Hummel in Ref. 13, on a slender delta wing at angle of incidence  $\alpha \approx 20^\circ$ , see Fig. 13. The theory describes in essence the characteristic feature, namely the main suction peak underneath the leading-edge vortex; it cannot take care of the secondary and tertiary vortices on the suction side. The observed pressure distribution on the lower surface of the wing is also given by the theory in its main features.

The predictions of the theories of Brown and Michael and of Mangler and Smith are now also compared to experimental results obtained in supersonic flow for various Mach numbers on a thin slender delta wing (with a rather small conical body) by W. Stahl in Ref. 95. Fig. 52 shows the lift coefficient versus angle of incidence as calculated from the theories in their original versions (for incompressible flow) as well as the results, when extended to take into account the influence of Mach number, in the manner proposed by R. Huerlimann and W. Stahl and discussed above. Again, the experimental results are overestimated by all the theoretical methods, though the extended versions of the theories lead to closer predictions than the original versions.

Comparison of predictions due to the theory of Gersten, with experimental results for rectangular wings of aspect ratio  $A = 0.5$  and  $A = 1.0$  are shown in Fig. 53. The theoretically pre-

dicted lift coefficients and the experimental results are seen to agree rather well. In Fig. 54 is given a comparison between predicted and measured lift coefficients for a swept wing. The theory of Gersten is seen to agree quite well with experimental data in this case, too.

Next we consider some results of the discrete-vortex method developed by O.A. Kandil. Fig. 55 shows the computed wake shape for a rectangular wing in the flow at angle of incidence  $\alpha = 15^\circ$ . There is no direct comparison given with a real wake, but the computed wake shows, to a certain degree, the rolling up process of the real side-edge vortex sheet. The computed wake of a slender delta wing at incidence  $\alpha = 15^\circ$  is depicted in Fig. 56, the leading-edge vortex-sheet is seen to have rolled up about a turn.

Numerical results obtained by S.M. Belotserkovskii, S.D. Ermolenko, and O.A. Kandil for the normal forces and pitching moments of a rectangular wing of aspect ratio  $A = 1$  are presented in Fig. 57a and 57b, respectively; and compared to experimental data. There is reasonable agreement of the predictions of Belotserkovskii and Kandil with most of the experimental results. The spanwise variation of the local normal-force coefficient for the rectangular wing at two angles of attack is given in Fig. 58; the predictions of K. Gersten, C. Rehbach, and O.A. Kandil are compared to experimental data. The normal-force and pitching-moment coefficients of an  $A = 2$  delta wing in incompressible and compressible flow have been computed by O.A. Kandil and compared to experimental data in Fig. 59.

The capability of the method of J.A. Weber et al to predict overall wing coefficients accurately is shown in Fig. 60 for a delta wing of aspect ratio 1 at  $M_\infty = 0$ . The figure shows the non-linear variation of the normal-force coefficient  $c_N$  with angle of attack  $\alpha$ . Several values of  $c_N$  were computed for angles of attack up to  $20^\circ$ ; they agree well with experimental data and theoretical results from the leading-edge-suction analogy of Polhamus. The corresponding load distribution at  $\alpha = 20^\circ$  is plotted in Fig. 61 and compared with experimental results. Although only 25 wing panels were used on one-half of the configuration, the completely three-dimensional non-conical load distribution is well predicted, including the location of the vortex-induced pressure peaks and the decrease of the load toward the trailing edge.

As a last remark, it should be stated that the material presented herein can by no means represent all the results of experimental and theoretical work available. The reader is also referred to the collection of various results on aerodynamic characteristics of low aspect ratio wings in the Engineering Sciences Data, Ref. 26; as well as to the review articles by A.G. Parker, Ref. 118, D.J. Peake, Ref. 119 and J.H.B. Smith, Ref. 120. The present paper was intended to acquaint the reader with some of the pertinent and interesting facts about low aspect ratio wings, their characteristic flow field and aerodynamic behaviour, as well as to introduce him to some of the more important theories available. The use of the references given should provide immediately a large amount of additional useful material.

#### REFERENCES

- 1 Küchemann, D. Types of flow on swept wings. J. Roy. Aeron. Soc., Vol. 57, 1953, pp. 683-699.
- 2 Küchemann, D. Vortex motions. Weber, J. ZAMM, Vol. 45, 1965, pp. 457-474.
- 3 Werlé, H. Sur l'éclatement des tourbillons. ONERA N.T. 175 (1971).
- 4 Ludwig, H. Vortex breakdown. DLR-FB 70-40, 1970.
- 5 Hall, M.G. Vortex breakdown. Ann. Rev. Fl. Mech., Vol. 4, 1972, pp. 195-218.
- 6 Hayashi, Y. Flow field in a vortex with breakdown above sharp-edged delta wings. Nakaya, T. Jap. Nat. Aerosp. Lab. TR-423, 1975.
- 7 Squire, L.C. Flow regimes over delta wings at supersonic and hypersonic speeds. Aeron. Quart., Vol. 27, 1976, pp. 1-14.
- 8 Szodruch, J. On the lee-side flow over delta wings at high angle of attack. Ganzer, U. AGARD-CPP-247, 1978, pp. 21.1 - 21.7.
- 9 Küchemann, D. On some threedimensional flow phenomena of the transonic type. Symp. Transsonicum ed. by K. Oswatitsch, Springer Verlag Berlin, Göttingen, Heidelberg, 1964, pp. 218-248.

- 10 Esch, H. Private communication, DFVLR, 1969.
- 11 Rainbird, W.J.  
Crabbe, R.S.  
Peake, D.J.  
Meyer, R.F. Some examples of separation in three dimensional flows.  
Can. Aeron. Space J., 1966, pp. 409-423.
- 12 Schlichting, H. A survey of some recent research investigations on boundary layers and heat transfer.  
J. Appl. Mech., Vol. 38, 1971, pp. 289-300.
- 13 Hummel, D. Zur Umströmung scharfkantiger schlanker Deltaflügel bei großen Anstellwinkeln.  
Z. Flugwiss., Vol. 15, 1967, pp. 376-385.
- 14 Hummel, D. On the vortex formation over a slender wing at large angles of incidence.  
AGARD-CPP-247, 1978, pp. 15.1 - 15.17.
- 15 Stahl, W.  
Hartmann, K.  
Schneider, W. Force and pressure measurements on a slender delta wing at transonic speeds and varying Reynolds numbers.  
AGARD-CP-83-71, 1971, pp. 9.1 - 9.12.
- 16 Smith, J.H.B.  
Kurn, A.G. Pressure measurements on a slender rhombic cone at incidence at Mach numbers from 0.4 to 1.1.  
ARC, RM 3626, 1970.
- 17 Hummel, D.  
Srinivasan, P.S. Vortex breakdown effects on the low speed aerodynamic characteristics of slender delta wings in symmetrical flow.  
J. Roy. Aeron. Soc., Vol. 71, 1967, pp. 319-322.
- 18 Schneider, W.  
Stahl, W.  
Hartmann, K. Interferenz-Erscheinungen an einer schlanken Flügel-Rumpf-Anordnung in kompressibler Strömung.  
DFVLR/AVA-Bericht 73 A 06, 1974.
- 19 Gersten, K.  
Hummel, D. Untersuchungen über den Einfluß der Vorderkantenform auf die aerodynamischen Beiwerte schiebender Pfeil- und Deltaflügel von kleinem Seitenverhältnis.  
DLR-FB 66-86, 1966.
- 20 Henderson, W.P. Effects of wing leading-edge radius and Reynolds number on longitudinal aerodynamic characteristics of highly swept wing-body configurations at subsonic speeds.  
NASA TN D-8361, 1976.
- 21 Bartlett, G.E.  
Vidal, R.J. Experimental investigation of influence of edge shape on the aerodynamic characteristics of low-aspect-ratio wings at low speeds.  
J. Aero. Sci., Vol. 22, 1955, pp. 517-533.
- 22 Gersten, K.  
Decken, J.v.d. Aerodynamische Eigenschaften schlanker Flügel in Bodennähe.  
WGLR Jahrbuch 1966, pp. 108-125.
- 23 Decken, J.v.d. Berechnung der Druckverteilung an schlanken dicken Flugkörpern in Bodennähe.  
Dissertation TU Braunschweig, 1969.
- 24 Ermolenko, S.D.  
Ragazin, Yu.A.  
Rogachev, G.V. Application of the nonlinearity theory of a lifting surface to the calculation of aerodynamic characteristics of a triangular wing moving close to the earth's surface.  
AD 785154, FTD-HC-23-1802-74.
- 25 Fox, C.H. Prediction of lift and drag for slender sharp-edge delta wings in ground proximity.  
NASA TN D-4891, 1969.
- 26a Low-speed longitudinal aerodynamic characteristics of slender wings.  
Engineering Sciences Data, Item Nr 71006.
- 26b Low-speed normal force and pitching moment of slender wings in ground effect.  
Engineering Sciences Data, Item No. 71007.

- 27 Harvey, J.K.                   Some measurements on a yawed slender delta wing with leading-edge separation.  
ARC RM 3160, 1961.
- 28 Hummel, D.  
Redeker, G.                   Über den Einfluß des Aufplatzens der Wirbel auf die aerodynamischen Beiwerte von Deltaflügeln mit kleinem Seitenverhältnis beim Schiebeflug.  
WGLR Jahrbuch 1967, pp. 232-240.
- 29 Schlottmann, F.               Stationäre und instationäre Rollmomentenderivativa schlanker Flügel in Rollbewegung.  
Z. Flugwiss., Vol. 22, 1974, pp. 331-344.
- 30 Parker, A.G.               Measurements on a delta wing in unsteady flow.  
J. Aircr., Vol. 14, 1977, pp. 547-552.
- 31 Cross, E.J.               Experimental and analytical investigation of the expansion flow field over a delta wing at hypersonic speeds.  
ARL 68-0027, 1968.
- 32 Rao, D.M.  
Whitehead, A.H.Jr:           Lee-side vortices on delta wings at hypersonic speeds.  
AIAA J., Vol. 10, 1972, pp. 1458-1465.
- 33 Tosti, L.P.               Low speed static stability and damping-in-roll characteristics of some swept and unswept low-aspect-ratio wings.  
NACA TN 1468, 1947.
- 34 Roy, M.               Caractères de l'écoulement autour d'une aile en flèche accentuée.  
C.R. Acad. Sci., Vol. 234, No. 26, Paris, 1952, pp. 2501-2504.
- 35 Örnberg, T.               A note on the flow around delta wings.  
Kungl. Tekn. Högsk., Stockholm, Aero TN 38, 1954.
- 36 Fink, P.T.               Wind tunnel tests on a slender delta wing at high incidence.  
Z. Flugwiss., Vol. 4, 1956, pp. 247-249.
- 37 Marsden, D.J.  
Simpson, R.W.  
Rainbird, W.J.           The flow over delta wings at low speed with leading edge separation.  
Coll. of Aeronautics, Cranfield, Rep. 114, 1958.
- 38 Emerson, H.F.           Wind-tunnel investigation of the effect of clipping the tips of triangular wings of different thickness, camber, and aspect ratio - Transonic bump method.  
NACA TN 3671, 1956.
- 39 Young, A.D.               Some special boundary layer problems.  
Z. Flugwiss. Weltraumforsch., Vol. 1, 1977, pp. 401-414.
- 40 Winter, H.               Strömungsvorgänge an Platten und profilierten Körpern bei kleinen Spannweiten.  
Forsch. Ing.-Wes., Vol. 6, 1935, pp. 40-50, 67-71.  
Also: Flow phenomena on plates and airfoils of short span.  
NACA Rep. 798, 1937.
- 41 Scholz, N.               Kraft- und Druckverteilungsmessungen an Tragflächen kleiner Streckung.  
Forsch. Ing.-Wes., Vol. 16, 1949/50, pp. 85-91; see also:  
J. Aer. Sci., Vol. 16, 1949, pp. 637-638.
- 42 Gersten, K.               Nichtlineare Tragflächentheorie für Rechteckflügel bei inkompressibler Strömung.  
Z. Flugwiss., Vol. 5, 1957, pp. 276-280.
- 43 Schlichting, H.  
Truckenbrodt, E.           Aerodynamik des Flugzeuges.  
Vol. 2, 2nd Ed. Springer, Berlin-Göttingen-Heidelberg, 1969.  
Also: Airplane aerodynamics, McGraw-Hill, Düsseldorf, in preparation.
- 44 Wickens, R.H.           The vortex wake and aerodynamic load distribution of slender rectangular plates; the effects of a 20-degree bend at mid-chord.  
NRC Canada, NAE LR-458, 1966.

- 45 Ahlborn, F. Die Wirbelbildung im Widerstandsmechanismus des Wassers. Jb. Schiffbautechn. Ges., Vol. 6, 1905, pp. 67-81.
- 46 Ahlborn, F. Die Widerstandsvorgänge im Wasser an Platten und Schiffskörpern. Die Entstehung der Wellen. Jb. Schiffbautechn. Ges., Vol. 10, 1909, pp. 370-431.
- 47 Prandtl, L. Führer durch die Strömungslehre. 6th Ed., Vieweg, Braunschweig, 1965, pp. 326, 333-336.
- 48 Mabey, D.G. Beyond the buffet boundary. Aeron. J., Vol. 77, 1973, pp. 201-215.
- 49 Cornish, J.J. High lift applications of spanwise blowing. 7th ICAS Congress, Rome, 1970, ICAS P. 70-09.
- 50 Dixon, C.J. Lift and control augmentation by spanwise blowing over trailing edge flaps and control surfaces. AIAA P. 72-781, 1972.
- 51 Werlé, H. Gallon, M. Contrôle d'écoulements par jet transversal. Aéron. Astron. No. 34, 1972, pp. 21-33.
- 52 Bradley, R.G. Whitten, P.D. Wray, W.O. Leading-edge-vortex augmentation in compressible flow. J. Aircr., Vol. 13, 1976, pp. 238-242.
- 53 Holmboe, V. The center of pressure position at low speed and small angles of attack for certain type of delta wings. SAAB TN 13, 1953.
- 54 Wentz, W.H. Jr McMahon, M.C. An experimental investigation of the flow fields about delta and double delta wings at low speeds. NASA CR 521, 1966.
- 55 Wentz, W.H. Jr McMahon, M.C. Further experimental investigation of delta and double delta wing flow fields at low speeds. NASA CR 714, 1967.
- 56 Krogmann, P. Experimentelle und theoretische Untersuchungen an Doppeldeltaflügeln. AVA Bericht 68 A 35, 1968.
- 57 Hopkins, E.J. Hicks, R.M. Carmichael, R.L. Aerodynamic characteristics of several cranked leading edge wingbody combinations at Mach numbers from 0.4 to 2.94. NASA TN D-4211, 1967.
- 58 Corsiglia, V.R. König, D.G. Morelli, J.P. Large scale tests of an airplane model with a double delta wing including longitudinal and lateral characteristics and ground effects. NASA TN D-5102, 1969.
- 59 Stahl, W. Zum Einfluß eines Strakes auf das Strömungsfeld eines Deltaflügels ( $\Lambda = 2$ ) bei schallnahen Geschwindigkeiten. DLR Mitt. 73-04, 1973, pp. 113-136, also (in Engl.): ESA TT 175, 1975.
- 60 Henderson, W.P. Huffmann, J.K. Effects of wing design on the longitudinal aerodynamic characteristics of a wing body model at subsonic speeds. NASA TN D-7099, 1972.
- 61 Staudacher, W. Verbesserung der Manöverleistungen im hohen Unterschall. DLR Mitt. 73-04, 1973, pp. 137-158, also: NASA TT-F-15,406; 1974.
- 62 Staudacher, W. Zum Einfluß von Flügelgrundrißmodifikationen auf die aerodynamischen Leistungen von Kampfflugzeugen. Jahrestagung DGLR/ÖGFT, Innsbruck, 24-28.9.1973, DGLR Nr. 73-71.



- 63 Schröder, W.                      Untersuchung über die Umströmung eines Tragflügels mit geknickter Vorderkante und ungepfeiltem Außenflügel bei mäßiger Unterschallgeschwindigkeit.  
DFVLR IB 080-72/16, 1972.
- 64 Schröder, W.                      Untersuchungen über die Umströmung von Tragflügeln mit geknickten Vorderkanten und gepfeilten Außenflügeln bei mäßiger Unterschallgeschwindigkeit.  
DFVLR IB 151-74/11, 1974.
- 65 Baumert, W.                      Messungen am Prinzipmodell Flügel mit Strake bei symmetrischer Anblasung.  
DFVLR IB 157-75 A 13, 1975.
- 66 Baumert, W.                      Druckverteilungsmessungen am Prinzipmodell Flügel mit Strake bei unsymmetrischer Anblasung.  
DFVLR IB 157-75 A 17, 1975.
- 67 Akcay, M.  
Richards, B.E.  
Stahl, W.  
Zarghami, A.                      Aerodynamic characteristics of a missile featuring wings with strakes at high angles of attack.  
AGARD-CP-247, 1978, pp. 20.1-20.7.
- 68 Fiddes, S.P.  
Smith, J.H.B.                      Strake-induced separation at moderately swept leading edges.  
RAE TR 77128, 1977.
- 69 Wedemeyer, E.                      Stable and unstable vortex separation.  
AGARD-CP-247, 1978, pp. 13-1 to 13-10.
- 70 Bollay, W.                      A nonlinear wing theory and its application to rectangular wings of small aspect ratio.  
ZAMM, Vol. 19, 1939, pp. 21-35.
- 71 Gersten, K.                      Nichtlineare Tragflächentheorie, insbesondere für Tragflügel mit kleinem Seitenverhältnis.  
Ing. Archiv, Vol. 30, 1961, pp. 431-452.  
see also: A non linear lifting surface theory especially for low aspect ratio wings.  
AIAA J., Vol. 1, 1963, pp. 924-925.
- 72 Legendre, R.                      Ecoulement au voisinage de la pointe avant d'une aile a forte flèche aux incidences moyennes.  
Rech. Aéron., No 30, 1952, pp. 3-8; No 31, 1953, pp. 3-6; No 35, 1953, pp. 7-8.
- 73 Jones, R.T.                      Properties of low aspect ratio pointed wings at speeds below and above the speed of sound.  
NACA R 835, 1946.
- 74 Adams, M.C.                      Leading edge separation from delta wings at supersonic speeds.  
J. Aero. Sci., Vol. 20, 1953, p. 430.
- 75 Edwards, R.H.                      Leading edge separation from delta wings.  
J. Aero. Sci., Vol. 21, 1954, pp. 134-135.
- 76 Brown, C.E.  
Michael, W.H.                      Effect of leading edge separation on the lift of a delta wing.  
J. Aero. Sci., Vol. 21, 1954, pp. 690-694, 706.
- 77 Mangler, K.W.  
Smith, J.H.B.                      A theory of the flow past a slender delta wing with leading edge separation.  
Proc. Roy. Soc., Vol. A 251, 1959, pp. 200-217.
- 78 Smith, J.H.B.                      Improved calculations of leading edge separation from slender delta wings.  
RAE TR 66070, 1966.
- 79 Sonnleitner, W.  
Kraus, W.                      Weiterentwicklung des Panelverfahrens, Teil 1: Nichtlineares Panelverfahren unter Berücksichtigung diskreter, abgelöster Wirbelschichten an gepfeilten, schlanken Tragflügelformen.  
Messerschmitt-Bölkow-Blohm GmbH UFE 1070, 1973.

- 80 Brown, C.E.  
Michael, W.H. On slender delta wings with leading-edge separation.  
NACA TN 3430, 1955.
- 81 Nenni, J.P.  
Tung, Ch. A second order slender wing theory for wings with leading edge separation.  
NASA CR 66762, 1969.
- 82 Nenni, J.P.  
Tung, Ch. A second order slender wing theory for wings with leading edge separation in supersonic flow.  
NASA CR 1860, 1971.
- 83 Pershing, B. Separated flow past slender delta wings with secondary vortex simulation.  
SSD TDR 64-151, 1964.
- 84 Levinsky, E.S.  
Su, F.Y.  
Wei, M.H.Y. Nonconical theory of flow past slender wing bodies with leading edge separation.  
NASA CR 13446, 1969.
- 85 Hanson, C.W.  
Lundberg, E.  
Sacks, A.H. A theoretical investigation of the aerodynamics of slender wing body combinations exhibiting leading edge separation.  
NASA CR 719, 1967.
- 86 Garner, H.C.  
Lehrian, D.E. Nonlinear theory of steady forces on wings with leading edge flow separation.  
NPL Aero R 1059, ARC 24, 523, 1963.
- 87 Lange, A.H. Nonlinear lifting surface theory for cambered low aspect ratio wings of arbitrary planform.  
Grumman Aircr. Rept. ADR 01-03-67.1, 1967.
- 88 Betz, A. Applied airfoil theory,  
in: Aerodynamic theory, ed. by W.F. Durand, Springer, Berlin, 1935.
- 89 Ermolenko, S.D. Nonlinear theory of small aspect ratio wings.  
Soviet Aeron., Vol. 9, 1966, pp. 5-11; NASA TT F-10, 915, 1967.
- 90 Legendre, R. Vortex sheets rolling up along leading edges of delta wings.  
Progr. Aero. Sci., Vol. 7, 1966, pp. 7-34.
- 91 Legendre, R. Effet de la forme des extrémités d'ailes sur l'enroulement des nappes tourbillonnaires.  
Rech. Aérosp., 1971, pp. 227-235.
- 92 Küchemann, D. A nonlinear lifting surface theory for wings of small aspect ratio with leading edge separation.  
RAE R Aero 2540, 1955.
- 93 Hürlimann, R. Über eine Erweiterung der nichtlinearen Theorie schlanker Tragflügel.  
DGLR-FB Vol. 3, 1968, Paper No 39.
- 94 Hürlimann, R. Zur Berechnung der Kräfte auf schlanke, zugespitzte Tragflügel.  
Z. Flugwiss., Vol. 16, 1968, pp. 69-81.
- 95 Stahl, W. Untersuchungen an schlanken, kegligen Rumpf-Flügel-Kombinationen in Überschallströmung, insbesondere hinsichtlich Volumenverteilung und Wölbung.  
Z. Flugwiss., Vol. 18, 1970, pp. 461-473.
- 96 Belotserkovskii, S.M. Calculation of the flow around wings of arbitrary planforms in a wide range of angles of attack.  
NASA TT F-12, 291, 1969.
- 97 Rehbach, C. Calculation of flows around zero thickness wings with evolutive vortex sheets.  
NASA TT, F-15, 183, 1973, also:  
Calcul découlements autour d'ailes sans épaisseur avec nappes tourbillonnaires évolutives.  
Rech. Aérosp. 1973-2, 1973, pp. 53-61.

- 98 Rehbach, C. Numerical investigation of vortex sheets issuing from separation line near the leading edge.  
NASA TT F-15, 530; 1974, also:  
Étude numérique de nappes tourbillonnaires issues d'une ligne de découlement près du bord d'attaque.  
Rech. Aérosp. 1973-6, 1973, pp. 325-330.
- 99 Kandil, O.A. Prediction of the steady aerodynamic loads on lifting surfaces having sharp-edge separation.  
Ph.D. Dissertation, Virginia Polytechnic Institute and State Univ. Blacksburg, Va., 1974.
- 100 Kandil, O.A.  
Mook, D.T.  
Nayfeh, A.H. Nonlinear prediction of the aerodynamic loads on lifting surfaces.  
J. Aircr., Vol. 13, 1976, pp. 22-28.
- 101 Kandil, O.A.  
Mook, D.T.  
Nayfeh, A.H. A numerical technique for subsonic flows past three dimensional canard-wing configurations with edge separations.  
AIAA P. 77-1; 1977.
- 102 Kandil, O.A.  
Mook, D.T.  
Nayfeh, A.H. Effect of compressibility on the nonlinear prediction of the aerodynamic loads on lifting surfaces.  
AIAA P. 75-121, 1975.
- 103 Atta, E.H.  
Kandil, O.A.  
Mook, D.T.  
Nayfeh, A.H. Nonlinear, unsteady aerodynamic loads on rectangular and delta wings.  
AIAA P. 77-156, 1977.
- 104 Barsby, J.E. Flow past conically-cambered slender delta wings with leading-edge separation.  
RAE TR 72179, ARC R M 3748, 1972.
- 105 Pullin, D.I. Calculations of the steady conical flow past a yawed slender delta wing with leading-edge separation.  
Imp. Coll., Lond., Aero R. 72-17, 1972.
- 106 Jones, I.P. Flow separation from yawed delta wings.  
Computers and Fluids, Vol. 3, 1975, pp. 155-177.
- 107 Cooper, R.K. Oscillatory slender wings with leading-edge vortex sheets.  
ARC 35922, 1975.
- 108 Clark, R.W. Non-conical flow past slender wings with leading-edge vortex sheets.  
Euromech 41, Norwich, 1973. RAE T R 76037, 1976.
- 109 Rehbach, C. Numerical calculation of three-dimensional unsteady flows with vortex sheets.  
AIAA P. 78-111, 1978.
- 110 Schröder, W. Berechnung der nichtlinearen Beiwerte von Flügeln mit kleinem und mittlerem Seitenverhältnis nach dem Wirbelleiter-Verfahren in inkompressibler Strömung.  
DFVLR IB 151-76/18, 1976.
- 111 Polhamus, E.C. Predictions of vortex-lift characteristics by a leading-edge suction analogy.  
J. Aircr., Vol. 8, 1971, pp. 193-199.
- 112 Polhamus, E.C. Charts for predicting the subsonic vortex-lift characteristics of arrow, delta, and diamond wings.  
NASA TN D -6243, 1971.
- 113 Lamar, J.E.  
Luckring, J.M. Recent theoretical developments and experimental studies pertinent to vortex flow aerodynamics - with a view towards design.  
AGARD - CPP - 247, 1978, pp. 24.1-24.31.
- 114 Weber, J.A.  
Brune, G.W.  
Johnson, F.T.  
Lu, P. & Rubbert, P.E. A three-dimensional solution of flows over wings with leading edge vortex separation.  
AIAA J., Vol. 14, 1976, pp. 519-525.

- 115 Belotserkovskii, S.M. Study of the unsteady aerodynamics of lifting surfaces using the computer.  
Ann. Rev. Fluid Mech., Vol. 9, 1977, pp. 469-494.
- 116 Sun, Y.C. Nicht-angestellte Deltaflügel mit Unterschall- und Schallvorderkanten.  
J. Mécanique, Vol. 3, 1964, pp. 141-163.
- 117 Sun, Y. C. Die Kopfwelle an einem nicht angestellten Deltaflügel in stationärer Überschallströmung beim Übergang von Unterschall- zu Überschallvorderkanten.  
J. Mécanique, Vol. 7, 1968, pp. 521-573.
- 118 Parker, A.G. Aerodynamic characteristics of slender wings with sharp leading edges - a review.  
J. Aircr., Vol. 13, 1976, pp. 161-168.
- 119 Peake, D.J. Controlled and uncontrolled flow separation in three dimensions.  
NRC Canada, NAE LR-591, 1976.
- 120 Smith, J.H.B. Inviscid fluid models, based on rolled-up vortex sheets, for three-dimensional separation at high Reynolds number.  
AGARD-LS-94, 1978, pp. 9.1-9.27.
- 121 Gersten, K. Calculation of non-linear aerodynamic stability derivatives of aeroplanes.  
AGARD R 342, 1961.
- 122 Bradley, R.G.  
Smith, C.W.  
Bhateley, I.C. Vortex-lift prediction for complex wing planforms.  
J. Aircr., Vol. 10, 1973, pp. 379-381.
- 123 Kandil, O.A. Personal communication.
- 124 Peckham, D.H. Low-speed wind-tunnel tests on a series of uncambered slender pointed wings with sharp edges.  
ARC R M 3186, 1961.
- 125 Polhamus, E.C. A concept of the vortex lift of sharp-edge delta wings based on a leading-edge-suction analogy.  
NASA TN D-3767, 1966.

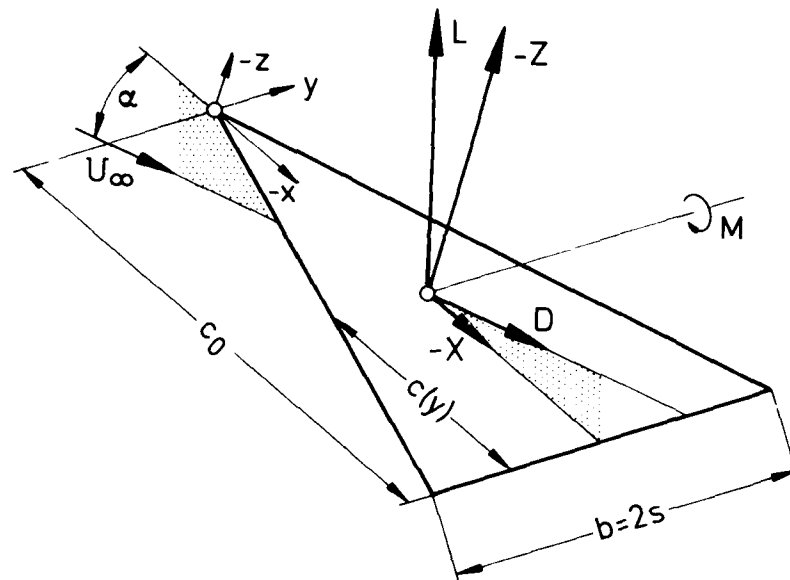


Fig.1 Notations and axes

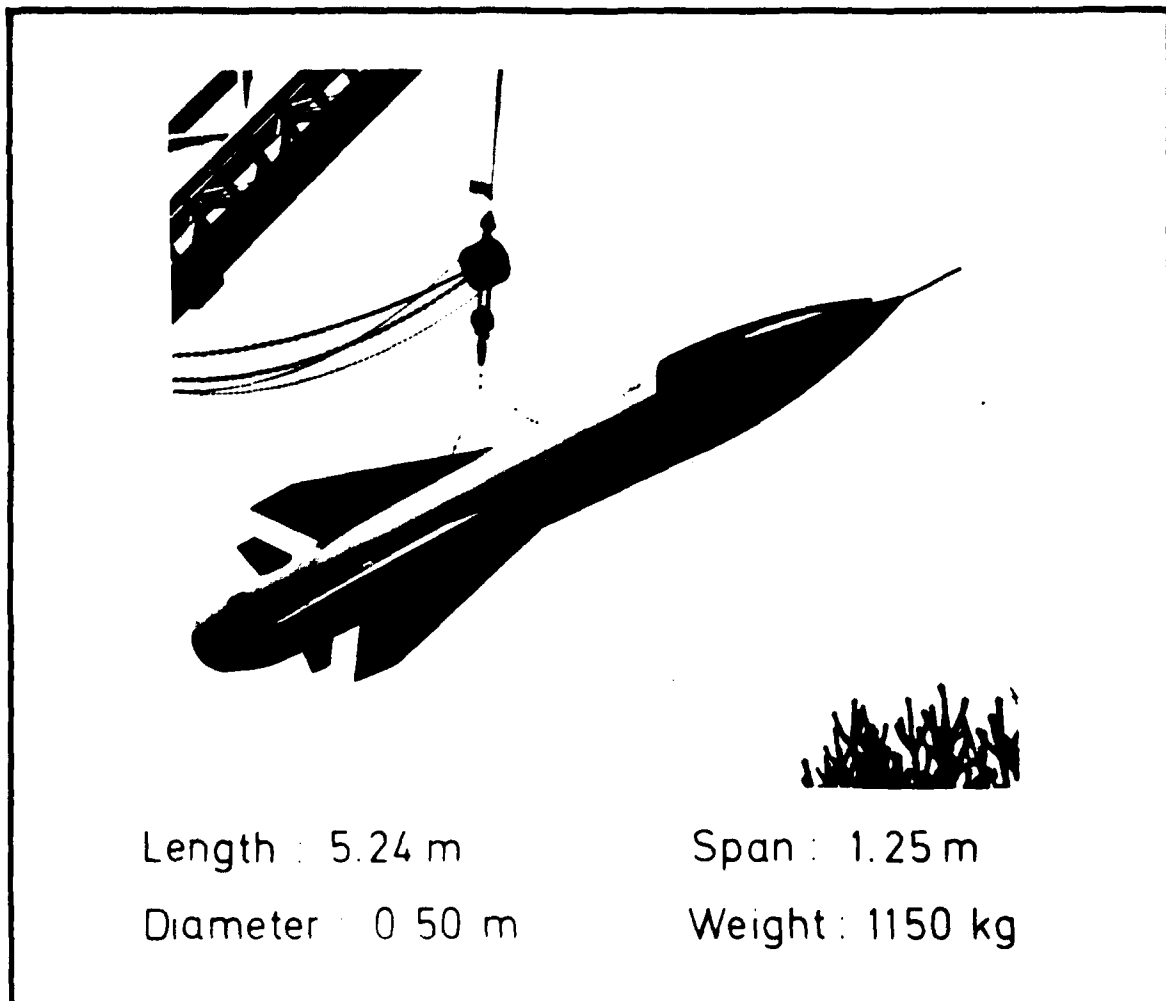


Fig.2 Air-ground guided missile JUMBO (MBB)

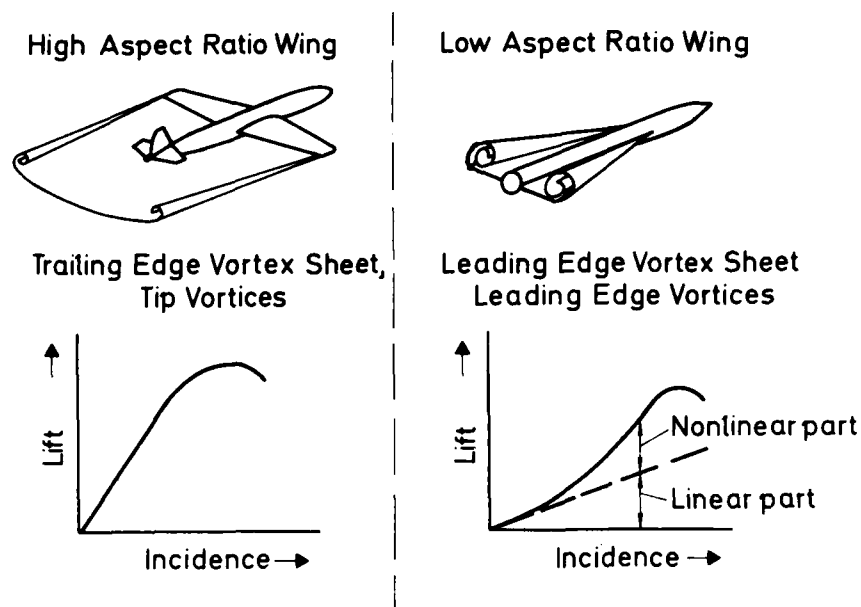


Fig.3 Vortices and lift for high and low aspect ratio wing

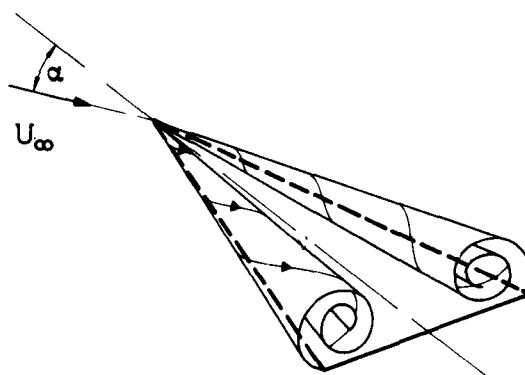


Fig.4 Flow field of slender delta wing (schematically)

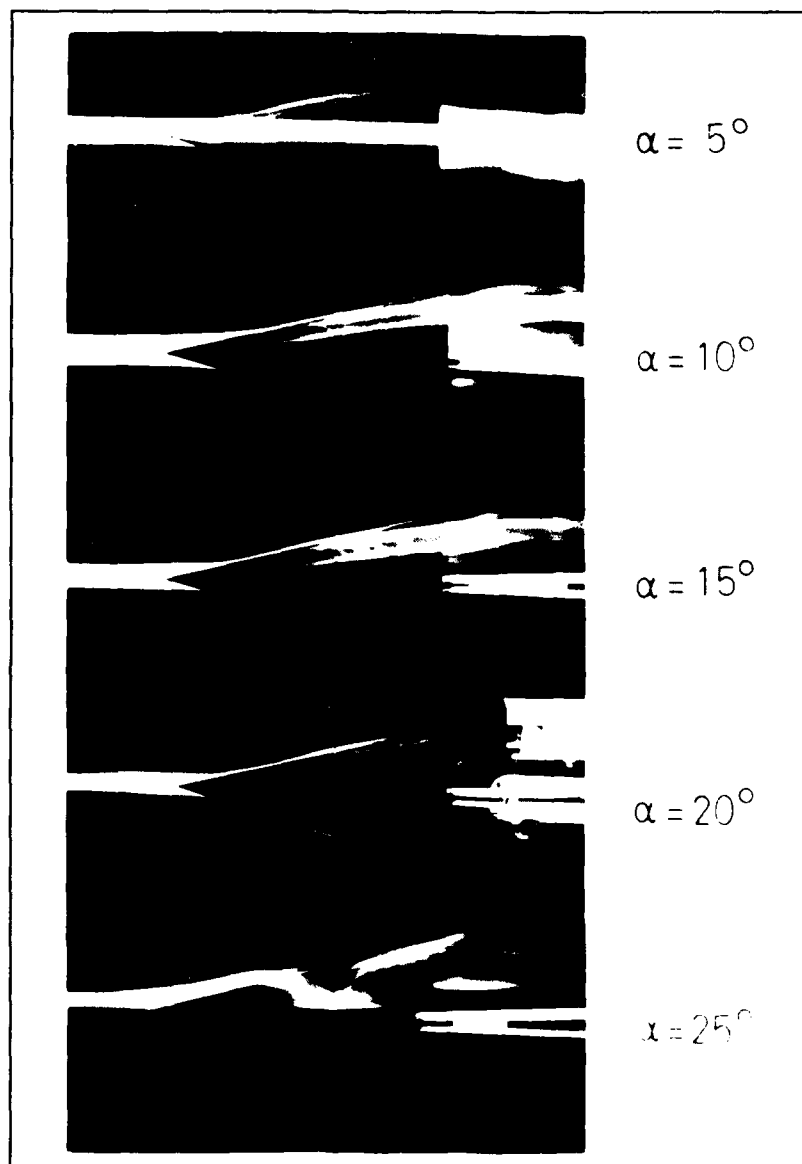


Fig.5(a) Flow visualization for delta wing  $M_\infty = 0.6$

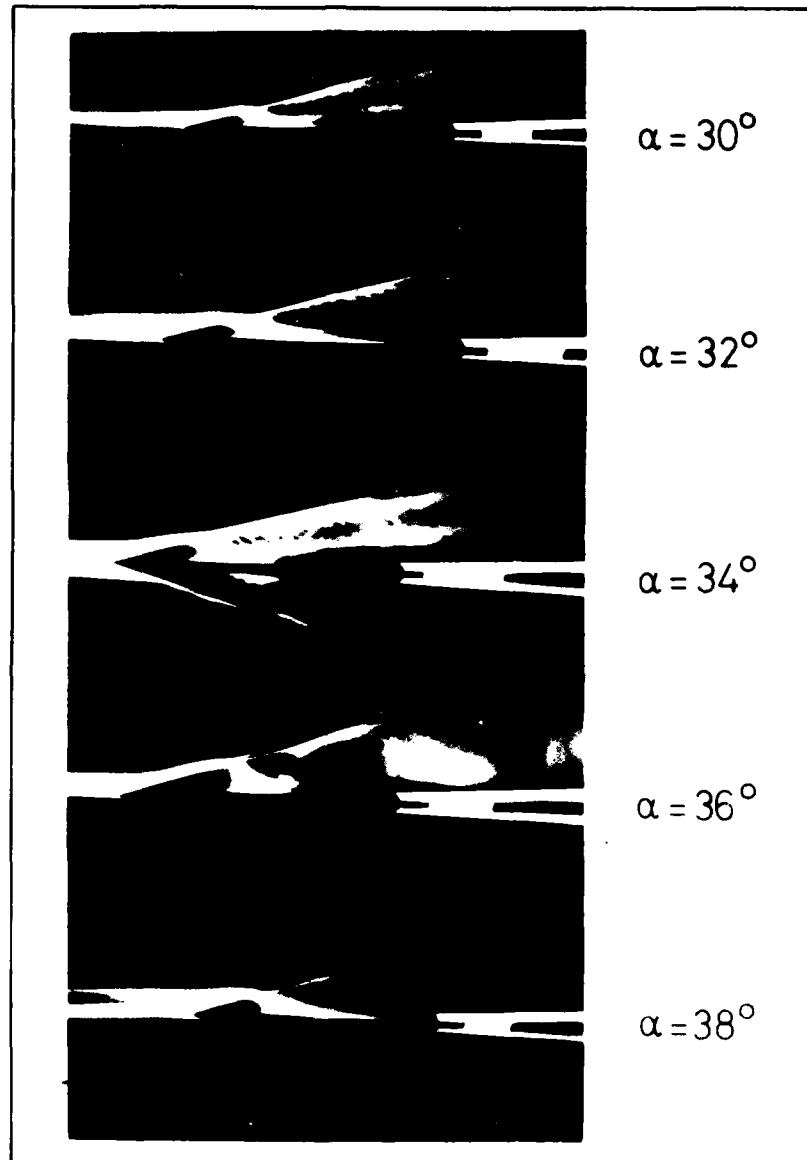


Fig.5(b) Flow visualization for delta wing  $M_\infty = 0.6$



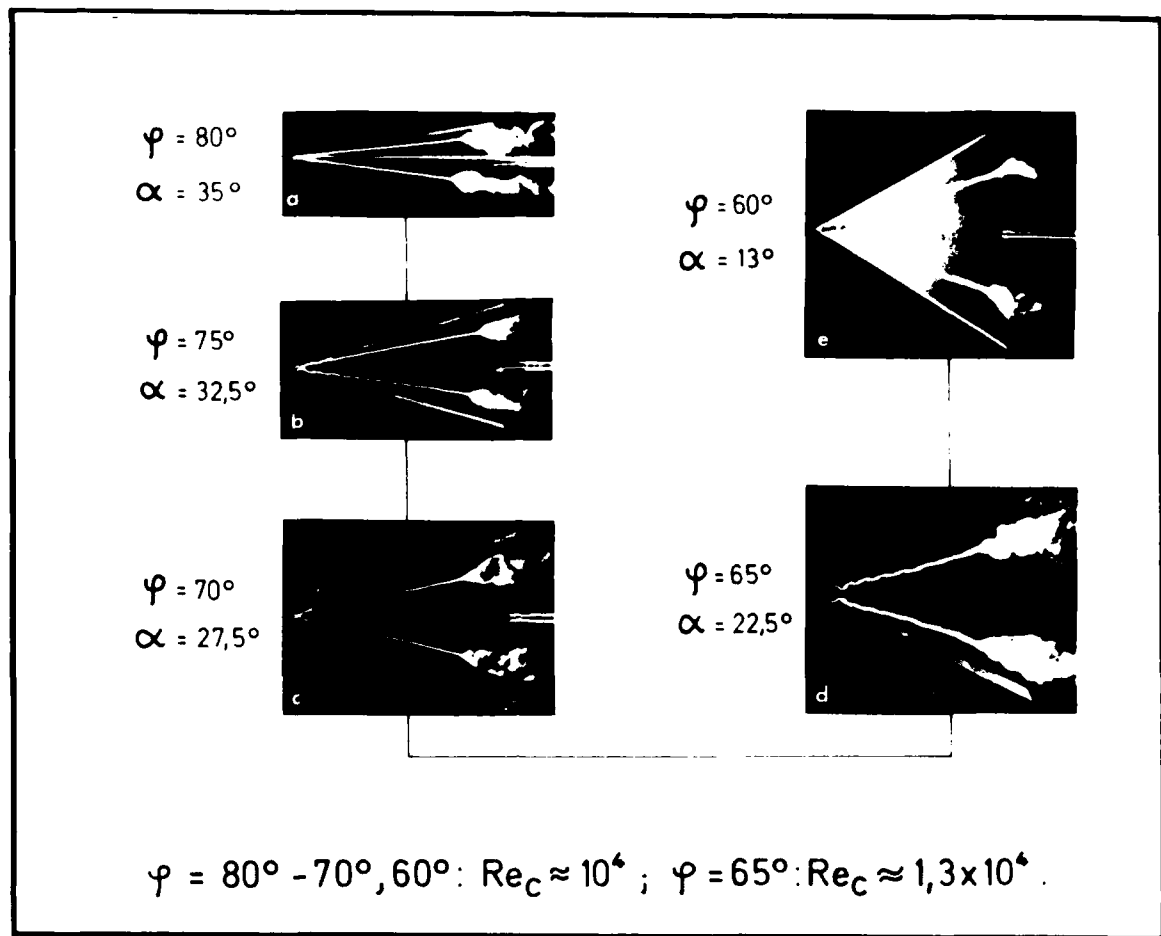


Fig.6 Vortex breakdown on delta wings, with various leading-edge sweep angles, from H.Werle, Reference 3

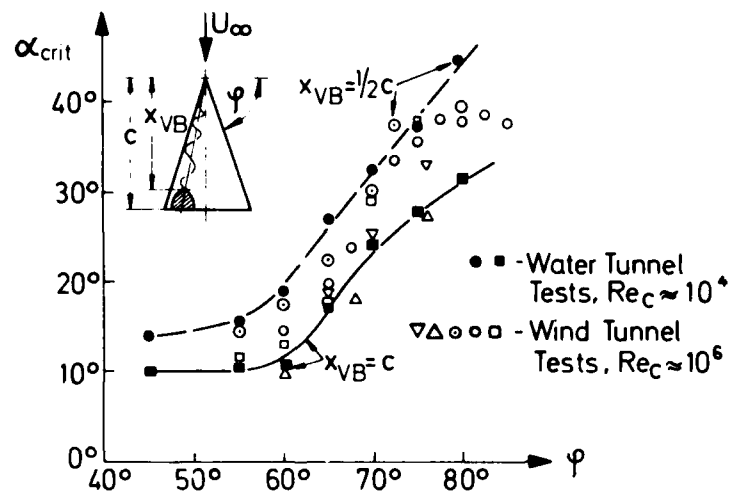


Fig.7 Vortex breakdown on a sharp-edged delta wing, influence of leading-edge sweep on the critical incidence, from Reference 3



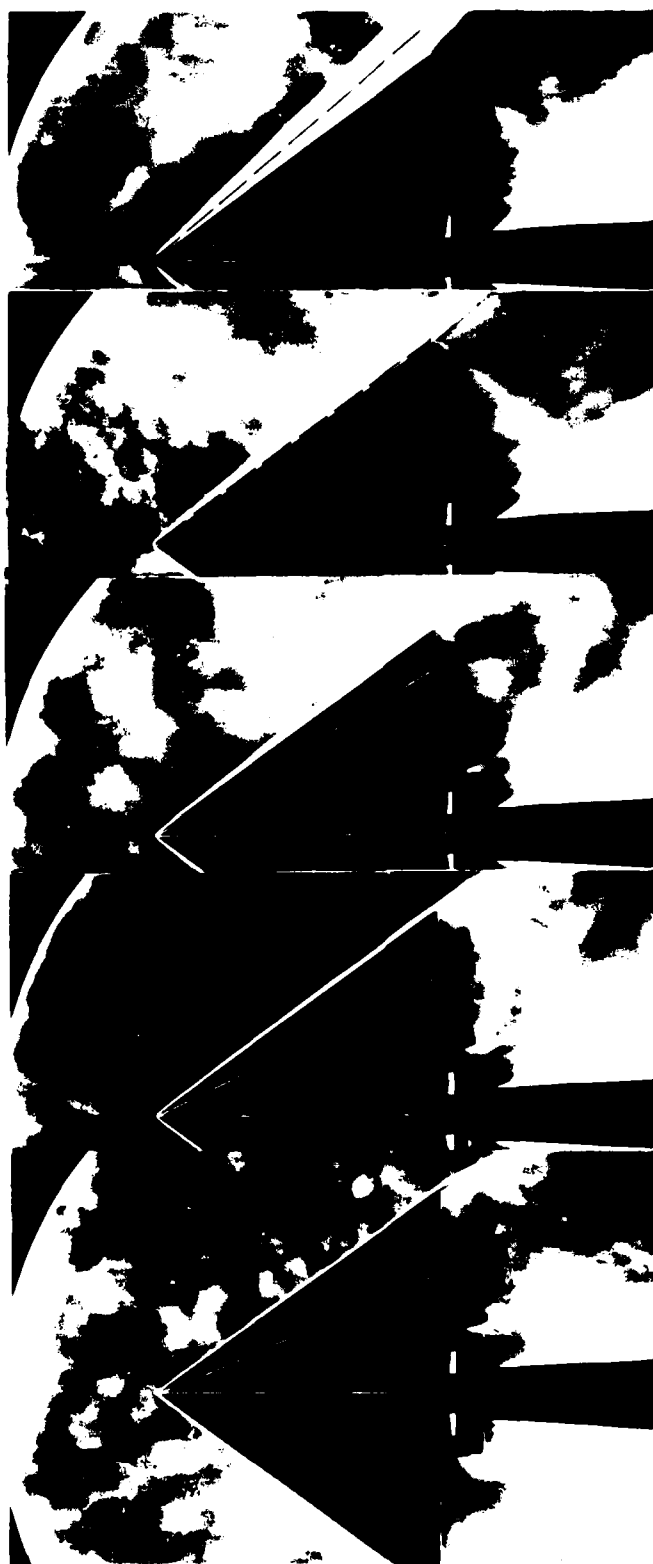
 $M_{\infty} = 1.56$  $M_{\infty} = 1.73$  $M_{\infty} = 2.00$  $M_{\infty} = 2.25$  $M_{\infty} = 2.50$ 

Fig. 9. Supersonic flow past a delta wing,  $\alpha = 0^\circ$ . Transition from subsonic to supersonic leading edge.  
H. H. Sch. Reference 10

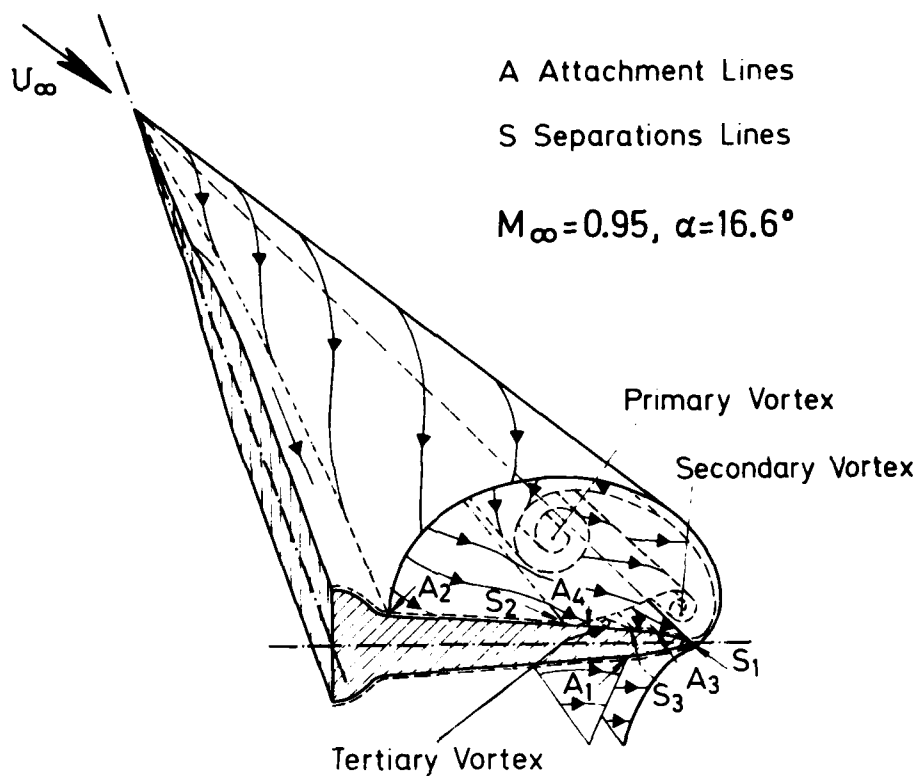


Fig.10 Flow field of slender delta wing, from Reference 11

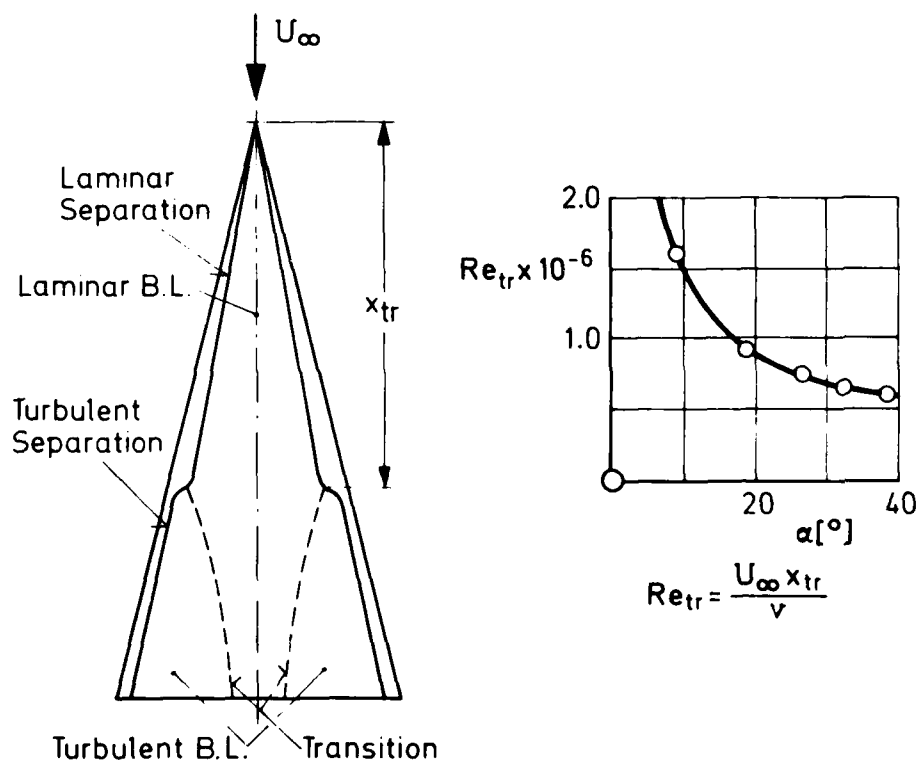


Fig.11 Boundary layer flow on suction side of slender delta wing, from Reference 12

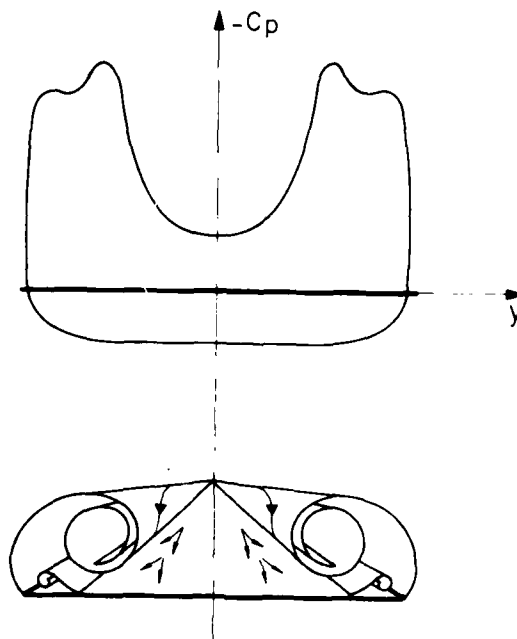


Fig.12 Spanwise pressure distribution on slender delta wing (schematically)

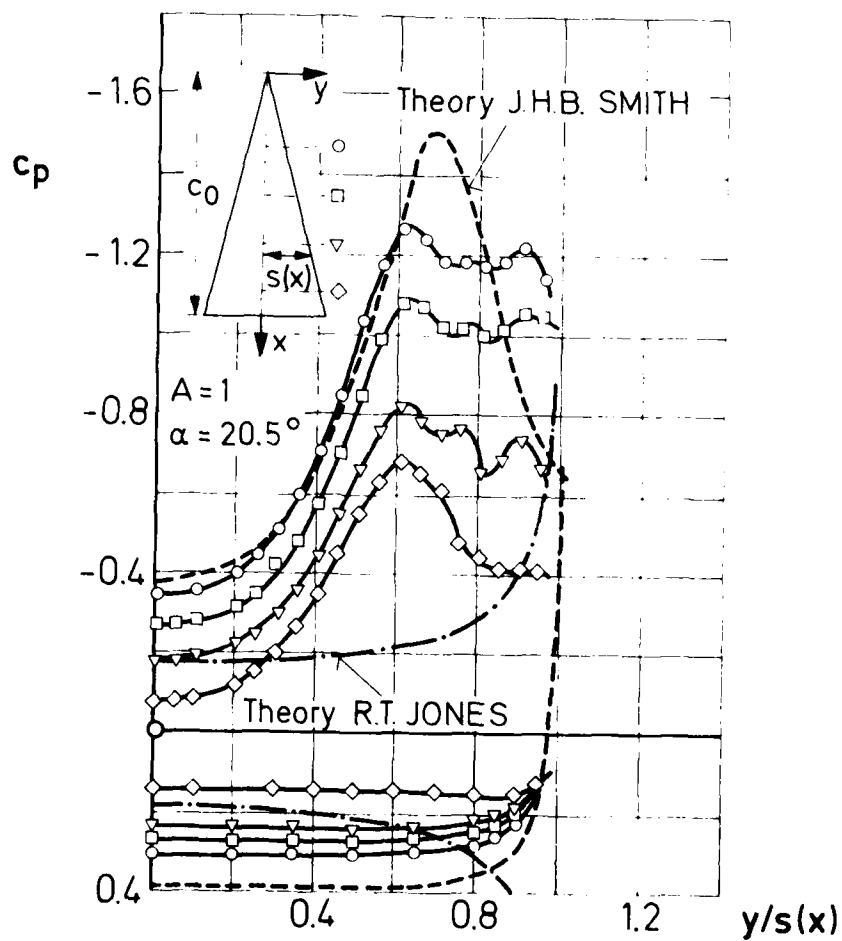


Fig.13 Pressure distributions on delta wing, from Reference 13

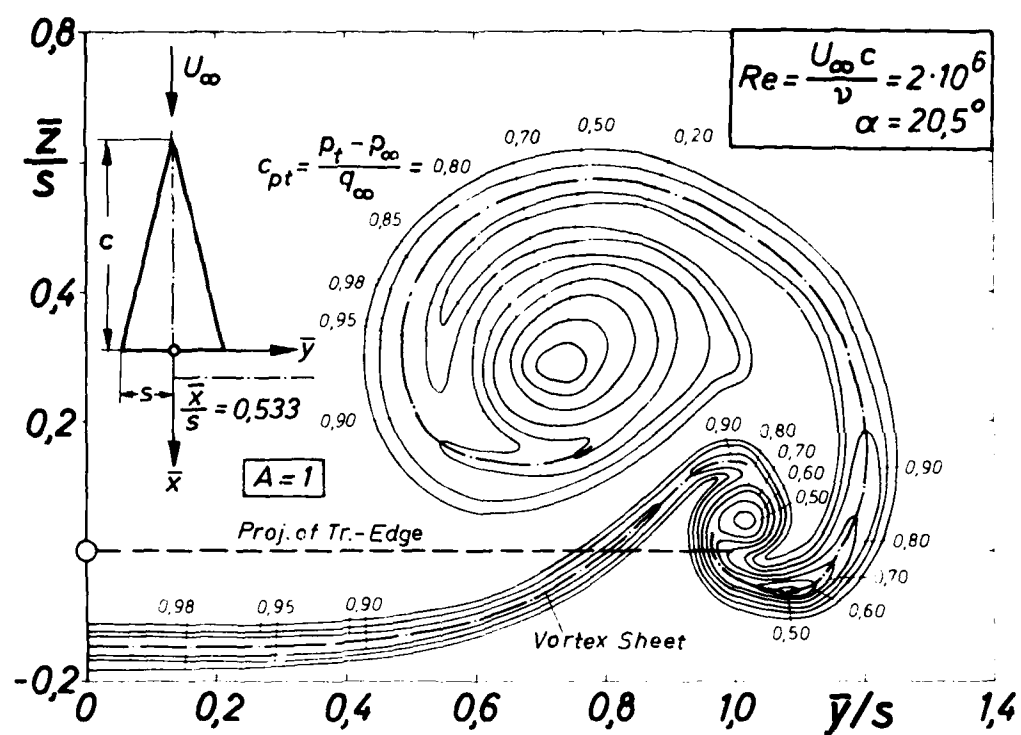


Fig. 14 Distribution of total pressure downstream of delta wing, from D. Hummel, Reference 14

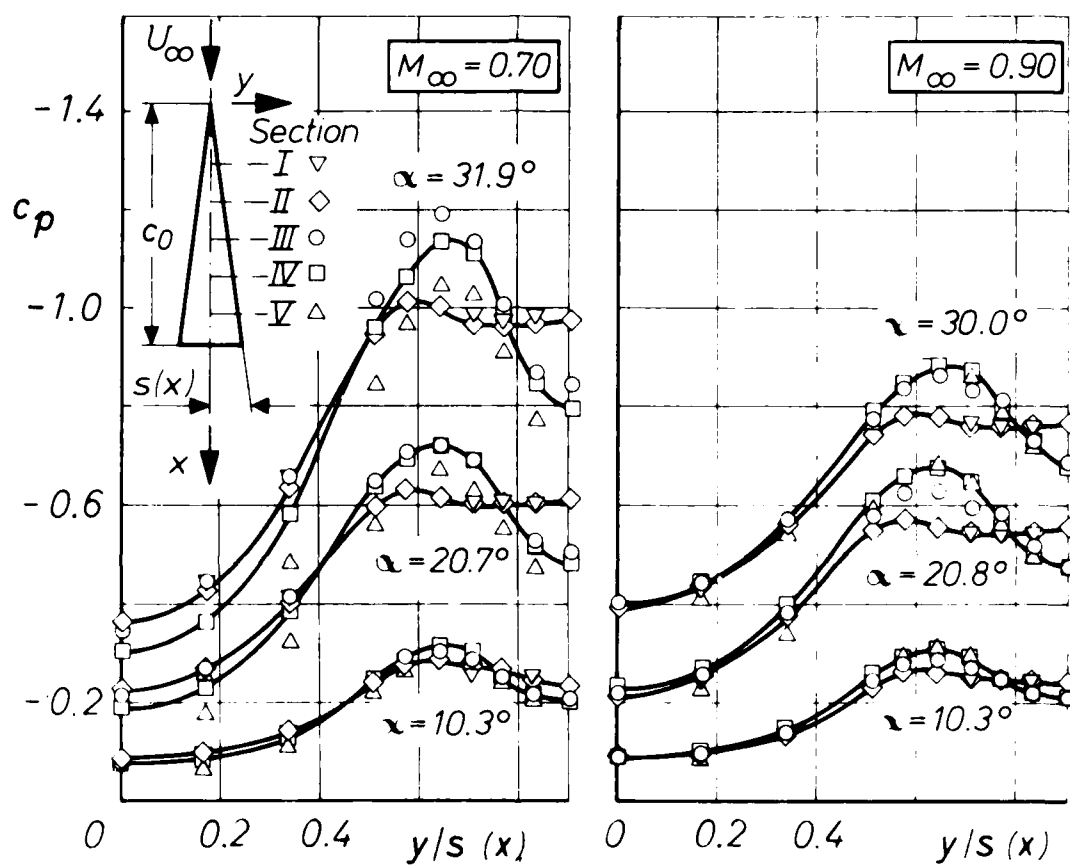


Fig. 15(a) Spanwise pressure distributions on suction side, from Reference 15

$$Re = \frac{U_\infty \cdot (2/3)c_0}{\nu_\infty} = 2.7 \cdot 10^6$$

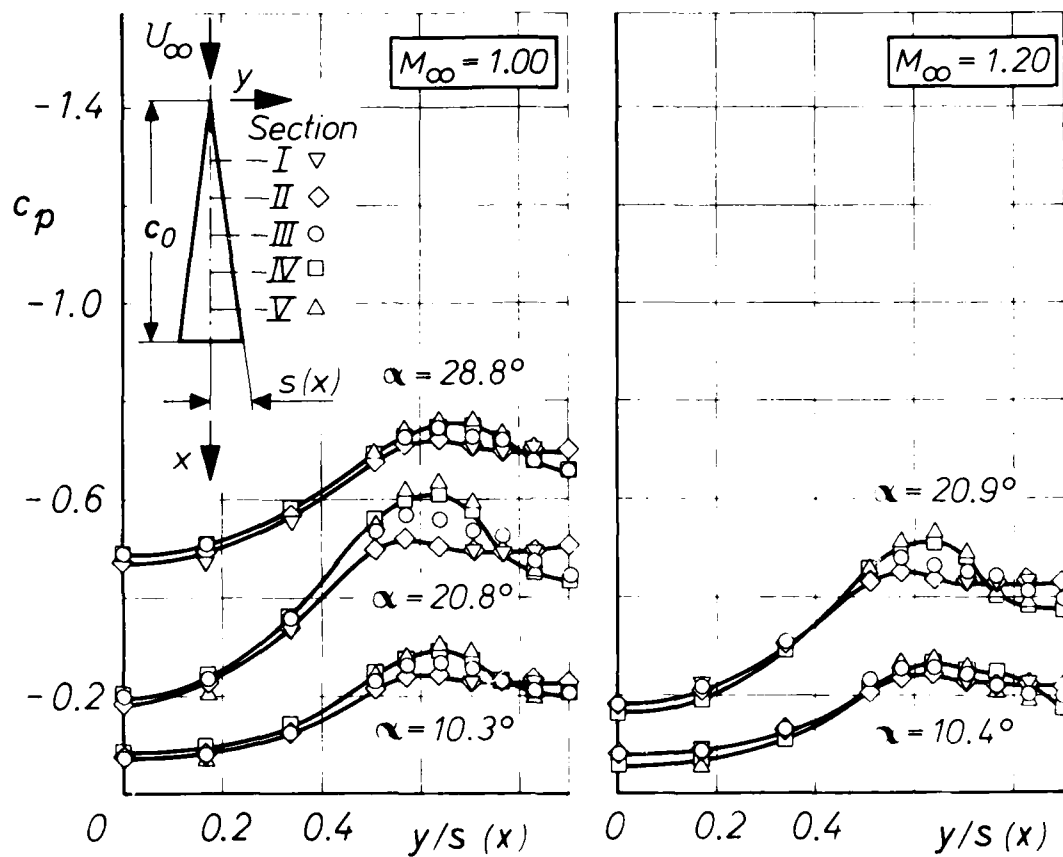


Fig. 15(b) Spanwise pressure distributions on suction side, from Reference 15

$$Re = \frac{U_\infty \cdot (2/3)c_0}{\nu_\infty} = 2.7 \cdot 10^6$$



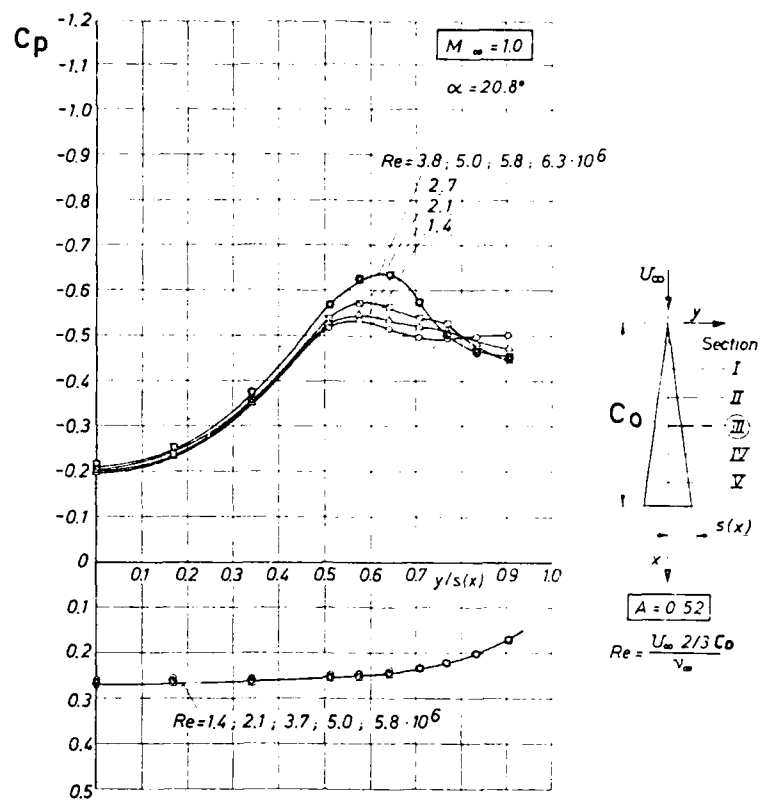


Fig.16 Influence of Reynolds number on pressure coefficient of slender delta wing, from Reference 15

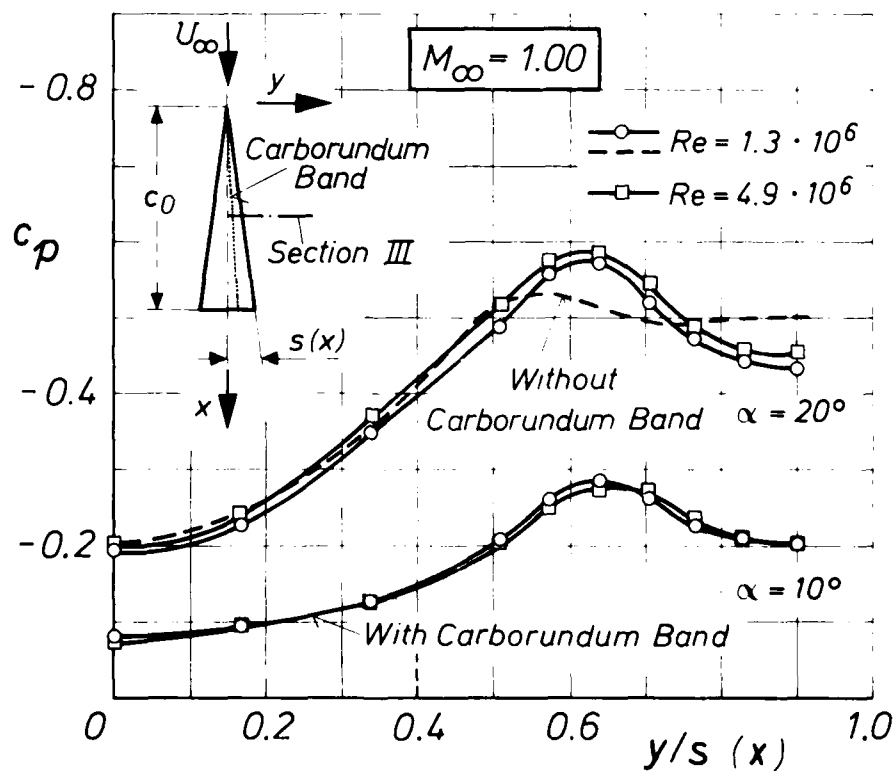


Fig.17 Spanwise pressure distributions on suction side with transition strip, from Reference 15

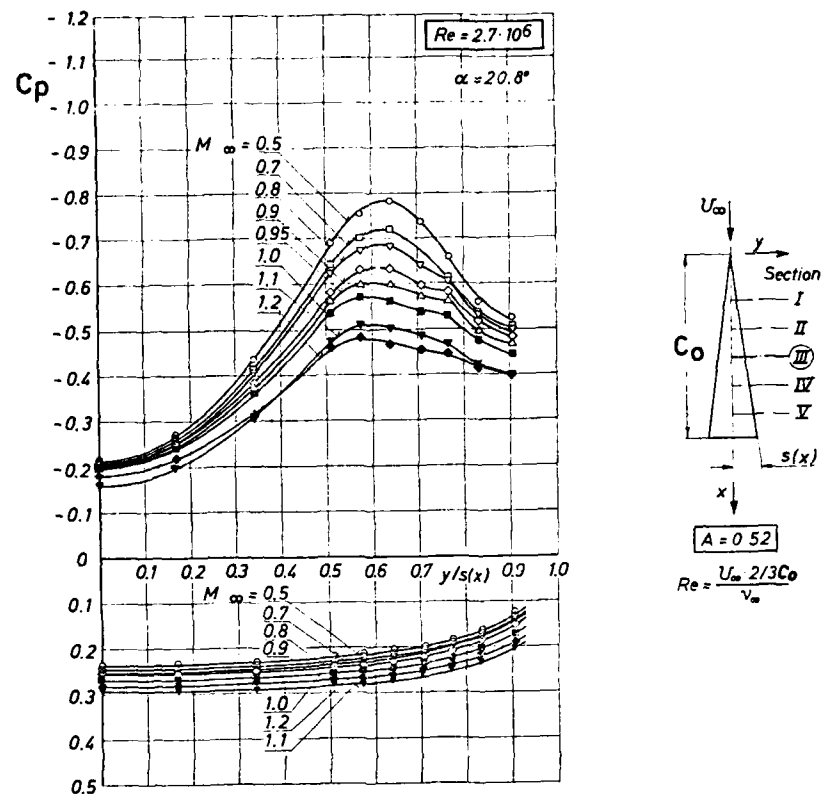


Fig.18 Influence of Mach number on pressure coefficient of slender delta wing, from Reference 15

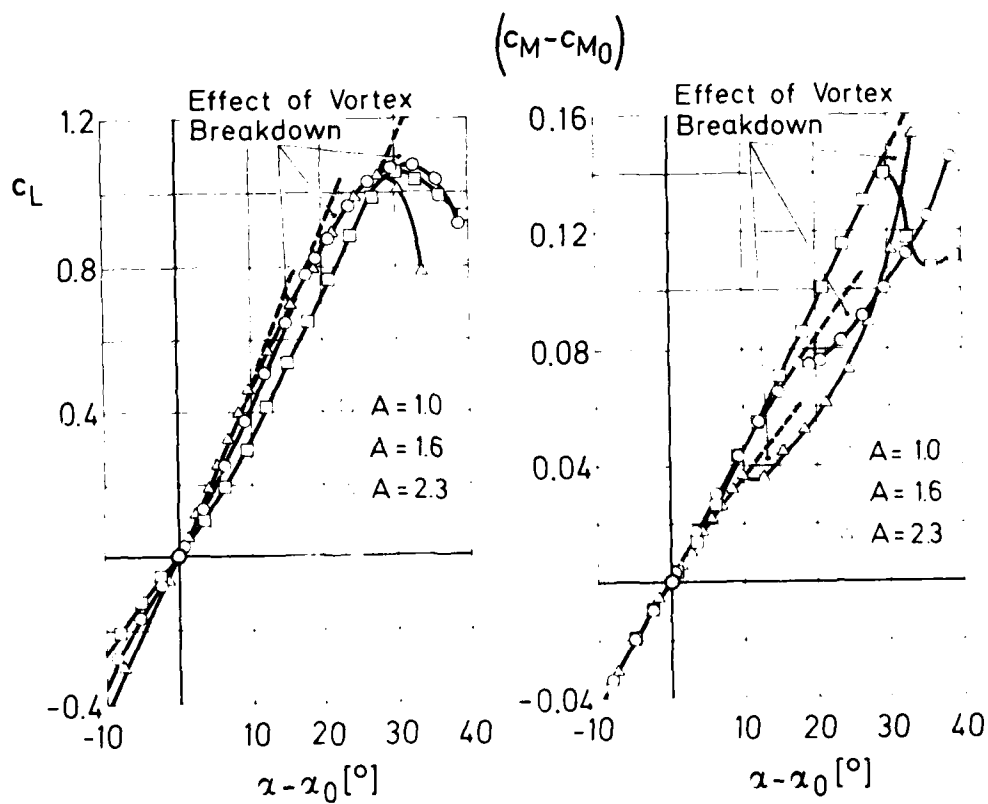


Fig.19 Lift and pitching moment curves for delta wings, from Reference 17

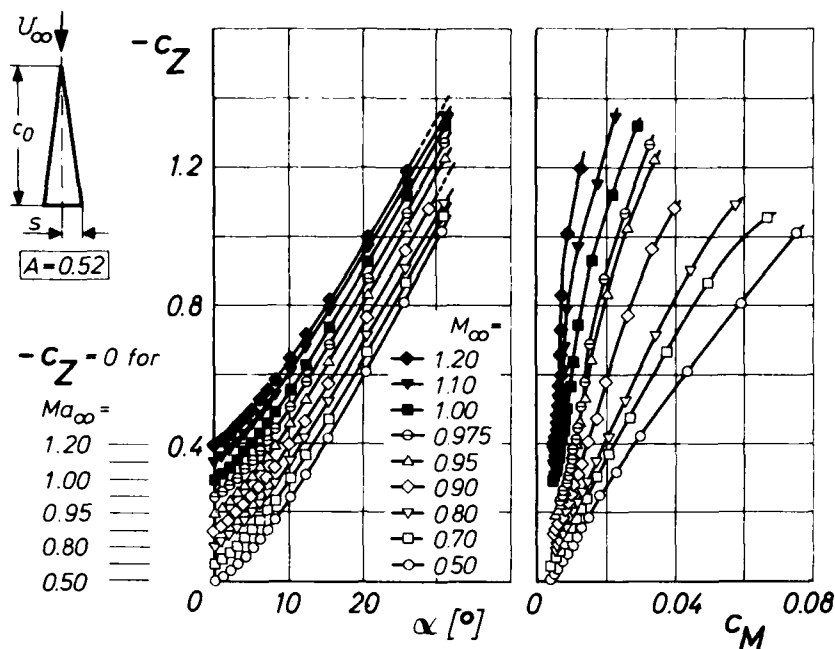


Fig.20 Influence of Mach number on normal force and pitching moment behaviour, from Reference 15

$$Re = \frac{U_\infty \cdot (2/3)c_0}{\nu_\infty} = 2.7 \cdot 10^6$$

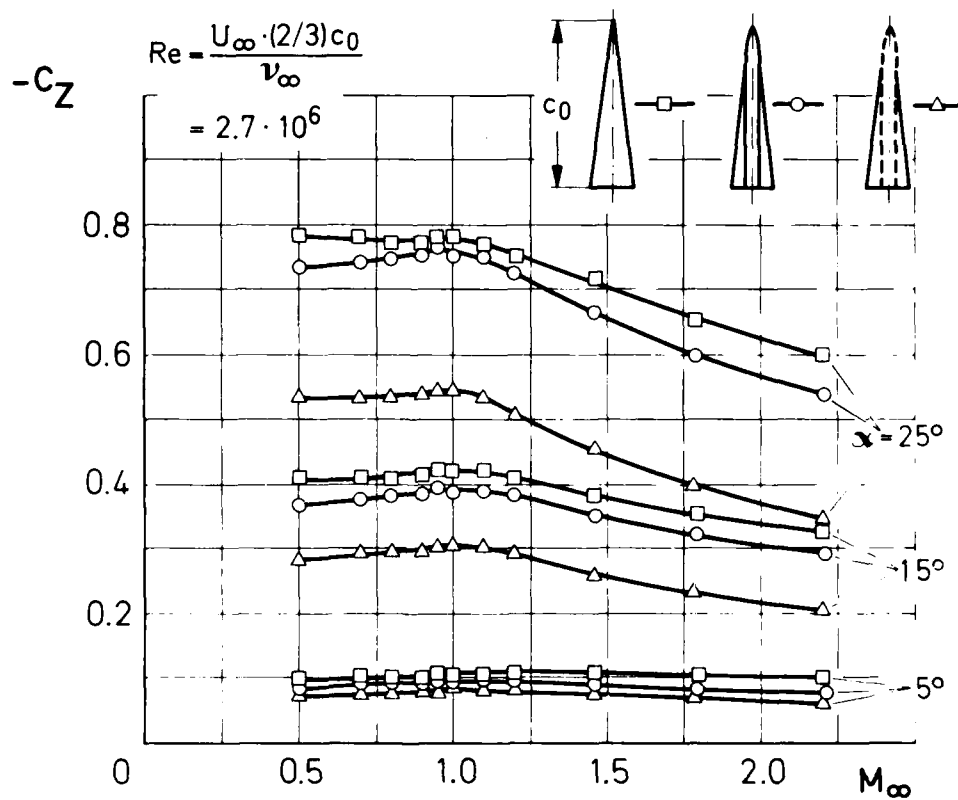


Fig.21 Dependence of normal force coefficients on Mach number, from Reference 18

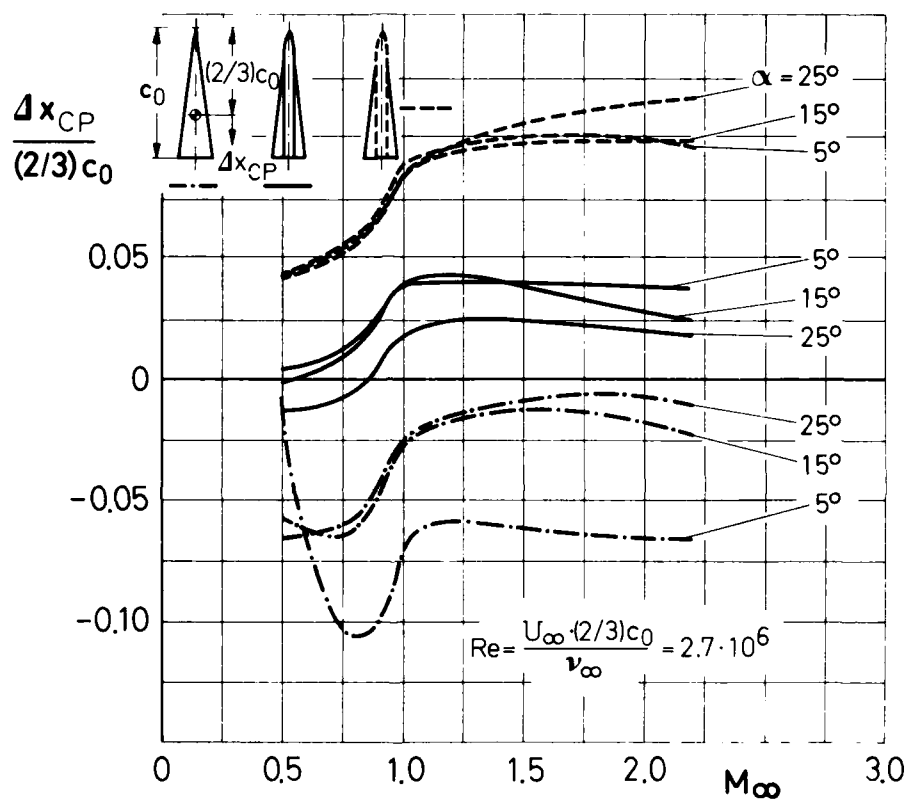


Fig.22 Dependence of position of center of pressure on Mach number, from Reference 18

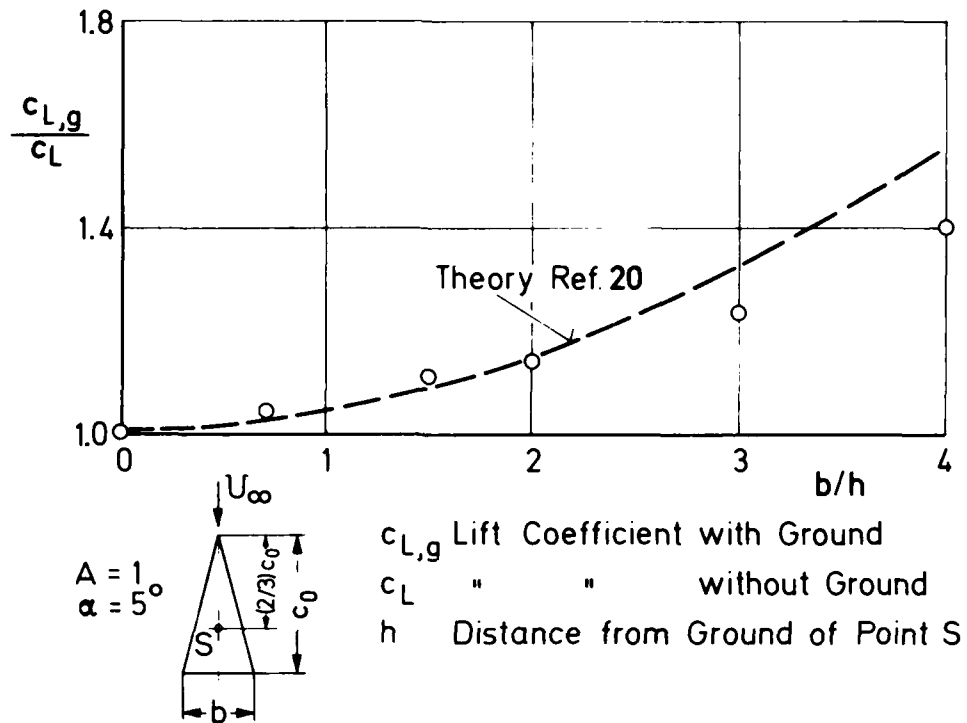


Fig.23 Influence of leading-edge shape on lift and moment coefficients for slender delta wing, from Reference 19

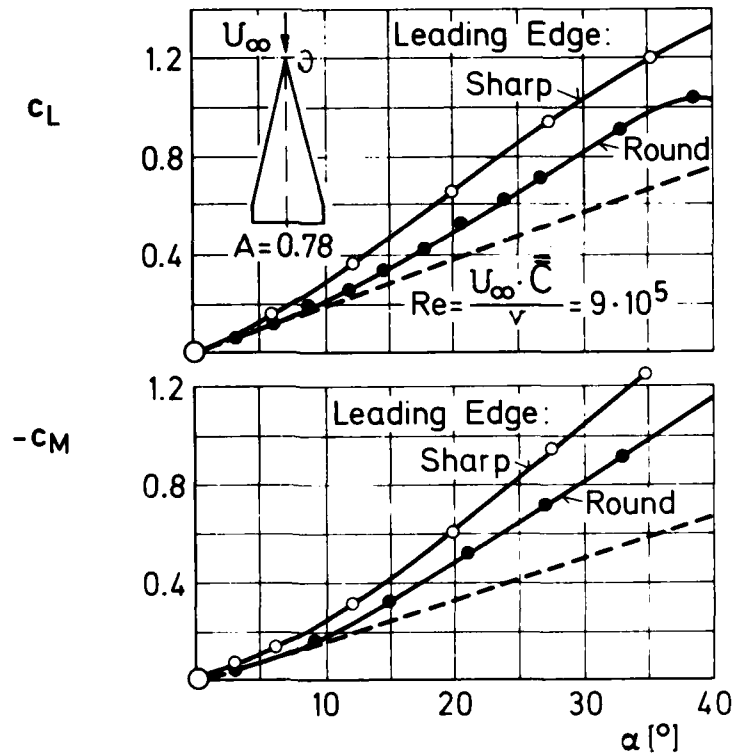


Fig.24 Ground effect on slender delta wing, from Reference 20

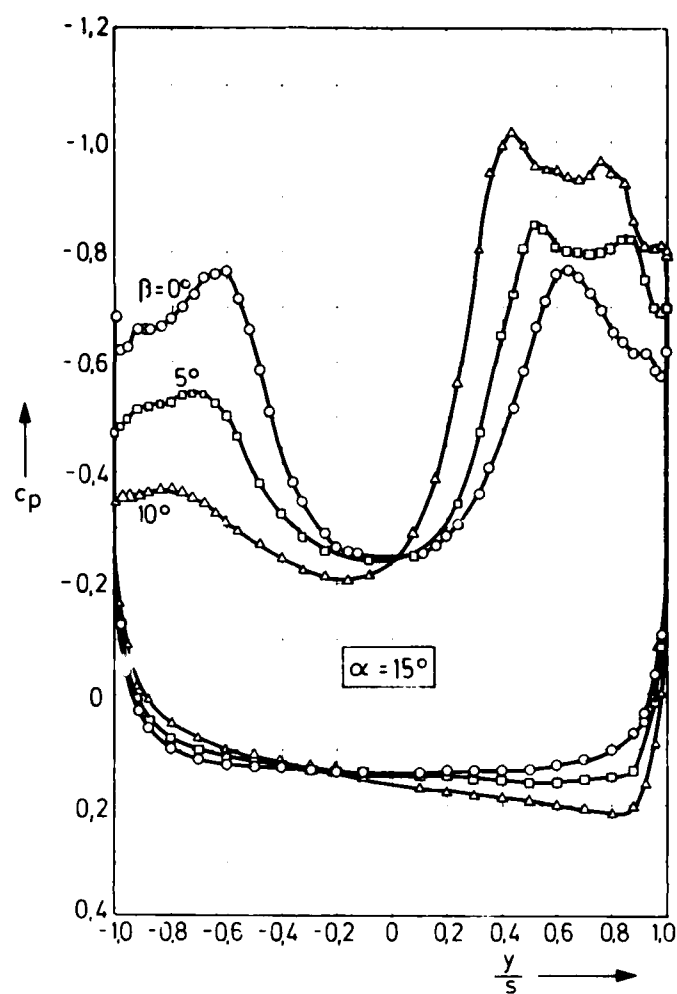


Fig.25 Pressure distribution on slender delta wing for various yaw angles, from J.K.Harvey, Reference 27

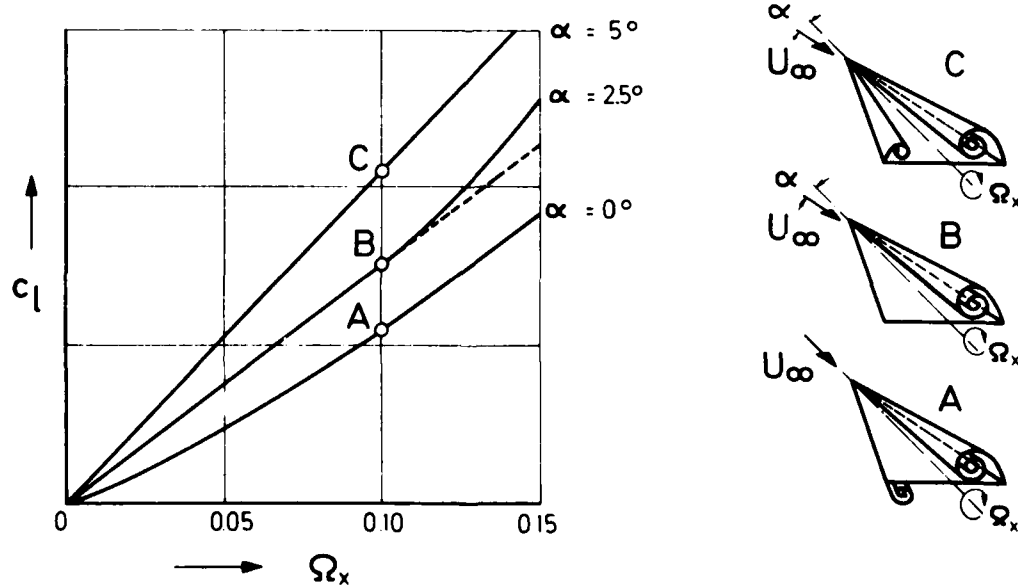
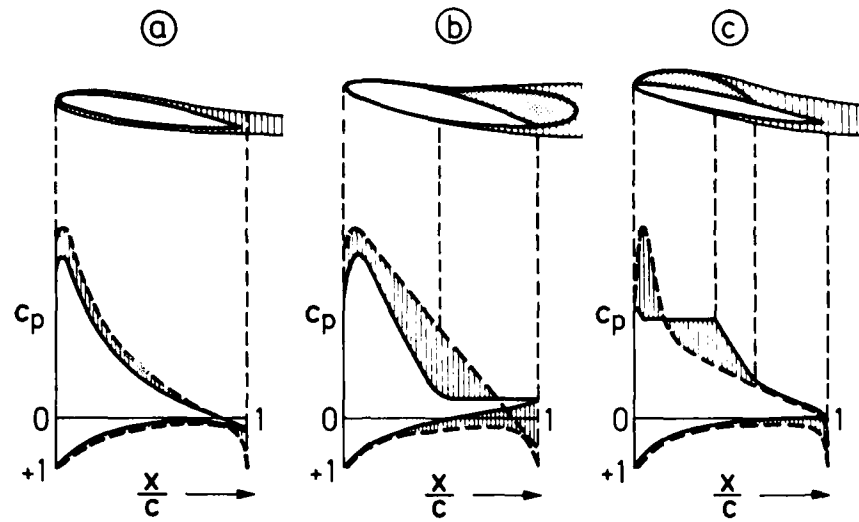


Fig.26 Influence of vortex configuration on rolling moment, from F.Schlottmann, Reference 29



Flow: --- Without Friction, — With Friction

Fig.27 Various types of flow about profiles (schematically), from Reference 47

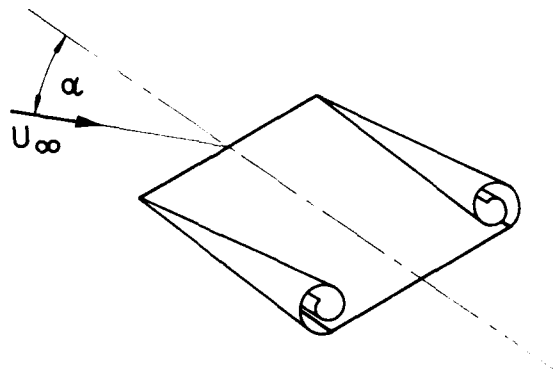


Fig.28 Side edge flow on rectangular wing (schematically)

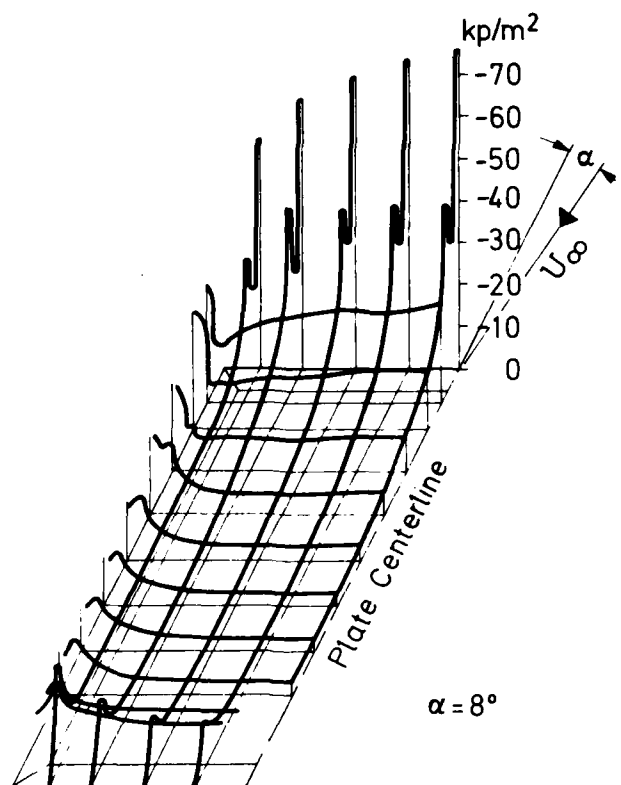


Fig.29(a) Pressure distribution on suction side of rectangular plate, from Reference 40

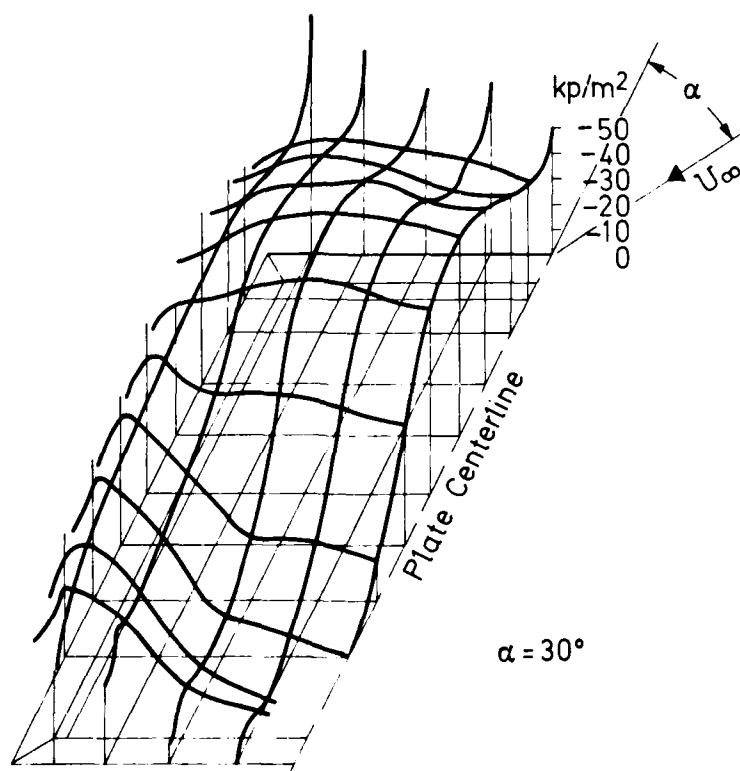


Fig.29(b) Pressure distribution on suction side of rectangular plate, from Reference 40



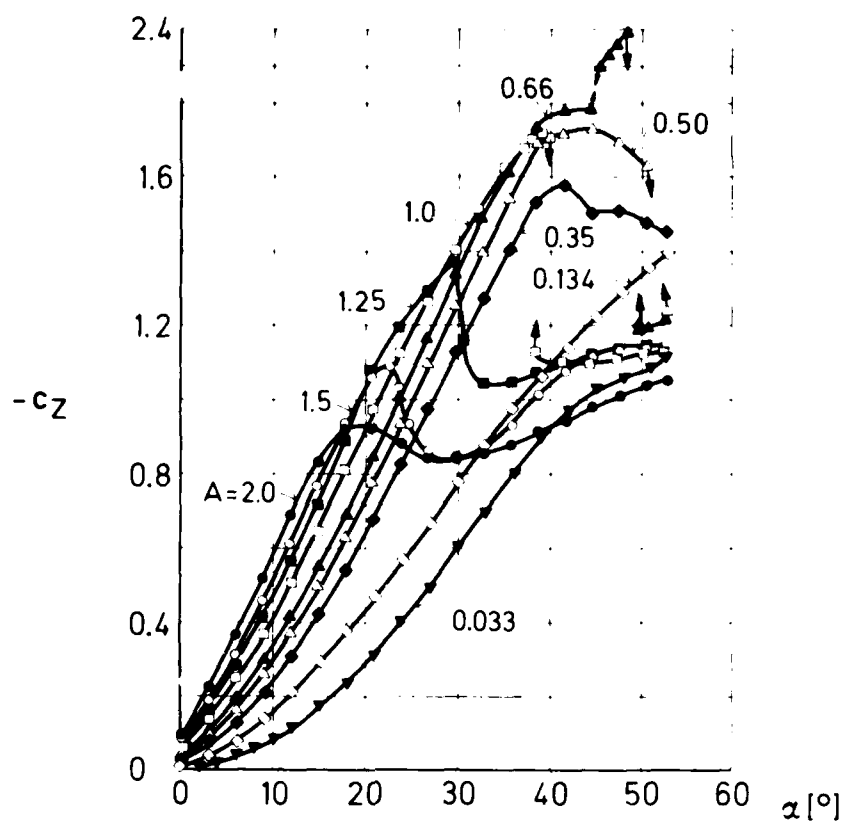


Fig.30 Normal force coefficient for rectangular plates of various aspect ratios, from Reference 40

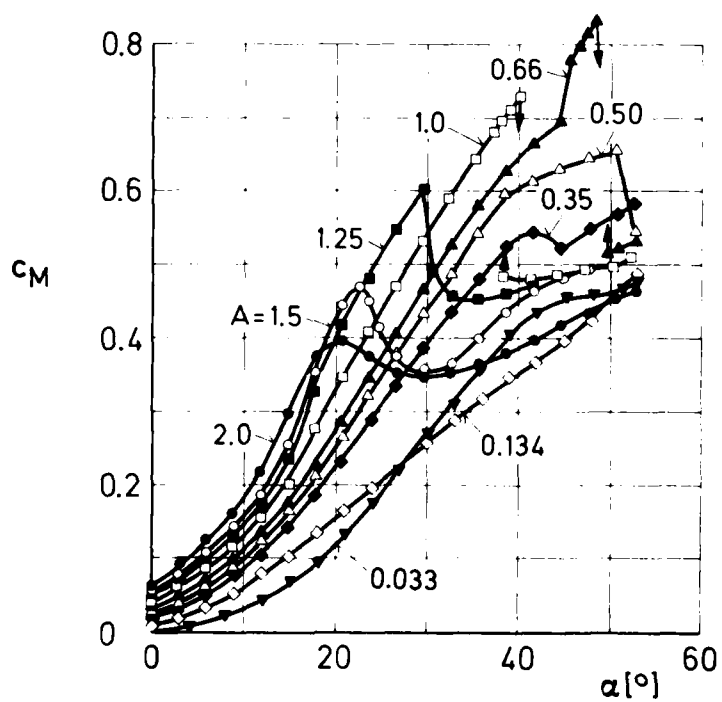
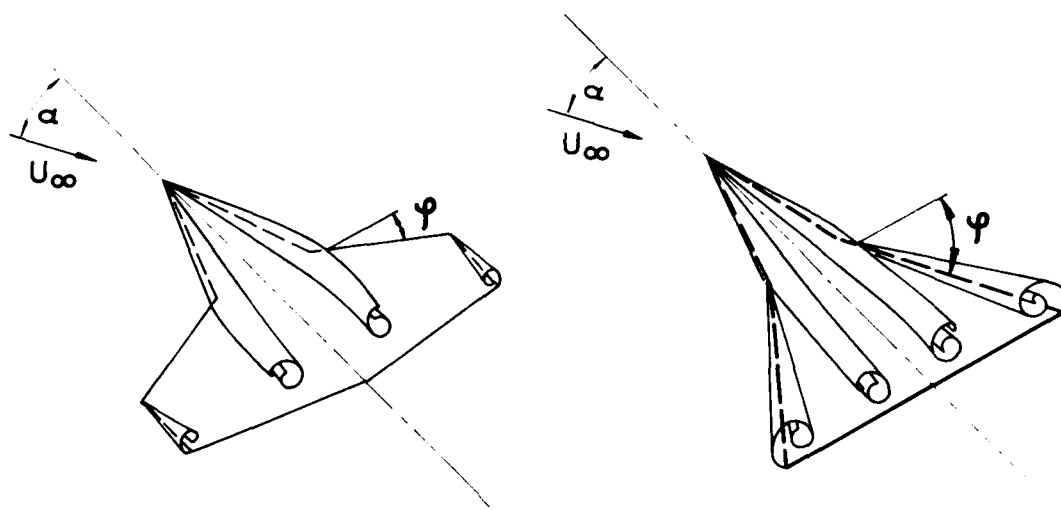


Fig.31 Moment coefficient for rectangular plates of various aspect ratios, from Reference 40



Trapezoidal Wing with Strake:

Low or Moderate Leading - Edge Sweep  
of Main Wing

Double Delta Wing:

High Leading - Edge Sweep  
of Main Wing

Fig.32 Vortex flows on wings with strakes (schematically)

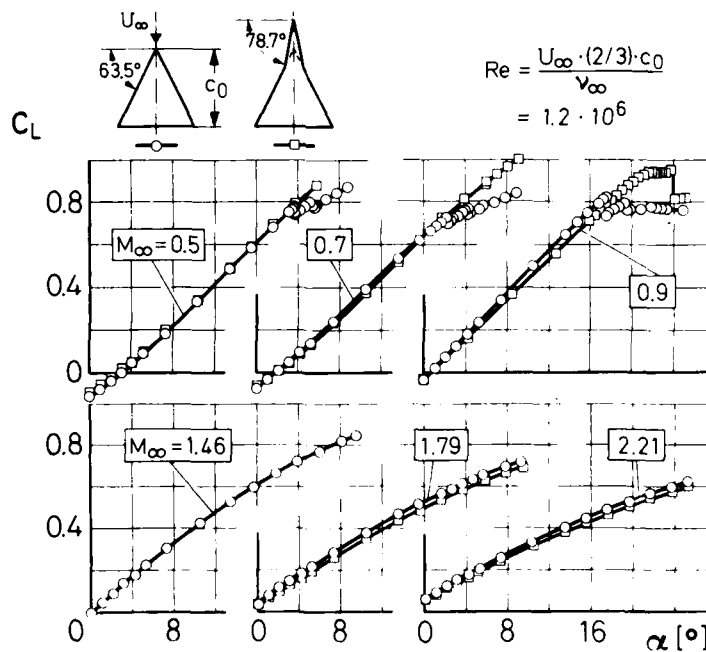


Fig.33 Lift coefficients for delta wing without and with strake, from Reference 59

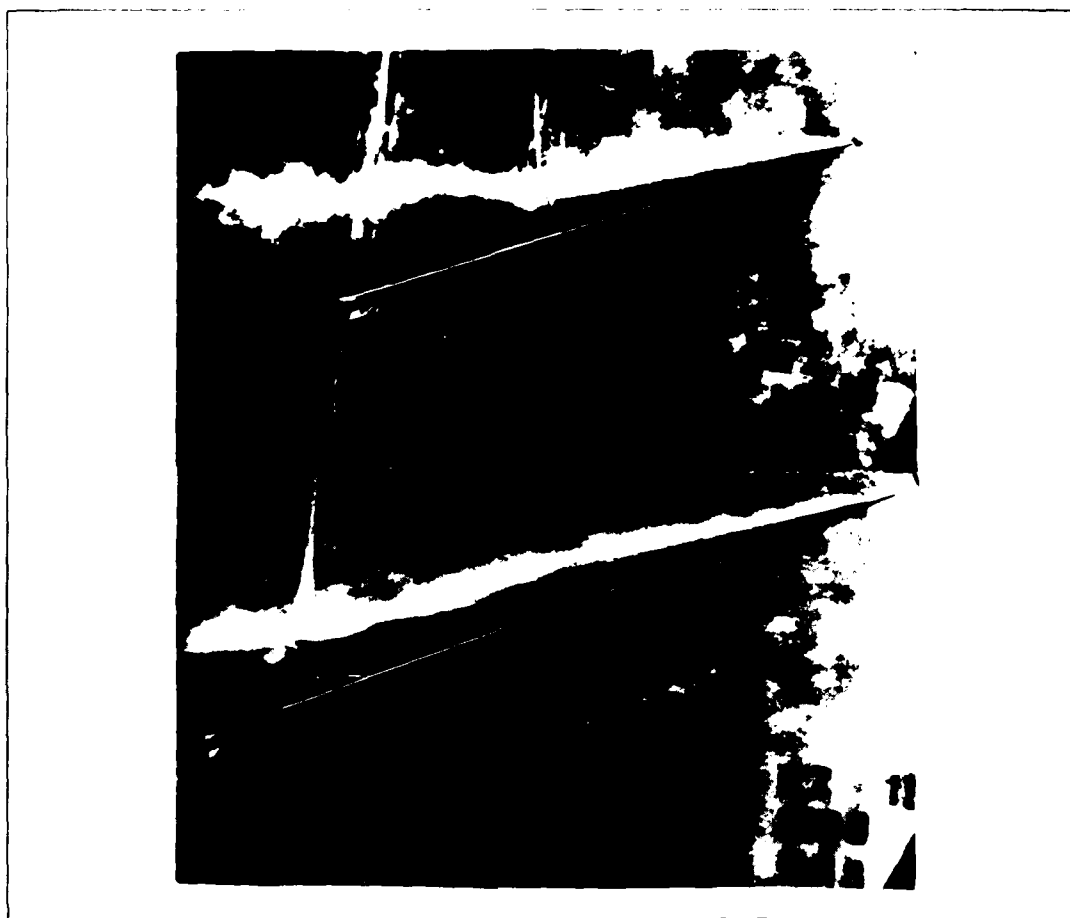


Fig.34 Flow for delta wing without and with strake:  
 $M_\infty = 0.9$ ,  $\alpha = 18^\circ$ , from Reference 59

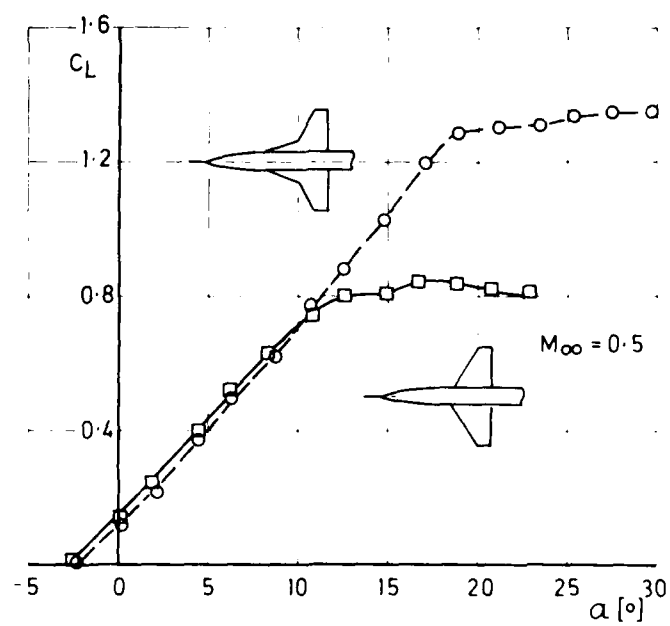


Fig.35 Lift coefficients for trapezoidal wing without and with strake,  
 from Reference 62

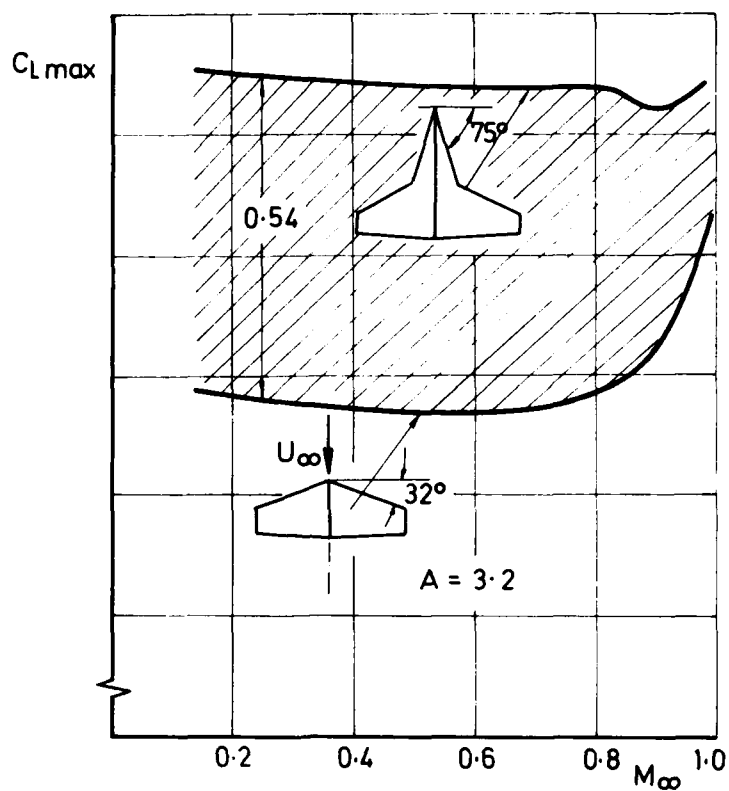


Fig.36 Maximum lift for trapezoidal wing without and with strake, from Reference 62

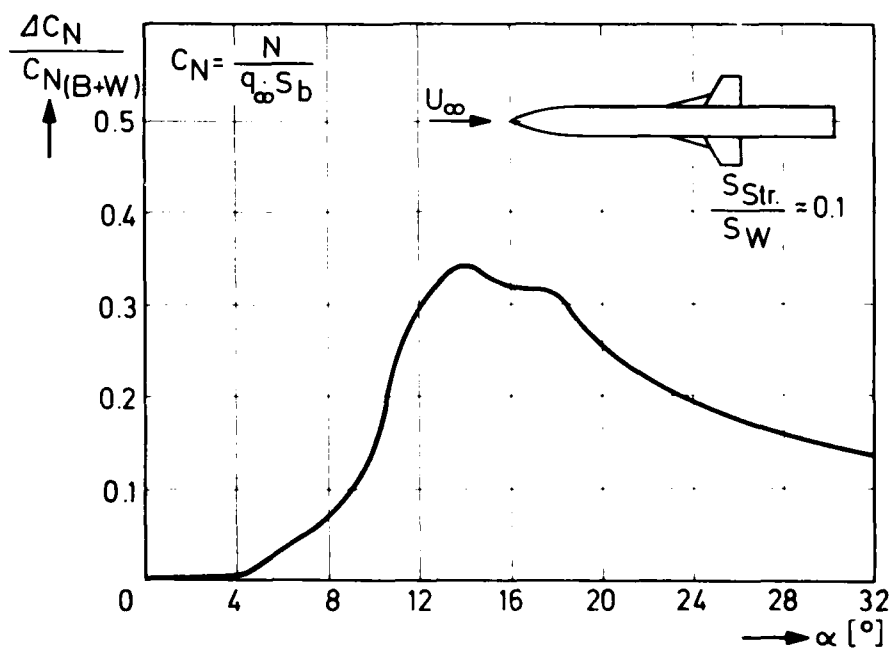


Fig.37 Influence of strake on missile configuration: relative increment of normal force coefficient due to strake vs incidence,  $M_\infty = 0.83$ ;  $Re = 1.4 \times 10^5$ , from M.Akçay, et al., Reference 67

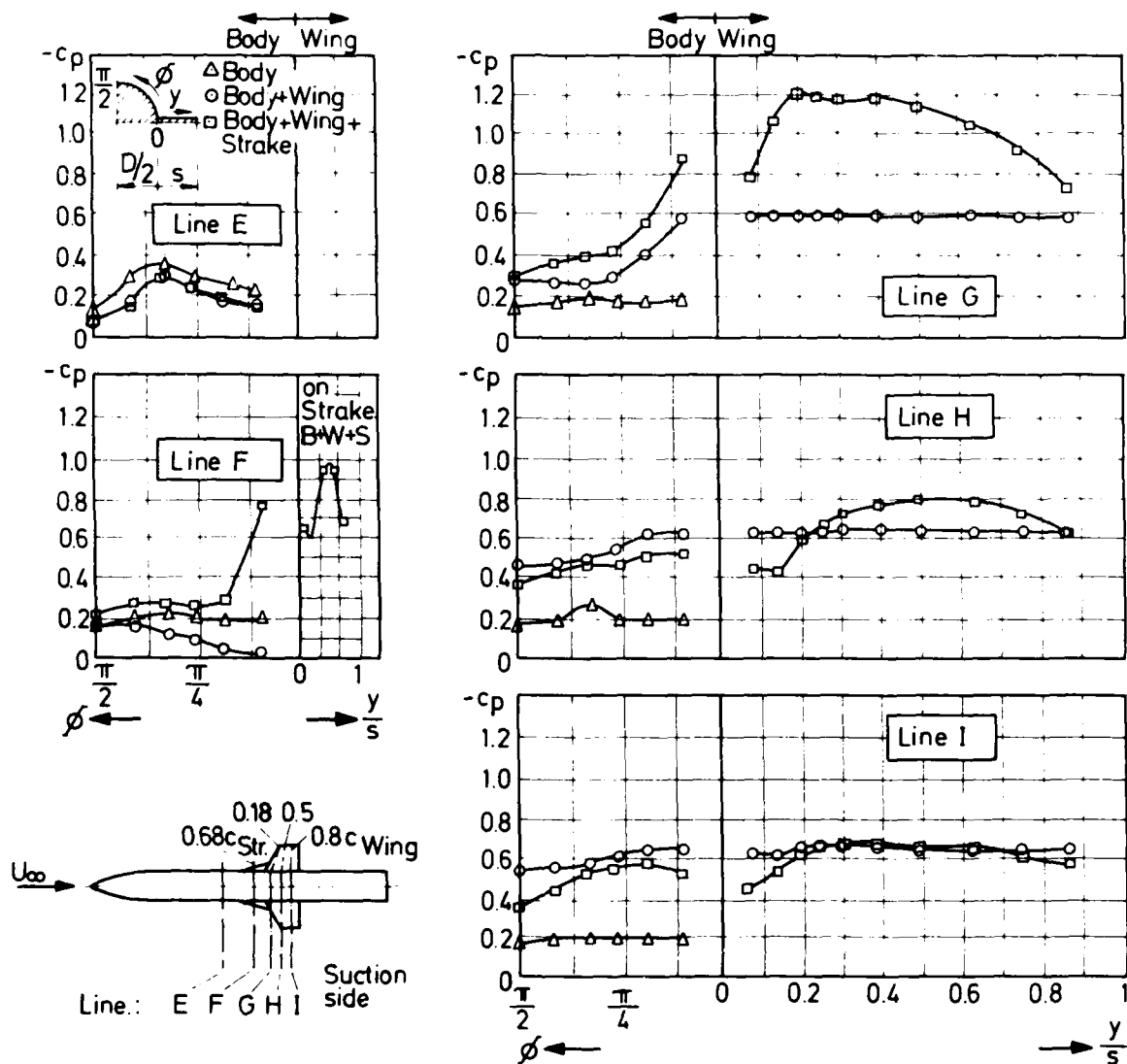


Fig.38 Influence of strake on missile configuration: comparison of measured pressure distributions  
 $M_\infty = 0.83$ ;  $Re_D = 1.4 \times 10^5$ ;  $\alpha = 21^\circ$ , from M.Akçay, et al., Reference 67

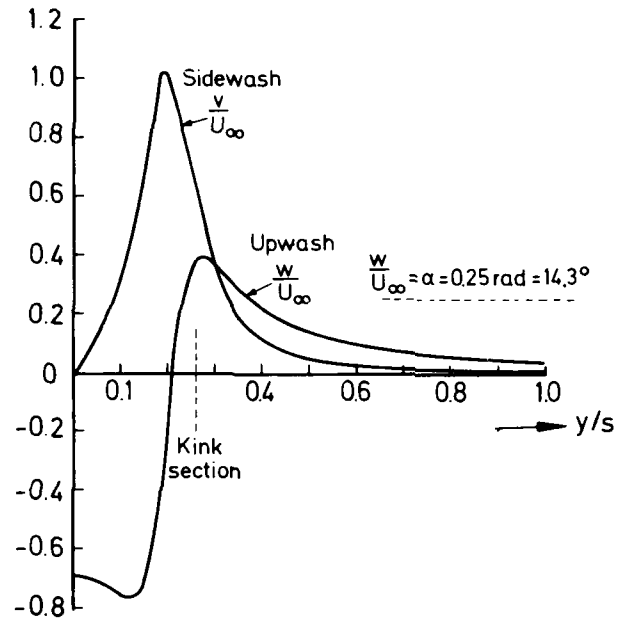


Fig.39(a) Velocities induced in wing plane by vortex pair,  $\alpha = 14.3^\circ$ ; acc. to S.P.Fiddes and J.H.B.Smith, Reference 68

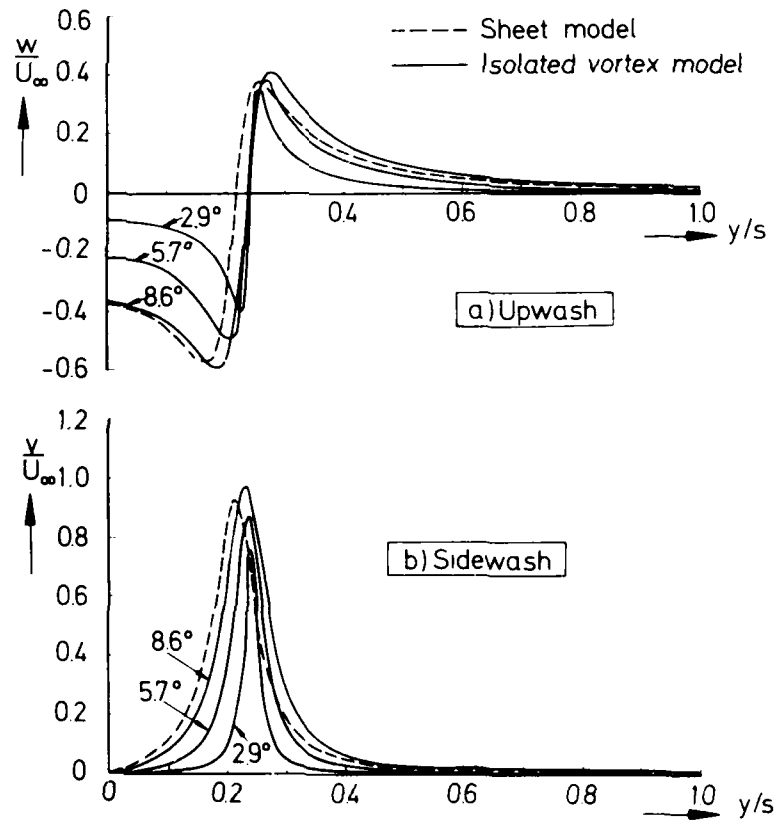


Fig.39(b) Variation of stroke vortex upwash and sidewash field with incidence acc. to S.P.Fiddes and J.H.B.Smith, Reference 68

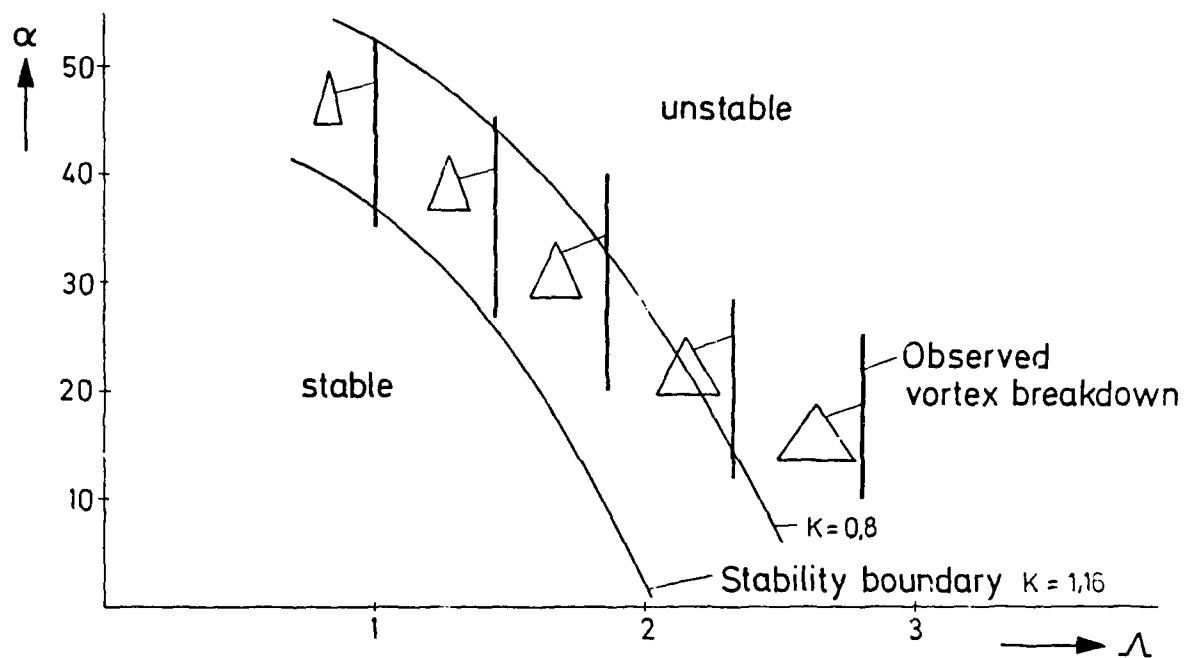


Fig.40 Theoretical stability boundary and experimental ranges of vortex breakdown, from W.Wedemeyer, Reference 69

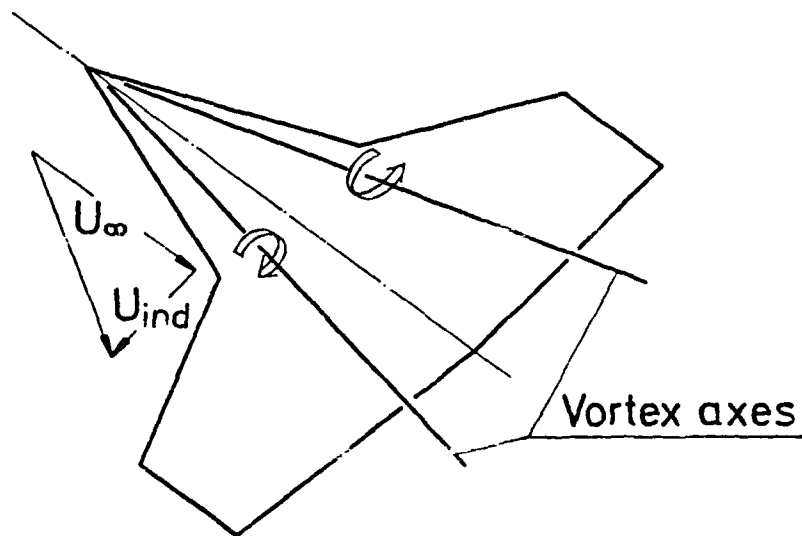


Fig.41 Effect of the strake vortices on the main wing, from E.Wedemeyer, Reference 69

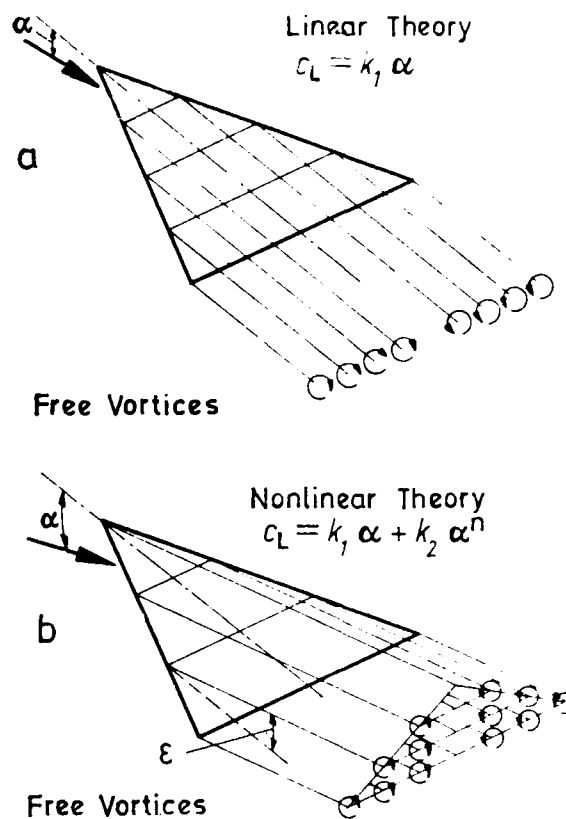


Fig.42 Vortex systems for wings

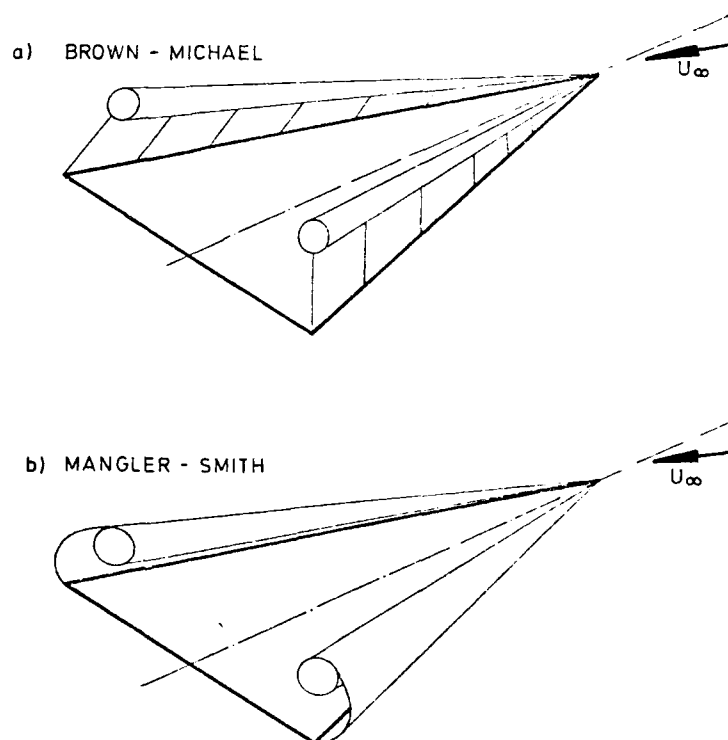
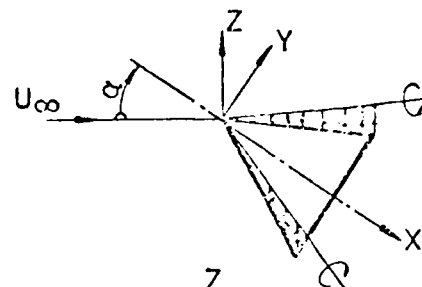


Fig.43 Flow models for slender delta wings  
 (a) Brown-Michael. (b) Mangler-Smith

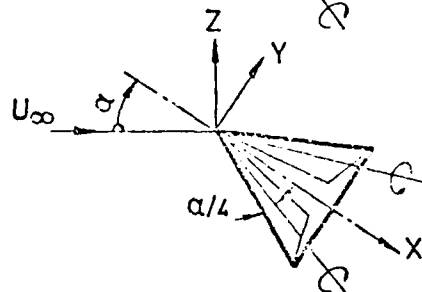


BROWN C.E./MICHAEL W.H.  
REF. 76,80.

NENNI J.P./TUNG CH.  
REF. 81,82.

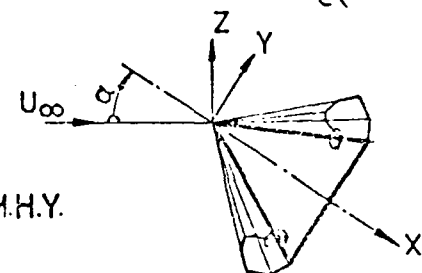


PERSHING B.  
REF. 83.

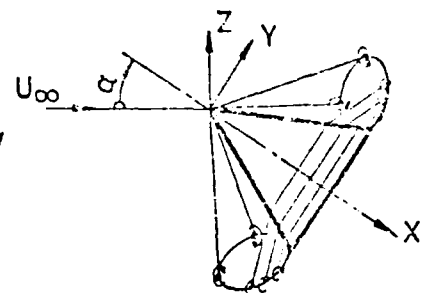


MANGLER K.W./SMITH J.H.B.  
REF. 77.

LEVINSKY E.S./SU F.H./WEI M.H.Y.  
REF. 84.



HANSON C.W./LUNDBERG E/  
SACKS A.H.  
REF. 85.



GERSTEN K. REF. 42,71.  
GARNER H.C./LEHRIAN D.E.  
LANGE A.H. REF. 86.  
REF. 87.

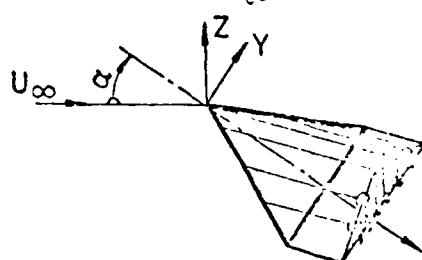
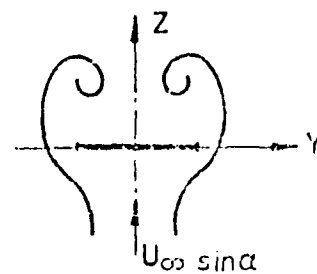
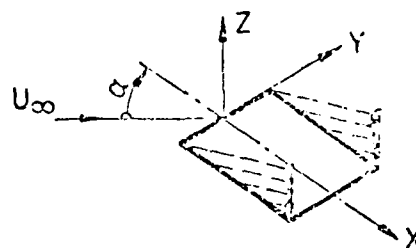


Fig.44(a) Various flow models for slender wings, from Reference 79

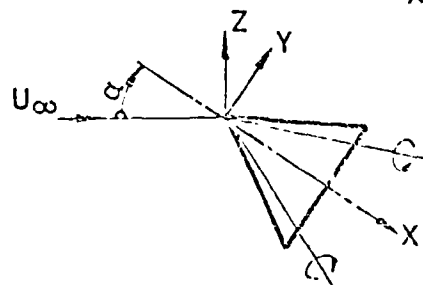
BETZ A.  
REF. 88.



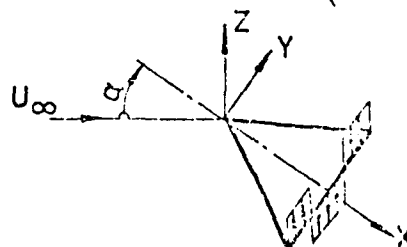
BOLLAY W.  
REF. 70.  
ERMOLENKO S.D.  
REF. 89.



LEGENBRE R.  
REF. 72, 90, 91.



KUECHEMANN D.  
REF. 92.



HUERLIMANN R.  
REF. 93, 94.

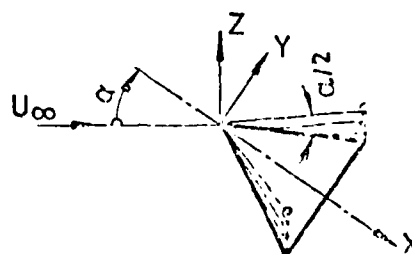
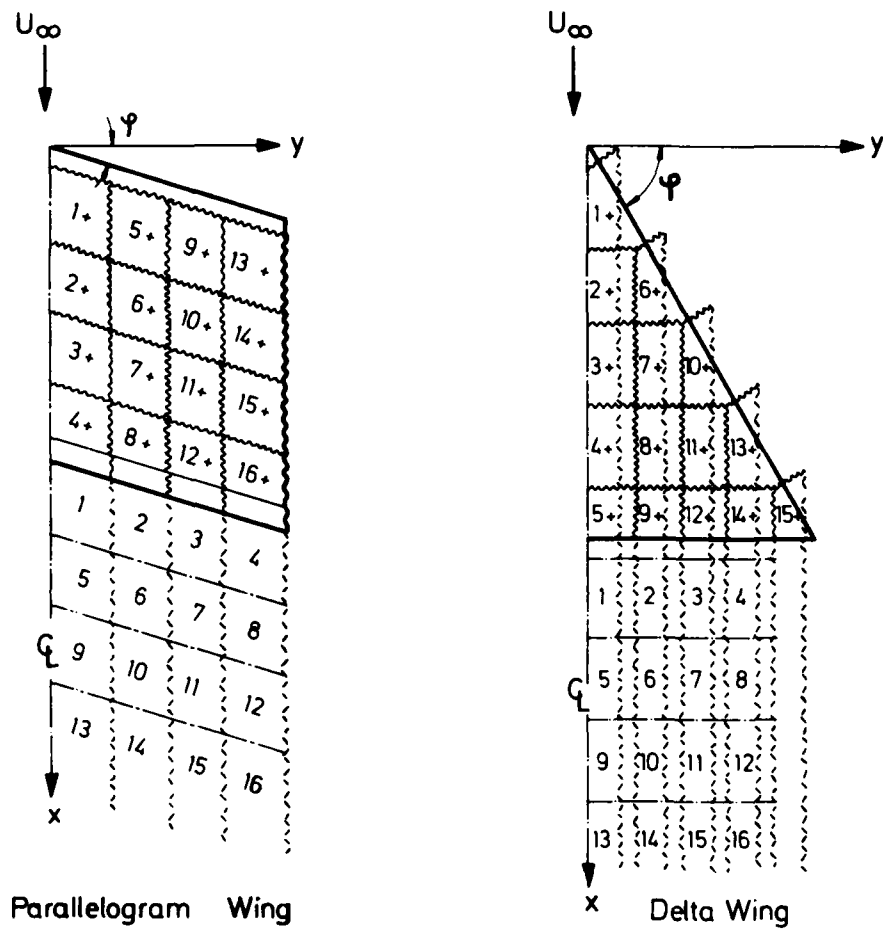


Fig. 44(b) Various flow models for slender wings, from Reference 79



+ Control Points; — Bound - Vortex Lattice; - - - - - Trailing - Vortex Lines.

Fig.45 Arrangement of the discrete-vortex model, acc. to O.A.Kandil, Reference 99

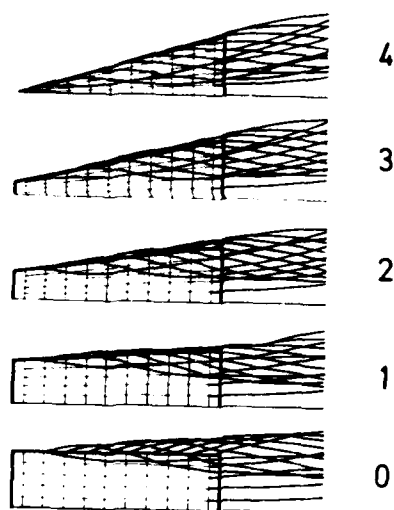
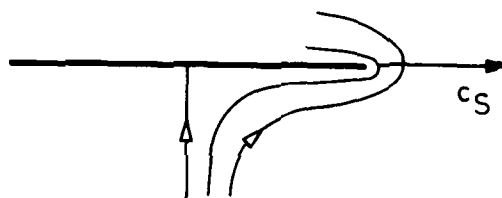
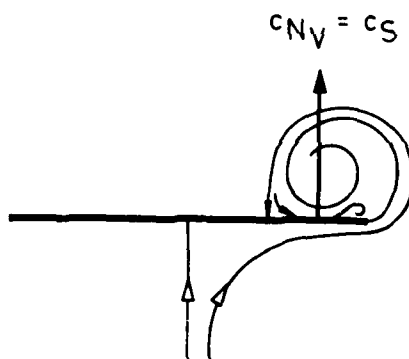


Fig.46 Calculation of delta wing by progressive deformation of a rectangular wing, acc. to C.Rehbach, Reference 98



Attached Flow with Leading-Edge Suction,  $c_S$ ;



Separated Flow with Vortex Suction,  $c_{N_V}$

Fig.47 Leading-edge suction analogy acc. to E.C.Polhamus, Reference 111

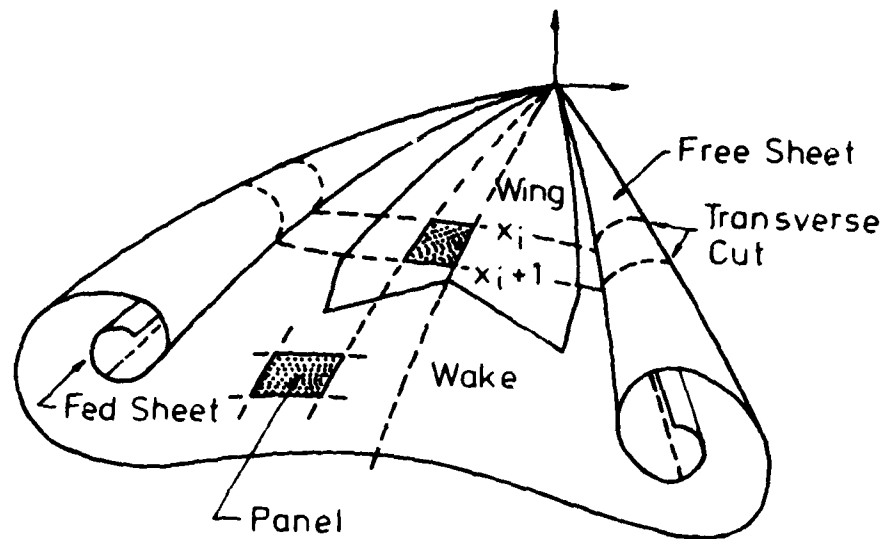


Fig.48 Schematic description of wing and flow model  
acc. to J.A.Weber, et al., Reference 114

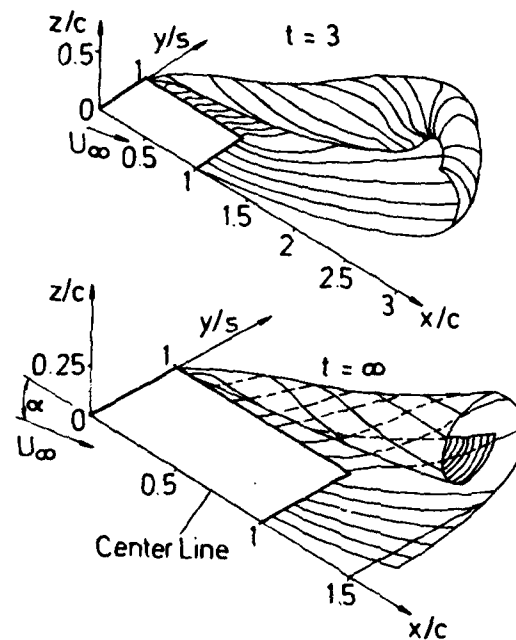


Fig.49 Computed development of vortex wake on rectangular wing,  
 $A = 1$ , at  $\alpha = 30^\circ$ , from Reference 115

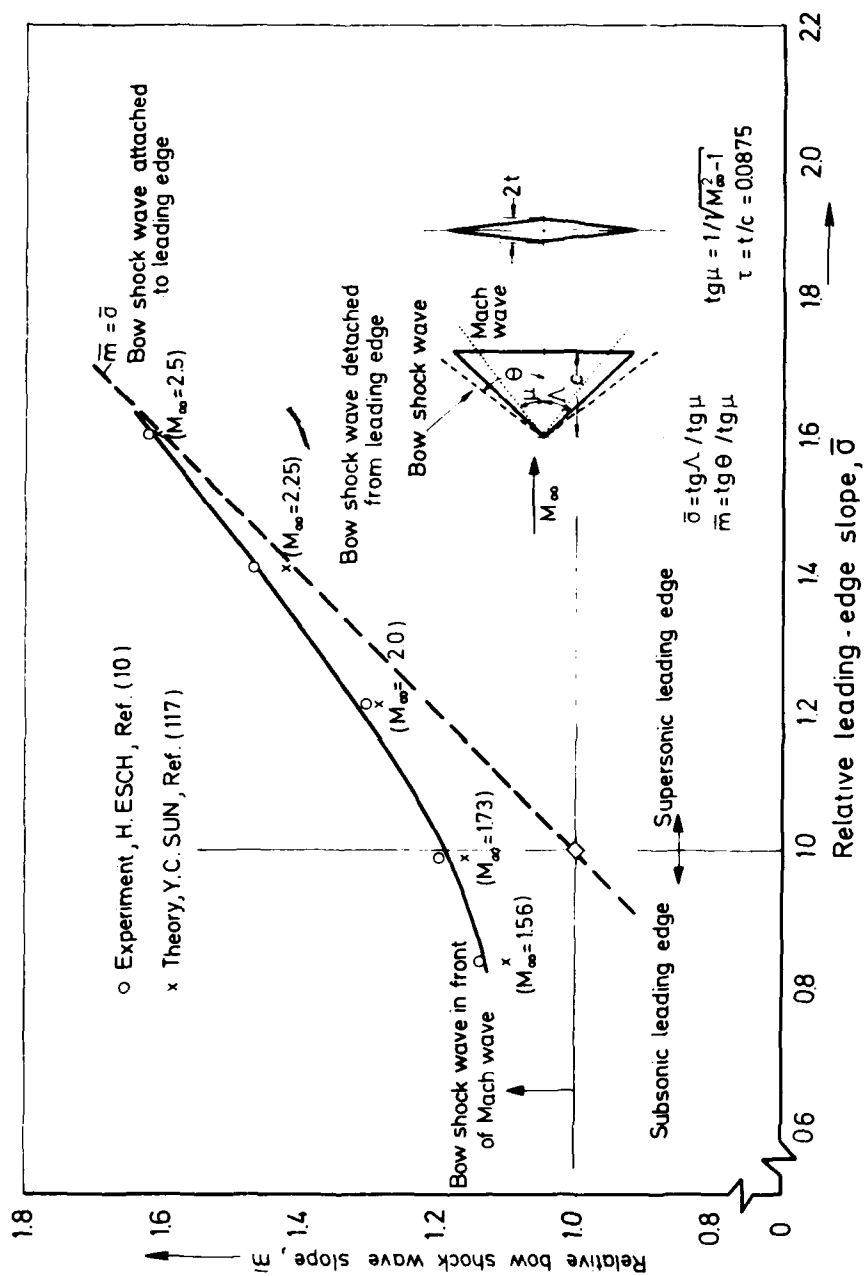


Fig.50 Bow shock wave slope for delta wing with rhombic cross-section at zero incidence. Transition from subsonic to supersonic leading edge

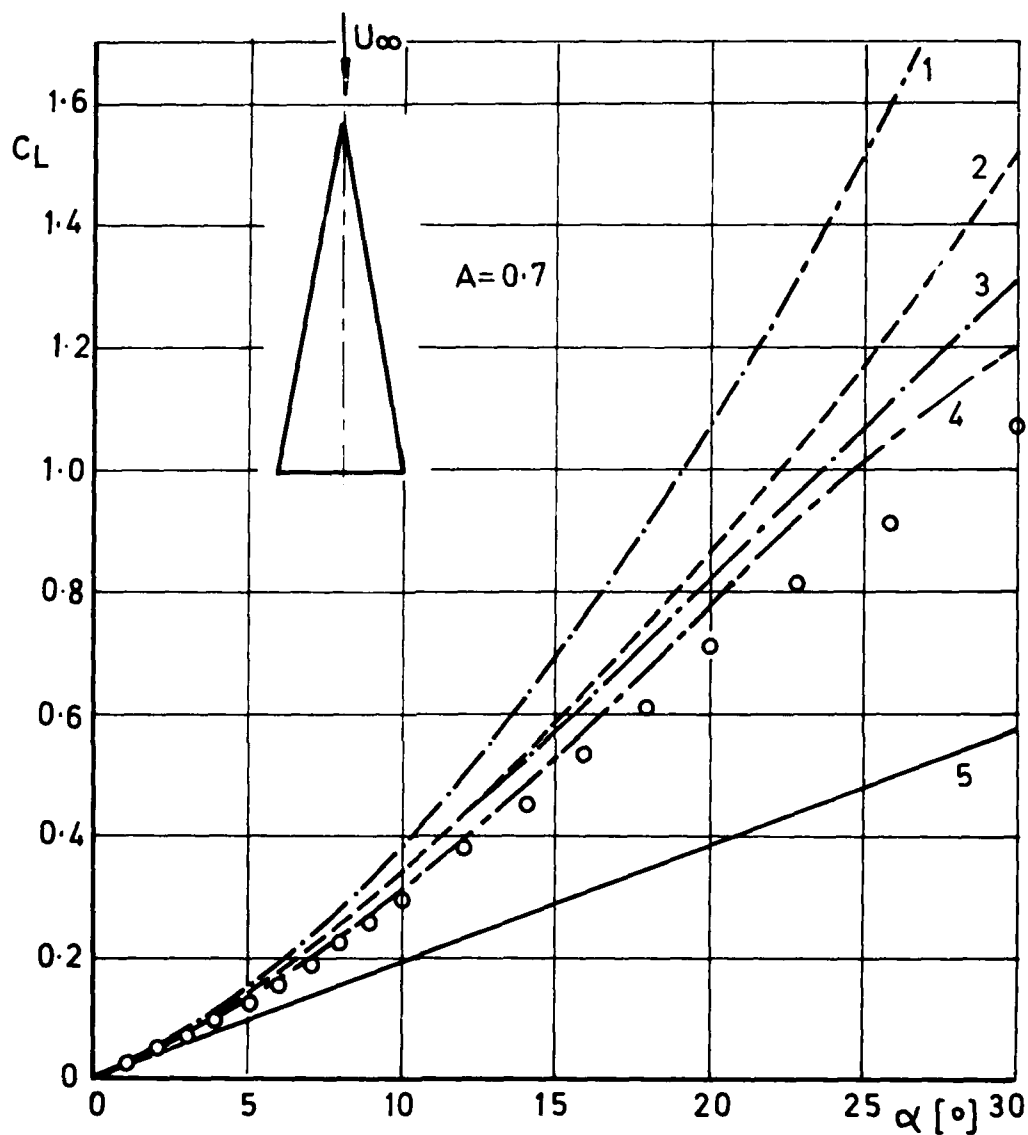


Fig.51 Comparison of various theories with experiment for slender delta wing, from Reference 94

- 1 C.E.Brown and W.H.Michael, Reference 80
- 2 R.H.Edwards, Reference 75
- 3 J.H.B.Smith, Reference 78
- 4 K.W.Mangler and J.H.B.Smith, Reference 77
- 5 R.T.Jones, Reference 73
- Experiment P.T.Fink, Reference 36

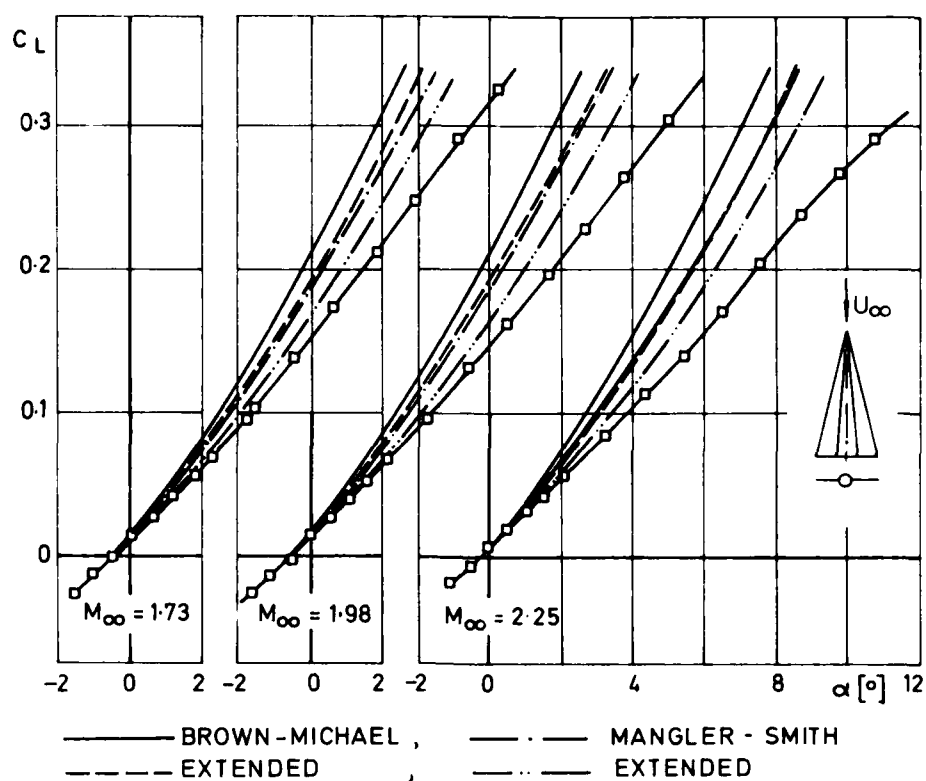


Fig.52 Comparison of theoretical predictions and experiment, from Reference 95

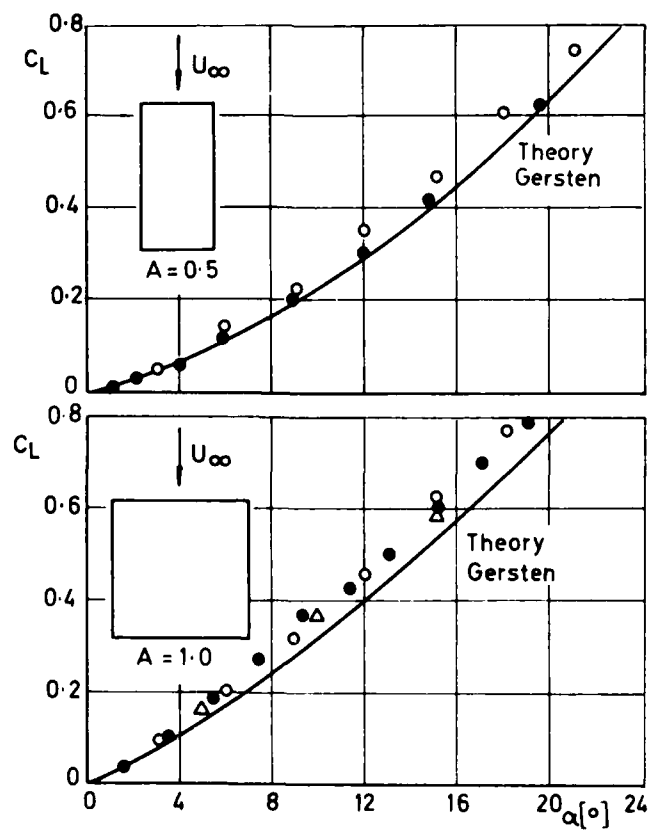


Fig.53 Comparison of theoretical predictions with experiment for rectangular wings, from Reference 43



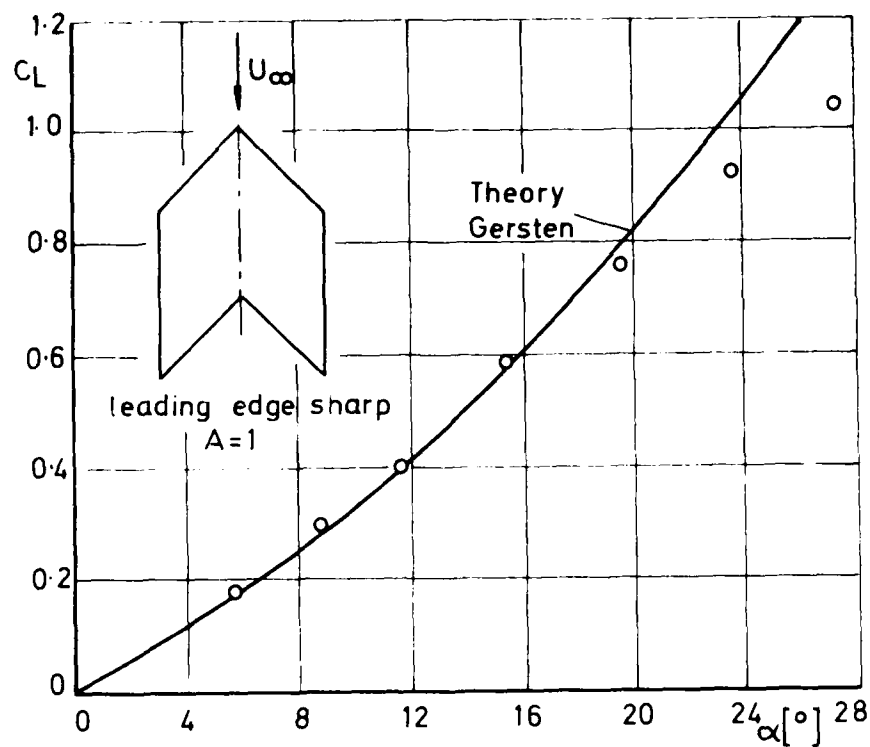


Fig.54 Comparison of theoretical predictions with experiment for swept wing. from Reference 43

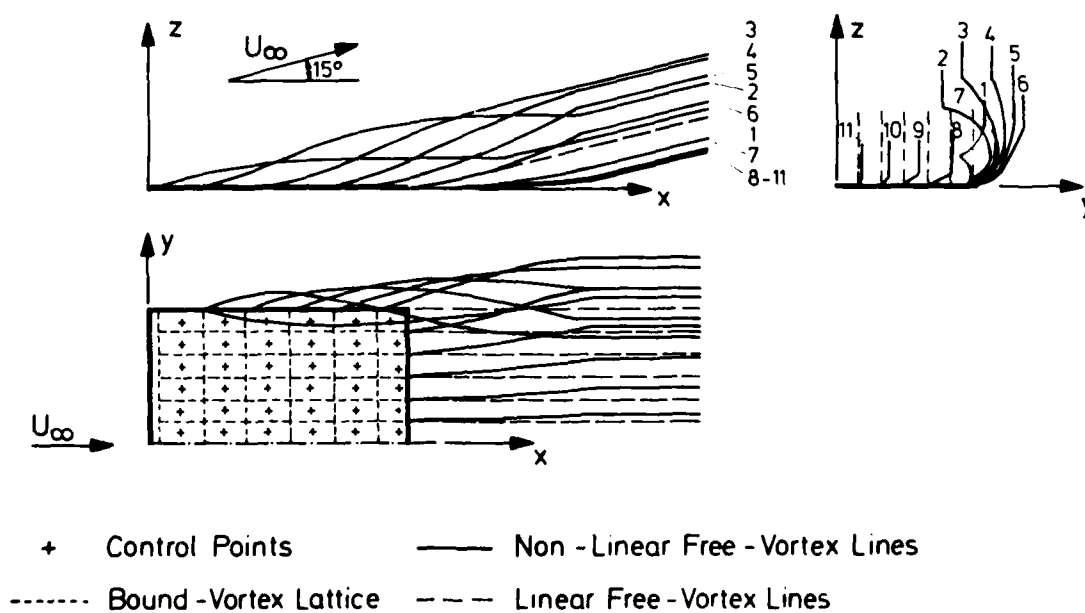


Fig.55 Wake shape of a rectangular wing.  $A=1$ , acc. to O.A.Kandil, Reference 99

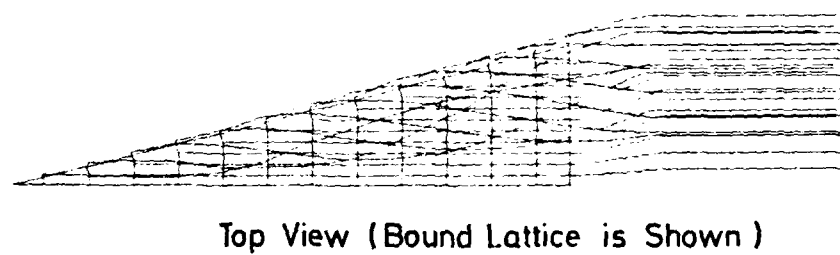
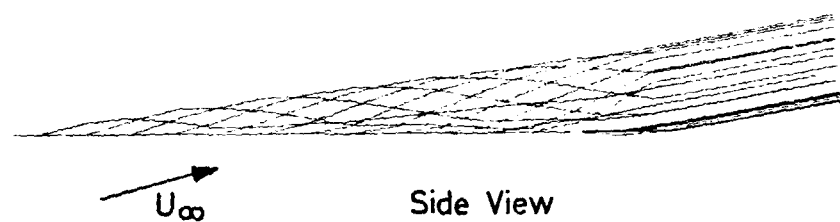
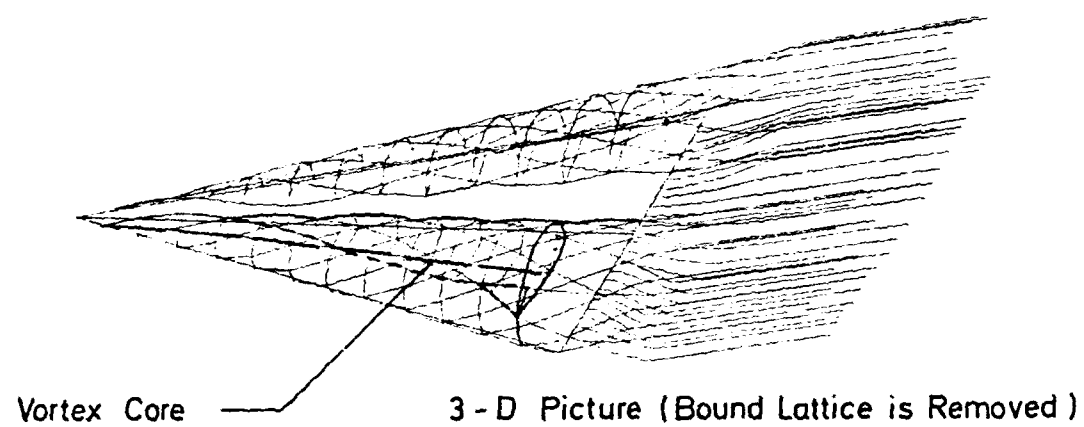
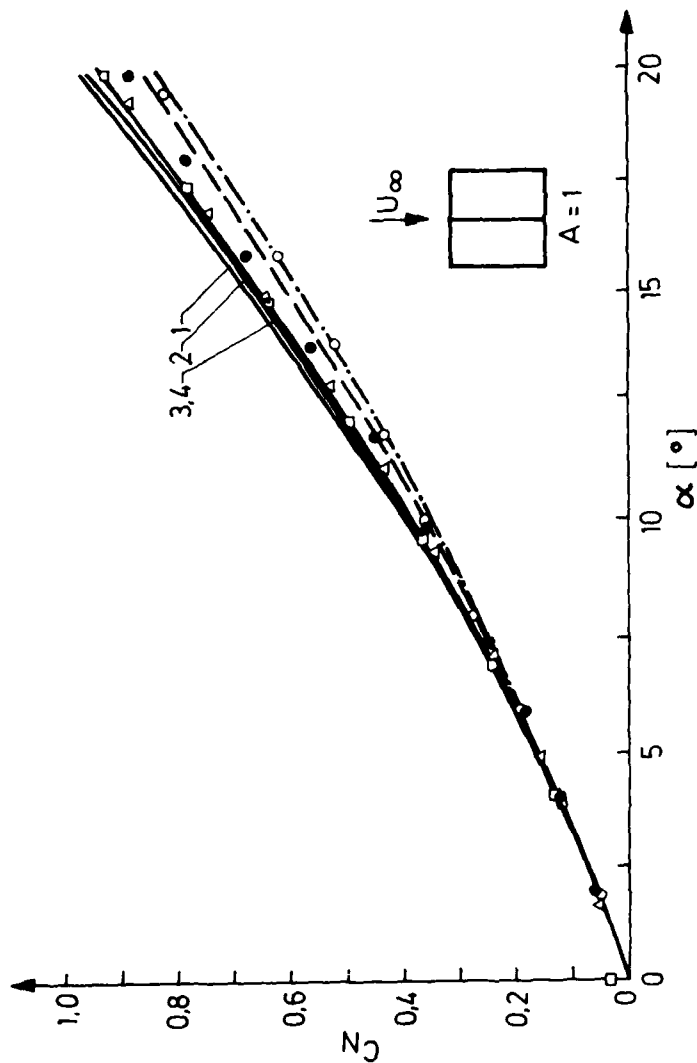


Fig.56 Wake shape of a delta wing,  $A = 1$ ,  $\alpha = 15^\circ$ , acc. to O.A.Kandil, Reference 123



#### Numerical Results

- Belotserkovskii, Ref. 96
- Ermolenko, Ref. 89
- Bradley, et al., Ref. 122
- Kandil, Ref. 99

Curve No. 1 = 4x4 lattice, No. 2 = 6x6,  
No. 3 = 9x7, No. 4 = 9x9

#### Experimental Results

- Belotserkovskii, Ref. 96
- Ermolenko, Ref. 89
- Winter, Ref. 40
- △ Scholz, Ref. 41

Fig. 57(a) Comparison of theoretical predictions and experiment for rectangular wing. Normal-force coefficient vs. angle of attack, from Reference 99

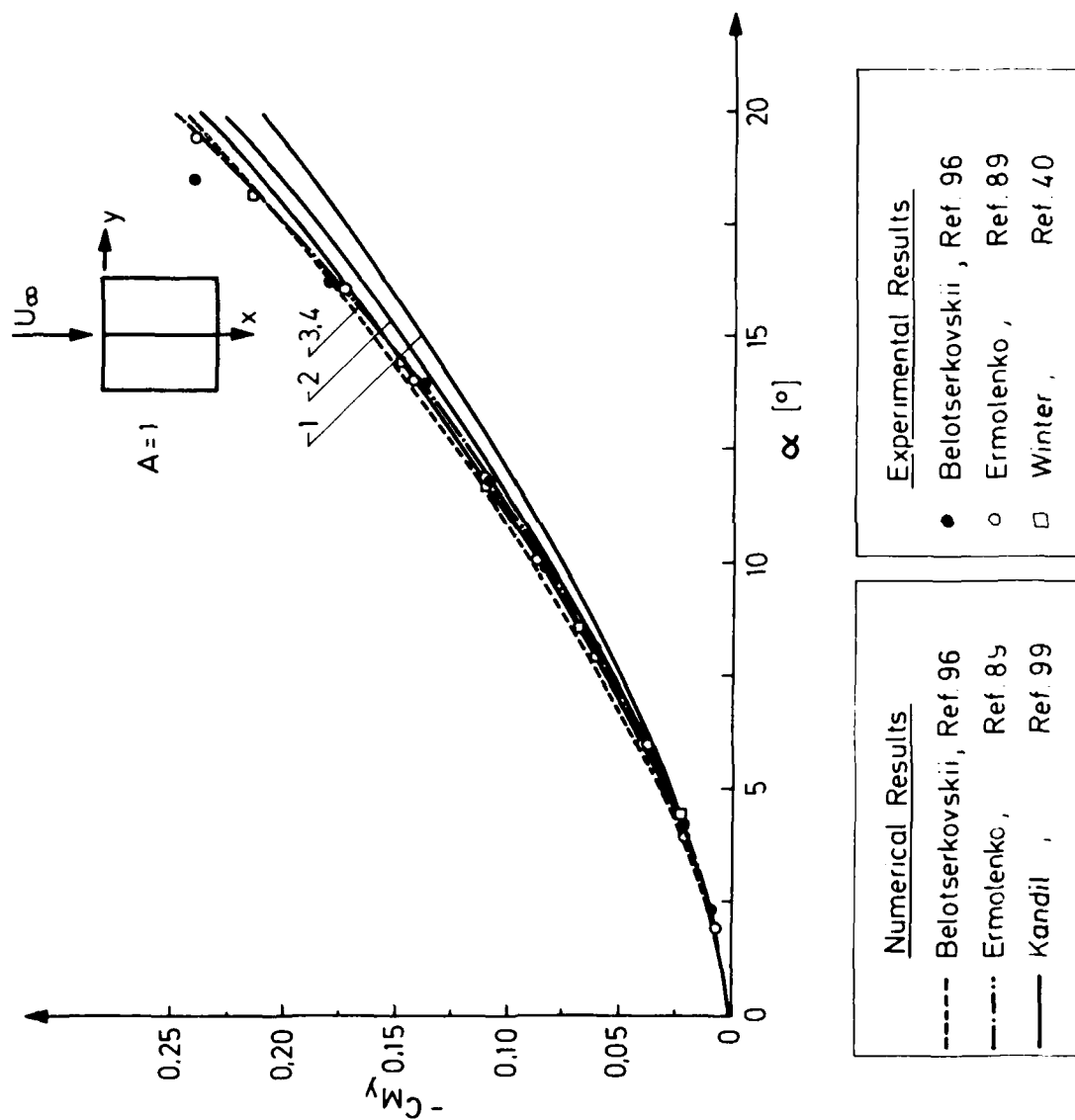


Fig.57(b) Comparison of theoretical predictions and experiment for rectangular wing. Pitching-moment coefficient vs. angle of attack, from Reference 99

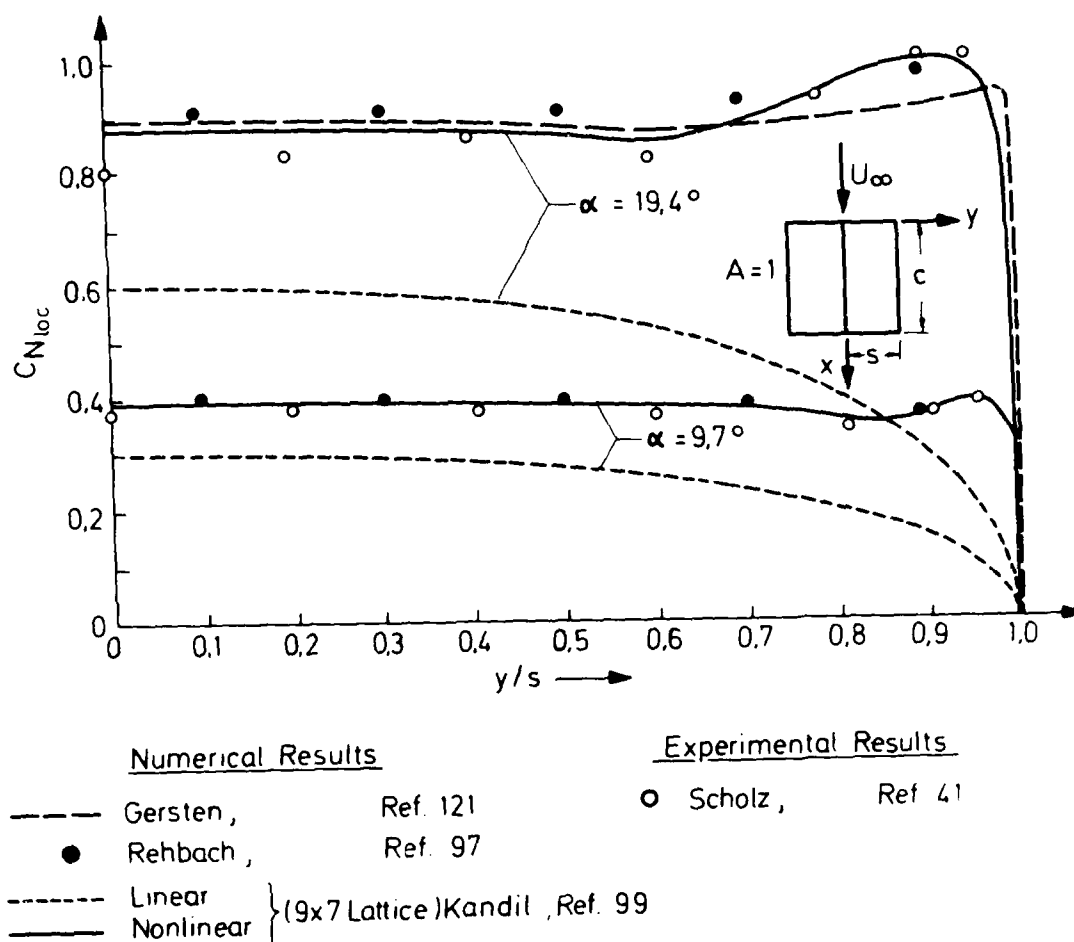


Fig.58 Comparison of theoretical predictions and experiment. Spanwise variation of normal-force coefficient, from Reference 99

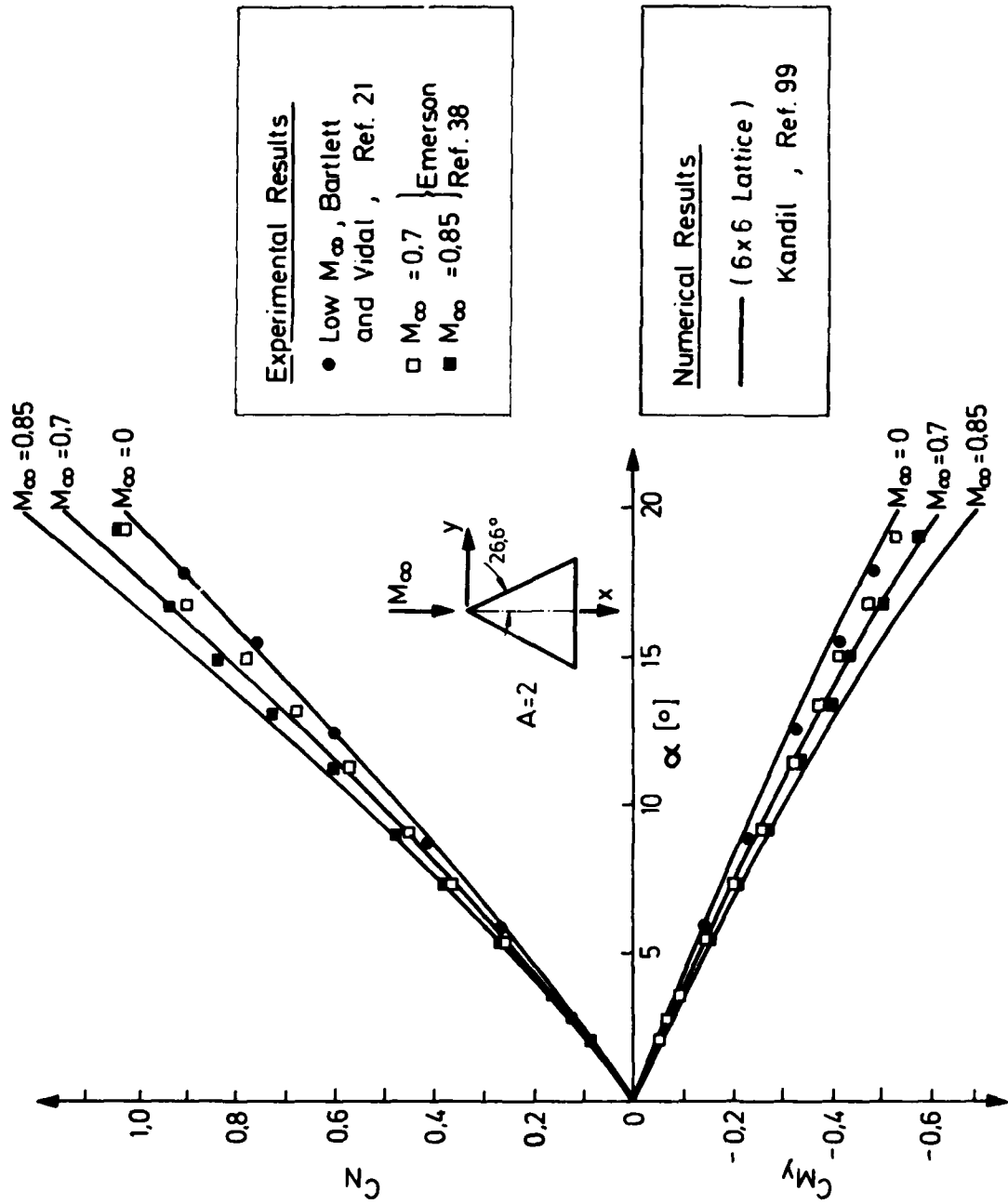
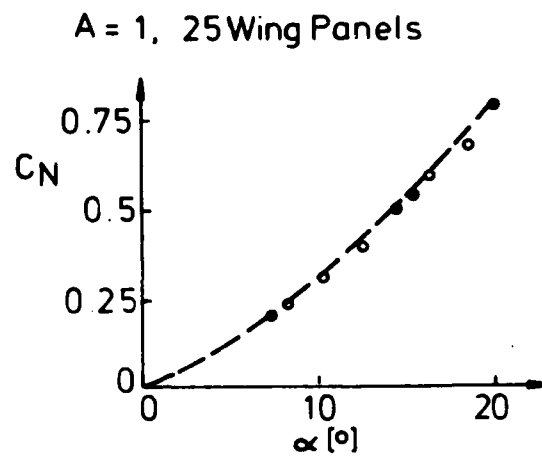


Fig.59 Comparison of theoretical predictions and experiment for delta wing. Normal-force and pitching-moment coefficients, from Reference 99



- Weber et al , Ref. 114
- Polhamus , Ref. 125
- Peckham Experiment , Ref. 124

Fig.60 Comparison of theoretical predictions and experiment for delta wing normal-force coefficient, acc. to J.A.Weber, et al., Reference 114

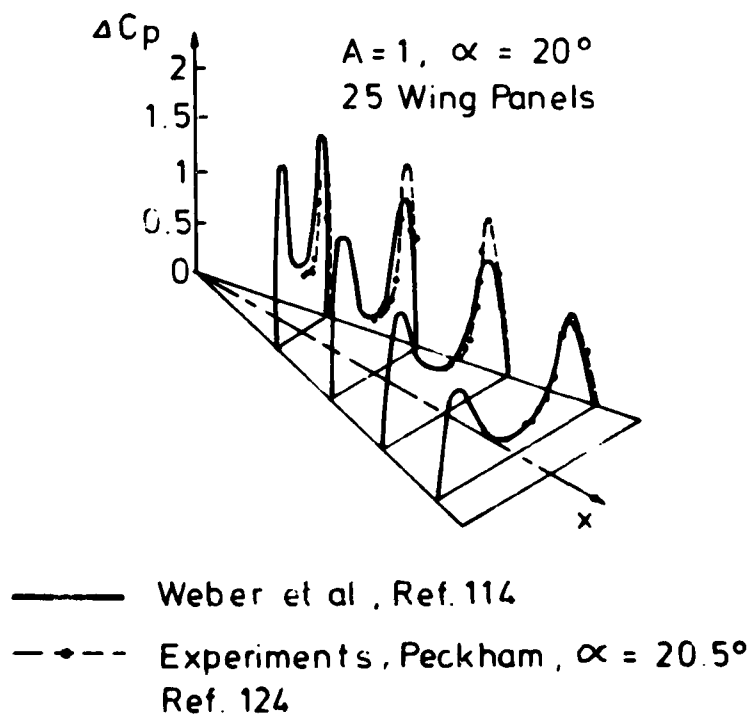


Fig.61 Comparison of theoretical predictions and experiment for delta wing load distribution, acc. to J.A.Weber, Reference 114

## BODIES

H. Esch

DFVLR  
Köln-Porz, Germany1. Introduction

Most missiles fly only a few seconds. They have no time to get back the money for an elaborate shape or a perfect surface finish. The production costs must be kept low. It is a reasonable aspect to drop a few percent of efficiency when by this the costs can be reduced. This means that the geometries of missiles are often relatively simple. The bodies have circular cross sections and often long cylindrical portions. In many cases the form is not given by aerodynamic requirements but by the payload, the infra-red head, the boxes, and launching devices, which are already in use when a new missile is designed. Fig. 1 shows some typical body shapes. They include short projectiles and multistage sounding rockets with fineness ratios of 20 or even more, nose and afterbody shapes, which have been optimized with respect to a minimization of drag, and blunted noses, which are given by guidance requirements. Lately one finds more complicated geometries with integrated air-intakes, noncircular cross sections a.s.o.

This lecture will deal with the determination of the static aerodynamic coefficients of axisymmetric bodies. According to physical aspects the forces are decomposed into potential flow, friction, and separated flow (fig. 2). For each of these 3 types of flow different computational methods must be applied. Here only relatively simple methods will be discussed which allow a quick estimation of the aerodynamics. By these methods only slender shapes can be treated. The problems which arise from the bluntness will therefore be discussed in every chapter of this lecture. Before undergoing flight tests missiles are tested in windtunnels. Besides this most of the design data are based on windtunnel experiments. As the Reynolds numbers of the windtunnel models and of the real missiles are often different and as this difference may have an influence on the aerodynamic coefficients the influence of the Reynolds number will be discussed too in every chapter. The discussion of the aerodynamics of bodies can't be complete within the frame of this lecture. Only some aspects of static coefficients will be treated. Other very important aerodynamic problems as for instance dynamic stability, Magnus forces, internal flow of bodies, stage separation are not considered.

2. Computational methods (potential flow)

In the following results of computational techniques and windtunnel experiments will be compared. Therefore at first some words about theoretical methods. There exist several methods for the computation of the potential flow over axisymmetric bodies. Since long the method of characteristics and the method of singularities are known. From these two methods several other methods have been derived, which one could call "classical" methods, e.g. the v. Karman-Tsien method (1932) [1], the slender body theory (Munk 1924, Jones 1946) [2], the "Second order shock expansion theory" (Syvertson, Dennis 1955) [3]. They compare partly well with experiments but are restricted in their application: to purely subsonic or supersonic flows (v. Karman-Tsien), to purely supersonic flow (second order shock expansion theory). Besides this restriction in the Mach number range only rather slender shapes can be treated (fig. 3).

The man in the industry who had to design missiles often could not use these theoretical methods. His missile for instance had to have a blunted infra-red head and it had to fly in the transonic Mach number range. Hence he had to build up his own procedure from his experience, from the literature, from different theories, and from windtunnel measurements. So several empirical methods have been developed, the best known of which is the Datcom method [4]. By use of lots of charts and tables and simple formulas the aerodynamic coefficients of all conventional missiles can be computed. There are also computer programs in which all these data have been stored which allow a rapid estimation of the stability and the performance of missiles e.g. [5]. One condition must be fulfilled when using empirical techniques. Problems similar to those which one wants to solve must have been treated before. This is often not the case with modern missile concepts. There don't exist enough data on integrated air intakes, complicated cross sections with shock-boundary layer interferences a.s.o.

In the last years work has begun on new methods in order to overcome the difficulties associated with the "classical" methods (slender shapes, purely subsonic or supersonic flow). E.g. in supersonic flow on blunt bodies at angle of attack the shape of the detached bow shock and the subsonic region with the sonic line are calculated by a three dimensional time dependent method (Rusanow difference scheme [6]). For the purely supersonic flow field downstream a more economical method is used. At the DFVLR in Köln-Porz C. Weiland [7] is working in this field with the aim to include the calculation of the attached three-dimensional boundary layer and in later years also the separated flow.

In the last years panel methods came more and more into use. They need big computers with large core storages and long computing times. From this one could conclude that these methods are more accurate than the simple "classical" methods. But this is true only as far as the geometry is concerned. Complete missile configurations can be represented by the panels. Hence one does not need to calculate the forces on the body and the wings separately and add the interferences. But the physical flow models are normally very



simple. The panel methods are well suited for configurations with large interferences but have no advantages over the "classical" methods when the flow over isolated bodies or isolated wings must be computed [8].

### 2.1 Method of linearized singularities

Axial- and normal forces are given by integration of the pressure distribution. The pressure coefficient is related to the velocity by the linearized Bernoulli-equation. The velocity is induced by a distribution of sources (thickness distribution) and of doublets (angle of attack). From this one gets an equation for the potential of the body. In this equation the strength of the singularities is unknown. The strength is determined by the boundary condition: on the body the flow must be tangential with the body contour. In the v. Karman-Tsien method the body is divided into frustums and the boundary condition is fulfilled in one point of each frustum. In slender body theory in addition to the simplifications already made - i.e. linearized Bernoulli - equation, squares of perturbation velocities neglected - the source strength is proportional to the slope of the cross section  $dS/dx$  and the boundary condition is fulfilled on the body axis and not on the body contour. From this follows that the pressure and normal force distributions are  $\neq 0$  only when  $dS/dx \neq 0$  (fig. 7).

A body is slender when it lies well within the Mach cone from the vertex. This means that in transonic flow also relatively blunt bodies may qualify as slender whereas at hypersonic Mach numbers all practical shapes are too blunt to be treated by slender body theory. In the literature the following limits are given for the application of the methods of linearized singularities in supersonic flow.

slender body theory:  $0 \leq \sqrt{M^2-1} / (l_N/D) \leq 0.05$

v. Karman-Tsien:  $0.05 \leq \sqrt{M^2-1} / (l_N/D) \leq 0.4$

The v. Karman-Tsien method really fails when the Mach angle is smaller than the slope of the contour (fig. 3).

### 2.2 Second order shock expansion method

The contour is approximated by a tangent-body. Mach number and pressure on the starting cone can be determined by known theories (e.g. from NACA Rep. 1135). For the flow over the juncture between two frustums the Prandtl-Meyer relation is used. From this one gets the conditions at the upstream end of the frustum. The pressure distribution over the frustum is determined with the aid of the equation for a streamwise pressure gradient  $\partial p / \partial s = 1/\cos \mu \cdot \partial p / \partial C_1$ . For bodies at angle of attack the normal force coefficients of cones are taken (for instance from NACA Rep. 1135) and corrected. The second order shock expansion method is only applicable in purely supersonic flow in the range

$0.4 < \sqrt{M^2-1} / (l_N/D) < \infty$ . A computer program for zero angle of attack which includes the calculation of the turbulent boundary layer has been published in [9].

### 2.3 Empirical methods (fig. 4)

Empirical methods are based on different data, very often on experimental results. As these data stem from different sources (theories, windtunnels with different Reynolds numbers, different types of tests: force- and pressure measurements, free flight) there may exist some discrepancies. But they are normally small. On the other hand the many different methods and data on which these techniques are based lead to a greater reliability.

### 2.4 Comparison of different computational methods for potential flows

The pressure distribution on slender bodies in the linear angle of attack range can be calculated with the aid of the relatively simple methods mentioned above. None of these techniques has decisive advantages over the others. Fig. 7 shows results for an ogive-cylinder body with nose fineness ratio 3.5. At  $M = 1.5$  and zero angle of attack the v. Karman-Tsien method and the second order shock expansion method give the same pressure distribution. But at  $M = 3.5$  the method of singularities reaches its limit. The Mach angle is nearly equal to the contour angle at the vertex ( $\sqrt{M^2-1} / (l_N/D) = 0.96$ ). Hence the lower pressure coefficient at the vertex and the lower pressure drag coefficient (fig. 7).

According to the very simple slender body theory the normal force distribution is proportional to the derivative of the cross section with respect to  $x$  - i.e. the normal force is zero on a cylindrical portion of a body - and it is independent of Mach number. This is a good approximation in subsonic and transonic flows (fig. 7). A nose fineness ratio of 3.5 at a Mach number of 3.5 is far outside the range of this simple theory (fig. 7). Nevertheless slender body theory can often be used when only rough approximations are needed.

In supersonic flow the point of zero local normal force is shifted downstream with increasing Mach number. This is predicted by the method of singularities (v. Karman-Tsien, FFA-panel) whereas the second order shock expansion method does not predict a change of sign for this configuration (fig. 7).

Before starting extensive calculations one has to check what is the cheapest method to solve a problem. Fig 5 shows an example where the v. Karman-Tsien method [1] gives the

same results as the method of Weiland [7] which for this case needed a 3000-times longer computing time. But if the ogive-cylinder body of fig. 5 were not pointed but spherically blunted the v. Karman-Tsien method would fail and the more complicated procedure would have to be used.

The agreement between experiments and the relatively simple theoretical methods is sometimes not good. Nevertheless they have their value. It is often not necessary to use complicated methods, e.g. one does not need a complicated boundary layer method which takes the heat transfer into account when the difference to the adiabatic wall temperature is small or when the contribution of the friction to the drag is small even if there exists a large heat transfer. Fig. 6 summarizes what was said about the different computational methods.

When applying the v. Karman-Tsien method or the second order shock expansion method it is useful to know how many steps are needed for the approximation of the contour by a tangent body, since the computing time is a function of these steps. When calculating the wave drag and the normal force of an ogive-cylinder body at  $M = 2$  by the v. Karman-Tsien method, the number  $n$  of disks in the nose region of the approximating body was varied. The axial force coefficient is relatively independent of  $n$  - less than 1% - whereas the normal force coefficient increases rapidly when  $n$  falls short of a certain amount. In this case a partition of the nose into 8 disks is sufficient (fig. 8).

When using computer programs one should know the ranges of their applicability. Nowadays the listings of many complicated programs are available. So one is able to do extensive calculations without having programmed the methods oneself and without possibly being well acquainted with the method. Hence one may run the risk to violate certain conditions without knowing it, e.g. fig. 9. In this case the normal force could be calculated by the v. Karman-Tsien method although the flow was locally subsonic. This error could easily be spotted, but in complicated computer programs with many subroutines it is very difficult to know the limits of the program. Normally one has no time to go through all the details of a program and may run the risk to get absurd results.

The references [5], [8], [9], [12], [14], [17] include program listings.

### 3. Axial force

#### 3.1 Drag coefficient at zero angle of attack

The drag is divided into the forebody pressure drag, the friction drag, and the base drag. These contributions are determined separately. Their importance for the total drag depends on the geometry of the body, the Mach number, and the Reynolds number. E.g.: When the nose shape is not too blunt the pressure drag in subsonic flow may be neglected, the base drag can be reduced by boattailing (conical afterbodies in supersonic flow:

$C_{Db} = C_{Db \text{ cylinder}} \cdot (db/D)^2$ ), and the largest contribution to the total drag of long slender bodies stems from the friction (fig. 10).

##### 3.1.1 Pressure drag

The pressure drag of not too blunt nose shapes is almost zero in subsonic flow. At supersonic Mach numbers the pressure drag can be calculated by the v. Karman-Tsien method or the second order shock expansion method. Fig. 11 shows a comparison of the results. There are differences of up to 15 % between both methods in the upper Mach number range where the method of singularities begins to fail. The agreement with experimental results is not bad when the uncertainties of the windtunnel tests are taken into account. The total drag is measured by a balance, the measured base drag and the computed friction drag are subtracted, so that the pressure drag is the difference of large figures. In addition there are errors in the measurement of  $C_{Dtotal}$  and  $C_{pb}$  and one has to make several assumptions (transition point of boundary layer, heat transfer) when calculating the friction drag. Hence the experimentally determined pressure drag coefficient is in this case not very accurate.

The v. Karman-Tsien method becomes less accurate with increasing Mach number. The nose shape must be slender i.e. the body must lie well within the Mach cone from the nose. But at  $M = 3.5$  the Mach angle is equal to the contour angle at the vertex. Hence the body is no longer slender. The low drag coefficient at high supersonic Mach numbers is due to a low pressure coefficient over the front part of the nose (fig. 7). The v. Karman-Tsien method and the second order shock expansion method can also be used for boattailed and slightly flared afterbodies. At Mach numbers around  $M = 1$  the pressure drag of slender nose shapes ( $l_N/D \geq 3$ ) can be calculated by the method of Wu and Aoyama [12].

#### Blunt shapes

Shapes which are not slender must be treated by other methods. In supersonic flow one could for instance use the method of Weiland [7] as long as no separation occurs (e.g. spherically blunted, not flat faced noses). Normally one has to refer to empirical methods. Many shapes have been investigated. Hence one has the chance when looking through the literature to find cases which are similar to the problem one has to solve. Here it is of course important to understand the flow phenomenon so that one is able to extrapolate correctly. As an example the pressure drag coefficient of blunt nose shapes in transonic flow is shown in fig. 12.

A tangent ogive nose of fineness ratio  $l_N/D = 2.5$  was cut to lengths of 2, 1.5, 1 and 0 calibers. The behaviour of the pressure drag coefficient with Mach number can be explained by the separation of the flow at the sharp corner of the face. The drag is divided into two parts, the drag of the flat face and the drag of the remaining ogival contour, which is negative at least in subsonic flow. The contribution of the face is  $C_{WD}$  (flat faced cylinder)  $\cdot (D_{face}/D)^2$ . The second part can be estimated from pressure measurements on a plane-nosed cylinder [13]. For Mach numbers  $M < 0.93$  the pressure coefficient in the separation bubble just behind the corner is  $c_p = -0.4$  independent of Mach number. Only the length of the separation bubble changes with Mach number from about 2.5 diameters at  $M = 0.7$  to about 3.5 diameters at  $M = 0.9$ . Hence the negative drag of the remaining ogival nose increasing with increasing Mach number as the drag of the flat face does so that the sum of both is almost constant in this Mach number range (Nose Nr. 7 and 8). When however the separation bubble extends already at low subsonic Mach numbers to the model shoulder the increasing separation length can no longer influence the pressure distribution on the nose and the drag coefficient goes up with the increasing drag of the face (Nose Nr. 11). At a Mach number of about 0.93 the flow field changes suddenly: a very short bubble is formed with a terminal shock and a high negative pressure coefficient at the corner which slowly decreases with Mach number ( $M = 0.95 : c_p = -1.4$ ;  $M = 1.2 : c_p = -0.9$ ). Blunted bodies where the distance between the face and the shoulder is shorter than or equal to the length of the supersonic separation bubble will have a drag reduction (Nose Nr. 11) due to the sudden jump of the pressure in the separation region. At higher Mach numbers, for the longer noses already at  $M = 0.95$ , the short separation length and the rising pressure lead to an increasing drag coefficient. The Mach number where the sudden change occurs cannot be fixed definitely. There is a hysteresis: both types of separation were observed between  $M = 0.95$  and  $M = 1.1$  [13].

#### Influence of Reynolds number on the pressure drag

The pressure drag is only slightly influenced by the Reynolds number. The influence stems from the thickening of the body contour by the boundary layer displacement thickness, i.e. the body becomes blunter by the boundary layer. Fig. 13 shows the pressure drag coefficient versus Reynolds number for a slender tangent ogive with fully turbulent boundary layer (calculated by use of [1], [14]). At a Reynolds number based on body diameter  $Re_D = 1 \cdot 10^6$ , which is typical for medium sized windtunnels, the difference may be 5 % for a 3.5 caliber tangent ogive, when the boundary layer is not taken into account.

#### 3.1.2 Friction drag

The friction drag is often the largest part of the total drag (fig. 10). It is therefore important to know it accurately. There are many different methods for the determination of the friction. But they will not be discussed in this lecture. In the figures shown here the boundary layer was calculated by the method of Rotta [14]. It is an integral method for compressible plane and axisymmetric flows which accounts for varying contour radii ( $r \neq \text{constant}$ ) and varying pressure coefficients ( $c_p \neq 0$ ) but no heat transfer is regarded. In empirical methods (e.g. Datcom) one normally uses tables or charts, which give the skin friction coefficient of the flat plate ( $r = \infty$ ,  $c_p = 0$ ) versus Reynolds number with only one parameter, the Mach number. So one possibly must take other influences into account: the pressure distribution, the surface roughness, the heat transfer a.s.o. In order to give an impression of the magnitude of these effects figs 14 and 15 were prepared.

On an ogive cylinder with a nose fineness ratio of 2.5 the local skin friction is in the forward part by about 15 % higher than the flat plate value. While the differences in  $c_f$  are restricted to the nose region, the influence on the boundary layer displacement thickness  $\delta_1$  is felt over the entire body (fig. 14).

Computer programs and charts normally give the skin friction coefficient for smooth surfaces. Rough surfaces have a higher friction drag provided that the roughness height is large enough e.g. the corn size must be larger than the laminar sublayer. The critical size can be determined by the Reynolds number based on the conditions at the roughness element.

$$\kappa_c \cdot u_\kappa / \nu \approx 250 \quad \begin{array}{l} \kappa_c \text{ critical roughness height} \\ u_\kappa \text{ velocity at the top of the roughness element} \end{array}$$

Roughness measurements on new air to air missiles and tip tanks showed roughness heights of about 0.01 mm. These surfaces are hydraulically smooth (see fig. 15). For special cases - the lacquer of missiles which have flown for a long time under an aircraft may crack off - one can estimate the influence of the roughness on the friction drag with the aid of fig. 15. The drag due to excrescences as for instance rivets, launcher hooks, cable ducts, small steps due to the malalignment of different segments of the missile is of the order of 10 % to 20 % of the clean configuration.

Heat transfer between the wall and the flow influences the friction drag. Its effect on  $c_f$  can roughly be estimated using fig. 15, when the wall temperature of the body is known. The temperature depends on a missiles geometry, structure, mission, inner heat transfer, flying time a.s.o. For an accurate determination of the surface temperature and the skin friction all these parameters must be taken into account. There exist computer programs for simple geometrical shapes e.g. [17]. In [18] a temperature-time history of a sounding rocket has been published. 30 seconds after the start at a Mach number  $M=6$  a temperature

ratio  $\theta = 0.7$  was measured on the inner wall of a 1.5 mm steel shell about 2 calibers behind the shoulder of the ogival nose. This heat transfer increases the skin friction by about 20 %.

### Blunt bodies

Most boundary layer methods, e.g. the method of Rotta [14], postulate that the stagnation conditions outside the boundary layer are constant. On blunt bodies in supersonic flow this assumption is no longer fulfilled. Behind a detached bow shock (fig. 16) the total pressure varies from the value of the pitot pressure (streamlines near the body) to the undisturbed value (streamlines far outside the body). The total pressure at the stagnation point of a hemisphere at  $M = 4$  is about 7 times smaller than the total pressure of the free stream and the Mach number far behind the nose is reduced to  $M = 2.7$ . When the changes of total pressure and Mach number are not taken into account too high skin friction coefficients will be calculated.

### Influence of Reynolds number on skin friction drag

The friction drag depends strongly on the Reynolds number. The influence can directly be read from charts, for instance for the reduction of windtunnel data to free flight conditions. Problems arise when the transition point of the boundary layer is not known. The transition point on windtunnel models is often fixed by roughness elements. But at high supersonic Mach numbers or in test series with strongly varying conditions (Mach number, Reynolds number, boundary layer thickness) an artificial tripping is problematic and hence not used. In such cases the transition point is not known but must be determined in special test runs or estimated from the model geometry and the transition Reynolds number of the windtunnel. Fig. 13 shows calculated forebody drag coefficients for a slender body. The differences in Reynolds number depend mainly on the type of the windtunnel: blow down tunnels need high stagnation pressures while in continuous and suck down windtunnels at high Mach numbers the pressures are considerably lower. Usual transition Reynolds numbers  $Re_{tr}$  at  $M = 3$  are between  $1 \cdot 10^6$  and  $4 \cdot 10^6$ . This means if the transition is not fixed artificially that at the lower unit Reynolds numbers the boundary layer may be laminar over long distances of the model and hence the friction drag will be considerably smaller than with a turbulent boundary layer.

#### 3.1.3 Base drag

The flow in the base region will be discussed in detail in another lecture. Therefore only some remarks. The base drag may attain 50 % or even more of the total body drag (fig. 10). Therefore it is worthwhile to try to reduce it. In addition the afterbody is sometimes the only part, which can be optimized - e.g. the nose shape (forebody drag) is given by the infrared head and the wetted surface area (friction drag) can't be varied very much for a given volume - Fig. 17 shows that the afterbody drag can be reduced by almost 90 %. If the 6-caliber body of figure 10 had a conical boattail ( $l_b/D = 1$ ,  $\beta = 15^\circ$ ) instead of a cylindrical base, the total drag would reduce in subsonic flow to 50 %. The optimum of cone-angle  $\beta$  depends on Mach number and geometric boundary conditions: For a fixed afterbody length  $\beta_{opt}$  is about  $7^\circ$  for supersonic flow and about  $16^\circ$  for subsonic flow and it varies in transonic flow with the critical Mach number. For a given base diameter ratio  $d_b/D$   $\beta_{opt}$  is different (see lower part of fig. 17).

### Influences of blunt nose shapes and of Reynolds number

The laminar and the turbulent base pressure coefficients of cylindrical afterbodies without jet are often given as a single curve [4], as function of the Mach number only, without regarding the Reynolds number - the boundary layer thickness is assumed to be very small - and the nose shape. From fig. 18 one can see the differences in  $C_{pb}$  when these two parameters are not taken into account. In the test series the nose fineness ratio varied between  $l_N/D = 0.5$  and 3.5 and the cylindrical body length  $l_z/D$  between 6 and 18. The base pressure  $p_b$  increases with increasing nose bluntness and increasing boundary layer thickness.

#### 3.1.4 Influence of Reynolds number on the total drag coefficient

In most cases the flow over a body can be decomposed into contributions due to potential flow, friction, and separated flow and the forces can be calculated separately. But sometimes the interactions between the different types of flow are so big that a distinction is not possible - e.g. the flow over a boattailed afterbody at subsonic speeds-. This is also true for the influence of the Reynolds number. When the body shapes are slender and the state of the boundary layer is known it is relatively easy to reduce windtunnel data to free flight conditions as the laws of reduction are known. But as soon as separation occurs the influence is usually unknown. Especially the flow over corners with small radii is very critical as the separation region depends on the state of the boundary layer at the separation point. At really sharp corners no influence of Reynolds number is felt since the flow must always separate at the same point independent of the state of the boundary layer. The measurements of Hayes and Henderson [20] clearly show the range of corner radii where the Reynolds number has the greatest influence. As the model was very short ( $l/D = 1$ ) the

base flow is also affected by the separation at the shoulder and hence the effect is very large (fig. 19).

### 3.2 Drag coefficient at angle of attack

In [4] several empirical methods are given by which the change of the drag with angle of attack can be calculated. Usually the axial force coefficient of the forebody  $C_{XF}$  remains almost constant up to  $\alpha \approx 8^\circ$  or increases only slightly ( $< 10\%$ ) so that the change of the forebody drag coefficient  $C_{DF}$  is mainly given by the contribution of the normal force  $C_Z \cdot \sin \alpha$ . Fig. 20 shows a comparison between theory (method of linearized singularities) and experiment. According to theory  $C_{XF}$  decreases slightly with  $\alpha$ , while it increases in the windtunnel test. It was assumed hereby that the contribution of the friction drag is constant with  $\alpha$  within the angle of attack range considered here. A confirmation whether this assumption is realistic could not be found.

The v. Karman-Tsien method and the FFA-panel method are linear methods. Therefore one cannot expect that at angles of attack which are no longer small the normal force coefficient  $C_Z$  and hence the forebody drag coefficient  $C_{DF}$  can be determined accurately by these methods. One must apply techniques which take flow separation on the body into account e.g. [21] (fig. 20).

As it is very difficult to compute the influence of the angle of attack on the base drag by theoretical methods one normally determines the base drag experimentally. In windtunnel tests one has to regard that the model sting affects the base pressure. It is almost impossible to give correction factors since the influence of the sting depends on many parameters: the diameter ratio, the model geometry, the Mach number, and also the angle of attack. The above mentioned effect of the nose shape on  $C_{pb}$  (fig. 18) varies with  $\alpha$  too. With increasing angle of attack the base lies in the region of streamlines which have gone through the bow shock outside the body axis at smaller shock angles (fig. 16). Hence the pressure losses decrease with  $\alpha$  and thereby also the differences between the base pressures of bodies with slender and blunt nose shapes.

### 4. Normal force and center of pressure

Like the axial force the normal force is divided into the contributions of potential flow, friction, and separated flow. The contribution of the friction to the normal force is usually so small that it is practically negligible.

At angles of attack around  $\alpha = 0^\circ$  the flow over slender bodies is well described by potential flow theories. With increasing angle of attack the boundary layer moves to the lee side of the body, accumulates there, and finally separates forming a pair of symmetrical vortices. When separation occurs the pressure distribution over the cross section changes fundamentally (fig. 21): on the lee side a region of low pressure forms which cannot be described by potential flow methods. It leads to an additional normal force which is no longer linear with  $\alpha$ . The boundary between the linear and nonlinear angle of attack ranges is not fixed but a function of body length (separation starts at the downstream end of a cylinder body, when  $\alpha$  increases), Mach number, Reynolds number, model geometry (fig. 22). When the angle of attack is further increased ( $\alpha \geq 25^\circ$ ) the vortex pattern becomes asymmetric leading in subsonic and transonic flow to side forces which may be greater than the normal forces.

What requirements must be satisfied by computational methods depends on the problem to be solved. On sounding rockets the contribution of the body alone to the normal force may be of the order of 50 % whereas for missiles with large wings and tails the body lift may decrease to about 10 % of the total lift. In the latter case a very simple method for the estimation of the forces on the body will be sufficient.

#### 4.1 Linear angle of attack range

Near  $\alpha = 0^\circ$  the normal force of slender bodies is a linear function of the angle of attack. For missiles which fly only at low angles of attack it is therefore sufficient to know the slopes  $dC_Z/d\alpha$  and  $dc/d\alpha$ . Fig. 23 shows the typical runs with Mach number determined in a windtunnel: a pronounced peak at  $M = 1$  and an increase with increasing supersonic Mach number. These curves are represented by the above mentioned methods only to some extent (fig. 25). The slender body theory does not account for the influences of Mach number, body length, nose shape on  $dC_Z/d\alpha$  but only for the effect of nose shape on the center of pressure. The results of the v. Karman-Tsien method and the second order shock expansion method are acceptable for Mach numbers  $M > 1.5$  with the exception of the influence of the body length. But this can be improved by taking the boundary layer into account. In this regard the v. Karman-Tsien method gives the best results. It predicts the crossing of the curves for body lengths of  $l_z/D = 6$  and 10 (fig. 24, 26). This cross over is caused by the downstream movement of the negative local normal force (fig. 7) with Mach number. The consideration of the boundary layer is important for long bodies. The differences in normal force and center of pressure of cylinders ( $l_z/D > 6$ ) are due only to the fact that the displacement thickness increases with body length (fig. 24).

In slender body theory the lift is  $L = q_\infty \cdot S_{\text{Base}} \cdot 2\alpha$ . This means that a closed body

( $S_{base} = 0$ ) has no lift but only a moment which is in contradiction to experiment. The reason for these differences is that the flow ceases to be potential when there is boattailing. One assumes that the point where this happens is in subsonic flow a function of the station at which  $dS/dx$  first reaches its maximum negative value [4].

The influence of the nose fineness ratio is correctly represented by simple theoretical methods in transonic and low supersonic flow as long as the limitations of the methods are taken into account. Even slender body theory describes well the movement of the center of pressure with nose fineness ratio. So it can be used, for example, to convert experimentally determined centers of pressure to other nose fineness ratios. At high supersonic Mach numbers the almost linear relation between the center of pressure and the nose fineness ratio is distorted. This is probably due to the influence of the strong bow shocks on the boundary layer since the influence increases with body length.

#### Blunt nose shapes

On blunt nose shapes and on shoulders with sharp corners (cone cylinders) the flow may separate even at zero angle of attack. Hence the flow is no longer a potential flow and cannot be determined by the above mentioned theoretical methods. Large separation regions exist especially in subsonic flow with sudden changes in the transonic regime. These jumps are observed when the flow in the nose region changes from subsonic to supersonic. They are mostly due to boundary layer shock interferences and they are connected with instationary pressure fluctuations [23] and hysteresis (fig. 28). The sudden changes increase with increasing separation, i.e. they increase with increasing cone angle of cone cylinders. The long separation bubble in subsonic flow leads to a higher static stability (fig. 27, 28). Fig. 29 shows schlieren pictures of the flow separation (compare also fig. 12).

On a hemisphere - cylinder a local supersonic flow is first observed just below  $M = 0.7$ , but a well-defined shock system is not obtained until nearly  $M = 0.9$ . This change in flow pattern leads to jumps of the normal force and the center of pressure similar to that of cone cylinders (fig. 27).

#### Influence of Reynolds number

It was shown in fig. 24, that the boundary layer has a great influence on the normal force of long bodies near zero angle of attack. Therefore one can expect that also the effect of the Reynolds number is appreciable [24] (fig. 31). It can be calculated for instance by the methods of v. Karman-Tsien [1] and Rotta [14]. But for quick estimates of single values and as subroutines of extensive computer programs in which the time and the available storage are limited simple approximate formulae will do. They were derived from slender body theory. With the pressure coefficient  $C_p(\phi, x) = 4 \cdot \alpha \cdot \cos \phi \cdot \frac{dr}{dx}$  and the body contour, enlarged by the displacement thickness  $\delta_1$ ,  $r(x) = R(x) + \delta_1(x)$  one obtains

$$\Delta C_Z = -8\alpha \frac{\delta_{1t}}{D} - 4\alpha \left[ C_{fL} \frac{L}{D} + C_{ft} \left( \frac{L}{D} - \frac{L}{D^2} \right) \right]$$

$$\Delta C_m = -4\alpha \left[ \frac{\delta_{1L}}{D} \frac{L}{D} + \left( \frac{\delta_{1t}}{D} - \frac{\delta_{1L}}{D^2} \right) \left( \frac{L}{D} + \frac{L}{D^2} \right) \right] -$$

$$-4\alpha \left\{ C_{fL} 0.5 \left( \frac{L}{D} \right) + C_{ft} \left( \frac{L}{D} - \frac{L}{D^2} \right) \right\} \times$$

$$\times \left[ \frac{L}{D} + 0.5 \left( \frac{L}{D} - \frac{L}{D^2} \right) \right]$$

$\Delta C_m$  pitching moment coefficient due to boundary layer, reference point: nose tip

$C_f$  average skin friction coefficient

subscript: L laminar  
t turbulent

For purely laminar or purely turbulent boundary layers the formulae simplify to

$$\Delta C_Z = -8\alpha \cdot \frac{\delta_1}{D} - 4\alpha \cdot C_f \cdot \frac{L}{D}$$

$$\Delta C_m = -4\alpha \cdot \frac{\delta_1}{D} \cdot \frac{L}{D} - 2\alpha \cdot C_f \cdot \left( \frac{L}{D} \right)^2$$

The displacement thicknesses  $\delta_{1L}$ ,  $\delta_{1t}$  and the mean skin friction coefficients  $C_{fL}$ ,  $C_{ft}$  should be calculated by a boundary layer method such as that of Rotta [14]. For quick estimates of single values the diagrams in fig. 30 were prepared. When the flow is partly

laminar and partly turbulent one can write approximately  $\delta_{1t} \approx \delta_{1t} (l_2=0) \frac{l-l_2}{l} + \delta_{1l}$ .

The formulae given above and the diagrams (fig. 30) are valid only for relatively long cylinders ( $l_2/D > 5$ ) and for slender nose shapes.

When comparing measurements in different windtunnels often differences are encountered which cannot be explained by inaccuracies of the test equipment. Here, too, the boundary layer may play a part, and this even if the Reynolds numbers are identical or differ only by a factor of 3 or 4 which by itself would not have a great influence. The differences are caused by different positions of boundary layer transition. The transition Reynolds number  $Re_{tr}$  can vary considerably in the different tunnels. If for one reason or another the transition point is not fixed on the model, differences in the normal force characteristics may possibly exist even if the experimental conditions are otherwise identical. As an example fig. 32 shows the slope of the normal force coefficient and the center of pressure for a slender ogive-cylinder body at  $M = 1.3$  plotted versus the transition Reynolds number  $Re_{tr}$ . Values of  $Re_{tr}$  for various American transonic windtunnels were taken from [25]. For example, if the model R 115 of reference [19] ( $D = 30$  mm) had been tested in these tunnels at a unit Reynolds number  $Re/cm = 1.3 \cdot 10^5$ , then apart from the usual measuring inaccuracies, the different positions of the transition point would have led to differences of up to 0.8 calibers in the center of pressure and of about 15 % in the normal force coefficient from one tunnel to the other. Of course, such differences only occur when on long bodies the transition point moves by several calibers, say, in the range  $6 < Re_{tr}/Re_D < l/D$ . No differences would have to be expected on this account when the models are appropriately smaller or larger (here:  $D = 10$  mm and 100 mm), because the boundary layer on the model would then be completely laminar in all the windtunnels or would become turbulent already in the nose region.

#### 4.2 Nonlinear angle of attack range

At angles of attack of about  $5^\circ$  - see figs. 21, 22 - the flow starts to separate from the body. This flow separation leads to an increase in the aerodynamic loads. At not too high incidences - say up to about  $25^\circ$  - a symmetric vortex pattern exists. This intermediate-angle-of-attack range will be briefly described here, not the complete area of high-angle-of-attack aerodynamics which is presented in another chapter.

There exist computational methods for three dimensional viscous flow fields about slender bodies, but they are very complicated and time consuming [26] or only partial problems can be treated as for instance the determination of the separation line in incompressible flow [27]. In order to estimate the normal force on slender bodies in the nonlinear  $\alpha$ -range simple semi-empirical methods are available. In these methods the flow is decomposed into the velocity components parallel with and normal to (cross flow  $U_\infty \sin \alpha$ ) the body axis and the drag of the cylinder due to the cross flow which is the viscous normal force must be determined.

$$Z_{visc} = \int_0^l d(x) \cdot C_{DC}(x) \cdot q \cdot \sin^2 \alpha \cdot dx$$

where  $d(x)$  is the local body diameter and  $C_{DC}(x)$  the drag coefficient of a cylinder element.

Allen [21] chose a mean value for  $C_{DC}(x)$  which is constant over the body length and which is only corrected for the influence of the fineness ratio of the body. So he got a very simple equation

$$C_{Zvisc} = \eta \cdot C_{DC2D} \cdot \frac{S_p}{S} \cdot \sin^2 \alpha$$

$C_{DC2D}$  is the drag coefficient of an infinitely long circular cylinder,  $\eta$  is a correction factor for the influence of the fineness ratio on  $C_{DC}$ ,  $S_p$  is the plan form area of the body, and  $S = \pi D^2/4$  the cross section.

This equation gives good agreement with experiments for long cylindrical bodies at high angles of attack (fig. 34). But especially in the nose region the cross-flow drag is not constant with the length. Kelly [28] developed a method which is based on the impulse-flow-analogy: the development of the cross-flow at any station on a body of revolution at incidence is analogous to that past a two-dimensional circular cylinder started impulsively into motion from rest. A potential cross-flow exists at the nose, with a gradual development of viscous cross-flow along the body. Schwabe and later others determined experimentally the cross-flow drag of cylinders set impulsively into motion from rest (fig. 33). The time  $t$  in the experiments can be related to the distance  $x$  of the body, since the parameter

$\frac{U_\infty}{R} \cdot t$  which he used is equal to  $\frac{x}{R} \cdot \tan \alpha$  of an inclined cylindrical body (the cross-flow velocity  $V_{cr} = U_\infty \sin \alpha$  and the time  $t = \frac{x}{U_\infty \cos \alpha}$ ). In order that the equation for the viscous

normal force may be readily integrated Kelly approximated Schwabe's results by a polynomial. The first term leads to the equation  $C_{Zvisc} = 0.49 \cdot (C_{DC} \cdot l^2/S) \cdot \alpha^3$  which is valid for subsonic flow if  $\alpha < 10^\circ$  and  $2l \tan \alpha < 5$ , as long as the boundary layer thickness does not increase

the base area appreciably. The drag coefficient of the circular cylinder  $C_{DC}$  is 1.2 for laminar and 0.35 for turbulent flow.

More modern experiments in impulsively started laminar flow which were extended to higher values of  $U_{\infty} \cdot t/R$  show a peak and then a decrease of the drag coefficient (fig. 33). This has been taken into account by Thomson [30], who also made allowance for the influence of axial pressure gradients on the separation. A favourable pressure gradient inhibits flow separation, reducing the cross-flow drag.

$$C_{Zvisc} = C_{DC} \cdot F \cdot G \cdot 4/\pi \cdot d/D \cdot \sin^2 \alpha.$$

In this equation the factors  $F$ ,  $G$ ,  $H$  represent the influences of the base, the strength of the wake vortices, and the effect of the axial pressure gradient. The cross-flow-drag coefficient  $C_{DC}$  includes the influences of the type of separation ( $C_{DC \text{ turbulent}}/C_{DC \text{ laminar}} \approx 0.6$  for  $0^\circ < \alpha < 20^\circ$ ) and of the distance from the nose tip ( $C_{DC} = f(x/D \cdot S \cdot \tan \alpha)$ ,  $S$  = Strouhal number). In [30] curves are shown which agree well with experimental results.

#### Blunt nose shapes

The influence of the nose shape on the separation pattern has been investigated theoretically [31] but there are no computational methods by which the influence on the viscous normal force could be calculated. From the windtunnel tests of Hartmann [11] one could conclude that an appreciable influence is only felt in subsonic and transonic flows. But the nose effect could have been hidden by the long cylinder ( $l/D = 19$ ). Oil flow pictures at least show big differences in the separation patterns of the flows in the nose regions of slender and hemispherical noses.

#### Influence of Reynolds number

The Reynolds number can have a strong influence on the viscous normal force. When the state of separation changes from laminar to turbulent the viscous normal force varies by a factor of about 3. This large variation in the drag coefficient of a circular cylinder is taken into account in the above mentioned methods. Nevertheless big differences between calculated and measured normal forces can occur. These differences are primarily caused by the fact that inadequate account is taken of the Reynolds number: it is only asked whether the boundary layer is laminar or turbulent, and no further distinction is made. But the drag coefficient of a circular cylinder is not a step function. In the critical cross-flow range it varies continuously between  $C_{DC} = 0.25$  and 1.25. Therefore the strong variations in the normal force coefficient and in the center of pressure in the critical range (fig. 35, 36).

For long bodies at high angles of attack the nonlinear contribution of the cross-flow to the normal force coefficient is primarily given by  $C_{DC} \cdot \sin^2 \alpha$ , where the drag coefficient  $C_{DC}$  of the cylinder depends mainly on the Reynolds number and the Mach number (fig. 38).

As the state of the boundary at the separation line is important for the pressure distribution in the wake, the Reynolds number  $Re_{AZ}$ , which is characteristic for the separation, is based on the freestream conditions and on the length of the streamline  $l_{AZ}$  from  $\phi = 0^\circ$  up to the separation line at  $\phi \approx 90^\circ$  and not on the cross-flow ( $Re_D \cdot \sin \alpha$ ).

The length of the streamlines is a function of the angle of attack:  $l_{AZ}$  and thereby also  $Re_{AZ}$  decrease with increasing  $\alpha$ . Consequently when changing the angle of attack during a windtunnel test one also passes through a certain range of Reynolds number  $Re_{AZ}$ . In fig. 36 the complete critical cross-flow range is covered. At  $M = 0.5$  and  $Re_D = 1.5 \cdot 10^5$ , for example,  $Re_{AZ}$  corresponding to  $\alpha < 6^\circ$  is so large that the boundary layer is turbulent before reaching the separation line. The steep decrease of  $C_{DC}$  is reached when  $\alpha \approx 6^\circ$  (point A). The minimum of the drag coefficient of the cylinder is passed as  $\alpha$  increases further, and at  $\alpha \approx 12^\circ$   $C_{DC}$  has a value which is more or less equal to that for a turbulent boundary layer at a low Reynolds number (point B). The drag coefficient then increases rapidly and eventually attains the almost constant laminar value. At larger Reynolds numbers  $Re_D$  the points A and B move towards higher angles of attack, the distance between them becomes greater, and the influence of the critical range is felt more strongly (fig. 38).

This is no longer true at higher Mach numbers. As soon as the cross-flow Mach number  $M_{cr} = M \cdot \sin \alpha$  reaches the critical value at about  $M_{cr} = 0.42$  at which the speed of sound is reached locally on the cylinder, the influence of the Reynolds number decreases markedly and eventually disappears completely (fig. 37, point C in fig. 38).

Changes in the normal force distribution, too, are noted when the critical cross-flow range is passed or when the cross-flow Mach number  $M_{cr}$  exceeds a value of about 0.42. This is caused by the interference between the non-viscous flow over the nose and the viscous cross-flow. In the subcritical range (laminar separation) or at  $M_{cr} > 0.42$  a region of high local normal force exists at the shoulder. This region increases in length with increasing cross-flow Mach number.



If one wants to avoid the critical separation region, one must limit oneself to a certain range of Reynolds number that depends on the angle of attack and on the Mach number. In low subsonic flow one has  $Re_{AZA} \approx 7 \cdot 10^5$  and  $Re_{AZB} \approx 2.5 \cdot 10^5$  -  $Re_{AZA}$ ,  $Re_{AZB}$  are the Reynolds numbers  $Re_{AZ}$ , based on the streamline length up to separation, at the points A and B (fig. 38) -. From this one obtains the relationship between the angle of attack and  $Re_D$  (fig. 3.). This relationship only holds when the cross-flow Mach number  $M_{cr}$  is lower  $\approx 0.42$ .

The importance of the state of the boundary layer for the normal force of bodies is demonstrated by fig. 35. At transonic and supersonic Mach numbers only small models of circular cross section come into the critical separation region (fig. 39) with its large changes in normal force and center of pressure. But this may happen also to large windtunnel models when, for instance, a body has a rectangular cross section with rounded corners (compare fig. 19).

#### References

- [1] SAUER, R. Einführung in die theoretische Gasdynamik  
Berlin: Springer, 1960.
- [2] ADAMS, M.C.  
SEARS, W.R. Slender-Body Theory-Review and Extension.  
J. aeron. Sci. Vol.20,2 (1953), p.85-97.
- [3] SYVERTSON, C.A.  
DENNIS, D.H. A Second-Order Shock-Expansion Method Applicable to Bodies  
of Revolution Near Zero Lift.  
NACA Rep. 1328 (1957).
- [4] USAF Stability and Control DATCOM.  
Wright-Patterson Air Force Base, Ohio (1969).
- [5] MOORE, F.G. Body Alone Aerodynamics of Guided and Unguided Projectiles  
at Subsonic, Transonic and Supersonic Mach Numbers.  
Naval Weapons Laboratory Dahlgren  
AD-754 098 (1972).
- [6] LYUBIMOW, A.N.  
RUSANOW, V.V. Gas Flow Past Blunt Bodies.  
NASA TT F-714 (1973).
- [7] WEILAND, C. Lösung der Euler-Gleichungen für räumliche Überschallströ-  
mungen um stumpfe Körper.  
DLR FB 76-60 (1975).
- [8] GUSTAVSSON, S.A.L. A Computer Program for the Prediction of Aerodynamic  
Characteristics of Wing-Body-Tail Combinations at Subsonic  
and Supersonic Speeds.  
FFA AU-635, Part 2 (1972).
- [9] JACKSON, C.M.  
SMITH, R.S. A Method for Determining the Total Drag of a Pointed Body  
of Revolution in Supersonic Flow with Turbulent Boundary  
Layer.  
NASA TN D-5046 (1969).
- [10] ESCH, H. Untersuchungen an schlanken Rotationskörpern im Transschall.  
DFVLR, Porz-Wahn 1 US F-69-1 (1969).
- [11] HARTMANN, K. Drei-Komponenten- und Druckverteilungsmessungen einschließ-  
lich Strömungsbeobachtungen an einem kreiszylindrischen  
Flugkörperperrumpf mit verschiedenen Kopfformen bei Machzahlen  
 $Ma_\infty = 0,5$  bis 2,2 und verschiedenen Reynoldszahlen.  
DFVLR-AVA 251 74 A 32 (1974).
- [12] WU, J.M.  
AOYAMA, K. Transonic Flow-Field Calculation Around Ogive Cylinders by  
Nonlinear-Linear Stretching Method.  
Redstone Arsenal RD-TR-70-12 (1970).
- [13] STANBROOK, A. A Correlation of the Forebody Drag of Cylinders with Plane  
and Hemispherical Noses at Mach Numbers from Zero to 2.5.  
RAE TN AERO 2875 (1963).
- [14] ROTTA, J.C. Fortran IV-Rechenprogramm für Grenzschichten bei kompres-  
siblen ebenen und achsensymmetrischen Strömungen.  
AVA, Göttingen 68 R 03 (1968).
- [15] GODDARD, F.E. Effect of Uniformly Distributed Roughness on Turbulent  
Skin-Friction Drag at Supersonic Speeds.  
J. aeron. Sci. Vol.26,1 (1959).
- [16] WALZ, A. Strömungs- und Temperaturgrenzschichten.  
Karlsruhe: G. Braun, 1966.

- [17] HERON, I.C.                   A Fortran Program for Predicting the Temperature - Time Histories of Hemispherical Shells Subjected to Aerodynamic Heating. Weapons Research Establishment, Australia WRE-TN-783 (WR & D) (1972).
- [18] WING, L.D.                   A Method for Calculating Aerodynamic Heating on Sounding Rockets. NASA TM-X-69896 (1973).
- [19] ESCH, H.                    Kraftmessungen an zylindrischen Rümpfen im Überschall. DFVLR, Porz-Wahn 1-US-F-72-8 (1972).
- [20] HAYES, W.C.  
    HENDERSON, W.P.           Some Effects of Nose Bluntness and Fineness Ratio on the Static Longitudinal Aerodynamic Characteristics of Bodies of Revolution at Subsonic Speeds. NASA TN-D-650 (1961).
- [21] ALLEN, H.J.  
    PERKINS, E.W.           A Study of Effects of Viscosity on Flow over Slender Inclined Bodies of Revolution. NACA Rep. 1048 (1949).
- [22] RIEDEL, H.  
    EMUNDS, H.  
    NIEZGODKA, F.J.       Einfluß der Dickenrücklage und der Rumpflänge von achsensymmetrischen Flugkörpern auf die aerodynamischen Beiwerte im Überschall. DLR FB 70-54 (1970).
- [23] CHEVALIER, H.L.  
    ROBERTSON, J.E.       Pressure Fluctuations Resulting from an Alternating Flow Separation and Attachment at Transonic Speeds. AEDC TDR-63-204 (1963).
- [24] ESCH, H.                   Der Einfluß der Reynoldszahl auf die Normalkraftcharakteristik schlanker zylindrischer Rümpfe. DLR FB 75-09 (1975).
- [25] DOUGHERTY, N.S.  
    STEINLE, F.W.       Transition Reynolds Number Comparisons in Several Major Transonic Tunnels. AIAA 8th Aerodynamic Testing Conference, Bethesda, Maryland, USA, July 8-10, 1974. AIAA Paper 74-627 (1974).
- [26] WALITT, L.  
    TRULIO, J.G.           A Numerical Method for Computing Three-Dimensional Viscous Supersonic Flow Fields About Slender Bodies. NASA CR-1963 (1971).
- [27] GEISSLER, W.           Calculation of the Three-Dimensional Laminar Boundary Layer Around Bodies of Revolutions at Incidence and with Separation. AGARD Conference Proceedings No. 168 on Flow Separation, AGARD-CP-168 (1975).
- [28] KELLY, H.               The Estimation of Normal-Force, Drag, and Pitching-Moment Coefficients for Blunt-Based Bodies of Revolution at Large Angles of Attack. J. aeron. Sci. Vol. 21, 8 (1954).
- [29] MELLO, J.F.           Investigation of Normal Force Distributions and Wake Vortex Characteristics of Bodies of Revolution at Supersonic Speeds. J. aeron. Sci. Vol. 26, 3 (1959).
- [30] THOMSON, K.D.       The Estimation of Viscous Normal Force, Pitching Moment, Side Force and Yawing Moment on Bodies of Revolution at Incidences up to 90°. Weapons Research Establishment, Australia WRE-Report-782 (WR & D) (1972).
- [31] WANG, K.C.           Separation Patterns of Boundary Layer over an Inclined Body of Revolution. AIAA J. Vol. 10, 8 (1972).

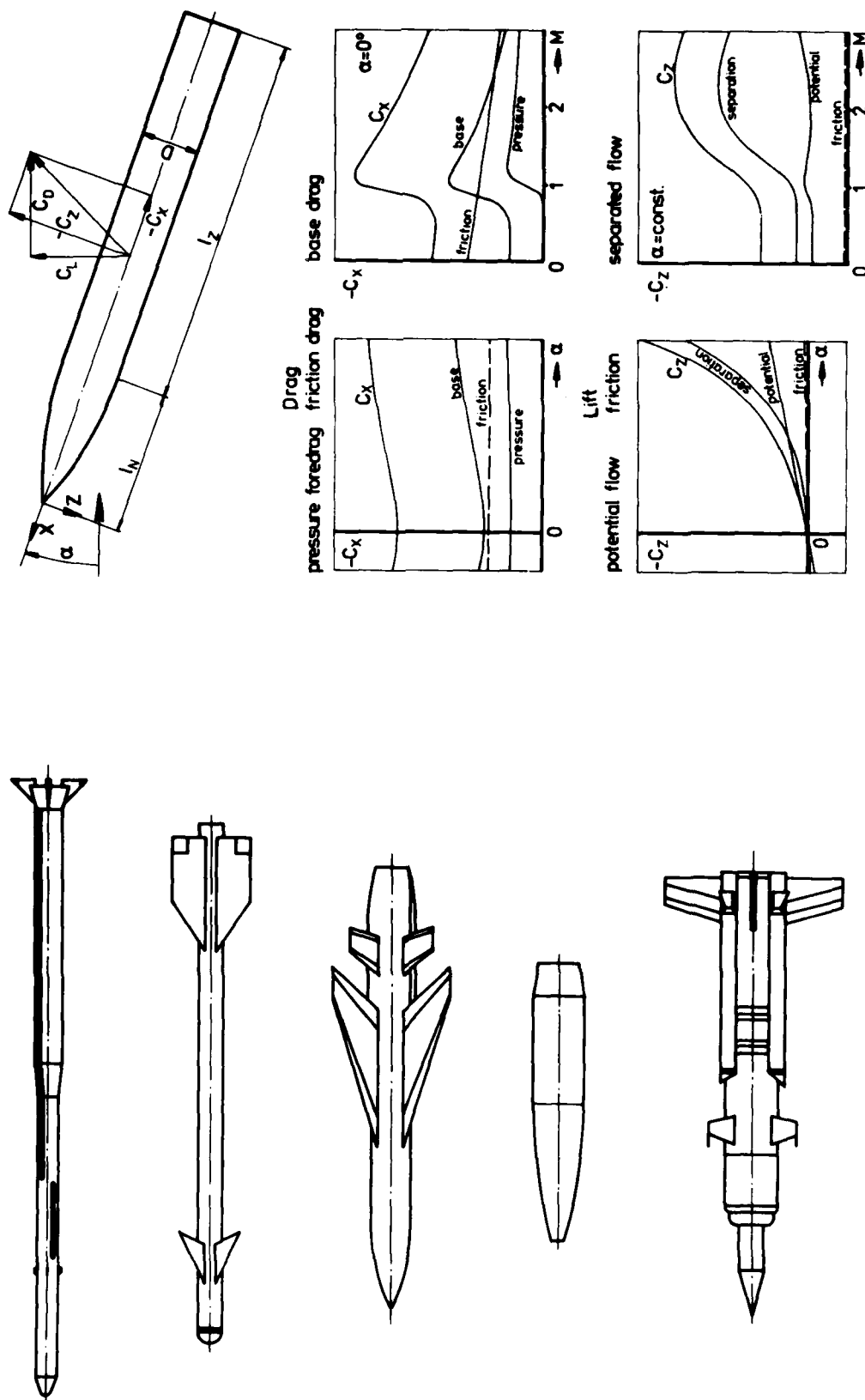


Fig. 1 Missile configurations

Fig. 2 Components of aerodynamic forces

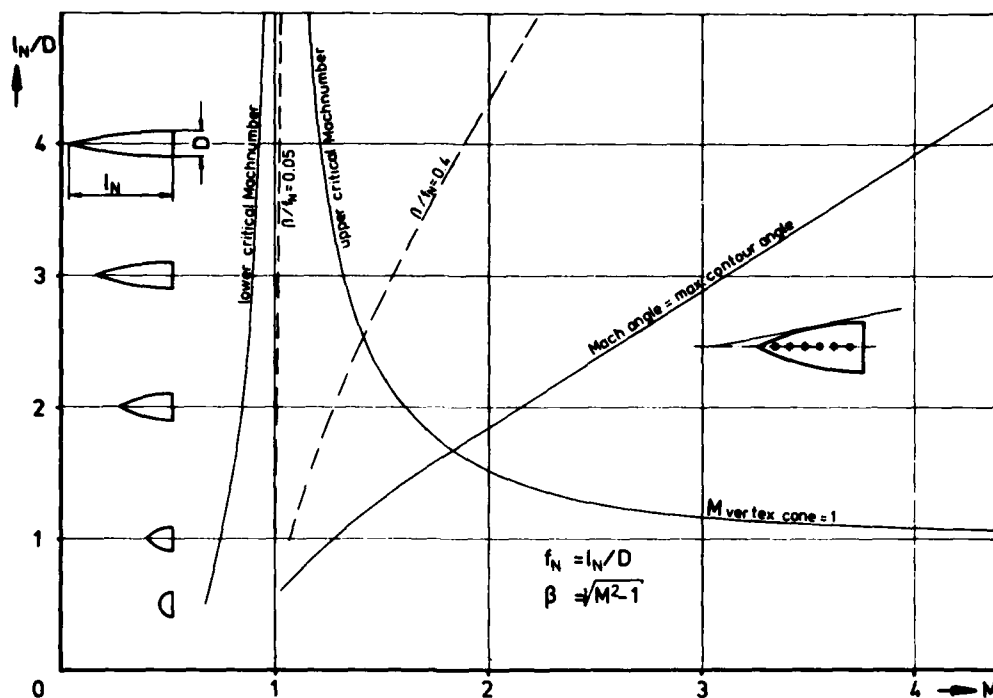


Fig. 3 Fineness ratio limitations of "classical" methods, tangent ogive noses shapes

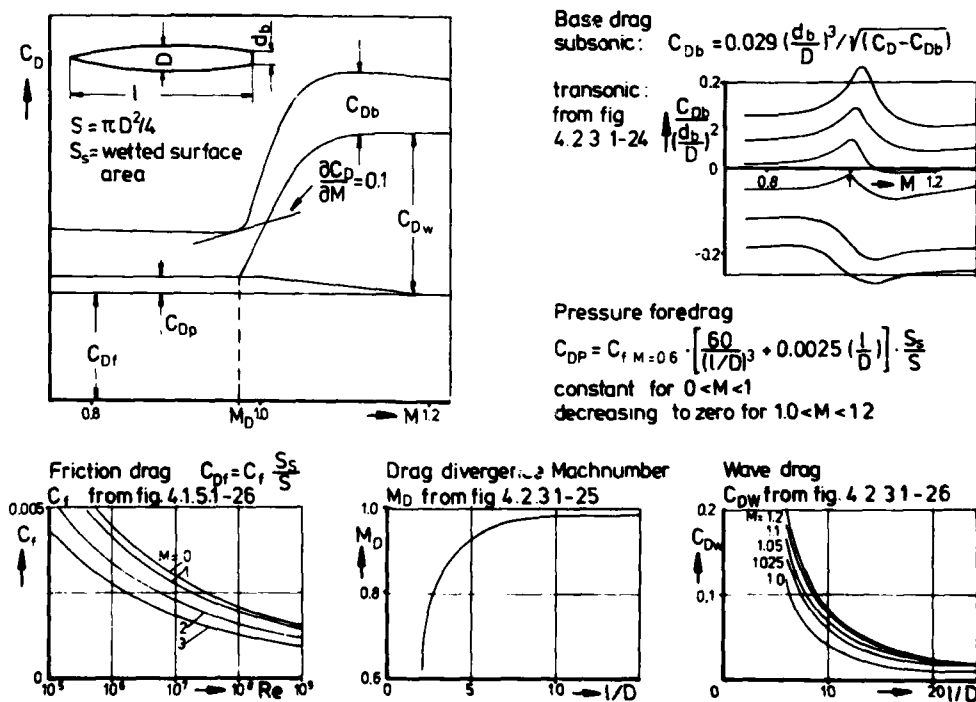


Fig. 4 Datcom method, zero-lift drag in transonic flow [4]

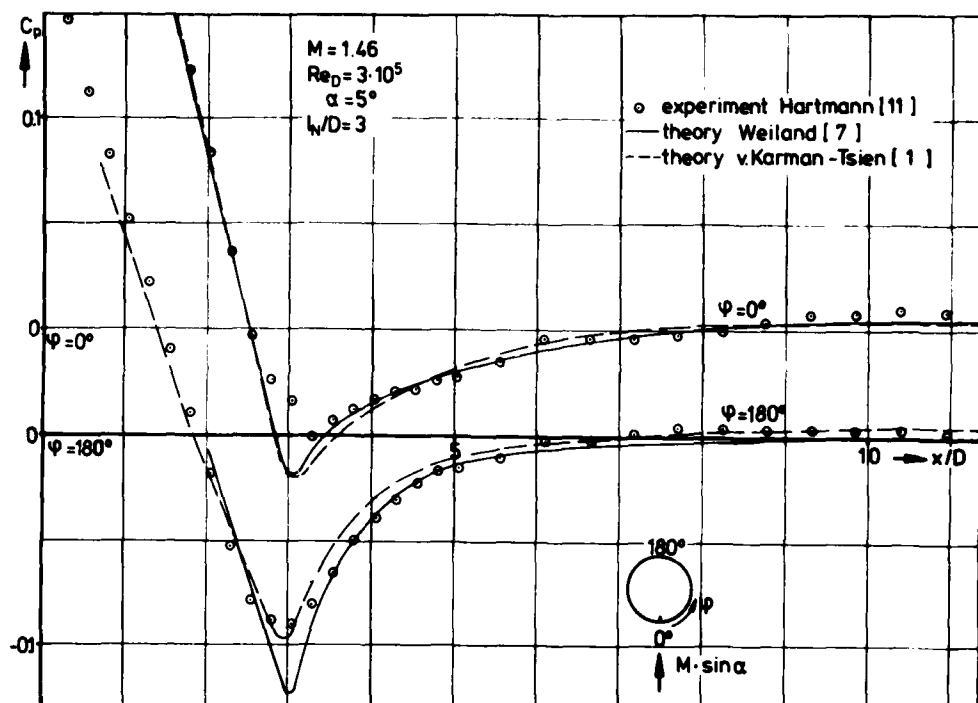


Fig. 5 Pressure distribution on a tangent ogive-cylinder body, comparison between theory and experiment

Method	Mach number range			Geometry				Results				Expenditure (isolated body $\alpha \neq 0$ , $M > 1$ )		Remarks
	subsonic	transonic	supersonic	pointed nose	blunt nose	non circular cross-section	flow field	shock shape	pressure	force		core storage	computing time (TR 440)	main application advantages disadvantages
empirical methods (DATCOM)	X	X	X	X	X	X				X				optimization of missiles reliability few geometric parameters, no flow details
slender body theory	X	X	X	X					X	X				subroutines, conversion of experim. results simplicity low accuracy
v. Karman - Tsien method	X		X	X	M		X		X	X		34K	7sec	
F FA -panel	X		X	X	M		X		X	X		60K	11sec	complete configurations versatility need of big computers
second order shock expansion			X	X			(X) $\alpha = 0$			X		28K	11sec	
Rusanow - difference (WEILAND)	M	X	X	X	X	X	X	X	X	X		55K <sup>1)</sup> 25K <sup>2)</sup>	10 hrs <sup>1)</sup> 20 min <sup>2)</sup>	research investigations, details of flow accuracy long computing times 1) nose region 2) purely supersonic flow field

Fig. 6 Computational methods (potential flow)

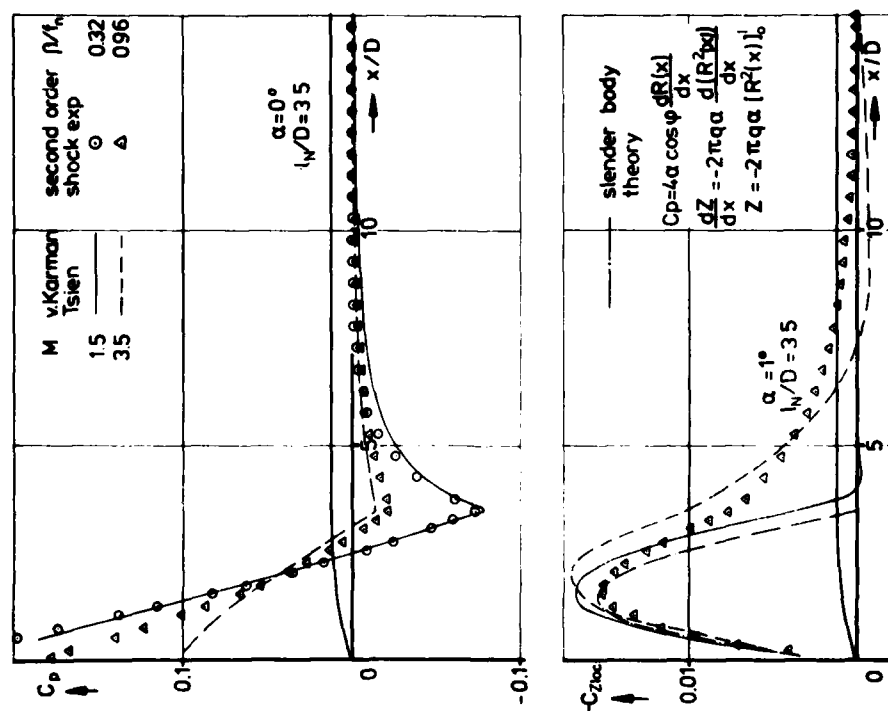


Fig. 7 Distributions of pressure coefficient and local normal force coefficient for an ogive-cylinder, theoretical methods [1], [2], [3]

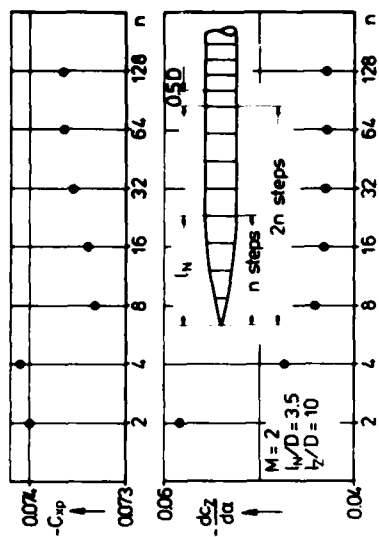


Fig. 8

v. Karman Tsien method, influence of number of steps  $n$  on axial force and normal force coefficients of an ogive-cylinder body

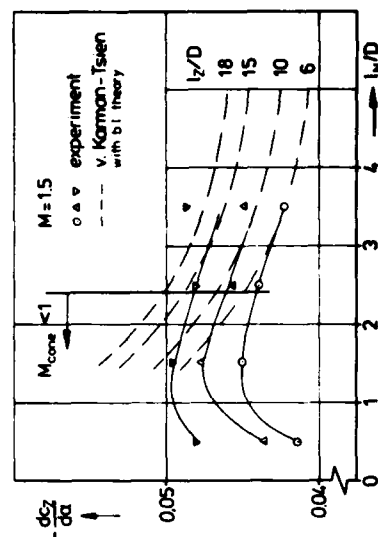


Fig. 9 Influence of nose fineness ratio on the normal force of ogive-cylinders at  $M=1.5$  [19]

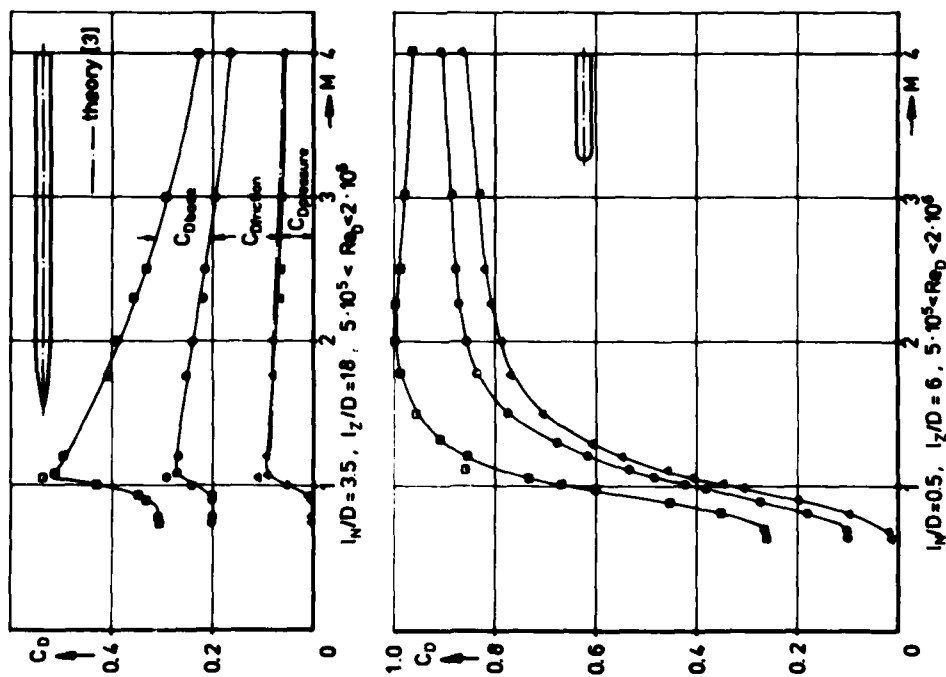


Fig. 10 Zero-lift drag coefficients of ogive-cylinder bodies

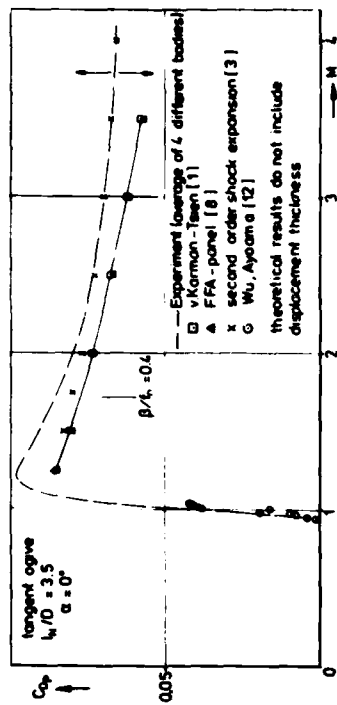


Fig. 11 Pressure drag coefficient of a 3.5 caliber tangent ogive body, comparison between experiment and theoretical methods

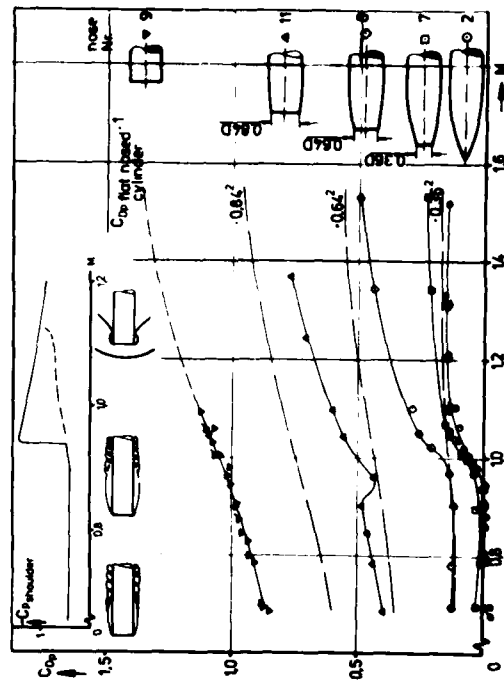


Fig. 12 Pressure drag coefficient of blunted ogival noses at  $\alpha = 0^\circ$  [10], fineness ratio of basic ogive  $l_w/D = 2.5$

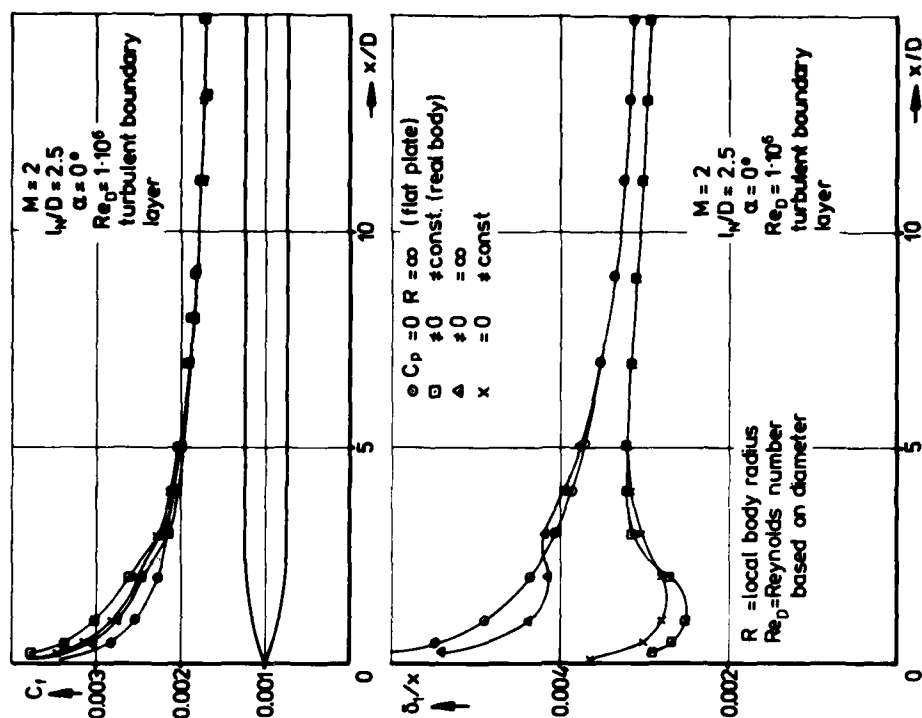


Fig. 14 Distribution of local skin friction coefficient  $C_f$  and displacement thickness  $\delta_1$  on an ogive-cylinder body;  $l_w/D=2.5$ ,  $M=2$ ,  $Re_D=10^6$ ; theoretical results [1], [14]

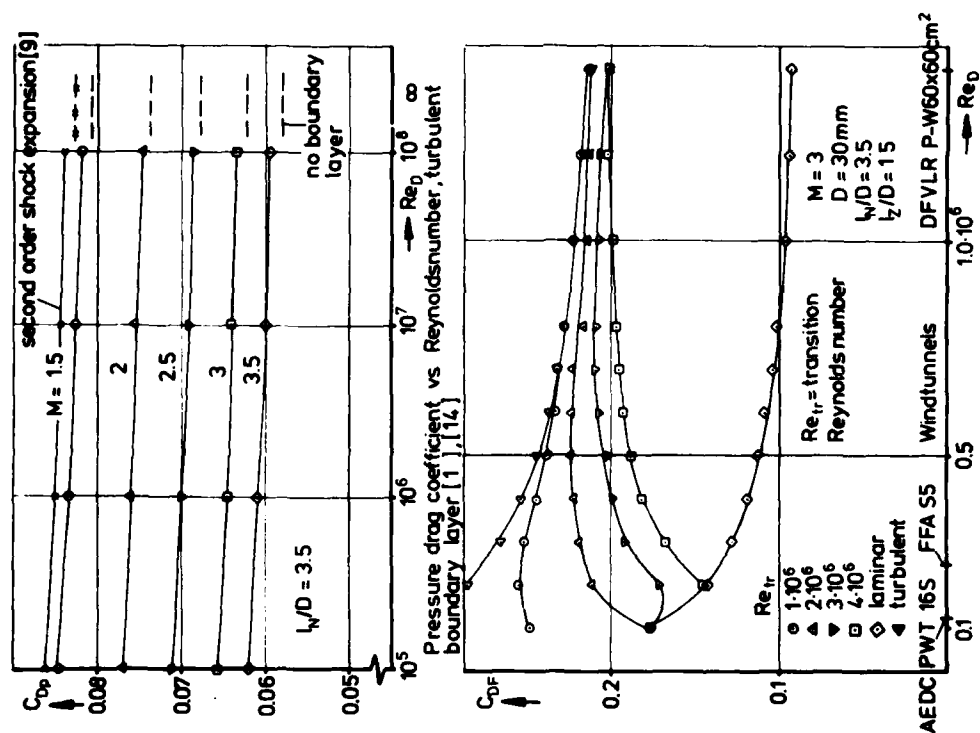
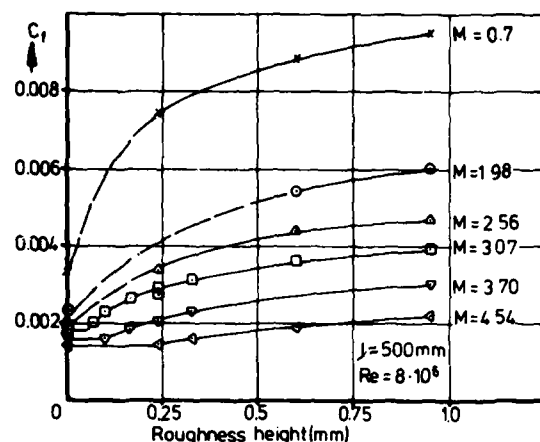
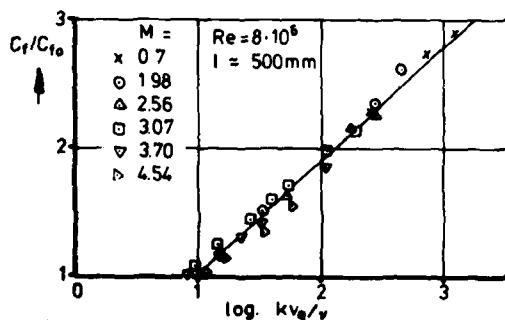


Fig. 13 Influence of Reynolds number on the drag of an ogive-cylinder body of nose fineness ratio 3.5

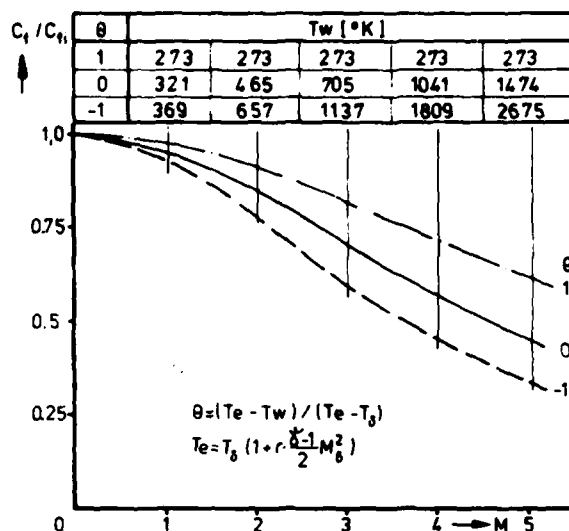




Average turbulent skin-friction-drag coefficient vs roughness height for various Mach Numbers [15]



Ratio of turbulent skin-friction-drag coefficient for a rough surface to that for a smooth surface vs.  $\log kv_0/v$  [15]  $v_0 = \sqrt{T_w/\rho_w}$



Influence of heat transfer and Machnumber on the skin friction coefficient of a flat plate, turbulent boundary layer,  $Re = 1 \cdot 10^7$  [16]

$T_w$  = wall temperature  
 $T_0$  = temperature at the outer edge of the boundary layer  
 $M_0$  = Mach number  
 $r$  = recovery factor ( $r = 0.88$ )  
 $C_{f0}$  = incompressible skin friction coefficient

Fig.15 Influences of roughness and heat transfer on turbulent skin friction

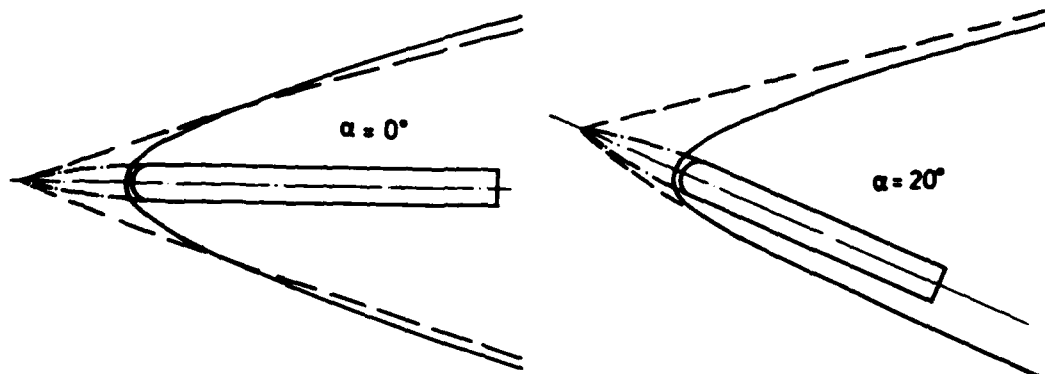


Fig.16 Shock shapes of tangent ogive cylinders with nose lengths of 0.5 and 3.5 calibers at  $M = 4$

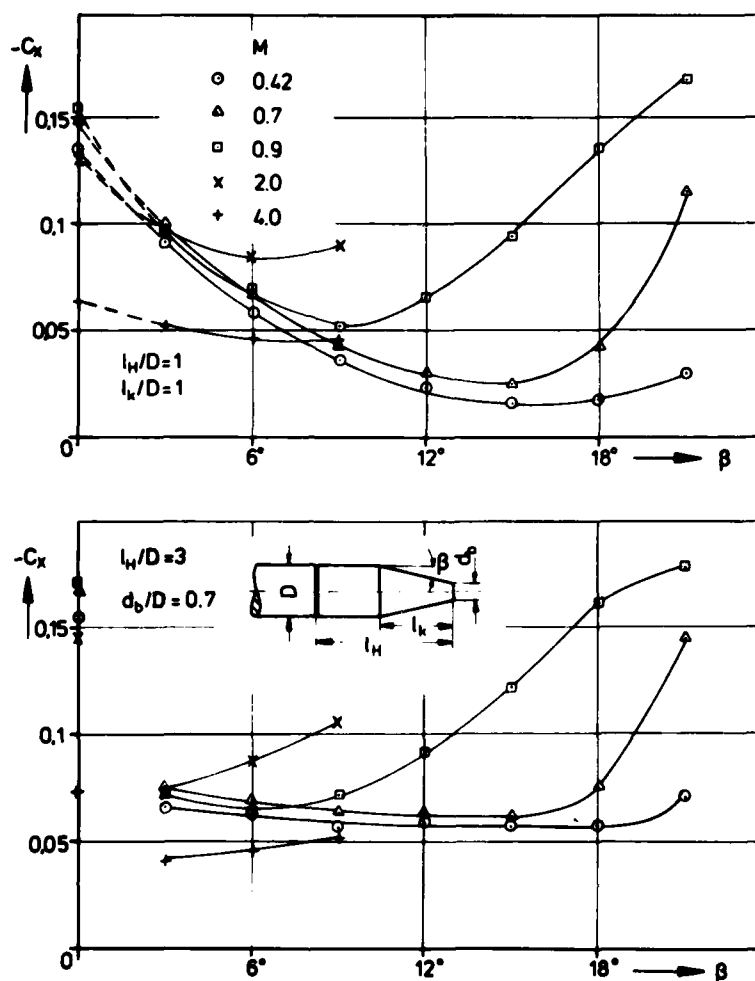


Fig. 17 Drag coefficient of conical afterbodies at zero angle of attack, no jet

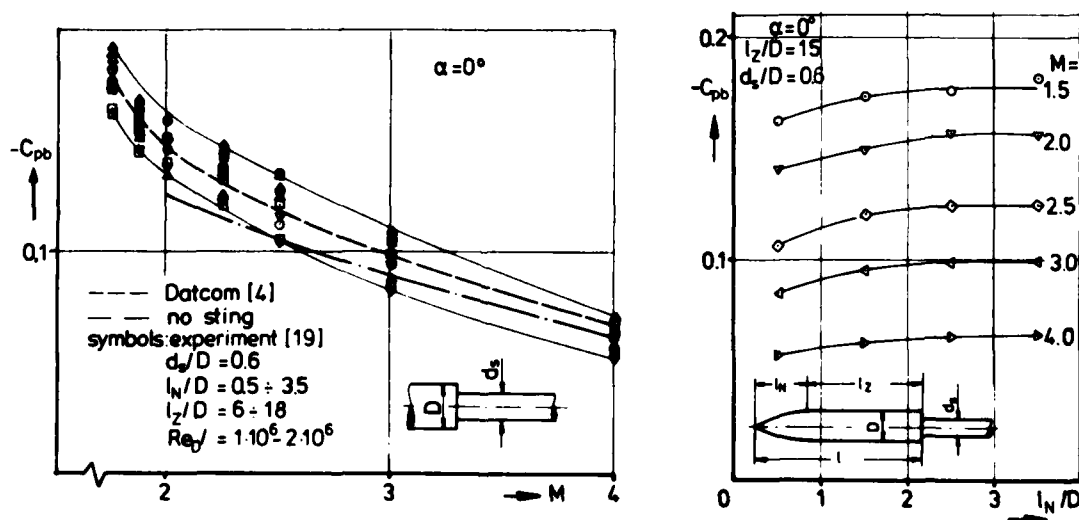


Fig. 18 Influences of nose fineness ratio and body length (Reynolds number) on the base pressure coefficient of ogive-cylinder bodies at  $\alpha=0^\circ$  [19]

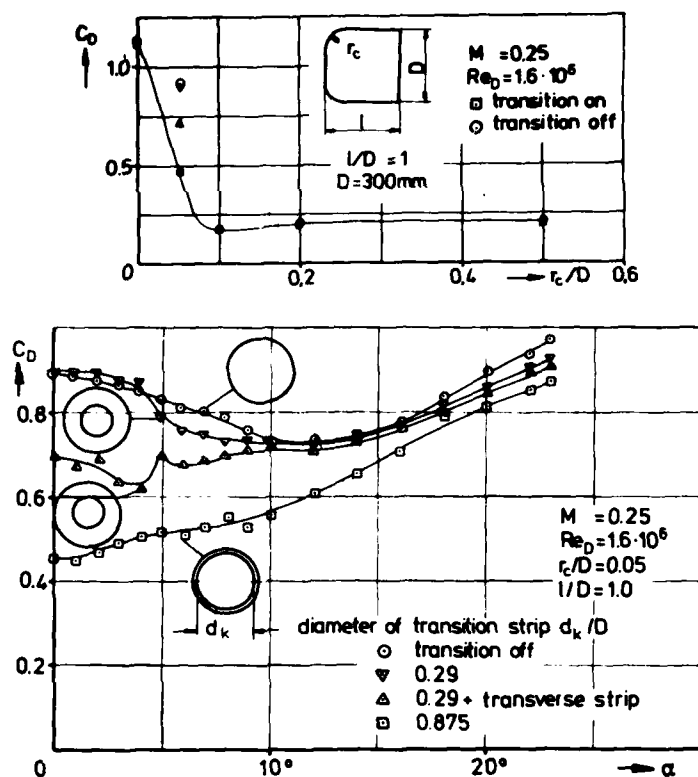


Fig. 19 Effects of corner radius  $r_c/D$  and transition location  $d_k/D$  on the drag of a body of fineness ratio 1 [20]

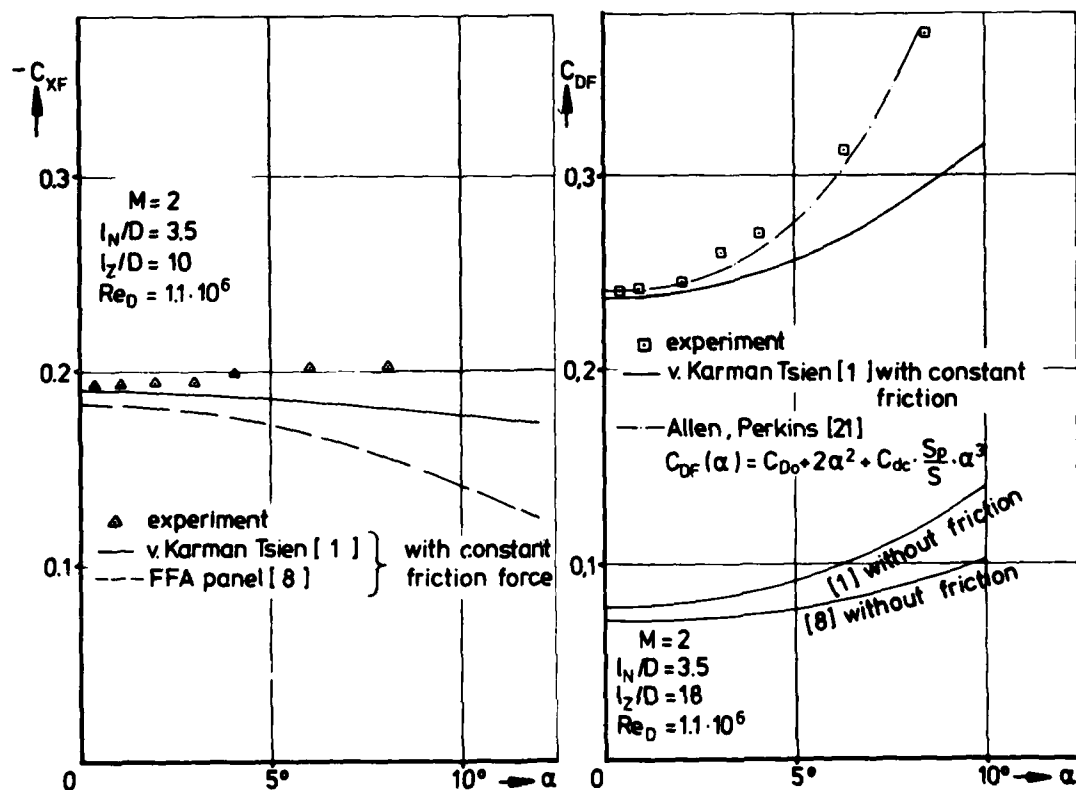


Fig. 20 Forebody drag ( $C_{DF}$ )- and forebody axial force ( $C_{XF}$ ) coefficients for ogive-cylinder bodies at angle of attack

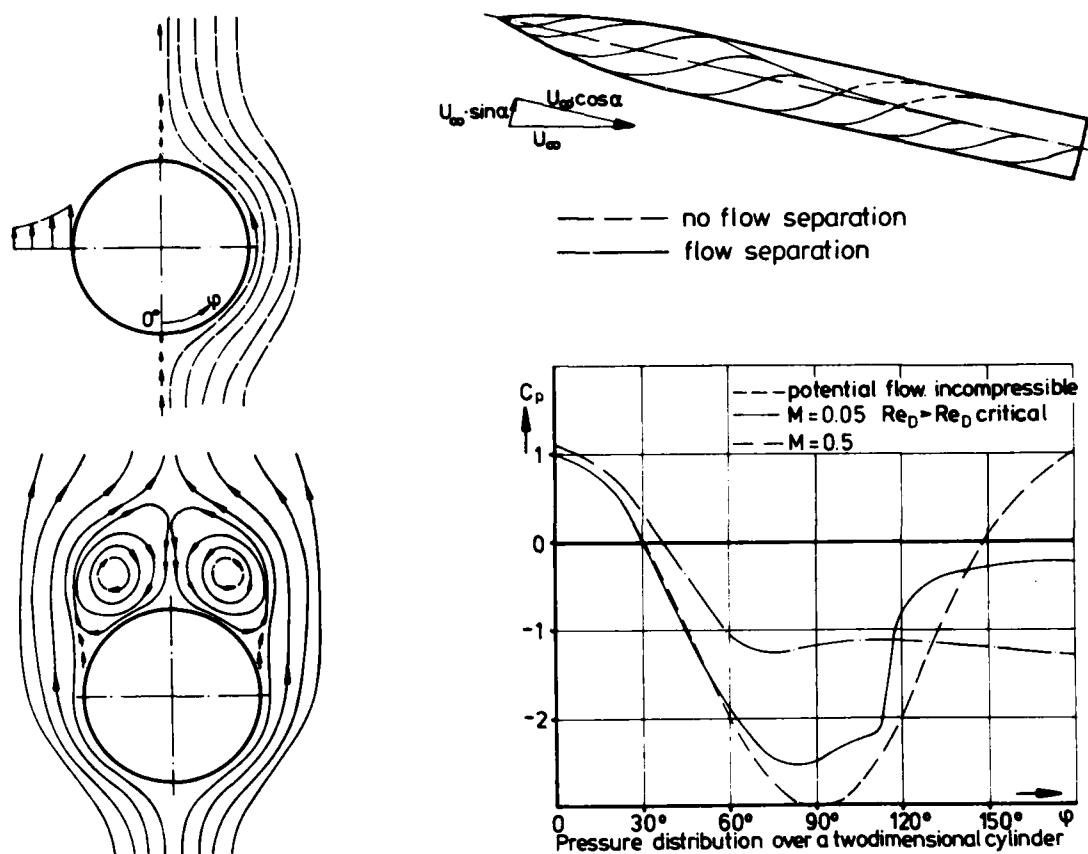


Fig. 21 Nonlinear  $\alpha$ -range, flow separation

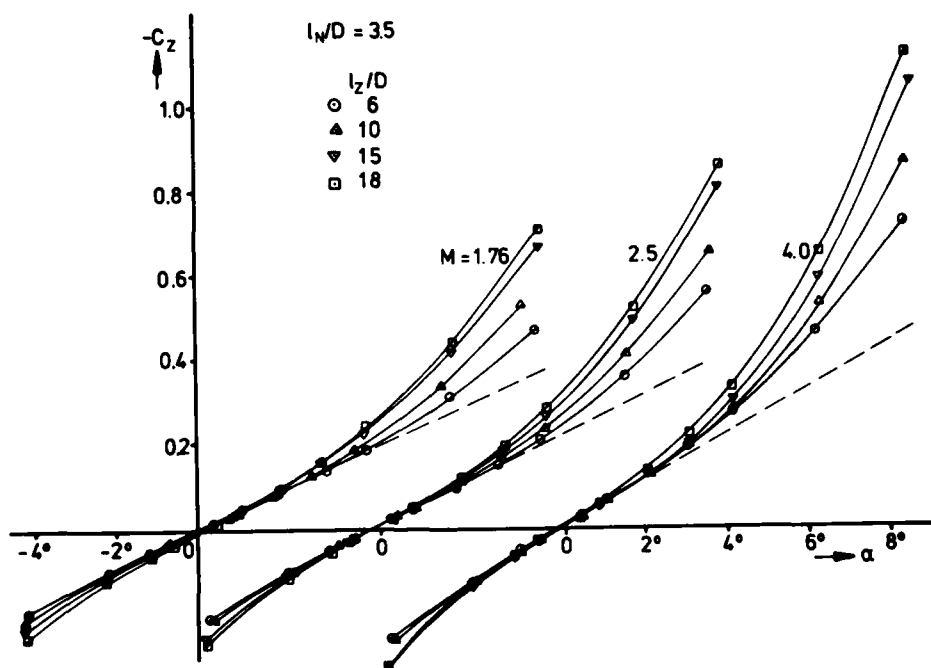


Fig. 22 Normal force coefficient of ogive cylinder bodies of different lengths [19]

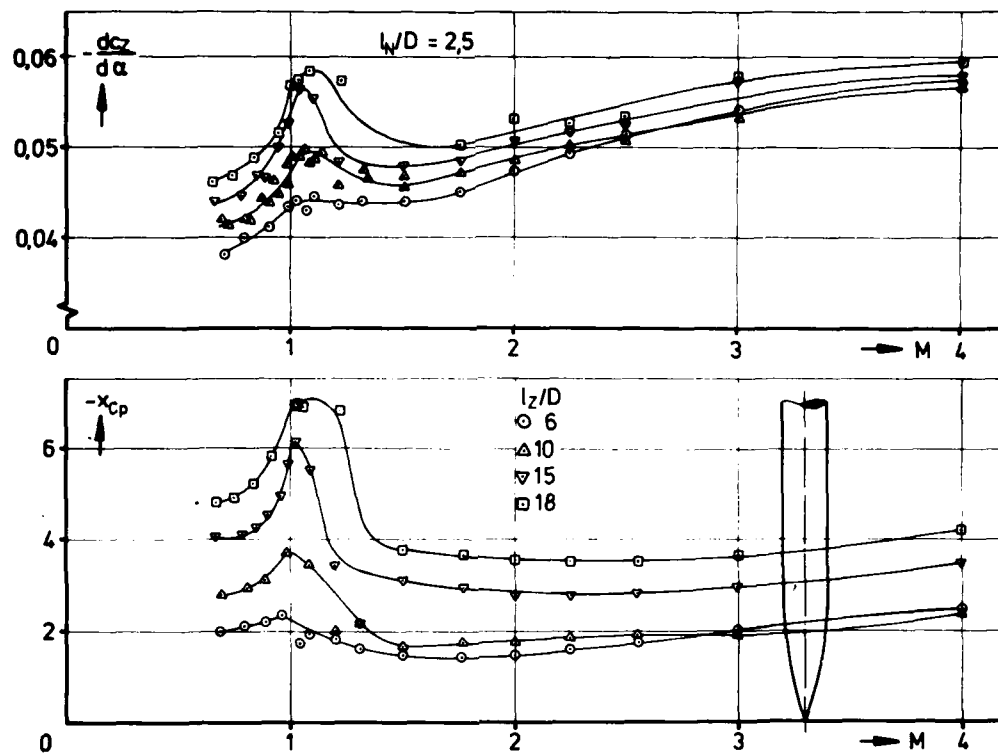


Fig. 23 Normal force slope and center of pressure of ogive-cylinder bodies at  $\alpha = 0^\circ$ , nose fineness ratio  $l_N/D = 2.5$ , experimental results [19]

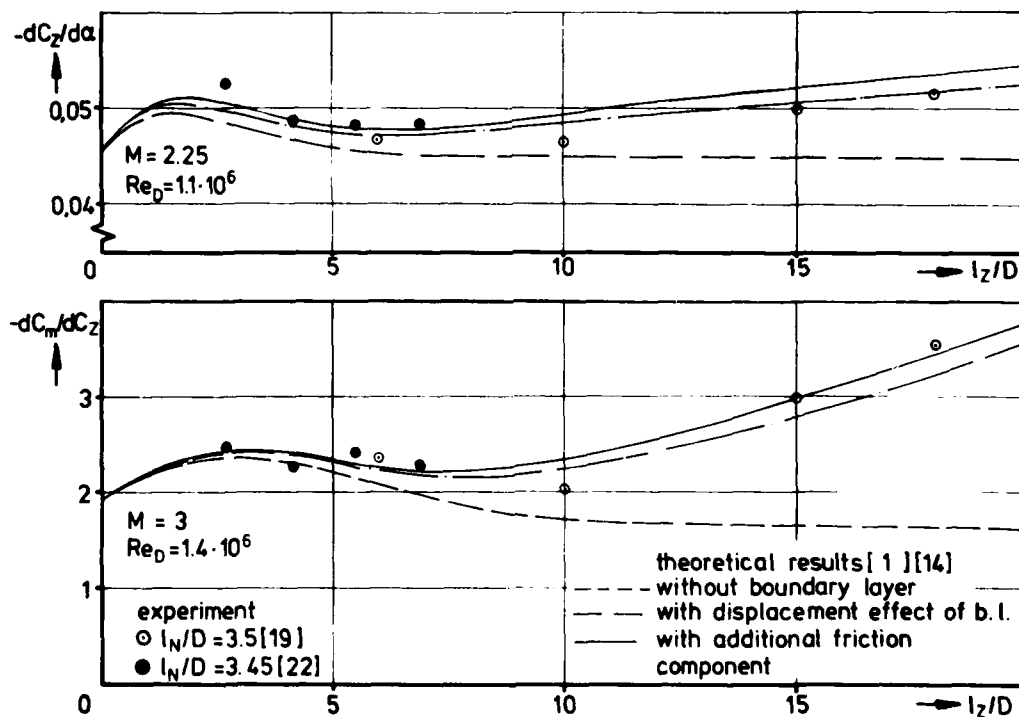


Fig. 24 Influence of the cylinder length on the normal force slope and the center of pressure of an ogive-cylinder ( $l_N/D = 3.5$ ) at  $\alpha = 0^\circ$ , comparison between experiment and theory [1], [14]

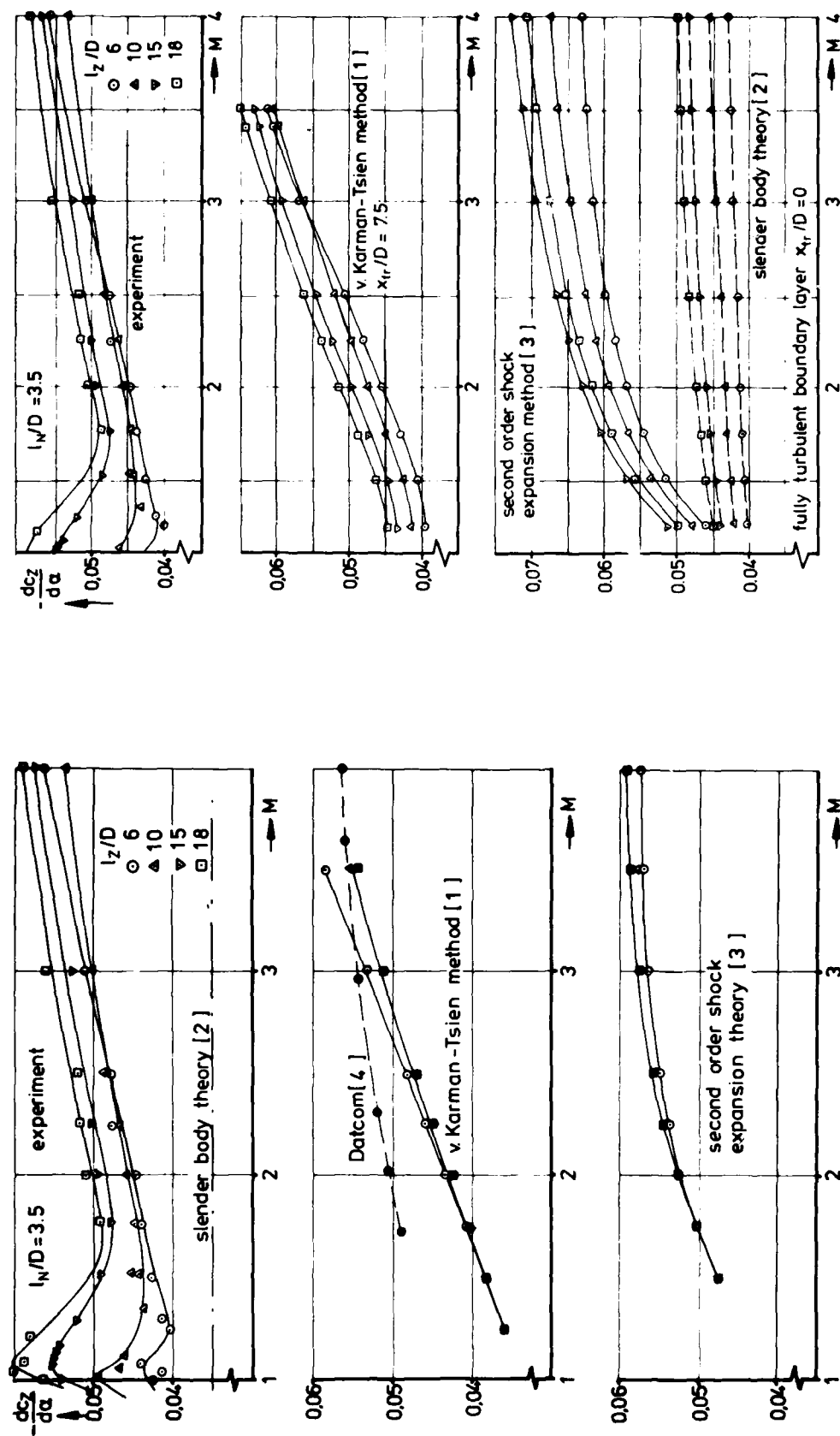


Fig. 25 Slope of normal force coefficient for ogive-cylinder bodies at  $\alpha=0$  [19], theoretical results without boundary layer thickness [19]

Fig. 26 Slope of normal force coefficient for ogive-cylinder bodies, theoretical results include displacement thickness [19]

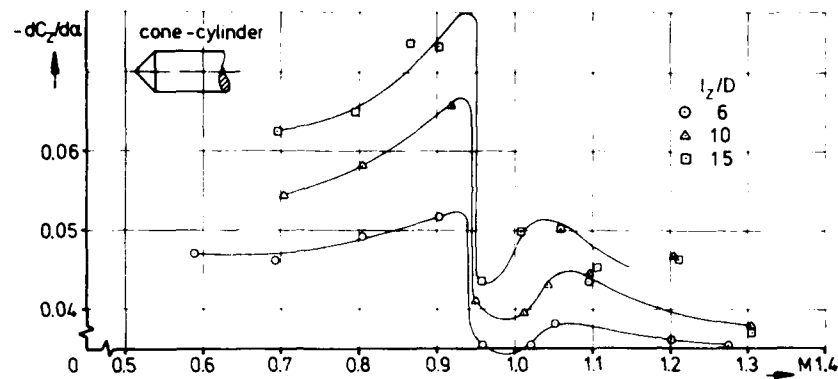


Fig. 27 Slope of normal force coefficient at  $\alpha=0^\circ$  for blunt cone cylinders,  $l_N/D=0.5$ ,  $0.5 \cdot 10^6 < Re_D < 1.1 \cdot 10^6$  [10]

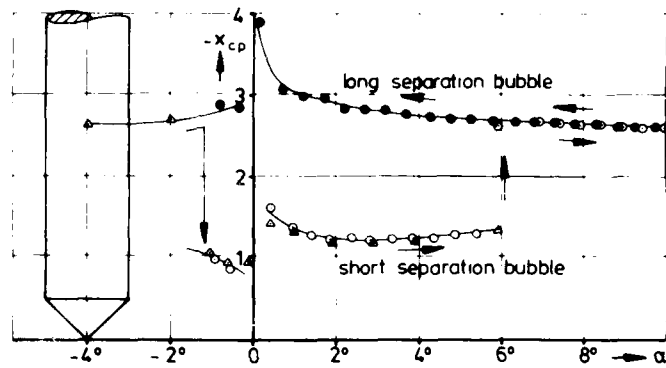


Fig. 28 Hysteresis in the center of pressure of a blunt cone-cylinder at transonic speeds [10]

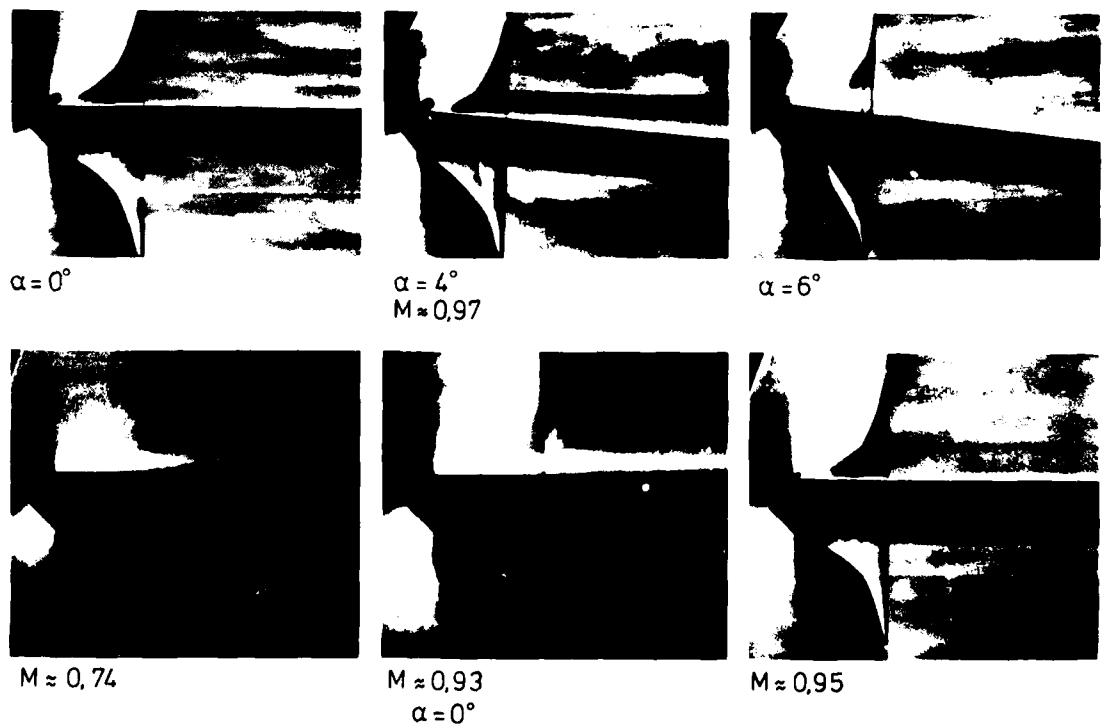


Fig. 29 Effects of angle of attack and Mach number on the flow separation on cone shoulders in transonic flow [10]

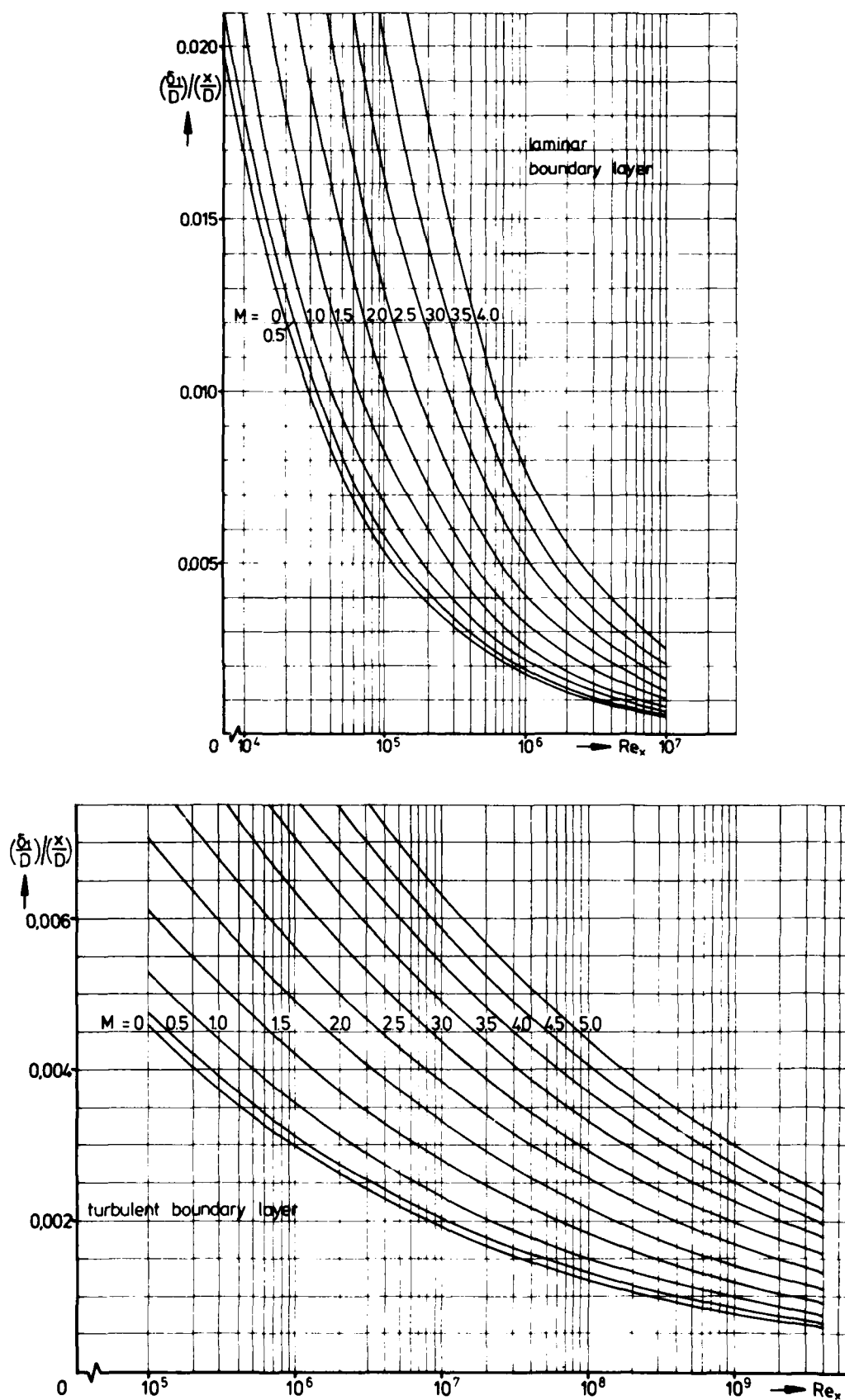


Fig. 30 Boundary layer displacement thickness on long cylinder bodies,  $l_z/D \geq 5$



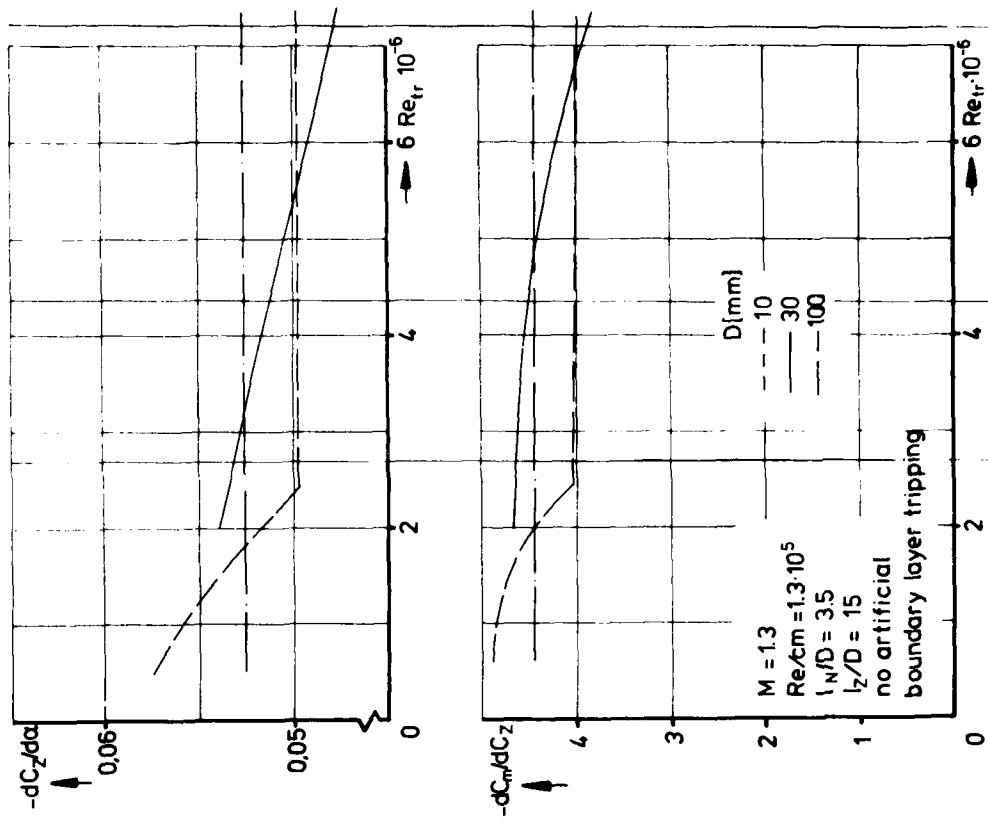


Fig. 32 Influence of the transition Reynolds number  $Re_{tr}$  on the normal force coefficient and the center of pressure of a slender cylindrical body under otherwise identical conditions [24]

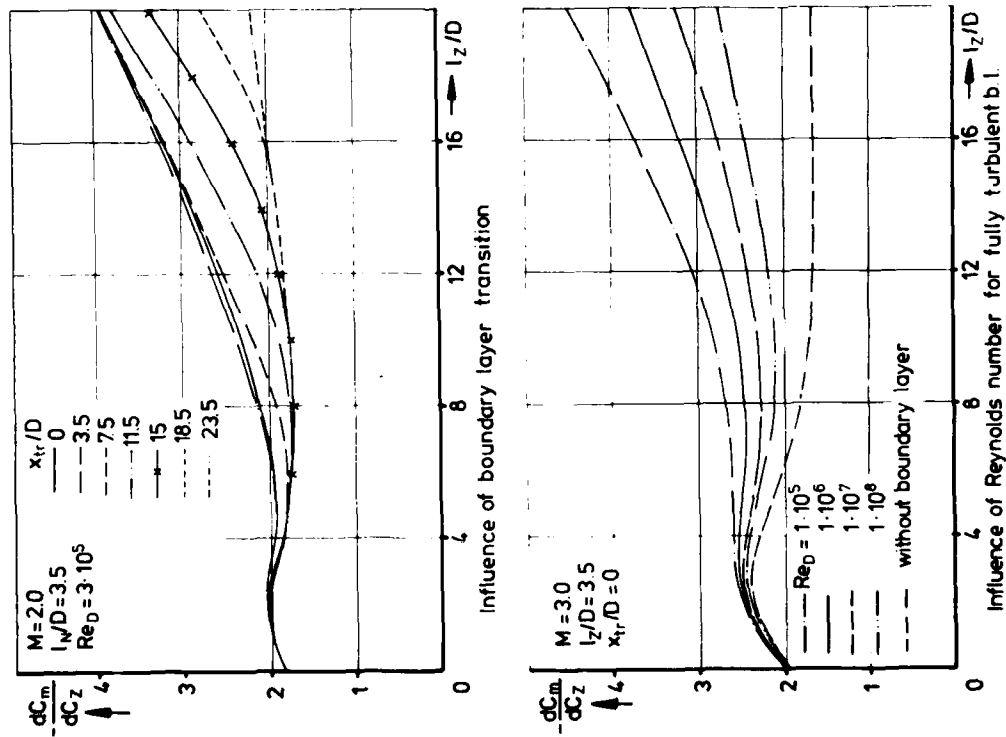


Fig. 31 Distance of the center of pressure from nose tip at  $\alpha = 0^\circ$ , theoretical methods [1], [14]

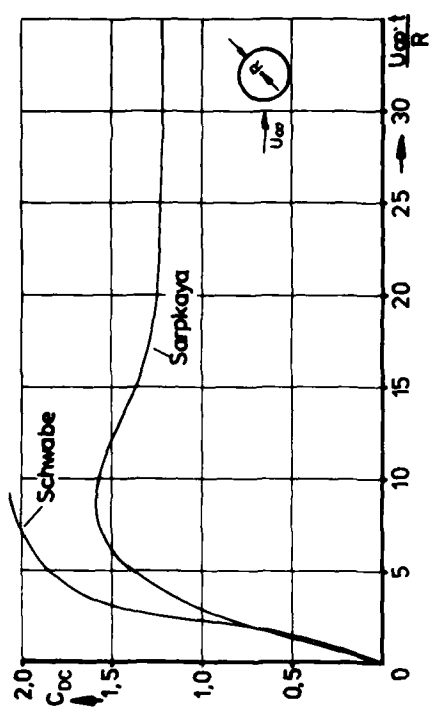


Fig. 33 Drag coefficient of a circular cylinder in impulsively started laminar flow

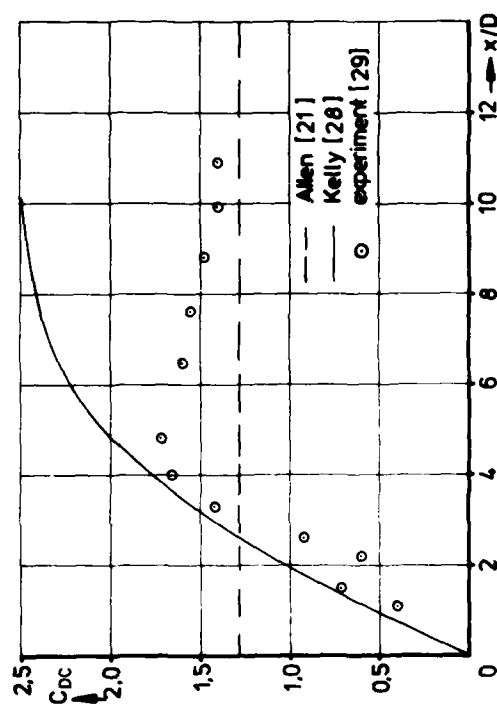


Fig. 34 Axial distribution of cross flow drag coefficient on a 30° cone-cylinder at  $\alpha = 23^\circ$ ,  $M = 2$  [29]

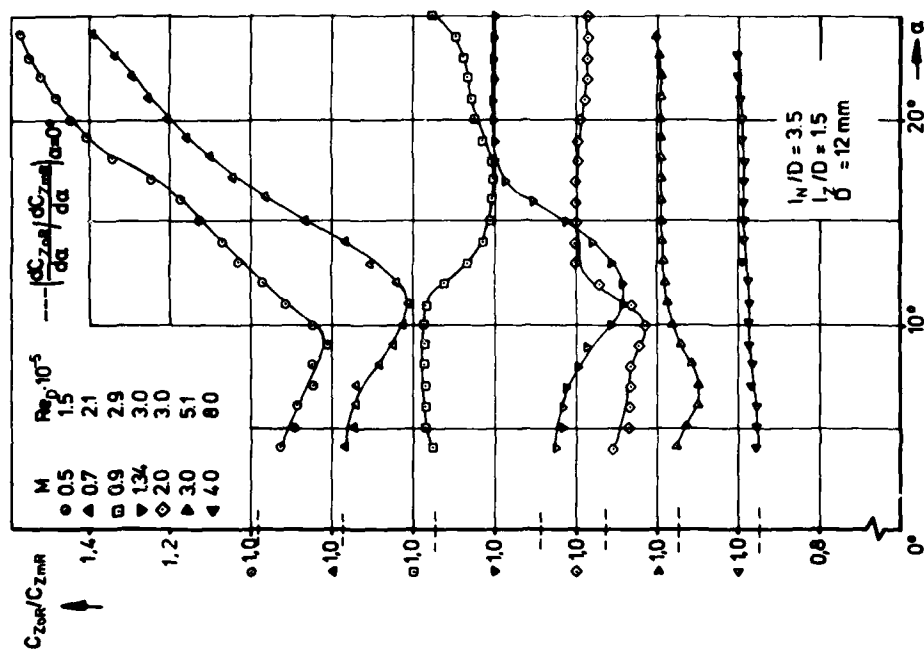


Fig. 35 Ratio of the normal force coefficients vs.  $\alpha$  for an ogive-cylinder body with ( $C_{ZmR}$ ) and without ( $C_{ZoR}$ ) transition strip [24]

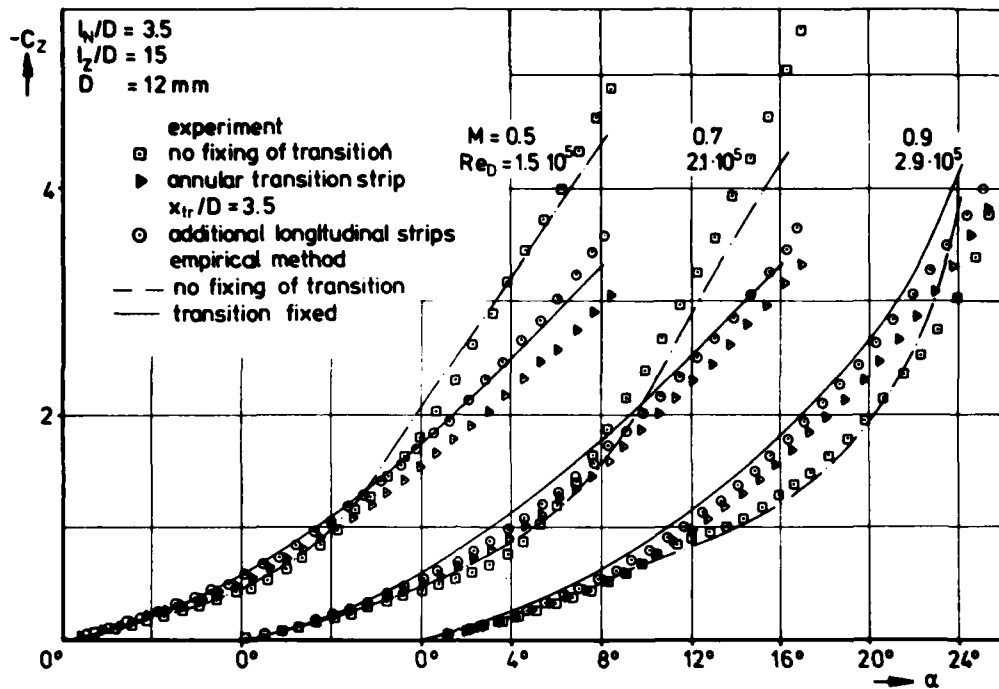


Fig. 36 Normal force coefficient of an ogive-cylinder in the critical cross flow range, influence of Reynolds number and boundary layer tripping [24]

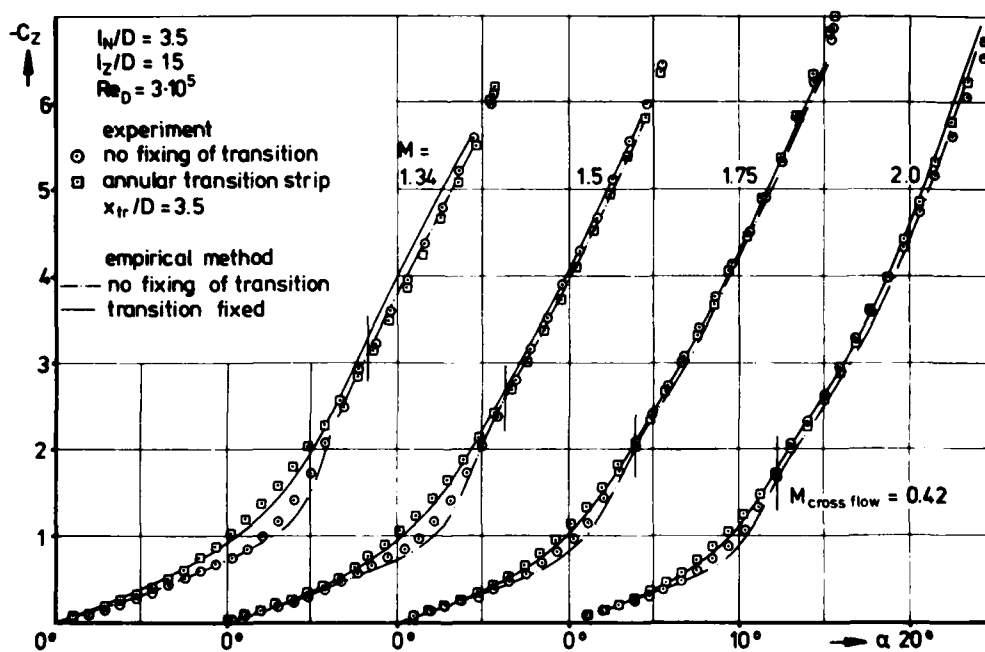


Fig. 37 Normal force coefficient of an ogive-cylinder, influence of Mach number at a constant Reynolds number [24]

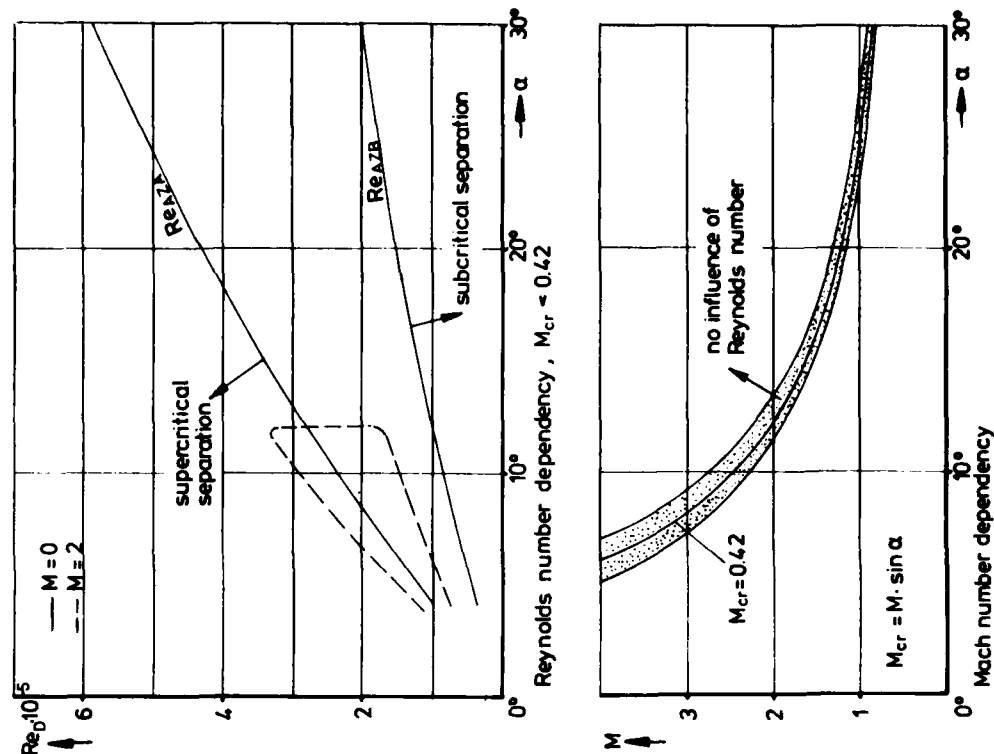


Fig. 39 Boundaries of critical separation region on a circular cylinder at angle of attack [24]

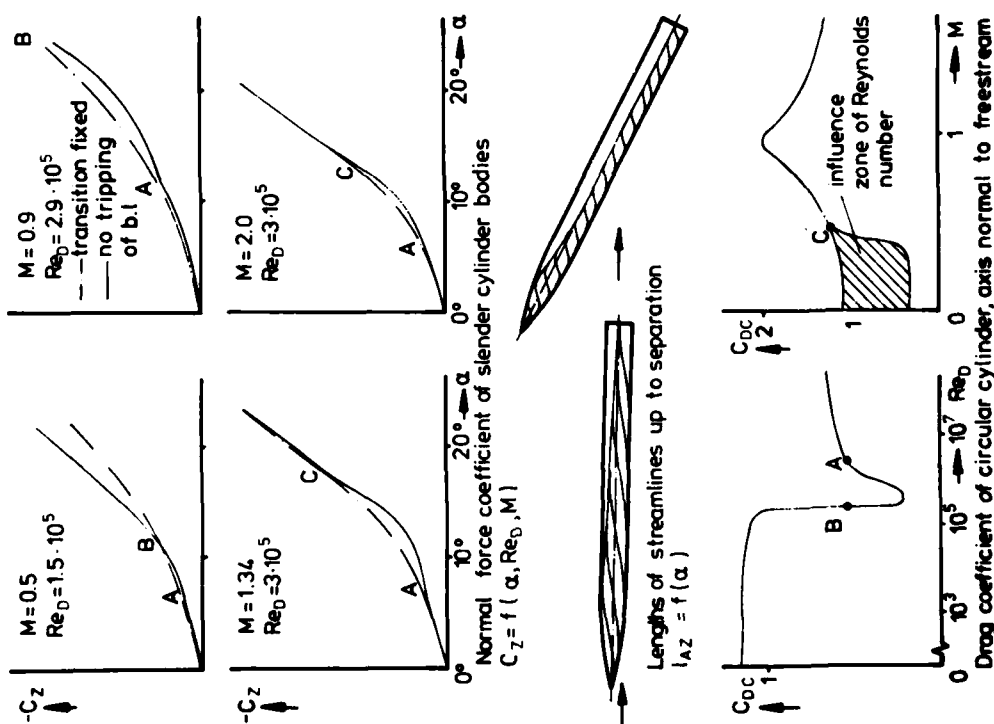


Fig. 38 Normal force coefficient of slender cylinder bodies in the critical cross flow range [24]

## HIGH-ANGLE-OF-ATTACK MISSILE AERODYNAMICS

Andrew B. Wardlaw, Jr.  
Naval Surface Weapons Center  
White Oak Laboratory  
Silver Spring, Maryland, USA

## SUMMARY

The large scale leeward flow separation occurring at high angles of attack precludes a tractable theoretical basis for determining missile aerodynamic characteristics. This has led to the development of predictive methods that rely heavily on experimental data and progress in creating such techniques is linked to the determination of a quantitative experimental description for the flow about and forces on missiles at high incidence. The following paper reviews experimental data on and predictive methods for bodies, fins and complete missile configurations. An outline and description is provided of the various vortex regimes that exist on a missile and its components at high angles of attack. Data is examined to determine quantitative trends in surface pressure distributions and loads. Available analytic, semi-empirical and empirical predictive methods are reviewed. On cylindrical bodies, analogies with cylinders in crossflow provide a convenient framework for constructing empirical predictive methodologies. However, for lifting surfaces and complete configurations, an apt analogy does not exist and predictive techniques consist of correlations of large force and moment data bases. Semi-empirical and theoretical methods model the flow field and from this information calculate loads on the missile configuration. Even though these approaches require less experimental information for development, they can have large computational requirements and tend to be restricted to subsonic flow.

## SYMBOLS

$a$	local body radius
$A$	area
$A_{ref}$	reference area
$R$	aspect ratio
$b$	wing alone semi-span
$C_r$	root chord
$C_{dc}$	crossflow drag coefficient
$C_{of}$	local side force coefficient normalized by the crossflow dynamic pressure
$C_L$	lift force coefficient
$C_n$	yaw moment coefficient
$C_N$	normal force coefficient
$C_{N_v}$	viscous contribution to the normal force
$C_{N_p}$	potential contribution to the normal force
$C_M$	pitching moment
$C_p$	$(p - p_\infty)/q$
$C_{ym}$	absolute value of the maximum $C_y$
$C_y$	yaw force coefficient
$d$	local diameter
$D$	reference diameter
$f_w, f_T$	y coordinate of wing vortex location at the wing and tail, respectively
$h$	width of a Karman vortex street
$i$	tail interference factor $(L_{T(V)}/L_{T_\alpha}) / \frac{\Gamma_m}{2\pi\alpha U} (s_T - r_T)$ . Also $\sqrt{-1}$ .
$l_n$	$L_n/D$
$l_t$	$L_t/D$
$\bar{l}_t$	$L_t/\bar{l}_t \int_0^{L_t} dx = L_t/\bar{D}$
$L$	lift force
$L_n$	nose length
$L_t$	total missile length
$M$	freestream Mach number
$M_c$	crossflow Mach number, $M \sin \alpha$
$p$	pressure
$q$	dynamic pressure
$r$	reference radius
$r_b$	nosetip radius/D

$R_{eD}$	freestream Reynolds number based on diameter
$r_W, r_T$	body radius at the wing and tail, respectively
$Re_C$	crossflow Reynolds number, $Re_D \sin \alpha$
$S$	Strouhal number
$s$	wing or tail semi-span in combination with body
$t$	time
$t^*$	$x \tan \alpha / D$
$U$	freestream velocity
$\vec{V}$	velocity vector
$\bar{V}$	body volume
$\vec{W}$	complex crossflow plane velocity, $v + iw$
$\hat{W}$	$W/U \sin \alpha$
$x_c$	distance from nose or leading edge to centroid of planform area
$x_m$	distance from nose to pitching moment reference center
$X_{cp}$	center of pressure
$x_s$	axial coordinate of initial vortex formation
$x, y, z$	cartesian coordinates (See Figure 1)
$y_v, z_v$	vortex location in the crossflow plane
$\alpha$	angle of attack
$\alpha_m$	angle of attack at which maximum side force occurs
$\alpha_o$	angle of attack at which side force or wake asymmetries start
$\beta$	$\sqrt{ M^2 - 1 }$
$\lambda$	taper ratio
$\Gamma$	circulation
$\Gamma_m$	circulation of wing vortex
$\epsilon$	semi-vertex angle of a delta wing
$\zeta$	complex crossflow plane coordinate, $y + iz$
$\zeta_j$	location of the $j^{\text{th}}$ vortex in the crossflow plane
$\zeta_o$	crossflow plane separation point
$\eta$	factor accounting for the finite body length in crossflow theory
$\theta_c$	cone half angle
$\theta_n$	semi-apex nose angle
$\theta_o$	angular location of separation in the crossflow plane
$\Lambda$	leading edge sweep angle of a delta wing ( $\Lambda \rightarrow 0$ as $M \rightarrow \infty$ )
$\xi$	angle between the extended vortex paths and a missile body
$\rho$	density
$\sigma$	standard error
$\chi$	$\tan \xi / \tan \alpha$
$\Phi$	complex velocity potential
$\phi$	velocity potential, roll angle
$\omega$	$\nabla \times \vec{V}$

## Subscripts

$B$	body
$T$	tail
$W$	wing
$BWT$	body-wing-tail combination
$BT$	body-tail combination
$B(W), B(T)$	body in the presence of the wing or tail
$W(B), T(B)$	wing or tail in the presence of the body
$B(W, T)$	body in the presence of the wing and tail
$T(V)$	tail in the presence of wing vortices
$\alpha$	derivative with respect to $\alpha$

## 1. INTRODUCTION

Increased missile performance requirements have recently stimulated interest in high angle of attack aerodynamics, a subject area which had been dormant for over a decade. This article considers the aerodynamics of missile configurations at angles of attack where separated flow dominates the leeward flow field. Special emphasis is given to phenomena which are unique to high angles of attack aerodynamics.

As a missile is exposed to increasing angles of attack the leeward flow field goes through several regimes. At incidences above 5 degrees the flow separates from the missile body and leading edges of lifting surfaces. This separated fluid rolls up to form well-defined vortices in the leeward flow field. Flow separation is accompanied by an increase in the aerodynamic loads while the presence of vortices introduces extreme loading nonlinearities. Small changes in the vortex paths and strengths can result in large variations in the aerodynamic forces. At sufficiently high incidences the steady vortex patterns disappear and flow about the missile body resembles a cylinder in crossflow.

The aerodynamic loads at high angles of attack differ qualitatively from those at low incidences. A much larger portion of the normal force and moment are contributed by the missile body. On missile configurations with pitch plane symmetry, induced forces arise. These loads which include roll moment, yaw force and yaw moment are absent at low angles of attack and their presence at high incidence seems in contradiction with the basic problem symmetry. They are produced by the asymmetric vortex pattern which develops in the leeward flow field.

The complex flow-field structure occurring at high angles of attack makes it very difficult to predict missile aerodynamic characteristics. Linear methods applicable at low incidences no longer are valid and a tractable theoretical approach does not exist. This has led to the development of empirical predictive methods which rely heavily on experimental data. For this reason, developing an experimental description of the high angle of attack flow field is a prerequisite for creating effective predictive methods.

These notes are divided into two sections. In the first, experimental information describing the flow field about and forces on missiles at high angles of attack will be reviewed. This will include a discussion of bodies alone, fins alone, complete configurations and high incidence testing problems. The second section will provide an overview of existing predictive methods.

## 2.1 EXPERIMENTAL DESCRIPTION OF FLOW ABOUT CIRCULAR BODIES

At an angle of attack greater than a few degrees the fluid on the leeward side of a body in subsonic flow rolls up to form vortices as shown in Figure 1. With increasing incidence a pattern containing two symmetrically disposed vortices gives way to an asymmetric flow field which may feature a large number of vortices. Both of these flow conditions are nominally steady and the latter gives rise to large, steady side forces. At incidences near 90 degrees the vortex pattern becomes unsteady and the resulting flow field resembles that behind a cylinder in crossflow. The vortex pattern in supersonic flow changes as the crossflow Mach number approaches unity. Vortices near the base of the body become elliptic in shape and with increasing Mach number degenerate into free shear layers. The leeside surface pressure distribution becomes very low due to compressibility effects and the flow field structure has relatively little influence on total body loads. A qualitative outline of the Mach number-incidence bounds of the various high angle of attack flow regimes is shown in Figure 2.

### 2.1.1 PARAMETERS FOR CORRELATING EXPERIMENTAL DATA

The analogy between the crossflow about a body at high angle of attack and flow about a two dimensional cylinder is often relied upon to interpret experimental data. Two different types of relations have been constructed. The simplest, which will be referred to as the crossflow analogy, assumes that the flow over an inclined body can be divided into a component parallel to the body axis and one perpendicular to it. The viscous flow in the crossflow plane of the inclined body is similar to that about the cylinder where the free stream conditions are  $Re \sin \alpha$  and  $M \sin \alpha$ . Figure 3 provides the circular cylinder drag coefficient and rms lift coefficient as a function of Mach number and Reynolds number.<sup>1,2</sup> From these charts it is evident that Reynolds number is an important parameter below the critical Mach number of .42. The onset of turbulence moves the separation point leeward narrowing the wake and reducing drag and lift. At Mach numbers greater than .42, separation is triggered by the formation of weak shock waves on the shoulders of the cylinder and Reynolds number no longer has an important effect on the force coefficients.

A more complex analogy, which will be referred to as the impulsive flow analogy, likens the development of the flow in the crossflow plane of an inclined body to that about an impulsively started cylinder. This analogy assumes that the crossflow plane is swept at the uniform rate,  $U \cos \alpha$ , down the body. The flow field in the crossflow plane at a distance  $x$  from the missile nose has thus been developing for the period of time  $t = x/U \cos \alpha$  and should be analogous to the flow field about an impulsively started cylinder at the same time after the start of flow. The free stream velocity of the impulsively started cylinder is  $U \sin \alpha$  and the dimensionless time parameter for a cylinder in crossflow,  $Ut/D$ , becomes:

$$t^* = x \tan \alpha / D \quad (1)$$

A problem with the impulsive flow analogy is that experimental data on impulsively started cylinders is difficult to generate. Available information from references 3, 4, 5 and 6 are shown in Figure 4. In addition, to accurately simulate the nose region, impulsively started flow experiments should initially feature an expanding cylinder. Despite these difficulties this analogy correctly predicts formation of a symmetric vortex pattern at low incidences (i.e. at small values of  $t^*$ ) and asymmetric vortex structures at higher angles of attack. Unfortunately it gives no criteria for the onset of unsteady flow.

The above two analogies suggest that important parameters correlating experimental measurements at high angles of attack should be:

1. Crossflow Reynolds number,  $Re \sin \alpha$
2. Crossflow Mach number,  $M \sin \alpha$
3. Dimensionless time from the start of the crossflow,  $x \tan \alpha / D$

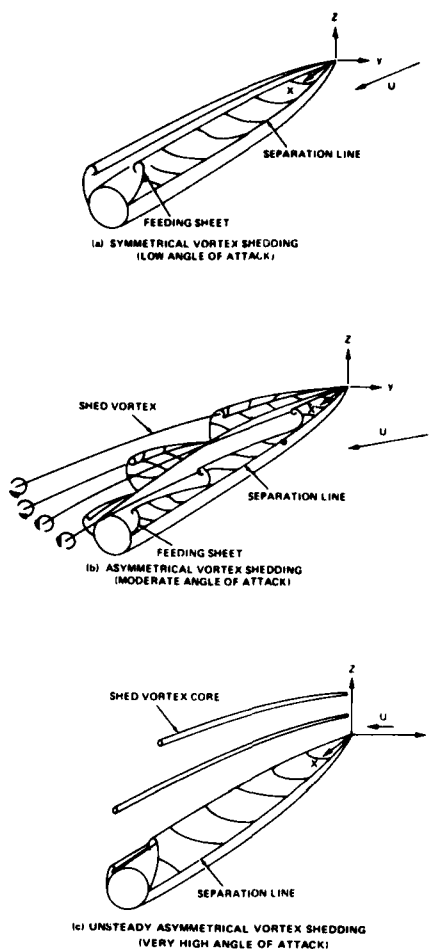


Figure 1. Leeward vortex structure in subsonic flow

nose and base. It will be shown in later sections that neither of these analogies can account for measured side force characteristics.

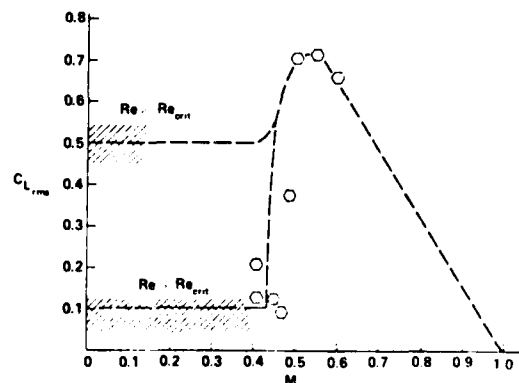
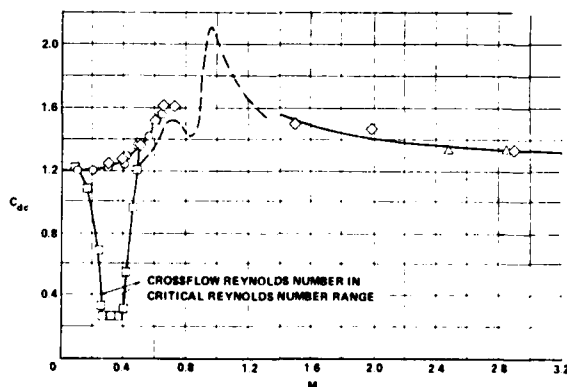


Figure 3. Cylinder drag<sup>1</sup> and rms lift coefficient<sup>2</sup> as a function of Mach for sub and supercritical Reynolds number

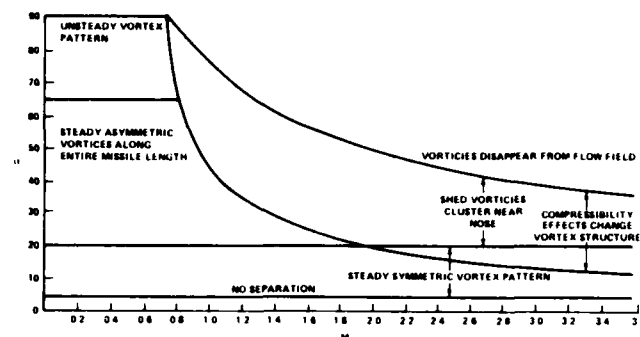


Figure 2. Leeward flow field regimes on a circular body,  $l_t \sim 10$

There seems to be little question that crossflow Mach number and  $t^*$  are effective parameters for correlating experimental data. However, as discussed by reference 7, at low incidences transition is determined by the axial Reynolds number,  $Re_{cos\alpha}$  while at high angles of attack the crossflow Reynolds number is likely to be most influential. It has been found on studies of infinite yawed cylinders that the streamwise Reynolds number  $Re_D/\sin\alpha$  is a single parameter grouping that produces appropriate Reynolds number values for predicting transition at both high and low incidences.<sup>8</sup> To illustrate this point experimental values of the average crossflow drag coefficient on inclined bodies have been plotted as a function of  $Re_D/\sin\alpha$  in Figure 5. These drag coefficients were obtained by using the experimental normal force<sup>9,10</sup> in Eq. (19) and solving for  $C_{cd}$ . Most of this data was taken at a crossflow Mach number of less than .35 and shows a sharp decline at Reynolds numbers greater than  $1.5(10^5)$  to  $4.0(10^5)$ . The remaining measurements reflect a sensitivity to Reynolds number that decreases with increasing crossflow Mach number. The influence of crossflow Mach number and streamwise Reynolds number on the crossflow drag is thus seen to be very similar to that of freestream Mach number and Reynolds number on the drag of a cylinder in crossflow.

Despite some success in applying the above analogies to inclined bodies, it should be kept in mind that flow about such a configuration is really three dimensional, particularly near the



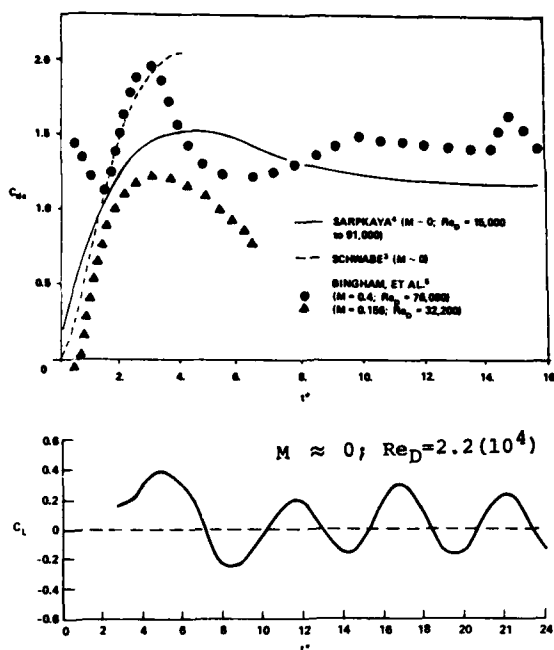


Figure 4. Time dependent drag and lift<sup>6</sup> on an impulsively started cylinder

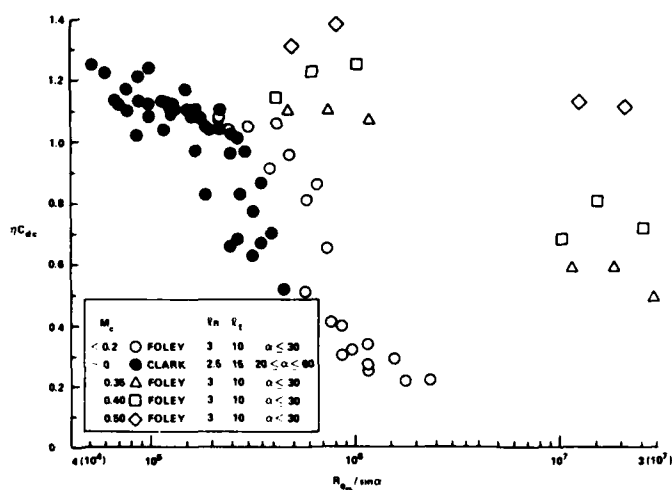


Figure 5. Measured  $nC_{Dc}$  on inclined bodies as a function of Reynolds number

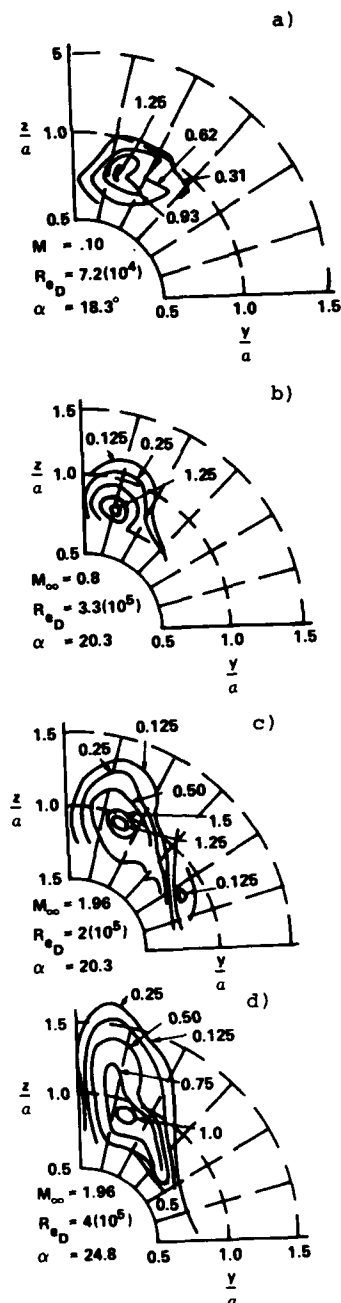


Figure 6. Crossflow plane vorticity ( $Dw/4U$ ). Case A is from reference 11, while remainder are from reference 12. Test body was a tangent ogive,  $\ell_n = 3$ ,  $x/D = 6$ .

### 2.1.2 THE SYMMETRIC VORTEX REGIME

The symmetric vortex pattern, depicted in Figure 1a, generally occurs at incidences up to 20 to 40 degrees, with the lower limit applying to longer bodies. The gross crossflow plane pattern is relatively insensitive to Mach number and Reynolds number as long as the crossflow Mach number is less than unity. With increasing  $Mc$ , starting near the base, vortices progressively become more elliptic and finally degenerate into free shear layers. This is illustrated in Figure 6 where experimentally determined crossflow plane velocities have been integrated to obtain the vorticity distribution<sup>11,12</sup>. The vortex structure remains qualitatively unchanged in Figure 6a, 6b, and 6c even though the freestream velocity Mach and Reynolds number vary over a wide range. A clear elongation of the vortex structure can be seen in Figure 6d which features a crossflow

Mach number near unity. This is more emphatically illustrated in Figure 7 using Oberkamp's supersonic crossflow measurements.<sup>13,14</sup>

The fully developed symmetric vortex pattern as viewed in the crossflow plane is shown in Figure 8 and features both a primary and secondary vortex of opposite circulation. The flow field can generally be characterized by the following three features:

1. Primary separation point
2. Vortex position
3. Vortex strength

In addition to the above quantities, the axial position of the initial leeward flow separation is found to be a useful correlative parameter. In the following section, experimental information describing these features is presented.

The axial position,  $x_s$ , at which vortices first appear has been determined experimentally in a number of different studies and the results have been correlated by Mendenhall<sup>15</sup>:

sharp nosed bodies:

$$\frac{x_s}{r} = 32 \left( 1 - \sqrt{\frac{\alpha - 4}{\theta_N - 4}} \right) \quad (2)$$

blunt nosed bodies:

$$\frac{x_s}{r} = \frac{10}{\alpha - 4} + 2 \quad (3)$$

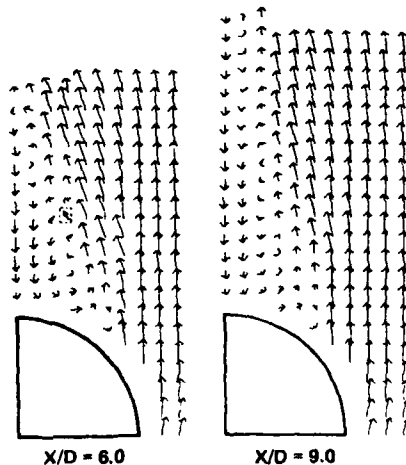


Figure 7. Crossflow plane velocity vector plot from reference 13.  
[ $M_\infty = 3.01$ ,  $\alpha = 25^\circ$ ,  $Re_D = 1.7 (10^6)$ ]

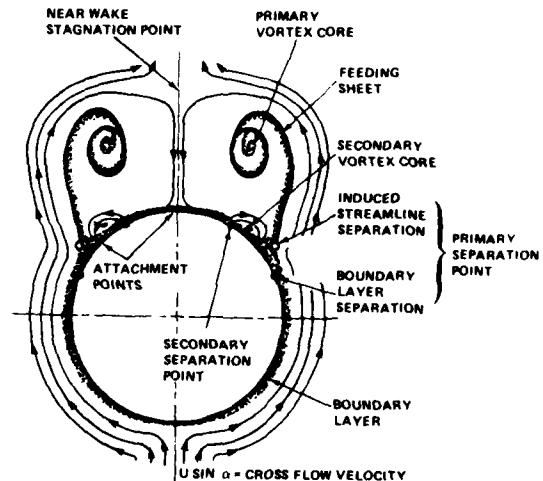


Figure 8. Symmetric flow field viewed from crossflow plane

Measurements of the primary separation point can be found in a number of different references.<sup>16-22,45</sup> Usually this quantity is determined using flow visualization techniques such as oil flow, dye injection or hydrogen bubbles. As discussed by Schindell<sup>16</sup>, these techniques do not always lead to the same results. Hydrogen bubbles mark the point of separation for the inviscid streamlines while the position of boundary layer separation is determined by dyes and oil flows. In addition to these discrepancies, interpretation of the flow visualization experiments is often very subjective. Despite these uncertainties, three distinct trends are visible in the separation point data:

1. The separation point moves windward with increasing distance from the nose.
2. With increasing angle of attack, the separation point moves windward.
3. At crossflow Mach numbers greater than .8, the separation point moves in the leeward direction.

This last point is illustrated in Figure 9 using the data correlated by Nielsen, et.al.<sup>23</sup> and adding to it measurements from Feldhuhn's<sup>17</sup> study on cones. Both this graph and the previously described changes of vortex structure at high crossflow Mach numbers indicates that the wake narrows under these conditions. The two other trends are depicted in Figure 10 which features separation angle as a function of  $t^*$ . The data plotted in this graph is representative of both symmetric and asymmetric vortex patterns, the latter case occurring for large  $t^*$ . Asymmetric vortex patterns generate different separation angles on each side of the inclined body and the plotted value is an average of the two. The quantity  $F'$ , determined from Figure 9 has been subtracted from measurements taken at crossflow Mach numbers greater than .8. The scatter in the results makes it difficult to draw firm conclusions, however, for  $t^* > 2$ , data are

roughly distributed between the laminar and turbulent cylinder separation angles, with the solid symbols representing turbulent separation (i.e.  $Re_p/\sin\alpha > 4(10^5)$ ,  $M_\infty < .4$ ) appearing to be closer to the turbulent cylinder in crossflow separation point.

The flow field surveys of Figure 6 show vorticity to be widely distributed throughout the crossflow plane. Nevertheless, it is convenient from the point of view of quantifying the flow field to characterize the vortex structure by a vortex center and a total circulation. The vortex center is usually taken to be the point of most intense circulation which closely coincides with the position of the minimum total pressure. Information on vortex strength and position can be found in a large number of places.<sup>11,12,14,24-29</sup> Ideally vortex strengths are determined by measuring flow field velocities and performing the integration

$$\Gamma = \int_C \vec{V} \cdot d\vec{s}$$

about contours which appear to enclose the vortex. However, in many cases, only the vortex position is measured directly. The vortex strength is calculated by combining position data and other experimental measurements with simple theoretical models. As will be discussed in Section 3.1, it is possible to derive an expression for normal force as a function of crossflow plane vortex position. Assuming symmetric vortices and solving for vortex strength yields:

$$\frac{\Gamma}{2\pi r U \sin\alpha} = \frac{(C_N - C_{N_P})r}{4\sin 2\alpha y_V [1 - a^2/(y_V^2 + z_V^2)]} \quad (5)$$

Here  $C_{N_P}$  is the slender body theory contribution to the normal force and  $y_V, z_V$  is the vortex location in crossflow coordinates. Circulation values obtained by integrating crossflow velocities are in good agreement with these results. An alternate approach is to measure the location of the near wake stagnation point.<sup>29</sup> Constructing a potential crossflow plane model with two symmetrically placed point vortices and requiring that the velocity be zero at the measured near wake stagnation point location also yields an expression for vortex strength.

Vortex positions and strengths from references 11, 14, and 24-29 have been correlated to determine relevant trends. Figures 11 to 13 indicate that vortices move away from the missile body and become stronger with increasing distance from the nose. As is evident in Figure 11, vortex strength increases in subsonic flow with increases in  $Re_p$ . Although the supersonic vortex strength appears to be larger than subsonic ones, this may be partly due to  $Re_p$  which is generally larger in the supersonic data. In Figure 12 subsonic vortices are seen to move away from the body along radial lines with constant angular orientations. The actual angular location appears linked to the separation point, moving leeward with transition and then windward with further increases in  $Re_p$ . In supersonic flow the vortex angular position decreases with increasing distance from the nose. Figure 13 illustrates that the radial vortex location is larger in supersonic flow. For subsonic conditions it is sensitive to  $Re_p$  decreasing after transition and then increasing with further increases in  $Re_p$ .

A new type of vortex structure has recently been reported to exist on the nose tip of blunt bodies at intermediate incidences in transonic flow.<sup>18</sup> This phenomenon which occurs in addition to the crossflow plane vortices, forms as a result of a leeside vortex separation bubble which is induced by axial rather than crossflow pressure gradients. The resulting vortex pair is illustrated in Figure 14 and features a circulation opposite in sign to that of the crossflow plane vortex. There is no information concerning the associated vortex strength, hence its importance in influencing aerodynamic loads is unknown.

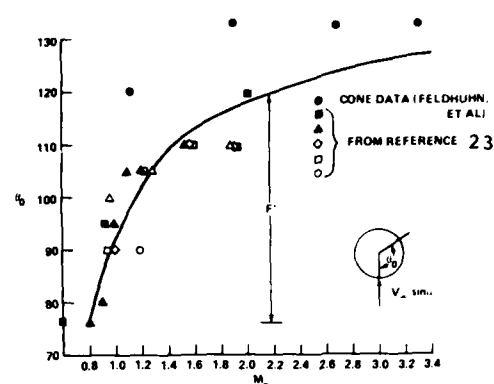


Figure 9. Steady state separation angle as a function of crossflow Mach number

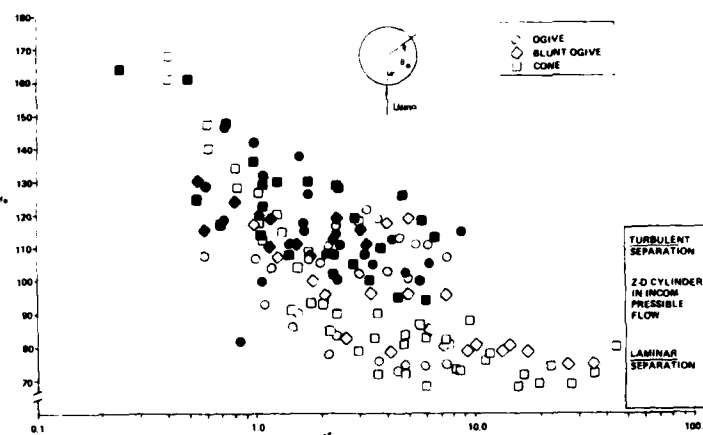


Figure 10. Average separation angle as a function of  $t^*$ . Solid symbols denote turbulent separation.

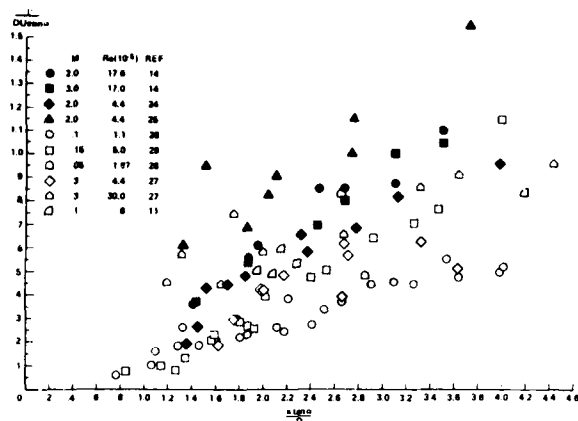


Figure 11. Strength of Symmetric Body Vortices

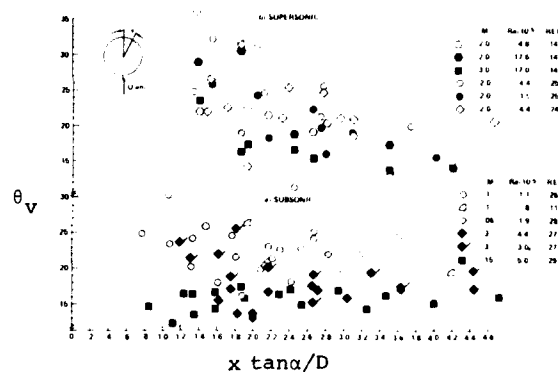


Figure 12. Angular Orientation of Symmetric Body Vortices

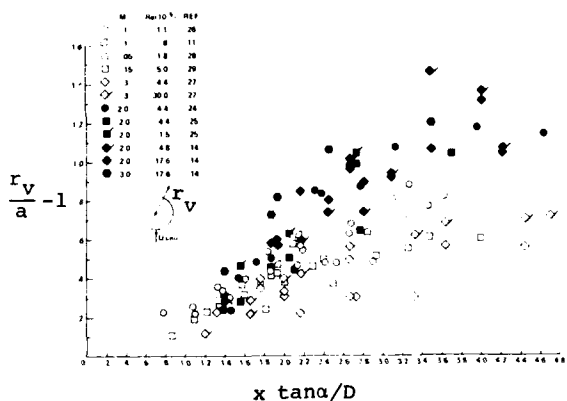
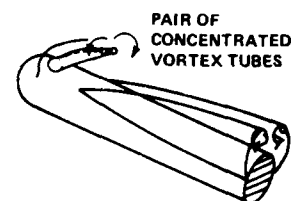
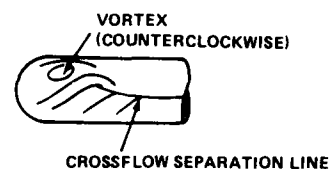


Figure 13. Radial Position of Symmetric Body Vortices

## a) VORTEX STRUCTURE



## b) SURFACE STREAMLINES

Figure 14. Nose Vortex Structure at  $\alpha \sim 19^\circ$  on a Blunt Body in Transonic Flow

## 2.1.4 DESCRIPTION OF THE ASYMMETRIC VORTEX PATTERN

At an intermediate range in angle of attack (25 to 70 degrees) a nominally steady asymmetric vortex pattern develops in the leeward flowfield. This pattern is not extremely stable; various vortex configurations have been reported for the same test conditions and in some cases unsteadiness has occurred. Examples illustrating the fickle nature of the flow field can be found throughout the literature. Gowen and Perkins<sup>30</sup> ran an extensive series of flow visualization studies on slender bodies of revolution at Mach 2 and observed the onset of an unsteady flow field in the incidence range 20 to 40 degrees. Gapcynski<sup>31</sup> ran similar tests and was unable to find flow unsteadiness. Thomson and Morrison<sup>32</sup> have observed unpredictable regions of instability in their flow field studies while Clark and Nelson<sup>23</sup>, and Deffenbaugh and Koerner<sup>21</sup> found that asymmetric vortex patterns would change to symmetric ones, and vice versa, with no discernible variation in test conditions. Clark<sup>10</sup> has also discovered that generating a small disturbance upstream of a body with an asymmetric vortex pattern will form a new, more stable vortex configuration. Gowen and Perkins<sup>30</sup> and Wardlaw and Morrison<sup>2</sup> both report altering asymmetric vortex patterns by changing the roll orientation of bodies of revolution. Results from the latter work are shown in Figure 15. These experiences suggest that very small changes in test procedure and irregularities in model machining can have a large influence on the asymmetric flow field. The importance of this last factor is underscored by the experiment carried out by Kruse<sup>34</sup> (see Figure 16). Here an axisymmetric model at high incidence was spun about its axis and the resulting side force which reflects the leeward vortex structure is seen to vary periodically with roll orientation.

Currently it is unclear what role unsteadiness plays in the case of the asymmetric vortex pattern. Pressure measurements in incompressible flow by Lamont and Hunt<sup>35</sup> support the hypothesis that it is central to an understanding of this flow regime. These workers have concluded that the flow field is unsteady and continuously changes between two mirror images patterns. A right-handed pattern is formed when the first shed vortex is on the right side of the body and a left handed pattern reflects the opposite situation. The steady state side force reflects the average amount of time that the flow spends in each orientation. Support for this point of view comes from surface pressure



Figure 15. Variation of the leeward flowfield with changes in roll orientation on an axisymmetric model,  $M = .7$ ,  $\alpha = 40^\circ$ .

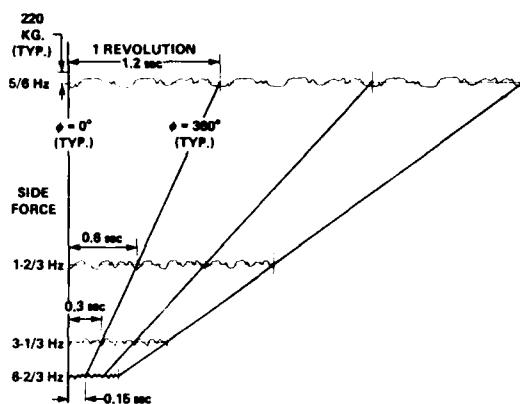


Figure 16. Side force as a function of roll orientation and spin rate

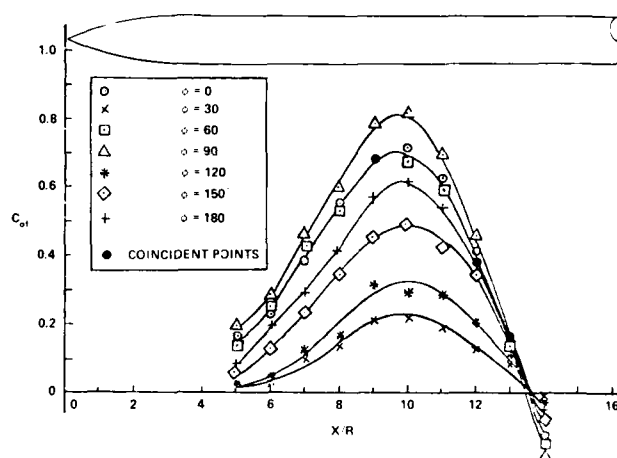


Figure 17. Local side force as a function of axial position and roll orientation

measurements which were integrated to produce the side force distribution. As is common experience, the steady state side force is seen to vary with roll angle, however, the functional form of the side force distribution curve does not (see Figure 17). Lament and Hunt were able to make the magnitude of the side force independent of roll orientation using an unsteady pressure measurement. At each roll angle the steady state side force was corrected by multiplying it by the ratio of peak to average pressure.

Thomson and Morrison have developed a general description of the steady asymmetric flow field using data covering the Mach number Range of .4 to 2.8 and a low enough Reynolds number to assure laminar separation. As with the symmetric vortex pattern, the gross features of the flow field are primarily dependent on crossflow Mach number. For  $M_C < .7$ , two weak, closely spaced nose vortices are followed by a series of constant strength ones as shown in Figure 18. As the crossflow Mach number is increased past .7, vortices cluster closer together and become increasingly concentrated near the nose tip. These changes are illustrated in the Schlieren photographs of Figure 19. A detailed view of the crossflow plane vorticity distribution provided by wake surveys is shown in Figure 20. At a crossflow Mach number of 1.2 an elliptic, almost symmetric vortex pair appears near the lee side of the body. Only far from the body does a weak asymmetric vortex pattern develop. This is in contrast to the vorticity distribution in subsonic flow from reference 11 shown in the same Figure where a strong asymmetric vortex pattern develops near the lee side of the body.

Water tunnel results by Clark and Nelson<sup>10,33</sup> covering both laminar and turbulent separations, in contrast to those of Thomson and Morrison, suggest that the flow field is dominated by two strong nose vortices. One or two additional vortices may be shed downstream of the nose vortices, and the flow field about the aft end of the model contains only diffuse vorticity. Introduction of an air bubble stream impinging on the nose tip was found to produce a more stable vortex pattern with the larger number of shed vortices. The various vortex patterns observed by Clark are shown in Figure 21.

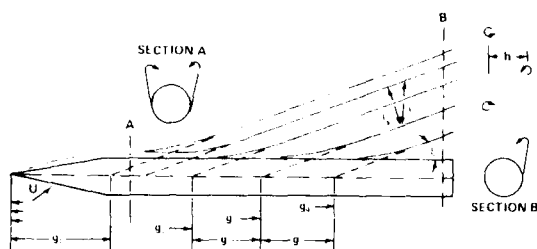


Figure 18. Terminology for Thomson and Morrison's Theory



c) Supersonic flow;  $M = 2.0$ ,  $\alpha = 45^\circ$ ,  $M_c = 1.4$   
Figure 19. Schlieren photographs of the leeward flow field



a) Subsonic flow;  $M = 0.6$ ,  $\alpha = 45^\circ$ ,  $M_c = 0.4$



b) Supersonic flow;  $M = 2.0$ ,  $\alpha = 35^\circ$ ,  $M_c = 1.1$

Thomson and Morrison appear to be the only reference developing a quantitative description of the asymmetric flow field. These results apply to the case of laminar separation with  $M_c < 0.7$  and were developed using a cone-cylinder model. In this study the leeward flow field is mapped using a Pitot probe and results are integrated to determine vortex strength. The emerging flow-field description indicates that the first two vortices are much weaker and clustered closer to each other than are subsequent ones. In an effort to supplement measured vortex strengths an indirect method of calculation is devised. The first two vortices are excluded from the analysis and the remainder are treated using a combination of the impulsive flow analogy, Karman vortex street theory<sup>36</sup>, and the concept of the yawed vortex street. This latter principle supposes that the shed vortices can be treated as a Karman vortex street traveling in a direction perpendicular to the shed vortex lines (see Fig. 18). The resulting theory allows vortex strengths to be determined from the vortex spacing which can readily be measured using Schlieren photographs.

The Strouhal number which describes the frequency for vortex shedding in two-dimensional flow is written:

$$S = \frac{D}{2tU} \quad (6)$$

where  $t$  is the time between the shedding of successive vortices. Using the impulsive flow analogy (Section 2.1.1), the time between the shedding of successive vortices is related to the axial distance between adjacent vortices,  $q'$ , by:

$$t = \frac{q'}{U \cos \alpha} \quad (7)$$

Replacing  $U$  in Eq. (6) by  $\sin \alpha$  (which is consistent with the impulsive flow analogy) and using (7) yields:

$$S = \frac{D}{2q' \tan \alpha} \quad (8)$$

The theory developed by von Kármán defines vortex strength in a two-dimensional street to be:

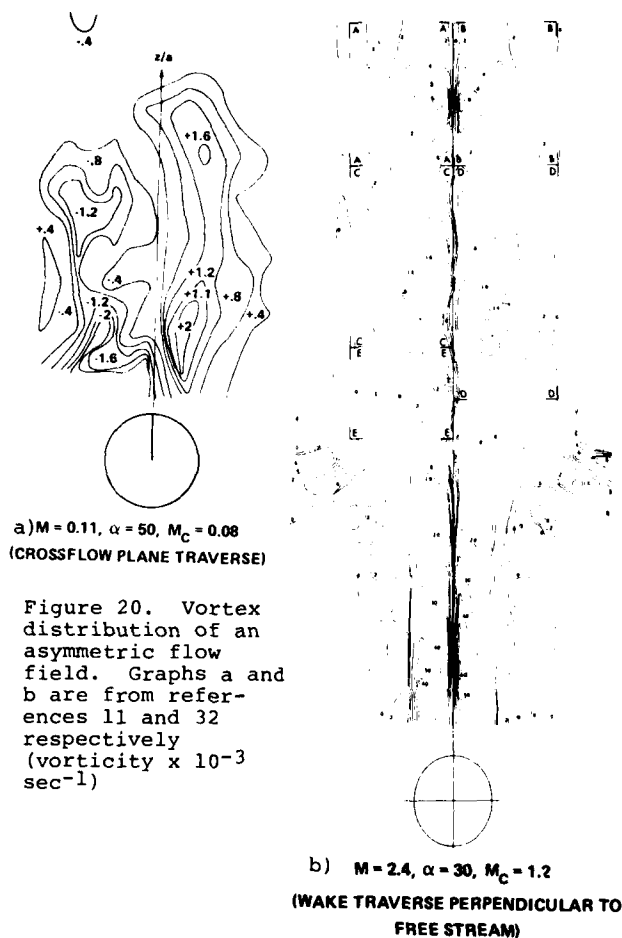


Figure 20. Vortex distribution of an asymmetric flow field. Graphs a and b are from references 11 and 32 respectively (vorticity  $\times 10^{-3}$  sec $^{-1}$ )

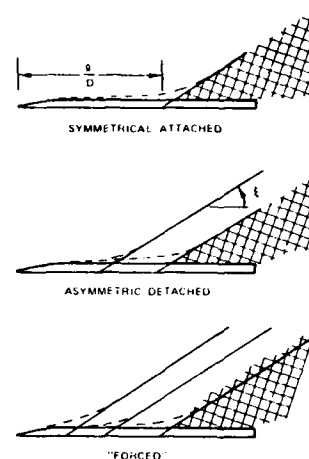


Figure 21. Vortex patterns observed by Clark. Crosshatched area shows diffuse vorticity and solid lines represent vortex paths.

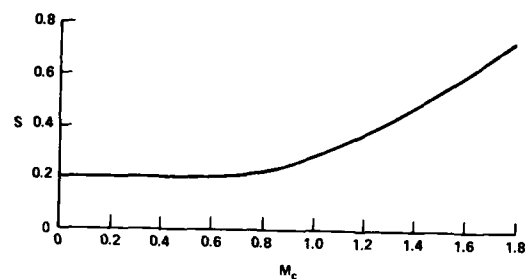


Figure 22. Strouhal number on an inclined body

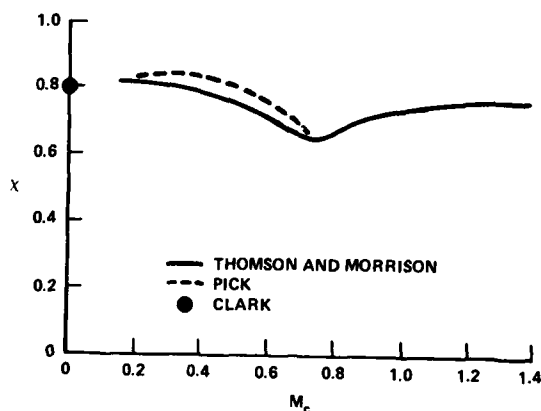


Figure 23. Mean values of  $\chi$

$$\Gamma = \frac{2l_s U_s}{\tanh(\pi h/l_s)} \quad (9)$$

Here  $l_s$  is the distance between vortices of like sign,  $h$  is the wake width, and  $U_s$  is the velocity of the vortices. These results are strictly applicable to an infinite, incompressible vortex street. Assuming shed vortices behind a body at incidence to be an infinite yawed vortex street leads to the following relations:

1.  $l_s = l \cos \xi$
2.  $h = 2g' \tan \xi$
3.  $U_s = U \sin(\alpha - \xi)$

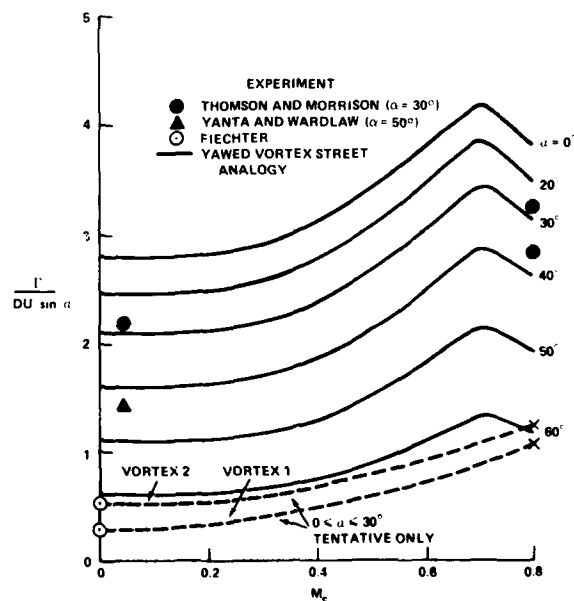


Figure 24. Vortex strength from experiment and yawed vortex street theory

Substituting the above and Eq. (8) into Eq. (9) and applying an experimentally determined value of  $h/l = .19$  yields the following relation for vortex strength:

$$\frac{\Gamma}{UD \sin \alpha} = 2 \left( \frac{\chi}{S} \right) (1 - \chi) \cos^2 (\xi) \coth \left( \frac{.60}{\cos \xi} \right) \quad (10)$$

The parameters,  $S$ ,  $\xi$ , and  $\chi$  are evaluated as functions of  $M_c$  using Figures 22 and 23. The results of Eq. (10) are plotted against  $\alpha$  and  $M_c$  in Figure 24. These values agree well with the experimentally measured vortex strengths over a wide range in crossflow Mach number.<sup>32</sup> Also indicated in this picture are the tentative strengths of the first two weaker vortices. The experimentally observed Strouhal numbers obtained using Eq. (8) agree closely with the incompressible value of  $S$  on circular cylinders in crossflow. Changes in vortex spacings do not occur until  $M_c$  becomes greater than .7.

Thomson and Morrison also provide experimental information for the points at which the extended vortex trails intersect the body centerline which is summarized in Figure 25. In addition, the orientations of the vortex paths can be found using the values of  $\chi$  given in Figure 23. Since  $\chi = \tan \xi / \tan \alpha$ :

$$\xi = \tan^{-1} \{ \chi \tan \alpha \}$$

Thomson and Morrison's results can be compared to information from several other sources. The break away points and values of  $\chi$  measured by Pick<sup>37</sup> and Clark<sup>10</sup> are shown in Figure 25 and are in relatively good agreement, however, only a qualitative correspondence exists between the measured break away points in all of these studies. Some of the difference may be due to a lack of uniformity in nose geometry. Also, the breakaway points measured by Clark represent the maximum number of such positions. As mentioned earlier, the number of shed vortices visible in this study varied. The wake measurements of Yanta and Wardlaw, shown in Figure 20 yield a mean shed vortex strength value which is in reasonable proximity to the results of Eq. (10) as shown in Figure 24.

The angle of attack at which the vortex pattern initially becomes asymmetric decreases with increasing body length and nose fineness. Experimental studies have suggested a number of different methods for determining the onset angle. In Figure 25 Thomson and Morrison provide a position for the start of asymmetry which is a function of the crossflow Mach number. The vertical scale on this graph indicates the point at which the extended vortex path intersects the body centerline. To obtain the axial location along the body where separation first starts, add .42 to the value read in Figure 25.<sup>6</sup> In contrast to this approach which is Mach number dependent, others are not. Also, other methods are usually derived from considering the onset of side force. Wardlaw and Morrison<sup>38</sup> found that the equation:

$$\alpha_o = \tan^{-1} \left( \frac{4}{\ell_t} \right) \quad (11)$$

was close to the mean value for a large data base. Chapman and Keener<sup>39</sup> have proposed the following relation for determining the onset of side forces on forebodies:

$$\alpha_o = 2.1 \theta_n \quad (12)$$

In a later study the above was extended to nose afterbody combinations.<sup>40</sup> Fiechter<sup>26</sup> also provides an expression for predicting the onset of asymmetry:

$$\alpha_o \sim 4.2 / \ell_t \text{ (rad)} \quad (13)$$

This relation was developed on long bodies ( $\ell_T > 10$ ) and hence it cannot really be expected to apply to forebodies alone. Lamont and Hunt<sup>35,44</sup> have suggested the following results which are based on pressure measurements:

$$\text{if: } 3+.05\alpha > 7-\ell_N \quad \alpha = \tan^{-1} \left( \frac{7-\ell_N}{2\ell_t} \right) \quad (14)$$

$$\text{otherwise: } \tan \alpha - \frac{.025\alpha}{\ell_t} = \frac{1.5}{\ell_t}$$

To facilitate comparison all of the above have been plotted in Figure 26.

In subsonic flow the vortex patterns become unsteady as the angle of attack is increased and the vortices are shed periodically from opposite sides of the body as is shown in Figure 1c. The incidence where this transition occurs depends on body length. Unsteadiness starts at the model base and progresses towards the nose with increasing angle of attack. On long bodies this transition occurs near an incidence of 60 degrees while on short forebodies a steady side load and hence steady asymmetric vortex patterns have been observed up to incidences of 80 degrees.<sup>39,40</sup> For supersonic flow the vortex pattern documented by Thomson and Morrison disappears before this incidence is reached and unsteady vortex patterns probably do not form. This conclusion is inferred from the observation that the flow field about a cylinder in supersonic flow is steady and devoid of vortex structures.



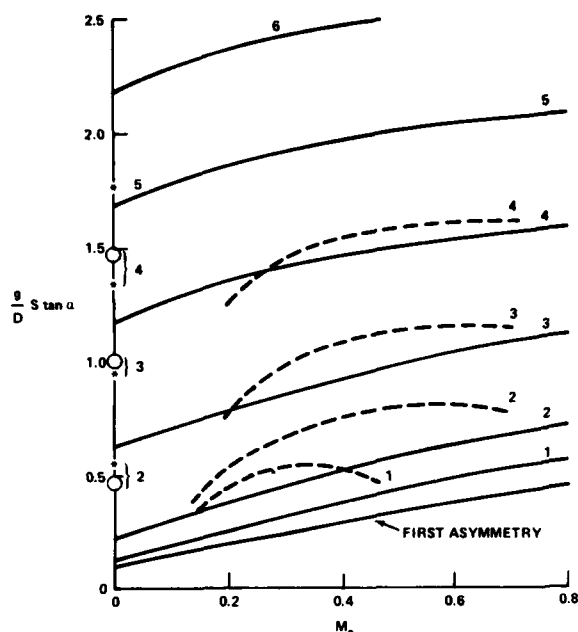


Figure 25. Mean measured intersection of extended vortex path and body centerline (see Figure 18 for definitions of  $g_1$  to  $g_4$ ).  
 — Thomson and Morrison<sup>32</sup> (cone cylinder);  
 --- Pick<sup>37</sup> (tangent ogive);  $\circ, *$  Clark<sup>10</sup>  
 sharp and blunt tangent ogive

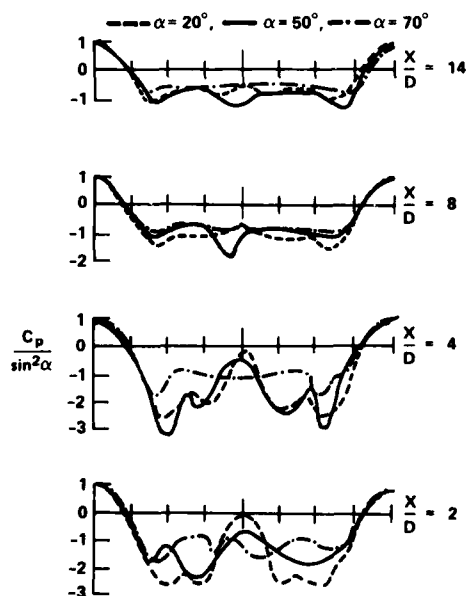


Figure 27. Circumferential pressure distribution on  $l_n = 3$  tangent ogive in low speed flow.  $Re_D = 1.1 (10^5)$

The normal force distribution of reference 26 is shown as a function of incidence in Figure 29 and features peak loads on the nose. Although this feature remains present throughout the angle of attack range, its relative magnitude is largest at low incidence which explains the aft motion of the center of pressure with increasing angle of attack.

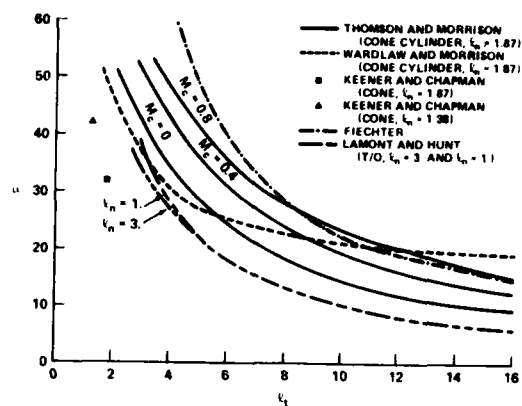


Figure 26. Predicted incidence at which a flow field becomes asymmetric

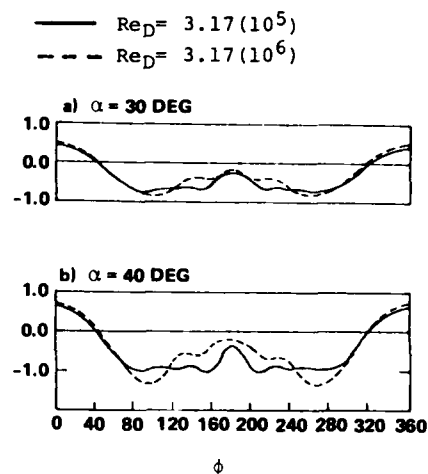


Figure 28. Influence of  $Re_D$  on the pressure distribution of a tangent ogive

#### 2.1.5 SURFACE PRESSURES AND FORCES ON BODIES AT HIGH INCIDENCE

The surface pressure distribution on a body in subsonic flow measured in reference 26 is shown at several incidences in Figure 27. The irregular pressure distribution on the lee side reflects the importance of the leeward vortex structures. Consistent with the onset of the asymmetric vortex structure discussed in the last section, the pressure distribution is clearly asymmetric at an incidence of 50 degrees. At an angle of attack of 70 degrees, circumferential pressures are again symmetric reflecting the existence of an unsteady flow field which produces a symmetric time averaged pressure distribution. The influence of Reynolds number on the circumferential pressure distribution is shown in Figure 28 using the data of reference 21. As might be expected from the analogy with a cylinder in cross-flow, the higher Reynolds number case which presumably corresponds to turbulent separation, reflects a higher leeside pressure and a narrower separation region.

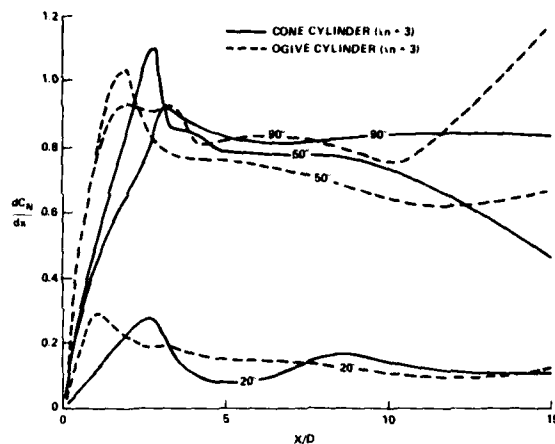


Figure 29. Force distribution on inclined cone and ogive cylinders ( $l_n = 3.0$ ) in incompressible flow.

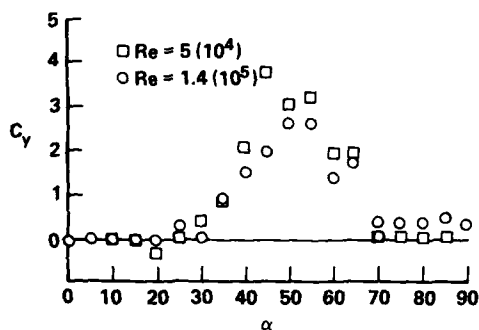


Figure 31. Side force coefficient variation with angle of attack for 2 Reynolds numbers on a tangent ogive ( $l_n = 3.$ ,  $l_t = 15$ ) in incompressible flow<sup>41</sup>

The typical normal force curve for a body in subsonic flow is shown in Figure 30. At very low incidences (i.e.  $\alpha < 5$ ) slender body theory accounts for the majority of the measured load. At higher angles of attack the flow separates reducing the leeside pressure and producing a large increase in normal force. Throughout most of the angle of attack range, the circumferential pressure distribution, normalized by crossflow dynamic pressure remains relatively constant producing a normal force curve which is functionally similar to a  $\sin^2 \alpha$  curve. The normal force curve in Figure 30 features a temporary decrease or stall at an incidence of 55 to 60 degrees. It has been postulated that this dip is due to unsteadiness during transition from an axial to crossflow dominated flow field structure.<sup>21,41</sup> As can be seen in Figure 30, Reynolds number has a large influence on the incidence at which the stall occurs. It has been suggested that peak side force values are accompanied by local increases in normal force such as that occurring immediately prior the stall<sup>22,42</sup> Qualitatively this observation is in agreement with the measured side force curves shown in Figure 31. However, as the Reynolds number is decreased from  $1.4(10^5)$  to  $5.0(10^4)$  the incidence at which the peak side force occurs moves from 55 to 50 degrees while the normal force stall point location changes from 55 to 60 degrees.

The surface pressure distribution on a body in supersonic flow is shown in Figure 32 at several different incidences. Unlike the subsonic case, the leeside pressure distribution is symmetric and shows the influence of leeward flow field vortices only at low incidences. As the incidence and hence crossflow Mach number increases the amplitude of the leeside pressure fluctuations decrease and at  $M_\infty \sim 1$  (i.e.  $\alpha = 30^\circ$ ), the pressure on the leeside of the body is nearly uniform. A typical normal force curve for a body in supersonic flow is shown in Figure 33. As in the subsonic case the general form of the normal force curve is a  $\sin^2 \alpha$  function. However, the stall point is not present in the supersonic case and there is no leveling off of the normal force coefficient for incidences in the vicinity of 90 degrees. The absence of the stall phenomena might be expected since this feature is essentially a product of the

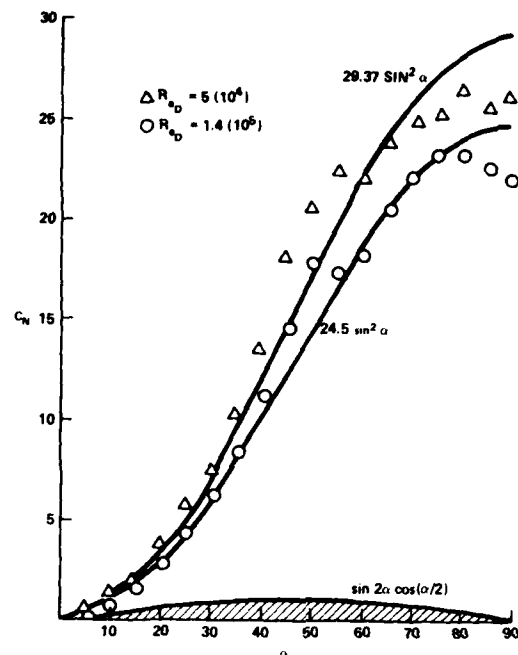


Figure 30. Normal force coefficient for an ogive cylinder ( $l_n = 3.$ ,  $l_t = 15$ ) in low speed flow.<sup>41</sup> Hatched area is slender body theory contribution

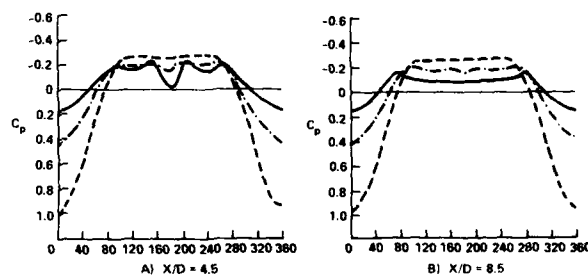


Figure 32. Pressure distribution about a tangent ogive ( $l_n = 3.5$ ) at Mach 2. Data from reference 31. —  $\alpha = 17^\circ$ , --  $\alpha = 30^\circ$ , ---  $\alpha = 50^\circ$ .

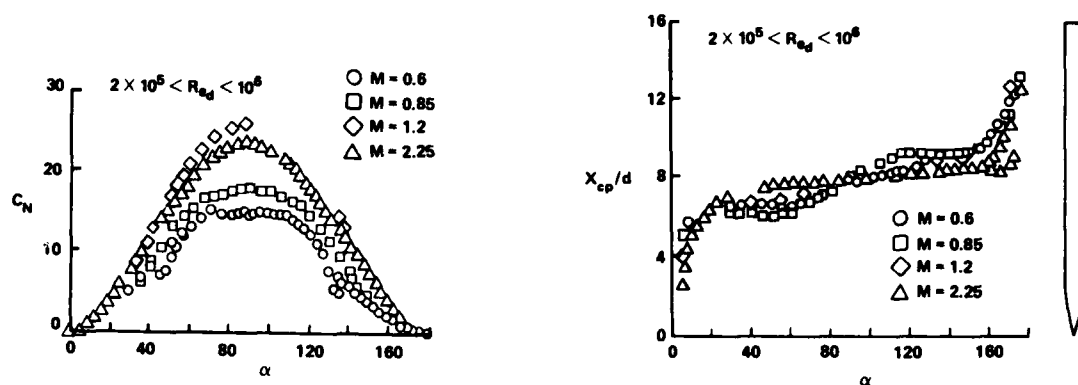


Figure 33. Influence of Mach number on normal force and center of pressure.<sup>43</sup>

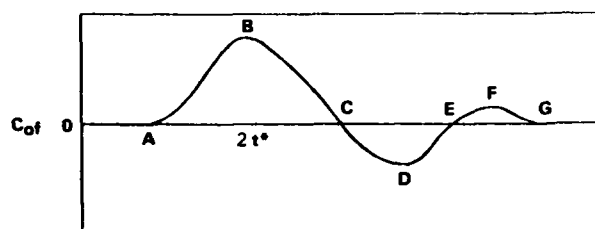


Figure 34. Local side force distributions on inclined bodies as a function of  $t^*$

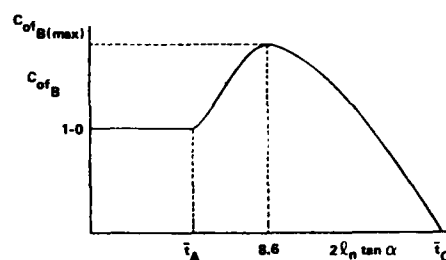


Figure 35. Amplitude of point B on the side force distribution curve. See Table 1 for definition of  $\ell_A$  and  $\ell_D$ .

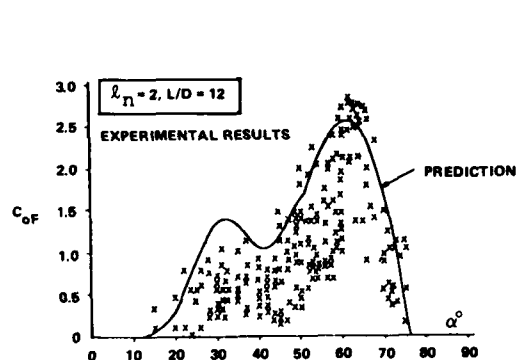


Figure 36. Comparison of Lamont and Hunt's prediction to a large body of experimental data on a single model<sup>44</sup>

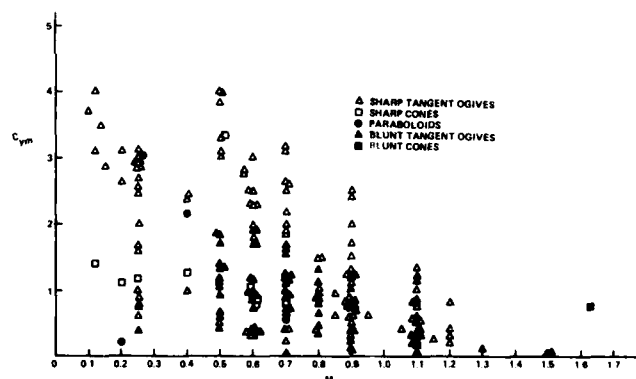


Figure 37. Peak side force coefficient as a function of Mach number

lee flow field. At high angles of attack in supersonic flow, the leeward pressure is so low that gross changes in its value have little effect on the overall vehicle aerodynamics. As is shown in Figure 33, the normal force coefficient increases with increasing Mach number in the subsonic-transonic regime, but decreases with increasing Mach number under supersonic conditions. Center of pressure location, also shown in this figure, is seen to be furthest aft in supersonic flow for  $\alpha \leq 90$ .

Lamont and Hunt<sup>35,44</sup> have measured the side force distribution on circular bodies with several different nose shapes in incompressible flow. The general form of the local side force coefficient normalized by the crossflow dynamic pressure is shown in Figure 34 and features a periodic distribution along the body which is in accord with the predictions of the impulsive flow analogy. However, the first peak is the largest and the remaining ones decrease in magnitude with distance from the nose. Only two of these peaks are significant which is at variance with the impulsive flow analogy that predicts a continuing series of equal amplitude peaks. The side force distribution is correlated with  $x \tan \alpha / D$ , however this parameter grouping does not completely remove the effects of nose shape and incidence. Expressions describing the motion of key positions on the side force distribution curve with changes in incidence and nose shape are listed in Table 1. The deduced unswitched amplitude of point B on the side force distribution curve is shown in Figure 35 and the entire curve is presumed to scale with this point. As previously explained, Lamont and Hunt have concluded that unsteady changes from a right to a left handed vortex pattern account for variation in the measured steady side force magnitude. These mirror image patterns produce side forces of the same magnitude

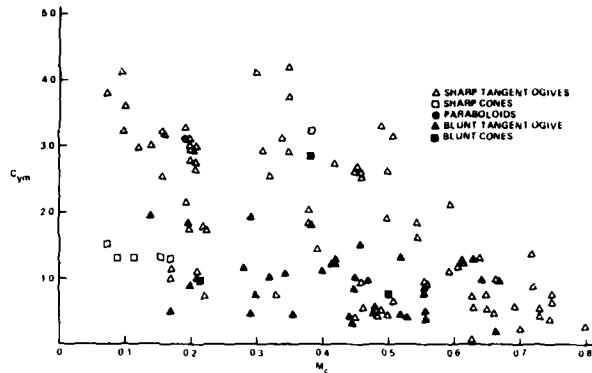


Figure 38. Peak side force coefficient as a function of crossflow Mach number

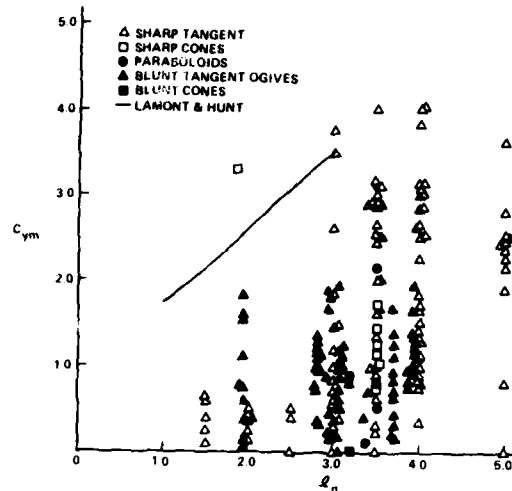


Figure 39. Peak side force coefficient as a function of nose fineness.  
— Predictions for a tangent ogive ( $l_t = 12$ ).

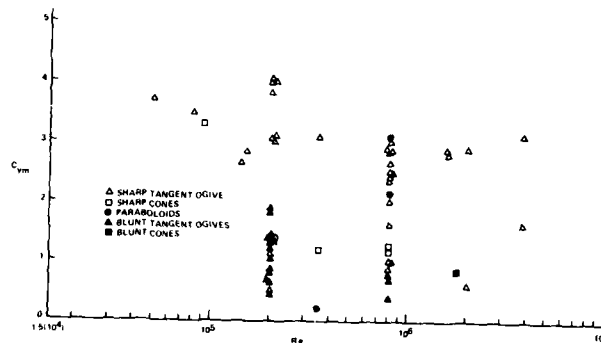


Figure 40. Reynolds number influence on side force for  $M_c < .42$

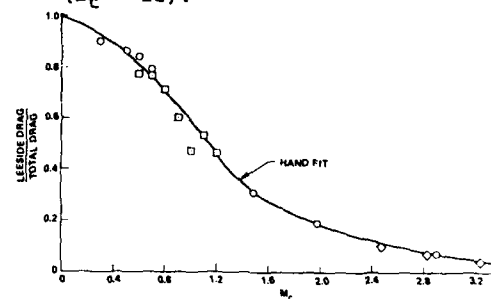


Figure 41. Ratio of leeward drag to total drag as calculated in reference 23

but opposite sign. The maximum possible side force magnitude occurs under test conditions where the vortex pattern stays locked in one configuration or is unswitched. As is illustrated in Figure 36, the total body side force produced by integrating the distribution curve with the unswitched magnitude bounds a large number of measurements made on a single body at varying roll angles.

The sensitive nature of side force makes a quantitative description difficult to obtain. Measured values have been observed to change with variations in the roll orientation of axisymmetric bodies. The data of references 37-41 and 43 suggest that the magnitude of these loads decreases with increasing Mach number, decreasing nose fineness and the introduction of bluntness. References 35 and 4 indicate that transition to turbulence decreases side force values while the addition of grit has been observed to increase these forces in some cases and decrease them in others. Wardlaw and Morrison<sup>38</sup> have developed a quantitative description of key side force characteristics such as maximum observed side force, angle of attack at which it occurs and the onset angle of incidence. A data base was assembled using information available in the open literature and private sources. Trends visible in the data base are illustrated in Figures 37 to 40. Figures 37 and 38 show the effect of  $M$  and  $M_c$  on  $C_{ym}$  while Figure 39 examines the influence of nose fineness. In all three cases, the greatest effect is found to exist at transonic Mach numbers where the crossflow Mach number is supercritical. The influence of Reynolds number at subcritical Mach numbers is explored in Figure 40. Results suggest a peak at transition with a decrease at the higher Reynolds numbers, but a strong trend is not evident.

In order to develop a quantitative description of the phenomena, a linear regression technique has been applied to the data base. Only those terms that are statistically significant are included in the final description of the phenomena. The following descriptive equations are developed:

## (a) Maximum observed side-force magnitude:

1. Sharp tangent ogives ( $r_b < .005$ )

$$C_{ym} = 4.20 - 12.50 h\left(\frac{M}{l_n}\right) - 1.06 f(R_{e_D}, M); \sigma_{C_{ym}} = .65 \quad (15)$$

where

$$h\left(\frac{M}{l_n}\right) = \begin{cases} .3 & \text{for } M/l_n \geq .3 \\ \frac{M}{l_n} & \text{for } \frac{M}{l_n} < .3 \end{cases} \quad f(R_{e_D}, M) = \begin{cases} 0 & \text{if } M > .57 \text{ or } Re_D < 6(10^5) \\ 1 & \text{if } M \leq .57 \text{ and } Re_D \geq 6(10^5) \end{cases}$$

2. Blunt tangent ogives ( $r_b > .005$ )

$$C_{ym} = 1.17 - .543 f(R_{e_D}, M) - 3.91 h^1\left(\frac{M}{l_n}\right); \sigma_{C_{ym}} = .38 \quad (16)$$

$$h^1\left(\frac{M}{l_n}\right) = \begin{cases} 0 & \text{if } M \leq .57 \\ \frac{M - .57}{l_n} & \text{if } M > .57 \end{cases}$$

## (b) Angle of attack at which the maximum side force occurs:

$$\alpha_m = 39.8 - 10.3 M + \frac{91.6}{l_T}; \quad \sigma_{\alpha_m} = 6.75 \quad (17)$$

## (c) Angle of side force onset:

$$\alpha_o = 18.72 + 425.7/\bar{l}_T^2; \quad \sigma_{\alpha_o} = 4.95 \quad (18)$$

The side force values obtained by integrating Lamont and Hunt's yaw force distribution curve are compared to the collected data plotted as a function of  $l_n$  in Figure 39. It can be seen that the predicted level of side force bounds the experimental measurements. This validates the general level of side force determined by Lamont and Hunt in Figure 35 but it does not necessarily affirm the rationale (i.e. presumed influence of flow unsteadiness) used in arriving at this level.

As can be determined by examining Figures 37 and 38, side force starts to decrease at a crossflow Mach number of .4 or a freestream Mach number of .6 and is not present in supersonic flow. There are three different mechanisms which can be expected to lead to the reduction of side force with increasing Mach number.

1. In supersonic flow the leeside pressures become a very small fraction of the stagnation value. Pressure changes induced by the flow field vortices will have little effect on body loads. This is illustrated in Figure 41, showing the ratio of leeside pressure drag to total drag for a circular cylinder as a function of Mach number.

2. At crossflow Mach numbers much greater than .7, the asymmetric vortex structure develops only in the far wake and hence can be expected to have little influence on surface pressures.

3. As the crossflow Mach number becomes greater than the critical value (.42 for a circular cylinder) portions of the flow near the cylinder shoulder become supersonic in the crossflow plane. Thus the influence of leeward asymmetric vortex structures is not sensed on surfaces near the cylinder shoulder.

The last mechanism is the only one which produces a demise of the side force consistent with the data of Figures 37 and 38. The other two possibilities lead to a reduction in side force at Mach numbers which are too high. Mechanism one should produce measurable forces values at crossflow Mach numbers as high as 1.5 or 2. Mechanism two suggests that side forces will start to decline at crossflow Mach numbers greater than .7.

Induced loads are very sensitive to test conditions and difficult to predict. These considerations have motivated an investigation into methods for suppressing or eliminating them. The following schemes have been tried for side forces and moments:

1. Vortex generators.<sup>45</sup> These consist of a large number of very small, low aspect ratio fins attached to the missile nose.

2. Use of grit.<sup>37,39,45</sup> Grit has been applied in a number of different ways, at the nose and along the body.

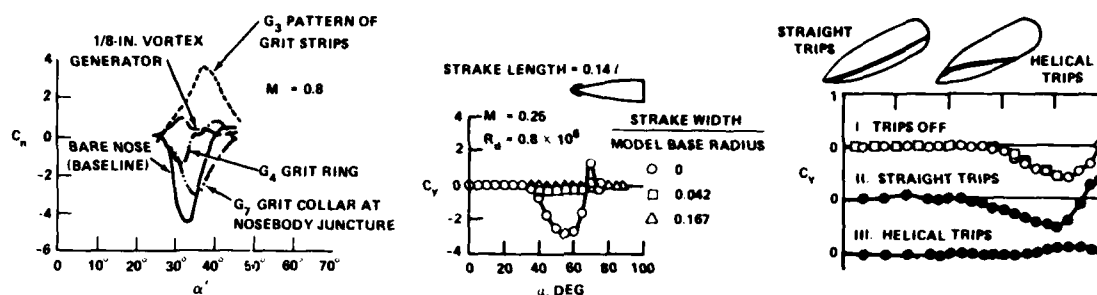


Figure 42. Yaw force and moment reduction using strakes, grit and boundary layer trips from references 45, 39 and 46 respectively

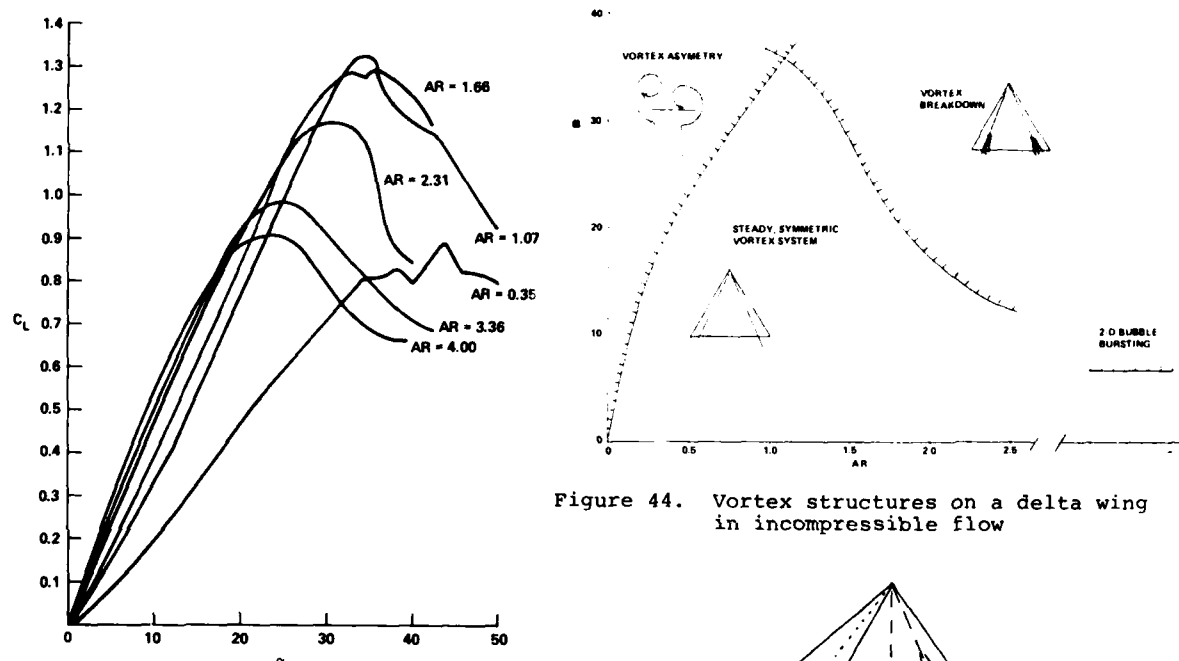


Figure 43. Lift curves for delta wings of various aspect ratio

3. Nose strakes and booms.<sup>39</sup>
4. A small degree of nose blunting.<sup>37,39</sup>
5. Separation trips<sup>46</sup>

Induced loads have been reported to be reduced substantially through the application of the above methods as is illustrated in Figure 42. Devices for suppressing side force and moment disrupt the flow in the nose region and prevent shed vorticity from rolling up into concentrated, well defined vortices. Addition of grit to a model has been observed to increase side forces in some cases and decrease it in others. Nose bluntness reduces the size of side forces and some studies have concluded that the maximum effect is obtained with only a small amount of nose bluntness. Helical boundary layer separation trips have apparently been very successful in suppressing side forces on a number of different bodies.

## 2.2 EXPERIMENTAL DESCRIPTION OF FLOW ABOUT LOW ASPECT RATIO WINGS

At incidences greater than a few degrees, the flow about a low aspect ratio wing separates. The resulting leeward flow field is dependent on the geometry of the wing; its planform area and leading edge radius. The present discussion is confined to sharp, low aspect ratio delta wings for which the most information is available. Brief mention will be made of the flow about low aspect ratio rectangular wings. Additional review articles on slender wings can be found in references 47, 48 and 49.

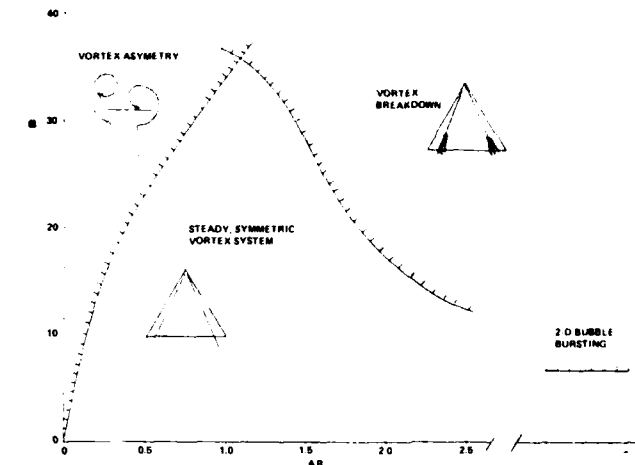


Figure 44. Vortex structures on a delta wing in incompressible flow

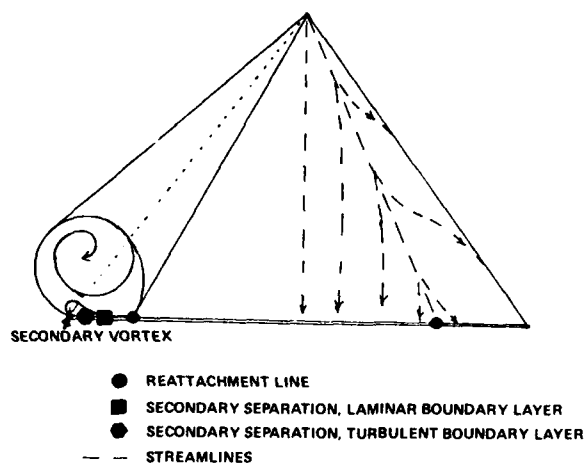


Figure 45. Leeward vortex structure on a delta wing

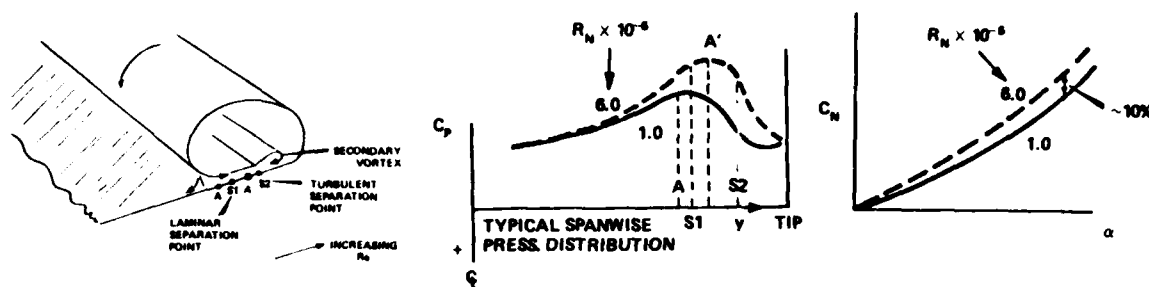


Figure 46. Reynolds number influence on slender delta wing.  
Reported in reference 49 using the results of reference 52.

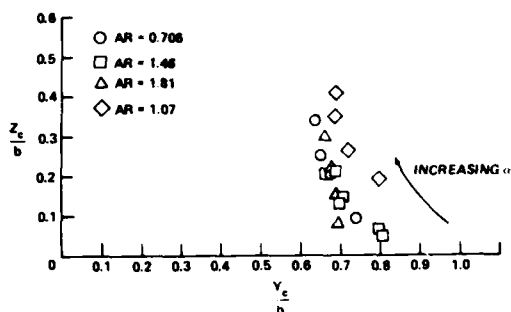


Figure 47. Crossflow plane position of wing vortices on delta wings in incompressible flow

In subsonic flow, the leeward flow field structure on a delta wing can be divided into two regimes. At low incidence the separated flow rolls up to form well defined, steady vortices while at high angles of attack an incoherent, unsteady flow field is present. The incidence-lift curves of reference 50 which are shown in Figure 43 clearly reflect these two regimes. At low incidences the leeward flow field vortices produce a large lift while at high angles of attack the unorganized flow field structure leads to a reduction in this quantity.

The actual demise of the organized vortex structure occurs as a consequence of vortex bursting or breakdown. This process which is promoted by a positive pressure gradient in the streamwise direction causes the vortex to lose its organized structure, with its kinetic energy being converted into higher pressure. With increasing angles of attack the point of vortex bursting moves from the far flow field toward the wing and finally crosses its trailing edge. Figure 44, which was taken from Reference 51, illustrates for incompressible flow the angles of attack at which vortex breakdown first occurs at, or forward of the trailing edge. Clearly, this incidence decreases with increasing aspect ratio. Figure 44 also indicates that for  $AR < 1$ , asymmetric vortices form at sufficiently high incidences.

The low incidence flow field which features well defined vortices is shown in Figure 45. Fluid impacts on the lower surface of the wing and flows out on it leaving the surface at the edge and rolling up to form a vortex on the upper side of it. This vortex generates a large suction increasing the wing lift. The streamline that passes over the top of the vortex, reattaches on the upper surface of the wing and divides. Part of the fluid moves toward the trailing edge while the remainder travels back to the leading edge. This latter fluid stream reseparates before reaching the leading edge due to the adverse pressure gradient imposed by the vortex. The flow rolls up to form a secondary vortex structure with opposite circulation as shown in Figure 45. The location of the secondary separation point is dependent on the state of the adjacent boundary layer. With increasing Reynolds number this boundary layer becomes turbulent and the point of separation moves toward the leading edge increasing the wing lift still further. An example of the variation in the wing surface pressure distribution and normal force with changes in Reynolds number is shown in Figure 46.

Experimental data on vortex position from several different studies have been correlated by Parker<sup>47</sup> and are shown in Figure 47. Despite the fact that different aspect ratio wings are represented, the data is fairly tightly grouped.

The portion of the total wing lift contributed by vortex suction increases with decreasing aspect ratio. This is illustrated in Figure 48 where the ratio of vortex

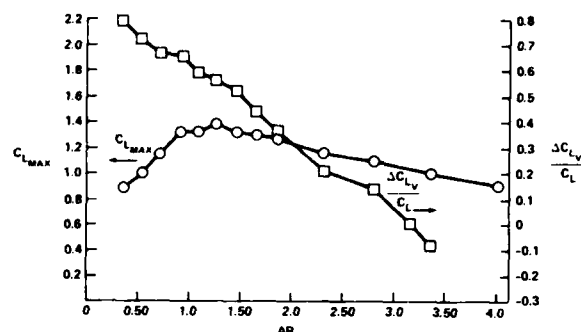


Figure 48. Variation in peak lift characteristics of delta wings in incompressible flow as a function of aspect ratio

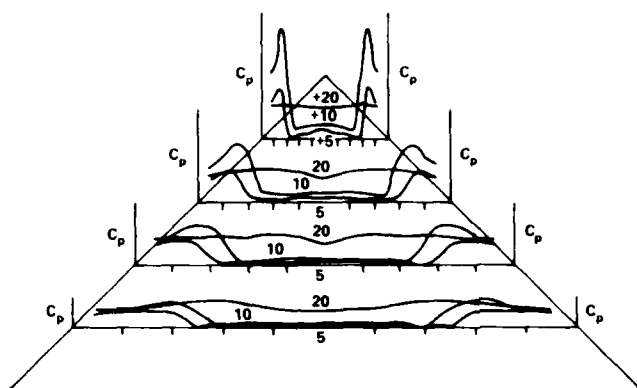


Figure 49. Pressure distribution on an  $AR = 4$  wing in low speed flow

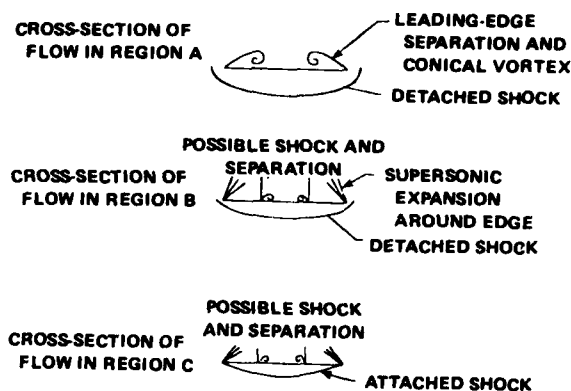
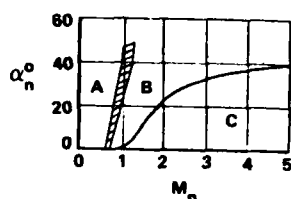


Figure 51. Influence of compressibility on the delta wing flow field

lift to total wing lift is plotted as a function of aspect ratio. The vortex contribution to the wing lift is estimated by subtracting the calculated potential lift (i.e. first term of Eq. 43) from the total lift measured by Wentz and Kolhman<sup>50</sup>. Clearly, for wings with aspect ratios greater than 3 or 4, the vortex induced lift is not important. The pressure distributions on an aspect ratio 4 wing, measured in reference 53 and shown in Figure 49, provides an explanation for this. As a consequence of near wing vortex breakdown on larger aspect ratio wings at low incidence, strong suction develops only near the apex.

The influence of aspect ratio on lift is shown in Figure 43. Stall occurs at an incidence that decreases with increasing aspect ratio. The chord-wise position of vortex breakdown at stall is documented in Figure 50 using the data of reference 50 and can be seen to move forward with increasing aspect ratio. On small aspect ratio wings, stall marks the incidence at which vortex bursting crosses the trailing edge. For larger aspect ratio wings the position of vortex breakdown is near the wing apex. As is shown in Figure 48 the peak lift increases with decreasing aspect ratio until  $AR \sim 1$ . For wings with lower aspect ratios there is a marked decrease in the peak lift. This has been attributed to the formation of an asymmetric leeside vortex pattern which is consistent with the bounds for this regime shown in Figure 44.

Squire<sup>54</sup> has outlined the changes in leeward flow field structure that occur in transonic and supersonic flow. As the Mach number normal to the leading edge approaches unity, the flow about the leading edges is increasingly turned by a Prandtl-Meyer

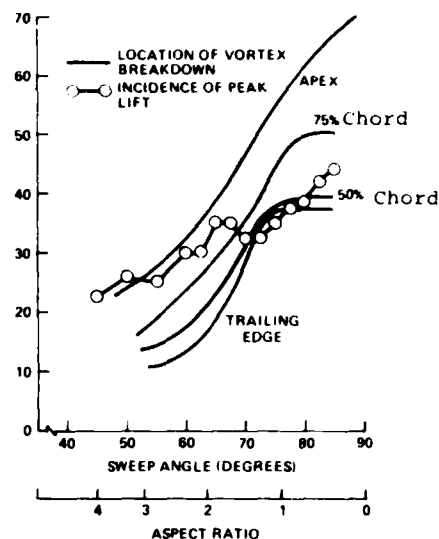


Figure 50. Vortex breakdown position and incidence of maximum lift

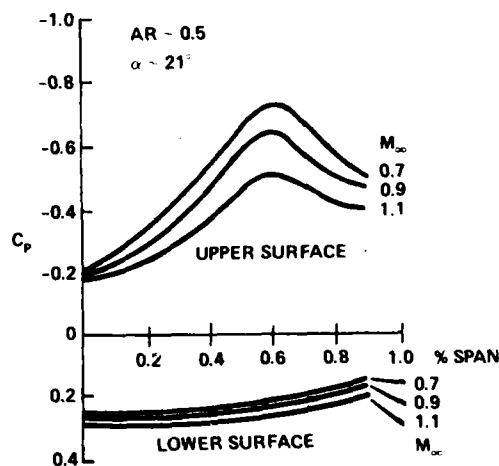
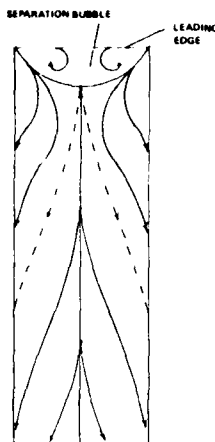


Figure 52. Influence of compressibility on delta wing surface pressure. Reported in reference 49 using the results of reference 52



Figure 53. Streamlines on the surface of a rectangular wing. Streamlines down stream of dotted lines cross trailing edge.



expansion which results in a weaker vortex that lies closer to the wing surface. At a sufficiently high Mach number the flow is able to expand completely about the leading edge and the tip vortex disappears. Under these conditions it is possible for a shock induced separation to occur near the middle of the wing. This type of separation moves outboard with increasing incidence and becomes indistinguishable from a leading edge separation which moves inboard. Further increases in Mach number lead to a windward shock which is attached to the leading edges. The bounds given by Squire for each of these flow field structures are shown in Figure 51 as a function of the leading edge incidence and normal Mach number:

$$M_n = M_\infty \sqrt{1 - \cos^2 \alpha \cos^2 \Lambda}$$

$$\alpha_n = \tan^{-1} \{ \tan \alpha / \cos \Lambda \}$$

The surface pressure distributions on a delta wing given in Figure 52 indicate that the vortex suction peak decreases with increasing Mach number as would be expected from the above discussion. However, compressibility effects increase the windward pressures compensating for at least part of the loss in leeside lift. Clearly, with increasing Mach number, the wing lift loses its dependency on vortex structure. The actual variation of lift magnitude with Mach number is dependent on aspect ratio. Very low aspect ratio wings which depend on vortex suction for a significant portion of their lift may experience a lift reduction at transonic and supersonic speeds. For larger aspect ratio wings compressibility effects will dominate and such lift losses will not occur.

On low aspect ratio wings with different planform shapes separation will occur on leading and sides edges. As long as the separated flow reattaches aft or inboard of the separation line a suction will be formed which will increase the wing lift. The similarity between the separation regions on delta and other planform shapes does not necessarily extend to the fine structure of the separation regions. For example, the surface streamlines measured by Wickens<sup>55</sup> for a very low aspect ratio rectangular wing, shown in Figure 53, do not indicate a region of secondary separation on either the leading or side edges. Regardless of fin planform, the peak lift coefficient will be obtained at a small but finite aspect ratio. In the limit as the aspect ratio goes to zero the wing will have insufficient surface area to allow flow separating at the side edge to reattach which will eliminate the vortex suction lift. It may also be expected that the peak lift will occur at an aspect ratio where the vortex pattern on the lee side of the wing becomes asymmetric. To illustrate the qualitative similarities between the rectangular and delta planform, the normal force curves for several rectangular wings provided in referenced 56 are shown in Figure 54.

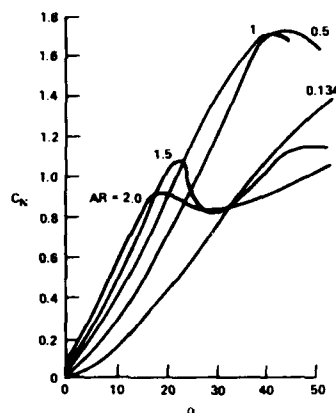


Figure 54. Normal force curve for rectangular wings

## 2.4 EXPERIMENTAL DESCRIPTION OF THE COMPLETE MISSILE CONFIGURATION

The vortex structures associated with the complete missile configuration can be constructed by superimposing those of the isolated components. For a wing-body-tail configuration this results in the type of flow field shown in Figure 55. Vortices shed from the forward lifting surfaces interact with body vortices and flow back over the tail inducing significant loads on this component. The quantitative description of the flow field structure is strongly influenced by the interaction between the various missile components. With increasing incidence the steady, well defined vortex structures disappear. In subsonic flow an organized flow field structure exists to a higher incidence on bodies alone ( $\alpha \sim 60^\circ$  to  $80^\circ$ ) than on wings alone ( $\alpha \sim 20^\circ$  to  $40^\circ$ ). Hence the disappearance of vortex structures can normally be thought of as starting on the fins with the onset of vortex bursting. However, the effective angle of attack of a fin which is part of a complete configuration is dependent on the configurations roll orientation and this may not always be the case. Also, the interaction between body and wing vortices can result in the suppression of wing vortex bursting to a higher incidence.<sup>57</sup>

Little systematic information is available describing quantitatively the interaction between body and wing vortices. One of the few available studies is that of reference 29 which measured vortex paths and strengths on circular bodies with and

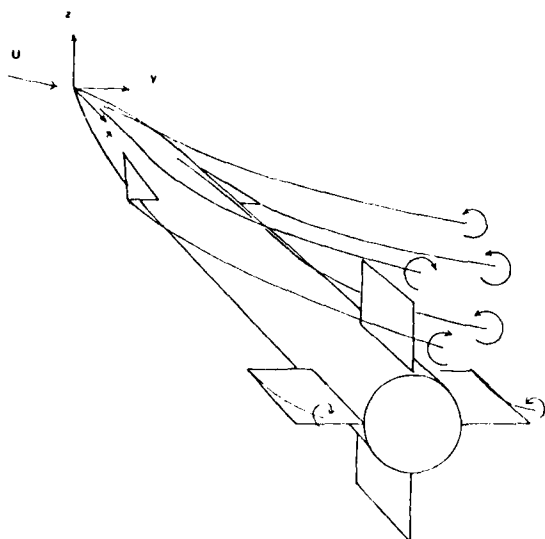


Figure 55. Vortex shedding on a complete missile configuration at high angles of attack

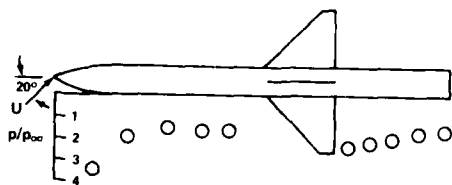


Figure 57. Windward symmetry plane body surface pressures on a cruciform missile  $\alpha = 20^\circ$ ,  $\phi = 0^\circ$ ,  $Re_D = 1.9 (10^5)$

without wings in subsonic flow. The position and strength of body vortices are not affected by the wings forward of the body wing junction. Aft of this point, body vortex strengths are reduced and paths are perturbed for both delta and rectangular wing planforms. In supersonic flow body vortices disappear at crossflow Mach numbers greatly in excess of unity and the leeward flow field structure is dominated by lifting surface vortices.

Inviscid or shock interactions become important in supersonic flow as shown in Figures 56 and 57. The actual effect of shock interaction is dependent on the specific configuration being tested and freestream Mach number. Data taken in reference 16 illustrates the types of phenomena present. At incidences in the neighborhood of 20 degrees, attached fin shocks intersect the body and adjacent fins while the bow shock interacts with the windward fin. This produces large gradients in the surface pressure as shown in Figure 56. The rapid rise in symmetry plane pressure down stream of the fins in Figure 57 is due to shocks from the horizontal fins. At angles of attack near 50 degrees fin shocks become detached and interact with the bow shock. At a roll orientation of 45 degrees (X configuration) the flow between the windward fins is reminiscent of that in a choked duct. A normal shock forms upstream of the fin leading edge producing high pressure and subsonic flow between the fins. The shock structure and surface pressures for this case are illustrated in Figure 58.

As a body-tail configuration, at incidence  $\alpha$ , is rolled, a fin which moves from the windward ( $\phi = 0^\circ$ ) to the leeward ( $\phi = 180^\circ$ ) plane experiences a change in normal force coefficient ( $C_{N_T}$ ) shown in Figure 59a with the data of reference 23. In the absence of body influence and vortex interactions, the wing angle of attack changes from 0 at  $\phi = 0^\circ$  to  $\alpha$  at  $\phi = 90^\circ$  to 0 at  $\phi = 180^\circ$  while the yaw angle varies from  $\alpha$  to  $0^\circ$  to  $-\alpha$  respectively. The accompanying fin normal force at Mach 3 peaks at  $\phi = 70$  degrees and then becomes negative at  $\phi = 140 \sim 160$  degrees. The location of peak normal force

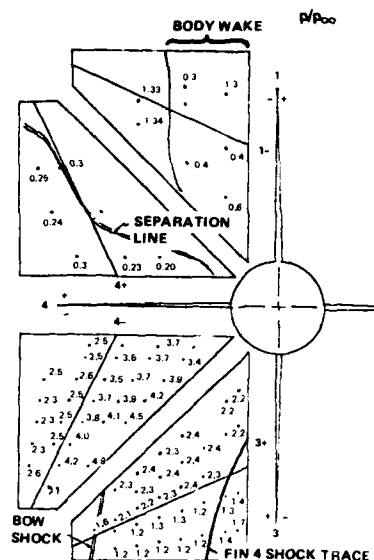


Figure 56. Fin surface pressures on a cruciform missile configuration,  $\alpha = 20^\circ$ ,  $\phi = 0^\circ$ ,  $Re_D = 1.9 (10^5)$

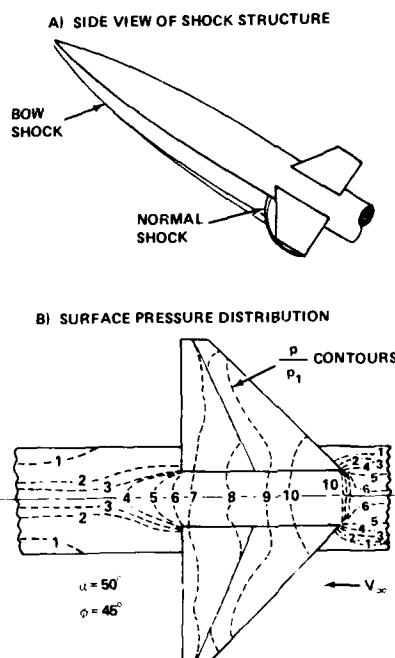


Figure 58. Surface pressure<sup>48</sup> and shock structure<sup>16</sup> on a finned missile at  $\alpha = 50^\circ$

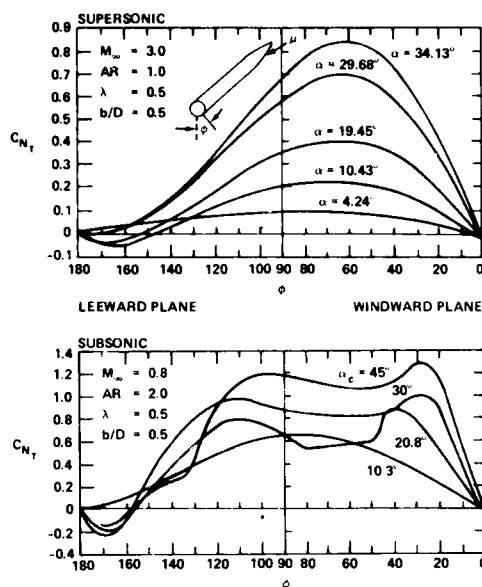


Figure 59a. Fin normal force as a function of body roll orientation<sup>23</sup>

is a result of the interaction between the yaw and pitch angle changes. Increases in both of these angles tend to increase the fin normal force. The negative normal force near the leeward plane of symmetry is attributable to vortex interaction since the wing never achieves a negative angle of attack. At a Mach number of .8 the variation of the fin normal force features a severe stall at roll orientations between 25 and 50 degrees which is greater than that measured in fin alone tests.<sup>23</sup> The degree of stall is highly dependent on fin planform geometry and abates quickly with increasing Mach number. The influence of asymmetric body vortices on fin normal force can be seen in Figure 59b to occur for  $\phi > 90$ . Here the value of  $C_{N_T}$  for fins positioned symmetrically about the pitch plane is seen to differ.

As a missile fin is rolled past the orientation,  $\phi = \phi_c$ , where the fin normal force is zero the chord and span-wise moments remain finite which moves the center of pressure off the fin to infinity. The actual behavior of the fin normal force, hinge moment and chord-wise center of pressure is shown in Figure 60 using the data from reference 58. Measurements of the fin center of pressure in the vicinity of  $\phi = \phi_c$  have been found very difficult to repeat accurately. This is not surprising since fin loads near this orientation are dominated by body vortex interference effects. As was discussed in Section 2.1, the positions and strengths of body vortices are very sensitive to small changes in the experimental procedure. Measurements of center of pressure from repeat tests are shown in Figure 61. Notice that even data from the same tests do not show pitch plane symmetry which indicates the presence of asymmetric body vortices.

Yaw forces, yaw moments and roll moments can arise on the complete missile configuration at all angles of attack due to such factors as lack of pitch plane symmetry or a yaw angle. At high angles of attack asymmetric vortices can also produce these loads on symmetric missile configurations at zero yaw angle. With increasing Mach number the pressures in the leeward flow field are reduced relative to the stagnation pressure and vortex structures lose their influence on loads causing induced forces to disappear.

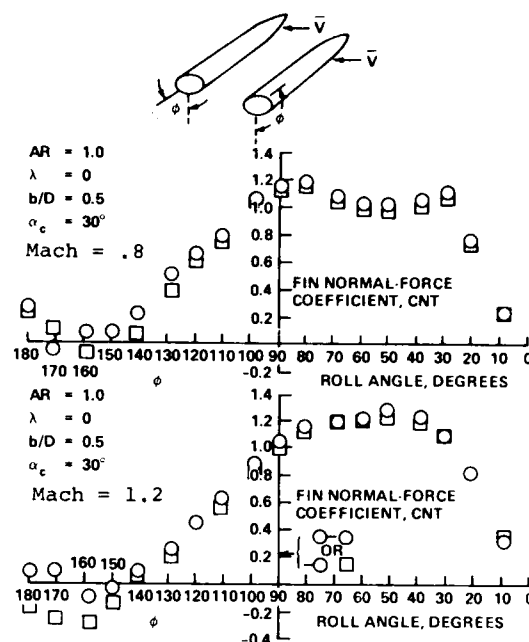


Figure 59b. Fin normal force asymmetries induced by asymmetric body vortices<sup>23</sup>

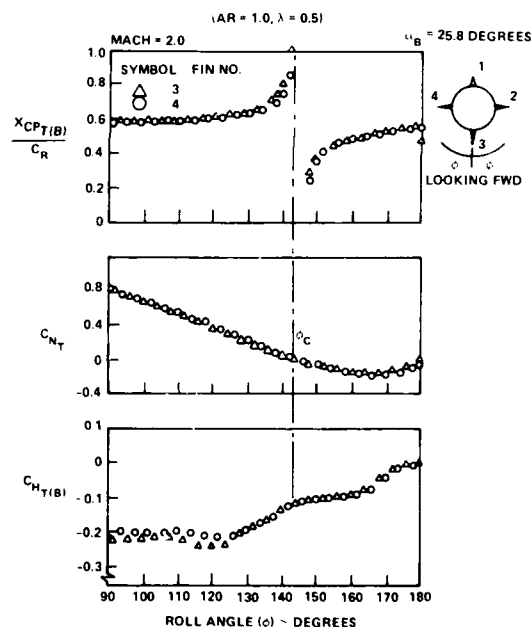


Figure 60. Fin normal force, chord-wise center of pressure, and hinge moment in leeward flow field<sup>58</sup>

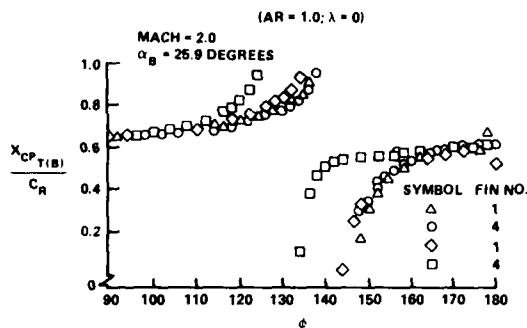


Figure 61. Near the roll orientation where  $C_N = 0$ , center of pressure measurements are difficult to duplicate<sup>58</sup> (See Figure 60 for definition of symbols)

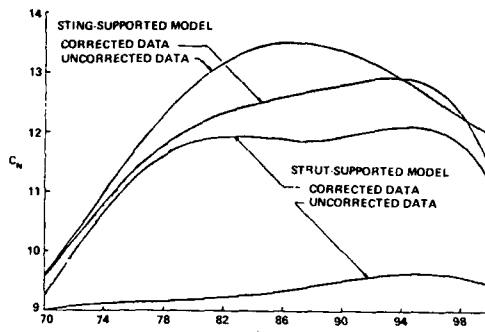


Figure 63. Influence of model support on normal force at Mach .6

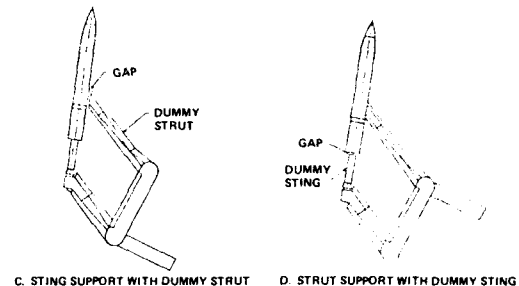
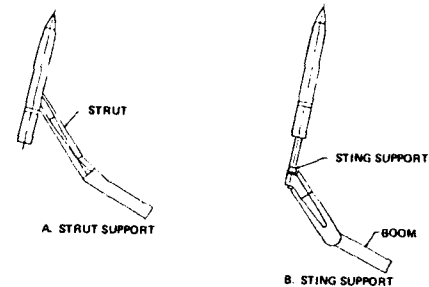


Figure 62. Model support systems tested in reference 61

## 2.5 EXPERIMENTAL PROBLEMS AND UNCERTAINTIES AT HIGH INCIDENCES

It has been common practice to apply the same testing procedure used in low incidence testing to high angle of attack experiments. However, little effort has been expended to check on the validity of such procedures and data taken in the Mach number range where viscous effects strongly influence aerodynamic loads must be regarded with scrutiny. For body alone tests, questionable measurements occur in the subsonic-transonic range while on fin alone results uncertainties exist from the subsonic to the supersonic regime. Two separate categories of problems affect the validity of the experimental results. The first is model support interference while the second is the instability of the viscous flow field.

In references 60 and 61, model support interference on bodies of revolution has been examined in the incidence range of 60 to 90 degrees. The four tested model support systems are shown in Figure 62 and consist of a sting support, a strut mount, a sting support with a dummy strut mount and a strut support with a dummy sting mount. The results of the testing are provided in Figures 63 and 64 which show measured  $C_N$  values with the sting and strut mounts and the corrected value inferred from the dummy combination support systems at Mach .6 and .9 respectively. The sting support appears to increase the normal force 5% to 10% by increasing the effective body length while the strut mount acts as a splitter plate in the crossflow plane decreasing the crossflow drag and hence the normal force by 30% to 40%. Figure 64 indicates that the largest interference occurs at the lowest Mach number which is to be expected since the viscous influence on the load is greatest under these conditions.

Force measurements on fin configurations have also been found to be influenced by the type of support system used. A comparison carried out in reference 23 between data obtained using reflection plate and sting supported models suggests that the reflection plate tests feature a premature stall as shown in Figure 65 which is attributable to a fin plate boundary layer shock interaction. The severity of this effect increases with decreasing aspect and taper ratio. The majority of high incidence data for fins has been taken using reflection plate mounting methods and relatively little sting support information is available for comparison. Hence the above conclusion has been drawn using a very limited amount of data. In supersonic flow the reflection plate support technique also induces flow separation forward of the fin at incidences greater than 60 to 70 degrees.<sup>62</sup> In effect the fin appears as a forward facing step to the oncoming flow.<sup>58</sup> This decreases the normal force coefficient as shown in Figure 66 with data from reference 62 and moves the lateral center of pressure outboard.

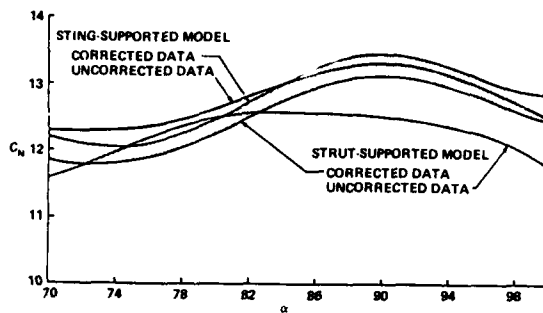


Figure 64. Influence of model support on normal force at Mach .9

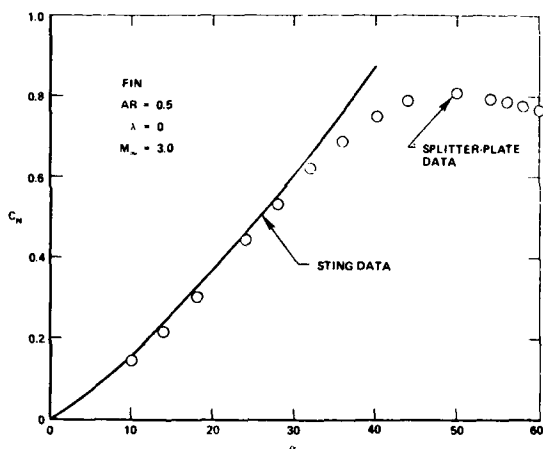


Figure 65. Fin alone support interference for reflection plate and sting mounts

The second category of experimental problems occurring at high angles of attack is that of viscous instability which results in significant variations of experimental data, particularly induced loads, for the same nominal test conditions and model. Such problems are most severe on sharp nosed bodies as shown in Figure 67 using Atraghji's<sup>63</sup> data. The change in normal and side force is probably due to either a steady or unsteady variation in the leeward flow field structure accompanying changes in the model orientation. The relative importance of these two mechanisms is at present unclear and it is difficult to prescribe a set of experimental rules which will lead to repeatable results. However, there are several guidelines which it is wise to follow, particularly when measuring induced loads. Tests should be carried out in a low turbulence tunnel, ideally with a free stream turbulence level of less than .1%.<sup>44</sup> A rigid support system should be used to minimize model vibration. When force tests are being conducted balance flexibility make this requirement difficult to meet. Light models in conjunction with stiff balances should be used to minimize this problem. Transient as well as steady state measurements should be taken and when induced loads are of interest axisymmetric models should be tested at several different roll orientations.

In the case of fins, viscous instabilities are not as severe a problem, probably because the separation points are fixed at the leading edge tip and asymmetric vortex patterns are not encountered as often. Here a lack of reproducibility from facility to facility has been noted in Reference 15 with regard to incidences at which vortex bursting occurs in subsonic flow as shown in Figure 68.

### 3. PREDICTIVE METHODS

The complete problem of high-angle-of-attack prediction involves determining the character of the leeward flow field; regions of separation, structure of the flow, and its steadiness or unsteadiness. The problem as defined in this manner cannot be addressed directly by the current state of the art. However, a large number of techniques have been developed for predicting the loads on bodies at high angles of attack under restricted conditions and for specific geometries.

The following sections provide a review of some of the existing predictive methods. The discussion is divided into three parts: body alone, wing alone, and complete missile configurations. Each of these sections is further divided into a review of empirical, semi-empirical and theoretical techniques. Empirical approaches are those based primarily on experimental observations while semi-empirical ones combine experimental observation with computations. Theoretical procedures use no experimental information.

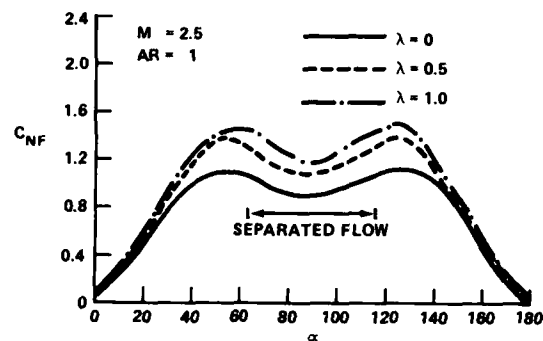


Figure 66. Supersonic reflection plate fin normal force data featuring separation near an incidence of 90°

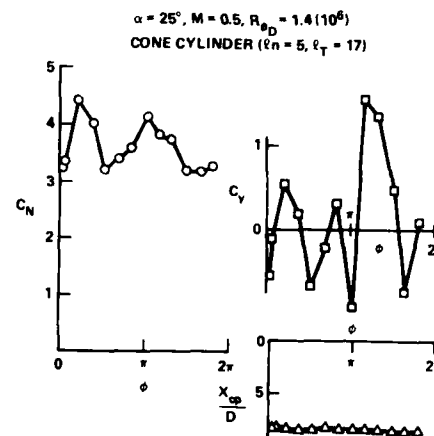


Figure 67. Variation of aerodynamic coefficients with roll on a cone-cylinder

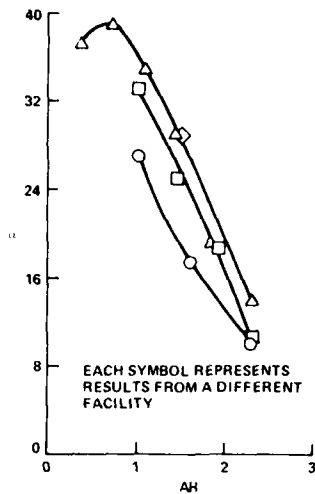


Figure 68. Angle of attack at which vortex bursting occurs at the trailing edge of a delta wing

### 3.1 Body Alone Methods

Empirical methods have been developed to provide estimates over the entire range of angle of attack from 0 to 90 degrees. Semi-empirical techniques are applicable to regimes where steady, well-defined vortices exist ( $\alpha < 50 \sim 60$  degrees). Currently there are few examples of theoretical methods.

#### 3.1.1 Empirical Methods for Body-Alone Configurations

Body-alone methods are generally based on the analogy between flow about a two-dimensional cylinder and that about an inclined body as discussed in Section 2.1.1. The total force is assumed to be the sum of the viscous force and the potential contribution determined from slender body theory. The simplest approach uses the crossflow analogy to evaluate the viscous term. The crossflow drag coefficient is assumed to be equal to the steady state cylinder drag, shown in Figure 3a, which is a function of crossflow Mach number ( $M \sin \alpha$ ) and crossflow Reynolds number ( $Re_D \sin \alpha$ ). This leads to:

$$C_N = \underbrace{\frac{\sin(2\alpha) \cos(\alpha/2) \pi D^2}{4A_{ref}}}_{\text{potential term}} + \underbrace{n C_{dc} \frac{A_p}{A_{ref}} \sin^2 \alpha}_{\text{viscous term}} \quad (19)$$

and the moment taken about  $x_m$  is:

$$C_M = \sin(2\alpha) \cos(\alpha/2) \left[ \underbrace{\frac{\bar{V} \pi D^2 (L_t - x_m)/4}{DA_{ref}}}_{\text{potential term}} \right] + \underbrace{n C_{dc} \frac{A_p (x_m - x_c)}{A_{ref} D}}_{\text{viscous term}} \sin^2 \alpha \quad (20)$$

In both of these equations the factor  $\eta$  is included to account for finite body length. In practice it has been found that  $\eta$  should be set to unit in supersonic flow and evaluated from Goldstein's<sup>64</sup> data, shown in Figure 69, for subsonic conditions.<sup>1</sup> In reference 65 the above equations have been extended to bodies with noncircular cross-section.

The crossflow analogy was originally suggested by Allen<sup>66</sup>, but the actual form of Eqs. (19) and (20) is from Jorgensen.<sup>1</sup> Although it is an extremely simple approach it

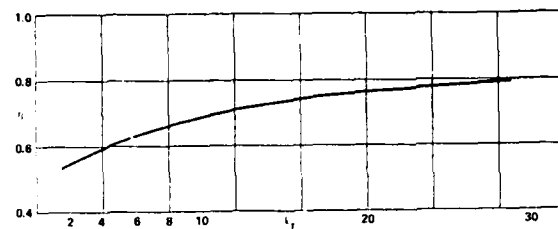


Figure 69. Body length correction factor.

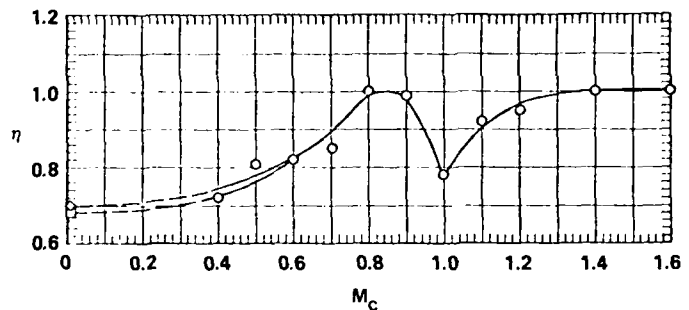


Figure 70. Correction factor of calculate from experimental data on inclined bodies with  $\lambda_T \sim 10$

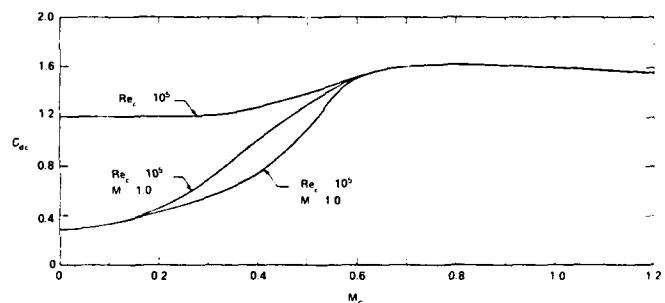


Figure 71. Crossflow drag coefficient as a function of crossflow Mach number determined from normal force data on inclined bodies

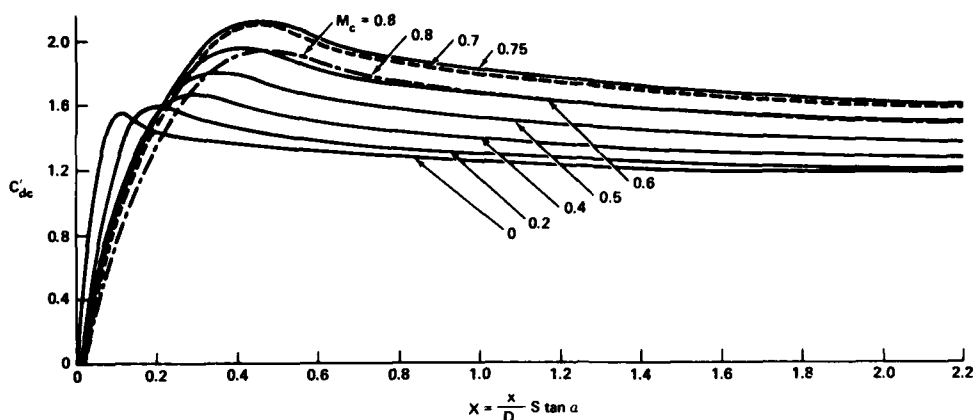


Figure 72. Thomson's adjusted crossflow drag curve

does very well at providing a rough estimate of normal force over a wide range of Mach number. When  $C_{dc}$  and  $\eta$  are determined as described above best results are obtained at supersonic crossflow Mach numbers. For  $M_c \sim 1$ , an uncertainty exists as to the most appropriate value of  $\eta$ . Jorgensen<sup>65</sup> has calculated  $\eta$  values by substituting  $C_{dc}$  values from Figure 3a and  $C_N$  measurements into Eq. (18). The results shown in Figure 70 indicate a rapid variation of  $\eta$  for  $M_c$  near unity. In subsonic crossflow where Reynolds number has a large influence on normal force the use of crossflow Reynolds number to determine the condition of the separating boundary layer is questionable. As discussed in Section 2.1.1 and shown in Reference 67 the crossflow Reynolds number is based on an inappropriate characteristic length. Particularly at low incidences ( $\alpha < 25$ ) a characteristic length representative of the surface streamline length (i.e.  $D/\sin\alpha$ ) is more appropriate. At incidences greater than 45 degrees, the ratio of the streamwise Reynolds number ( $Re_D/\sin\alpha$ ) to the crossflow Reynolds number is less than two and the discrepancy introduced by using this latter parameter is probably small.

A variation on the crossflow analogy as defined above is to calculate  $C_{dc}$  values by substituting the measured normal force coefficient on inclined bodies into Eq. (19). A crossflow drag curve suggested by Baker<sup>62,68</sup> is shown in Figure 71 and features the supercritical curve determined by Fidler<sup>49</sup> and a subcritical one from DATCOM<sup>69</sup>. In conjunction with the  $C_{dc}$  values in this Figure, the following function is given to blend subsonic values of  $\eta$  to unity in supersonic flow<sup>68</sup>:

$$\eta = \eta + \left( \frac{1-\eta}{2} \right) \left\{ 1 + \tanh \left[ \frac{15(M-1)}{M^4} \right] \right\} \quad .95 < M < 1.35$$

As apposed to Jorgensen's curve fit for  $\eta$  the above is based on freestream Mach number rather than crossflow Mach number.

Force Prediction methods based on the impulsive flow analogy (see Section 2.1.1) produce equations for  $C_N$  and  $C_M$  similar to those shown above:

$$C_N = \underbrace{\frac{\sin(2\alpha)\cos(\alpha/2)\pi D^2}{4 A_{ref}}}_{\text{potential term}} + \underbrace{\frac{\eta}{A_{ref}} \sin^2(\alpha) \int_0^{L_t} d C_{dc} dx}_{\text{viscous term}} \quad (21)$$

$$C_M = \sin(2\alpha)\cos(\alpha/2) \left[ \frac{\bar{y} - \pi D^2 (L_t - x_m)/4}{D A_{ref}} \right] + \frac{\eta \sin^2(\alpha)}{A_{ref} D} \int_0^{L_t} d C_{dc} (x_m - x) dx \quad (22)$$

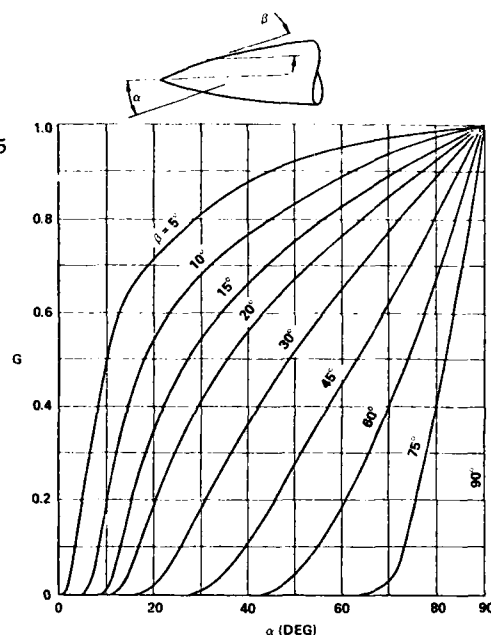


Figure 73. Correction of crossflow drag due to axial pressure gradient

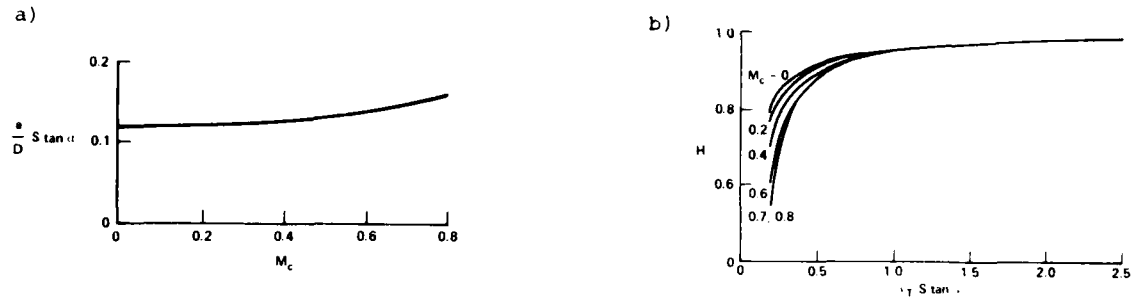


Figure 74. Reduction factor  $H$  to account for base influence. Apply to the drag coefficient within a distance  $e$  from the base.

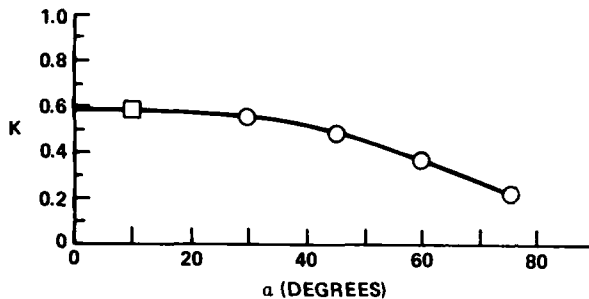


Figure 75. Crossflow drag reduction due to turbulence

Here again the total force and moment is assumed to be the sum of a potential and viscous contribution. However, the crossflow drag coefficient is assumed to be a function of distance along the missile axis. Available experimental data for  $C_{dc}$  on an impulsively started cylinder is shown in Figure 4a where the crossflow drag is given as a function of  $t^* = xt \tan \alpha / D$ .

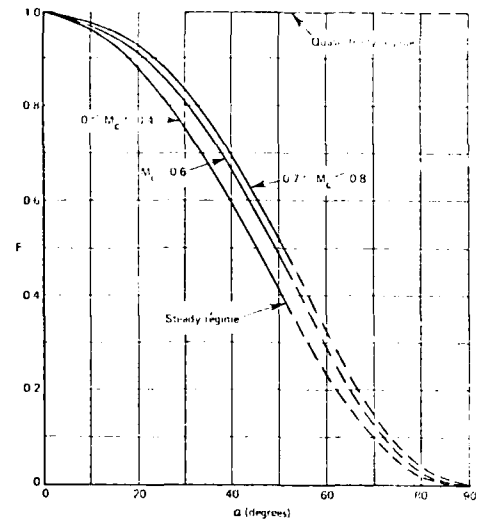


Figure 76. Correction for use of impulsive flow analogy

The impulsive flow analogy was initially suggested by Kelly<sup>70</sup> who used a polynomial fit to Schwabes' data<sup>3</sup> to evaluate Eqs. (21) and (22). Unfortunately, Schwabes' results are now generally considered to be superseded by Sarpkaya's.<sup>4</sup> However, there is little data on impulsively started cylinders and this is a major impediment in using this approach.

Thomson<sup>6</sup> has developed a method of prediction based on an extensive modification of the impulsive flow analogy which is applicable at  $M_c < .8$ . Sarpkaya's  $C_{dc}$  curve is scaled by the steady-state cylinder drag value to introduce a Mach number effect. In addition, the functional form of this curve is altered by matching times at which Sarpkaya observed vortices to be shed to those points along a missile where the corresponding vortex breaks away. This adjusted  $C'_{dc}$  curve is shown in Figure 72.

Thomson's theory also makes adjustments for additional effects which are generally ignored in other empirical approaches. The nose geometry produces a favorable pressure gradient on the boundary layer which reduces the width of the separation region on forward portions of the body. The method of correction is based on slender body theory pressure distributions and assumes that separation occurs at the point of minimum pressure. Taking this minimum value to be the pressure throughout the separation region allows the ratio of crossflow drag with and without axial pressure gradient to be determined as shown in Figure 73. The base influence is determined by assuming that in the region shown in Figure 74a, the vortices grow at only a fraction of their normal value. Taking this as .4 results in the base region crossflow drag reduction factor provided in Figure 74b. The judgment concerning the state of the boundary layer is made by examining both the crossflow and axial Reynolds numbers. The turbulence reduction in crossflow drag coefficient is dependent on incidence as shown in Figure 75. Finally, the factor  $F$  in Figure 76 is used to account for the error of applying the impulsive flow analogy instead of the yawed vortex street concept. Inherent in the impulsive flow analogy is the assumption that vortex cores are parallel to the body axis while in fact they are skewed at an angle  $\epsilon$ . The crossflow drag coefficient is determined by multiplying all of the above correction factors times the value of  $C'_{dc}$  provided in Figure 72. Hence at any point along the crossflow drag coefficient is:

$$C_{dc} = C'_{dc} FGHK$$

where  $F$ ,  $G$ ,  $H$  and  $K$  are determined using Figures 73 to 76.



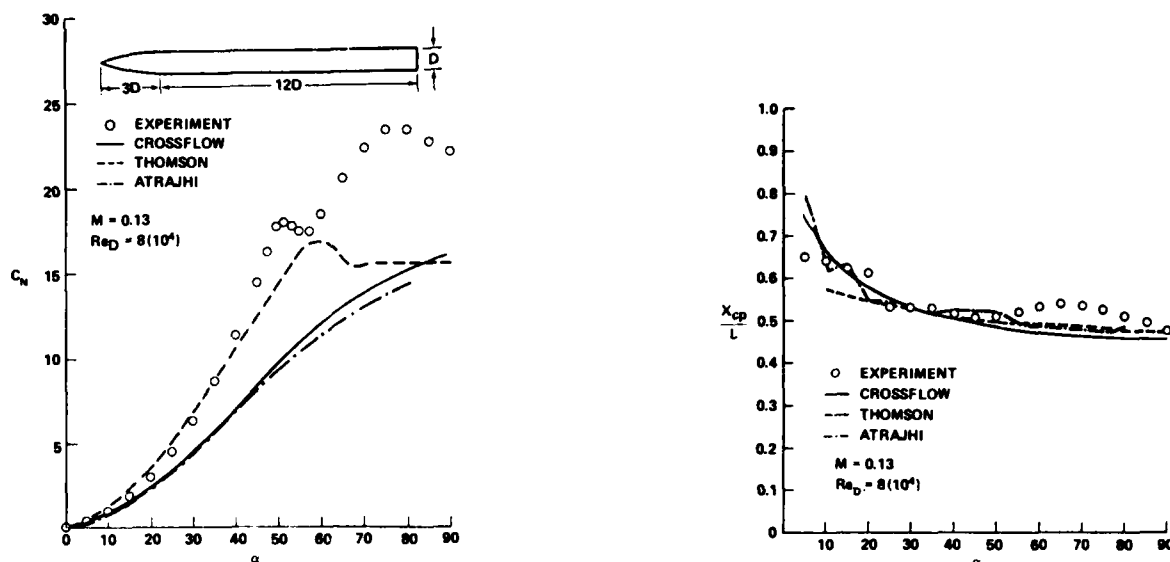


Figure 77. Measured and predicted normal force coefficients and center of pressure in incompressible flow

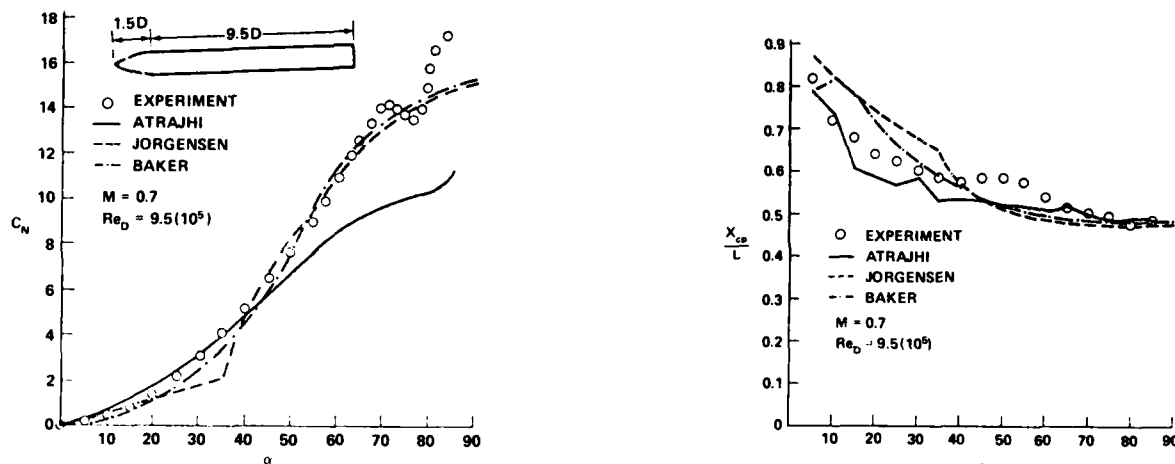


Figure 78. Measured and predicted normal force coefficients and center of pressure in transonic flow

The above methodology applies up to an incidence of 40 degrees. In the angle of attack range of 40 to 60 degrees a similar procedure is used with the F correction factor of Figure 76 set to unity. This is to account for the unsteadiness of vortices far from the nose. At higher incidence the standard crossflow analogy is applied with  $C_{dc}$  determined at  $X = 2.2$  in Figure 72. With the exception of turbulence, the remainder of the correction factors are dropped in favor of  $\eta$  which is determined from Figure 69.

An alternative application of the impulsive flow analogy is provided by Atraghji.<sup>63</sup> This method uses the analogy to extend impulsive and Karman vortex street drag terms to the three dimensional case. To estimate these quantities a sinusoidal bound vorticity distribution is assumed, the level of which is determined based on Karman vortex street analysis. This approach is applicable to bodies in incompressible flow only.

The above predictive methods have been compared to experimental data in reference 71 and some of these cases are shown in Figures 77 to 79. All of the predictions tend to underestimate the sting measured normal force at high incidence in the case of incompressible flow with laminar separation (see Figure 77). As discussed in Section 2.5, force data taken on sting mounted models tends to overestimate the normal force which may account for some of this difference. However, there is also a wide variation among predicted results. Better agreement is obtained at Mach .7, at a supercritical Reynolds number as is shown in Figure 78. The abrupt change in the crossflow predictions using Jorgensen's method corresponds to the incidence at which the crossflow Mach number becomes supercritical and the Reynolds number loses its influence of normal force. A better prediction of normal force is obtained using the crossflow drag coefficients of Figure 71 which show a more gradual change of the supercritical crossflow drag curve with Mach number. A final comparison is carried out in Figure 78 at Mach 2 and shows very good agreement between theory and experiment. The method labeled

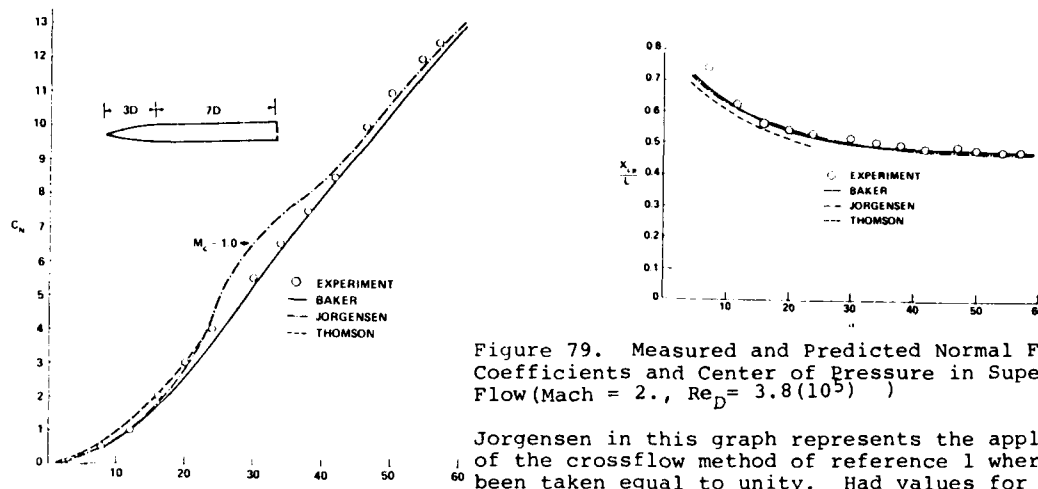


Figure 79. Measured and Predicted Normal Force Coefficients and Center of Pressure in Supersonic Flow (Mach = 2.,  $Re_D = 3.8(10^5)$ )

Jorgensen in this graph represents the application of the crossflow method of reference 1 where  $\eta$  has been taken equal to unity. Had values for  $\eta$  suggested in Figure 70 been used, the hump in the predicted normal force curve near  $M_C \approx 1$  would have been reduced.

Attempts to develop analogous empirical methods for predicting yaw force and moment have not been nearly as successful. The crossflow analogy cannot be used since lift forces on a cylinder in crossflow are unsteady with a time averaged value of zero. In principle the impulsive flow analogy can be applied by replacing the quantity  $C_{dc}$  in Eq. (21) by  $C_L$  and dropping the potential force contribution. Until very recently experimental information on the development of lift on an impulsively started cylinder was not available. Hence to obtain an upper bound on  $C_y$  reference 2 used the root-mean-square  $C_L$  value whose approximate behavior with Mach number and Reynolds number is shown in Figure 3b. In a more detailed approach Lamont and Hunt<sup>72</sup> have inferred the unsteady impulsively started cylinder's lift characteristic using Sarpkaya's observed vortex spacing and wind tunnel data.

Using a different approach, Thomson<sup>6</sup> has applied his own data concerning vortex strengths and trajectories to provide upper and lower bounds for side force. The upper limit is determined by assuming that the circulation around the missile body at any given cross section is equal in magnitude but opposite in sign to the strength of all the vortices in the crossflow plane. The force at each crossflow plane is determined using the Kutta-Joukowski theorem:

$$F_y = U \sin \alpha \rho \Gamma \quad (23)$$

The total force acting on the missile body is determined by integrating the contribution of each crossflow plane along the length of the missile. The lower limit is arrived at in a similar manner, but in this case the circulation of only the growing vortices are used.

In a similar vein Kao<sup>73</sup> has developed a method of predicting side force using Thomson's data and an experimentally determined onset angle. Again, lift is computed using the Kutta-Joukowski theorem, but the final solution provides an estimate for the local side force peaks, not an upper and lower bound as produced by Thomson.

One of the most recent predictive methods for side force is that of Lamont and Hunt<sup>44</sup> which is based on the experimental pressure data discussed in Section 2.1.5. This information is integrated to produce a crossflow side force coefficient which is correlated as a function  $x \tan \alpha / D$  as is shown in Figure 34. This correlation does not completely remove the incidence and nose shape dependency of the data. Key positions on the side force distribution curve are defined as a function of these parameters in table 2. The local side force coefficient is integrated to determine  $C_y$  using the unswitched amplitude of Figure 35.

The sensitive nature of side force makes it difficult to evaluate predictive theories. Most of the procedures are compared to limited experimental measurements at the time of development and hence produce side forces of the correct order of magnitude. However, for these methods to have general applicability, they should exhibit trends evident in a large data base (see Section 2.1.5). In low speed flow the side force magnitude clearly declines with decreasing nose fineness. To describe the nose region accurately, the impulsive flow analogy should model flow about an expanding impulsively started cylinder. The impulsive flow methods of references 2 and 73 neglect the expanding aspect of this analogy and hence do not accurately describe nose fineness effects. Techniques such as Thomson's<sup>6</sup> and Kao's<sup>73</sup> which are dependent on observed vortex strength could conceivably satisfy this requirement, however there is an absence of data defining the influence of nose geometry on vortex strength. Atraghji's<sup>63</sup> prediction of side force does not seem to show a decrease in side force with decreasing nose fineness. The only predictive method that can be shown to satisfy this trend is that of Lamont and Hunt.<sup>44</sup> The predicted peak side force values accurately bound experimental data when plotted as a function of nose fineness as is shown in Figure 39.

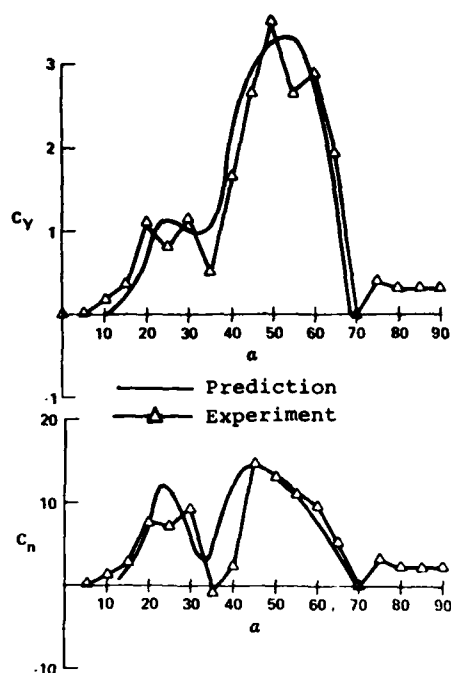


Figure 80. Predicted side force and moment by Lamont and Hunt<sup>44</sup> compared to the measurements of Smith and Nunn<sup>41</sup> on an ogive model ( $l_n = 3$ ,  $l_t = 15$ ).  $M = .13$ ,  $Re_D = 8 (10^5)$

number. The same problem probably exists with Thomson's method since vortex strengths do not decrease until a crossflow Mach number of .7 is achieved. At present there appears to be no proven method of estimating side forces at crossflow Mach numbers greater than .4 or free stream Mach numbers of greater than .6.

### 3.1.2 Semi-Empirical Methods for Body-Alone Configurations

Semi-empirical methods can only handle steady flow fields and thus are limited to incidences of less than 60 degrees. These theories use ad-hoc formulations that to varying degrees force the observed problem structure into the solution. The resulting theories can provide useful predictive tools; however, their validation requires a broad comparison between experiment and theory since a firm basis for expecting close quantitative agreement does not exist. Available techniques are formulated using potential theory and thus are restricted to subsonic flow.

Most of the available methods are based on the impulsive flow analogy with the flow in the crossflow plane being taken as incompressible. The root of this latter assumption is a loose application of slender body theory which is based on the small disturbance equation:

$$(1 - M_\infty^2) \frac{\partial^2 \phi}{\partial x^2} + \frac{\partial^2 \phi}{\partial y^2} + \frac{\partial^2 \phi}{\partial z^2} = 0 \quad (24)$$

The above expression applies to bodies which are of sufficient slenderness to insure that the flow velocities caused by their presence are small compared to the free-stream velocity. This limits the application of the above equation to missile-like configuration at angles of attack near zero degrees. Slender body theory shows that the first term in the above equation can be neglected and hence, that the crossflow component can be treated by Laplace's equation and is therefore incompressible. Application of this assumption at high angles of attack is theoretically unfounded in transonic or supersonic flow. However, its use reduces the problem to manageable proportions.

Semi-empirical methods describe the incompressible, viscous crossflow plane by superimposing point vortices on the potential solution for flow about a cylinder. Expressed in complex coordinates (see Figure 81 for a definition of notation) the complex potential for flow over a circular cylinder with free-stream velocity  $U \sin \alpha$  is:

$$\phi = -U \sin \alpha \left( \zeta - \frac{a^2}{\zeta} \right) i \quad (25)$$

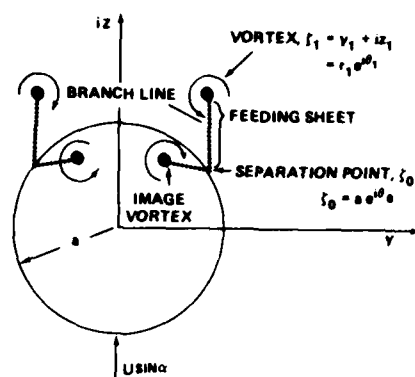


Figure 81. Symmetric concentrated vortex crossflow plane model used by Bryson

In addition, close agreement is obtained between select side force and moment measurements of which Figure 80 is an example. The selected data sets come from experiments in which the magnitude of the side force is fairly independent of roll angle. At present the Lamont and Hunt method for predicting side force is the only one which is supported by a wide body of experimental data.

Predictive methods applicable to transonic Mach numbers should exhibit a decreasing side force magnitude with increasing Mach number. According to the data presented in Figures 37 and 38 side force starts decaying at a free stream Mach number of .6 or at a crossflow Mach number of .4. The results of reference 2 do not decrease rapidly enough with increasing Mach

Using the circle theorem<sup>36</sup> the solution for an isolated vortex at location  $\zeta_1$  in the presence of a circular cylinder is:

$$\phi = -\frac{i\Gamma}{2\pi} \left[ \ln(\zeta - \zeta_1) - \ln\left(\zeta - \frac{a^2}{\zeta_1}\right) + \ln \zeta \right] \quad (26)$$

The first term in this equation represents the vortex in the flow, the second term is its image which is located inside the cylinder, and the third term is a vortex at the center of the cylinder. The image vortex is located at a point such that the combination of its velocity and that of the external vortex satisfy the normal flow condition on the circular cylinder boundary. The central vortex allows the total circulation about the cylinder to be set to zero. Generally it is assumed that vorticity shed into the wake leaves a circulation of opposite strength on the cylinder and hence this term is neglected.

The crossflow plane of a body of revolution containing  $N$  vortices of strengths  $\Gamma_1, \Gamma_2, \dots, \Gamma_N$  and located at positions  $\zeta_1, \zeta_2, \dots, \zeta_N$ , respectively, can be constructed by superimposing Eqs. (25) and (26):

$$\phi = U \sin \alpha \left[ -\left(\zeta - \frac{a^2}{\zeta}\right)i - \frac{i}{2\pi U \sin \alpha} \sum_{j=1}^N \Gamma_j \ln \left\{ \frac{\zeta - \zeta_j}{\zeta - \frac{a^2}{\zeta_j}} \right\} \right] \quad (27)$$

Differentiating this expression with respect to  $\zeta$  the complex velocity in the crossflow plane ( $W = v + iw$ ) is obtained:

$$\bar{W} = v - iw = -i U \sin \alpha \left\{ \left(1 + \frac{a^2}{\zeta^2}\right) + \sum_{j=1}^N \frac{\Gamma_j}{2\pi U \sin \alpha} \left[ \frac{1}{(\zeta - \zeta_j)} - \frac{1}{(\zeta - a^2/\zeta_j)} \right] \right\} \quad (28)$$

A source term is often added to Eqs. (27) and (28) to account for the expanding body radius near the missile nose. The complete flow field as described by the above two expressions is irrotational everywhere except at the vortex locations where the velocity is singular.

Using Eqs. (27) and (28) it is possible to construct a crossflow plane containing any number of vortices of arbitrary strengths and locations. The problem addressed by semi-empirical techniques is that of calculating the distributions and strengths of vortices in the crossflow plane. This task is divided into two distinct parts:

- (1) Determination of the rate and manner of vorticity production.
- (2) Tracing the transport of vorticity throughout the crossflow plane.

Once these steps have been accomplished the problem is completed by calculating the loads in each crossflow plane resulting from the predicted flow field.

Two different schemes have commonly been used to determine the rate of vorticity production or the instantaneous strengths of vortices in the flow field. The first involves satisfying the Kutta condition at the separation point:

$$W(\zeta_0) = 0 \quad (29)$$

The second method assumes that the rate at which vorticity is shed into the wake is:

$$\frac{d\Gamma}{dt} = K W^2(\zeta_0) \quad (30)$$

This expression is derived by considering the vorticity flux across the two-dimensional boundary layer:

$$\left| \int_0^{\delta} y \left( \frac{\partial v}{\partial x} - \frac{\partial u}{\partial y} \right) u dy \right| \approx \frac{u^2(\delta)}{2} = \frac{W^2(\zeta_0)}{2} \quad (31)$$

The factor  $K$  arises by taking into account a detailed picture of the crossflow plane separation pattern as shown in Figure 8. The primary and secondary separation points generate vorticity of opposite sign and vorticity from the secondary separation point annihilates some of that from the primary separation point, hence the factor  $K$ .

Vorticity transport in the crossflow plane is traced by following the paths of the vortices introduced into the flow field. The motion of a vortex can be described in several ways. Most simply the velocity of the vortex is assumed to be equal to that of the local fluid velocity at its own location (excluding its own contribution which is singular at this point). Hence:

$$\frac{d\zeta_j}{dt} = W_j \quad (32)$$

or using the impulsive flow analogy:

$$\frac{d\zeta_j}{dx} = \tan \alpha \hat{W}_j$$

To obtain vortex paths, this equation is broken into its real and imaginary parts and integrated numerically. This approach is always applied to vortices of constant strength. However, the motion of growing vortices is often assumed governed by:

$$\frac{d\zeta_j}{dt} + \frac{(\zeta_j - \zeta_0)}{r_j} \frac{dr_j}{dt} = W_j$$

or

(33)

$$\frac{d\zeta_j}{dx} + \frac{(\zeta_j - \zeta_0)}{r_j} \frac{dr_j}{dx} = \tan \alpha \hat{W}_j$$

The need for Eq. (33) can be explained by considering Helmholtz's theorem which states that vorticity of fluid elements in a potential flow field cannot change. As a consequence, each growing vortex develops a pressure discontinuity along an arbitrary path or branch line extending from its core to infinity. Mathematically the pressure jump arises from the velocity potential which is a function of  $\theta$  and therefore double valued. This can be seen by considering an isolated vortex located at the origin. Here the complex potential is  $-i\Gamma/2\pi \ln \zeta$  and the velocity potential is  $\theta/2\pi$ . Substituting into the unsteady Bernoulli equation which is

$$\frac{p}{\rho} = -\frac{1}{2} V^2 + \frac{\partial \phi}{\partial t} + C(t) \quad (34a)$$

and noting that the velocity distribution for a point vortex is  $\Gamma/2\pi r$  yields:

$$\frac{p}{\rho} = -\frac{\Gamma^2}{8\pi^2 r^2} + \frac{d\Gamma}{dt} \frac{\theta}{2\pi} + C(t) \quad (34b)$$

The function  $\theta$  jumps in value by  $2\pi$  whenever the branch line is crossed. Hence, unless  $d\Gamma/dt$  is zero a pressure discontinuity will exist.

The branch line of a vortex in the presence of a cylinder is taken as extending through the nearer separation point, the image vortex, and then to infinity along image vortex branch line. Since a vortex and its image are of opposite strength, the pressure jump along the two concurrent branch lines cancels leaving only a discontinuity along the line connecting a vortex with its image of  $\rho(d\Gamma/dt)/\text{unit length}$ . Balancing the total force on the portion of the branch line crossing the flow field,  $i\rho(\zeta_j - \zeta_0) d\Gamma_j/dt$ , by the lift force on the vortex due to Kutta-Joukowski theorem,  $-i\rho\Gamma(d\zeta_j/dt - W_j)$ , produces Eq. (33). Here,  $d\zeta_j/dt - W_j$  is the vortex velocity with respect to the local fluid. The portion of the branch line crossing the flow field is known as the feeding sheet.

Once the flow-field structure is known, forces on the missile body must be calculated. The most direct approach is to use the vortex impulse theorem. This provides a closed-form expression for determining the force on a body induced by  $N$  vortices:

$$(C_{N_V} - iC_Y) = \frac{2 \cos \alpha}{\pi U r^2} \sum_{j=1}^N \Gamma_j \left\{ \zeta_j - \frac{a^2}{\bar{\zeta}_j} \right\} \quad (35)$$

Here  $\zeta_j$  is the location of the  $j^{\text{th}}$  vortex in the base crossflow plane. To determine moments, this expression is evaluated at a number of different points along the body length. The above equation is derived in a number of different ways.<sup>74,75,76</sup> Considering each crossflow plane as a two-dimensional cylinder, an extension of Lagally's theorem can be applied.<sup>76</sup> Results from this approach are identical with Eq. (35) provided that the pressure jump across a feeding sheet is assumed balanced by a growing vortex's lift. Generally, the total force on the body is assumed to be the viscous component described by Eq. (35) plus a potential term. Hence:

$$C_N - iC_Y = \sin 2\alpha \left( \frac{a^2}{r^2} \right) + \frac{2 \cos \alpha}{\pi U r^2} \sum_{j=1}^N \Gamma_j \left\{ \zeta_j - \frac{a^2}{\bar{\zeta}_j} \right\} \quad (36)$$

If the method of derivation uses a momentum balance about a missile body the potential term is automatically included.<sup>75</sup> Implicit in Eq. (35) and (36) is the assumption that in each crossflow plane the flow field can be represented by vortices of infinite extent with cores which are parallel to the missile body. Accordingly, this expression is most applicable to low angles of attack. However, its use at large incidences is consistent with the impulsive flow analogy.

An alternate method for obtaining loads on a missile is to numerically integrate calculated pressures at the model surface using Eq. (34b).<sup>77</sup> Although this approach would seem to be extraneous in view of the vortex impulse theorem, these two methods are not entirely equivalent. The vortex impulse theorem does not include viscosity or damping, and

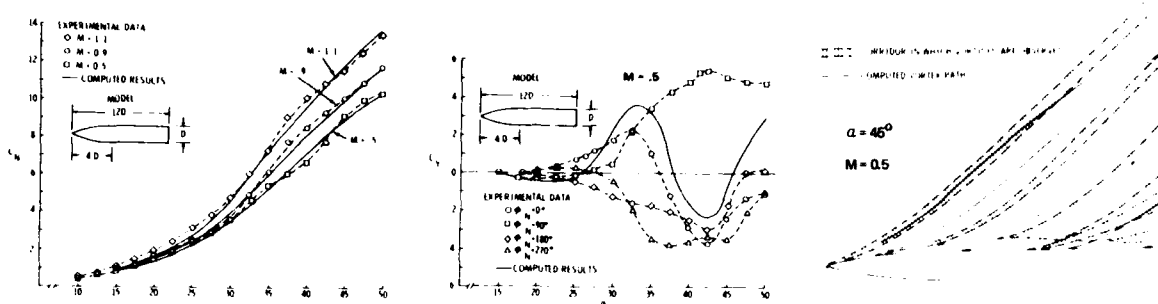


Figure 82. Results of asymmetric concentrated vortex model used in reference 81

vortices which are located a great distance from the body can still generate large loads. If the forces are calculated numerically, artificial damping will be introduced due to numerical error and the influence of distance vortices will be diminished.

Semi-empirical models have applied methods for calculating vorticity production, vorticity transport and aerodynamic loads in a variety of different ways. The simplest approach is to use a concentrated vortex model. Here a single vortex is used to describe each visible vortex in the wake. This method was first used in conjunction with delta wings and later was applied by Bryson<sup>78</sup> to describe the crossflow plane on a body at incidence. The original approach suggested by Bryson describes the motion of a growing pair of symmetric vortices using Eq. (33). The strengths of the vortices are determined by applying the Kutta condition at the separation point. The assumed problem formulation is illustrated in Figure 81. This method requires that the point at which the boundary layer separates be described empirically. In addition, the position at which vortices first form must be specified. This includes the point along the body and the crossflow plane location. Using a perturbation analysis, Bryson was able to show that the nascent vortices initially move away from the separation point along a line  $\theta_0 \pm \pi/3$  relative to the freestream. In the case of a cone his analysis indicated that vortices do not form until:

$$\frac{\tan \alpha}{\tan \theta_c} = \frac{1.5}{\sin \theta_0} \quad (37)$$

This criterion can be applied to missile-like bodies to determine the start of separation if the local body slope is used in place of the cone angle. The initial radial location must be determined through numerical experimentation. Bryson's solution is obtained numerically using a series of steps in the solution. At the start of each step the Kutta condition is applied to determine vortex strength. Vortex motion is then traced using Eq. (33). The drag produced by Bryson's method on an impulsively started cylinder is in good agreement initially but at moderate times ( $t^* = 3$ ) decreases and becomes negative.

A number of studies have followed Bryson's which are essentially an extension of his approach. Schindel<sup>79</sup> generalized the method to bodies of elliptic cross section, while Kuhn, et. al.,<sup>80</sup> treated the asymmetric wake containing two vortices in conjunction with a body undergoing coning motion. Wardlaw<sup>81</sup> has applied this approach to the asymmetric wake containing an arbitrary number of vortices. The solution is started by placing two point vortices near the body nose using Bryson's criteria for location. Asymmetry is immediately introduced by perturbing the radial location of each vortex. The solution is continued until the difference in radial position of these two vortices becomes greater than 10 percent. At this point the first vortex is shed and its circulation is assumed to be constant from this point on. A new vortex is started on the side of the body from which the vortex is shed. The nascent vortex is placed a small distance from the body along the broken feeding sheet of the shed vortex. Further vortices are shed at regular intervals along the body using the Strouhal number as the criterion.

This approach includes a large number of free parameters which must be specified before a solution can be achieved and much of the observed physics is forced into the problem. However, it is possible to choose a set of free parameters that correctly predicts vortex paths, yaw and pitch plane force on a sharp body at low subsonic Mach numbers as is shown in Figure 82. One problem with this method is that it is unable to account for increases in normal force and decrease in side force accompanying an increase in Mach number to transonic values. Nikolitsch<sup>82</sup> has improved upon the above method by taking into consideration the angle between the shed vortex core and the missile axis when computing loads.

Another approach for describing the developing crossflow plane is the multivortex method. Here a large number of point vortices are used to describe each wake vortex or primary vortex. The solution proceeds by introducing small point vortices periodically into the flow which are assumed to be of constant strength after addition. The crossflow plane location of nascent vortices is taken to be near the separation point. These vortices, whose paths are traced using Eq. (32), roll up to form large groups of vortices corresponding to the primary vortices visible in the leeward flow field. This process is depicted in Figure 83. By introducing an asymmetry into the problem, groups

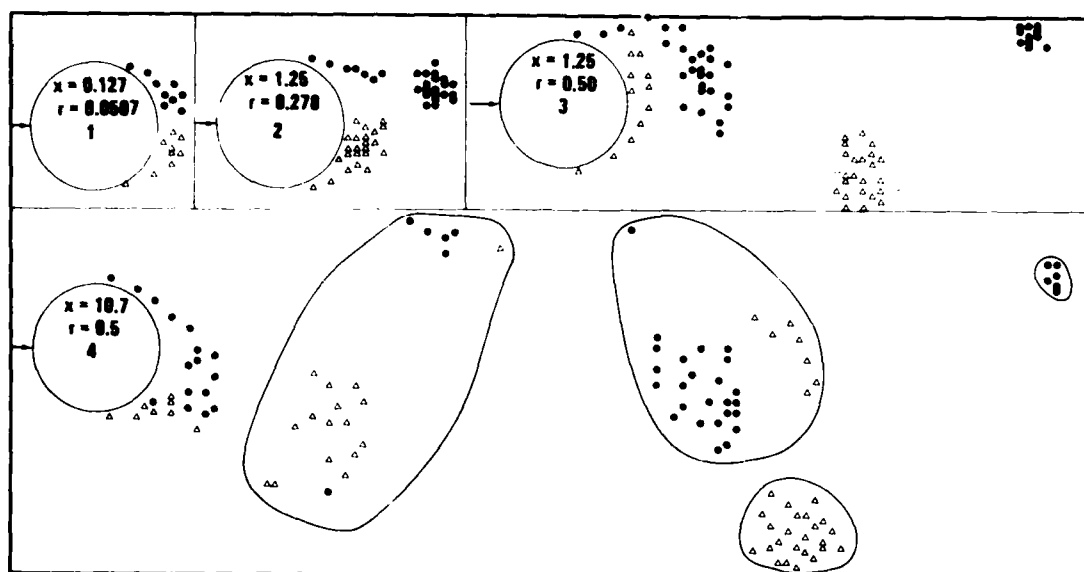


Figure 83. Leeward flow field on a tangent ogive predicted using a multivortex model

of point vortices can be observed to shed from the body at a rate which is compared to the experimentally measured Strouhal frequency.<sup>83</sup>

The multivortex or discrete vortex modeling method has been widely applied to viscous, unsteady, two dimensional flows with regions of flow separation. Clements<sup>84</sup> provides a recent review of such work. This approach was first applied to bodies at incidence by Angellucci<sup>85</sup> who developed a multivortex model of the symmetric wake. In this case the Kutta condition was used to determine the rate at which vorticity is shed into the flow field. This method is distinctive in that vorticity is assumed to lie in a continuous filament near the separation point. At a small distance from it, the strength of short lengths of filament are lumped into point vortices which are simpler to handle numerically. Wardlaw<sup>83</sup> has used the multivortex approach to model the asymmetric flow field. In this case the expression  $KU^2$  is used to determine the rate at which vorticity is shed into the flow field. Compressibility effects are simulated using Gothert's rule and the flow field is initially perturbed by increasing the circulation of vortices on one side of the model for the first few steps. Sample results for the developed wake are shown in Figure 83. The most sophisticated example of the application of this method is that of Deffenbaugh, et al.<sup>77,21</sup> which will be discussed in the next section.

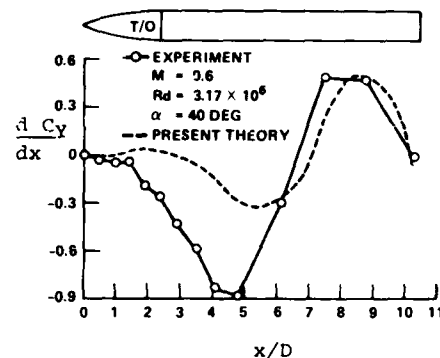
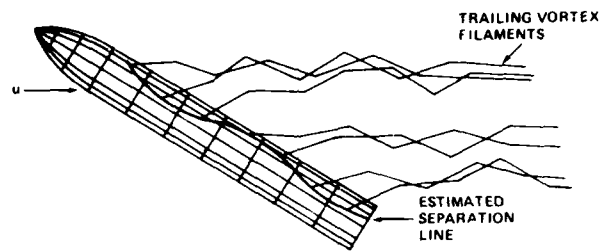


Figure 84. Predicted<sup>21</sup> and measured local side force distribution,  $M = .6$ ,  $Re_D = 3.7 (10^6)$ ,  $\alpha = 40^\circ$

The multivortex approach reduces the number of free parameters required to generate a description of the asymmetric wake. In particular it eliminates the requirement for specification of the axial positions at which vortices shed. However, it suffers from stability problems, particularly at high angles of attack which have plagued most application of multivortex methods. The crux of the difficulty is the velocity singularity at the center of each vortex. When a close encounter occurs between two vortices, one or both can be moved an extremely large distance in a single step playing havoc with the calculated loads. One method for dealing with this problem is to surround each vortex with a rotational core so that the velocity at the vortex location is zero. Another is to coalesce vortices in close proximity to one another into a single structure. Both of these techniques introduce free parameters into the solution which are difficult to determine on a physical basis. Fink and Soh<sup>86</sup> have considered point vortices as a discretization of a vortex filament. A linear constant strength vortex filament of finite length induces a velocity along its length except at its center. Hence only at this point does the self induced vortex velocity of zero computed using the standard approach agree with this point of view. These two methods can be brought into coincidence by redefining a set of equally spaced vortices at the end of each integration step. Instituting this method increases computational time and complexity, however, it avoids introducing new free parameters. At present this approach has not been applied to the modeling of the crossflow plane on missile bodies.

Most of the reported attempts to model the crossflow plane using the multivortex approach have successfully matched normal force and to a lesser degree center of pressure measurements with experiment. Also the predicted side force is of the correct order of magnitude. The calculated side force distribution of reference 21 is shown in

Figure 84 and places the majority of the load closer to the base than does experiment.<sup>7</sup> Since other concentrated and multivortex models also produce similar force distributions, the problem may be intrinsic to the use of the impulsive flow analogy. At high angles of attack or on very long bodies, the multivortex approach requires a significant computational effort which limits the use of this method as a design tool.



Currently there are studies in progress to develop three dimensional, steady potential models of the flow field about an inclined body.<sup>87</sup> Vortex filaments are trailed from the separation points and allowed to roll up to form vortices. Each filament is divided into a series of straight segments which are aligned through an iterative procedure with the local fluid velocity. The inviscid boundary conditions are satisfied on the body surface using a distribution of sources and sinks as shown in Figure 85. Such a model is very similar to those of low aspect ratio wings at high incidence to be discussed in the next section.

Figure 85. Three dimensional vortex model. Distributed sources are used to satisfy boundary conditions and the flow field is modeled using vortex filaments.

### 3.1.3 Theoretical Methods

The very few available theoretical techniques for the Mach number range ( $0.3 < M < 3$ ) are based on the impulsive flow analogy. As far as providing an engineering tool, these approaches have the major drawback of extremely large computational requirements. However, they also have the greatest potential for future development.

The method developed by Marshall and Deffenbaugh<sup>77</sup> uses a multivortex method similar to those discussed in the previous section to model the outer flowfield. In addition, the two-dimensional unsteady boundary layer in the crossflow plane is simulated using finite difference methods, eliminating the requirement for an observed separation point. Using the shape of the imposed velocity on the forward boundary layer and the calculated separation point, the separation of the rear shear layer is inferred. Assuming that the vorticity generated at each separation point is  $U^2/2$  the need for the previously discussed separation factor,  $K$ , disappears. The initial crossflow location of nascent vortices are such that the no-slip boundary condition is imposed on the outer flow contribution at the separation point. Although this method does not require experimental information, it has been found that empirically adjusting the rate of vorticity production (i.e.  $K$ ) improves results. As reported in Reference 77, this method is applicable only to the symmetric case. However, Deffenbaugh has extended the method to include the asymmetric situation and transition.<sup>21</sup> Turbulent separation points are predicted using Stratford's separation criteria.

The method of Walitt and Trulio<sup>88</sup> solves the crossflow plane using the full Navier Stokes equations. In this effort, the hypersonic version of the impulsive flow analogy, the equivalence principle is used to reduce the three-dimensional steady problem to a two-dimensional unsteady one. The method is designed to be used in supersonic flow where the analysis shows that the error due to the application of the equivalence principle is small. Calculations have been carried out on circular as well as noncircular cross sections. Flow-field characteristics such as embedded shocks and the point of boundary-layer separation (which is assumed to be two dimensional) are computed. This method has only been applied to angles of attack of less than 15 degrees assuming a symmetric flow field. Even under these conditions it has an exceptionally long run time.

## 3.2 Fin Alone

This section reviews the predictive techniques applicable to low-aspect-ratio wings at high angles of attack. The geometry of fin edges has a large effect on the resulting aerodynamics forces and the methods discussed are restricted to sharp-edged configurations. The only predictive methods available for the entire range of incidence, 0 to 90 degrees are empirical ones. The theoretical and semi-empirical techniques are valid only to incidences below stall (i.e., typically 20 to 35 degrees).

### 3.2.1 Empirical Methods

Use of the crossflow analogy for development of a predictive methodology is a natural approach which has been considered. Unfortunately, it does not provide as convenient a method as in the body-alone case. Flow on the upper surface of a wing is highly dependent on the planform geometry. Rectangular wings feature separations from three different edges while deltas experience separation from only two. The flow-field structure provided by the crossflow analogy does not account for these changing flow patterns with varying planform. As discussed in Section 2.2, Reynolds number is not a first-order influence on aerodynamic loads since the primary separation point is always fixed at the edge of the wing. In this respect the prediction of wing normal force is simplified as compared to the body alone case.



A crossflow expression for predicting normal force on a wing can be written:

$$C_N = \frac{\sin 2\alpha}{2} C_{N_\alpha} + C_{dc} \sin^2 \alpha \quad (38)$$

In incompressible flow the drag coefficient of a two dimensional flat plate is 2. Use of this value for  $C_{dc}$  gives satisfactory results on certain delta wing geometries but not in general.<sup>89</sup> On rectangular plates separation which increases lift occurs on both the sides and leading edge and a larger  $C_{dc}$  value produces best results. Efforts to take planform into account have resulted in Figure 86 which provides  $C_{dc}$  as a function of aspect and taper ratio.<sup>90,91</sup> Unfortunately, this graph does not include a Mach number correction and hence can only provide rough estimates. In addition, crossflow methods which use a fixed value of  $C_{dc}$  throughout the angle of attack range can only be expected to be valid up to the incidence of stall. At higher angles of attack, the functional form of the lift or normal force curve is no longer  $\sin^2 \alpha$ .

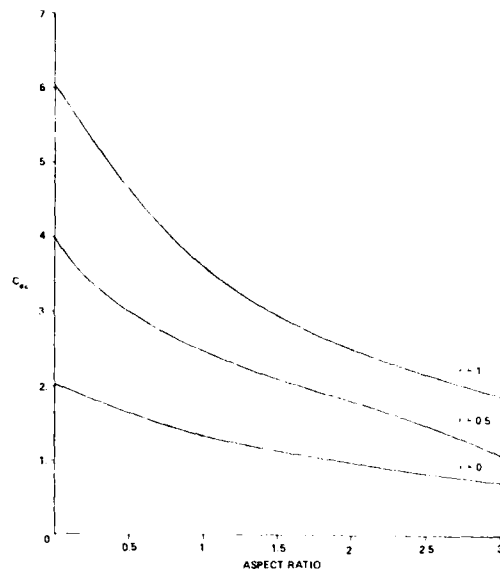


Figure 86. Crossflow drag coefficient on fins as a function of aspect and taper ratio<sup>90</sup>

Methods to circumvent the shortcomings of directly applying the crossflow analogy have been developed in DATCOM.<sup>69</sup> Here the basic formulation of the crossflow analogy is retained (i.e. Eq. (38) is unchanged), however,  $C_{dc}$  is defined as a function of planform shape and incidence. In subsonic flow the methodology for calculating  $C_{dc}$  is divided into a pre and post-stall section. At pre-stall incidences a correction, dependent on fin geometry and angle of attack, is applied to the value of  $C_{dc}$  producing the maximum lift. At post-stall angles of attack  $C_{dc}$  is interpolated from the maximum lift value and the crossflow drag value at  $\alpha = 90^\circ$ .

References 49, 58 and 68 have correlated extensive wind tunnel tests on fins with aspect ratios of .5, 1., and 2. and taper ratios of 0., .5, and 1. Baker's<sup>68</sup> results are restricted to a Mach number range of .6 to 1.3. The predictive form of this method is:

$$C_N = B_0 + B_1 \lambda + B_2 \lambda^2 + B_3 \lambda^3 \quad (39)$$

The coefficients  $B_0$  to  $B_3$  are provided in tabular form as a function of incidence and Mach number.

The predictive method devised in references 49 and 58 is divided into a pre-stall ( $\alpha \leq 30^\circ$ ) and post-stall ( $30^\circ < \alpha < 90^\circ$ ) regime. It covers the Mach number range of .8 to 3. and is applicable to fins with aspect ratios between .5 and 2. and taper ratios equal to or less than 1. Within each of these regimes the normal force is assumed described by the power series:

$$C_N = \sum_{n=0}^{\infty} A_n \alpha^n$$

Experimental data and other considerations are used to evaluate the coefficients of this series. For  $\alpha < 30^\circ$ , six terms are retained and it is assumed that:

- (1)  $C_N(0) = 0$
- (2)  $C_{N_\alpha}(90) = 0$
- (3)  $C_{N_\alpha}(180) = 0$
- (4)  $C_{N_\alpha}(180) = -C_{N_\alpha}(0)$
- (5)  $C_{N_\alpha}(0)$  is known
- (6)  $C_N(90) = A$ , which is empirically determined

Applying the above to the power series results in the expression:

$$C_N = C_{N_\alpha}(0) A(\alpha) + C_N'(90) B(\alpha) \quad (40)$$

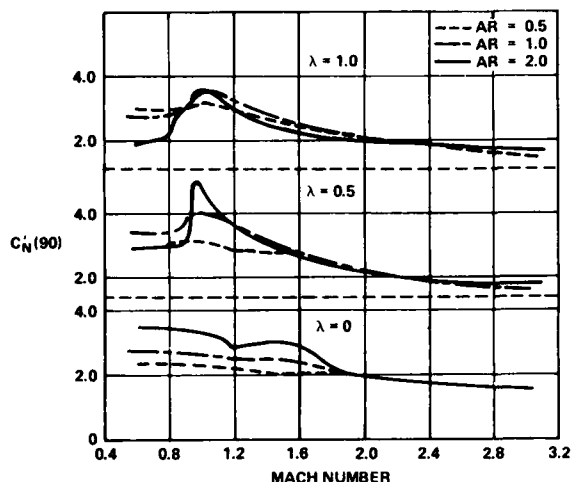


Figure 87.  $C_N'(90)$  as a function of Mach number and taper ratio

where

$$A(\alpha) = \alpha - \frac{5}{\pi} \alpha^2 + \frac{8\alpha^3}{\pi^2} - \frac{4\alpha^4}{\pi^3}$$

$$B(\alpha) = \frac{16\alpha^2}{\pi^2} - \frac{32\alpha^3}{\pi^3} + \frac{16\alpha^4}{\pi^4}$$

The constant  $C_{N_\alpha}(0)$  can be evaluated from linear theory or experiment while the parameter  $C_N'(90)$  is empirically determined using Figure 87. In the vicinity of  $\alpha = 30^\circ$  where stall occurs, a correction is applied to the method using Figures 88 and 89. Figure 88a indicates the incidence,  $\alpha'$ , where the correction is first applied. Using Figure 88b and 89,  $\Delta C_{N_M}$  and  $\Delta C_N/\Delta C_{N_M}$  are determined respectively for the appropriate geometry. Now  $C_N$  is calculated using the following expression where  $C_N(\alpha')$  is determined from Eq. (40):

$$C_N = C_N(\alpha') + \Delta C_{N_M} \left( \frac{\Delta C_N}{\Delta C_{N_M}} \right)$$

These adjustments are made only for subsonic flow.

In the angle-of-attack range 30 to 90 degrees the power series is truncated after four terms. Here the constraints are taken to be:

- (1)  $C_N(30)$  is known
- (2)  $C_{N_\alpha}(30)$  is known
- (3)  $C_{N_\alpha}(90) = 0$
- (4)  $C_N(90)$  is known

This produces:

$$C_N = C(\alpha)C_N(30) + D(\alpha)C_{N_\alpha} + E(\alpha)C_N(90) \quad (41)$$

where

$$C(\alpha) = + 4.2973\alpha - 5.472\alpha^2 + 1.7416\alpha^3$$

$$D(\alpha) = 1 - 4.297\alpha + 5.472\alpha^2 - 1.742\alpha^3$$

$$E(\alpha) = - 1.178 + 3.750\alpha - 3.342\alpha^2 + .9119\alpha^3$$

The constants  $C_N(30)$ ,  $C_{N_\alpha}(30)$ , and  $C_N(90)$  are determined from Figures 90, 91 and 92.

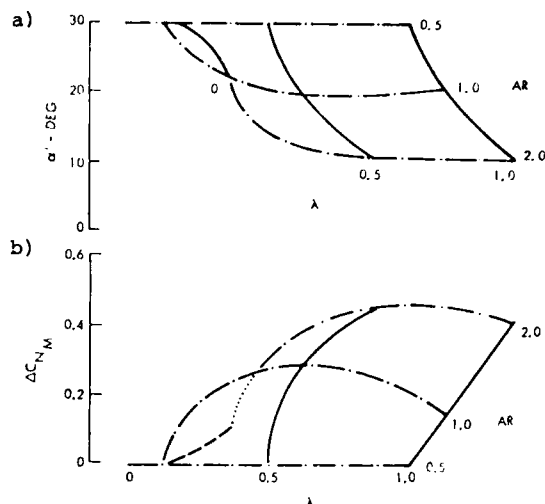


Figure 88. Charts for determining  $\alpha'$  and  $\Delta C_{N_M}$

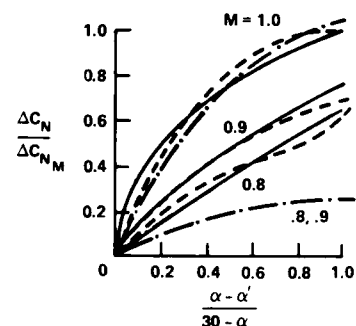
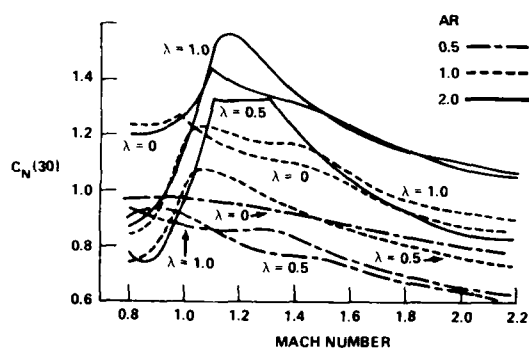


Figure 89. Chart for determining  $\Delta C_N/\Delta C_{N_M}$ ; —  $\lambda=1$   
---  $\lambda=.5$ , -.-  $\lambda=0$ .

Figure 90. Chart for determining  $C_{N(30)}$ 

Calculated results are compared to each other and to experiment in Figure 93. Also shown are the test data corrected for the estimated reflection plate interference effect as provided in reference 23. In subsonic flow the data correlation methods of references 58 and 68 are in good agreement with the uncorrected test results. The DATCOM prediction is significantly higher and agrees more closely with the corrected data. The crossflow method provides acceptable predictions up to an incidence of 25 degrees. Similar trends are evident in supersonic flow. Here the spread between the corrected and uncorrected data is much smaller.

The prediction of the center of pressure as a function of incidence is facilitated by the smooth behavior of this variable. At low incidence the position is well predicted by linear theory. With increasing incidence the center of pressure moves aft and is positioned at the planform centroid at  $\alpha = 90^\circ$ . Techniques for predicting this quantity can be found in references 58, 68 and 69. The DATCOM approach makes use of  $x_{cp}$  calculated at  $\alpha = 90^\circ$  by linear theory, and at the incidence of maximum lift. Baker<sup>68</sup> uses a correlation of the form of Eq. (39). The DATCOM method is limited to subsonic Mach numbers while Baker's correlation applies to Mach numbers between .6 and 1.3. The method developed in reference 58 is applicable over the Mach number range of .6 to 3. The center of pressure at Mach .98 is provided by Figure 94. To correct for Mach number effects, the following relation is used:

$$\frac{x_{cp}}{c_r} \alpha, M = \frac{x_{cp}}{c_r} \alpha = 90^\circ + \left[ \frac{x_{cp}}{c_r} \alpha = 90^\circ - \frac{x_{cp}}{c_r} \alpha = 90^\circ \right]_{M = .98} (F(M) + 1.) \quad (42)$$

Here  $F(M)$  is defined in Figure 95. Calculated center of pressure positions are compared to experiment in Figure 96. Clearly, the results of the predictive methods are in good agreement with themselves and experimental data.

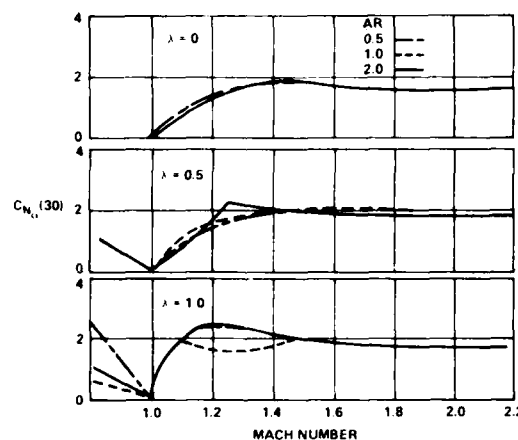
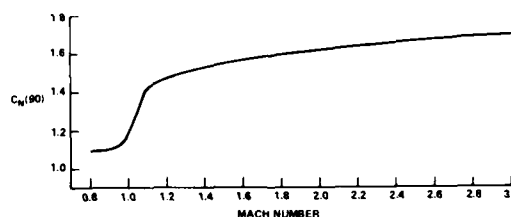
### 3.2.2 Semi-Empirical Methods

The only method to be discussed in this section is the leading edge suction analogy. As originally proposed by Polhamus<sup>92</sup> this approach is completely analytic; however, further work<sup>15</sup> has shown that use of an empirical factor can improve predictions. Although this approach was devised for delta wings, the concept can be applied to arbitrary wing planform and is valid at incidences below stall. The great utility of the leading edge suction analogy is that it allows lifting surface programs to be extended into the nonlinear angle of attack range.

The basic idea is to develop a method of prediction which circumvents the need to determine the separation vortex position and strength. The predictive equation is of the form:

$$C_N = K_p \sin \alpha \cos \alpha + K_v \sin^2 \alpha \quad (43)$$

which is similar to the crossflow flow equation. The first term represents the potential contribution and  $K_p$  is  $C_{N(0)}$  which can be determined from experiment or linear theory. The second term is the viscous contribution, but the constant  $K_v$  is found using the leading edge suction analogy, not the crossflow relation.

Figure 91. Chart for determining  $C_{N(30)}$ Figure 92. Chart for determining  $C_{N(90)}$

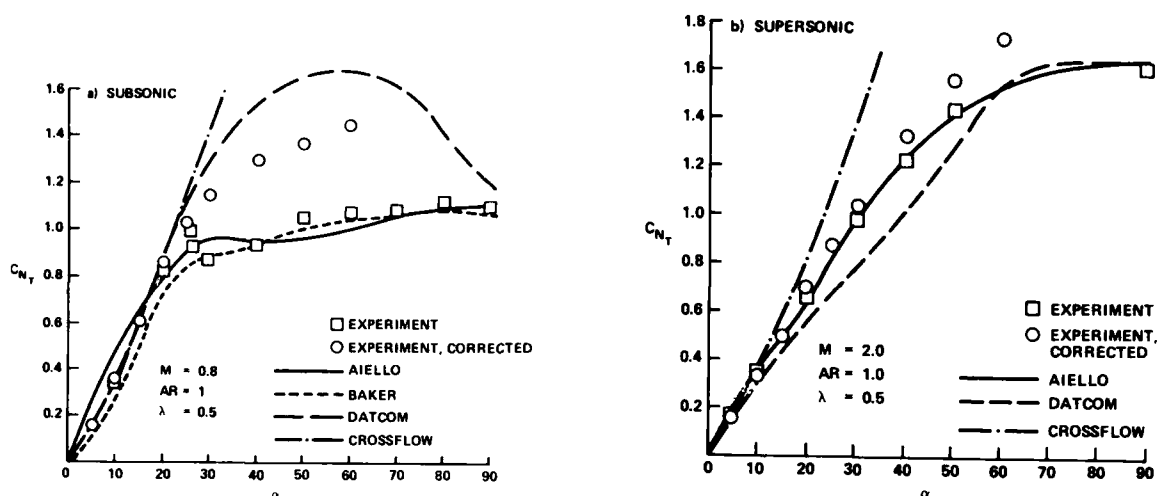
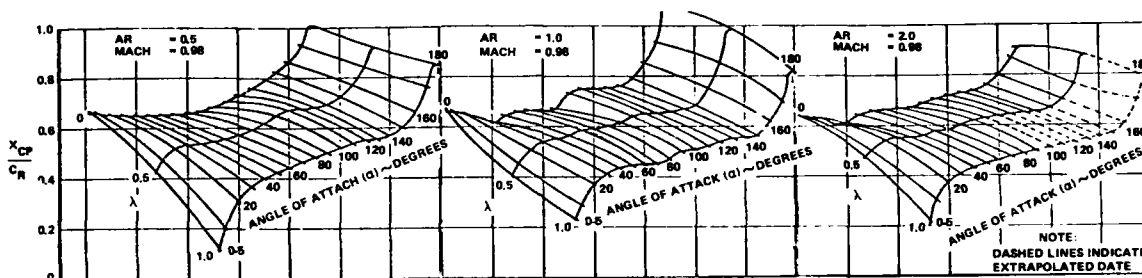


Figure 93. Calculated and measured fin normal force

Figure 94. Chordwise fin center of pressure at  $M = .98$ 

The leading edge suction analogy can be understood by considering potential (attached) flow about a sharp wing edge as shown in Figure 97. The fluid streamlines flow around the wing leading edge and then along the upper surface of the wing. In moving about the wing edge the fluid is accelerated and as a consequence its pressure is reduced which results in a leading edge suction. The same type of flow pattern occurs about thick leading edges as is shown in Figure 97. The calculated leading edge suction force is independent of wing-tip radius and hence is the same for both cases. Figure 97c shows the actual separated flow about a sharp wing edge. The path followed by the fluid in going about the vortex is similar to that about a thick wing edge rotated 90 degrees in a counterclockwise direction. The leading edge suction analogy assumes that the suction force calculated by potential lifting surface theory is equal to the lift force on a wing due to vortex separation. Both constants in Eq. (44) can be evaluated using a lifting surface program. To predict the center of pressure on wings with sharp edges, the suction load can be applied to the edge where it is generated.

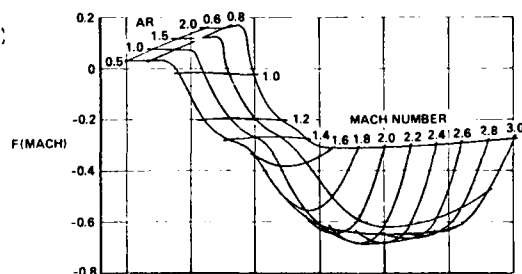


Figure 95. Mach number correction for fin center of pressure

Direct implementation of the leading edge suction analogy requires the use of a lifting surface program in subsonic flow. Fortunately, results can be summarized in graphical form as shown in Figures 98 and 99 for delta and arrow wings.<sup>93</sup> Correction for compressibility effects is obtained using the Prandtl-Glauert transformation. Supersonically,  $K_V$  and  $K_P$  for delta wings can be expressed:

$$K_P = \pi AR / 2E$$

$$K_V = \pi [(16 - (AR \beta)^2) (AR^2 + 16)]^{1/2} / 16E^2$$

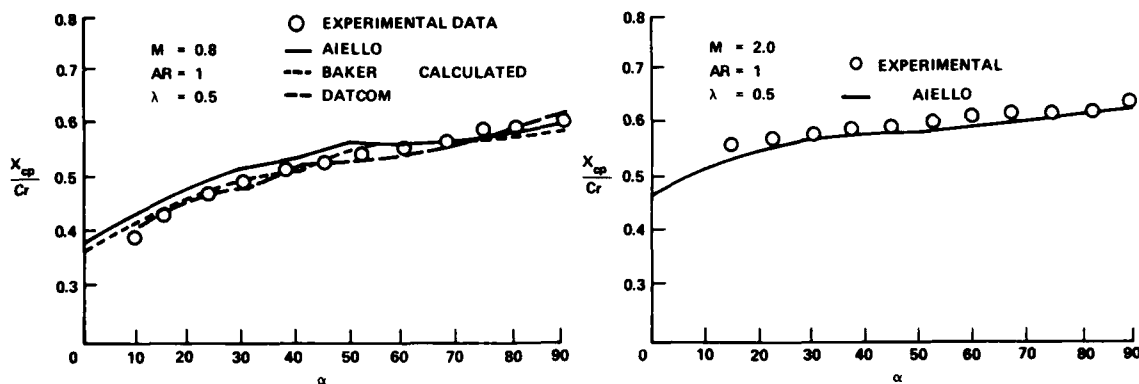


Figure 96. Measured and calculated center of pressure

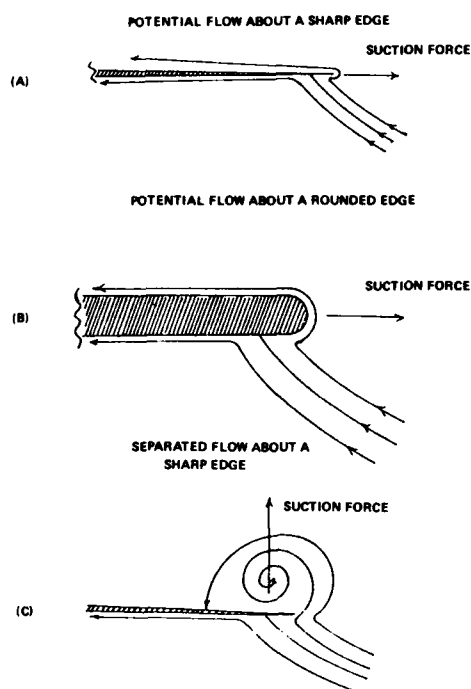


Figure 97. Leading edge flow conditions

Here  $E$  is an elliptic integral of the second kind with a modulus of  $[1 - (\beta \cot \Lambda)^2]^{1/2}$ . The leading edge suction disappears when the Mach number of the flow perpendicular to the leading edge reaches unity.

The leading edge suction has been applied to a wide variety of planforms in both subsonic and supersonic flow. Values for  $K_p$  and  $K_v$  applicable to many different planforms can be found in References 93 and 94.

An examination of experimental data indicates that the leading edge suction analogy tends to overpredict the normal force on delta wings for aspect ratios much greater or less than unity. For very small aspect ratio wings this is probably due to the formation of asymmetric vortices. Mendenhall and Nielsen<sup>15</sup> have examined a large number of experimental cases to determine the portion of the leading edge suction force that is converted into lift. A correction factor,  $K_C$ , which represents the

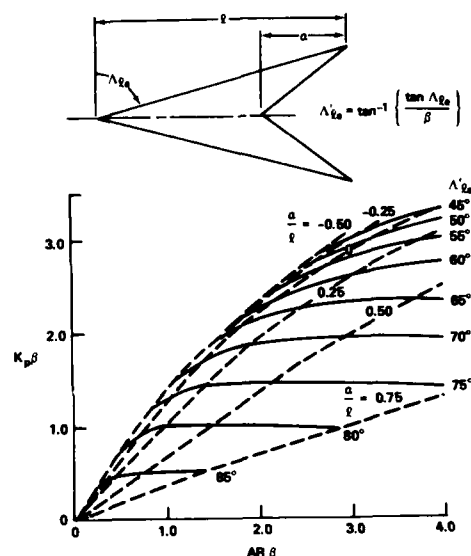


Figure 98. Variation of potential lift on arrow wings

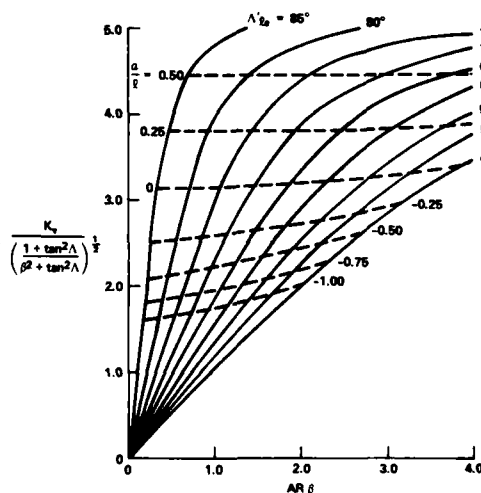


Figure 99. Variation of vortex lift on arrow wings

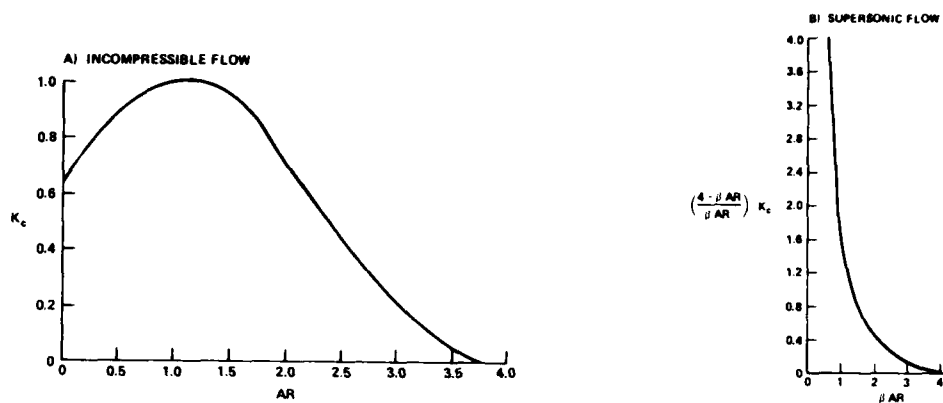


Figure 100. Portion of the leading edge suction converted into lift on a delta wing in subsonic and supersonic flow.

ratio of the actual to the theoretical suction force is shown in Figure 100 for incompressible and supersonic flow. To use this parameter, Eq. (44) is written:

$$C_N = K_p \sin \alpha \cos \alpha + K_c K_v \sin^2 \alpha \quad (44)$$

### 3.2.3 Theoretical Models

Available theoretical models for small aspect ratio wings at high incidence can be conveniently grouped into three classes:

- (1) Crossflow plane models (usually applicable to delta wings).
- (2) Lifting surface theories which vary the angle at which vortex filaments leave the wing as the function of incidence.
- (3) Lifting surface theories that model the trailing vortex wake structure.

This section will mention some of the existing theories in each of these classes. Extensive detail will not be provided since a large amount of material is available and because few of these approaches have actually been applied to missile configurations. The crossflow plane models are of interest because they are closely related to body alone techniques. Theories that model the vortex wake appear to show the greatest promise for improvement and application to missile geometries.

The crossflow plane models are generally based on slender body theory and often assume conical flow. As discussed in Section 3.1.2, slender body theory defines an incompressible crossflow plane which can be modeled by superimposing vortices on potential flow solutions. The use of a conical flow field on delta wings is strictly valid only in the supersonic case upstream from the trailing edge where the Kutta condition must be satisfied. In subsonic flow the limitations of this assumption are clearly illustrated in Figure 49.

One of the earlier models is that of Brown and Michael,<sup>95,96</sup> which was later adapted to bodies of revolution by Bryson<sup>77</sup> as discussed in Section 3.1.2. Here the vortex behind the leading edge is modeled using a single concentrated vortex as shown in Figure 101a. The motion of the vortex is governed by the conical form of Eq. (33) which can be obtained by replacing  $d\Gamma/dx$  and  $d\zeta_1/dx$  by  $\epsilon\Gamma/a$  and  $\epsilon\zeta_1/a$ , respectively. Applying the Kutta condition at the wing tip results in a set of algebraic equations which must be solved numerically in an iterative fashion to determine the vortex position and strength as a function of angle of attack and semi-vertex wing angle,  $\epsilon$ . Fortunately, an approximate solution can be obtained which agrees closely with the numerical one. These results are:

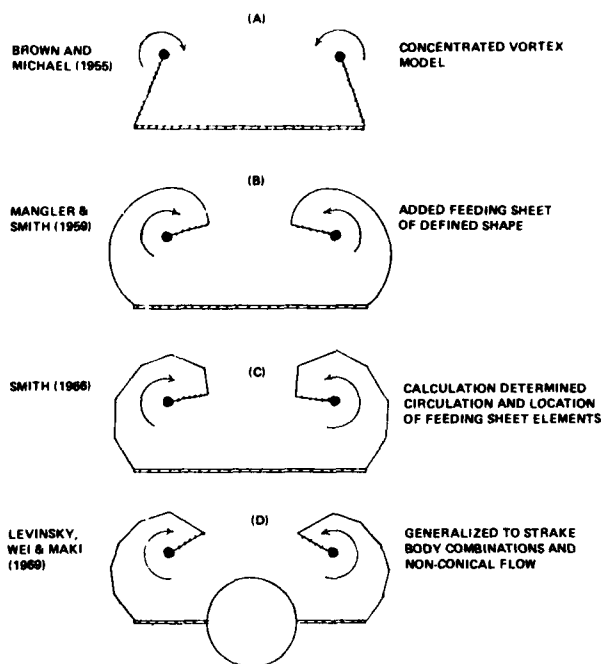


Figure 101. Crossflow plane theories

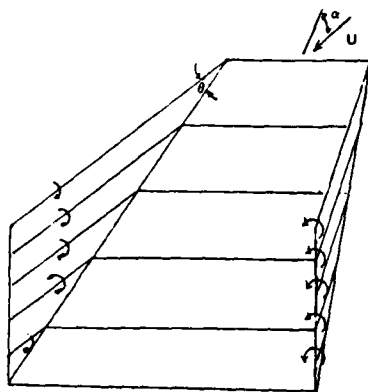


Figure 102. Bollay's nonlinear lifting surface theory model  
 $\theta$  is generally near  $\alpha/2$ .

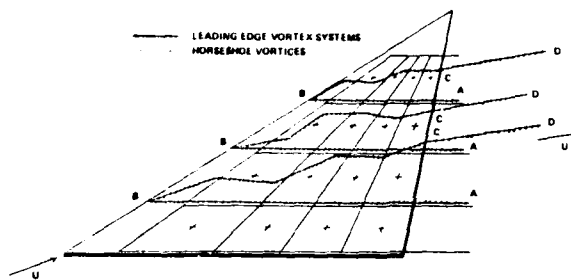


Figure 103. The extended lattice model of reference 108.

$$\begin{aligned} \frac{y_v - b}{b} &= \frac{1}{2} \left( \frac{z_v}{b} \right)^{2/3} \left[ 1 - \frac{3}{4} \left( \frac{z_v}{b} \right)^{2/3} \right] \\ \frac{\alpha}{\epsilon} &= 4 \frac{z_v}{b} \left[ 1 + \frac{1}{2} \left( \frac{z_v}{b} \right)^{2/3} \right] \\ \frac{\Gamma}{2\pi\epsilon U b} &= \frac{1}{2} \left[ 1 + \frac{3}{2} \left( \frac{z_v}{b} \right)^{2/3} \right] \frac{\alpha}{\epsilon} \end{aligned} \quad (45)$$

Using the above, lift can be calculated:

$$\frac{C_L}{2} = \frac{2\pi\alpha}{\epsilon} + 16\pi \left( \frac{\alpha}{4\epsilon} \right)^{5/3} \left[ 1 + \frac{2}{3} \left( \frac{\alpha}{4\epsilon} \right)^{2/3} \right] \quad (46)$$

An improved model of leading edge separation on a delta wing has been suggested by Mangler and Smith<sup>97</sup> (Fig. 101b) and later by Smith<sup>98,99</sup> (Fig. 101c). This latter work is essentially a refined version of the first made possible through advances in computational equipment and attention is focused on it. This approach seeks to describe the vortex sheet as well as the vortex core. The assumed model features a vortex sheet extending from the wing tip into the leeward flow field. The end of the filament is visualized as being connected to the vortex core which is represented by a concentrated vortex via a branch line. The motion of the concentrated vortex is again governed by the conical equivalent of Eq. (33) and the Kutta condition is also satisfied at the wing tips. In implementing the model the feeding sheet is divided up into  $n$  segments as is shown in Figure 101c. At the center of each segment the following conditions are satisfied:

- (1) Vortex sheets are assumed to lie along the local stream surfaces.
- (2) Pressure is assumed to be continuous across the vortex sheets.

The resulting algebraic equations contain the following unknowns which are solved for as a function of  $\alpha/\tan \epsilon$ :

- (1) Concentrated vortex position
- (2) Concentrated vortex strength
- (3) Vortex strength at  $n$  positions along the feeding sheet
- (4) Position of the vortex sheet at  $n$  different locations.

To obtain the solution an iterative procedure is devised. The final results provide a good estimate of the vortex location, however, the computed position tends to be too far outboard. The calculated surface pressure distribution agrees well with experiment provided that the cross section in question is well upstream of the trailing edge. The largest discrepancies occur near the leading edge on the upper surface of the wing. Smith's model has been extended in References 100 and 101 to include a body strake combination in conical and nonconical flow.

The second class of methods are lifting surface theories that require the vortex filament to leave the wing at some angle relative to the wing surface. This angle is often specified as one-half the angle of incidence and in other cases is calculated by assuming the vortex filaments to be straight lines which are parallel to the flow at the point which they leave the wing. The displacement of the trailing vortex filaments reduces the downwash on the wing increasing the required circulation and the calculated lift. By adopting a problem formulation which varies this orientation with angle of attack, the resulting solution is made nonlinear. Specification of the trailing vortex

filaments as straight lines is, of course, a simplification of the true situation. At every point the vortex filaments should be parallel to the local fluid velocity. The mutual interaction between the filaments will cause them to roll up to form large vortex structures downstream of the wing.

A number of different approaches have been put forth on this subject, one of the earliest being that of Bollay.<sup>102</sup> This model is shown in Figure 102 and features a vorticity distribution over the surface of the wing. The orientation of the trailing vortex filaments is calculated as described in the preceding paragraph. The vortex distribution is assumed to be constant in the span-wise direction and the functional form is prescribed along the chord. By satisfying the tangency flow condition in the mean on the surface of the wing the absolute magnitude of the vorticity distribution is determined. In the limit  $AR \rightarrow \infty$ , Prandtl's lifting line theory is recovered indicating that the orientation of the wing-tip vortices does not have a large effect in this case. The small aspect ratio limit,  $AR \rightarrow 0$  results in the Newtonian solution  $2 \sin^2 \alpha$  which is also the viscous crossflow normal-force term. More recent development of this type of method can be found in the works of Gersten,<sup>103-4</sup> Kucheman,<sup>105</sup> Garner,<sup>106</sup> and Ermolenko.<sup>107</sup>

There are several examples of modified lifting surface theories that model the vortex wake. Mook and Maddox<sup>108</sup> have developed a method which is an extension of vortex lattice techniques and is applicable to thin delta wings with leading edge separation. The approach augments the traditional vortex lattice techniques with a leading edge vortex system shown in Figure 103. The vortex filaments comprising the leading edge vortex system can be broken down into three sections. The first section, A-B consists of a straight-line vortex coincident with the lines of the trailing horse-shoe vortex of the regular lattice. The second part, B-C, is comprised of a series of straight-line filaments while section C-D is again a single straight-line segment, this time coincident with the freestream. Control points are also placed near the leading edge allowing Kutta condition to be approximately satisfied along it. The final boundary conditions applied by this method are:

- (1) Flow tangency at the control points on the wing.
- (2) The Kutta condition at the leading and trailing edge.
- (3) The line filaments in part B-C of the leading edge vortex system are aligned so that the flow is parallel to their upstream end.

To satisfy these conditions an iterative procedure is necessary since neither the strengths nor locations of the leading edge vortex filaments are known. This method has been further developed to apply to sharp wings and to account for compressibility.<sup>109,110</sup>

The final lifting surface method to be considered is described in Reference (111) and applies to wing and wing-body combinations in subsonic flow. This approach uses a distribution of doublet sheets to simulate the wing, wake, and leading edge vortex as shown in Figure 104. Panels describing the wing are subjected to the flow tangency condition. Both this condition and the constraint of pressure continuity across the doublet sheet are applied to the remaining panels accounting for the wake and leading edge separation. The vortex cores are treated with doublet sheets to which no boundary conditions are applied. The formulated problem is nonlinear since the shape and the strengths of the free doublet sheets are not known and an iterative scheme must be used to obtain a solution. Results compare favorably with experiment, particularly for the pressure distribution along the upper surface of the wing as illustrated in Figure 105. In addition to calculating the total lift, the wing load distribution is accurately determined.<sup>112</sup>

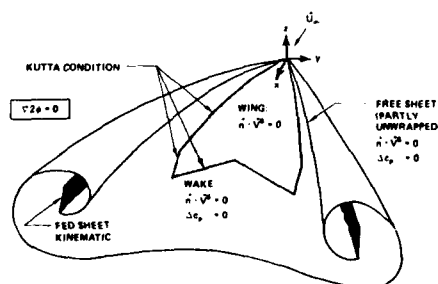


Figure 104. Dipole distribution used in reference 111.

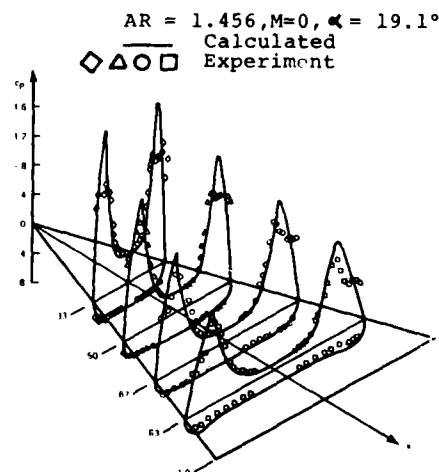


Figure 105. Comparison of the results of reference 111 to experiment



### 3.3 COMPLETE CONFIGURATION

The problems encountered in predicting the aerodynamic characteristics of body and wing alone are greatly compounded in the case of a complete missile configuration. The degree of difficulty is least for a cruciform body-tail configuration at zero roll and greatest for a canard-body-tail missile at arbitrary roll orientation. Empirical methods have been formulated for calculating the aerodynamic characteristics up to an angle of attack of 90 degrees. Semi-empirical methods are limited to incidences where steady, well defined vortices are formed. At present there are no completely theoretical methods applicable to missile configurations at high angles of attack.

#### 3.3.1 Empirical Predictive Methods

A large number of different approaches have been formulated for calculating the aerodynamics of missiles to high angles of attack. A listing and brief description of some of these methods is provided in Table 2. At present there is no single method applicable to a wide variety of canard-body-tail configurations which can be relied upon to incidences of 90 degrees. The more accurate methods tend to be restricted to body-tail missiles and are applicable to narrow Mach number and incidence ranges. The actual procedures available for calculating missile loading are too lengthy to be described in detail and this section will attempt to outline the various types of approaches that have been used. For simplicity fin and canard deflection will not be considered and center of pressure determination will not be discussed.

A premise behind most of the methods for calculating loads on complete missile configuration is that the total force is equal to the sum of that on the isolated components plus a correction for the interference between various components. The interference effects accounted for include body-wing, body-tail and wing vortex-tail interaction. At high angles of attack this interaction between the various components may enhance or delay stall on lifting surfaces and this framework may not always be appropriate. A standard method valid for unbanked configurations at low incidence and using the sum of the component forces approach is that of Pitts, Nielsen, and Kattari<sup>17</sup> (P,N,K method). The normal force on the complete configuration is:

$$C_N = C_{N_{B(W,T)}} + C_{N_{W(B)}} + C_{N_{T(B)}}$$

The total body normal force is given by:

$$C_{N_{B(W,T)}} = C_{N_{B_\alpha}}^{(0)} \left( \frac{A_B}{A_{ref}} \right) + K_{B(W)} \alpha C_{N_{\alpha_W}}^{(0)} \left( \frac{A_W}{A_{ref}} \right) + K_{B(T)} \alpha C_{N_{\alpha_T}}^{(0)} \frac{A_T}{A_{ref}} \quad (47)$$

$$- \frac{4\Gamma_m}{A_{ref}U} \left[ \frac{(f_W^2 - r_W^2)}{f_W} - f_T + \frac{r_T^2}{\sqrt{f_T^2 + r_T^2}} \right]$$

The first term is the potential contribution of the nose, while the second and third are the lift carryover onto the body from the wing and tail. The last term reflects the effect of trailing vortices from the wing on the body. The normal force on the wing is:

$$C_{N_{W(B)}} = K_{T(B)} \alpha C_{N_{\alpha_W}}^{(0)} \left( \frac{A_W}{A_{ref}} \right) \quad (48)$$

while that on the tail includes an additional term to account for the wing vortex-tail interaction:

$$C_{N_{T(B)}} = K_{T(B)} \alpha C_{N_{\alpha_T}}^{(0)} \left( \frac{A_T}{A_{ref}} \right) +$$

$$\left[ \frac{C_{N_{\alpha_W}}^{(0)} C_{N_{\alpha_T}}^{(0)} i (s_T - r_T)}{2\pi R_T (f_W - r_W)} \right] K_{W(B)} \alpha \left( \frac{A_W}{A_{ref}} \right)$$

The factor  $i$  can be evaluated from charts in References (74) and (117). Usually the wing vortex is assumed to move along a straight path parallel to  $U$  and intersecting the center of the wing alone vorticity.

The empirical predictive methods available in the literature generally fall into three classes:

1. Crossflow Methods: A noncircular body crossflow drag term is added to the linear theory.
2. Correlation of force measurements using data on isolated components and complete configurations.

### 3. Extension of the P-N-K method to high incidences.

Jorgensen<sup>65</sup> has extended the crossflow approach to missiles with wings and tails. The normal force on the complete configuration is written:

$$C_N = (C_N)_{P-N-K} \frac{\sin 2\alpha}{2\alpha} + \frac{n C_{dc} \sin^2 \alpha}{A_{ref}} \int_0^{L_t} \left( \frac{C_n}{C_{n_0}} \right)_{Newt} dx \quad (50)$$

The first term is the linear contribution which is determined using the P-N-K method. Here  $C_{dc}$  is the crossflow drag coefficient of a circular cylinder and  $(C_n/C_{n_0})_{Newt}$  is the ratio of the crossflow drag of the winged configuration crosssection to that of a circular crosssection determined using Modified Newtonian theory. Jorgensen has compared the results of the above method to experiment and has gotten fairly good agreement on center of pressure but poor agreement with normal force measurements. The problem is with the linear term which overpredicts the normal force at incidences greater than 10 to 15 degrees. In the vicinity of 90 degrees angle of attack, the linear term will be near zero and the above method should produce improved results. The principal advantage of this technique is its simplicity. However, this approach has not been extensively used by other workers..

Methods based on a correlation of force measurements on complete configurations and isolated components are generally easily applied and relatively accurate. However, they are usually applicable to a restricted range in flow conditions and missile geometries. The correlative expressions are not based on a detailed understanding of the flow field which circumvents the need to model flow field vortices. However, it is these structures that produce much of the observed nonlinearity at high incidence and an extensive data base is thus needed in order to obtain accurate results. In addition, the applicability of the predictive method is limited to the bounds of the data base used to develop it. The available predictive methods of this type are limited to body-tail configurations. Extension to a wing-body-tail configuration would greatly increase the number of parameters effecting the aerodynamic coefficients and a very large data base would be required.

Recent examples of methods based on a correlation of force measurements are provided by Baker<sup>68</sup> and Aiello.<sup>58</sup> In both of these studies force measurements were taken on isolated fins and on fins attached to the missile configuration allowing the influence of the body on the fin loads to be directly measured. Both approaches are restricted to body tail configurations and Baker's method is applicable over the angle attack range of 0 to 180 degrees for Mach numbers between .6 and 1.3 but is restricted to unbanked configurations. Here the normal force on the complete configuration is written:

$$C_N = C_{N_B} + C_{N_F} \left( \frac{A_F}{A_{ref}} \right) + \Delta C_{N_{FOB}} \left( \frac{A_F}{A_{ref}} \right) + \Delta C_{N_{BOF}} \left( \frac{A_F}{A_{ref}} \right) \quad (51)$$

The calculation of body alone normal force,  $C_{N_B}$ , is accomplished using a crossflow method while the fin normal force is expressed by Eq. (39). The interaction terms,  $\Delta C_{N_{BOF}}$  and  $\Delta C_{N_{FOB}}$ , which represent the increment in tail lift due to the presence of the body and change in body normal force due to the presence of the fin respectively, are expressed by the functions:

$$\beta_0 + \beta_1 \lambda + \beta_2 \lambda^2 + \beta_3 R + \beta_4 \left( \frac{d}{2s} \right) \quad (52)$$

The coefficients  $\beta_0$  to  $\beta_4$  are provided in tabular form as a function of Mach number, Reynolds number and angle of attack and were obtained using a regression analysis of the data base. Comparison between calculated results and experimental data not used to formulate the predictive method indicates an overall prediction accuracy of 10% to 15%. Worse results are obtained at incidences near 90° where support interference may occur.

The predictive method of Aiello<sup>58</sup>, which is an extension of the work in references 49 and 118, is applicable at arbitrary roll angles to incidences of 45 degrees and over the Mach number range .6 to 3. The total normal force on the complete configuration is:

$$C_{N_{TOTAL}} = C_{N_B} + \sum_{j=1}^4 C_{N_{T_j}} R_{T_B}(\phi_j) \sin \phi_j + I_{BT} \quad (53)$$

The first term is the body-alone contribution which is made up of an inviscid and a viscous term and is calculated using a power series variation of the crossflow analogy. The second term represents the normal force on the tail in the presence of the body while the third is the residual which can be interpreted as the force carry over from the wing on to the body. The fin normal force is calculated using Aiello's method presented in Section 3.2.1. To determine  $R_{T_B}$  and  $I_{BT}$ , the data was examined to establish visible trends. The general strategy was to use power series in  $\phi$  and  $\alpha$  and to apply separate fitting functions on the windward and leeward sides. Comparison between this method and data from other studies indicates an overall prediction accuracy of  $\pm 7.5\%$ . However the method tends to underpredict normal force at high

incidence.<sup>119</sup>

To adapt the P-N-K method to high angles of attack several modifications are required:

(1) The viscous or nonlinear body force must be included in  $C_{B(W,T)}$ . If the crossflow analogy is used, the first term in Eq. (47) is replaced by Eq. (19). An alternate approach is to use the experimentally determined vortex paths and strengths to calculate the viscous force via the impulsive flow theorem (Eq. (35)). This technique is only valid for the angle of attack - Mach number range for which well-defined, steady vortices exist (see Fig. 2).

(2) The effect of body vortices on the missile wings and tail should be accounted for, particularly if banked configurations are to be considered.

(3) The lift or normal force coefficient of wing or tail surfaces should be estimated using nonlinear theories or data as discussed in Section 3.2.

(4) The interference factors ( $K_{W(B)}$ ,  $K_{B(W)}$ ) should be estimated using nonlinear theories or data.

An early extension of the P-N-K method to unbanked missiles at high angles of attack is provided by Howard, Brooks and Saffell<sup>191</sup> using considerations (1) and (3). The wing and tail lift coefficients are expressed using Eq. (38) and Figure 86. Only the potential term is assumed to participate in the interference effects. Hence for the wing or tail:

$$C_{L_{W(B)}} = K_{W(B)} C_{L_{\alpha_W}}(0) \left( \frac{A_W}{A_{ref}} \right) \sin \alpha \cos \alpha + C_{dc} \sin^2(\alpha) \cos(\alpha) \left( \frac{A_W}{A_{ref}} \right) \quad (54)$$

The carryover lift on the body due to either the wing or tail is

$$K_{B(W)} C_{L_{\alpha_W}}(0) \sin \alpha \cos \alpha \frac{A_W}{A_{ref}} \quad (55)$$

and the slender body theory values of interference parameters are used. Predictions, which have been compared to experimental data on body-tail configurations in reference 68, are most accurate in supersonic flow. In the subsonic and transonic regime, normal force is overpredicted and center of pressure is only accurate to within 1/2 caliber.

A more recent example of the extension of the P-N-K type of approach to wing-body-tail configurations is provided in reference 23. This method is applicable to angles of attack of 45 degrees at arbitrary roll orientations. Central to this approach is the experimentally determined normal force coefficients for wings alone. The basic idea is to determine the effective or equivalent angle of attack of a missile fin or wing which takes into account body interference, vortex influence and roll orientation. The resulting expression for equivalent angle of attack is:

$$\tan(\alpha_{eq}) = \frac{K_{W(B)} \sin \alpha_c \sin \phi + \frac{4}{AR} K_{\phi} \sin^2 \alpha_c \sin \phi \cos \phi + \cos \alpha_c \tan(\Delta \alpha_{eq,v})}{\cos \alpha_c} \quad (56)$$

where the first term accounts for body interference, the second fin yaw induced by roll orientation and the third for vortex influence. It is assumed that  $K_{W(B)}$  and  $K_{\phi}$  are exclusively a function of missile angle of attack which allows these constants to be determined from experimental data once the vortex influence is assessed. The positions and strengths of body vortices are calculated using a multi-vortex model (see Section 3.1.2). The slender body ratio of  $K_{W(B)}/K_{B(W)}$  is used to determine the lift carry over onto the body. The nonlinear forces on the missile body are determined using a combination of the body vortex models, similar to those discussed in section 3.1.2, and crossflow methods.

The important aspect of the above method is that it postulates a physical model of the flow and then uses experimental data to determine unknown parameters. The net result is an approach which attempts to model the nonlinearities (i.e. vortex effects) of the problem. The great advantage of this technique is that it can be developed with less experimental data and can be extrapolated with more confidence. A disadvantage is that it is more difficult to apply. Comparison of predictions for total configuration and fin loads with experiment for  $M < 1.3$  indicate relatively good agreement for cases without control deflection. Also, situations where canard vortices pass very close to the afterbody combination can not be handled accurately. For Mach numbers greater than 1.3 suitable test cases are not available.

### 3.3.3 Semi-Empirical Methods for Complete Configurations

These types of methods combine the semi-empirical and theoretical techniques discussed in Section 3.1 and 3.2 for isolated components.

A method of this type has been developed by Mendenhall and Nielsen<sup>15</sup> which applies to incidences where body vortices are symmetric. The position and strength of body

vortices upstream of the wing leading edge are assumed described by empirical data correlations. At this point the strengths of the vortices are fixed and their paths over the wing are traced using Eq. (32) with vortex velocities being obtained through the use of conformal transformation techniques. This allows the velocity induced on the wing by the body and body vortices to be determined. A lifting surface program is applied to the isolated wing using these induced velocities at each control point. Thus, the calculated lift takes into account body and vortex interference. The particular lifting surface program used applies the leading edge suction analogy as described in Section 3.2.2 to determine the nonlinear contribution to the lift. In the supersonic case the lift carryover from the wing to the body is estimated using linear methods. Subsonically it is calculated using the vortex lift theorem (Nielsen pp. 138 to 140). Once the potential and nonlinear lift on the wing has been determined, the shed vorticity is divided into two vortices. One vortex includes the effect of the potential lift while the second accounts for the leading and side edge separations. The normal force on the afterbody is calculated by tracing the wing and body vortices back to the missile tail and using the impulsive flow theorem (Eq. (35)). The tail is treated in the same fashion as the wing. In this case there are at least three pairs of vortices in the crossflow plane.

Nikolitsch<sup>82</sup> reports the development of a method along similar lines. In this case the body vortex positions and strengths are calculated by the concentrated vortex model of reference 81. The wing is modeled using a low aspect ratio lifting surface technique developed by Gersten which features vorticity trailing from the wing at an orientation  $\alpha/2$  with respect to the wing planform. The velocities calculated from the vortex model are imposed on the wing in order to obtain the solution. The lift carry over from the wing to the body is estimated using the methods of reference 117. Results compare favorably with experiment up to incidences of 20 to 35 degrees, depending on wing location.

#### 4. CONCLUSION

The separated flow field about a missile at high angles of attack is extremely complex and the accompanying vortex structures create nonlinear loads. Linear theories which are valid at low incidences no longer apply and a tractable theoretical basis for calculating missile aerodynamic characteristics is not available. This has led to the creation of predictive methods which are dependent on experimental data and progress in developing such techniques is closely related to developing a quantitative description of flow about and forces on missiles at high incidence. Unfortunately, obtaining accurate, repeatable data has been a difficulty in itself. Force measurements which are the easiest, quantitative data to obtain are subject to support interference problems. Strut mounts on bodies and reflection plate supports for fins have recently been found to introduce substantial error at very high incidences. Flow field velocity measurements, useful for determining vortex strength and position, are extremely tedious and it is difficult to generate sufficient information to draw general conclusions. Particularly in subsonic flow where viscous effects are dominant, repeatability of some results is difficult to achieve. Principal examples of this are the magnitude of yaw forces induced by asymmetric body vortices and the incidence of vortex bursting on wings. In the case of the induced yaw forces there is some evidence to indicate that free stream turbulence levels and error in the model construction on the order of machining tolerance may influence results. For the most part, a qualitative understanding is available of the flow field about and forces on missiles at high incidence. A necessary step in improving predictive methods is to increase the amount of quantitative data available.

Predictive methods for bodies alone are fairly well in hand. Analogies with cylinders have provided a basic framework for constructing simple, reliable, empirical methods. These methods are of least utility in subsonic flow where the influence of Reynolds number is important. More elaborate methods have been developed which predict body vortex strength and position and then calculate forces from this information. Although such approaches have been reasonably successful, they require substantial computational effort and the principal justification for their development is in conjunction with complete configuration analysis. Here the calculated vortex position and strength is used to determine boundary conditions for wing or fin analysis.

Empirical methods for calculating the forces and moments on isolated fins have been developed that span the incidence range from 0 to 180 degrees. The crossflow approach is not found to be useful and polynomial fits are used to correlate the experimental data. Above stall incidences, the accuracy of these methods is questionable. The data base used to develop the predictive equations was measured using reflection plate mounted fins and there is evidence to suggest that this type of support produces a premature wing stall. Lifting surface theories have also been developed which estimate the nonlinear increase in wing lift at high incidences due to leading and side edge separation. Such methods are in principal feasible up to the incidence at which stall occurs.

Predictive methods applicable to complete configurations are generally restricted in scope. Techniques valid over the incidence range 0 to 90 degrees are either very approximate or limited to unbanked body-tail configurations. Several predictive methods applicable to incidences of 45 degrees are available for arbitrary roll angle. Most of these techniques are strongly dependent on force measurements. A few semi-empirical models have been developed which combine body alone vortex models with nonlinear lifting surface theories. Such methods are limited to incidences below stall.

## REFERENCES

1. Jorgensen, L. H., NASA, "Prediction of Static Aerodynamic Characteristics for Space-Shuttle-Like and Other Bodies at Angles of Attack from  $0^\circ$  to  $180^\circ$ ," 1973, TN D-6996
2. Wardlaw, A. B., Jr., and Morrison, A. M., NSWC, "Induced Side Forces on Bodies of Revolution at High Angle of Attack," 1975, TR-75-176
3. Schwabe, M., NACA, "Pressure Distribution in Nonuniform Two-Dimensional Flow," 1943, TM 1039.
4. Sarpkaya, T., "Separated Flow About Lifting Bodies and Impulsive Flow About Cylinders," *AIAA Journal*, Vol. 4, No. 3, pp 414-420, 1966
5. Bingham, H. H., Weimer, D. K. and Griffith, W., Princeton University, "The Cylinder and Semicylinder in Subsonic Flow," 1952, TR 11-13
6. Sarpkaya, T., "Impulsive Flow Analogy-Analysis and Experiment," Summary of Working Group Meeting on High Angle of Attack Missile Aerodynamics, March 1978, NASA Langley
7. Thomson, K. D., WRE, "The Estimation of Viscous Normal Force, Pitching Moment, Side Force and Yawing Moment on Bodies of Revolution at Incidences up to  $90^\circ$ ," 1972, Report-782 (WR&D)
8. Burtnall, W. J. and Loftin, L. K., Jr., NACA, "Experimental Investigation of the Pressure Distribution about a Yawed Circular Cylinder in the Critical Reynolds Number Range," 1951, TN 2463
9. Foley, J. E., Chrysler Corp., "Results of a Study of Mach Number and Reynolds Number Effects on the Crossflow Drag Characteristics of Ogive-Cylinders and Ogive-Cylinder-Frustrum-Cylinders at Angles of Attack up to 30 Degrees," 1971, CR-61365
10. Clark, W. H., "Body Vortex Formation on Missiles in Incompressible Flows," 1977, AIAA Paper No. 77-1154
11. Yanta, W. J. and Wardlaw, A. B., "Laser Doppler Velocimeter Measurements of Leeward Flowfields on Slender Bodies at Large Angle-of-Attack," 1977, AIAA Paper 77-660
12. Foley, J. E., Chrysler Corp., "Results of a Study of Mach Number and Reynolds Number Effects on the Lee Side Vortex Flow Field Characteristics of an Ogive-Cylinder-Frustrum-Cylinder at Angles of Attack to 25 Degrees," 1972, TN-AP-72-565
13. Oberkampf, W. L., Bartel, T. J. and Martindale, W. R., "Supersonic Flow Measurements in the Body Vortex Wake of an Ogive Nose Cylinder," 1978, AIAA Paper 78-787
14. Oberkampf, W. L., Bartel, T. J., "Symmetric Body Vortex Wake Characteristics in Supersonic Flow," 1978, AIAA Paper 78-1337
15. Mendenhall, M. R. and Nielsen, J. N., NFAR, "Effect of Symmetrical Vortex Shedding on the Longitudinal Aerodynamic Characteristics of Wing-Tail-Body Combinations," 1975, NASA CR-2473
16. Agnone, A. M., Zakkay, V. and Tory, E., "Aerodynamics of Slender Finned Bodies at Large Angles of Attack," June 1977, AIAA Paper 77-666
17. Feldhuhn, R. H., Winkelmann, A. E. and Pasiuk, L., "An Experimental Investigation of the Flowfield Around a Yawed Cone," *AIAA Journal*, 9, 6, June 1971, pp 1074-1081
18. Hsieh, Tsuying, "Low Supersonic Flow Over Hemisphere-Cylinder at Incidence," *JSR*, 14, 11, Nov 1977, pp 662-668
19. Rainbird, W. J., Crabbe, R. S., Peake, D. J. and Meyers, R. F., "Some Examples of Separation in 3-Dimensional Flows," *CAS Journal*, 12, 10, Dec 1966, pp 409-422
20. Schindel, L. H., MIT Aerophysics Laboratory, "Effect of Vortex Separation on Lifting Bodies of Elliptic Crosssection," Sep 1965, TR 118
21. Deffenbaugh, F. D. and Koerner, W. G., "Asymmetric Vortex Wake Development on Missiles at High Angles of Attack," *JSR*, 14, 3, Mar 1977, pp 155-162
22. Atraghji, E. G., National Aeronautics Establishment, "The Influence of Mach Number, Reynolds Number, Semi-nose Angle and Roll Rate on the Development of Forces and Moments over a Series of Long Slender Bodies of Revolution at Incidence," 1967, Report 5X5/0020
23. Nielsen, J. N., Hensch, M. J. and Smith, C. A., NEAR, "A Preliminary Method for Calculating the Aerodynamic Characteristics of Cruciform Missiles to High Angles of Attack Including Effects of Roll Angle and Control Deflection," Nov 1977, ONR-CR215-226-4F
24. Mello, J. F., "Investigation of Normal Force Distribution and Wake Vortex Characteristics of Bodies of Revolution at Supersonic Speeds," *J. Aero-Space Sci.*, 26, 1959, pp 155-168
25. Jorgensen, L. H. and Perkins, E. W., NACA, "Investigation of Some Wake Vortex Characteristics of an Inclined Ogive-Cylinder Body at Mach Number 2," 1955, Report 1371
26. Fiechter, M., Deutsch-Franzosisches Forschungsinstitut, Saint-Louis, "Über Wirbelsysteme an Schlanken Rotationskörpern und Ihren Einfluss auf die Aerodynamischen Beiwerte," 1966, Bericht 10/66
27. Tingley, B. E. and Allen, C. O., NASA, "An Investigation of the Normal Force and Vortex Wake Characteristics of an Ogive-Cylinder Body at Subsonic Speeds," 1962, TN D-1207
28. Fidler, J. E., Schwind, R. G. and Nielsen, J. N., "Investigation of Slender-Body Vortices," *AIAA Journal*, 15, 12, Dec 1977, pp 1736-41
29. Grosche, F. R., "Wind Tunnel Investigation of the Vortex System Near an Inclined Body of Revolution With and Without Wings," 1971, AGARD, *Aerodynamic Interference*, pp 2-1, 2-13
30. Gowens, F. E. and Perkins, E. W., NACA, "Study of the Effects of Body Shape on the Vortex Wakes of Inclined Bodies at  $M = 2$ ," 1953, RM A53117
31. Gapcynski, J. P., NACA, "An Experimental Investigation of the Flow Phenomena Over Bodies at High Angles of Attack at a Mach Number of 2.01," 1955, NACA RM L55H29
32. Thomson, K. D. and Morrison, D. F., "The Spacing, Position and Strength of Vortices in the Wake of Slender Cylindrical Bodies at Large Incidence," *JFM*, 50, 4, 1971, pp 751-783

33. Clark, W. C. and Nelson, R. C., "Body Vortex Formation on Missiles at High Angles of Attack," 1976, AIAA Paper 76-65
34. Kruse, R. L., "Influence of Spin Rate on Side Force of an Axisymmetric Body," *AIAA Journal*, 16, 4, Apr 1978, pp 415-16
35. Lamont, P. J. and Hunt, B. L., "Pressure and Force Distributions on a Sharp-nosed Circular Cylinder at Large Angles of Inclination to a Uniform Subsonic Stream," *JFM*, 76, 3, 1976, pp 519-559
36. Milne-Thomson, L. W., *Theoretical Hydrodynamics*, MacMillan and Co., Limited, 1938
37. Pick, G., "Investigation of Side Forces on Ogive-Cylinder Bodies at High Angles of Attack in the  $M = .5$  to  $1.1$  Range," 1971, AIAA Paper No. 71-570
38. Wardlaw, A. B. and Morrison, A. M., "Induced Side Forces at High Angles of Attack," *JSR*, 13, 10, Oct 1976, pp 589-593
39. Keener, E. R. and Chapman, G. T., "Onset of Aerodynamic Side Forces at Zero Sideslip on Symmetric Forebodies at High Angles of Attack," 1974, AIAA Paper 74-770
40. Keener, E. R., Chapman, G. T. and Kruse, R. L., "Effects of Mach Number and After-body Length on Onset of Asymmetric Forces on Bodies at Zero Sideslip and High Angles of Attack," 1976, AIAA Paper No. 76-66
41. Smith, L. H. and Nunn, R. H., NPS, "Aerodynamic Characteristics of an Axisymmetric Body Undergoing a Uniform Pitching Motion," 1975, NPS-59Nn75021
42. Reding, J. P. and Ericson, L. E., "Maximum Vortex-Induced Side Forces on Slender Bodies," 1977, AIAA Paper 77-1155
43. Fleeman, E. L. and Nelson, R. C., "Aerodynamic Forces and Moments on a Slender Body with a Jet Plume for Angles of Attack up to  $180^\circ$  Degrees," 1974, AIAA Paper No. 74-110
44. Lamont, P. J. and Hunt, B. L., "Prediction of Aerodynamic Out-of-Plane Forces on Ogive-Nosed Circular Cylinders," *JSR*, 14, Jan 1977, pp 38-44
45. Clark, W. H., Peoples, J. R. and Briggs, M. M., "Occurrence and Inhibition of Large Yawing Moments During High Incidence Flight of Slender Missile Configurations," *JSR*, 10, 8, 1973, pp 510-519
46. Rao, D. M., "Side Force Alleviation on Slender Pointed Bodies at High Angles of Attack," 1978, AIAA Paper 78-1339
47. Parker, A. G., "Aerodynamic Characteristics of Slender Wings with Sharp Leading Edges - A Review," 13, 3, Mar 1976, pp 161-8
48. Neilsen, J. N., "Nonlinearities in Missile Aerodynamics," Jan 1978, AIAA Paper No. 78-20
49. Fidler, J. E. and Bateman, M. C., Martin Marietta, "Aerodynamic Methodology (Isolated Fins and Bodies)," 1973, OR 12,399
50. Wentz, W. H. and Kohlman, D. L., U. of Kansas Center for Research, "Wind Tunnel Investigations of Vortex Breakdown on Slender Sharp-Edged Wings," 1968, FRL 68-013
51. Polhamus, E. C., "Predictions of Vortex-Lift Characteristics by a Leading-Edge Suction Analogy," *J. of Aircraft*, 8, 4, 1971, pp 193-199
52. Stahl, W., Hartman, K., and Schneider, W., "Force and Pressure Measurements on a Slender Delta Wing at Transonic Speeds and Varying Reynolds Number," AGARD Conference on Facilities and Techniques for Aerodynamic Testing at Transonic Speeds and High Reynolds Number, 1971, Pre-Print No. 83
53. Nathman, J. K., Norton, D. J., and Rao, B. M., Texas A&M Research Foundation, "An Experimental Investigation of Incompressible Flow Over Delta and Double Delta Wings," Dec 1976, Technical Report
54. Squire, L. C., "Flow Regimes Over Delta Wings at Supersonic and Hypersonic Speeds," *Aeronautical Quarterly*, 27, 1, Feb 1976, pp 1-14
55. Wickens, R. H., Nat. Res. Council of Canada, "The Vortex Wake and Aerodynamic Load Distribution of Slender Rectangular Plates. The Effects of  $20^\circ$ -Degree Bend at Midchord," Aero. Report 1966
56. Winter, H., "Flow Phenomena on Plates and Airfoils of Short Span," 1936, NACA-TM-798
57. Hemsch, M. J., Smith, C. A., Nielsen, J. N. and Perkins, S. C., Jr., "Calculation of Component Forces and Moments of Arbitrarily Banked Cruciform Missiles with Control Deflection," Nov 1976, ONR-CR215-226-3
58. Aiello, G. F., Martin Marietta, "Aerodynamic Methodology (Bodies with Tails at Arbitrary Roll Angles) (Transonic and Supersonic)," April 1976, OR 14,145
59. Fidler, J. E. and Bateman, M. C., "Asymmetric Vortex Effects on Missile Configurations," *JSR*, 12, 11, pp 674-681, 1975
60. Dietz, W. E., Jr. and Alstatt, M. C., "Experimental Investigation of Support Interference on an Ogive Cylinder at High Incidence," Jan 1978, AIAA Paper No. 78-165
61. Alstatt, M. C. and Dietz, W. E., Jr., AEDC, "Support Interference on an Ogive-Cylinder Model at High Angles of Attack in Transonic Flow," March 1978, AEDC-TR-78-8
62. Baker, W. B., AEDC, "Static Aerodynamic Characteristics of a Series of Generalized Slender Bodies with and without Fins at Mach Numbers from  $.6$  to  $3.$  and Angles of Attack from  $0$  to  $180^\circ$  Degrees," May 1976, AEDC-TR-75-124
63. Atraghji, E., "A Method for Estimating the Loading Distribution on Long Slender Bodies of Revolution at High Angles of Attack in Incompressible Flow," Sep 1976, Conference Proceedings No. 204 on Prediction of Aerodynamic Loading
64. Goldstein, S., *Modern Developments in Fluid Dynamics*, Oxford, The Clarendon Press, Vol. 2, 1938, pp 439-440
65. Jorgensen, L. H., NASA, "Prediction of Static Aerodynamic Characteristics for Slender Bodies Alone and With Lifting Surfaces to Very High Angles of Attack," Sep 1977, NASA TR-R-474
66. Allen, H. J., NACA, "Estimation of the Forces and Moments on Inclined Bodies of Revolution of High Fineness Ratio," RM A9126, 1949
67. Esch, H., Institut für Angewandte Gasdynamik, "Der Einfluss der Reynoldszahl auf die Normalkraftcharakteristik schlanker zylindrischer Rumpfe," 1975, DLR-FB 75-09

68. Baker, W. B., An Aerodynamic Coefficient Prediction Technique for Slender Bodies with Low Aspect Ratio Fins at Transonic Mach Numbers and Angles of Attack to 180 Degrees, U. of Tennessee, Ph.D. Thesis, 1976
69. U. S. A. F. STABILITY & CONTROL DATCOM, Flight Control Division, AFFDL, Wright Patterson AFB, Ohio, 1960, revised 1975
70. Kelly, H. R., "The Estimation of Normal Force, Drag, and Pitching Moment Coefficients for Blunt Based Bodies of Revolution at Large Angles of Attack," J. Aeronautical Science, Vol. 21, No. 8, Aug 1954
71. Wardlaw, A. B., "Survey of High Incidence Predictive Methods," Proceeding of the Third Meeting of the Technical Cooperation Program, Naval Postgraduate School, Monterey, Calif., July 1976, pp 1-69
72. Lamont, P. J., and Hunt, B. L., "Out-of-Plane Force on a Circular Cylinder at Large Angles of Inclination to a Uniform Stream," Aeronautical Journal, Jan 1973, pp 41-45
73. Kao, H. C., "Side Force on Unyawed Slender Inclined Aerodynamic Bodies," J. Aircraft, 12, 3, Mar 1975, pp 142-150
74. Nielsens, J. N., Missile Aerodynamics, New York, N. Y., McGraw-Hill Book Co., 1960
75. Schindel, L. H. and Chamberlain, T. E., MIT Aerophysics Laboratory, "Effects of Vortex Separation on Lifting Bodies of Elliptic Cross Section," 1967, TR 138
76. Sarpkaya, T., "An Analytic Study of Separated Flows about Circular Cylinders," J. Basic Engineering, Transactions of ASME, 1968, pp 511-520
77. Marshall, F. J. and Deffenbaugh, F. D., "Separated Flow Over a Body of Revolution," J. Aircraft, 12, 2, 1975, pp 78-85
78. Bryson, A. E., "Symmetric Vortex Separation on Circular Cylinders and Cones," J. Applied Mechanics, Vol. 26, Dec 1959, pp 643-648
79. Schindel, L. H., "Effects of Vortex Separation on the Lift Distribution on Bodies of Elliptic Cross Section," J. Aircraft, Vol. 6, No. 6, 1969, pp 537-543
80. Kuhn, G. D., Spangler, S. B., and Nielsen, J. N., NEAR, "Theoretical Study of Vortex Shedding From Bodies of Revolution Undergoing Coning Motion," Oct 1969, CR-1448
81. Wardlaw, A. B., Jr., "Prediction of Yaw Force at High Angle of Attack," AIAA Journal, 12, 8, pp 1142-1144, 1974
82. Nikolitsch, D., "Normal Force and Pitching Moment Coefficients of Bodies and Wing-Body Combinations at Very High Angles of Attack," 1978, AIAA Paper No. 78-63
83. Wardlaw, A. B., Jr., "Multivortex Model of Asymmetric Shedding on Slender Bodies at High Angle of Attack," Jan 1975, AIAA Paper No. 75-123
84. Clements, R. R., "Flow Representation, Including Separated Regions, Using Discrete Vortices," Computational Fluid Dynamics, AGARD-VKI Lecture Series, March 1977
85. Angelucci, S. B., "A Multivortex Method for Axisymmetric Bodies at Angle of Attack," J. Aircraft, Vol. 8, No. 12, 1971, pp 959-966
86. Fink, P. T. and Soh, W. K., "Calculation of Vortex Sheets in Unsteady Flow and Applications in Ship Hydrodynamics," Tenth Symp. Naval Hydrodynamics, Cambridge, Mass., U.S.A., 1974
87. Van Tuyl, A., Private Communication, Applied Mathematics Branch, NSWC/WOL, Silver Spring, Maryland
88. Walitt, L. and Trulio, J. G., NASA, "A Numerical Method for Computing Three-Dimensional Viscous Supersonic Flow Fields About Slender Bodies," Nov 1971, NASA CR-1963
89. Bartlett, G. E. and Vidal, R. J., "Experimental Investigation of Influence of Edge Shape on the Aerodynamic Characteristics of Low Aspect Ratio Wings at Low Speed," J. Aero. Sci., 22, 8, 1955, pp 517-533
90. Eaton, P. T., David Taylor Model Basin, "A Method for Predicting the Static Aerodynamic Characteristic of Flow Aspect-Ratio Configurations," June 1966, DTMB Report 2216
91. Saffel, B. F., Howard, M. L., and Brooks, E. N., NSRDC, "A Method for Predicting the Static Aerodynamic Characteristics of Typical Missile Configurations for Angles of Attack to 180 Degrees," Mar 1971, Report 3645
92. Polhamus, E. C., NASA, "A Concept of the Vortex Lift of Sharp-Edge Delta Wings Based on a Leading-Edge-Suction Analogy," 1966, NASA TN D-3767
93. Polhamus, E. C., NASA, "Charts for Predicting the Subsonic Vortex-Lift Characteristics of Arrow, Delta, and Diamond Wings," 1971, NASA TN D-6243
94. Lamar, J. E., NASA, "Extension of Leading Edge Suction Analogy to Wings with Separated Flow Around the Side Edges at Subsonic Speeds," Oct 1974, NASA TR R-428
95. Brown, C. E. and Michael, W. H., Jr., "Effect of Leading-Edge Separation of the Lift of a Delta Wing," J. Aero. Sciences, 21, 10, 1954, pp 690-694 and 706
96. Brown, C. E. and Michael, W. H., NACA, "On Slender Delta Wings with Leading Edge Separation," NACA TN 3430
97. Mangler, K. W. and Smith, J. H. B., "A Theory of the Flow Past a Slender Delta Wing with Leading Edge Separation," Proc. Roy. Soc. A., 251, 1959, pp 200-217
98. Smith, J. H. B., RAF, "Improved Calculations of Leading-Edge Separation from Slender Delta Wings," Mar 1966, RAF Report No. 66070
99. Smith, J. H. B., "Improved Calculations of Leading-Edge Separation from Slender, Thin, Delta Wings," Proc. Roy. Soc. A., 306, 1968, pp 67-90
100. Levinsky, E. S. and Wei, M. H. Y., Air Vehicle Corp., "Nonlinear Lift and Pressure Distribution of Slender Conical Bodies with Strakes at Low Speed," 1969, NASA CR-1202
101. Levinsky, E. S., Wei, M. H. Y. and Maki, R. L., Air Vehicle Corp., "Theoretical Studies of Vortex Flow on Slender Wing-Body Combinations," Analytic Methods in Aircraft Aerodynamics, NASA SP-228, Oct 1969, pp 113-129
102. Bollay, William, "A Nonlinear Wing Theory and its Application to Rectangular Wings of Small Aspect Ratio," ZAMM, 19, 1, 1939, pp 21-35
103. Gersten, K., "Non-Linear Airfoil Theory for Rectangular Fins in Incompressible Flow," Feb 1959, NASA RF 3-2-59W

104. Gersten, K., "Calculation of Non-Linear Aerodynamic Stability Derivatives of Aeroplanes," Apr 1961, AGARD Rept 342
105. Kuchemann, D., RAE, "A Non-Linear Lifting Surface Theory for Wings of Small Aspect Ratio and Edge Separations," Apr 1955, RAE Rept., Aero 7540
106. Garner, H. C. and Lehrian, D. H., ARC, "Non-Linear Theory of Steady Forces on Wings with Leading-Edge Flow Separation," 1964, ARC R. and M. No. 3375
107. Ermolenko, S. D., "Nonlinear Theory of Small Aspect Ratio Wings," Soviet Aeronautics, (in English), 9, 1966, pp 5-11
108. Mook, D. T., "Maddox, S. A., "Extension of a Vortex-Lattice Method to Include Effects of Leading-Edge Separation," J. Aircraft, 11, 2, 1974, pp 127-128
109. Kandil, O. A., Mook, D. T. and Nayteh, A. H., "Nonlinear Prediction of the Aerodynamic Loads on Lifting Surfaces," J. Aircraft, 13, 1, 1976, pp 22-8
110. Kandil, O. A., Mook, D. T. and Nayteh, A. H., "Subsonic Loads on Wings having Sharp Edges and Tips," J. Aircraft, 13, Jan 1976, p 62-3
111. Johnson, F. T., Lu, P., Brune, G. W., Weber, J. A., "An Improved Method for the Prediction of Completely Three-Dimensional Aerodynamic Load Distributions of Configurations with Leading Edge Vortex Separation," 1976, AIAA Paper No. 76-4
112. Kuhlman, J., "Load Distribution on Slender Delta Wings having Vortex Flow," J. Aircraft, 14, 7, July 1977, pp 699-702
113. Thomson, K. D., "Subsonic Wing-Body Interference for Missile Configurations at Large Angles of Attack," Aeronautical Quarterly, Aug 1977, pp 163-175
114. Hensch, M. J., Nielsen, J. N., Smith, C. A., and Perkins, S. C., "Component Aerodynamic Characteristics of Banked Cruciform Missiles with Arbitrary Control Deflections," 1977, AIAA Paper 77-1153
115. Howard, M. L., Brooks, E. N., Jr. and Saffell, B. F., Jr., "A Method for Predicting the Static Aerodynamic Characteristics of Typical Missile Configurations for Angles of Attack to 180 Degrees," Aug 1970, AIAA Paper 70-981
116. Tipping, Derrick E., et al., Martin Marietta, "Computer-Aided Missile Synthesis (CAMS)," June 1972, OR 12,034
117. Pitts, W. C., Nielsen, J. N., and Kattari, G. E., NACA, "Lift and Center of Pressure of Wing-Body-Tail Combinations at Subsonic, Transonic and Supersonic Speeds," 1957, NACA Report 1307
118. Fidler, J. E., Bateman, M. C., Martin Marietta, "Aerodynamic Methodology (Body with and without Tails in Transonic Flow)," Jan 1974, OR 12,851
119. Spring, D. J., Derrick, J. N., Winn, G.C., Redstone Arsenal, "An Assessment of Martin-Marietta High Angle of Attack Aerodynamic Methodology for Body Tail Missiles," June 1976, TR-RD-76-33

TABLE 1

Description of Key Points on the Side Force Distribution Curves  
 Point is Determined by the Expression in the Definitions Column  
 Unless, Limiting Value is Exceeded, in which Case it Applies

Position	Definition	Limiting Value
$\bar{\tau}_A$	$3 + .052\alpha$	$7 - \ell_n$
$\bar{\tau}_B$	$\bar{\tau}_A + (\bar{\tau}_C - \bar{\tau}_A)(.6 + .1 \cos 2\alpha)$	
$\bar{\tau}_C$	$11 + 4.7 \tan \alpha$	$21 - 2\ell_n$
$\bar{\tau}_D$	$.5(\bar{\tau}_C + \bar{\tau}_E)$	
$\bar{\tau}_E$	$\bar{\tau}_C + 4. + 2.6 \tan \alpha$	
$\bar{\tau}_F$	$.5(\bar{\tau}_G + \bar{\tau}_E)$	
$\bar{\tau}_G$	$\bar{\tau}_E + 4. + 2.6 \tan \alpha$	



Table 2

Originating Facility or Author	Related Reference	Mach Range	Limitations Incidence Range	Configuration	Approach	Calculated Quantities	Date	Comments
CAMS116 (Martin Marietta)	None	$.5 \leq M \leq .9$ $M \approx 1$ $1.2 \leq M \leq 10$	$0 \leq \alpha \leq 180$	Unbanked wing-body-tail with planar, triform, cruciform (both + and x), and conventional tail (A). Control deflections allowed	Extended P-N-K	All pitch plane loads and centers of pressure	June 1972	Comparison in reference 68 shows relatively accurate CN throughout Mach number range on body-tail configuration
NSRDC91	115	$BR \leq 10$	$0 \leq \alpha \leq 180$	Unbanked wing-body-tail with control deflections	Extended P-N-K	All pitch plane loads and centers of pressure	Mar 1971	Comparison in reference 68 shows CN over predicted in transonic and subsonic flow on B-T configurations. Xcp accurate to $\pm .5$ calibers
Thomson113	6	Subsonic	$0 \leq \alpha \leq 90^\circ$	Unbanked wing-body. Control deflections not considered	Extended P-N-K	Pitch plane loads except for drag	Aug 1977	
Nielsen, Hensen and Smith13	114	$.8 \leq M \leq 3$	$0 \leq \alpha \leq 45^\circ$	Arbitrary roll orientation of wing-body-tail configurations with control deflections	Extended P-N-K	Pitch and yaw plane loads and moments and rolling moment	Nov 1977	Insufficient data to check out method completely. Test cases for $M < 1.3$ indicate satisfactory results for no control deflection.
Aiello58	49,118	$.6 < M < 3.0$	$0 \leq \alpha \leq 45^\circ$	Arbitrary roll of body tail configuration without control deflection	Force Data Base	All pitch plane loads and moments	Apr 1976	Deemed of acceptable accuracy for design trade-off studies19
Baker68	62	$.6 < M < 1.3$	$0 \leq \alpha \leq 180^\circ$	Unbanked body-tail. No control deflection	Force Data Base	All pitch plane loads and moments except drag	Aug 1976	
Jorgensen65	1	arbitrary	$0 \leq \alpha \leq 180^\circ$	Unbanked wing-body tail. No control deflections	Crossflow	All pitch plane loads, except drag	Sept 1977	Overpredicts normal force

## ÉCOULEMENTS DE CULOT

par Jean DELFRY et Maurice SIRIEIX

Office National d'Etudes et de Recherches Aéronautiques (ONERA)  
92320 Châtillon (France)

♦

### Résumé

Les phénomènes qui se produisent dans la région du culot sont susceptibles d'avoir une répercussion importante sur les performances et en conséquence la définition d'un missile. Les domaines qu'ils concernent sont nombreux et complexes : traînée de l'arrière-corps, flux de chaleur, interaction écoulement externe - écoulement interne. Le présent exposé est essentiellement centré sur les implications pratiques des phénomènes de culot dans le cas réaliste de couches limites turbulentes et dans un domaine de nombres de Mach excluant l'hypersonique. Également, les problèmes plus spécifiques liés aux lanceurs ne seront que peu ou pas évoqués.

L'exposé est divisé en deux parties principales :

- la première est consacrée à une analyse phénoménologique des écoulements de culot avec ou sans jet propulsif, en subsonique et en supersonique. On examine l'effet des principaux facteurs d'influence : forme du missile, incidence, ailetage, géométrie de la tuyère d'éjection, rapport de détente du jet, facteurs thermiques ... Des méthodes empiriques de corrélations sont présentées.
- la seconde partie porte sur les théories actuellement disponibles pour traiter pratiquement les problèmes de culot. Les principes de base de ces théories sont d'abord exposés dans le cas fondamental et plus simple du recollement sur paroi (méthodes globales ou analytiques, méthodes d'interaction forte). Les extensions aux problèmes de culot en écoulement de révolution sont ensuite présentées : en premier lieu celles applicables au culot sans jet propulsif en supersonique et en subsonique, en second lieu celles qui permettent de traiter les configurations d'arrière-corps avec tuyère propulsive. La validité de ces méthodes est discutée par confrontation avec les résultats expérimentaux disponibles.

Sont également évoqués les moyens mis en oeuvre pour réduire la traînée de culot par injection de masse ou combustion.

## BASE FLOWS BEHIND MISSILES

### Summary

The phenomena taking place around the base of a vehicle can have important repercussions on its performance, and consequently on the design of a missile. The fields they concern are many and complex : afterbody drag, heat flux, interaction between internal and external flows. The present paper is essentially centered on the practical implications of the base flow phenomena in the realistic case of turbulent boundary layers and in a Mach number range up to, but excluding hypersonics. The problems pertaining more specifically to space launchers will also be hardly approached.

The paper is divided into two main parts :

- the first is devoted to a phenomenological analysis of the base flows, with or without propulsive jet, at subsonic and supersonic velocities. The effects of the main factors of influence are surveyed : missile shape, angle of attack, fins, exhaust nozzle geometry, jet expansion ratio, thermal factors, etc... Empirical correlation methods are presented.
- the second part concerns the presently available theories for the practical treatment of base flow problems. The basic principles of these theories are first presented in the fundamental and simplest case of reattachment on a wall (global or analytic methods, strong interaction methods). The extensions to base problems for axisymmetrical flows are then presented : first those applicable to a base without propulsive jet at subsonic and supersonic speed, second those allowing the treatment of afterbody configurations with propulsive nozzle. The validity of these methods is discussed by comparison with available experimental results.

The paper also mentions the means implemented to reduce the base drag by mass injection or combustion.

## INTRODUCTION

Aussi bien aux vitesses subsoniques que supersoniques, la pression  $p_c$  qui s'établit au culot d'un projectile comme d'un missile, en vol propulsé ou non, est presque toujours notablement inférieure à la pression  $p_\infty$  du milieu non perturbé. Il en résulte une force de traînée, proportionnelle à la surface du culot et qui représente une fraction importante de la résistance totale lorsque cette surface est voisine de l'aire du maître couple. Dans des cas particulièrement défavorables, cette contribution, qui dépend du nombre de Mach, peut avoisiner 70 % de la traînée totale, en transsonique par exemple.

En raison de l'importance du problème, sur le plan pratique, de nombreux efforts de recherches ont été consacrés, depuis longtemps, à la détermination de la pression de culot au moyen de méthodes, qui, à l'origine, reposaient largement sur des corrélations expérimentales déduites de mesures de  $p_c$  en vol ou en souffleries.

Des progrès décisifs dans les méthodes de prévision ont été accomplis il y a 25 ans lorsqu'une analyse expérimentale détaillée de l'écoulement de culot a permis d'élaborer des modèles théoriques plus réalistes que les schématisations rudimentaires utilisées jusqu'alors.

Depuis cette époque les phénomènes de culot ont fait l'objet de très nombreuses études, aussi bien théoriques qu'expérimentales qui ont conduit, d'une part au perfectionnement des méthodes de calcul dont le champ d'application a été étendu (arrière-corps avec jet propulsif, traitement des configurations subsoniques, optimisation d'arrière-corps, engins multi-tuyères), d'autre part, grâce à la mise en oeuvre de techniques de mesure plus raffinées, à une meilleure connaissance de l'organisation des zones décollées (champs moyen et turbulent, effets instationnaires).

Néanmoins, la structure des écoulements de culot est encore loin d'être entièrement élucidée, spécialement dans les circonstances complexes rencontrées sur les missiles : écoulements tridimensionnels, interaction de nappes tourbillonnaires, effets d'ondes de choc, confluence de flux de compositions et d'états thermodynamiques très différents, instabilités, etc....

Le présent exposé est essentiellement centré sur les implications pratiques des phénomènes de culot dans le cas réaliste de couches limites turbulentes, en amont du décollement et dans un domaine de nombres de Mach excluant l'hypersonique.

Egalement, les problèmes plus spécifiques liés aux lanceurs (configurations multi-tuyères, problèmes thermiques liés à l'éclatement des jets, séparation d'étages, etc...) ne seront que peu ou pas évoqués.

L'exposé a été divisé en deux parties :

- la première est consacrée à une analyse phénoménologique des écoulements de culot avec ou sans jet propulsif en subsonique et en supersonique. Les effets des principaux facteurs d'influence sont discutés sur des exemples et des méthodes empiriques de corrélations présentées ;
- la seconde porte sur les théories actuellement disponibles pour traiter pratiquement les problèmes de culot avec ou sans jet propulsif. La validité de ces méthodes est discutée par confrontation avec les résultats expérimentaux disponibles.

## P R E M I E R E   P A R T I E

### 1. ANALYSE PHENOMENOLOGIQUE DES ECOULEMENTS DE CULOT

#### 1.1 Aspects phénoménologiques de l'écoulement au culot d'un missile non propulsé : cas de référence

##### 1.1.1 Généralités :

Malgré de très nombreuses recherches [1 à 9] la compréhension des mécanismes régissant le décollement qui se produit au culot d'un engin ou d'un projectile est encore incomplète.

Il n'est donc pas inutile pour aborder ce difficile problème de faire l'inventaire de nos connaissances par l'analyse d'un cas très schématique dont l'étude expérimentale peut être menée à bien à l'aide du montage d'essai défini figure 1.

Ce montage permet de simuler l'écoulement autour d'un arrière-corps cylindrique dont l'axe  $XX'$  est parallèle à la vitesse de l'écoulement général, uniforme en amont du domaine d'interaction de l'écoulement de culot.

Le nombre de Reynolds  $Re_\delta$  formé avec l'épaisseur de la couche limite en  $D$  doit être suffisamment grand pour qu'un régime turbulent soit établi, même lorsqu'une aspiration à travers une paroi poreuse a été effectuée pour diminuer l'épaisseur  $\delta_0$  et faire varier le rapport  $\delta_0/r$ .

C'est sur cette configuration, dite de référence, que nous examinerons en détail, le décollement qui s'établit en aval du culot, et plus particulièrement, les effets sur ce décollement du nombre de Mach  $M_\infty$  de l'écoulement amont.

### 1.1.2 Écoulement subsonique subcritique

La structure du décollement est dans ce cas peu dépendante des effets de compressibilité de telle sorte que nous utiliserons comme premiers éléments d'analyse les résultats fournis par la visualisation au tunnel hydrodynamique [ 10 ].

Les clichés reproduits figures 2a et 2b ont été obtenus avec des temps de pose très différents. Figure 2a où la durée d'exposition est de 1 seconde environ, les traceurs constitués ici de fines bulles d'air en suspension dans l'eau, observés dans une mince tranche passant par l'axe, permettent de définir assez bien la structure de l'écoulement moyen. Celui-ci, parfaitement reproductible, s'organise autour d'un tourbillon principal torique situé dans un domaine fermé par la ligne de courant  $DR$ . Le décollement se produit pratiquement à l'arête  $D$ , un processus de mélange se développe le long de  $DR$  et l'écoulement entraîné au cours de ce processus reflue dans la zone fermée sous l'effet de la compression qui s'établit au voisinage du point d'arrêt  $R$ .

Sur le cliché 2b, où le temps d'exposition est beaucoup plus faible (0,01 s environ) le caractère instationnaire des couches dissipatives turbulentes est clairement mis en évidence, ainsi que le mécanisme de formation de grosses structures, entraînées au sein de la couche de mélange et évacuées ensuite vers l'aval d'une manière quasi périodique.

Les répercussions de tels phénomènes sont essentiellement de deux ordres :

- tout d'abord, induction de fluctuations sensibles de la pression dans le décollement ;
- ensuite modification profonde de la structure de la turbulence, déterminante pour l'évolution du sillage lointain.

En ce qui concerne le champ moyen, des explorations détaillées à l'aide de sondes de pression et du fil chaud, de la zone décollée et de son voisinage, permettent de compléter les observations fournies par la visualisation.

Sur l'exemple donné figure 3 [ 11 ] dans le cas d'un écoulement à basse vitesse ( $U_{\infty} \approx 40$  m/s), on remarquera plus particulièrement :

- le développement rapide et l'extension transversale des couches de mélange ;
- la relative compacité de la zone décollée dont la longueur est un peu supérieure à un diamètre ;
- l'importance des vitesses négatives de retour qui peuvent atteindre et même dépasser 30 % de la vitesse extérieure ;
- enfin, l'évolution très continue des profils de vitesse turbulent et leur passage progressif d'une situation de type couche de mélange avec courant de retour à une situation du type sillage et vitesse croissant sur l'axe.

Cette évolution peut être caractérisée par la définition d'une famille de profils à 1 ou 2 paramètres [11,12] dont on verra l'utilisation dans la 2ème partie de cet exposé, consacrée aux méthodes de calcul.

Au cours de ce processus, une forte production de turbulence apparaît au voisinage de  $DR$  (figure 4). Cette turbulence diffuse très vite vers l'axe du sillage comme vers l'extérieur et se maintient à un niveau assez élevé dans la zone décollée, par le jeu de la recirculation.

En ce qui concerne le champ des pressions, la courbe  $\bar{p}^*(x)$  obtenue par intégration du champ des vitesses moyennes, définit la frontière de l'obstacle "équivalent" au décollement.

L'évolution du coefficient  $K_R$  déduit des mesures de pression pariétales (figure 5) montre que cet effet d'obstacle se fait sentir en amont du culot jusqu'à une distance égale à environ 1 diamètre \*. L'accélération que subit l'écoulement, très marquée près du culot, assure le raccordement continu des pressions en  $D$  de part et d'autre du décollement.

L'évolution axiale des pressions statiques en aval du culot présente l'allure caractéristique reproduite figure 5. Cette évolution, lorsque  $X$  augmente, est marquée tout d'abord par une légère décroissance de  $p$  jusqu'à une valeur minimale située à une distance égale à environ  $X = \zeta$ . Cette décroissance de  $p$  peut être associée à l'augmentation de la vitesse de retour (figure 3). La recompression qui fait suite est importante. Elle résulte de la confluence de l'écoulement sur l'axe, la pression maximale, nettement supérieure à  $p_0$ , étant atteinte un peu en aval du point d'arrêt  $R$ .

Dans l'exemple qui vient d'être analysé extrait de la référence [11] l'épaisseur relative de la couche limite en  $D$  est assez faible ( $\delta^*/r_c = 0,012$ ). L'effet de ce paramètre sur le niveau de la pression de culot sera discuté dans la seconde partie de cet exposé, mais on peut dès à présent examiner quelques résultats typiques obtenus au cours de la même étude.

---

\* Cet effet d'influence amont peut entraîner des erreurs assez importantes dans la détermination expérimentale du coefficient de pression de culot  $K_{Rc}$ , lorsque la prise de pression de référence est située trop près de  $D$  [13].

On constate (figure 6) que la pression de culot diminue lorsque  $Q/r_c$  décroît, d'une manière d'autant plus marquée que  $Q/r_c$  est plus petit. Par contre pour des valeurs de  $Q/r_c$  supérieures à environ 0,02 l'évolution de la pression de culot est très faible. Cette tendance est confirmée par d'autres observations [1, 17] et explique l'effet peu important d'une variation appréciable du nombre de Reynolds enregistré par les expérimentateurs lorsque la couche limite en amont du culot est turbulente et que les valeurs de  $Q/r_c$  balayées lorsque  $Q_0$  varie sont supérieures à 0,02.

L'effet de couche limite initiale se fait également peu sentir sur l'étendue longitudinale  $L_s$  du décollement (figure 7). Toutefois la détermination assez imprécise de  $L_s$ , au vu de ces résultats, ne permet de porter qu'un jugement qualitatif.

Ainsi que nous l'avons annoncé au début de ce paragraphe, l'effet du nombre de Mach est peu important. Le coefficient de pression de culot  $\lambda_{rc}$  n'évolue que très faiblement lorsque  $M_0$  est inférieur à 0,85 (figure 8). Il en est de même des lois de distribution axiale de la pression (figure 9) et de la vitesse de retour (figure 10), à condition toutefois que la distance  $X$  au culot soit rapportée à l'étendue  $L_s$  du décollement. Par contre  $L_s$  varie de manière significative et croît avec  $M_0$  comme le montre la figure 11.

### 1.1.3 Ecoulement supersonique :

Dans ce cas, la visualisation stroboscopique constitue un moyen d'observation privilégié qui met en évidence les traits essentiels du décollement de culot en supersonique (figure 12a, b, c).

Ces visualisations montrent clairement :

- la détente quasi centrée à l'arête du culot qui dévie brutalement l'écoulement vers l'axe ;
- la couche turbulente fortement dissipative, séparant l'écoulement non visqueux du bulbe de décollement ;
- la recompression continue dont les ondes se focalisent pour former un choc ;
- le sillage relativement épais qui suit cette recompression.

On notera, tout d'abord, la disparition de l'effet d'interaction amont, le décollement en supersonique étant précédé d'une détente pratiquement centrée à l'arête qui est souvent limitée par la présence d'un choc faible ("lip shock" [14]). Ensuite, sur le cliché b, où le temps d'exposition est plus réduit, la nature tourbillonnaire et instationnaire du sillage en aval de la recompression, marquée par la présence de structures turbulentes à plus grande échelle, dont on n'observe pas la présence à la frontière de la zone décollée, contrairement au cas subsonique.

Pour entrer plus en détail dans la description de l'organisation de tels décollements, nous suivrons le même ordre qu'au paragraphe 1.1.2.

#### Champs moyen et turbulent :

Les éléments typiques représentés figure 13a et 13b sont extraits de la référence [15] qui donne une analyse très détaillée des champs moyen et turbulent obtenus lors d'une étude du cas de référence à  $M_0 = 2,3$ .

La figure 13a fournit le tracé des lignes de courant dans un plan diamétral. Le schéma de la zone décollée ne diffère du cas subsonique que par les conditions de séparation en  $D$ , le décollement supersonique étant caractérisé par une variation brutale de la direction de la vitesse liée à la détente initiale. Les profils de vitesse (pondérée par la masse) qui décrivent l'écoulement dans la zone décollée et à son voisinage appartiennent à la même famille qu'en subsonique (§ 1.1.2). Ainsi, mis à part les effets d'échelle, les différences entre les cas subsonique et supersonique intéressent essentiellement l'écoulement extérieur non dissipatif et interviennent au niveau du "couplage" avec la décollée (détente initiale, formation d'ondes de choc ...).

Sur la figure 13b sont présentés les profils du frottement apparent turbulent  $\tau$ , rapportés au frottement pariétal  $\tau_0$  de la couche limite en  $D$ , à différentes distances en aval du culot. Des effets analogues à ceux enregistrés en subsonique sont mis en évidence. On notera les niveaux élevés de  $\tau$  relevés en fin de zone de mélange. L'influence de la compressibilité se traduit notamment par des variations sensibles avec le nombre de Mach, du paramètre de mélange  $\sigma$  qui définit l'échelle transversale des couches dissipatives en amont de  $R$  (voir seconde partie de l'exposé § 2.2.2).

#### Champs de pressions :

La distribution des pressions statiques sur l'axe en aval du culot [16] reflète l'évolution de l'écoulement extérieur (figure 14). On enregistre comme en écoulement subsonique tout d'abord une légère décroissance de  $p$  suivie d'une compression continue, d'abord brutale, passant ensuite par un maximum et décroissant plus lentement jusqu'à un niveau sensiblement égal à  $p_0$ . Cette forme de la recompression, assez différente de celle observée dans le cas bidimensionnel plan supersonique, est spécifique du décollement de culot d'un arrière-corps de révolution. En effet, la présence d'une zone décollée quasi isobare à la frontière de l'écoulement supersonique extérieur entraîne, lorsque cet écoulement se rapproche de l'axe une croissance sensible de sa direction locale  $\varphi$  [2]. Cette situation contribue, lorsque l'écoulement reprend une direction sensiblement parallèle à l'axe, à la création d'une compression dont le niveau est supérieur à  $p_0$  d'une manière d'autant plus marquée que le nombre de Mach est plus grand (figure 14).

#### Effet de la couche limite turbulente initiale :

Nous retiendrons simplement les aspects essentiels suivants, une discussion plus détaillée étant faite dans la deuxième partie.

On observe de la même manière qu'en écoulement subsonique une croissance de la pression de culot lorsque  $q/r_c$  augmente, le taux de croissance devenant très faible à partir d'une certaine plage de valeurs de  $q/r_c$ . Ainsi dans la plupart des applications l'évolution de  $p_c/p_0$  avec le nombre de Reynolds  $Re$  peut être négligée, à condition toutefois que  $Re$  soit suffisamment grand pour qu'aucune relaminarisation ne se produise après la détente initiale précédant le décollement.

#### Effet du nombre de Mach $M_0$ :

Dans ces conditions, on peut définir, en vue d'estimations utiles pour un Bureau d'Etude, un coefficient de pression de culot  $K_{pc}$  pratiquement peu dépendant du nombre de Reynolds, dont l'évolution en fonction du nombre de Mach est donnée figure 8. Les résultats portés sur cette figure qui mettent en évidence une décroissance continue de  $K_{pc}$  lorsque  $M_0$  augmente, proviennent de compilations effectuées notamment référence [2,3,17]. La dispersion des résultats n'est pas très grande et cette courbe moyenne constitue une référence empirique permettant d'obtenir des estimations assez précises pour des cas proches de la configuration de base.

#### 1.1.4 Ecoulement transsonique :

Dans ce domaine très étroit ( $0,95 < M_0 < 1,10$ ), peu étudié dans son détail, les résultats expérimentaux présentent une marge d'incertitude nettement plus marquée que dans les cas précédents. Diverses causes contribuent à cette situation.

Tout d'abord, l'interaction entre le décollement et l'écoulement extérieur est souvent fort complexe par suite de la présence d'ondes de choc quasi normales dont la position est instable ou rapidement évolutive pour de faibles variations de  $M_0$ .

Ensuite les effets de limitation de l'écoulement sont particulièrement sévères et il est souvent difficile, sinon impossible, d'en tenir compte par une correction des résultats expérimentaux.

Enfin il existe relativement peu d'essais publiés contenant une analyse détaillée de la configuration de référence définie figure 1, de telle sorte que dans la plupart des cas connus où la maquette est maintenue par un support latéral ou un dard arrière, l'effet de ce support tend à fausser les résultats d'une manière significative.

Nous nous bornerons donc à représenter figure 8 par une zone hachurée le domaine dans lequel on peut inclure les résultats expérimentaux disponibles.

#### 1.2 Perturbations du cas de référence

1.2.1 L'analyse qui vient d'être faite avait pour but de préciser la structure des écoulements de culot, en choisissant une situation volontairement simplifiée correspondant au cas où l'écoulement est uniforme en amont du domaine d'interaction lié au décollement. Ces conditions ne sont donc réalistes que pour des corps cylindriques de grand allongement, possédant une ogive très élancée et placés à l'incidence nulle dans l'écoulement général.

Dans le cas d'un projectile ou d'un missile non propulsé on est conduit à envisager d'une part des formes plus complexes, imposées par les contraintes associées à une mission donnée (compacité du corps, problèmes d'échauffement, guidage, recherche d'une optimisation des formes en vue d'une réduction de la traînée, etc...), d'autre part des situations différentes de celle correspondant à l'incidence nulle.

Nous examinerons les conséquences de ces effets, dans un certain nombre de cas typiques que nous avons classés de la manière suivante :

- influence des formes géométriques du corps axisymétrique ;
- effet de l'incidence ;
- effets associés à la présence d'ailétages ;
- effet de mise en rotation du corps ;
- effet de ventilation au culot

#### 1.2.2 Effet des formes géométriques de l'obstacle sur la pression de culot

Dans le cas où l'écoulement est supersonique la non-uniformité associée à la présence de formes rapidement évolutives est marquée en premier lieu par l'existence d'ondes de choc créées soit par l'avant corps pseudo ogival, éventuellement émoussé, soit par un évasement de l'arrière-corps, tel qu'une jupe, qui peuvent produire un écoulement inhomogène et rotationnel. Ainsi l'état de l'écoulement immédiatement en amont du culot (nombre de Mach, pression, direction de la vitesse) est fort différent de l'état uniforme  $M_\infty$ ,  $p_\infty$ . D'autre part, la frontière du décollement est soumise, comme le montre la figure 15a, aux perturbations créées par la non-uniformité du champ, qui contribuent à modifier la courbure et la direction locale de cette frontière. Enfin, le développement de la couche limite est fortement conditionné par les circonstances locales de l'écoulement et notamment par la présence éventuelle d'interactions du type choc - couche limite.

La prise en compte de ces divers effets ne peut en toute rigueur être effectuée que par l'intermédiaire d'une méthode de calcul, comme nous le verrons plus loin. Toutefois, des règles simples ont été proposées [2, 3] pour assurer une corrélation avec le cas de base décrit paragraphe 1.1.3 et obtenir ainsi une estimation de la pression de culot dans des cas plus généraux.

La plus communément admise consiste à définir, à partir de l'état local de l'écoulement immédiatement en amont du culot ( $M_1, \rho_1, \beta_1$ ) un état de référence ( $M_r, \rho_r, \beta_r = 0$ ) pour lequel la direction de la vitesse serait parallèle à l'axe du corps et qui se déduit de l'état réel ( $M_1, \rho_1, \beta_1$ ) soit par une compression ou une détente isentropique locale d'angle  $\beta_1$  [ 18 ], soit en utilisant la procédure indiquée figure 15b [ 2 ]. L'expérience montre qu'une bonne approximation de la pression de culot peut être obtenue en utilisant la courbe relative au cas de base reproduite figure 8, à condition de remplacer  $M_0, \rho_0$  par  $M_r, \rho_r$ . C'est ce que nous allons voir dans les exemples que nous allons présenter maintenant et qui serviront en outre à illustrer un certain nombre d'effets typiques concernant les variations de forme.

#### Effet d'émoussement sur un corps conique

Les résultats reproduits figures 16 et 17, déduits de la référence [ 18 ] concernent l'évolution, en fonction du nombre de Mach, de la pression de culot d'un obstacle conique de demi-angle  $\theta = 9^\circ$  comportant ou non un effet d'émoussement. La présence d'un nez arrondi provoque une variation sensible du nombre de Mach  $M_r$ , immédiatement en amont du culot et entraîne, lorsque le nombre de Mach  $M_0$  varie, une évolution du rapport  $p_c/p_1$  très différente pour les deux maquettes, la pression de culot étant plus élevée dans le cas de la maquette émoussée, comme le montre la figure 16. Le concept de nombre de Mach de référence permet d'harmoniser les résultats et conduit à une prévision très bonne de la pression de culot. Il faut noter que ces essais ont été effectués à très grand nombre de Reynolds et que, par conséquent, les couches limites sont très minces (devant le diamètre du culot). Une correction de l'effet du nombre de Reynolds a été appliquée à la courbe de base définie figure 8 [ 18 ].

#### Effets de rétreint et de jupe

Parmi les moyens de réduire la traînée de culot d'un arrière corps, l'utilisation d'un rétreint est l'un des plus usités.

Son action met en jeu divers effets complémentaires qui ont pour but :

- d'une part de réduire la surface exposée à une pression de culot faible, donc génératrice de traînée ;
- d'autre part de bénéficier de la recompression naturelle qui atténue en écoulement axisymétrique, lorsque la paroi se rapproche de l'axe, l'effet des détentes isentropiques liées à une augmentation de la pente locale, ce qui a pour conséquence de diminuer le nombre de Mach de référence  $M_r$  ;
- enfin d'accroître les facteurs de courbure de la ligne de jet à la frontière de la zone décollée. Ces deux derniers effets vont dans le sens d'une augmentation de la pression de culot.

L'expérience confirme pleinement ces hypothèses, comme le montrent les figures 18 et 19. La première [ 19, 20 ] met en évidence le gain obtenu dans le cas d'arrière-corps coniques ou paraboliques pour un nombre de Mach de l'écoulement amont uniforme égal à 2.

La seconde (figure 19), extraite de la référence [ 3 ] est relative à des essais effectués à  $M_0 = 2,9$ . On notera que l'angle maximal du rétreint constitue un paramètre caractéristique de son effet, permettant de regrouper des résultats obtenus sur des corps de forme variée. On retiendra, en outre, que l'utilisation du concept du nombre de Mach de référence assure une prévision tout à fait correcte de la pression de culot.

Bien qu'une augmentation sensible de la pression de culot soit obtenue par l'effet de rétreint, il ne faut cependant pas perdre de vue que, dans le bilan de traînée, la part revenant à l'arrière-corps augmente de façon très notable lorsque  $\beta$  croît, de telle sorte que la traînée optimale de l'ensemble arrière-corps - culot est obtenue par un compromis ne correspondant pas nécessairement à la valeur de  $\beta_c$  la plus élevée (figure 20).

Comme on pouvait le prévoir, l'effet de jupe (valeurs positives de  $\beta$ ), à l'inverse de l'effet de rétreint, conduit à des pressions de culot plus basse comme le montre l'exemple de la figure 19.

Lorsque l'écoulement est subsonique il n'est pas possible en toute rigueur de dissocier les effets d'interaction entre le décollement de culot et l'écoulement autour du corps, de telle sorte que ces effets sont en général pris en compte dans le cadre d'une méthode de calcul incluant le traitement du décollement. Toutefois, lorsque l'obstacle possède un grand allongement et une forme quasi-cylindrique sur la plus grande partie de son étendue, il est alors possible de considérer isolément les effets de rétreint dans un bilan de traînée. A titre d'exemple la figure 21 fournit des courbes de variations du coefficient de pression de culot obtenues à  $M_0 = 0,9$  pour différentes valeurs de l'angle maximal du rétreint dans le cas d'arrière-corps circulaires ou paraboliques. Ces résultats qui proviennent de la compilation d'un certain nombre d'expériences sont extraits de la référence [ 21 ]. Ils mettent en évidence l'effet très favorable du rétreint sur la pression de culot en écoulement subsonique et peuvent être utilisés pour des nombres de Mach inférieurs à 0,9.

#### 1.2.3 Effet de l'incidence

La mise en incidence ( $\alpha \neq 0$ ) introduit une dissymétrie de l'écoulement qui se répercute très directement sur le décollement de culot et qui est d'autant plus marquée que  $\alpha$  est plus grand.

Cette dissymétrie intéresse non seulement l'écoulement non dissipatif, mais également les couches dissipatives turbulentes dont l'épaisseur se trouve alors répartie d'une manière fort irrégulière à la périphérie du culot.

La visualisation au tunnel hydrodynamique présentée figures 22a et 22b en donne un exemple [ 22 ].

On observe notamment figure 22b sur la vue de dessus la tendance du sillage à s'enrouler suivant deux structures tourbillonnaires distinctes.

Cette tendance a été observée dans le cas d'essais effectués en écoulement supersonique sur une maquette libre de tout support matériel et tenue par suspension magnétique [ 23 ]. L'exploration du sillage de cette maquette a conduit les auteurs à l'interprétation présentée figure 23, conforme pour l'essentiel à ce que laisse supposer l'observation à basse vitesse.

Comme indiqué figure 23, à grande incidence, existent des structures décollées tridimensionnelles, dont l'analyse a été effectuée dans les leçons consacrées à l'aérodynamique des missiles. L'interaction de ces structures avec le sillage en aval du culot constitue un problème extrêmement complexe sur le plan théorique comme sur le plan expérimental sur lequel il n'existe que très peu d'informations.

Ceci est en particulier dû à la quasi impossibilité d'éviter les interactions de supports, qui conduisent à des résultats entachés d'erreur. C'est pourquoi nous nous bornerons à donner sur quelques exemples où les effets de support sont réduits ou inexistants, les tendances générales qui se dégagent de l'évolution  $\kappa/\rho_\infty = f(\alpha)$ .

Le premier concerne le cas d'écoulements subsoniques et transsoniques ( $0,6 \leq M_\infty \leq 1,4$ ) autour d'un cône de section elliptique placé à des incidences comprises entre 0 et 20° [ 24 ]. Les résultats obtenus (figure 24) mettent en évidence :

- l'effet peu important enregistré aux faibles incidences ( $\alpha \leq 4^\circ$ ) ;
- une diminution d'abord sensible puis plus lente de la pression de culot lorsque l'incidence croît ( $4^\circ < \alpha < 16^\circ$ ) ;
- une tendance à l'inversion de cet effet à plus grande incidence.

En dehors d'un domaine proche de l'unité, les variations  $\Delta \kappa/\rho_\infty = f(\alpha)$  sont peu dépendantes du nombre de Mach  $M_\infty$  en écoulement subsonique. Le second exemple est celui d'un cône circulaire d'angle d'ouverture 20°, étudié à grand nombre de Mach ( $M_\infty = 5,3$ ) jusqu'à des incidences élevées ( $\alpha \sim 55^\circ$ ), par une technique de largage de maquettes dans une veine supersonique, donc sans interaction de support [ 25 ].

L'évolution avec l'incidence de la pression de culot (figure 25) indique, comme dans le cas précédent un faible effet de  $\alpha$  au voisinage de  $\alpha = 0$ , suivi d'une décroissance de  $\kappa/\rho_\infty$  lorsque  $\alpha$  augmente jusqu'à environ 12°. Au-delà de cette incidence on enregistre une croissance de la pression de culot d'autant plus marquée que  $\alpha$  est plus grand.

Les tendances observées dans les 2 exemples précédents concernant des corps coniques sont également confirmées dans la plage d'incidence expérimentée, dans le cas d'un corps fuselé (maquette NACA RM 10) essayé à  $M_\infty = 1,49$  (figure 26).

#### 1.2.4 Effet d'ailletages

La présence d'empennages et de gouvernes au voisinage d'un culot modifie également de manière importante les écoulements visqueux et non visqueux, et introduit de fortes hétérogénéités du champ des pressions, des épaisseurs des couches dissipatives aussi bien sur le corps qu'en aval de celui-ci. En particulier la présence des sillages tourbillonnaires de l'ailletage constitue un facteur de perturbation important du décollement.

Les paramètres qui régissent ces perturbations sont très nombreux (nombre des ailettes, forme en plan et flèche, épaisseur relative des profils, position relative par rapport au culot, etc...). Aussi, nous nous contenterons de dégager certains effets caractéristiques, en nous inspirant de l'analyse effectuée référence [ 3 ] dans le cas où l'écoulement est supersonique.

L'exemple présenté figure 27 concerne l'influence de la position par rapport au plan du culot d'un arrière-corps cylindrique, d'un empennage cruciforme, de profil lenticulaire dont l'épaisseur relative (10 %) est constante en envergure. Les expériences ont été faites pour 2 valeurs du nombre de Mach :  $M_\infty = 1,5$  et 2.

Une diminution importante de la pression de culot est créée par le champ de perturbation des ailettes, spécialement à  $M_\infty = 1,5$ , lorsque les bords de fuite de l'ailletage sont situés dans le plan du culot.

Un déplacement de l'empennage vers l'amont, réduit d'une manière sensible cette perte ; toutefois, la pression de culot correspondant au cas de référence sans ailletage n'est pas toujours atteinte pour un déplacement vers l'amont atteignant une corde.

Le second exemple (figure 28) concerne l'effet de l'épaisseur relative du profil de l'empennage. Comme prévu, la variation de la pression de culot est d'autant plus marquée que le champ de perturbation est plus accusé, c'est-à-dire que l'épaisseur relative du profil est plus grande ou encore que le nombre de Mach est plus faible.

Dans le cas où l'interaction est la plus sévère ( $\kappa_c = 0$ ), le champ de perturbation des ailettes crée une distribution du nombre de Mach local à la surface de l'arrière-corps périodique et fortement hétérogène avec toutefois une nette prédominance des détonations dont l'action en aval du culot, sur la frontière de la zone décollée, explique la décroissance de la pression de culot.

Une estimation assez grossière de ces effets peut être obtenue en prenant comme état de référence  $\rho_r, M_r$  pour le calcul de la pression de culot, des valeurs moyennées sur la périphérie du culot.



Un meilleur résultat est enregistré en définissant l'état moyen de référence, non pas au niveau de l'arête, mais en aval sur le corps prolongé fictivement d'une longueur égale à  $0,6 D$  pour tenir compte des perturbations induites sur la frontière du décollement.

Des effets analogues sont observés lorsque l'écoulement externe est subsonique. Ils sont en outre compliqués par les modifications qu'apporte le décollement de culot à l'écoulement sur l'ailetage.

### 1.2.5 Effet de mise en rotation du corps

Ce procédé concerne un grand nombre d'applications (projectiles, missiles). Cependant l'étude de son action sur la pression de culot n'a fait l'objet que d'un nombre très limité de travaux, seulement en écoulement subsonique. Nous avons extrait de la référence [ 26 ], un exemple montrant le type d'influence que l'on peut obtenir

Sur la figure 29 sont représentées, dans le cas d'un arrière-corps cylindrique, les variations du coefficient de pression de culot, en fonction du rapport de vitesse  $U_r/U_\infty$ ,  $U_r$  étant la vitesse à la périphérie de l'obstacle. On observe que pour des valeurs de ce paramètre inférieures à 0,25, une augmentation de pression de culot est obtenue pouvant entraîner une réduction de traînée de culot de l'ordre de 16 % lorsque  $U_r/U_\infty$  est égal à 0,15.

Pour des valeurs de  $U_r/U_\infty$  supérieures à 0,2 on enregistre à l'opposé une augmentation de la traînée de culot qui croît de façon significative lorsque  $U_r/U_\infty$  augmente dans le domaine des valeurs expérimentées ( $U_r/U_\infty < 0,5$ ).

### 1.2.6 Ventilation du culot par un écoulement à faible vitesse

L'idée d'utiliser une injection à très faible vitesse dans le décollement, pour diminuer la résistance de culot en écoulement supersonique est très ancienne [ 106 ]. La démonstration expérimentale de l'efficacité du procédé et des conditions d'utilisation optimales est présentée figure 30 dans le cas d'un arrière-corps cylindrique placé dans un écoulement uniforme de nombre de Mach  $M_0 = 2$ .

L'injection dans le décollement de culot d'un flux d'air dont la température génératrice est égale à celle de l'écoulement extérieur ( $T_e$ ), est pratiquée à travers un orifice circulaire.

Différentes configurations caractérisées par un rapport  $D/r_c$  compris entre 0,2 et 0,8 ont été expérimentées de manière à étudier systématiquement pour un débit  $q_j$ , l'effet du nombre de Mach d'injection  $M_j$  à la sortie de l'orifice.

Les courbes de la figure 30 donnent l'évolution du rapport  $p_c/p_0$  en fonction du débit réduit

$$\bar{q} = \frac{q_j \sqrt{\gamma R T_e}}{\gamma p_0 S_c \pi r_c^2}, \text{ pour différentes valeurs du rapport } D/r_c.$$

On observe immédiatement que l'efficacité du procédé est d'autant plus grande que  $M_j$  est plus faible, c'est-à-dire que la section de passage du flux de ventilation  $q_j$  est plus importante. Dans le cas le plus favorable une augmentation de la pression du culot atteignant 40 % est obtenue pour des débits  $q_j$  petits correspondant à un nombre de Mach  $M_j$  de l'ordre de 0,25.

Une justification théorique parfaitement claire de cet effet sera donnée dans la 2ème partie.

## 1.3 Ecoulement du culot d'un missile en présence du jet propulsif

1.3.1 Nous abordons maintenant l'étude des aspects spécifiques de la phase propulsée du vol d'un missile où sont mis en jeu des phénomènes très complexes spécialement lors de l'amorçage de la tuyère d'éjection. Ces phénomènes sont créés par la confluence de deux écoulements dont les états générateurs et locaux (nombre de Mach, inclinaison de la vitesse, etc...) ainsi que les compositions chimiques sont très différents.

Nous examinerons en premier lieu le cas de l'écoulement externe supersonique qui conduit aux effets d'interaction les plus marqués. [27, 28].

### 1.3.2 Ecoulement externe supersonique

Nous analyserons d'abord un exemple typique extrait de la référence [ 27 ]. La configuration géométrique étudiée (arrière-corps cylindrique muni d'une tuyère coaxiale) est définie figure 31. Les écoulements interne et externe sont alimentés par de l'air ayant la même température ( $T_j = T_e$ ). Le nombre de Mach  $M_0$  de l'écoulement externe est uniforme en amont du culot et égal à 2, de même que le nombre de Mach nominal  $M_0$  de la tuyère d'éjection du flux interne. L'équipement en prises de pression statique indiqué figure 32 permet la mesure simultanée de la pression de culot et des pressions à la paroi de la tuyère. Le résultat des mesures obtenues lorsque le rapport  $p_j/p_e$  varie est représenté figures 31 et 32.

La courbe donnant l'évolution de  $p_c/p_0$  en fonction de  $p_j/p_e$  (figure 31) peut être divisée en 3 domaines.

Le premier (I) qui correspond à des débits très petits est marqué, comme on l'a vu au paragraphe 1.2.6, par une croissance continue de  $p_c/p_0$  jusqu'à une valeur maximale.

Dans le second domaine (II) on observe une décroissance brutale et rapide de la pression culot jusqu'à une valeur minimale très basse ( $p_c/p_0 = 0,18$ ). Durant cette phase on enregistre successivement :

- l'amorçage de la tuyère d'éjection jusqu'à son extrémité (de a à b, figures 31 et 32) ;

- l'établissement d'un régime de confluence des écoulements interne et externe entièrement supersonique (de b en c, figure 31).

Dans le domaine III la pression de culot augmente uniformément lorsque la détente du jet interne se poursuit. L'écoulement est alors très stable.

Cet exemple fait apparaître une évolution rapide mais continue des phénomènes qui n'est pas toujours réalisée, comme le montre la figure 33 [28].

Aux variations de  $P_c/P_o$ , représentées ici en fonction du taux de détente  $P/P_o$ , sont associées des clichés de visualisation strioscopique de l'écoulement qui illustrent les différentes circonstances décrites précédemment.

On observe sur ce deuxième exemple que la phase d'amorçage de l'éjecteur (domaine II) se termine par une discontinuité brutale, l'écoulement extérieur se comportant vis à vis du jet central comme un diffuseur de soufflerie supersonique à second col réglable.

D'autre part un phénomène d'hystérésis apparaît. Lorsque, l'éjecteur une fois amorcé, on fait décroître le taux de détente  $P/P_o$ , le désamorçage se produit pour une valeur de  $P/P_o$  différente de celle qui correspond aux conditions d'amorçage.

Ces deux exemples montrent qu'au cours de la phase II la structure du décollement subit un bouleversement considérable qui se traduit par le passage d'une situation analogue à celle du paragraphe 1.1.3 comportant une zone décollée étendue avec un point d'arrêt sur l'axe et des effets axisymétriques importants, à une situation de confluence autour d'une zone décollée réduite dont la structure présente un caractère bidimensionnel dominant.

Dans ce dernier cas l'organisation interne de la zone décollée est presque toujours marquée par la présence d'une circulation de fluide, favorisant les échanges entre écoulements interne et externe, comme indiqué figure 34. L'écoulement le plus lent cède un certain débit entraîné par l'écoulement le plus rapide [9].

Après avoir décrit les phénomènes observés au culot en présence du jet d'un propulseur, nous allons examiner maintenant, à l'aide de résultats extraits de la référence [37] les effets des principaux paramètres qui les régissent. Pour simplifier, nous nous placerons dans le cas d'un arrière-corps cylindrique.

#### Effet des dimensions transversales $r/r_c$ de la tuyère propulsive

Cet effet est analysé figure 35, les résultats présentés couvrant un large domaine de variation du rapport  $r/r_c$  ( $0,2 \leq r/r_c \leq 0,8$ ).

Lorsque  $r/r_c$  diminue on observe :

- une décroissance marquée de la pression de culot maximale (voir § 1.2.6) ;
- un accroissement très sensible de l'étendue du domaine II ; les valeurs de  $P/P_o$  conduisant à la pression de culot minimale (frontière du domaine III) sont d'autant plus élevées que  $r/r_c$  est plus faible ;
- corrélativement une diminution sensible de  $P_c/P_o$  dans le domaine III.

On notera que la valeur de  $P_c/P_o$  la plus faible, enregistrée à la frontière des domaines II et III est par contre pratiquement indépendante de  $r/r_c$ .

#### Effet du nombre de Mach nominal $M_o$ de la tuyère propulsive

Les résultats présentés figure 36 concernent 2 configurations d'arrière-corps qui ne diffèrent que par le nombre de Mach nominal  $M_o$  de la tuyère d'éjection, respectivement égal à 1 et 2.

La diminution de  $M_o$  entraîne :

- une augmentation du niveau de la pression de culot dans le domaine III. Dans le cas d'une valeur sonique de  $M_o$  cette variation est très sensible et compense dans une certaine mesure la perte de poussée d'une telle tuyère ;
- des différences assez notables dans le domaine II liées à l'apparition de régimes instables différant d'une tuyère à l'autre.

#### Effet des formes géométriques et de la position de la tuyère propulsive

La figure 37 montre l'évolution de  $P_c/P_o$  en fonction de  $P/P_o$  pour 3 tuyères de nombre de Mach nominal égal à 2, ayant même section de sortie et différant seulement par l'inclinaison  $\beta$  de la paroi au bord de fuite ( $0 \leq \beta \leq 10^\circ$ ).

L'effet que provoque cette modification de forme est faible et n'apparaît que pour la valeur de  $\beta$  la plus élevée. Il se traduit par un léger accroissement de la pression de culot dans le domaine III, la borne inférieure de ce domaine étant pratiquement la même pour les 3 tuyères.

La distance  $X_f$  qui définit la position du plan de sortie de la tuyère propulsive par rapport au plan du culot est également un paramètre géométrique important intervenant de manière significative dans les calculs d'optimisation de la poussée.

Les configurations pour lesquelles  $\lambda_T$  est négatif (tuyères enterrées) sont généralement utilisées dans le domaine de l'Aéronautique. Elles ont permis d'obtenir de très bons résultats pour l'adaptation de tuyères convergentes dans les domaines de vol subsonique et transsonique [ 29 ].

Nous nous intéresserons ici aux situations pour lesquelles  $\lambda_T$  est positif (figure 38 ).

Le cas limite représenté figure 38b correspond au recollement de l'écoulement externe sur la paroi extérieure de la tuyère prolongée en aval du culot à la manière d'un dard. La zone décollée est alors soustraite aux effets d'induction du jet et la pression de culot, pour les taux de détente faibles ou modérés est supérieure à celle qui est obtenue pour  $\lambda_T = 0$  (figure 38a ), spécialement lorsque  $\gamma/\epsilon$  est petit.

Pour des valeurs de  $\lambda_T$  inférieures à la précédente, la confluence des écoulements internes et externes peut se produire. L'étendue longitudinale de la couche de mélange du jet est plus faible qu'en a) et  $p_c$  est également plus élevée.

Ces quelques exemples illustrent les effets sur la pression de culot des facteurs d'influence les plus significatifs de la présence du jet propulsif.

D'autres cas seront traités dans la seconde partie de cet exposé, à titre de contrôle des méthodes de calcul appliquées en particulier à l'optimisation des formes d'un arrière-corps. L'utilisation de ces méthodes requiert notamment la connaissance aussi précise que possible de la frontière des domaines II et III (point C, figure 31 ).

La corrélation empirique proposée référence [ 30 ] a pour objet de définir la valeur de  $p_j/p_c$  en C.

Cette corrélation de diverses expériences (figure 39 ) est basée sur l'existence d'une loi de comportement reliant  $(p_j/p_c)_C$  en C et  $p_c/\rho_j$  de la forme :

$$\log \left( \frac{p_j}{p_c} \right)_C = K_1 \log \frac{p_c}{\rho_j} + K_2$$

dans laquelle  $K_1$  et  $K_2$  sont des fonctions de  $M_{j0}$  fournies par l'expérience.

L'utilisation conjointe de cette loi et des méthodes de calculs usuelles de la pression de culot en écoulement supersonique permet de prévoir la valeur de  $p_j/p_c$  au point C.

### 1.3.3 Ecoulement externe subsonique

Un exemple typique de variation de la pression de culot en présence d'un jet, dont le taux de détente augmente, dans le cas d'un écoulement externe subsonique ( $M_{e0} = 0,9$ ) est donné figure 40 . Cette évolution est comparée à celle qui est obtenue lorsque le nombre de Mach  $M_{e0}$  est faiblement supersonique ( $M_{e0} = 1,2$ ) et qui reproduit les traits essentiels définis paragraphe 1.3.2. Cet exemple est extrait de la référence [ 31 ].

On remarquera tout d'abord l'analogie qui existe dans l'évolution de ces 2 courbes pour les taux de détente faible ( $p_j/p_c < 1,5$ ).

L'inflexion très caractéristique qui se produit ensuite lorsque l'écoulement externe est subsonique est toujours observée. Elle coïncide avec la formation et la phase initiale de développement d'un jet supersonique en aval du col de la tuyère.

Les effets du paramètre  $\gamma/\epsilon$  sur le coefficient de pression de culot [ 31 ] sont présentés figure 41 pour différents taux de détente  $p_j/p_{e0}$  et pour deux valeurs du nombre de Mach externe encadrant le domaine transsonique ( $M_{e0} = 0,9$  et  $M_{e0} = 1,1$ ).

Ces résultats révèlent comme en supersonique (1.3.2) une action importante et complexe de ce paramètre sur le niveau de  $K/p_c$ , qui se traduit, en général, par une décroissance de la pression de culot lorsque  $\gamma/\epsilon$  diminue, pour les valeurs élevées du taux de détente. Pour des valeurs faibles de  $p_j/p_{e0}$ , la tendance inverse est observée, ce qui entraîne dans le domaine intermédiaire une évolution de  $K/p_c + f(\gamma/\epsilon)$  caractérisée par la présence d'un minimum.

### 1.3.4 Effets liés à la température et à la composition chimique du jet

Les résultats présentés jusqu'à présent concernent le cas d'écoulements d'air ayant la même température génératrice. Il n'existe que peu d'études où l'influence du rapport  $T_j/T_c$  ait été systématiquement analysée. Les variations de  $T_j/T_c$  expérimentées sont en général faibles, inférieures à 3 et s'accompagnent, compte tenu du mode de chauffage le plus souvent utilisé (combustion de kérosène) de variations du rapport  $\gamma$  des chaleurs spécifiques du gaz chaud (variables avec la température  $T_j$  et la composition des produits de combustion), ce qui entache les résultats d'un effet parasite dont l'importance ne peut être appréciée que par le calcul.

Il ressort toutefois de ces études que l'effet de  $T_j/T_c$  tant qu'il demeure modéré ( $T_j/T_c \leq 3$ ) ne modifie pas fondamentalement l'évolution des phénomènes, comme le montrent les exemples présentés figures 42 et 43 [ 32 ].

Les expériences correspondantes ont été effectuées pour 2 valeurs du nombre de Mach extérieur,  $M_{e0} = 0,9$  et 2, sur un arrière-corps cylindrique équipé soit d'une tuyère sonique, soit d'une tuyère en forme dont le nombre de Mach théorique est voisin de 2.

Les résultats sont donnés sous forme de courbes exprimant l'écart relatif sur la traînée de culot obtenu en fonction du rapport  $\gamma/\pi_c$  pour différentes valeurs du taux de détente  $\gamma/\pi_0$ , le cas  $\gamma/\pi_c = 1$  étant pris comme référence. (figure 42)

Ces écarts sont très faibles à  $M_0 = 2$  et ne dépassent guère 5 %, par contre le sens de leur évolution permet d'envisager des différences plus importantes lorsque  $\gamma/\pi_c$  est plus grand. En revanche, ces écarts deviennent plus importants à  $\gamma_c = 0,9$  (figure 43), lorsque le taux de détente est faible ( $\gamma/\pi_0 \sim 2$ ) et vont dans le sens d'une diminution de la traînée de culot.

Les corrélations expérimentales données figure 44 [21], permettent de définir la correction correspondante, dans le cas plus général où l'arrière-corps comporte un rétreint. Ces corrélations établies pour  $M_0 = 0,9$  dans le cas de corps fuselés de grand allongement peuvent être utilisées à des nombres de Mach plus faibles.

En ce qui concerne les effets des propriétés physiques des gaz en présence, une discussion théorique du problème sera effectuée dans la seconde partie de l'exposé.

### 1.3.5 Configurations "multituyères"

Les décollements qui s'établissent au culot d'un missile lorsque l'effet propulsif est réparti entre plusieurs tuyères groupées sont beaucoup plus complexes que ceux qui ont été analysés jusqu'à présent. La structure de l'écoulement en aval de la ligne de séparation est alors fortement tridimensionnelle, y compris dans le domaine de recirculation, de telle sorte que la pression n'est en général plus uniforme sur la surface du culot, comme dans le cas d'une configuration monotuyère où les écarts enregistrés d'un point à un autre sont toujours faibles.

Des résultats typiques d'une telle situation sont présentés figure 45 pour un écoulement externe supersonique [33]. Les non uniformités les plus marquées apparaissent lorsque le taux de détente est important et lorsque la disposition des tuyères entraîne, par suite de la confluence des jets en présence, une sorte de cloisonnement de la partie centrale du culot.

Nous examinerons cette situation dans le cas particulier des quadrituyères qui a fait l'objet de nombreuses études [33, 34]. Les schémas déduits de l'expérience et représentés figure 46 définissent l'organisation de la zone décollée pour différents taux de détente d'un tel système propulsif.

A basse altitude, lorsque  $\gamma/\pi_0$  est faible (schéma a), l'effet d'entraînement des jets assure l'évacuation d'un flux provenant de l'écoulement externe dans la zone centrale située au voisinage de l'axe. La non-uniformité des pressions dans le plan du culot est alors peu marquée (figure 45).

Lorsque le taux de détente devient plus élevé (schéma b) l'expansion des jets en sortie de tuyère provoque leur confluence; les gradients de pression positifs importants qui en résultent assurent le développement d'un flux de recirculation intense de l'écoulement interne dirigé d'abord vers le plan du culot et évacué ensuite à la périphérie des jets. La présence en C d'un point d'arrêt pour cet écoulement de retour à grande vitesse entraîne des valeurs élevées de la pression en ce point et à son voisinage.

A haute altitude, lorsque  $\gamma/\pi_0$  devient très grand, cet effet s'accuse (schéma c), le débit de recirculation s'accroît de manière très notable jusqu'au blocage sonique des sections de passage disponibles entre les tuyères.

Dans une telle situation le coeur du culot est le siège de pressions élevées (figure 45) et de flux de chaleur importants (figure 47).

### 1.3.6 Phénomènes liés à l'éclatement du jet interne

Dans l'exemple précédent, il est intéressant de suivre l'évolution de la pression  $\pi_c$  à la périphérie du culot lorsque  $\gamma/\pi_0$  augmente.

A basse altitude (a), on enregistre une forte détente de l'écoulement externe, la pression  $\pi_c$  étant très inférieure à  $\pi_0$ .

A moyenne altitude (b) l'augmentation de  $\gamma/\pi_0$  provoque un accroissement de  $\pi_c$  et par suite une réduction de la détente en D.

A haute altitude (c)  $\pi_c$  devient supérieur à  $\pi_0$  et une onde de choc se forme au voisinage de l'arête D. L'intensité de cette onde augmente avec  $\gamma/\pi_0$  et entraîne un décollement de l'écoulement externe en amont du culot.

Le phénomène que nous venons de décrire et qui est associé à la forte détente de l'écoulement interne se produisant lorsque l'altitude de vol est très supérieure à l'altitude d'adaptation, n'est évidemment pas spécifique des configurations multituyères.

L'exemple présenté figure 48 concerne l'étude à  $M_0 = 2,01$  d'un arrière-corps muni d'un rétreint tronconique et équipé d'une tuyère centrale unique [36]. La progression vers l'amont du point de décollement situé sur le rétreint se produit d'une manière régulière lorsque le taux de détente augmente.

Les effets associés à cette progression vers l'amont du décollement sont par ailleurs très importants. Le bilan de puissance dans la mesure où ils réduisent les pertes provenant de la sous-détente de la tuyère.

Par contre dans le cas d'un arrière-corps muni d'ailettes ou de gouvernes, l'interaction provoquée par le décollement, aggravée éventuellement des dissymétries dues à l'incidence de vol du missile peut conduire à des effets néfastes sur sa stabilité statique ( 27 ).

#### 1.4 Effets instationnaires dans les écoulements de culot

Comme nous l'avons vu paragraphe 1.1, le décollement de culot est le siège de phénomènes instationnaires en partie provoqués par la formation plus ou moins aléatoire de grosses structures turbulentes à sa frontière, en particulier dans le cas du vol non propulsé et spécialement en écoulement subsonique et transsonique.

Les fluctuations de pression ainsi créées peuvent avoir des fâcheuses répercussions, aussi bien sur le plan de la tenue mécanique des structures que sur le plan du pilotage. C'est pourquoi l'analyse de ces fluctuations (intensités, spectre) est très importante.

L'exemple reproduit figure 49 est extrait de [ 38 ]. Il concerne un corps à nez semi-sphérique équipé d'une jupe, étudié dans un large domaine de nombre de Mach.

Dans ce cas, l'analyse des fluctuations de la pression de culot a été effectuée sur une maquette tenue par un dard dont la présence peut créer un effet stabilisateur sur le décollement.

Les courbes de la figure 49 montrent l'évolution avec la fréquence réduite  $\pi = f/q_\infty$  de la fonction spectrale  $\sqrt{\pi} F(\pi)$  dont nous rappellerons les définitions :  $F(\pi) d\pi$  représente la contribution, dans la bande de fréquence  $d\pi$ , à l'intensité moyenne des fluctuations de pression de culot, mise sous forme adimensionnelle :  $(\bar{p}_c/q_\infty)^2$ . On observe :

- dans le domaine  $0,3 \leq M_\infty \leq 0,85$ , une indépendance du spectre des fluctuations vis à vis du nombre de Mach, le niveau moyen  $\bar{p}_c/q_\infty$  étant élevé (0,025) ;
- un accroissement du niveau général, sans modification de la forme du spectre, en transsonique ( $\bar{p}_c/q_\infty = 0,029$  à  $M_\infty = 0,9$ ) ;
- en revanche, une décroissance sensible de ce niveau en supersonique, d'autant plus marquée que  $M_\infty$  est plus grand.

Dans le cas du vol propulsé, le niveau des fluctuations de  $\bar{p}_c$  est très faible lorsqu'une configuration de confluence en écoulement supersonique est réalisée. Par contre des effets instationnaires marqués apparaissent dans la phase d'établissement du régime amorcé, qui dépendent fortement de la configuration étudiée (géométrie, nombre de Mach, etc...).

Lorsque l'écoulement extérieur est subsonique, des fluctuations extrêmement importantes de la pression de culot peuvent se produire, lorsqu'un effet de couplage est réalisé entre l'intermittence des frontières turbulentes du jet et les perturbations créées à l'origine des couches de mélange par les ondes de pression instationnaires que ces frontières émettent [ 39 ]. Ce phénomène peut être extrêmement violent dans le cas d'une configuration multivoyère pour laquelle la zone confinée centrale contribue à exacerber ces effets.

## DEUXIEME PARTIE

### 2. METHODES DE CALCUL DES ECOULEMENTS DE CULOT

#### 2.1 Remarques préliminaires

Ainsi que nous venons de le voir, l'écoulement dans la région du culot d'un engin est extrêmement complexe et dépendant de nombreux paramètres : nombres de Reynolds et de Mach, couche limite initiale, géométrie de l'arrière corps, conditions de fonctionnement de la (ou des) tuyère, etc... Par ailleurs, dans le cas des missiles, le régime est dans la très grande majorité des cas turbulent, ce qui rend encore problématique le développement de méthodes exactes basées sur la résolution numérique des équations de Navier-Stokes, en raison principalement de la difficulté de modéliser convenablement la turbulence dans des régions décollées où existent des effets fortement perturbateurs.

En conséquence, les théories qui sont proposées pour traiter les problèmes de culot ont un caractère approché et utilisent une schématisation parfois sommaire des phénomènes réels. Elles ne sont donc pas en mesure de prédire la structure détaillée de l'écoulement (champ des vitesses, par exemple), mais elles permettent néanmoins de déterminer, avec une précision correcte, certaines caractéristiques globales (pression et/ou flux de chaleur au culot, dimensions de la zone décollée) dont la connaissance est souvent suffisante dans la pratique.

La seconde partie de la conférence est consacrée à la présentation de certaines de ces méthodes, parmi les plus usitées. Nous ne prétendons pas être exhaustif, car un très grand nombre de théories ont vu le jour dans ce domaine. Beaucoup d'entre elles ne diffèrent d'ailleurs que par des variantes secondaires. Nous avons retenu celles qui nous paraissent les plus typiques, ainsi que celles dont nous avons une bonne expérience. On trouvera dans la référence [40], une revue plus complète des méthodes de calcul.

Avant d'exposer les méthodes développées pour traiter le problème de l'écoulement au culot d'un arrière corps de révolution, il nous a semblé instructif de faire un rappel sur les théories relatives au recollement turbulent, en considérant le cas plan pour simplifier. En effet, les méthodes appliquées aux écoulements de culot font appel aux mêmes concepts et aux mêmes règles fondamentales, mais dans des circonstances plus complexes dont la prise en considération peut masquer les principes de base sous jacents.

#### 2.2 Rappels sur les théories du recollement turbulent bidimensionnel sur paroi en écoulement supersonique

Nous ne donnerons ici qu'un exposé succinct des théories consacrées au problème du recollement d'un écoulement turbulent à sa frontière et stationnaire en moyenne. Des revues plus complètes de ces méthodes sont présentées, en particulier références [16, 41]. Nous considérerons uniquement le cas supersonique car c'est celui qui a donné lieu aux recherches les plus nombreuses en raison de son importance pratique pour les missiles ou les lanceurs et, probablement aussi, de la simplification relative apportée par le caractère hyperbolique des équations régissant l'écoulement non visqueux. Les quelques méthodes développées en subsonique, qui seront citées plus loin, s'inspirent d'ailleurs de concepts analogues.

##### 2.2.1 Aperçu phénoménologique

Les études théoriques sur le recollement supersonique turbulent ont été largement inspirées par l'analyse expérimentale détaillée de l'écoulement bidimensionnel plan en aval d'une marche descendante. Aussi, avant d'entrer dans l'exposé des méthodes, il n'est pas inutile d'examiner l'organisation d'un tel écoulement telles qu'elle ressort de l'observation expérimentale.

Les visualisations strioscopiques ou interférométriques de la Figure 50 mettent clairement en évidence les caractères essentiels de l'écoulement.

L'écoulement supersonique non visqueux subit d'abord une détente pratiquement centrée à l'arête de la marche et se trouve ainsi fortement dévié vers la paroi. A l'impact, se forme une recompression par ondes convergentes se focalisant en un choc. Vers l'aval, l'écoulement redevient uniforme et parallèle à la paroi.

Une couche turbulente et fortement dissipative sépare le fluide non visqueux d'un domaine fermé accolé à la marche, appelé communément "eau morte".

La distribution pariétale des pressions reflète l'évolution de l'écoulement extérieur (Figure 51). Elle présente à l'origine une détente initiale de  $p_0$  à  $p_c$ , suivie d'une très légère décroissance dans la zone d'eau morte. La recompression continue qui s'établit ensuite est d'abord rapide puis elle s'infléchit progressivement jusqu'à une pression  $p_s$  constante et très voisine de  $p_0$ .

Ce type de décollement est stable et l'observation avec un temps d'exposition très bref, de l'ordre de la  $\mu$ s (Figure 50), donne une description de l'écoulement, à l'extérieur de la zone décollée, à peine différente de celle qui est obtenue avec une pose longue (0,02 s). Dans la photographie éclair apparaît cependant en détail le caractère instationnaire et fortement tourbillonnaire des couches dissipatives turbulentes.

Pour compléter cet aperçu général, considérons le schéma de la Figure 52, établi à partir d'une analyse expérimentale très détaillée effectuée à un nombre de Mach  $M_0$  voisin de 2 par Taguiev. Cette étude permet de définir de façon précise l'organisation de l'écoulement dans la zone décollée et à son voisinage.

Dans son ensemble, la zone de décollement apparaît comme un domaine fermé au sein duquel l'écoulement moyen s'organise autour d'un tourbillon principal. Un tourbillon secondaire contrarotatif est situé au pied de la marche, mais ne joue pas un rôle important dans l'évolution du courant de retour. L'écoulement dissipatif peut être divisé en cinq régions. La première, située au voisinage immédiat de D est limitée à la détente initiale et au décollement de la couche limite (I). En aval, se développe une zone de mélange quasi-isobare (II) qui est suivie par une première recompression s'étendant jusqu'au point de recollement R. En aval de R, la recompression se poursuit jusqu'à un nouvel état d'équilibre (IV). Au sein de la zone décollée, délimitée par (I), (II) et (III), nous distinguerons le domaine de recirculation (V) à l'intérieur duquel reflue le courant alimentant la couche de mélange.

La considération de chacune de ces régions permet de définir la structure des couches dissipatives et de préciser le mécanisme du recollement. Cette décomposition a généralement présidé à l'élaboration des modèles de calcul. Il faut toutefois souligner le caractère assez arbitraire de ce partage ; en particulier, il n'est pas usuel de séparer le domaine (V) des régions (II) et (III) adjacentes, spécialement dans l'optique d'un traitement du décollement à partir des équations de la couche limite (voir § 2.2.3).

Il est intéressant de noter ici que l'analyse expérimentale des conditions de recollement d'un écoulement turbulent incompressible en aval d'une marche descendante, conduit à un partage de la zone décollée pratiquement identique à celui qui est envisagé ici. Toutefois, dans le cas subsonique, le décollement de la couche limite au voisinage de l'arête se produit sans variation aussi brutale de la pression.

Après cet aperçu phénoménologique, nous allons présenter des théories dont l'objectif essentiel est de calculer la pression  $p_c$  qui s'établit dans la zone décollée isobare, et qui s'exerce sur la marche (pression de culot). Dans une analyse du problème de la pression de culot, Chapman a montré que, dans l'hypothèse du fluide parfait, il existait une infinité de solutions possibles. La pression  $p_c$  demeure indéterminée. En conséquence, une théorie en fluide strictement non visqueux est inapplicable dans la pratique.

L'indétermination ne peut être levée qu'en faisant intervenir la viscosité. Les méthodes de calcul devront donc être en mesure de schématiser correctement le comportement des zones dissipatives. Les théories existantes peuvent être classées grossièrement en deux catégories :

- les premières décomposent l'écoulement en des parties discrètes qu'elles analysent séparément ; elles s'inspirent pour cela de l'examen expérimental, tel que celui qui vient d'être présenté. Ce mode de résolution est appelé par Nash [42] l'"approche analytique". Pratiquement, toutes les théories développées dans ce cadre découlent du modèle de Chapman-Korst [43 à 45].
- dans la seconde catégorie, entrent les théories dénommées par Nash "méthodes intégrales". Elles consistent à appliquer à l'ensemble de la couche dissipative les équations de la couche limite qui sont généralement résolues après mise sous forme intégrale. Il serait d'ailleurs plus exact d'appeler ces théories "méthodes d'interaction forte" pour les raisons que nous verrons plus loin. La première tentative dans cette voie est due à Crocco-Lees [46].

### 2.2.2 Théories dérivées du modèle de Chapman-Korst

Le modèle fondamental dont il est ici question a été proposé indépendamment par Chapman et Korst au début des années 1950. Les deux théories reposent sur les mêmes concepts de base, mais l'une, celle de Chapman traite le cas laminaire, tandis que l'autre, due à Korst, s'applique au turbulent. Nous porterons donc essentiellement notre attention sur la méthode de Korst.

Dans ce modèle, la couche dissipative est divisée en deux régions :

- une zone de mélange isobare dont la pression  $p_c$  est égale à celle de l'écoulement contigu non visqueux, de nombre de Mach  $M_c$  (région (I)),
- une zone de recompression (région (II)) où l'écoulement décollé reprend contact avec la paroi.

Examinons d'abord le comportement des particules fluides qui parcourent la couche de mélange et abordent la zone de recollement. Le maintien du régime permanent exigeant la conservation de la masse fluide contenue dans l'eau morte, c'est la ligne de courant (j) issue exactement du point de décollement D qui doit aboutir au point de recollement R. (voir Figure 53).

Toute ligne de courant située au-dessus de (j), doit se prolonger en aval de R, et toute ligne de courant située au-dessous de (j) doit retourner vers l'eau morte. Le courant de reflux qui s'établit ainsi, immédiatement en amont de R, implique l'existence d'un gradient de pression antagoniste, c'est-à-dire que dans l'écoulement non visqueux, se produit une onde continue de compression qui remplace l'onde de choc du modèle relatif au fluide parfait.

Le schéma précédent peut être généralisé pour tenir compte d'une injection éventuelle de masse dans l'eau morte de débit  $q_m$  (voir Figure 54). Alors, la ligne de courant ( $\ell$ ) qui aboutit au point de recollement R et qu'on appellera la ligne de courant limite, est distincte de la ligne de jet (j). Le principe de conservation de la masse implique que  $q_m$  est égal au débit compris entre (j) et ( $\ell$ ).

R étant un point d'arrêt sur ( $\ell$ ), il est nécessaire que la quantité de mouvement disponible sur ( $\ell$ ) au point C, immédiatement en amont de la recompression, soit d'un niveau strictement déterminé par la condition de s'annuler en R sous l'effet du gradient de pression adverse et des forces de viscosité rencontrées entre C et R. Si cette condition est réalisée, il est évident que les particules fluides cheminant au-dessous de ( $\ell$ ), animées d'une vitesse plus faible, rebrousseront chemin avant d'avoir atteint R, alors que les particules s'écoulant au-dessus de ( $\ell$ ), plus rapides, pourront surmonter l'action de freinage entre C et R et s'échapper du côté aval.

Les trois problèmes fondamentaux qui se dégagent de cette analyse, sont donc les suivants :

1. Déterminer l'état du fluide dans la zone de mélange. Nous caractériserons cet écoulement en chaque point par les variables :

$$\frac{\mu}{\mu_{ec}} = \varphi(y) \quad \frac{\rho}{\rho_{ec}} = \theta(y)$$

Le problème correspondant est dit "problème du mélange isobare".

2. Connaissant les profils  $\varphi(y)$  et  $\theta(y)$  dans la couche de mélange, au niveau du point C où commence le phénomène de recollement, définir quelle est la ligne de courant ( $\ell$ ) qui aboutira au point d'arrêt.
3. Enoncer une condition qui permettra d'assurer l'unicité de la solution. C'est le problème du "critère de recollement".

#### 1. Mélange turbulent isobare

La distribution de vitesse dans la zone de mélange peut être décrite par une solution approchée due à Korst.

Pour l'obtenir, on définit un premier système de coordonnées (X,Y) orthogonal et, en général, curviligne dont l'axe X suit la frontière isobare de l'écoulement décollé non visqueux, puis un deuxième système intrinsèque ( $x, y$ ) tel que :

$$X \equiv x \quad Y = y - y_m(x)$$

Après diverses simplifications, et l'introduction d'un modèle de viscosité tourbillonnaire, l'équation du mouvement se met sous la forme :

$$(1) \quad \frac{\partial u}{\partial x} = \frac{\varepsilon}{\mu_{ec}} \frac{\partial^2 u}{\partial y^2}$$

L'expérience des jets incompressibles conduit à prendre pour  $\varepsilon$  l'expression :

$$\varepsilon = \frac{1}{4 \sigma^2} \mu_{ec} x$$

où  $\sigma$  est le paramètre de mélange turbulent.

Korst a donné une solution générale de l'équation (1) qui tient compte du profil de vitesse de la couche limite initiale à l'origine de la zone de mélange. L'expression présente l'inconvénient de conduire à des calculs assez longs, c'est pourquoi, dans la pratique, on utilise le plus souvent la solution correspondant au cas d'une couche limite initiale nulle et qui s'écrit :

$$(2) \quad \varphi = \frac{1}{2} (1 + \operatorname{erf} \eta)$$

La relation (2) peut être employée si la couche limite n'est plus très petite devant l'étendue du décollement à condition d'utiliser le concept d'origine fictive du mélange introduit par Kirk [47] et repris par de nombreux auteurs [41]. En présence d'une couche limite non négligeable, le processus de mélange turbulent est supposé se développer d'une manière analogue à celle qui serait obtenue en l'absence de couche limite à partir d'une origine fictive O située en amont du point de séparation D, la distance OD dépendant, en première analyse, de l'épaisseur de quantité de mouvement  $\theta_c$  de cette couche limite et du nombre de Mach  $M_{ec}$  de l'écoulement extérieur non visqueux.



Le décalage correspondant  $x_0 = 00$  peut être obtenu de diverses manières. En particulier, Solignac et al. [48] ont proposé une relation établie à partir de l'hypothèse que la quantité de mouvement contenue en D dans la couche de mélange fictive, au-dessus de la ligne de jet (j), est identique à celle de la couche limite réelle en ce même point ; ce qui conduit à la relation :

$$x_0 = \sigma \frac{\theta_c}{I}$$

dans cette expression, I est la fonction du nombre de Mach  $M_{e_c}$  définie par :

$$I = \int_{\eta}^{\infty} \frac{\rho}{\rho_{e_c}} \varphi (1 - \varphi) d\eta$$

calculable d'après les lois connues du mélange isobare dans l'état asymptotique.

La relation (2), appliquée compte tenu d'un décalage fictif éventuel de l'origine du mélange, permet donc de déterminer le profil de vitesse à toute abscisse  $x$ . Le calcul de  $\rho/\rho_{e_c}$  suppose que soit également résolue l'équation de l'énergie. Le plus souvent, il est supposé que le nombre de Prandtl turbulent est égal à 1. Dans ces conditions, la distribution de température génératrice dans le mélange isobare est de la forme :

$$\frac{T_i}{T_{e_c}} = \alpha + \beta \varphi$$

soit, compte tenu des conditions aux limites :

$$\begin{aligned} \varphi \rightarrow 0 & \quad T_i = T_m \quad (\text{température de l'eau morte}) \\ \varphi \rightarrow 1 & \quad T_i \rightarrow T_{e_c} \end{aligned}$$

$$\Lambda = \frac{T_i}{T_{e_c}} = \frac{T_m}{T_{e_c}} + (1 - \frac{T_m}{T_{e_c}}) \varphi = \Lambda_m + (1 - \Lambda_m) \varphi$$

D'où, en introduisant le nombre de Crocco :  $C_{e_c}$  tel que :

$$C_{e_c}^2 = \frac{u_{e_c}^2}{2 C_p T_{e_c}} = \frac{\frac{\gamma-1}{2} M_{e_c}^2}{1 + \frac{\gamma-1}{2} M_{e_c}^2}$$

$$(3) \quad \frac{\rho}{\rho_{e_c}} = \frac{1 - C_{e_c}^2}{\Lambda - C_{e_c}^2 \varphi^2}$$

## 2. Détermination de la ligne de courant limite (l)

Considérons la zone de mélange isobare à la pression  $p_c$  qui se développe depuis le point de décollement D (voir Figure 55). En D existe une couche limite initiale dont les épaisseurs caractéristiques après détente de  $p_0$  à  $p_c$  sont  $\delta_c$ ,  $\delta_c^*$ ,  $\theta_c$ . Supposons en outre que soit opérée dans l'eau morte une injection de débit masse  $q_m$  et de quantité de mouvement  $i_m$ . L'application des théorèmes de conservation à la surface de contrôle isobare  $(-\infty, E E', +\infty)$  où EE' est une ligne de courant assez éloignée pour être en dehors de la zone visqueuse et dans le cas où la paroi est rejetée à l'infini (vitesse de retour négligeable) conduit aux relations suivantes :

- conservation de la quantité de mouvement

$$(4) \quad \int_{-\infty}^{\eta_{e'}} \frac{\rho}{\rho_{e_c}} \varphi^2 d\eta = \frac{\sigma}{x+x_0} \left( \frac{i_m}{\rho_{e_c} u_{e_c}^2} + \int_0^{\eta_{e'}} \frac{\rho u^2}{\rho_{e_c} u_{e_c}^2} d\eta \right)$$

Le second membre étant connu par hypothèse et  $\varphi(\eta)$ ,  $\rho/\rho_{e_c}$  déterminés, cette relation définit la cote  $\eta_{e'}$  à donner à la ligne de courant EE', c'est-à-dire détermine le calage en  $y$  du profil des vitesses et des températures tel que la conservation de la quantité de mouvement soit respectée à l'abscisse  $x$ . Le décalage  $y_m$  du système intrinsèque par rapport au système de référence se trouve donc déterminé.

- conservation de la masse

Pour que la masse fluide contenue dans l'eau morte se conserve, il faut et il suffit que entre (l) et EE' on trouve, à chaque abscisse, un débit égal au débit dans la tranche  $x=0$  soit :

$$(5) \quad \int_{\eta}^{\eta_{e'}} \frac{\rho}{\rho_{e_c}} \varphi d\eta = \frac{\sigma}{x+x_0} \left( \frac{q_m}{\rho_{e_c} u_{e_c}} + \int_0^{\eta_{e'}} \frac{\rho u}{\rho_{e_c} u_{e_c}} d\eta \right)$$

En formant ( 4.5 ) puis en remarquant que :

$$\int_0^{\eta_c} \frac{\rho u}{\rho_c u_c} \left( 1 - \frac{u}{u_c} \right) dy = \theta_c$$

il vient :

$$(6) \quad \int_{-\infty}^{\eta_c} \frac{\rho}{\rho_c} \varphi d\eta = \frac{\sigma}{x+x_0} \left( \frac{i_m}{\rho_c u_c^2} - \frac{q_m}{\rho_c u_c} + \theta_c \right) + \int_{-\infty}^{\eta_c} \frac{\rho}{\rho_c} \varphi (1-\varphi) d\eta$$

Dans cette expression, le deuxième membre est connu : la seule inconnue est donc  $\eta_c$  qui se trouve ainsi déterminé, d'où résultent les conditions sur la ligne limite  $\varphi(\eta_c)$  et  $\rho/\rho_c(\eta_c)$ .

La relation (6), établie par Carrière [49] permet d'introduire le coefficient d'injection généralisé :

$$(7) \quad Cq = \frac{q_m}{\rho_c u_c L} + \frac{\theta_c}{L} - \frac{i_m}{\rho_c u_c^2 L} \quad (L = x+x_0)$$

qui montre que l'effet de couche limite initiale peut être assimilé à une injection. En définitive, on constate que :

$$\varphi_f = \varphi_f (M_{e_c}, Cq, \Lambda_\pi, \gamma)$$

$$(8) \quad \frac{\rho_f}{\rho_c} = R (M_{e_c}, Cq, \Lambda_\pi, \gamma)$$

dans le cas, bien sûr, d'un gaz calorifiquement parfait.

Les calculs qui précèdent ayant montré l'influence de la couche limite initiale, la question se pose de déterminer dans chaque cas particulier l'état de cette couche limite à l'origine du mélange isobare, c'est-à-dire après la détente en D de  $p_0$  à  $p_c$ .

Plusieurs méthodes ont été proposées pour calculer l'état de la couche limite après la détente centrée [50,51,52]. Elles font en général l'hypothèse que la détente est un processus si rapide que les phénomènes de viscosité sont négligeables.

Une formule commode, et souvent utilisée, est celle proposée par Nash :

$$(9) \quad \frac{\rho_c u_c}{\rho_0 u_0} \frac{\theta_c}{\theta_0} = \frac{M_{e_0}^2}{M_{e_c}^2}$$

Il est également possible d'employer les relations établies par Reshotko et Tucker [53] dans l'étude des effets d'une discontinuité de pression sur les caractéristiques de la couche limite.

### 3. Critère de recollement

Les relations précédentes permettent de déterminer les caractéristiques de la couche de mélange ainsi que les conditions sur la ligne de courant limite en fonction de facteurs d'influence représentés par le coefficient  $Cq$  et pour une pression de décollement  $p_c$  (ou un nombre de Mach  $M_{e_c}$ ) donnée.

La "fermeture" du problème, exige l'introduction d'une loi ou condition supplémentaire, appelé communément "critère de recollement".

Historiquement, le premier critère proposé est le "critère d'échappement" de Chapman-Korst. Il consiste d'abord à supposer qu'entre la fin du plateau isobare et le point de recollement, les forces de viscosité sont négligeables devant les termes d'inertie et de pression. En conséquence, la compression s'effectue isentropiquement sur chaque ligne de courant.

Il est ensuite admis que la pression d'arrêt  $p_{i_f}$  sur la ligne limite ( $\ell$ ) au moment où elle aborde le recollement est juste égale à la pression statique  $p_s$  régnant dans l'écoulement en fin de compression (voir Figure 51).

$$(10) \quad p_{i_f} = p_s$$

La méthode pratique de calcul consiste, par exemple, à se donner la pression de culot  $p_c$ . On en déduit immédiatement  $M_{ec}$ ,  $q_c$ ,  $\sigma$ ,  $x_c$  ainsi que le nombre de Mach  $M_{es}$  (en considérant soit une compression isentropique, soit une compression par choc). La relation (6), jointes aux formules (2) et (3) permet de déterminer  $q_s$ ,  $q_m$  et  $x_m$  étant donnés, d'où  $\varphi_c$ . Le nombre de Mach  $M_s$  sur la ligne limite se calcule ensuite aisément à partir de  $\varphi_c$ . Dans le cas iso-énergétique ( $T_{te}$ ) on a simplement :

$$M_s^2 = \frac{\varphi_c^2 M_{ec}^2}{1 + \frac{\gamma-1}{2} M_{ec}^2 (1 - \varphi_c^2)}$$

d'où :

$$p_{is} = p_c \left( 1 + \frac{\gamma-1}{2} M_s^2 \right)^{\frac{\gamma}{\gamma-1}}$$

Il convient alors de s'assurer que la condition (10) est bien satisfaite. Si ce n'est pas le cas, on essaye une nouvelle valeur de  $p_c$ , l'opération étant répétée jusqu'à ce que  $p_{is} = p_s$ .

Les premières applications de la théorie effectuées par Korst, en considérant la couche limite initiale comme négligeable, donnaient un assez bon recouplement avec l'expérience. En fait, on a constaté plus tard, que le bon accord était fortuit et provenait de la compensation de deux erreurs : la première consistant à négliger la couche limite, la seconde résidant dans l'inexactitude du critère d'échappement (10).

De nombreuses modifications ont alors été proposées pour améliorer le critère de Chapman-Korst. Nous ne mentionnerons que les plus marquantes en nous étendant toutefois davantage sur la notion de "critère angulaire" qui est à la base des méthodes développées à l'ONERA pour traiter les problèmes de culot.

#### Critère de Nash

Le modèle d'écoulement de culot utilisé par Nash est essentiellement le même que celui de Korst. La différence essentielle porte sur le fait que Nash, sans doute le premier, a mis en évidence que la pression statique au recollement  $p_R$ , est inférieure à la pression aval  $p_s$ , ce qui explique l'inexactitude du critère de Chapman-Korst. Pour tenir compte de cette constatation, Nash introduit le rapport :

$$N = \frac{p_R - p_c}{p_s - p_c}$$

qui doit être demandé à l'expérience. La condition  $p_{is} = p_R$  est conservée, mais maintenant  $p_R < p_s$ . Le coefficient  $N$  varie avec le nombre de Mach  $M_{ec}$  (Figure 56a), l'évolution étant toutefois moins sensible en supersonique. Pour cette raison, Nash a initialement adopté une valeur moyenne  $N = 0,35$ . En fait,  $N$  est également fonction de la couche limite initiale [54].

#### Critère de Roberts

Le critère de recollement proposé par Roberts est basé sur une analogie entre la variation de pression de  $p_R$  à  $p_s$  dans un recollement et la croissance de pression de  $p_0$  à  $p_D$  au cours d'un processus de décollement. Roberts introduit un paramètre de recollement  $R$  défini par :

$$R = \frac{M_{es}}{M_{eR}}$$

et donné par la relation empirique :

$$R = 0,799 + 0,1560 M_{ec} - 0,08237 M_{ec}^2 + 0,009564 M_{ec}^3$$

qu'il a déduit de résultats sur le décollement supersonique.

Ainsi qu'on le constate Figure 56b, le paramètre  $R$  conduit à une meilleure corrélation que le coefficient  $N$  de Nash.

#### Critère de Mac Donald [55]

Bien qu'assez différente de la méthode de Korst, le modèle de Mac Donald suit également l'approche analytique selon la définition de Nash. Très succinctement, la zone dissipative est découpée en trois régions :

- le mélange isobare s'étendant jusqu'à une abscisse  $x_c$ ,
- le recollement de  $x_c$  à l'abscisse  $x_R$  du point de recollement,
- la réhabilitation entre  $R$  et l'état final correspondant à la pression  $p_s$ .

A partir d'une analyse simplifiée consistant à négliger l'action du frottement au delà de  $x_c$  et à utiliser des relations de conservation globales pour la masse et la quantité de mouvement, Mc Donald détermine, pour une pression  $p_c$  donnée, les caractéristiques de la couche visqueuse en fin de réhabilitation. La solution est obtenue quand le paramètre de forme de la couche limite dans l'état final est égal à la valeur résultant d'une loi de plaque plane.

#### Critère angulaire de recollement (Carrière et Sirieix [51])

Les différents critères que nous venons de passer en revue présentent probablement l'inconvénient majeur de faire intervenir, directement ou indirectement, le niveau de pression  $p_s$ , c'est-à-dire des conditions situées bien en aval du recollement. Or, au cours d'expériences systématiques, Carrière [56], puis Sirieix et al. [57] ont clairement mis en évidence que la pression en aval du point R pouvait être perturbée (entre certaines limites), sans que la partie initiale du processus de recollement, et donc la pression de culot  $p_c$ , soit modifiées. Une telle observation tend à démontrer que tout critère faisant intervenir l'état S a peu de chance de donner des résultats satisfaisants.

Le concept de "critère angulaire de recollement" tient compte de ce fait en retenant comme idée de base que le phénomène est entièrement déterminé par l'état de la couche dissipative au moment où elle aborde la zone de recollement, état qui peut être caractérisé par :

- la direction  $\psi$  de l'écoulement extérieur non visqueux relativement à la paroi (voir Figure 53a)
- le nombre de Mach extérieur  $M_{\infty}$
- les lois de distribution des vitesses et des masses spécifiques dans la couche turbulente.

Si l'on admet que pour  $M_{\infty}$  et un rapport  $\Lambda_m$  donnés, la condition de recollement est définie par la variable  $\eta$  caractérisant l'écoulement sur la ligne de courant limite ( $l$ ), il est clair, d'après les expressions établies plus haut (relations 8, 9 et 10), que cette condition ne dépend que du paramètre  $C_q$ .

En conséquence, la loi angulaire recherchée doit nécessairement être de la forme :

$$\psi = \psi(M_{\infty}, \Lambda_m, C_q) \quad (\text{pour } \gamma \text{ fixé})$$

Dans la mesure où  $C_q$  est un petit paramètre, on peut l'écrire :

$$(M) \quad \psi = \bar{\psi}(M_{\infty}, \Lambda_m) + C_q \frac{\partial \psi}{\partial C_q}(M_{\infty}, \Lambda_m)$$

On est ainsi amené à déterminer les deux fonctions

$$\bar{\psi}(M_{\infty}, \Lambda_m) \quad \text{et} \quad \frac{\partial \psi}{\partial C_q}(M_{\infty}, \Lambda_m)$$

A cet effet, la fonction  $\bar{\psi}(M_{\infty})$ , pour le cas iso-énergétique, a été déduite d'un certain nombre d'expériences systématiques, pour lesquelles les conditions d'essais ont été choisies aussi voisines que possible du cas idéal  $C_q = 0$

La fonction  $\partial \psi / \partial C_q$  est calculée à partir de la variation de la pression génératrice à travers la couche de mélange [51] en écrivant la déviation  $\psi(M_{\infty})$  sous la forme :

$$\psi(M_{\infty}) = \Delta \psi + \psi_R$$

$\Delta \psi$  étant la déviation subie par l'écoulement extérieur entre D et R et  $\psi_R$  l'inclinaison résiduelle au point de recollement R, par rapport à la paroi.

Si l'on admet que la pression en R est égale à la pression d'arrêt  $p_{R0}$  sur la ligne limite, ce qui est bien vérifié expérimentalement,  $\Delta \psi$  se met sous la forme, dans le cas iso-énergétique ( $T_i = \text{constante}$ ) :

$$\Delta \psi = P(M_R) - P(M_{\infty}) = P(M_{\infty} \sqrt{1 - \varphi_i^2}) - P(M_{\infty})$$

où  $P(M)$  est le nombre de pression de Busemann.

Par conséquent, compte tenu de l'expression connue de  $P(M)$ , et que pour  $C_q = 0$ ,  $\varphi_i = \varphi_j$

$$\frac{\partial \psi}{\partial C_q} = - \frac{\sqrt{M_{\infty}^2 - 1}}{1 - \varphi_i^2} \varphi_i \frac{\partial \varphi_i}{\partial C_q} \left/ \left( 1 + \frac{1-\gamma}{2} M_{\infty}^2 \right) \right. + \frac{\partial \psi_R}{\partial C_q}$$

Il est supposé que la couche dissipative en R est peu sensible aux variations de  $C_q$  (pour  $C_q \ll 1$ ) donc  $\partial \eta / \partial C_q = 0$

Finalement, tenant compte de (2.3 et 6), on trouve pour  $\partial \psi / \partial C_q$  l'expression :

$$(12) \quad \frac{\partial \psi}{\partial C_q} = - \frac{\sigma}{\sqrt{\pi}} e^{-\eta^2} \frac{\sqrt{M_{ec}^2 (1 - \eta^2)} - 1}{1 - \eta^2}$$

qui peut sans difficulté se généraliser au cas non iso-énergétique

Les calculs précédents, et en particulier l'expression (12), font intervenir le paramètre de mélange  $\sigma$  qui caractérise le taux d'expansion de la zone de mélange turbulent. Les valeurs de  $\sigma$  doivent être demandées à l'expérience et, malheureusement, la mesure de  $\sigma$  est délicate si bien que les données dont on dispose présentent une forte dispersion. La Figure 57 montre des lois d'évolution de  $\sigma$  en fonction du nombre de Mach  $M$  proposées par différents auteurs. On constate de larges différences entre les diverses corrélations (la valeur  $\sigma_{\infty}$ , correspondant au cas incompressible, est généralement prise égale à 12).

La loi de recollement, exprimée sous la forme du critère angulaire, a été généralisée au cas des écoulements de révolution afin de pouvoir traiter les problèmes d'application intéressant le domaine de la propulsion où les configurations présentent en général une symétrie axiale.

L'extension à de telles configurations des lois angulaires obtenues en écoulement plan se présente, a priori, d'une manière quelque peu décevante comme le montre la Figure 58 où sont portés, en fonction de  $M_{ec}$ , les angles théoriques  $\bar{\psi}$  déterminés pour des cas où l'effet de révolution se fait sentir. On observe une dispersion importante des résultats et des écarts notables par rapport à l'écoulement plan ; ces écarts peuvent être attribués non seulement à des facteurs de perturbation liés à la non uniformité du champ extérieur à la zone décollée, mais aussi à l'influence de l'effet de révolution sur le développement de la zone de mélange lorsque des variations significatives de la distance à l'axe le long de la frontière isobare sont enregistrées.

Il est toutefois possible d'établir une corrélation permettant d'exprimer l'écart sur les lois de recollement [58]

$$\bar{\psi}(M_{ec}) \text{ révolution} - \bar{\psi}(M_{ec}) \text{ plan}$$

en fonction du rapport :

$$F = \frac{\sigma \text{ plan}}{\sigma \text{ révolution}}$$

qui caractérise l'évolution du paramètre de mélange  $\sigma$  suivant la géométrie de la frontière isobare (voir Figure 59).

Une étude simplifiée du mélange, basée sur le modèle de viscosité turbulente de Prandtl, montre que F est donné par la relation :

$$F = \int_0^L \frac{r}{r_h} \frac{ds}{L}$$

dans laquelle les notations de la figure 59 sont utilisées. La valeur F résulte immédiatement de la forme de la ligne de jet théorique (frontière isobare) calculée, par exemple, par la méthode des caractéristiques.

L'angle de recollement  $\bar{\psi}$  peut également dépendre des effets thermiques (leur influence est faible tant que la température génératrice ne dépasse pas 1000°K [59]), ainsi que de la nature du gaz (effet de  $\gamma$ ). Des expériences effectuées à l'ONERA ont montré qu'effectivement,  $\bar{\psi}$  variait sensiblement en fonction de  $\gamma$  (voir Figure 60) [59]. Adoptant une démarche purement intuitive, l'écart observé peut être assez bien représenté au moyen du raisonnement suivant.

Dans le cas de l'air ( $\gamma = 1,4$ ), connaissant  $M_{ec}$  et  $\bar{\psi}(M_{ec})$ , il est possible de calculer le nombre de Mach final  $M_{ef}$  après recollement. En admettant que la compression de  $M_{ec}$  à  $M_{ef}$  est un processus quasi-isentropique et par ondes simples,  $M_{ef}$  est donné par :

$$\nu(M_{ef}) = \nu(M_{ec}) - \bar{\psi}(M_{ec})$$

$\nu(M)$  étant la fonction bien connue :

$$\nu(M) = \sqrt{\frac{\gamma+1}{\gamma-1}} \operatorname{Arctg} \sqrt{\frac{\gamma-1}{\gamma+1} (M^2 - 1)} - \operatorname{Arctg} \sqrt{M^2 - 1}$$

Si on postule que , à valeur de  $M_{ec}$  identique,  $M_{ef}$  est le même pour tout  $\gamma$  , l'angle de recollement pour  $\gamma \neq 1,4$  sera donné par :

$$\bar{\psi}(M_{ec}, \gamma) = \psi(M_{ec}, \gamma) - \psi(M_{ef}, \gamma)$$

Les courbes tracées Figure 60 , montrent que cette interprétation rend compte de la réalité de manière très correcte si  $\gamma = 1,667$ . Mais, évidemment, des expériences seraient souhaitables pour confirmer l'évolution prédite quand  $\gamma < 1,4$ .

A partir de ces données théoriques et des corrélations empiriques permettant de prendre en compte les différents facteurs (géométrie, nature du gaz), le calcul du recollement s'effectue, en règle générale, de la manière suivante.

Pour une pression  $p_c$  , fixée a priori, la méthode des caractéristiques détermine, dans le cas du fluide parfait (non visqueux) de nombre de Mach  $M_{ec}$  : la ligne de jet isobare théorique  $DR_r$  et définit, à l'impact  $R_r$  avec la paroi, la déviation  $\psi$  assimilée à l'angle de recollement. Les facteurs de courbure qui apparaissent lorsque l'écoulement extérieur n'est pas uniforme ou est de révolution, sont ainsi pris en compte (voir Figure 61 ).

$\psi$  et  $M_{ec}$  étant alors connus, le paramètre  $C_q$  est calculé par (11). Il lui correspond, si l'on connaît l'épaisseur de quantité de mouvement  $\theta_c$  à l'origine du décollement (donnée, par exemple, par (9)) un débit  $q_m$  (relation (7)) assurant l'équilibre massique de l'eau morte, qui est comparé à la valeur  $\bar{q}_m$  effectivement injectée (le plus souvent  $\bar{q}_m = 0$ ). Une itération sur  $p_c$  permet d'assurer l'égalité de ces deux grandeurs.

L'exemple choisi pour mettre en évidence la précision de cette méthode, par comparaison avec l'expérience et d'autres théories concerne l'influence de la couche limite initiale sur la pression de culot dans un cas où l'écoulement supersonique amont est uniforme (voir Figure 62 ). Les théories retenues sont celles que nous avons évoquées plus haut, (plus la méthode de Cooke [60] ). Un accroissement progressif de l'épaisseur  $\theta_0$  , immédiatement en amont de D (pour une hauteur  $h$  de culot donnée), se traduit par une croissance d'abord rapide de la pression de culot  $p_c$  , s'atténuant très vite lorsque  $\theta_0$  augmente, la valeur de  $p_c$  restant ensuite quasi-constante pour une large plage de variation de  $\theta_0$  . On constate sur la Figure 62 , que la théorie de Korst, appliquée en négligeant  $\theta_0$  recoupe assez bien l'expérience dès que  $\theta_0/h > 0,03$ , valeur au delà de laquelle  $p_c$  demeure sensiblement constante.

Des confrontations plus nombreuses de cette théorie avec l'expérience seront présentées plus loin où son application à des problèmes de culot plus réalistes sera envisagée.

### 2.2.3 Méthodes d'interaction forte (méthodes intégrales)

Le recollement turbulent est un exemple de couplage fort entre une zone visqueuse et un écoulement extérieur quasi-isentropique. Un tel phénomène s'observe chaque fois qu'il y a formation, au sein d'un écoulement, d'une zone décollée pouvant résulter, par exemple, d'un décrochement de paroi (problème de culot).

Le principe de base de la plupart des méthodes d'interaction forte repose sur la description de la zone dissipative au moyen des équations de la couche limite qui, le plus souvent, sont résolues au moyen d'une technique intégrale. La différence essentielle avec la théorie de Prandtl est qu'ici la loi de pression imposée à la frontière de la couche limite n'est plus une donnée indépendante, mais résulte du couplage entre le champ externe (non visqueux) et la zone visqueuse. Elle doit en conséquence être déterminée soit au fur et à mesure de la progression du calcul (cas supersonique), soit par itération avec relaxation (cas subsonique et transsonique).

La première application d'une méthode d'interaction à un problème de recollement supersonique, est due à Crocco-Lees [46] . Leur publication a inspiré un vaste effort de recherches qui se poursuit encore activement. Nous n'analyserons pas ici les nombreuses variantes de cette méthode qui ont été publiées à ce jour [61-62-63-64] . Mentionnons, à part, la critique expérimentale très détaillée de "de Krasinski" [65] qui, en outre, étendit la formulation au cas de révolution.

La formulation de la méthode fut ensuite améliorée par Lees et Reeves [66] , en laminaire, puis, dans cet esprit, étendue au cas turbulent par Alber [67] et Hunter et Reeves [68] .

Nous nous limiterons ici à la présentation de la formulation d'Alber qui, dans le cadre plus simple du cas supersonique plan, permet de dégager les aspects fondamentaux de la méthode dont nous verrons, plus loin, l'application au problème du culot axisymétrique.

Les équations de départ pour décrire la zone dissipative sont celles de la couche limite turbulente appliquées au mouvement moyen, soit :

$$\text{continuité} \quad (13) \quad \frac{\partial(\rho u)}{\partial x} + \frac{\partial(\rho v)}{\partial y} = 0$$

. quantités de mouvement

$$(14) \quad \rho u \frac{\partial u}{\partial x} + \rho v \frac{\partial u}{\partial y} = - \frac{\partial p}{\partial x} + \frac{\partial \tau}{\partial y}$$

$$0 = \frac{\partial p}{\partial y}$$

Ici  $\tau$  désigne le frottement total, somme du terme laminaire  $\tau_l$  (le plus souvent négligé) et de la tension de Reynolds  $\tau = -\rho \overline{u'v'}$ . Nous nous placerons dans le cas adiabatique, et supposons la température génératrice  $T_e$  constante, ce qui nous dispense de faire intervenir l'équation de l'énergie.

L'équation (14) est mise sous la forme intégrale de Von Karman :

$$(15) \quad \frac{d\theta}{dx} + \theta \left( \frac{\delta^*}{\theta} + 2 - \frac{2m_e}{\delta-1} \right) \frac{1}{1+m_e} \frac{dM_e}{dx} = \frac{C_f}{2}$$

où :  $M_e$  est le nombre de Mach à la frontière  $\delta$  de la couche dissipative,

$\delta^*$  l'épaisseur de déplacement,

$\theta$  l'épaisseur de quantité de mouvement et  $m_e = \frac{\delta-1}{2} M_e^2$

Le coefficient de frottement  $C_f$  est généralement négligé. L'approximation est justifiée par le fait que,  $C_f$ , nul au recollement, est partout faible dans la zone étudiée dont l'étendue longitudinale est de surcroît réduite (quelques  $\delta$ ).

A l'équation intégrale des quantités de mouvement, est adjoint une relation supplémentaire. A l'origine, Crocco et Lees ont proposé une équation de "mélange" ou "d'entraînement" de la forme :

$$\frac{d\bar{m}}{dx} = k \rho_e u_e$$

où  $\bar{m} = \int_0^\delta \rho u dy$  est le flux de masse à travers la couche dissipative, et  $k$  un coefficient de mélange supposé connu. Par la suite, on a préféré utiliser l'équation intégrale du premier moment de quantité de mouvement encore appelée équation de l'énergie cinétique. Elle est obtenue en multipliant (14) par  $u$  :

$$\rho u^2 \frac{\partial u}{\partial x} + \rho u v \frac{\partial u}{\partial y} = - u \frac{\partial p}{\partial x} + u \frac{\partial \tau}{\partial y}$$

d'où, après intégration en  $y$  de 0 à  $\delta$  :

$$(16) \quad \frac{d\theta^*}{dx} + \theta^* \left[ 3 + \frac{2(\delta-2)}{\delta-1} m_e \right] \frac{1}{1+m_e} \frac{1}{M_e} \frac{dM_e}{dx} = \phi$$

avec

$$\theta^* = \int_0^\delta \frac{\rho u}{\rho_e u_e} \left( 1 - \frac{u^2}{u_e^2} \right) dy \quad \phi = \frac{2}{\rho_e u_e^3} \int_0^\delta \tau \frac{\partial u}{\partial y} dy$$

La fonction  $\phi$  est souvent désignée sous le nom d'intégrale de dissipation.

Une variante, utilisée en particulier par Kuhn et Nielsen [69], consiste à multiplier (14), non pas par  $u$ , mais par  $y$ . On peut ainsi former une autre équation intégrale.

L'équation fondamentale qui assure le couplage entre la couche dissipative et l'écoulement contigu non visqueux est obtenue en intégrant de la paroi à  $\delta$  l'équation de continuité (13), ce qui donne :

$$(17) \quad \frac{d\delta^*}{dx} - (\delta - \delta^*) \frac{1 - M_e^2}{1 + m_e} \frac{1}{M_e} \frac{dM_e}{dx} = \frac{v_e}{u_e} = \eta \theta$$

où  $\theta$  représente l'inclinaison du vecteur vitesse  $\vec{V}_e$  à la frontière  $\delta$ .

Il est à noter que certains auteurs utilisent des équations de couplage différentes (voir à ce sujet Le Balleur [70]) consistant à assurer le couplage :

- soit sur la surface de déplacement  $\delta^*(x)$ , alors (17) devient : (18)  $\frac{d\delta^*}{dx} = \eta \theta$

- soit en transposant la condition de compatibilité à la paroi, alors la relation s'écrit :

$$(10) \quad \frac{d\delta^*}{dx} + \delta^* \frac{1-M_e^2}{1+M_e} \frac{1}{M_e} \frac{dM_e}{dx} = \tan \theta$$

Les équations (15 - 16 - 17) constituent le système décrivant l'interaction entre la couche dissipative et l'écoulement extérieur. En supersonique, l'intégration peut se faire en progressant de l'amont vers l'aval, l'écoulement externe étant calculé conjointement en utilisant, par exemple la méthode des caractéristiques qui fournit une relation liant  $\theta$  et  $M_e$ . Si cet écoulement s'effectue par ondes simples,  $\theta$  et  $M_e$  sont reliés directement par la relation de Prandtl-Meyer :

$$\theta - \theta_\infty = \nu(M_e) - \nu(M_\infty)$$

En fait, pour que le système différentiel soit fermé, il faut en plus faire une hypothèse sur les profils de vitesse dans la couche limite, afin de pouvoir exprimer les épaisseurs  $\delta, \delta^*, \theta, \theta^*$  en fonction d'un nombre réduit de paramètres. Le plus souvent, on utilise une famille à un paramètre de forme A, si bien que :

$$\frac{\theta}{\delta^*} = \mathcal{X}(A, M_e) \quad \frac{\theta^*}{\delta^*} = J(A, M_e)$$

$$\frac{\delta - \delta^*}{\delta^*} = \mathcal{Z}(A, M_e)$$

sont des fonctions connues de A et  $M_e$

L'intégrale de dissipation est exprimée, en fonction de A,  $M_e$  (plus éventuellement du nombre de Reynolds), soit à partir d'une formule empirique, soit à partir des profils de vitesse et d'une hypothèse sur le frottement turbulent

Le système différentiel s'écrit en définitive :

$$\mathcal{X} \frac{d\delta^*}{dx} + \delta^* \frac{\partial \mathcal{X}}{\partial A} \frac{dA}{dx} + Q_1 \frac{\delta^*}{M_e} \frac{dM_e}{dx} = \frac{C_f}{2} = (0)$$

$$J \frac{d\delta^*}{dx} + \delta^* \frac{\partial J}{\partial A} \frac{dA}{dx} + Q_2 \frac{\delta^*}{M_e} \frac{dM_e}{dx} = \phi$$

$$\frac{d\delta^*}{dx} + Q_3 \frac{\delta^*}{M_e} \frac{dM_e}{dx} = \tan \theta$$

$Q_1$ ,  $Q_2$  et  $Q_3$  sont des fonctions de A et  $M_e$  que nous n'explicitons pas ici (voir la référence [9]).

Il est souvent commode d'adopter comme paramètre A, caractérisant la forme des profils de vitesse, le rapport

$$\mathcal{H}_i = \frac{\theta_i}{\delta_i^*}$$

des épaisseurs de quantité de mouvement et de déplacement incompressibles. Nous adopterons dorénavant ce paramétrage.

La méthode originale d'Alber est, dans son esprit, analogue à la formulation que nous venons d'établir. Toutefois, afin d'éliminer la dépendance des fonctions  $\mathcal{X}$ ,  $J$ ,  $\mathcal{Z}$  à l'égard du nombre de Mach, Alber effectue, préalablement à la mise sous forme intégrale, une transformation compressible-incompressible sur les équations de départ (13 - 14). A cette fin, il introduit les variables transformées : X, Y, telles que :

$$dX = \frac{a_\infty \rho_\infty}{a_\infty \rho_\infty} dx$$

$$dY = \frac{a_\infty \rho}{a_\infty \rho_\infty} dy$$

$$\psi = \psi \text{ (fonction de courant)} \quad u_i = \frac{a_\infty}{a_e} u$$

Pour que la transformation soit effective, Alber fait une hypothèse sur la viscosité turbulente  $\epsilon$  ( $\tau = \rho \epsilon \frac{\partial u}{\partial y}$ ) qui est prise telle que :

$$\rho^* \epsilon = f(x) = \rho_r^* \epsilon_r$$

où  $\rho_r$  est une masse spécifique de référence,  $\epsilon_r$  étant de la forme :

$$\epsilon_r = K_\theta \mu_e \theta$$

$$\rho^* \epsilon = \rho_r^* K_\theta \mu_e \theta = \rho_r^* \frac{\rho_\infty}{\rho_e} K_\theta \mu_{e_i} \theta_i$$



où  $\theta_i$  est l'épaisseur de quantité de mouvement transformée :

$$\theta_i = \int_0^{\delta_i} \frac{u_i}{u_{ie}} \left( 1 - \frac{u_i}{u_{ie}} \right) dy$$

Posant  $\tilde{\epsilon} = \left( \frac{\rho_r}{\rho_e} \right)^2 K_0 u_{ei} \theta_i$ , les équations "incompressibles" s'écrivent :

$$\frac{\partial u_i}{\partial x} + \frac{\partial v_i}{\partial y} = 0$$

$$u_i \frac{\partial u_i}{\partial x} + v_i \frac{\partial u_i}{\partial y} = u_{ei} \frac{du_{ei}}{dx} + \tilde{\epsilon} \frac{\partial^2 u_i}{\partial y^2}$$

$$u_i^2 \frac{\partial u_i}{\partial x} + u_i v_i \frac{\partial u_i}{\partial y} = u_i u_{ei} \frac{du_{ei}}{dx} + \tilde{\epsilon} u_i \frac{\partial^2 u_i}{\partial y^2}$$

Mises sous forme intégrale, elles deviennent :

quantité de mouvement :  $\mathcal{R}_i \frac{d\delta_i^*}{dx} + \delta_i^* \frac{d\mathcal{R}_i}{dx} + (2\mathcal{R}_i + 1) \frac{\delta_i^*}{M_e} \frac{dM_e}{dx} = 0$

énergie cinétique :  $J_i \frac{d\delta_i^*}{dx} + \delta_i^* \frac{\partial J_i}{\partial \mathcal{R}_i} \frac{d\mathcal{R}_i}{dx} + 3 J_i \frac{\delta_i^*}{M_e} \frac{dM_e}{dx} = K_0 \left( \frac{\rho_r}{\rho_e} \right)^2 \mathcal{R}_i R_i$

couplage :  $G \frac{d\delta_i^*}{dx} + \delta_i^* \frac{dG}{dx} + \int \frac{\delta_i^*}{M_e} \frac{dM_e}{dx} = \frac{t_g \theta}{m_e}$

$$R_i = \frac{2\delta_i^*}{u_{ei}^2} \int_0^{\delta_i} \left( \frac{\partial u_i}{\partial y} \right)^2 dy$$

que nous n'explicitons pas.

$f$  et  $G$  sont des fonctions de  $m_e$  et  $\mathcal{R}_i$

Le système à intégrer - transformé ou non - peut s'écrire sous la forme :

$$(20) \quad \frac{d\delta^*}{dx} = \frac{N_1}{D}, \quad \frac{d\mathcal{R}_i}{dx} = \frac{1}{\delta^*} \frac{N_2}{D}, \quad \frac{dM_e}{dx} = \frac{M_e}{\delta^*} \frac{N_3}{D}$$

(forme analogue avec les quantités incompressibles).

Le système (20) n'est généralement appliqué qu'à la recompression. La zone de mélange quasi-isobare qui précède le recollement ne peut en effet être convenablement décrite par une famille à un seul paramètre. Cette région peut être calculée à l'aide des méthodes particulières, déjà citées, qui relèvent de la théorie du mélange turbulent ou en utilisant une famille de profils à deux paramètres (voir § 2.3.1.2).

Le principe général de résolution d'un problème de recollement consiste donc à calculer séparément le mélange quasi-isobare, puis la recompression. Les deux solutions sont ensuite raccordées en assurant la continuité de certaines grandeurs ; par exemple, le nombre de Mach  $M_e$ , la vitesse  $u_j$  sur la ligne de jet et de débit passant au-dessus de cette dernière (voir la référence [67] pour plus de détail).

Partant d'un état initial, en fin de zone isobare, le système (20) peut être intégré en cheminant vers l'aval, de façon à rejoindre un état de couche limite recollée. En fait, il apparaît, qu'au cours de cette intégration, le dénominateur  $D$  s'annule généralement (dans le cas où les équations de couplage (17) ou (18) sont utilisées), rendant ainsi la solution singulière sauf si les numérateurs s'annulent simultanément (on vérifie que si  $D$  et l'un des  $N_i$  sont nuls en même temps, les autres le sont aussi). Il est commode de discuter de ce comportement dans le plan de phase  $(\mathcal{R}_i, M_e)$  où, pour  $M_{e,0}$  donné (compression par ondes simples), il est possible de tracer les courbes  $\mathcal{R}_1, \mathcal{R}_2, \mathcal{R}_3$  et  $D$  sur lesquelles  $N_1 = N_2 = N_3 = D = 0$  respectivement. En vertu de la remarque qui précède, ces courbes ont un point commun  $K$  (voir figure 63). Il est aisé de s'assurer qu'une courbe intégrale continue partant de  $A$  (début de la recompression) ne peut joindre  $B$  (sillage réhabilité en aval) qu'à la condition de passer par  $K$ . Toute autre trajectoire dans le plan de phase correspond à une solution physiquement inacceptable pour un recollement (apparition d'un extremum pour  $M_e$  ou  $\mathcal{R}_i$ ).

La conséquence fondamentale de l'existence du point singulier K est de rendre la solution de A en K indépendante des conditions imposées en aval de K qui joue ainsi un rôle de "blocage" à la manière du col d'une tuyère convergente divergente amorcée. L'existence du "point critique K" a été démontrée pour la première fois par Crocco et Lees.

C'est le passage régulier de la solution par le point critique K qui assure l'unicité de la solution pour le problème du recollement, c'est-à-dire la condition qui définit la pression de culot  $p_c$ . Les valeurs initiales en A, et en particulier  $M_{ac}$ , donc  $p_c$ , doivent être telles que la trajectoire dans le plan de phase passe par K (voir figure 63). Cette condition constitue un "critère" de recollement, (le comportement des solutions au voisinage de K ainsi que les méthodes d'intégration qui permettent d'assurer la régularité en K sont discutées plus en détail, références [9] et [71]).

Ce schéma théorique est évidemment très séduisant car il semble interpréter parfaitement la notion de point critique mise en évidence expérimentalement par Carrière et Sirieix (voir précédemment). Toutefois, la position de K et même son existence sont étroitement fonctions de l'équation de couplage utilisée. Ainsi, la singularité qui se manifeste par l'annulation de D disparaît lorsqu'on assure le couplage à la paroi (équation (19)). La signification physique du point critique K est donc loin d'apparaître clairement.

Nous allons maintenant examiner un certain nombre de méthodes proposées pour résoudre les problèmes de culot qui nous préoccupent plus particulièrement. La plupart d'entre elles s'inspirent des théories que nous venons d'évoquer en les généralisant à des configurations pratiques :

- culot axisymétrique sans jet,
- culot axisymétrique avec un ou plusieurs jets propulsifs.

Nous commencerons par envisager le problème du calcul de la pression au culot d'un missile en l'absence de jet.

## 2.3 Ecoulement au culot d'un arrière corps de révolution sans jet

### 2.3.1 Ecoulement supersonique

#### 2.3.1.1 Méthodes globales (analytiques)

La détermination de la pression en aval d'un culot de révolution, en l'absence de jet, pose un problème particulier en raison des difficultés analytiques rencontrées dans le calcul de fluide parfait quand l'écoulement converge vers l'axe. L'artifice employé pour tourner cette difficulté consiste à imaginer que l'écoulement recolle sur un dard matérialisant le coeur du sillage visqueux ; le problème est alors de trouver le diamètre de ce dard.

. Théorie de Mueller. [8]

La méthode proposée par Mueller suit de très près le schéma de Chapman-Korst, mais en l'adaptant au cas de révolution.

Le modèle d'écoulement adopté est représenté Figure 64 .

L'écoulement est, selon l'approche classique, décomposé en trois régions :

- a/ un champ externe non visqueux,
- b/ une zone de mélange dissipative
- c/ une région de recollement

Les différentes hypothèses sont effectuées :

1. la couche limite initiale est négligée mais sa nature est turbulente.
2. l'écoulement non visqueux, contigu à la zone de mélange, est supposé se développer, entre D et  $R_T$ , le long d'une surface tronconique d'angle de convergence  $\varphi$ . Cette modélisation due à Zumwalt [72], repose sur des observations expérimentales montrant que la zone à pression constante, le long de l'axe, est relativement courte, la variation de pression étant proche de celle sur un arrière corps tronconique. L'écoulement de fluide parfait est calculé par la méthode des caractéristiques. Il résulte de cette hypothèse que le mélange n'est plus isobare et les nombres de Mach en D et  $R_T$  sont différents.
3. néanmoins, les profils de vitesse dans la zone de mélange sont toujours supposés être représentés par la relation (2).

4. La recompression en  $R_T$  s'effectue au travers d'une onde de choc oblique qui fait passer la pression à la valeur  $p_c$ . Le point  $R_T$  est situé sur un dard dont le rayon  $r_d$ , est donné par une corrélation proposée par Chapman [2] sous la forme  $r_d/r_c$  fonction du nombre de Mach  $M_{c_0}$  ( $r_c$  est le rayon du culot) (voir Figure 65). Dans une version ultérieure de la méthode, Roache [73] détermine la valeur de  $r_d$  selon un critère consistant à adopter le rayon  $r_d$  qui rend la pression de culot  $p_c$  maximale. On s'affranchit ainsi d'une donnée expérimentale dont le caractère de généralité peut être mis en doute.
5. l'unicité de la solution est assurée en satisfaisant au critère d'échappement de Korst.

Dans cette méthode, l'effet de révolution intervient essentiellement dans l'établissement des relations de bilan (4) et (5) qui permettent de positionner la ligne de courant limite. Le volume de contrôle utilisé est limité par deux sections situées en D et  $R_T$  respectivement, et par deux lignes de courant E et - E (voir Figure 64) définies de façon telle que la section droite offerte à l'écoulement demeure quasi-constante et que le terme de pression  $p dA$  puisse être négligé dans l'équation pour la quantité de mouvement. Les relations de bilan ainsi obtenues tiennent compte du fait que les nombres de Mach en  $R_T$  et D sont différents, ce qui conduit à une équation implicite assez compliquée pour  $\eta_c$  (ou  $\eta$ ) en  $R_T$ . Les effets de compressibilité et de nature du gaz sur le paramètre de mélange  $\sigma$  sont représentés par la formule de Channapragada [74].

La méthode permet également de tenir compte d'un effet d'injection de masse au culot.

Les figures (66a) et (66b) montrent des exemples d'application pour un culot cylindrique (où les points de comparaison expérimentaux sont nombreux), et un culot présentant un rétreint. L'accord avec l'expérience est généralement très bon.

La Figure 67 met en évidence l'effet de nature du gaz pour un arrière corps avec rétreint. L'augmentation de  $\gamma$  entraîne une croissance de la pression de culot, ce qui est en accord avec l'évolution du critère angulaire de recollement notée expérimentalement (voir Figure 60).

#### Théorie de Délery et Sirieix

La méthode développée à l'ONERA par Délery et Sirieix utilise le concept de critère angulaire de recollement. Ses caractéristiques essentielles sont les suivantes :

1. le mélange turbulent qui se développe depuis le point de décollement est supposé isobare à la pression de culot  $p_c$ . La frontière de l'écoulement décollé non visqueux est calculée par la méthode des caractéristiques.
2. la ligne de courant limite ( $\ell$ ) du mélange est déterminée en écrivant les relations de conservation globale pour la masse et la quantité de mouvement, compte tenu de l'effet de révolution, et de l'existence éventuelle d'une couche limite initiale.
3. le recollement est supposé se produire sur un dard de rayon  $r_d$ , ce qui permet de définir l'angle de recollement  $\psi$  (voir Figure 68) et d'appliquer les lois angulaires de recollement.
4. le rayon  $r_d$  est assimilé à l'épaisseur de déplacement  $\delta_R^*$  du sillage au niveau du recollement R,  $\delta_R^*$  étant défini par :

$$2\pi \int_0^{\delta_R} \rho u y dy = 2\pi \int_{\delta_R^*}^{\delta_R} \rho_{eR} u_{eR} y dy$$

où  $\rho_{eR}$ ,  $u_{eR}$  sont les conditions à la frontière  $\delta_R$  du sillage au niveau de R. Ces conditions sont calculées, à partir de  $p_c$ ,  $M_{c_0}$  en supposant une compression isentropique de l'écoulement sur la ligne limite ( $\ell$ ).

5. l'épaisseur de déplacement  $\delta_R^*$  est déterminée en admettant que le profil de vitesse  $u/u_{eR} = f(y/\delta_R)$  au recollement est universel et donné par des résultats obtenus en incompressible (l'effet de compressibilité sur ce profil est négligé). Dans ces conditions,  $\delta_R^*$  peut être calculée en supposant que le débit passant en R, dans le sillage, est égal au débit de la couche de mélange situé au dessus de la ligne de courant limite.

La procédure de calcul adoptée est la suivante : on se donne, a priori, un ensemble de valeurs  $r_d$  ; pour chacune d'elles, la pression de culot  $p_c$  est calculée, compte tenu de l'état de la couche limite initiale. Le calcul fournit également l'épaisseur  $\delta_R^*$ . La solution, obtenue par interpolation, correspondant à la valeur de  $p_c$  qui assure l'égalité de  $\delta_R^*$  et de  $r_d$ .

L'évolution expérimentale de la pression au culot d'un arrière corps cylindrique est comparée, Figure 69, aux résultats donnés par cette méthode et celle de Mueller (appliquée par Roache). Les points de mesure concernent des maquettes d'allongement géométrique variable pour lesquelles les caractéristiques de la couche limite sont rarement communiquées par les auteurs. L'allure générale de l'évolution est bien prédite par le calcul. La dispersion expérimentale peut s'expliquer par des variations importantes du paramètre  $\theta_0/r_c$ .

### 2.3.1.2 Méthodes d'interaction forte (intégrales)

Nous allons maintenant présenter des méthodes basées sur la notion de couplage fort entre un écoulement externe considéré comme non visqueux, et une couche dissipative. Nous avons déjà exposé le principe de ces théories dans le cadre, plus simple, du recollement plan sur paroi. Elles ont été étendues au cas du sillage de révolution, d'abord par de Krasinsky [65] qui suivait la formulation originale de Crocco Lees, puis plus récemment par Weng [75] et par Mehta [12]. Nous retiendrons ici la méthode de Mehta qui traite vraiment le problème du culot franc, celle de Weng supposant la présence d'un dard central.

#### . Théorie de Mehta.

Le schéma d'écoulement adopté par Mehta est représenté figure 70. Le fluide est divisé en une région externe, non visqueuse, pouvant donc être calculée par la méthode des caractéristiques, et une zone visqueuse interne à laquelle sont appliquées des équations du type couche limite. L'influence du "lip-shock" qui prend généralement naissance à proximité immédiate du point de séparation D est négligée [14] ; approximation très probablement justifiée tant que le nombre de Mach de l'écoulement amont est modéré ( $M_\infty < 4$ ).

Par ailleurs, s'appuyant sur des observations expérimentales [76] montrant clairement que du fait de la détente rapide au culot, les forces visqueuses sont prédominantes uniquement dans la partie la plus inférieure de la couche limite, Mehta inclut dans la région non visqueuse la portion externe de la couche limite initiale qui est ainsi considérée comme un écoulement de fluide parfait rotationnel. Le partage entre les deux zones est défini selon la procédure expliquée dans ce qui suit. Nous allons maintenant examiner les modélisations qui sont appliquées aux différentes parties de l'écoulement.

#### . Détente initiale au point de séparation

Le procédé adopté pour déterminer la frontière de la zone où les effets visqueux sont prédominants est le suivant (voir le schéma de la Figure 71). L'épaisseur  $\Delta_1$  de la zone visqueuse détendue de  $\rho_0$  à  $\rho_c$  (que l'on se donne a priori) est définie par la condition :

$$\left(\frac{\partial u}{\partial y}\right)_{\Delta_1} = \left(-\frac{\partial u}{\partial y}\right)_{\rho_c}$$

qui exprime que le gradient de vitesse à  $\Delta_1$  est le même que celui à la frontière de la couche limite initiale, avant détente.  $(\partial u / \partial y)_{\rho_0}$  est évalué en supposant un profil de vitesse en puissance  $1/7$ . Par  $\Delta_1$  (couche limite détendue) passe une ligne de courant issue de  $\Delta_0$  dans la couche limite initiale. L'écoulement situé au-dessus de cette ligne de courant est supposé isentropique. La localisation de  $\Delta_0$  est effectuée par tâtonnements. Au départ, on considère  $\Delta_{0,1}$  tel que  $M_{\Delta_{0,1}} = 1$ . Connaissant la loi de vitesse  $u(y)$ , on en déduit  $\Delta_{0,1}$ , puis  $u_{0,1}$ ,  $\rho_{0,1}$  etc... Une détente isentropique est ensuite effectuée de  $\rho_0$  à  $\rho_c$  ; d'où  $M_{1,1}$ ,  $u_{1,1}$ ,  $\rho_{1,1}$  sur  $\Delta_{1,1}$ . Un incrément  $\epsilon_0$  est donné à  $\Delta_{0,1}$  de façon à obtenir  $\Delta_{0,1,1}$ ,  $M_{0,1,1}$ ,  $u_{0,1,1}$ ,  $\rho_{0,1,1}$  etc... puis  $M_{1,1,1}$ ,  $u_{1,1,1}$  etc... L'incrément correspondant  $\epsilon_1$  pour l'épaisseur  $\Delta_{1,1}$  se déduit en écrivant l'équation de continuité. La pente du profil à la station 2 est alors égale à  $(u_{1,1,1} - u_{1,1})/\epsilon_1$ . Elle est comparée à  $(\partial u / \partial y)_{\rho_c}$  ; la procédure étant répétée par déplacement de  $\Delta_0$  jusqu'à ce qu'il y ait égalité.

Après quoi, le nombre de Mach, l'entropie, .... sur la caractéristique initiale (avant détente de  $\rho_0$  à  $\rho_c$ ) sont fournis par la distribution de vitesse  $u(y)$  et en supposant la pression statique constante. Il est à noter que la caractéristique initiale part du culot (l'effet d'interaction amont est négligée) à une distance de la paroi, non pas égale à  $\Delta_0$ , mais à  $\delta_0$ , épaisseur de la couche visqueuse après décollement, dont la répartition de vitesse est celle du profil de décollement de la famille choisie.  $\delta_0$  et  $\Delta_1$  sont reliées par l'équation de conservation de la masse.

#### . Ecoulement externe non visqueux

En raison de l'effet de révolution et du fait également que l'entropie n'est pas constante (couche rotationnelle), l'écoulement non visqueux ne peut être calculé par la relation de Prandtl-Meyer qui constituerait ici une approximation beaucoup trop grossière. Pour connaître à chaque pas d'intégration en X, les conditions à la frontière de la couche visqueuse, il faut utiliser la méthode des caractéristiques, formulée en écoulement de révolution non isentropique. Nous ne donnerons pas ici de détail sur cette formulation qui est classique. Afin de gagner du temps de calcul, Mehta met en oeuvre une procédure simplifiée dont le principe apparaît Figure 72.

Le réseau de base, correspondant aux points répartis sur la dernière caractéristique du faisceau de détente, a un espacement assez large ; le resserrement des points étant insuffisant pour le calcul couplé. En conséquence, les points intermédiaires, espacés de  $\Delta x$ , sont calculés à partir des conditions interpolées entre deux points initiaux, tels que 1 et 2 (voir Figure 72), en négligeant les caractéristiques montantes dans une maille telle que 1.2.2'. Les deux relations caractéristiques ne sont utilisées que lorsque le point 2 est dépassé. On calcule alors 3' exactement à partir de 3 et 2', puis on refait un calcul approché comme précédemment, entre 2' et 3'). Ce procédé est une amélioration de la technique proposée par Webb [77]. Il est également appliqué dans la région externe.

Ecoulement interne dissipatif

L'écoulement dissipatif est décrit par des équations du type couche limite (la pression est donc supposée transversalement constante) qui s'écrivent (pour le mouvement stationnaire moyen) :

continuité 
$$\frac{\partial}{\partial x} (\rho u) + \frac{1}{r} \frac{\partial}{\partial r} (\rho v r) = 0$$

quantité de mouvement 
$$\rho u \frac{\partial u}{\partial x} + \rho v \frac{\partial u}{\partial y} = - \frac{dp}{dx} + \frac{1}{r} \frac{\partial}{\partial r} (r \tau)$$

énergie 
$$h_i = h + \frac{u^2}{2} = \text{constante}$$

Suivant la démarche exposée plus haut, les équations appliquées à la couche dissipative sont résolues par une méthode intégrale utilisant les trois équations suivantes :

continuité (21) 
$$\frac{d}{dx} (\rho_c u_c A_1) - \rho_c u_c \delta \frac{d\delta}{dx} = - \rho_c v_c \delta$$

quantité de mouvement (22) 
$$\frac{d}{dx} (\rho_c u_c^2 A_2) - u_c \frac{d}{dx} (\rho_c u_c A_1) = - \frac{\delta^2}{2} \frac{dp}{dx} + \delta \tau_f$$

énergie cinétique : (23) 
$$\frac{d}{dx} \left( \frac{1}{2} \rho_c u_c^2 A_3 \right) - \frac{u_c}{2} \frac{d}{dx} (\rho_c u_c A_1) = - u_c A_u \frac{dp}{dx} - \rho_c u_c^2 R_1 + \delta u_c \tau_f$$

où,  $A_1, A_2, A_3, A_u$  sont des quantités ayant la dimension d'une surface et définies par :

$$A_1 = \int_0^\delta \frac{\rho u}{\rho_c u_c} r dr \quad A_2 = \int_0^\delta \frac{\rho u^2}{\rho_c u_c^2} r dr \quad A_3 = \int_0^\delta \frac{\rho u^3}{\rho_c u_c^3} r dr \quad A_u = \int_0^\delta \frac{u}{u_c} r dr$$

$R_1$  est "l'intégrale de dissipation" :

$$R_1 = \frac{1}{\rho_c u_c^2} \int_0^\delta r \tau \frac{\partial u}{\partial r} dr$$

$\tau_f$  est le frottement à la frontière  $\delta$  qui est non nul ici en raison de l'existence de la couche rotationnelle.

Le frottement turbulent  $\tau$  (la contribution laminaire est négligée) est exprimé à partir du concept de viscosité apparente sous la forme :

$$\tau = \rho \mathcal{E} \frac{\partial u}{\partial y}$$

La viscosité cinématique  $\mathcal{E}$  est représentée par un modèle algébrique :

$$\mathcal{E} = k \ell_c u_c$$

où  $\ell_c$  et  $u_c$  sont une longueur et une vitesse caractéristiques. Celles-ci sont définies en écoulement incompressible par les relations suivantes :

en amont du point de recollement

$$\ell_{c,i} = \sqrt{\int_{\eta^*}^{\bar{\eta}} \frac{u_i - u_{\eta i}}{u_{\eta i} - u_{\eta i}} \left( 1 - \frac{u_i - u_{\eta i}}{u_{\eta i} - u_{\eta i}} \right) \eta d\eta}$$

où  $\eta$  est la distance à l'axe,  $\eta^*$  la valeur de  $\eta$  telle que :

$$\int_0^{\eta^*} \frac{u_i}{u_{e,i}} \eta d\eta = 0$$

et  $u_{e,i}$  la vitesse sur l'axe.

en aval du point de recollement

$$l_{e,i} = \sqrt{\int_0^{\eta^*} \frac{u_i}{u_{e,i}} \left(1 - \frac{u_i}{u_{e,i}}\right) \eta d\eta}$$

La considération de résultats expérimentaux conduit à adopter pour  $k$  la même valeur constante ( $k = 0,07$ ) aussi bien en amont qu'en aval du recollement.

S'inspirant de l'approche d'Alber (voir § 2.2.3), Mehta utilise une transformation compressible-incompressible pour prendre en compte simplement l'effet de compressibilité dans l'évaluation des intégrales  $A_1, A_2, A_3, A_4$  et des expressions faisant intervenir le frottement ( $\tau_f$  et  $R_f$ ). Pour cela, il introduit les variables transformées  $\xi$  et  $\eta$  telles que :

$$d\xi = \frac{\rho_e a_e}{\rho_\infty a_\infty} dx \quad \text{et} \quad \eta d\eta = \frac{\rho a_e}{\rho_\infty a_\infty} r dr$$

Dans le plan incompressible,  $\xi$  se transforme en  $\tilde{\xi}$  tel que :

$$\tilde{\xi} = \frac{\rho^2 r^2}{\rho_e \rho_\infty \eta^2} \quad \xi = \tilde{\xi}(x)$$

Faisant les hypothèses (même démarche qu'Alber)

$$\frac{\rho^2 \xi}{\rho_e \rho_\infty} = \frac{\rho_e^2}{\rho_e^2} \xi_i = \frac{\rho_e^2}{\rho_e^2} k l_{e,i} u_{e,i}$$

$$\frac{r^2}{\eta^2} = \sqrt{\frac{\delta^2}{\delta_i^2}} \frac{\rho_e}{\rho_e}$$

on obtient :

$$\tilde{\xi} = k \left(\frac{\rho_e}{\rho_e}\right)^{\frac{1}{2}} \delta \left(\frac{l_{e,i}}{\delta_i}\right) u_{e,i}$$

La masse spécifique de référence  $\rho_e$  est calculée sur l'axe. La transformation permet d'exprimer les quantités compressibles sous la forme :

$$\delta^2 = \frac{\rho_\infty a_\infty}{\rho_e a_e} \frac{1 - 2 C_e^2 A_{2,i}}{1 - C_e^2} \delta_i$$

$$A_1 = \frac{1 - C_e^2}{1 - 2 C_e^2 A_{2,i}} \delta^2 A_{2,i}$$

$$A_2 = \frac{1 - C_e^2}{1 - 2 C_e^2 A_{2,i}} \delta^2 A_{2,i}$$

$$A_3 = \frac{1 - C_e^2}{1 - 2 C_e^2 A_{2,i}} \delta^2 A_{3,i}$$

$$A_4 = \frac{\delta^2}{1 - 2 C_e^2 A_{2,i}} (A_{1,i} - C_e^2 A_{3,i})$$

$$R_f = \frac{\tilde{\xi}}{\mu_e} \frac{a_e}{a_\infty} R_{f,i}$$

où

$$A_{1,i} = \int_0^1 \frac{u_i}{u_{e,i}} \eta' d\eta' \quad A_{2,i} = \int_0^1 \frac{u_i^2}{u_{e,i}^2} \eta' d\eta' \quad A_{3,i} = \int_0^1 \frac{u_i^3}{u_{e,i}^3} \eta' d\eta'$$

$$R_{f,i} = \int_0^{\delta} \left[ \frac{\partial(u_i/\mu_{e,i})}{\partial \eta'} \right]^2 \eta' d\eta' \quad \text{avec} \quad \eta' = \frac{\eta}{\delta_i}$$

$C_e$  étant le nombre de Crocco déjà défini (§ 2.2.2).

Les différentes intégrales qui précèdent peuvent être évaluées en représentant les distributions de vitesse dans la couche visqueuse au moyen d'une famille de profils.

A proximité du culot, Mehta utilise les profils de Green [78] qui sont constitués de deux parties (voir Figure 73) :

- une région de hauteur  $h_i$  à vitesse constante dans la région centrale du proche sillage :

$$\frac{u_i}{u_{e,i}} = 1 - 2A \quad (0 \leq \eta \leq h_i)$$

- une loi en cosinus dans le mélange

$$\frac{u_i}{u_{e,i}} = 1 - A - A \cos \pi \left( \frac{\eta - h_i}{\delta_i} \right) \quad (h_i < \eta \leq \delta_i)$$

où  $\delta_i = \delta_i - h_i$  est l'épaisseur de la couche visqueuse.

Ces profils dépendent donc de deux paramètres, à savoir : A et  $P = h_i/\delta_i$ . Au culot, A est égal à 0,5 en l'absence d'injection et inférieur à 0,5 si une injection est pratiquée.

Loin du culot, les distributions sont représentées par les profils de Kubota et al. [79] qui ne sont fonction que d'un seul paramètre (ces profils sont des solutions de similitude pour le sillage axisymétrique).

Compte tenu de ces représentations, les équations de base (21, 22, 23) pour la région proche du culot se mettent sous la forme :

$$(24) \quad \left| \alpha_{i,j} \right| \left| \frac{dA}{dx} \frac{dP}{dx} \frac{d\delta}{dx} \right|^T = \delta_i \quad (i = 1,3 ; j = 1,3)$$

Les coefficients  $\alpha_{i,j}$  sont des fonctions connues, les seconds membres contiennent les grandeurs à la frontière  $\delta$  de la couche dissipative :  $u_e$ ,  $S_e$  (entropie),  $v_e$ .

La méthode des caractéristiques fournit deux relations qui permettent d'exprimer, par exemple,  $v_e$  et  $S_e$  connaissant  $u_e$  (ou bien la pression  $p_e$ ). Dans cette région, une autre équation est donc nécessaire. L'auteur utilise l'équation des quantités de mouvement sur l'axe :

$$(25) \quad \frac{dp}{dx} = -\rho_0 u_i \frac{du_e}{dx} \quad (p = p_e)$$

Le processus d'intégration est le suivant : A, P et  $\delta$  sont calculés au pas  $x + dx$  en résolvant le système (24) ; la pression est ensuite évaluée par (25) ; puis la méthode des caractéristiques appliquée pour trouver  $v_e$  et  $S_e$ .

Loin du culot, là où la représentation à un paramètre est suffisante, il n'est plus nécessaire de faire intervenir l'équation (25). Le système à intégrer peut s'écrire :

$$(26) \quad \left| \beta_{i,j} \right| \left| \frac{d\eta}{dx} \frac{d\delta}{dx} \frac{du_e}{dx} \right|^T = \delta_i \quad (i = 1,3 ; j = 1,3)$$

où  $\eta$  est le "paramètre de forme" de la famille choisie. Les membres de droite contiennent  $v_e$  et  $S_e$  qui se calculent en fonction de  $u_e$  par la méthode des caractéristiques.

Le raccord entre les deux régions est effectué en imposant la continuité du débit à travers la couche visqueuse, de l'épaisseur de la couche visqueuse, du nombre de Mach  $M_e$  à sa frontière. Pour assurer l'unicité de la position du point de raccord, on doit aussi imposer l'égalité des rapports d'épaisseurs :

$$H_i = \frac{A_{1,i} - A_{2,i}}{0,5 - A_{1,i}}$$

Toutefois, des difficultés sont généralement rencontrées pour assurer le raccord entre les deux familles de profils. Ainsi, l'utilisation de l'équation (25) entraîne une décroissance irréaliste de la pression en amont du point où le raccord devient possible. On doit la remplacer par la relation :

$$\frac{dp}{dx} = \left( \frac{dp}{dx} \right)_{x_0} + \left( \frac{d^2p}{dx^2} \right)_{x_0} (x - x_0)$$

en aval du point ( $x = x_0$ ) où la dérivée seconde  $d^2u/dx^2$  de la vitesse sur la ligne limite s'annule. Par ailleurs, dans le cas où la couche limite initiale est très épaisse, le nombre de Mach élevé ou l'injection au culot importante, le raccord entre les deux familles devient impossible. La difficulté est tournée en conservant partout les profils de Green, mais en fixant le paramètre  $P$  à la valeur 0,2 à partir du moment où  $P$  tend à devenir inférieur à 0,2.

Dans la région du recollement, le système décrivant la couche visqueuse est donc toujours de la forme (26). Il présente une singularité analogue à celle du cas plan (point critique de Crocco-Lees), qui permet d'assurer, comme nous l'avons expliqué § 2.2.3, l'unicité de la solution, c'est-à-dire qui fixe la valeur de la pression de culot  $p_c$  jusqu'à présent indéterminée.

Nous allons maintenant présenter quelques comparaisons théorie-expérience extraites de la thèse de Mehta.

La Figure 74 montre des répartitions de pression sur l'axe du sillage pour des nombres de Mach amont  $M_0$  voisins de 2. L'accord théorie-expérience est généralement satisfaisant, en particulier, la pression de culot est prédite avec précision. L'écart important observé pour  $M_0 = 1.85$  est dû vraisemblablement à des effets perturbateurs provoqués par les parois de la soufflerie. Les lettres R, K, C et E désignent respectivement le point de recollement (R), le point critique (K), le col du sillage (C) et le point sonique sur l'axe (E).

La Figure 75 suivante donne l'évolution du coefficient de pression de culot en fonction du nombre de Mach  $M_0$  et met en évidence l'effet de couche limite initiale. La prédiction peut être considérée comme correcte, compte tenu d'une assez large dispersion expérimentale qui ne permet pas de dégager clairement l'influence de la couche limite initiale. Dans le cas du culot de révolution, ce paramètre semble d'ailleurs jouer rapidement un rôle secondaire, l'effet principal, pour une géométrie donnée, provenant du nombre de Mach amont. Une telle tendance a déjà été constatée dans le cas du recollement plan (voir § 2.2.2 et Figure 62) où l'on observe que la couche limite n'affecte fortement le phénomène qu'au voisinage du cas limite  $\delta_0 \rightarrow 0$ .

Enfin, la Figure 76 montre l'influence d'une injection au culot. La prédiction théorique se situe assez nettement au-dessous de l'évolution expérimentale, la pente des deux courbes différant surtout au voisinage de l'origine.

D'autres théories, semblables dans leur esprit à celles que nous venons de présenter, ont été proposées pour traiter le problème du culot en écoulement supersonique de révolution [80]. Elles diffèrent essentiellement par la façon de traiter l'effet de la détente de  $p_0$  à  $p_c$  sur la couche limite initiale ainsi que par le choix d'autres représentations des profils de vitesse dans la zone visqueuse.

### 2.3.2 Écoulement subsonique incompressible

Nous limiterons ici notre revue aux méthodes proposées pour traiter le cas d'un sillage subsonique supposé stationnaire.

Les régimes instationnaires ne peuvent être convenablement calculés que par résolution (numérique) des équations de Navier-Stokes. En suivant cette approche, des résultats très intéressants ont été obtenus, pour le laminaire, en particulier par Fromm [81]. En turbulent, se pose le problème de la modélisation de la turbulence qui soulève de grandes difficultés s'ajoutant d'ailleurs aux questions d'ordre numérique. Dans ce domaine, les méthodes n'en sont donc encore qu'au stade du développement sur le plan fondamental.

Différentes théories ont été développées pour calculer la pression de culot en écoulement subsonique plan et stationnaire. La plupart d'entre elles adoptent des schémas analogues à ceux définis pour traiter le cas supersonique : c'est-à-dire qu'elles font appel soit à des concepts du genre modèle de Chapman-Korst consistant à superposer les effets de viscosité sur une structure d'écoulement de fluide parfait [41, 82], soit à une technique d'interaction forte [78, 83] avec, souvent, l'utilisation de corrélations empiriques.

Plus récemment ont été développées des méthodes basées sur la résolution numérique des équations de Navier-Stokes avec introduction de modèles de turbulence du type algébrique ou à équations de transport [84, 85].

Pour le cas du culot en écoulement de révolution, les théories sont moins nombreuses. Nous retiendrons ici celle de Butsko [86] et celle de Vanwagenen [11]. Il s'agit de théories simplifiées reposant sur une schématisation des phénomènes réels.



### Théorie de Butsko

Nous ne donnerons que quelques indications sur la méthode de Butsko. Elle prend comme point de départ l'évaluation du coefficient de pression de culot  $K_{p_c}$  en écoulement bidimensionnel plan. Le calcul de  $K_{p_c}$  est effectué dans le cadre de la théorie de Nash avec détermination de l'écoulement non visqueux par une technique de transformation conforme. On obtient ainsi un  $(K_{p_c})_{2D}$  qui est écrit sous la forme :

$$(K_{p_c})_{2D} = \left[ \left( \frac{K_{p_c}}{K_{p_c \text{ lim}}} \right)_{2D} \right]_{\theta_0, \beta} \times \left[ (K_{p_c \text{ lim}})_{\beta=0} \right]_{2D}$$

$\beta$  est l'angle de rétreint et  $K_{p_c \text{ lim}}$  correspond au cas "limite"  $\theta_0 = 0$  (couche limite initiale nulle).

Butsko introduit ensuite des coefficients empiriques pour tenir compte de l'effet de tridimensionnalité, si bien que  $(K_{p_c})_{3D}$  est donné par :

$$(K_{p_c})_{3D} = \left[ \left( \frac{K_{p_c}}{K_{p_c \text{ lim}}} \right)_{2D} \right]_{\theta_0, \beta} \times \left[ (K_{p_c \text{ lim}})_{\beta=0} \right]_{2D}$$

$$\left[ \frac{(K_{p_c \text{ lim}})_{3D}}{(K_{p_c \text{ lim}})_{2D}} \right]_{\beta=0} \times \left[ \frac{(K_{p_c \text{ lim}})_{\beta}}{(K_{p_c \text{ lim}})_{\beta=0}} \right]_{3D}$$

Le cas d'une configuration réellement tridimensionnelle peut être traité en décomposant le culot en un ensemble de géométries plus simples puis en définissant pour chacune d'elles, une épaisseur  $\theta_0$  et un angle  $\beta_{\text{eff}}$  moyens sur le périmètre  $P$  du culot. L'effet tridimensionnel est caractérisé par le coefficient

$$P / 2 \sqrt{\pi S_c}$$

où  $S_c$  est la surface du culot (ce coefficient vaut 1 pour un écoulement de révolution).

La Figure 77 montre la précision de la méthode, appliquée en particulier à des configurations géométriques complexes. L'accord théorie-expérience est ici plutôt satisfaisant. La théorie de Butsko offre l'avantage d'une grande simplicité de mise en oeuvre, et peut être très utile si l'on se contente d'une évaluation de la pression de culot sans avoir besoin de renseignements sur l'organisation du sillage. La théorie de Vanwagenen que nous allons maintenant présenter en détail, permet d'aller plus loin, au prix bien sûr, d'une plus grande complexité.

### Théorie de Vanwagenen

Dans la théorie de Vanwagenen l'écoulement de culot est schématisé comme indiqué Figure 78. L'arrière corps est un cylindre prolongé indéfiniment vers l'amont. Une couche limite turbulente, dont les caractéristiques sont connues, est présente au niveau du point de décollement D. D est l'origine de la surface de courant séparatrice  $\psi_s$  qui délimite une cavité emprisonnant un écoulement dit "interne".  $\psi_i$  aboutit en L sur l'axe de révolution.  $\psi_s^*$  désigne la surface de déplacement de la région dissipative. Elle constitue la surface solide fictive le long de laquelle s'écoule le fluide externe considéré comme non visqueux.  $\psi_e$  est la surface de courant de cet écoulement qui passe en L' par la frontière externe de la couche dissipative au niveau du point L.

On désigne par  $p_c$  la pression s'exerçant sur le culot et par  $p_L$  la pression sur l'axe en L.

Le principe général de la solution consiste à assurer la compatibilité entre l'écoulement externe non visqueux et la couche dissipative le long de la surface de déplacement  $\psi_s^*$ .

L'écoulement potentiel est calculé par une méthode de singularités (sources et puits) réparties sur l'axe d'un écoulement de révolution uniforme. Les étapes du calcul sont les suivantes :

1. l'algorithme itératif est démarré en se donnant la forme de la surface séparatrice  $\psi_s$ . On choisit comme section méridienne une ellipse tangente au cylindre en D et normale à l'axe en L. La longueur  $L_s$  du demi-grand axe est donnée a priori. Elle constitue une des inconnues du problème.
2. l'écoulement potentiel est calculé le long d'une frontière constituée par : le cylindre, la surface  $\psi_s$  et, en aval de L, l'axe de révolution.

3. l'effet de déplacement de la couche limite initiale se détermine aisément à partir du profil de vitesse. L'épaisseur de déplacement au niveau de L est évaluée en procédant ainsi :
- on estime d'abord le débit de masse  $q_e$  qui pénètre dans la couche de mélange jusqu'au point L ( $q_e$  est la somme de débit de la couche limite initiale et du débit entraîné par effet visqueux entre D et L). Au départ,  $q_e$  est estimé à partir des résultats connus sur le mélange turbulent bi-dimensionnel.
  - la frontière externe  $\delta_e^*$  de la couche dissipative en L est déterminée connaissant  $q_e$  et en faisant l'hypothèse que le profil de vitesse, en L, est représenté par une loi en fonction d'erreur (Formule 2, § 2.2.2)
  - l'épaisseur de déplacement en L,  $\delta_L^*$  est ensuite calculée en écrivant que le débit  $q_e$  est égal au débit de fluide parfait passant entre  $\delta_L$  et  $\delta_L^*$ .
4. cette étape consiste à définir la forme de la surface de déplacement  $\psi_{\delta^*}$  dans la partie initiale du mélange, c'est-à-dire jusqu'à une distance  $x_3 \approx L_s/2$

Pour cela, il faut d'abord mettre en place la zone de mélange relativement à la surface limite  $\psi_{\delta^*}$ . A cette fin, on écrit les équations de bilan pour la quantité de mouvement et la masse en adoptant le volume de contrôle DEE'L'B représenté Figure 78 (le procédé est analogue, dans son principe, à ce qui a été exposé § 2.2.2).

. quantité de mouvement selon  $\vec{x}$

$$2\pi \int_{r_0}^{r_e} \rho u^2 r dr + 2\pi \int_0^{r_e} p r dr = 2\pi \int_0^{r_e'} \rho u^2 r dr + 2\pi \int_0^{r_e'} p r dr + 2\pi \int_{r_e}^{r_e'} p_{\infty} r dr$$

Dans cette expression  $u = \bar{u} + u'$  est la vitesse instantanée.  $\bar{u}'^2$  est négligée dans la couche limite initiale et pris égal à  $0,02 \bar{u}^2$  dans la zone de mélange. Nous obtenons donc l'équation :

$$2\pi \int_{r_0}^{r_e} \rho \bar{u}^2 r dr + 2\pi \int_0^{r_e} p r dr = 2\pi \int_0^{r_e'} \rho \bar{u}^2 r dr + 2\pi (0,02) \int_0^{r_e'} \rho \bar{u}^2 r dr + 2\pi \int_0^{r_e'} p r dr + 2\pi \int_{r_e}^{r_e'} p_{\infty} r dr$$

. conservation de la masse

$$2\pi \int_{r_0}^{r_e} \rho \bar{u} r dr = 2\pi \int_0^{r_e'} \rho \bar{u} r dr = 2\pi \int_{r_e}^{r_e'} \rho \bar{u} r dr$$

Dans la partie extérieure de la couche de mélange, les profils de vitesses sont supposés donnés par :

$$\frac{\bar{u}}{\bar{u}_e} = \frac{1}{2} (1 + \operatorname{erf} \eta)$$

où  $\eta = \sigma \frac{y}{x'}$  ( $y$  ordonnée locale)

$\sigma$  est pris égal à 12 et  $x' = x + 2,57 \sigma \theta_0$  pour tenir compte de l'effet de couche limite initiale (concept d'origine fictive, voir § 2.2.2 ).

Dans la cavité, les profils sont représentés par la formule :

$$\frac{\bar{u}}{\bar{u}_e} = \left( \frac{\bar{u}_s}{\bar{u}_e} - a \right) \sqrt{1 - \frac{r^2}{b^2}} + a$$

où  $a$ ,  $b$ ,  $\bar{u}_s$  sont définis par les conditions de raccord avec la famille (2) sur la ligne séparatrice et par :

$$\int_0^{r_2} \frac{\bar{u}}{\bar{u}_e} r dr = 0 \quad (r_2 \text{ distance à l'axe sur } \psi_f)$$

Une fois que la couche visqueuse est mise en place par rapport à  $\psi_f$ , on peut calculer son effet de déplacement en un ou plusieurs points.

5. La frontière de déplacement du sillage, en aval de L, est représentée par la formule (empirique) :

$$(27) \quad \frac{r}{\delta_L^*} = 0,4 + 0,6 \exp \left[ -C_3 (x - L_s) / \delta_L^* \right]$$

La constante  $C_3$  est ajustée de manière à assurer la continuité des pentes au raccordement avec la surface de courant de l'écoulement potentiel passant par  $\delta_L^*$ .

La méridienne de la surface de déplacement entre D et le sillage est assimilée à un arc d'ellipse tangent à l'épaisseur de déplacement de la couche limite en D et à la forme exponentielle (27) adoptée pour le sillage et passant au plus près des points définis dans l'étape précédente (ajustement par une méthode des moindres carrés).

6. L'écoulement potentiel est recalculé le long de la surface de déplacement  $\psi_f^*$  définie par :

- . la couche limite sur le cylindre,
- . l'arc d'ellipse entre D et L,
- . la relation (27) en aval.

Une nouvelle estimation de  $\delta_L^*$  peut ainsi être obtenue et comparée à la valeur précédente. Si l'écart est jugé trop important, le processus est répété jusqu'à ce que l'accord soit satisfaisant.

7. La procédure suivie jusqu'à maintenant fournit une solution de fluide parfait compatible (approximativement) avec l'effet de déplacement de la couche visqueuse et correspondant à des valeurs  $\theta_0$ ,  $L_s$  et  $q_f$  fixées. En fait,  $\theta_0$  est une donnée, mais  $L_s$  et  $q_f$  sont encore arbitraires.

Le débit  $q_c$  est déterminé en satisfaisant au théorème de la quantité de mouvement appliqué au volume de contrôle DEL'LB (voir Figure 70), c'est-à-dire :

$$(28) \quad 2\pi \int_{r_D}^{r_E} \rho \bar{u}^2 r dr + 2\pi \int_0^{r_E} p r dr = 2\pi (1,02) \int_0^{r_E} \rho \bar{u}^2 r dr + 2\pi \int_0^{r_L} p r dr + 2\pi \int_{r_E}^{r_L} p_{sur} \bar{u}_e r dr$$

Connaissant le champ de pression statique, fourni par le calcul de fluide parfait (la pression est supposée constante entre l'axe et  $\psi_f^*$ ), ainsi que le profil des vitesses en L (voir étape 3, ci-dessus), la relation (28) conduit à une expression pour le coefficient de pression de culot  $K_{p_c}$ .

La condition à satisfaire est que  $K_{p_c}$  déduit de (28), soit égal au coefficient  $K_{p_{s_D}^*}$  correspondant à la pression dans le fluide parfait sur la frontière de déplacement  $\delta_D^*$  en D. Ainsi, l'égalité  $K_{p_c} = K_{p_{s_D}^*}$  détermine la valeur de  $q_f$ , pour  $L_s$  fixée.

8. La longueur de cavité  $L_s$  est ensuite définie par le critère suivant. A une certaine abscisse  $x_3$ , la pression sur la surface de séparation  $p_s$  redevient égale à la pression de culot  $p_c$ . Cette station est appelée "début de la recompression de la couche dissipative". Il est alors supposé que la pression d'arrêt sur  $p_s$  est constante entre  $x_3$  et  $L$  (hypothèse de recompression isentropique de Chapman-Korst). Ainsi :

$$p_c + \frac{1}{2} \rho u_s^2 = p_s$$

Rappelons que  $u_s$  peut être évalué par application des relations de conservations (voir étape 4). Les pressions  $p_c$  et  $p_s$  résultent du calcul de fluide parfait, (la pression statique est supposée transversalement constante entre  $L$  et  $x_3$ ). L'unicité de la solution est donc assurée par la condition :

$$p_s - p_c = \frac{1}{2} \rho u_s^2$$

qui fixe la longueur  $L_s$

Afin d'illustrer l'application de la méthode sur un cas concret, la Figure 79 montre la façon pratique de déterminer le débit  $q_c$  dans le cas où trois longueurs de cavité  $L_s$  sont envisagées ( $L_s/r_c = 2,33 - 2,67$  et 3). Le théorème des quantités de mouvement (20) d'une part, et le calcul potentiel d'autre part fournissent chacun une valeur du coefficient  $K_{p_c}$ . L'intersection des deux évolutions, ainsi définies, détermine, pour chaque  $L_s$ , le débit  $q_c$  et  $K_{p_c}$ .

On porte ensuite, en fonction de  $L_s$ , les écarts  $K_{p_s} - K_{p_c}$  donnés respectivement par l'écoulement potentiel et par la recompression isentropique sur la surface limite. L'intersection des deux courbes fixe la longueur  $L_s$ , puis les coefficients  $K_{p_c}$  et  $K_{p_s}$  correspondant à la solution cherchée (voir Figure 80).

Les exemples d'application qui suivent permettent de juger la précision de la méthode. La Figure 81 montre l'évolution de  $K_{p_c}$  en fonction de l'épaisseur de quantité de mouvement de la couche limite au point de décollement  $D$ . L'accord entre la théorie et l'expérience est ici très satisfaisant pour  $\theta_s/r_c$  inférieur à 0,014. Au delà, l'effet de  $\theta_s$  tend à être surestimé. Les expériences montrent, qu'en fait, l'influence de  $\theta_s$  devient de moins en moins sensible,  $K_{p_c}$  s'établissant à une valeur pratiquement indépendante de  $\theta_s$  pour  $\theta_s/r_c > 0,015$ . En extrapolant l'évolution, pratiquement linéaire, de  $K_{p_c}$  il est possible de définir la valeur limite correspondant à une couche limite évanescence :

$$(K_{p_c})_{lim} = -0,132$$

d'où une formule approchée, pouvant être utile pour une estimation rapide de la traînée d'un culot cylindrique dans le cas d'une couche limite initiale de faible épaisseur ( $\theta_s/r_c < 0,014$ )

$$K_{p_c} = 1,375 \left( \theta_s/r_c \right) - 0,132$$

La pression au point de fermeture de la cavité (recollement théorique) est un peu moins bien prédite (Figure 82a), la théorie étant d'environ 5 % supérieure à l'expérience. Le désaccord provient vraisemblablement de l'hypothèse d'effets dissipatifs négligeables lors du processus de recollement.

Egalement, la théorie surestime légèrement la longueur de la cavité (Figure 82b), l'écart demeurant toutefois modéré (3 à 4 %). Pour les besoins pratiques,  $L_s$  peut être évaluée avec une bonne précision par la relation :

$$\frac{L_s}{r_c} = 2,42 + 12,7 \left( \frac{\theta_s}{r_c} \right)$$

La théorie de Vanwagenen a été adaptée par Champigny, de l'ONERA, pour traiter des géométries plus complexes que le simple cylindre. La Figure 83 montre un exemple d'application au cas d'une maquette dont l'arrière corps comporte une jupe d'angle  $\beta$ . La prévision recoupe bien l'expérience pour  $\beta = 0$ , mais elle tend à s'en écarter lorsque  $\beta$  augmente. Le désaccord est d'environ 15 % pour  $\beta = 15^\circ$ . Il faut cependant préciser que le calcul de l'écoulement potentiel suppose, qu'en amont de la jupe, la maquette est un cylindre semi-infini. Un calcul de fluide parfait sur la géométrie exacte permettrait, peut être, de résorber une partie de l'écart constaté.

### 2.3.3. Ecoulement transsonique

A notre connaissance, il n'existe pas encore de méthode vraiment opérationnelle pour calculer un écoulement de culot quand le nombre de Mach de l'écoulement extérieur est voisin de l'unité. Dans ce domaine de vitesse, les travaux théoriques n'envisagent pour le moment que le cas du recollement bidimensionnel sur paroi [87]. L'extension à une configuration de révolution est envisageable mais ne semble pas avoir été faite.

## 2.3. Ecoulement au culot d'un arrière corps de révolution avec jet propulsif

### 2.3.1 Ecoulements externe et interne supersoniques

#### 2.3.1.1 Schématisation des écoulements.

La structure de l'écoulement au culot d'un arrière corps équipé d'une tuyère propulsive a été analysée dans la première partie de cet exposé (voir § 1.3.2 et Figure 34). Elle est extrêmement complexe et les seules méthodes pratiques dont on dispose actuellement pour traiter ce genre de problème sont du type global et reposent sur une schématisation assez grossière des phénomènes réels. Néanmoins, comme nous le verrons dans ce qui suit, elles donnent le plus souvent une très bonne prédiction de la pression de culot. A notre connaissance, peu de méthodes intégrales ont été développées pour traiter ce genre de problème. Signalons toutefois les tentatives théoriques de Klineberg et al.

[88] et de Boger et al [89] pour résoudre le problème du décollement de l'écoulement externe causé par l'éclatement d'un jet propulsif très sous détendu. Bien qu'intéressantes, ces méthodes sont encore trop peu développées pour que nous en parlions ici.

Les deux théories qui vont être présentées constituent une extension des méthodes développées pour le recollement bidimensionnel sur paroi : la première utilise le concept de critère angulaire de recollement, la seconde due à Addy [90] s'inspire plus étroitement du modèle initial de Korst.

En fait, les deux méthodes sont basées sur des schématisations très voisines dont les traits essentiels sont les suivants :

- la zone décollée, délimitée grossièrement par le triangle  $D_c R D_i$  ( $D_i$  est le diamètre en sortie tuyère) est à la même pression  $p_c$  que les deux écoulements non visqueux décollés (écoulements interne et externe.)
- les processus visqueux sont superposés à une structure d'écoulement de fluide parfait entièrement déterminée si la pression du culot  $p_c$  est fixée. Pour les deux théories, la première étape consiste donc à effectuer un calcul de fluide parfait en procédant de la manière suivante (voir Figure 84). Les écoulements non visqueux amont sont supposés connus jusqu'en  $D_c$  et  $D_i$  (c'est une donnée du problème en même temps que les épaisseurs de quantité de mouvement des couches limites initiales). On dispose donc, par exemple, d'une distribution de points sur les caractéristiques de départ ( $\Gamma_c$ ) et ( $\Gamma_i$ ) où vitesse, pression, entropie sont connues.

Ayant fixé  $p_c$ , il est possible de calculer, par la méthode des caractéristiques, les frontières isobares ( $\Gamma_c$ ) et ( $\Gamma_i$ ) des deux écoulements de fluide parfait. Dans le cas où  $p_c$  est inférieure à la fois à  $p_{c0}$  et  $p_{ci}$  (pressions en  $D_c$  et  $D_i$  respectivement),  $D_c$  et  $D_i$  sont à l'origine d'un faisceau de détentes centrées (circonstance schématisée, Figure 84). Il n'en est pas obligatoirement ainsi. Si le jet est sous détendu,  $p_c$  peut être supérieure à  $p_{c0}$  et alors une onde de choc part de  $D_c$ . A l'inverse, si le jet est surdétendu, un choc peut se propager depuis  $D_i$ . Les deux lignes ( $\Gamma_c$ ) et ( $\Gamma_i$ ) se rencontrent généralement en un point d'impact  $R_m$ , distinct du point de recollement R.  $R_m$  constitue le point de confluence en fluide non visqueux. En aval de  $R_m$ , le calcul peut être en principe poursuivi en imposant que sur la frontière commune (G), les deux écoulements aient même direction et même pression (condition de compatibilité le long d'une ligne de glissement). Il n'est, en fait, pas nécessaire de calculer (G), seule sa direction initiale  $\beta_0$  en  $R_m$  est nécessaire à la suite du calcul. En leur point de rencontre, les deux écoulements subissent des déviations brutales qui entraînent la formation des ondes de choc ( $C_c$ ) et ( $C_i$ ). Les intensités de ces chocs doivent être telles, qu'immédiatement en aval de  $R_m$ , les pressions statiques sont identiques dans les deux écoulements, ce qui détermine  $\beta_0$  et la pression commune  $p_s$ . La méthode basée sur le critère angulaire utilise un mode de résolution du problème de confluence où les chocs sont remplacés par des compressions isentropiques. L'expérience montre, en effet, que les ondes de choc se forment par focalisation d'ondes de compression à une certaine distance de  $R_m$ . L'hypothèse d'une évolution isentropique doit donc conduire à une évaluation plus précise de  $\beta_0$ .

- l'étape suivante, qui va faire intervenir les relations de fermeture assurant l'unicité de la solution, consiste à appliquer la théorie du recollement aux deux écoulements. Pour cela, on admet que tout se passe comme si chacun d'eux recollait sur une paroi matérialisant la direction commune de confluence  $\beta_0$ . Une telle hypothèse est justifiée par l'observation expérimentale qui montre que la matérialisation par une plaque mince du plan de symétrie d'un écoulement de culot n'introduit que des effets mineurs dans le domaine proche du point de partage R où le frottement pariétal est faible. Les exemples présentés Figure 85 permettent de constater que la pression de culot n'est pas affectée de façon sensible, même dans le cas où une injection de masse à faible vitesse est pratiquée dans l'eau morte.

Nous allons maintenant distinguer les deux approches qui conduisent, à partir de là, à des formulations différentes.

### 2.3.1.2 Théorie utilisant le critère angulaire de recollement (Carrière, Sirieix, Delery)

Le calcul de fluide parfait, effectué comme il vient d'être indiqué brièvement, fournit les éléments suivants :

- longueurs d'échange assimilées aux longueurs  $L_e$  et  $L_j$  des frontières isobares comprises entre les points de décollement et  $R_T$  :

$$L_e = \overline{D R_T}, \quad L_j = \overline{D_j R_T}$$

- angles de recollement  $\psi_e$  et  $\psi_j$  (définis Figure 84 ),
- nombres de Mach  $M_{e_c}$  et  $M_{j_c}$  sur les frontières ( $J_e$ ) et ( $J_j$ ).

La relation (11) du § 2.2.2 est alors appliquée pour déterminer les coefficients d'injection généralisés,  $C_{q_e}$  et  $C_{q_j}$ , relatifs à chacun des écoulements. Dans l'évaluation des angles  $\psi$  ( $\psi(M_{e_c}, \psi_e)$ ,  $\psi(M_{j_c}, \psi_j)$  respectivement), il est tenu compte de l'effet de révolution au moyen de la fonction  $F$  calculée à partir de la géométrie des frontières isobares ( $J_e$ ) et ( $J_j$ ).

Les débits massiques d'échange,  $q_e$  et  $q_j$ , sont ensuite évalués par :

$$q_e = 2\pi r_T \rho_{e_c} u_{e_c} L_e \left( C_{q_e} - \frac{\theta_{e_c}}{L_e} \right) + \frac{I_e}{u_{e_c}}$$

$$q_j = 2\pi r_T \rho_{j_c} u_{j_c} L_j \left( C_{q_j} - \frac{\theta_{j_c}}{L_j} \right) + \frac{I_j}{u_{j_c}}$$

- où -  $\rho_{e_c}$ ,  $u_{e_c}$ ,  $\rho_{j_c}$ ,  $u_{j_c}$  sont relatifs aux conditions sur les frontières isobares ( $J_e$ ) et ( $J_j$ ) respectivement,

- $\theta_{e_c}$ ,  $\theta_{j_c}$ , sont les épaisseurs de quantités de mouvement en  $D_e$  et  $D_j$ , après détente (ou compression) de  $p_{e_0}$  à  $p_c$  et  $p_{j_0}$  à  $p_c$ .
- $L_e = L_e + x_{e_0}$ ,  $L_j = L_j + x_{j_0}$  ( $x_0$  étant le décalage de l'origine fictive du mélange, voir § 2.2.2).

La prise en compte des termes de quantité de mouvement  $I_e$  et  $I_j$  nécessite, en général, une itération puisqu'ils sont fonction de la vitesse d'injection du fluide au culot qui dépend de  $q_e$  et  $q_j$ .

Dans sa version actuelle, la méthode suppose les phénomènes isoénergétiques (pas de bilan thermique), si bien que l'unicité de la solution (pression de culot  $p_c$ ) est assurée par la seule condition :

$$q_e + q_j = q_m$$

- où  $q_m$  est le débit injecté au culot (dans la plupart des cas  $q_m = 0$ ).

Les exemples d'application qui suivent permettront de juger de la validité de la méthode :

- le premier cas, Figure 86, est relatif à un arrière corps cylindrique placé dans un écoulement uniforme de nombre de Mach  $M_{e_0} = 1,97$ . L'arrière corps est équipé d'une tuyère conique. Deux valeurs du nombre de Mach en sortie sont considérées :  $M_{j_0} = 2$  et  $M_{j_0} = 3$ . Les résultats présentés montrent l'évolution de la pression de culot en fonction du rapport de détente de la tuyère. Le calcul prend en compte l'effet des couches limites initiales.
- dans le deuxième exemple, Figure 87, le nombre de Mach de la tuyère est fixe ( $M_{j_0} = 2,5$ ) et deux valeurs du nombre de Mach externe sont considérées :  $M_{e_0} = 2,01$  et  $M_{e_0} = 3,27$  (les mesures sont extraites de la référence [91])
- le troisième exemple, présenté Figure 88, correspond à une configuration où la tuyère émerge largement de l'arrière corps, ce qui conduit à des longueurs de ligne de jet très différentes.
- enfin, la Figure 89 montre une application à un cas où une injection de masse est pratiquée au culot, pour plusieurs valeurs du rapport de détente.

Il ressort de l'ensemble de ces confrontations théorie-expérience, que la méthode conduit à une prédiction en général satisfaisante de l'influence des différents paramètres envisagés.

## 2.3.1.3. Théorie d'Addy.

Le modèle d'Addy utilise, pour chacun des écoulements, l'analyse du mélange turbulent isobare développée § 2.2.2, les couches limites initiales étant négligées. Les frontières isobares ( $\ell$ ) et ( $j$ ) constituent les axes de référence par rapport auxquels les zones de mélange sont positionnées. Les équations de conservation sont écrites en négligeant l'effet de révolution, mais on considère le cas où les écoulements ne sont pas isoénergétiques, ce qui se produit, en particulier, quand les deux flux sont à des températures génératrices différentes ( $T_e$  et  $T_j$ , respectivement).

Dans ces conditions, la température  $T_m$  du fluide emprisonné dans l'eau morte est une inconnue supplémentaire dont la détermination oblige de recourir à une relation de bilan pour l'énergie.

Nous allons reprendre rapidement la formulation utilisée par Addy qui est très voisine de ce qui a été exposé § 2.2.2.

La zone de mélange est schématisée Figure 90. Les profils de vitesse et de température sont de la forme :

$$\frac{u}{u_{e_c}} = \varphi = \frac{1}{2} (1 + \operatorname{erf} \eta) \quad \eta = \sigma \frac{y}{x}$$

$$\frac{T_i}{T_e} = \Lambda = \frac{T_m}{T_e} + (1 - \frac{T_m}{T_e}) \varphi = \Lambda_m + (1 - \Lambda_m) \varphi$$

Le système de coordonnées intrinsèques ( $x, y$ ) est mis en place par rapport au système de référence ( $X, Y$ ) en satisfaisant globalement l'équation des quantités de mouvement pour le volume de contrôle dessiné Figure 90. D'où la relation :

$$\eta_m = \eta_e - \int_{-\infty}^{\eta_e} \frac{\rho}{\rho_{e_c}} \varphi^2 d\eta$$

La ligne de jet ( $j$ ) est définie par la conservation du débit et résulte de :

$$(29) \quad \int_{\eta_j}^{\eta_e} \frac{\rho}{\rho_{e_c}} \varphi d\eta = \int_{-\infty}^{\eta_e} \frac{\rho}{\rho_{e_c}} \varphi^2 d\eta$$

Le transfert de masse  $q$  (par unité d'envergure) associé au processus de mélange est égalé au débit passant entre ( $j$ ) et la ligne limite ( $\ell$ ), soit, sous forme adimensionnelle :

$$\frac{\sigma q}{x \rho_{e_c} u_{e_c}} = \int_{\eta_j}^{\eta_e} \frac{\rho}{\rho_{e_c}} \varphi d\eta$$

Considérons maintenant les équations de bilan pour l'énergie.

L'énergie transférée à l'eau morte par conduction et par travail des forces de frottement le long de la ligne de jet ( $j$ ) est donnée par :

$$e_j = \int_{y_j}^{y_e + y_m} \rho C_p (T_e - T_i) u dy$$

ou, sous forme adimensionnelle :

$$\frac{\sigma}{x} \frac{e_j}{\rho_{e_c} u_{e_c} C_p T_e} = \int_{\eta_j}^{\eta_e + \eta_m} (1 - \Lambda) \frac{\rho}{\rho_{e_c}} \varphi d\eta$$

Cette expression peut également s'écrire, compte tenu en particulier de (29) :

$$\frac{\sigma}{x} \frac{e_j}{\rho_{e_c} u_{e_c} C_p T_e} = \int_{-\infty}^{\eta_j} (\Lambda - \Lambda_m) \frac{\rho}{\rho_{e_c}} \varphi d\eta$$

L'énergie convectée avec la masse entre ( $j$ ) et ( $\ell$ ) est donnée par :

$$e_\ell = \int_{y_j}^{y_e} \rho C_p u T_i dy$$

soit :

$$\frac{\sigma}{x} \frac{e_l}{\rho_{ec} \mu_{ec} C_p T_{ic}} = \int_{\eta_l}^{\eta_e} \frac{\rho}{\rho_{ec}} \Lambda \varphi d\eta$$

ou encore :

$$\frac{\sigma}{x} \frac{e_l}{\rho_{ec} \mu_{ec} C_p T_{ic}} = \int_{-\infty}^{\eta_e} \frac{\rho}{\rho_{ec}} \Lambda \varphi d\eta - \int_{-\infty}^{\eta_l} \frac{\rho}{\rho_{ec}} \Lambda \varphi d\eta$$

Le transfert total d'énergie est donc :

$$e = e_j + e_l$$

ou :

$$\frac{\sigma}{x} \frac{e}{\rho_{ec} \mu_{ec} C_p T_{ic}} = \int_{-\infty}^{\eta_e} \frac{\rho}{\rho_{ec}} \Lambda \varphi d\eta - \Lambda_m \int_{-\infty}^{\eta_l} \frac{\rho}{\rho_{ec}} \varphi d\eta$$

Dans le cas de la confluence de deux écoulements, la condition de conservation de l'énergie impose :

$$e_m = e_1 + e_2 = 0$$

où -  $e_1$  est l'énergie transférée par l'écoulement 1

-  $e_2$  est l'énergie transférée par l'écoulement 2

-  $e_m$  est l'énergie transférée au niveau du culot

La conservation de la masse dans l'eau morte s'exprime par la relation, déjà utilisée :

$$q_m + q_1 + q_2 = 0$$

$q_m$  et  $e_m$  sont des données du problème. Dans la plupart des applications traitées par Addy,  $q_m = e_m = 0$ . La condition  $e_m = 0$  correspond à un culot en équilibre thermique avec l'eau morte. S'il n'en n'est pas ainsi,  $e_m$  doit être égal au flux de chaleur au culot (voir à ce sujet (97), (98) )

Pour les écoulements de révolution, nous écrirons en adoptant les indices  $e$  et  $j$  pour distinguer l'écoulement extérieur et le jet de la tuyère :

$$q_e + q_j = 2\pi r_T (\bar{q}_e + \bar{q}_j)$$

$$e_e + e_j = 2\pi r_T (\bar{e}_e + \bar{e}_j)$$

où  $\bar{q}_e, \bar{q}_j, \bar{e}_e, \bar{e}_j$  sont évalués à partir de la théorie du mélange bidimensionnel. La longueur de mélange  $x$ , qui intervient dans les formules précédentes, est prise souvent égale, pour chacun des écoulements, à la longueur de frontière isobare comprise entre le décollement et  $R_T$ . Cette convention ne correspond pas très fidèlement à la réalité, le mélange isobare ne représentant qu'une fraction de  $L_e$  ou  $L_j$ . Pour cette raison, Addy a proposé une modification consistant à introduire des longueurs  $(L_e)_{eff}$  et  $(L_j)_{eff}$  effectives déterminées, approximativement, en situant le point de rencontre des deux zones de mélange

Rappelons que la position de la ligne limite ( $\eta_l$  puis  $\varphi_l$ ) est obtenue en satisfaisant au critère d'échappement qui, dans sa forme originale, consiste à écrire que la pression d'arrêt sur ( $l$ ) soit  $p_{il}$ , est égale à la pression statique  $p_s$  après recollement. Afin de tenir compte de l'effet de révolution, Addy [92] a modifié ce critère en l'exprimant sous la forme :

$$\frac{p_{il}}{p_s} = k \left( \frac{r_l}{r_s} \right)$$

où  $k$  est une fonction du rapport des rayons en  $D_e$  et  $D_j$  :

$$\bar{r} = \frac{r_j}{r_e}$$

qui peut être représentée par :

$$k = 0,483 + 1,088 \bar{r} - 0,874 \bar{r}^2 + 0,303 \bar{r}^3$$

La figure 91 montre la corrélation des valeurs expérimentales qui a permis de définir cette courbe.

Le mode d'obtention de la solution, pour  $q_m = e_m = 0$ , est le suivant (voir Figure 92 )

a. une valeur de  $p_{il}/p_{s0}$  est fixée a priori,



- b. différentes valeurs de  $\Lambda_m = T_m / T_{ic}$  sont considérées.  
 Pour chacune d'elles, les débits  $\Delta e = e_e + e_j$  et  $\Delta q = q_e + q_j$  sont calculés, puis on recherche, par interpolation, les rapports  $(\Lambda_m)_{\Delta q=0}$  tel que  $\Delta q = 0$  et  $(\Lambda_m)_{\Delta e=0}$  tel que  $\Delta e = 0$ .
- c. les valeurs  $(\Lambda_m)_{\Delta q=0}$  et  $(\Lambda_m)_{\Delta e=0}$  sont comparées. Si  $|(\Lambda_m)_{\Delta q=0} - (\Lambda_m)_{\Delta e=0}| < \varepsilon$ , la solution est trouvée. Sinon, les étapes a et b sont répétées pour d'autres pressions de culot.

La théorie donne en général de bons résultats, bien que les couches limites soient négligées. Nous ne présenterons ici qu'un nombre limité de confrontations théorie-expérience choisies parmi les nombreux cas calculés par Addy

- la Figure 93a montre l'effet du nombre de Mach  $M_{j_0}$ . L'arrière corps est placé dans un écoulement uniforme de nombre de Mach  $M_{e_0} = 2$
- la Figure 93b met en évidence l'effet de géométrie (rapport  $\bar{r} = r_j / r_c$ ) pour des conditions  $M_{e_0}$  et  $M_{j_0}$  fixées.
- la Figure 94 donne l'influence des effets thermiques (rapport  $T_j / T_e$  variant de 1 à 3,5). On constate que l'effet de température se répercute assez faiblement sur la pression de culot, du moins pour des valeurs de  $T_j$  pas trop élevées.

Il pourrait en être autrement, comme nous le verrons dans la suite, dans le cas de missiles équipés d'un propulseur à poudre : alors  $T_j \sim 10 T_e$ . Il est à noter que pour de telles configurations intervient également la nature du gaz (effet de  $\gamma_j$ ).

Il ressort des comparaisons avec l'expérience que les théories que nous venons de présenter ont une bonne fiabilité. Leur intérêt, outre la possibilité de prédiction sur une configuration particulière dont les caractéristiques sont figées, et de permettre une étude systématique et analytique de l'influence des nombreux paramètres qui affectent la pression de culot, chose qu'il serait très difficile et très coûteux de faire par l'expérience. Elles constituent en outre un outil précieux pour l'optimisation d'un arrière corps en vue d'une traînée minimale.

Les variations paramétriques présentées Figures 95 à sont extraites d'une publication d'Addy [90]. L'arrière corps considéré est cylindrique.

- la Figure 95a montre l'effet d'une variation du nombre de Mach externe  $M_{e_0}$  ( $M_{j_0} = 2,5$ ). Pour un rapport de détente  $p_{j_0} / p_{e_0}$  fixé, une diminution de  $M_{e_0}$  fait augmenter la pression du culot.
- la Figure 95b montre l'effet d'une variation de  $M_{j_0}$  ( $M_{e_0} = 2$ ). A  $p_{j_0} / p_{e_0}$  fixé,  $p_c / p_{e_0}$  croît quand  $M_{e_0}$  diminue.
- la Figure 96 montre l'influence des facteurs géométriques  $\bar{r} = r_j / r_c$  et  $\beta_j$  (demi-angle d'ouverture de la tuyère conique). La pression de culot augmente quand  $\bar{r}$  ou  $\beta_j$  augmentent.
- la Figure 97 met en évidence l'effet du  $\gamma_j$  du jet interne, pour une géométrie de tuyère fixée. Il y a donc également variation du nombre de Mach  $M_{j_0}$ , si bien qu'il peut y avoir compensation entre les deux effets.
- la Figure 98 montre l'influence du rapport des températures génératrices  $T_j / T_e$ . Une augmentation de  $T_j / T_e$  entraîne une croissance de la pression de culot qui peut être très sensible quand  $T_j$  est élevée (de l'ordre de 20 % pour  $T_j / T_e = 10$ ).
- la Figure 99 donne l'évolution de la traînée globale (culot plus rétreint) d'un arrière corps dont on fait varier l'angle de rétreint  $\beta_e$ . On voit qu'il existe un optimum dont la valeur est une fonction du taux de détente de la tuyère.

#### 2.3.1.4. Autres théories.

Avant de clore ce chapitre sur les méthodes de calcul de la pression de culot pour des écoulements confluents supersoniques, nous mentionnerons brièvement la théorie de Dixon et al [93] qui suit l'approche d'Addy aux modifications suivantes près :

- la frontière externe ( $\sqrt{e}$ ) n'est plus isobare mais est supposée rectiligne, sa direction résultant de la détente (ou compression) de  $p_{e_0}$  à  $p_c$ .
- la frontière ( $\sqrt{j}$ ) est calculée en lui imposant la répartition de pression trouvée le long de ( $\sqrt{e}$ )
- il est tenu compte de l'effet de révolution sur les profils de mélange, par la transformation de Mangler, et dans l'écriture des équations de bilan qui définissent  $\eta_j$  et  $\eta_e$ .

- la variante du critère de Korst, due à Goethert [94] est utilisée : si le nombre de Mach  $M_\ell$  sur la ligne limite ( $\ell$ ) est subsonique, le fluide se recomprime isentropiquement jusqu'à  $p_s$  ; Si  $M_\ell > 1$ , l'écoulement sur ( $\ell$ ) subit d'abord un choc droit, puis se comprime ensuite isentropiquement jusqu'à  $p_s$ .

Egalement, Hong [95] a proposé une théorie très voisine qui présente les caractéristiques suivantes :

- frontières ( $f_c$ ) et ( $f_j$ ) isobares,
- effet de révolution sur les équations de bilan,
- critère modifié de Goethert

Nous retiendrons un exemple d'application qui est intéressant car il est comparé à des mesures en vol (Lanceur THOR "de base" S/N 419). Comme on le voit Figure 100, la prédiction est plutôt bonne, (au delà d'une altitude de 90 000 pieds, les mesures sont incertaines).

Signalons enfin des extensions ou aménagements de ces schémas théoriques pour traiter les problèmes aérothermiques relatifs au culot d'engins multi-tuyères qui intéressent davantage les lanceurs multi-étages que les missiles utilisés en tant qu'armes [96 à 100].

### 2.3.2. Ecoulement externe subsonique et jet interne supersonique

Hormis des tentatives donnant des résultats surtout qualitatifs [101], il n'existe pas, à notre connaissance, de méthodes disponibles pour calculer un écoulement de culot dans le cas d'un vol subsonique ou transsonique. En revanche, des théories ont été développées pour calculer l'interaction entre le jet propulsif et un écoulement externe sub. ou transsonique sur des configurations d'arrière corps sans culot [102 à 105]. L'exposé de ces théories sortirait du cadre de la présente conférence, aussi nous n'en parlerons pas ici.

Toutefois, il n'est pas exclu qu'elles puissent servir de guide à l'élaboration d'un modèle qui tiendrait compte de l'existence d'un culot.

### 3. METHODES DE REDUCTION DE LA TRAINEE DE CULOT

Depuis les expériences de Cortright et Schroeder [106], on sait que l'injection d'un faible débit de masse dans la zone décollée est susceptible d'entraîner une augmentation sensible de la pression de l'eau morte, et donc de réduire la traînée de culot. Les traits essentiels du phénomène ont déjà été analysés au § 1.2.6 de la première partie.

Ce résultat est d'ailleurs parfaitement prédit par les théories que nous avons présentées, en particulier celles qui sont inspirées du schéma de Korst. L'effet peut être caractérisé simplement par l'introduction du coefficient d'injection généralisé  $C_q$ , défini § 2.2.2, et dont nous rappelons ici l'expression (le terme de quantité de mouvement de la couche limite initiale est omis pour raison de simplicité) :

$$(30) \quad C_q = \frac{q_m}{\rho_c u_c L} - \frac{i_m}{\rho_c u_c^2 L}$$

$i_m$  représente la quantité de mouvement (par unité d'envergure) associée obligatoirement à l'introduction du débit massique unitaire  $q_m$ . Si nous supposons que le fluide est injecté avec une vitesse  $v_m$  constante,  $i_m$  s'écrit :

$$i_m = q_m v_m$$

Il ressort de la formule (30) que l'effet de quantité de mouvement se retranche de l'effet de masse. Il y a donc intérêt, pour  $q_m$  donné, à ce que la vitesse d'injection soit la plus faible possible. De toute façon, pour un dispositif d'injection donné,  $v_m$  augmente obligatoirement avec  $q_m$  et on doit s'attendre à ce que son influence négative finisse par l'emporter. Il existe donc un débit  $q_m$  optimal, au delà duquel  $p_c$  se met à décroître.

Ce comportement est parfaitement confirmé par l'expérience, comme le montre les mesures présentées Figure 30 (voir § 1.2.6 de la première partie). Le rapport  $p_c/p_\infty$  passe par un maximum qui est d'autant plus élevé que le rayon  $r_j$  de l'orifice d'injection est plus grand, c'est-à-dire que la vitesse  $v_m$  est plus petite, à  $q_m$  donné. Le dispositif optimal, de ce point de vue, consiste à injecter le fluide à travers une paroi poreuse qui couvre toute la surface du culot. On peut alors obtenir des augmentations de la pression de culot  $p_c/p_\infty$  de plus de 100 %.

L'injection au culot peut également être bénéfique sur le plan de la traînée de l'arrière corps, dans le cas où celui-ci est équipé d'une tuyère propulsive. Nous avons déjà présenté (Figure 89) un exemple d'application de la théorie sur une configuration de ce genre. Toutefois, l'intérêt d'un soufflage au culot pour un engin de croisière à propulsion aérothermique est discuté.

Un bilan global montre, en effet, que la traînée de captation du débit  $Q_m$  peut l'emporter sur le gain de traînée de culot résultant de l'augmentation de  $\lambda_c$  [108]. En revanche, le procédé peut s'avérer très utile pour accroître la portée d'obus d'artillerie ou de missiles en vol non propulsé. Le problème fait donc l'objet de recherches actives dont nous allons donner un aperçu. Pour des vols de courte durée (cas des armes), on peut envisager d'agir autrement que par simple injection d'air au culot et obtenir ainsi des efficacités bien plus grandes.

L'analyse théorique [109] montre que l'effet est encore plus bénéfique si le gaz injecté a une masse moléculaire faible et si sa température est élevée (effet d'apport d'enthalpie).

L'influence de ces facteurs a été mise en évidence, expérimentalement, en particulier par Baker et al. [110] puis par Townend [111]. Des expériences de ce dernier, il ressort notamment, qu'à même débit injecté, l'hydrogène (masse moléculaire  $M = 2$ ) peut donner un accroissement  $\lambda_c/\lambda_0$  1,5 fois supérieur à celui de l'azote ( $M = 28$ ). Ce résultat n'est évidemment pas général, il dépend des circonstances de l'écoulement. Parfois, un gain plus important peut être obtenu. Townend a également montré qu'une pression  $\lambda_c \approx \lambda_0$  pouvait être réalisée par combustion de l'hydrogène dans la zone du sillage. L'intérêt d'injecter des gaz chauds au culot a été également démontré par Clayden et al. [112] dans des expériences de soufflerie et par Andersson et al. [113] sur des projectiles d'artillerie (réduction de la traînée de culot d'environ 70 %).

L'augmentation de  $\lambda_c$ , jusqu'à l'obtention d'un effet propulsif ( $\lambda_c > \lambda_0$ ), peut aussi être réalisée par combustion externe. Dans ce procédé, un mélange combustible riche est injecté transversalement dans l'écoulement externe supersonique en amont du culot. Par mélange avec l'air, il se produit alors une combustion dans le fluide non visqueux contigu au sillage. L'apport de chaleur et de masse engendre une compression qui interagit avec l'écoulement de culot et provoque une remontée de la pression  $\lambda_c$ . Des valeurs de  $\lambda_c$  supérieures à  $\lambda_0$  peuvent, en principe, être obtenues par cette méthode [114 à 116]. L'aspect purement aérodynamique du phénomène a été étudié par Neale et al. en simulant l'effet de la combustion par l'action d'une onde de compression agissant sur le proche sillage d'un arrière corps cylindrique.

Une analyse de l'action des différents paramètres que nous venons de passer rapidement en revue a été effectuée récemment par Schadow et Chieze [117] sur un montage bidimensionnel constitué d'une marche placée dans un écoulement uniforme à Mach 2. Les auteurs ont examiné l'efficacité des différents procédés suivants, utilisés séparément ou simultanément :

- injection au culot de gaz inertes (hélium et azote) désignée par BI
- combustion externe avec injection latérale supersonique (EB)
- combustion externe avec injection latérale subsonique. Dans ce cas, il se produit également une combustion au culot, une partie du mélange combustible étant entraîné dans l'eau morte par l'intermédiaire de la couche limite (EB/BR).

Examinons les résultats obtenus dans les différents cas :

- Figure 101 : influence de BI seul et de EB et EB/BR seules. Il est bien vérifié que le gaz léger ( $H_2$ ,  $M = 4$ ) est nettement plus efficace que l'azote ( $M = 28$ ). Le procédé EB/BR donne une augmentation de pression nettement supérieure à EB,
- Figure 102 : effets cumulés de BI et EB,
- Figure 102 : effets cumulés de BI et EB/BR (injection d'hélium). Cette dernière combinaison conduit à des pressions  $\lambda_c$  légèrement supérieures à  $\lambda_0$ , d'où un effet propulsif.

En fait, d'après les conclusions des auteurs (et la suggestion de Townend), il semble que le procédé le plus efficace consisterait à associer une combustion au culot, par injection directe d'un combustible, avec une combustion externe du type EB.

#### 4. CONCLUSION

Dans cet exposé, nous nous sommes efforcés de présenter d'une manière aussi complète que possible un état des connaissances actuelles sur les problèmes d'écoulement de culot en se plaçant d'un point de vue essentiellement pratique. Un examen phénoménologique de ces écoulements a permis d'en préciser la structure et de dégager les principaux facteurs d'influence. Sur le plan théorique, un certain nombre de méthodes, parmi les plus usitées, ont été présentées. Celles-ci conduisent le plus souvent à une bonne prévision des caractéristiques essentielles de l'écoulement de culot pour des configurations à symétrie de révolution, en subsonique comme en supersonique. Dans ce dernier cas elles permettent de tenir compte de la présence d'un jet propulsif.

Il n'en demeure pas moins, que de nombreux aspects des phénomènes de culot restent encore insuffisamment explorés.

Ainsi, sur le plan expérimental, on retiendra :

- l'absence d'études fondamentales vraiment fiables concernant les vitesses transsoniques ;
- le manque d'analyses détaillées de la structure du décollement de culot en tridimensionnel et plus spécialement lorsque cet effet est produit par la mise en incidence. Dans ce domaine, l'expérimentation est particulièrement difficile en raison des interactions de support et on peut regretter que le développement des systèmes de suspension magnétique n'ait pas été activement poursuivi ;
- la nécessité d'entreprendre des recherches sur la structure de la turbulence dans les écoulements de culot ainsi que sur les phénomènes instationnaires qui lui sont associés. L'utilisation de la vélocimétrie laser doit rendre ici de précieux services.

Sur le plan théorique, il conviendrait :

- d'étendre les méthodes existantes au transsonique et au cas subsonique avec jet, ce qui ne devrait pas soulever de difficultés majeures et de perfectionner les techniques d'interaction forte ;
- de développer des modèles pour traiter les configurations tridimensionnelles (effet d'incidence, interaction sillage tourbillonnaire - culot) spécialement en subsonique. Dans cette perspective, les méthodes de singularités tourbillonnaires ponctuelles, en cours de développement à l'ONERA [118, 119] sont particulièrement prometteuses ;
- d'étendre aux écoulements turbulents axisymétriques la résolution numérique des équations de Navier-Stokes, la définition et l'adaptation des modèles de turbulence appropriés devant se faire en étroite liaison avec l'expérimentation.

## REFERENCES

- [1] CHANG P.K. - Separation of flow - Pergamon Press, 1970
- [2] CHAPMAN D.R. - An analysis of base pressure at supersonic velocities and comparison with experiment - NACA Report 1051, 1951
- [3] LOVE E.S. - Base pressure at supersonic speeds on two dimensional airfoils and on bodies of revolution with and without fins having turbulent boundary layers - NACA T.N. 3819, 1957
- [4] KORST H.H., CHOW W.L. - ZUMWALT G.N. - Research on transonic and supersonic flow of a real fluid at abrupt increase in cross section (with special consideration of base drag problems) - University of Illinois, ME T.R. 3925, 1959
- [5] McDONALD H. - An analysis of the turbulent base flow problem in supersonic axisymmetric flow - The Aeronautical Quarterly, Vol. 16, Part 2, 1965
- [6] HUTSKO H.E. - CARTER W.V. - HERMAN W. - Development of subsonic base pressure prediction methods ; results of experimental investigation - AFFDL T.R. 65 157, Vol. 2, 1965
- [7] SIRIEIX M. - DELERY J. - Analyse expérimentale du proche sillage d'un corps élané libre de tout support latéral, AGARD CP 19, 1967
- [8] MUELLER T.J. - Determination of the turbulent base pressure in supersonic axisymmetric flow - Journal of Aircraft, vol. 5 n° 1, 1968
- [9] CARRIERE P. - SIRIEIX M. - DELERY J. - Méthodes de calcul des écoulements turbulents décollés en supersonique - Progress in Aerospace Sciences, Vol. 16, n° 4, 1975
- [10] WERLE H. - Document ONERA non publié
- [11] VANWAGENEN R. - A study of axially-symmetric subsonic base flow - Ph. D. Thesis, University of Washington, 1968
- [12] MEHTA G. - A theory of the supersonic turbulent axisymmetric near wake behind bluff-base bodies - Ph. D. Thesis, Georgia Institute of Technology, 1977
- [13] MERZ R.A. - PAGE R.H. - PRZIREMBEL C.E.G. - Subsonic axisymmetric near wake studies, - AIAA Journal Vol. 16, n° 7, 1978
- [14] HAMA F.R. - Experimental studies on the lip shock, AIAA Journal, Vol. 6, N° 2, 1968
- [15] GAVIGLIO J. - DUSSAUGE J.P. - DEBIEVRE J.P. - FAVRE A. - Behavior of a turbulent flow, strongly out of equilibrium, at supersonic speeds - The Physics of Fluids, Vol. 20, n° 10, 1977
- [16] SIRIEIX M. - DELERY J. - MONNERIE B. - Etude expérimentale du proche sillage d'un corps de révolution en écoulement supersonique - 19ème Congrès International d'Aéronautique, 1968
- [17] ROM J. - VICTOR M. - REICHENBERG M. - SALOMON M. - Wind tunnel measurements of the base pressure of an axially symmetric model in subsonic, transonic and supersonic speeds at high Reynolds numbers - TAE Report 134, 1972
- [18] WHITFIELD J.D. - POTTER J.L. - On base pressures at high Reynolds numbers and hypersonic Mach numbers - AEDC T.N. 60-61, 1960
- [19] BOWMAN J.E. - CLAYDEN W.A. - Boat-tailed afterbodies at  $M_\infty = 2$  with gas ejection - AIAA Journal, Vol. 6, n° 10, 1968
- [20] REID J. - HASTINGS R.C. - Experiments on the axisymmetric flow over afterbodies and bases at  $M = 2$  - ARC Report 21.707, 1959
- [21] McDONALD H. - HUGUES R.F. - A correlation of high subsonic afterbody drag in the presence of a propulsive jet or support sting - Journal of Aircraft, vol. 2, n° 3, 1965
- [22] WERLE H. - Document ONERA non publié
- [23] BROWAND F.K. - FINSTON M. - McLAUGHLIN D.K. - Wake measurements behind a cone suspended magnetically in a Mach number 4.3 stream - AGARD CP 19, 1967
- [24] STIVERS L.S. - LEVY L.L. - Effects of sting support diameter on the base pressure of an elliptic cone at Mach numbers from 0.6 to 1.4 - NASA T.N. D-354, 1961
- [25] PICK G.S. - Base pressure distribution of a cone at hypersonic speeds - AIAA Journal, Vol 10 n°12, 1972
- [26] SACHIDANANDA KANGOVI - Base flow of a spinning axisymmetric body - AIAA Paper 76-212, 1976
- [27] REID J. - HASTINGS R.C. - The effect of a central jet on the base pressure of a cylindrical afterbody in a supersonic stream - ARC R.M. 3224, 1961

- [28] CARRIERE P. - Recherches sur l'écoulement autour d'avions ou de fusées - 2ème Conférence Otto Lilienthal, Braunschweig, 1961
- [29] CARRIERE P. - SIRIEIX M. - HARDY J.M. - Problèmes d'adaptation de tuyères - T.P. ONERA n° 600 1968
- [30] HARRIES M.H. - Pressure on axisymmetric base in a transsonic or supersonic free stream in the presence of a jet - PFA Report 111, 1967
- [31] CUBBAGE J.M. - Jet effect on base and afterbody pressures of a cylindrical afterbody at transonic speeds NACA R.M. L56C21, 1956
- [32] REID J. - The effect of jet temperature on base pressure - RAE T.R. 68176, 1968
- [33] CHARCZENKO N. - HAYES C. - Jets effects at supersonic speeds on base and afterbody pressures of a missile model having single and multiple jets - NASA T.N. D-2046, 1963
- [34] GOETHERT B.H. - MATZ R. - Experimental investigation of base flow characteristics of four nozzle cluster-rocket models - AGARDograph 87, Vol. 2, 1964
- [35] MUSIAL N.T. - WARD J.J. - Base flow characteristics for several four-clustered rocket configurations at Mach numbers from 2 to 3.5 - NASA T.N. D-1093, 1961
- [36] ADDY A.L. - KORST H.H. - WHITE R.A. - WALKER B.J. - A study of flow separation in the base region and its effects during powered flight, AGARD CP 124, 1973
- [37] MCGHEE R.J. - Some effects of jet pluming on the static stability of ballistic bodies at Mach number of 6. - NASA T.N. D-3698
- [38] MABEY D.G. - Some measurements of base pressure fluctuations at subsonic and supersonic speeds - A.R.C. C.P. n° 1204, 1972
- [39] POL DER VAART L.J. - WIJNANDS A.P.J. - BRONKHORST I. - Sound pulse-boundary layer interactions studies - Film 16 mm, Technische Hogeschool, Eindhoven, 1974
- [40] CARPENTER P.W. - TABAKOFF - Survey and evaluation of supersonic base flow theories - Cincinnati University, Ohio, Institute of Space Sciences - NASA CR 97129, 1968
- [41] TANNER M. - Theoretical prediction of base pressure for steady base flow - Progress in Aerospace Sciences, Vol. 14, pp. 177-225, 1973
- [42] NASH J.F. - A discussion of two-dimensional turbulent base flows - ARC R & M 3468, 1967
- [43] CHAPMAN D.R. - Laminar mixing of a compressible fluid - NACA Rep. 958, 1950
- [44] CHAPMAN D.R. - KUEHN D.M. - LARSON H.K. - Investigation of separated flows in supersonic and subsonic streams with emphasis on the effect of transition - NACA Rep. 1356, 1958
- [45] KORST H.H. - A theory for base pressures in transonic and supersonic flow - J. Appl. Mech. 23, 1956, p. 593-600
- [46] CROCCO L. - LEES L. - A mixing theory for the interaction between dissipative flows and nearly isentropic streams - J. Aero. Sci. 19, p. 649-676, 1952
- [47] KIRK F.N. - An approximate theory for base pressure in two-dimensional flow at supersonic speeds - RAE TN Aero 2377, 1959
- [48] SOLIGNAC J.L. - SIRIEIX M. - Contribution à l'étude expérimentale de la couche de mélange turbulent isobare d'un écoulement supersonique - AGARD CP 4, 1960
- [49] CARRIERE P. - Effet d'une injection de fluide dans l'eau morte sur les conditions de recollement d'un écoulement plan supersonique - Compte-rendus de l'Académie des Sciences de Paris, t. 521, p. 2877-2879, 1960
- [50] NASH J.F. - An analysis of two-dimensional turbulent base flow including the effect of the approaching boundary layer - ARC R and M 3344, 1962
- [51] CARRIERE P. - SIRIEIX M. - Facteurs d'influence du recollement d'un écoulement supersonique - 10ème Congrès international de Mécanique Appliquée, STRESA, Italie, 1960
- [52] ROBERTS J.B. - On the prediction of base pressure in two-dimensional supersonic turbulent flow - ARC, R & M 3434, 1966
- [53] ROSHOTKO E. - TUCKER M. - Effect of a discontinuity on turbulent boundary layer thickness parameters with application to shock induced separation - NACA TM 3454, 1955
- [54] NASH J.M. - Comments on "Review of Recent Developments in turbulent supersonic base flow" - AIAA Journal vol. 4, n° 3, Mars 1966
- [55] McDONALD H. - Turbulent shear layer reattachment with special emphasis on the base pressure problem - Aero Quart. 15, p. 247-280, 1964

- [56] CARRIERE P. - Recherches récentes effectuées à l'ONERA sur les problèmes de recollement - 7ème Symposium de Mécanique des Fluides, Jurata, Pologne et T.P. ONERA n° 275, 1965
- [57] SIRIEIX M. - MIRANDE J. - DELERY J. - Expériences fondamentales sur le recollement d'un jet supersonique - AGARD CP 4, 1966
- [58] SOLIGNAC J.L. - DELERY J. - Contribution à l'étude aérodynamique des systèmes propulsifs à double flux - Israël Journal of Technology, vol. 10, n° 1-2, 1972, p. 97-111, 1972
- [59] ROUGIER P. - Etude expérimentale des phénomènes dynamiques et thermiques liés au recollement d'un jet supersonique. Application à l'étude des éjecteurs supersoniques - Thèse d'Ingénieur Docteur, Université de Lyon, 1970
- [60] COOKE J.C. - Separated supersonic flow - RAE TN Aero 2879, 1963
- [61] BRAY K.N., GADD G.E. - WOODGER L. - Some calculations by the Crocco-Lees and other methods of interaction between shock waves and laminar boundary layers including the effect of heat transfer and suction- ARC Report 21-834, FM 2937, 1960
- [62] GLICK H.S. - Modified Crocco-Lees mixing theory for supersonic separated and reattaching flows - Cal. Inst. of Tech., Memo n° 53, 1960
- [63] ROM J. - Theory for supersonic two-dimensional laminar base type flows using Crocco-Lees mixing concept - Technion Israël Inst. Of Tech., TAE Report 20, 1962
- [64] SEGNER A. - ROM J. - Integral method for the calculation of heat transfer in laminar supersonic separated flows - Technion Israël Inst. of Tech., TAE Report 78, 1967.
- [65] KRASINSKI (de) J.S. - A study of separated base flow behind bodies of revolution in supersonic streams IIAE, Cordoba, Argentine, Informe INF 01-66, 1966
- [66] LEES L. - REEVES B.L. - Supersonic separated and reattaching laminar flows : 1) general theory and application to adiabatic boundary layer shock wave interactions - AIAA Journal, vol 2 n° 11, 1964
- [67] ALBER I.E. - Integral theory for turbulent flows at subsonic and supersonic speeds - Cal. Inst. of Tech., Ph. D Thesis, 1967
- [68] HUNTER L.G. - REEVES B.L. - Results of a strong interaction wake-like model for supersonic separated and reattaching turbulent flow - AIAA Journal, vol. 9, n° 4, 1971
- [69] KUHN C.D. - NIELSEN J.N. - Prediction of turbulent separated boundary layers - AIAA Journal, vol 12 n° 7, 1974
- [70] LE BALLEUR J.C. - Calculs couplés visqueux-non visqueux incluant décollements et ondes de choc en écoulement bidimensionnel - AGARD LS 94, 1978
- [71] AI D.K. - On the critical point of the Crocco-Lees mixing theory in the laminar near wake - Journal of Engineering Mathematics, vol. 4, N°2, 1970
- [72] ZUMWALT G.W. - Analytical and experimental study of the axially symmetric base pressure problem - Ph. D dissertation, Department of Mechanical Engineering University of Illinois, 1959
- [73] ROACHE P.J. - Base drag calculations in supersonic turbulent axisymmetric flows - Journal of Spacecraft and Rockets, Vol. 10, n° 4, 1973
- [74] CHANNAPRAGADA R.S. - Compressible jet spread parameter for mixing zone analyses - AIAA Journal, Vol 1 n° 9, 1963
- [75] WENG CHI-HSIUNG - Base pressure problems associated with supersonic axisymmetric external flow configurations - Ph. D Thesis, University of Illinois, 1975
- [76] HASTINGS R.C. - Turbulent flow past two-dimensional bases in supersonic streams - RAE Tech. Note, Aero 9931, 1963
- [77] WEBB W.H. - An approximate pressure-angle relation for the axisymmetric supersonic near-wake - AIAA Journal, Vol 6, n° 7, 1968
- [78] GREEN J.E. - Two-dimensional turbulent reattachment as a boundary value problem - AGARD CP 4, Part 1, 1966
- [79] KUBOTA T. - REEVES B.L. - BUSS H. - A family of similar solutions for axisymmetric incompressible wakes - AIAA Journal Vol 2, n° 8, 1964
- [80] PETERS C.D. - PHARES W.J. - Analytical model of supersonic turbulent near-wake flows, AEDC - TR - 76-127, 1976
- [81] FROMM J. - A method for computing non-steady, incompressible viscous flows - Los Alamos Scientific Laboratory Report n° LA-2910, 1963

- [82] BOURQUE C. - NEWMAN B.G. - Reattachment of a two-dimensional jet to an adjacent flat plate - Aeronautical Quarterly, Vol. 11, Part 3, 1960
- [83] LE BALLEUR J.C. - MIRANDE J. - Etude expérimentale et théorique du recollement bidimensionnel turbulent incompressible - AGARD CP 168, 1975
- [84] GOSMAN A.D. - FUN W.M. - RUNCHAL A.K. - SPALDING D.B., WOLFSTEIN M. - Heat and mass transfer in recirculating flows - Academic Press, 1969
- [85] HA-MINH-HIEU - Décollement provoqué d'un écoulement turbulent incompressible, Etude théorique et expérimentale - Thèse Docteur ès Science, Institut National Polytech. de Toulouse, 1976
- [86] BUTSKO J.E. - Prediction of the subsonic base drag of hypersonic re-entry vehicles, - AIAA Paper n° 66-991, 1966
- [87] CHOW W.L. - SHIH T.S. - The viscous-inviscid interaction associated with a two-dimensional transonic flow past a backstep - University of Illinois, ME-TR-395-3, 1975
- [88] KLINEBERG J.M. - KUBOTA T. - LEES L. - Theory of exhaust-plume/boundary layer interactions at supersonic speeds - AIAA Journal, Vol. 10, n° 5, 1972
- [89] BOGEP R.C. - ROSENBAUM H. - REEVER B.L. - Flowfield interactions induced by underexpanded exhaust plumes - AIAA Journal, vol 10, n° 3, 1972
- [90] ADDY A.L. - Analysis of the axisymmetric base pressure and base temperature problem with supersonic interacting freestream nozzle flows based on the flow model of KORST et al. Parts I and II - Report n° RD-TR-69-12, U.S. Army Missile Command, Redstone Arsenal, Ala, 1969
- [91] AGRELL J. - WHITE R.A. - An experimental investigation of supersonic axisymmetric flow over boattails containing a centered propulsion jet - FFA Technical Note AU-913, 1974
- [92] ADDY A.L. - Experimental-theoretical correlation of supersonic jet on base pressure for cylindrical afterbodies - Journal of Aircraft, Vol. 7, N° 5, 1970
- [93] DIXON R.J. - RICHARDSON J.M. - PAGE R.H. - Turbulent base flow on a axisymmetric body with a single exhaust jet - Journal of Aircraft, Vol 7, n° 7, 1970
- [94] GOETHERT B.H. - Base flow characteristics of missiles with cluster rockets exhausts, - IAS Paper 69-89, 1969
- [95] HONG Y.S. - Base flow environment analysis of a single engine booster - AIAA Paper n° 71-643, 1971
- [96] PAGE R.H. - DIXON R.J. - Theoretical analysis of launch vehicle base flow - AGARD CP 4, 1966
- [97] LAMB J.P. - ABBUD K.A. - LENZO C.S. - A theory for base pressures in multi-nozzle rocket configuration - AIAA Paper n° 69-570, 1969
- [98] PAGE R.H. - DIXON R.J. - Base heating on a multiple propulsion nozzle missile - AIAA Paper n° 63-179, 1963
- [99] TANG H.H. - GARDINER C.P. - ANDERSON W.A. - NAVICKAS J. - Space shuttle booster multi-engine base flow analysis - NASA TMX 2507, 1971
- [100] HONG Y.S. - Base flow analysis for a dual engine booster - Journal of Spacecraft and Rockets, Vol 11, n° 4, 1974
- [101] CRAVEN A.H. - Base pressure at subsonic speeds in the presence of a supersonic jet - The College of Aeronautics, Cranfields, Report n° 129, 1960
- [102] MARIA SUBE R., CHATTOT J.J. - GILLON G. - Couplage entre l'écoulement autour d'un arrière-corps et le jet propulsif en théorie de fluide parfait - AGARD CP 150, 1974
- [103] GROSSMAN B. - MELNICK R.E. - The numerical computation of the transonic flow over afterbodies including the effect of jet-plume and viscous interactions - AIAA Paper 75-62, 1962
- [104] HOLST T.L. - Numerical solution of axisymmetric boattail fields with plume simulators - AIAA Paper 77-224, 1977
- [105] WILMOTH R.G. - Computation of transonic boattail flow with separation - NASA Technical Paper 1070, 1977
- [106] CORTRIGHT E.M. - SCHROEDER A.H. - Preliminary investigation of effectiveness of base bleed in reducing drag of blunt base bodies in supersonic stream - NACA RM E51 A 26, 1951
- [107] VALENTINE D.T. - PRZIREMBEL C.E.G. - Turbulent axisymmetric near-wake at Mach four with base injection - AIAA Journal, Vol 8, n° 12, 1970
- [108] ROBERTS J.B. - GOLESWORTHY G.T. - An experimental investigation of the influence of base bleed on the base drag of various propelling nozzle configurations - ARC - CP n° 892, 1966



- [109] PAGE R.H. - KORST H.H. - Non isoenergetic turbulent compressible jet mixing with consideration of its influence on the base pressure - Ph. D. dissertation, Mechanical Engineering Dept., Univ. of Illinois, 1955
- [110] BAKER W.T. - DAVIS T. - MATTHEWS S.E. - Reduction of drag of a projectile in supersonic stream by the combustion of hydrogen in the turbulent wake - John Hopkins Univ. Applied Physics Lab., CM-673, 1951
- [111] TOWNEND L.H. - Some effects of stable combustion in wake formed in a supersonic stream, RAE Tech. Note n° Aero 2872, 1963
- [112] CLAYDEN W.A. - BOWMAN J.E. - Cylindrical afterbodies at  $M = 2$  with hot gas ejection, AIAA Journal Vol 6, n° 12, 1968
- [113] ANDERSSON K. - GUNNERS N.E. - HELLGREN R. - Swedish base bleed-increasing the range of artillery projectiles through base flow - Propellants and Explosives, Vol. 1, p. 69-73, 1976
- [114] STRAHLE W.C. - Theoretical consideration of combustion effects on base pressure in supersonic flight 12th Symposium (International) on Combustion - The Combustion Institute, Pittsburgh, 1969, p. 1163
- [115] DIRECTOR M.N. - Evaluation of an external burning experiment - AIAA Paper 77-926, 1977
- [116] NEALE D.H. - HUBBARTT J.E. - STRAHLE W.C. - WILSON W.W. - Effects of external compression on an axisymmetric turbulent near wake - AIAA Journal, Vol 16, n° 9, 1978
- [117] SCHADOW K.C. - CHIEZE D.J. - Experimental study on base drag reduction with combined lateral and axial injection - AIAA Journal, Vol 16, n° 10, 1978
- [118] C. REHBACH - Numerical calculation of three-dimensional unsteady flows with vortex sheets, AIAA Paper n° 78-111, Janvier 1978
- [119] F. CHOMETON - P. FONTANET - Etude de l'écoulement tridimensionnel décollé autour de véhicules terrestres - A paraître

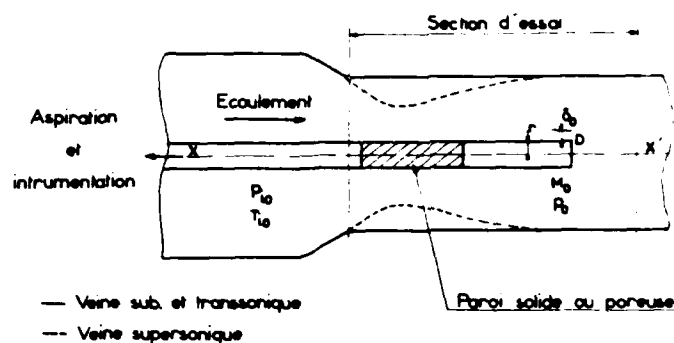
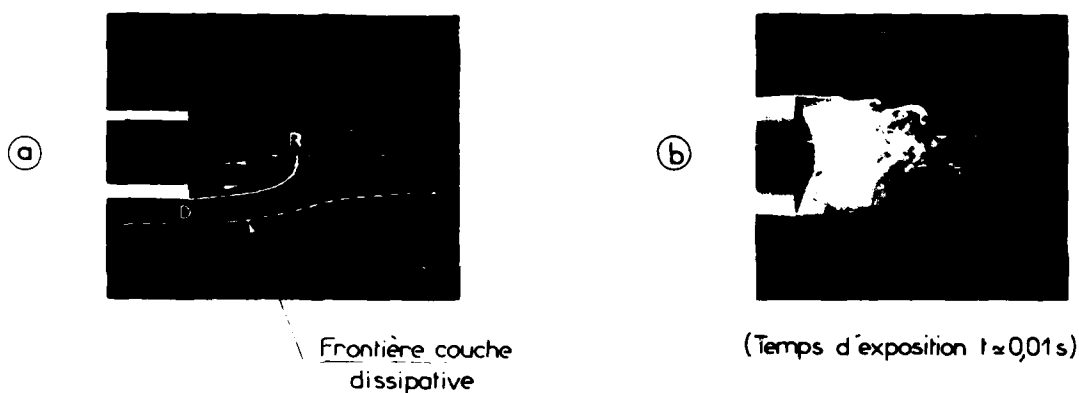
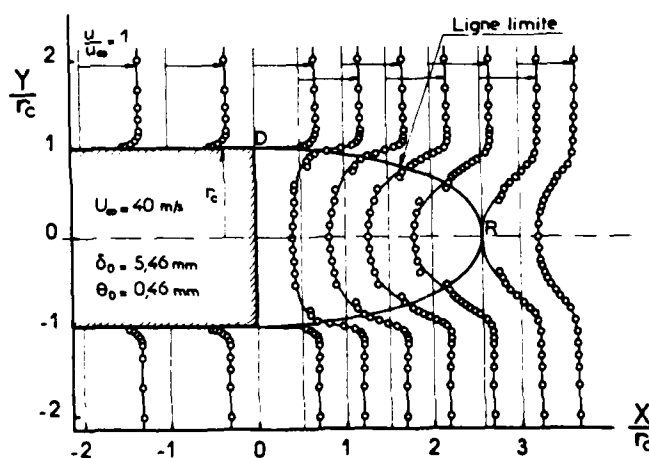


Fig. 1 MONTAGE D'ESSAI POUR L'ETUDE DES ECOULEMENTS DE CULOT

Fig. 2 ECOULEMENT DE CULOT VISUALISE  
AU TUNNEL HYDRODYNAMIQUE (d'après [ 10 ])Fig. 3 PROFILS DE VITESSE EN AVAL D'UN CULOT  
EN ECOULEMENT INCOMPRESSIBLE (d'après [ 11 ])

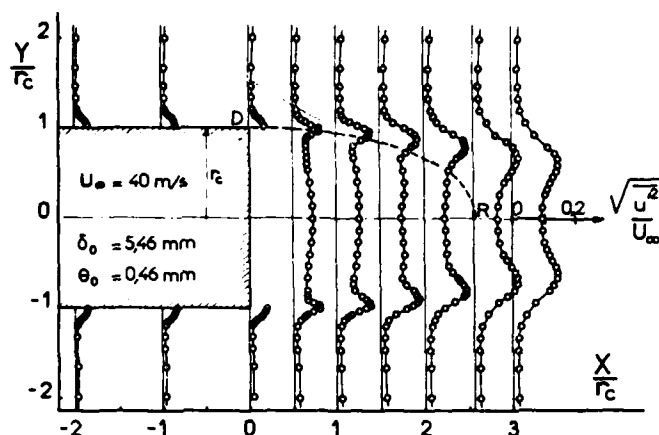


Fig. 4 TAUX DE TURBULENCE EN AVAL D'UN CULOT  
EN ECOULEMENT INCOMPRESSIBLE (d'après [11])

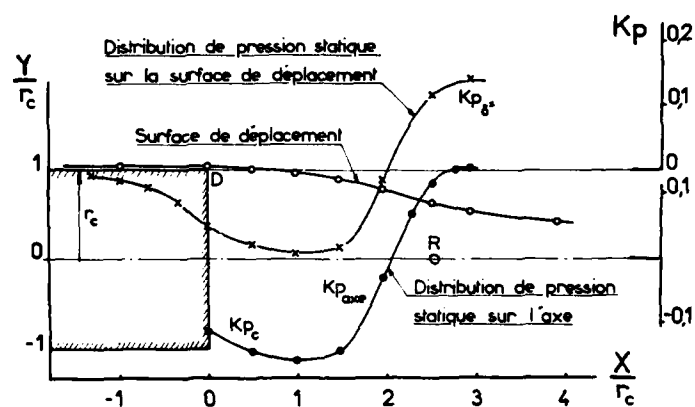


Fig. 5 COEFFICIENTS DE PRESSION SUR LA SURFACE DE DEPLACEMENT  
ET SUR L'AXE DU SILLAGE. ECOULEMENT INCOMPRESSIBLE (d'après [11])

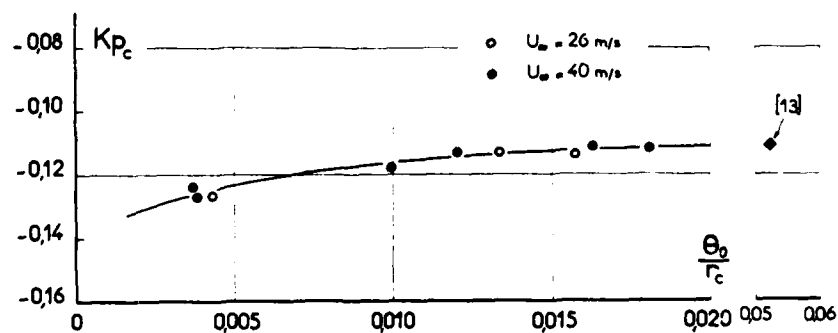


Fig. 6 EFFET DE COUCHE LIMITE INITIALE SUR LE COEFFICIENT  
DE PRESSION DE CULOT. ECOULEMENT INCOMPRESSIBLE (d'après [11])

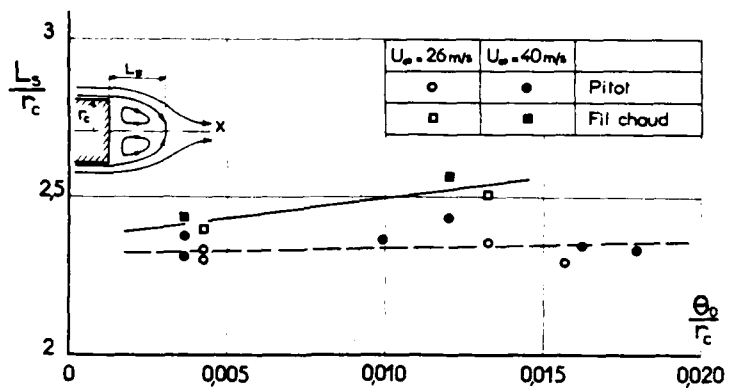


Fig. 7 EFFET DE LA COUCHE LIMITE INITIALE  
SUR LA LONGUEUR DE LA ZONE DE RECIRCULATION  
ÉCOULEMENT INCOMPRESSIBLE (d'après [ 11 ])

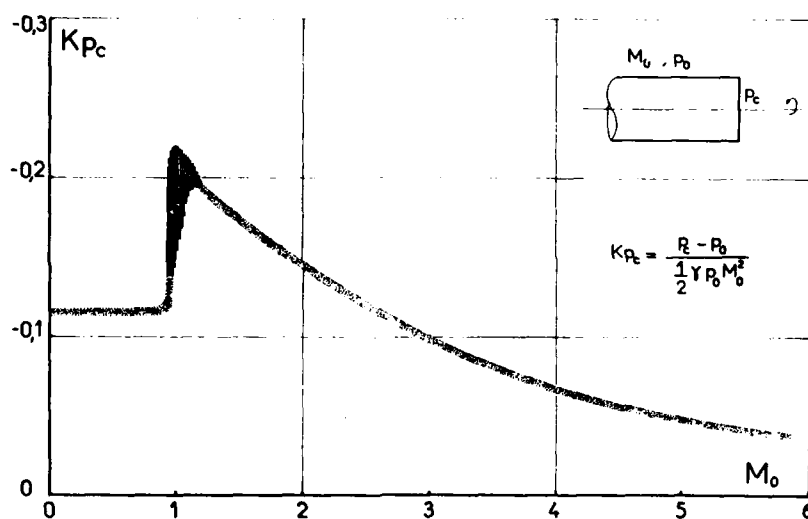


Fig. 8 COEFFICIENT DE PRESSION DE CULOT EN FONCTION DU NOMBRE DE MACH  
COURBE DE BASE ARRIERE CORPS CYLINDRIQUE [ 2.3.17 ]

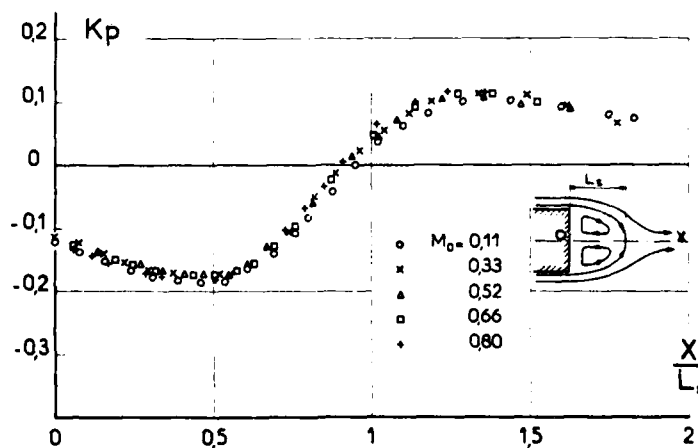


Fig. 9 ÉVOLUTION DU COEFFICIENT DE PRESSION SUR L'AXE  
ÉCOULEMENT SUBSONIQUE (d'après [ 13 ])

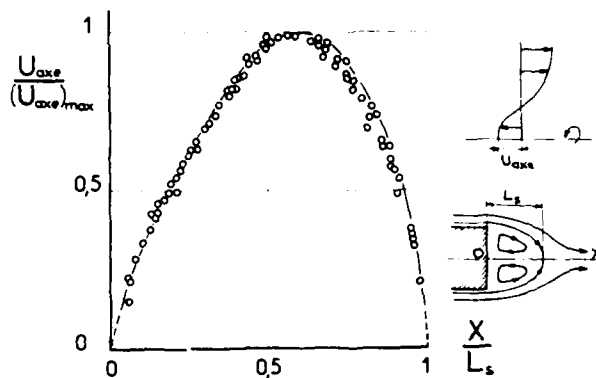
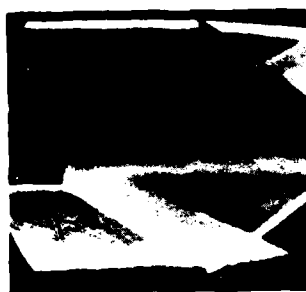
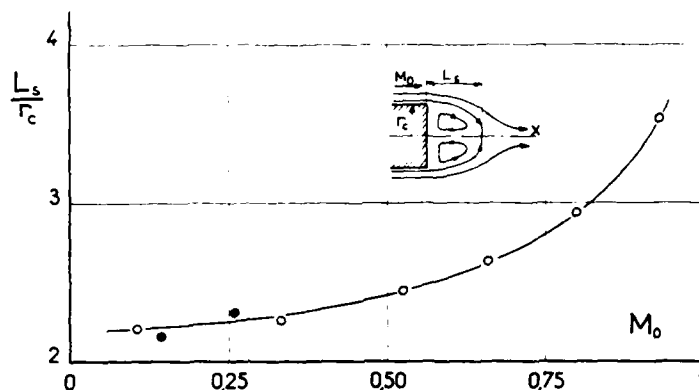
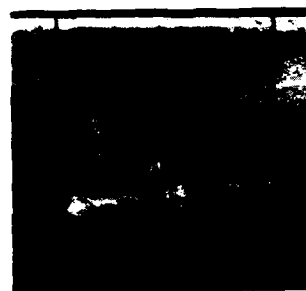


Fig. 10

EVOLUTION DE LA VITESSE DE RETOUR SUR L'AXE  
ECOULEMENT SUBSONIQUE ( $0,1 \leq M \leq 0,8$ ) (d'après [13])

Fig. 11 EFFET DU NOMBRE DE MACH  
SUR LA LONGUEUR DE LA ZONE DE RECIRCULATION  
ECOULEMENT SUBSONIQUE (d'après [13])

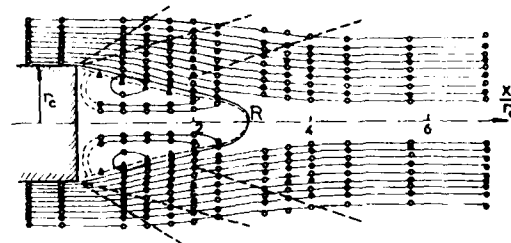
-a.  $M_0 = 2$ 

-b.  $M_0 = 2$   
temps d'exposition  $\sim 1 \mu s$

-c.  $M_0 = 4$ 

Fig. 12 VISUALISATION DE L'ECOULEMENT EN AVAL  
D'UN CULOT CYLINDRIQUE - ECOULEMENT SUPERSONIQUE

$M_0 = 2,3$  -a. lignes de courant



-b. profils de frottement

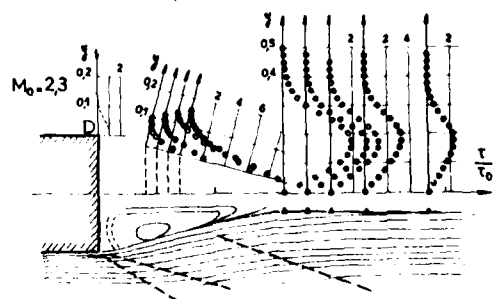


Fig. 13 STRUCTURE DE L'ECOULEMENT AU CULOT  
D'UN ARRIERE-CORPS CYLINDRIQUE  
ECOULEMENT SUPERSONIQUE (d'après [15])

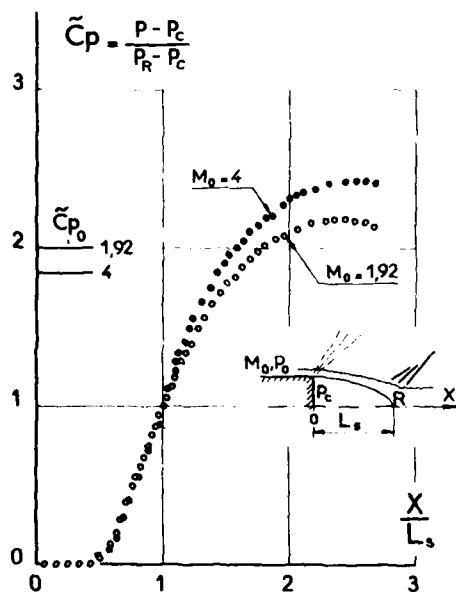


Fig. 14 REPARTITION DE PRESSION SUR L'AXE  
ECOULEMENT SUPERSONIQUE (d'après [ 16 ])

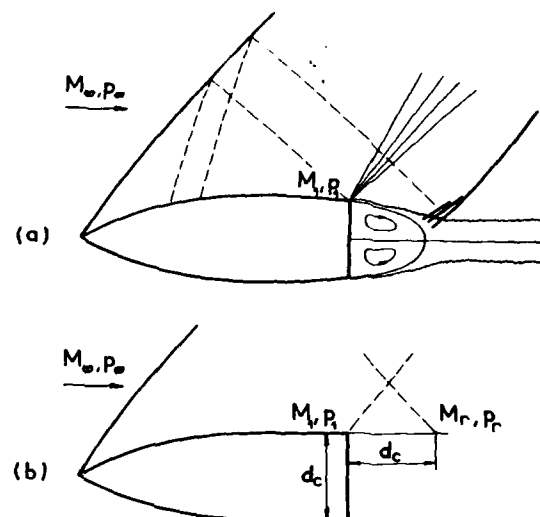


Fig. 15 DEFINITION DU NOMBRE DE MACH DE REFERENCE  
( d'après [ 2 ] )

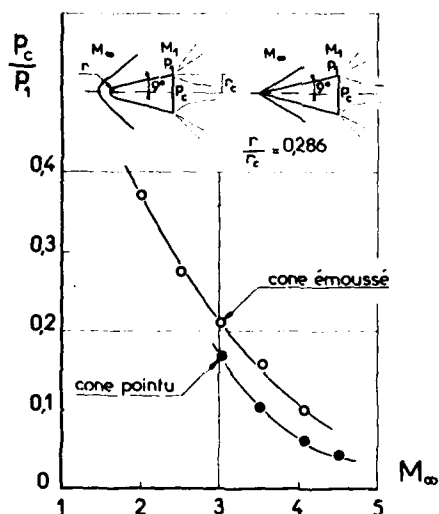


Fig. 16 PRESSION AU CULOT DE PROJECTILES CONIQUES  
ECOULEMENT SUPERSONIQUE ( d'après [ 18 ] )

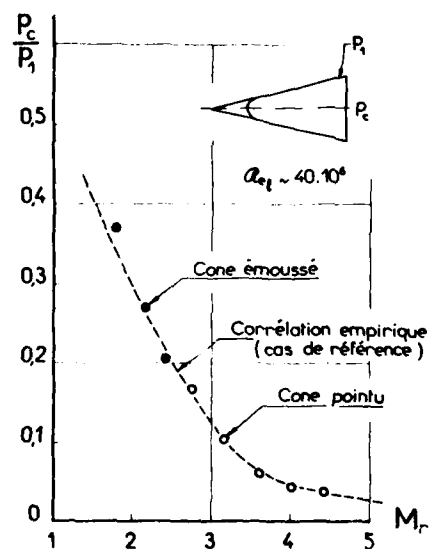


Fig. 17 CORRELATION DES PRESSIONS DE CULOT  
SUR CORPS CONIQUES (d'après [ 18 ])

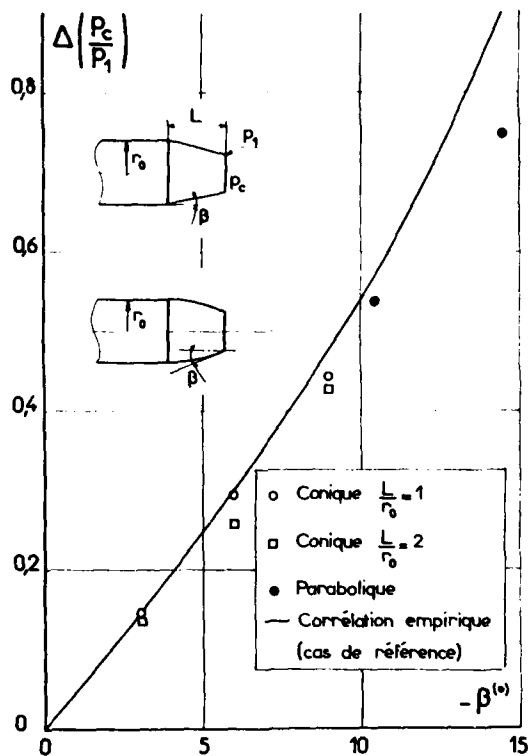


Fig. 18 EFFET DE RETREINT SUR LA PRESSION DE CULOT  
ECOULEMENT SUPERSONIQUE A  $M_0 = 2$  (d'après [19.20])

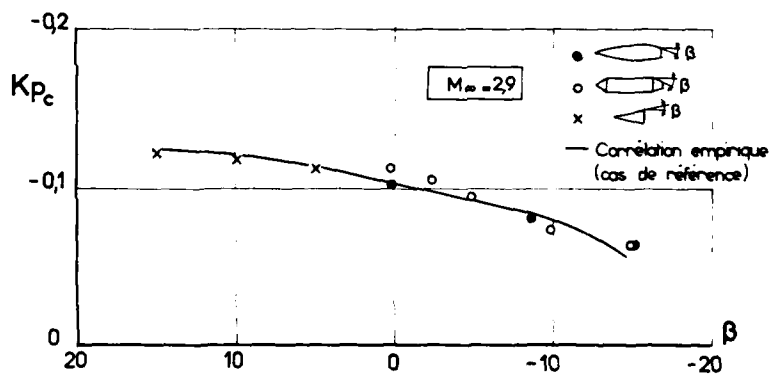


Fig. 19 EFFET D'INCLINAISON DE LA PAROI  
SUR LE COEFFICIENT DE PRESSION DE CULOT (d'après [3])

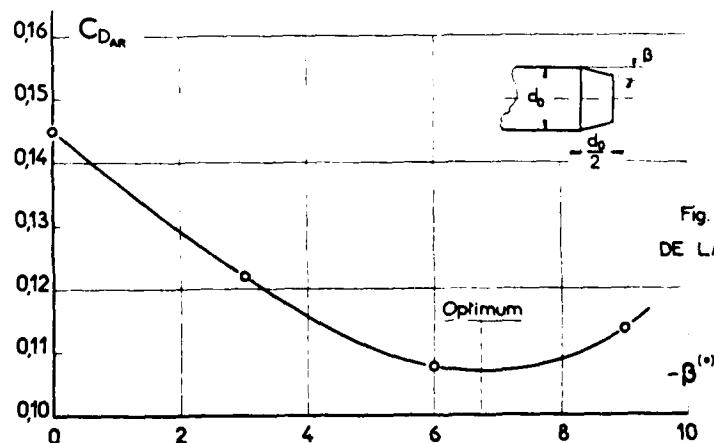


Fig. 20 EXEMPLE D'OPTIMISATION  
DE LA TRAINEE D'UN ARRIERE CORPS  
(d'après [19])

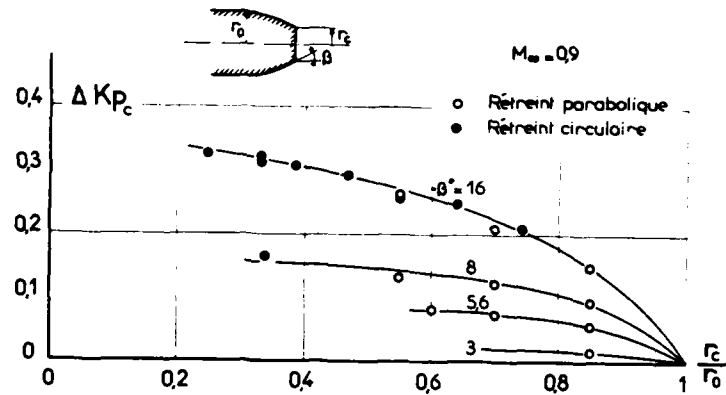


Fig. 21 EFFET DE RETREINT  
SUR LE COEFFICIENT DE PRESSION DE CULOT EN SUBSONIQUE (d'après [ 21 ])



(a) Vue de côté  
 $\alpha = 12,5^\circ$



(b) Vue de dessus

Fig. 22 EFFET D'INCIDENCE SUR L'ÉCOULEMENT DE CULOT  
VISUALISATION AU TUNNEL HYDRODYNAMIQUE (d'après [22])

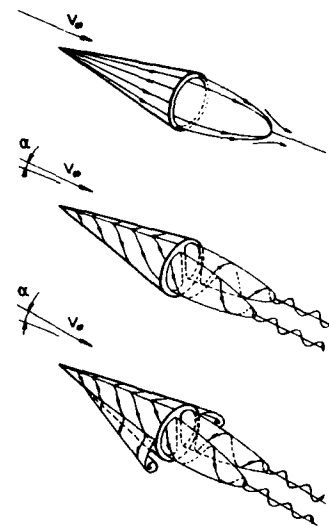
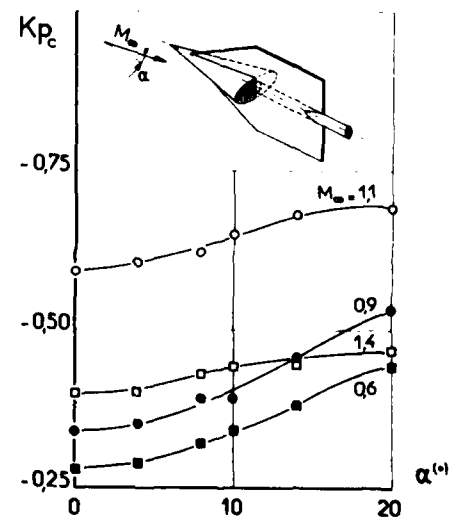


Fig. 23 EFFET D'INCIDENCE  
SUR LA STRUCTURE DE L'ÉCOULEMENT DE CULOT  
EN ÉCOULEMENT SUPERSONIQUE (d'après [ 23 ])

Fig. 24 EFFET D'INCIDENCE SUR LA PRESSION AU CULOT  
D'UN CONE ELLIPTIQUE ( d'après [ 24 ] )





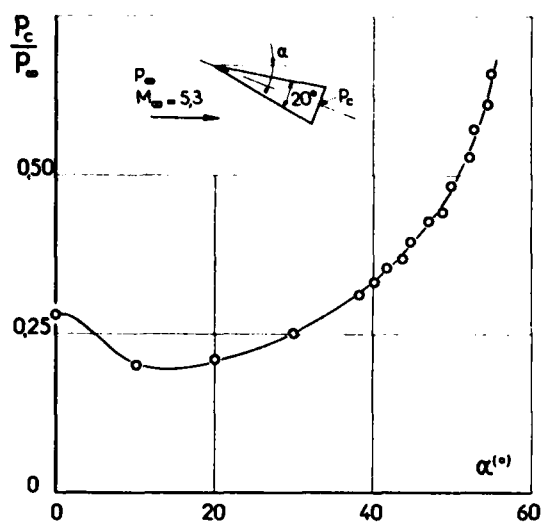


Fig. 25 EFFET D'INCIDENCE SUR LA PRESSION AU CULOT D'UN PROJECTILE CONIQUE ( d'après [ 25 ] )

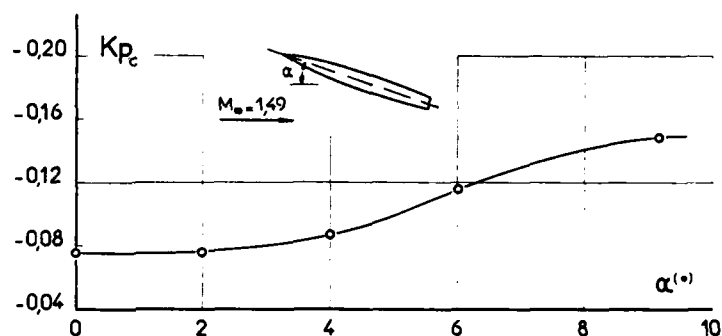


Fig. 26 EFFET D'INCIDENCE SUR LE COEFFICIENT DE PRESSION DE CULOT (maquette RM10. d'après[ 3 ])

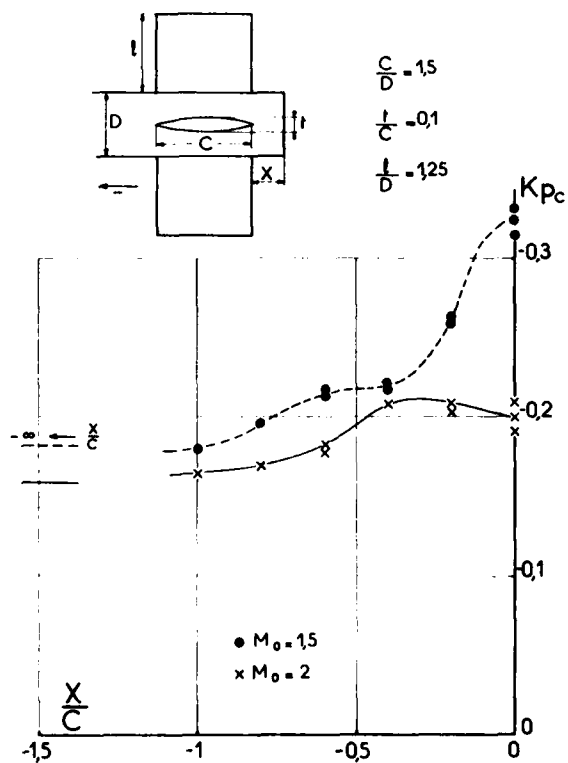


Fig. 27 EFFET D'AILETAGE SUR LE COEFFICIENT DE PRESSION DE CULOT (d'après[ 3 ])

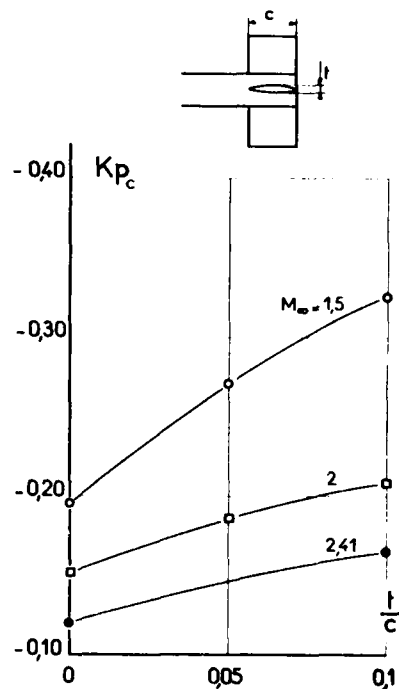


Fig. 28 EFFET D'EPaisseur RELATIVE DES AILETAGES SUR LE COEFFICIENT DE PRESSION DE CULOT (d'après[ 3 ])

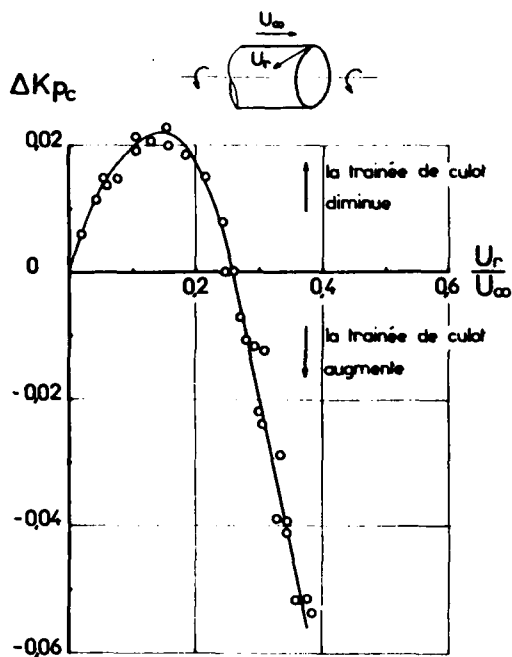


Fig. 29 EFFET DE ROTATION SUR LA PRESSION DE CULOT  
ÉCOULEMENT SUBSONIQUE (d'après [26])

Symbole	$\frac{r_1}{r_2}$
x	0,8
•	0,6
◦	0,4
◻	0,2

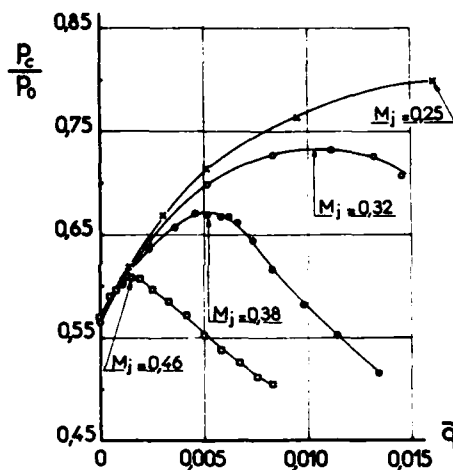
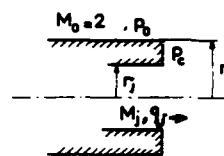


Fig. 30 EFFET DE VENTILATION SUR LA PRESSION DE CULOT  
ÉCOULEMENT EXTERNE SUPERSONIQUE (d'après [27])

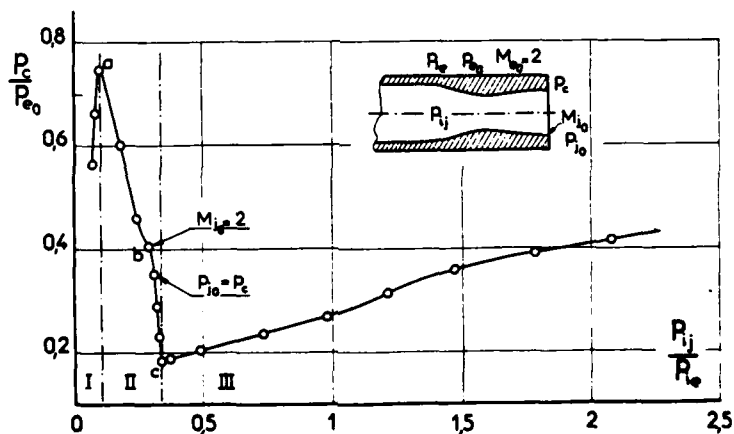


Fig. 31 PRESSION AU CULOT D'UN ARRIERE-CORPS ÉQUIPÉ D'UNE TUYÈRE  
EN ÉCOULEMENT SUPERSONIQUE (d'après [27])

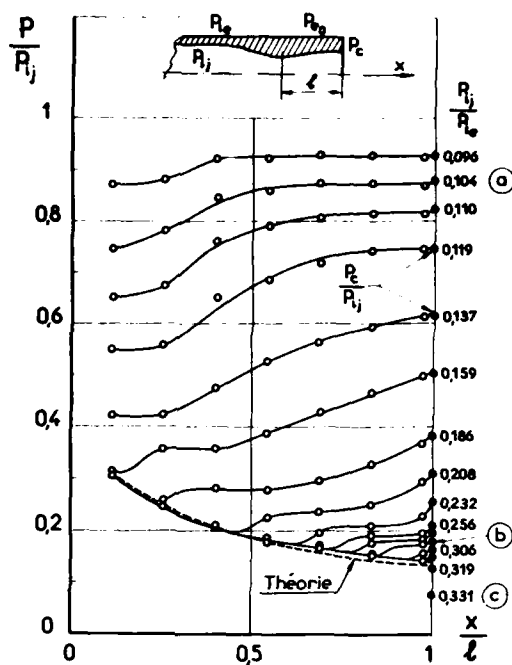


Fig. 32 REPARTITIONS DE PRESSION DANS LA TUYERE  
( essais de la fig. 31 - d'après [ 27 ] )

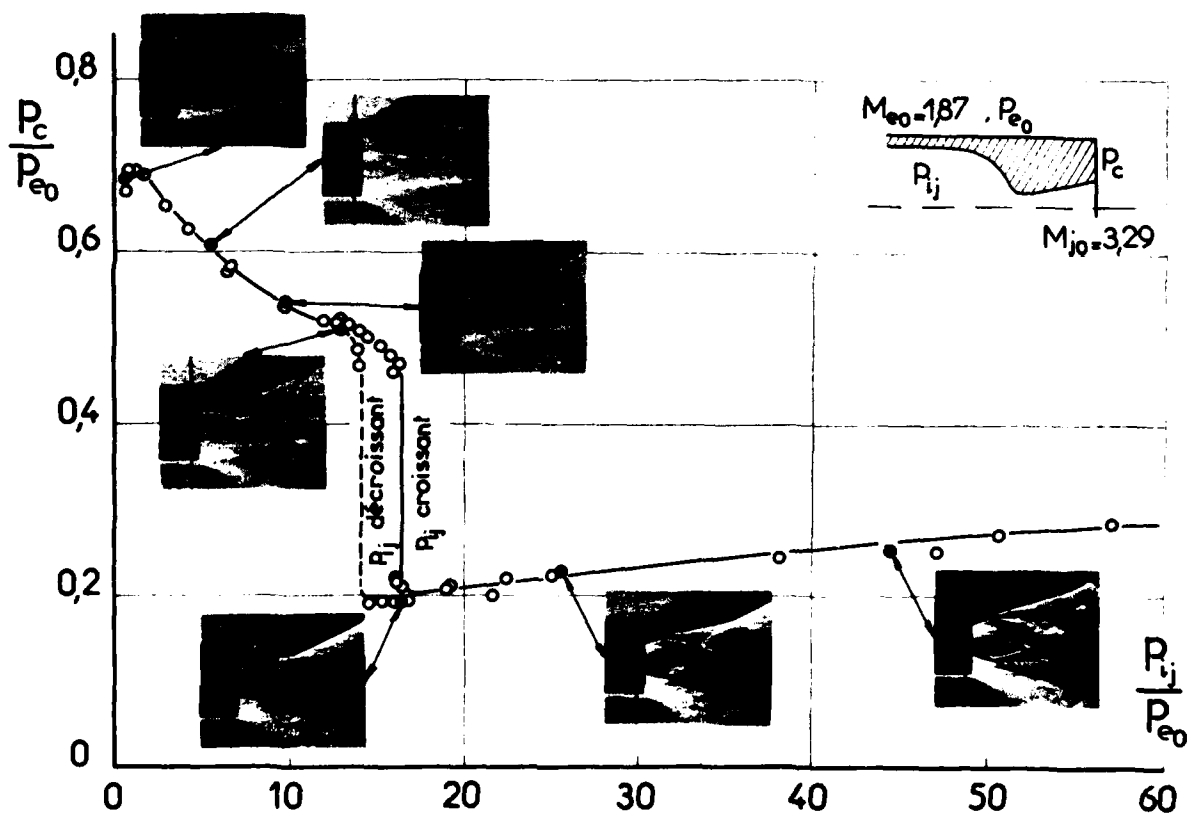


Fig. 33 EVOLUTION DE LA PRESSION DE CULOT EN FONCTION DU RAPPORT  
DE DETENTE DE LA TUYERE (résultats ONERA [28])

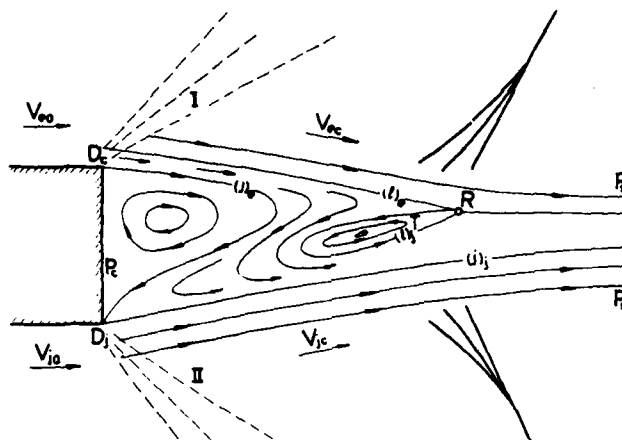
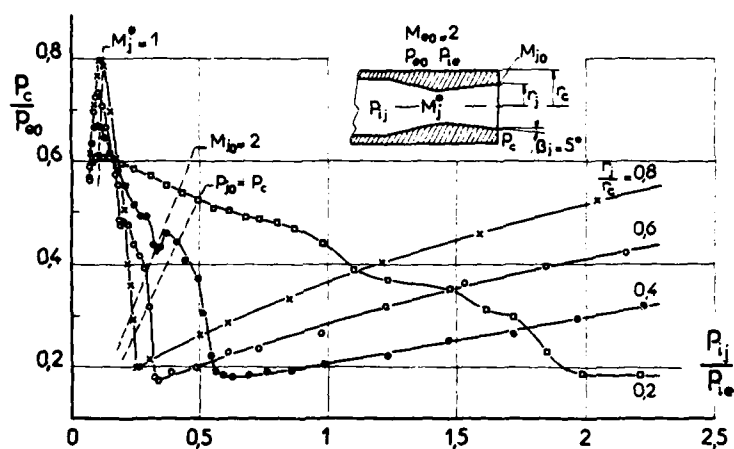
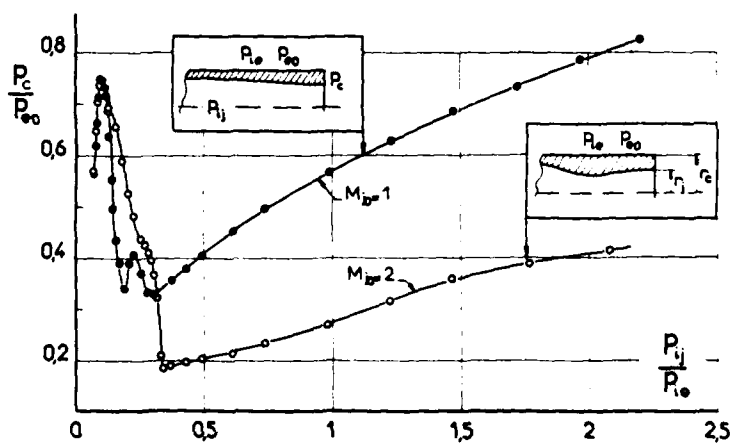


Fig. 34 SCHEMATISATION DE LA CONFLUENCE EN AVAL D'UN CULOT

Fig. 35 EFFET DES DIMENSIONS DE LA TUYERE  
SUR LA PRESSION DE CULOT (d'après [27])Fig. 36 EFFET DU NOMBRE DE MACH DE LA TUYERE  
SUR LA PRESSION DE CULOT (d'après [27])

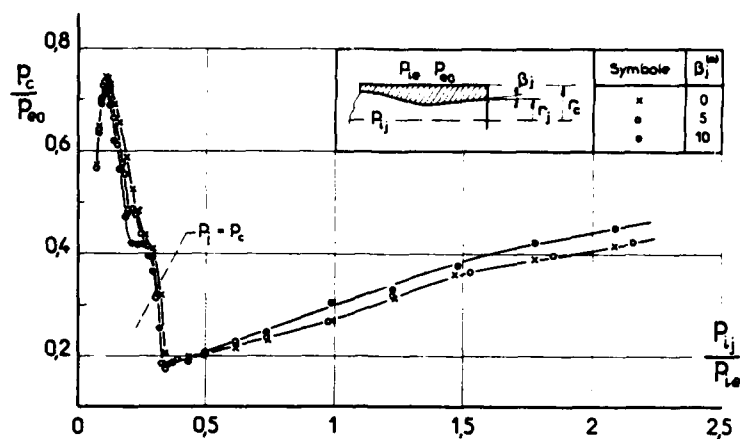


Fig. 37 EFFET DE L'ANGLE DE DIVERGENCE DE LA TUYERE SUR LA PRESSION DE CULOT (d'après [27])

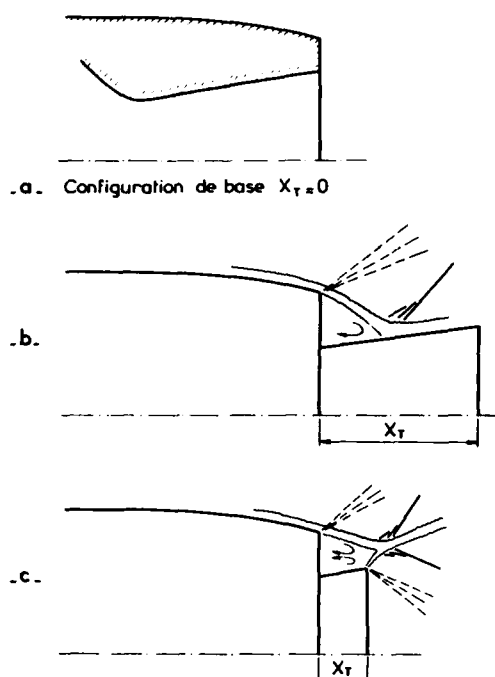


Fig. 38 EFFET D'EMERGENCE DE LA TUYERE

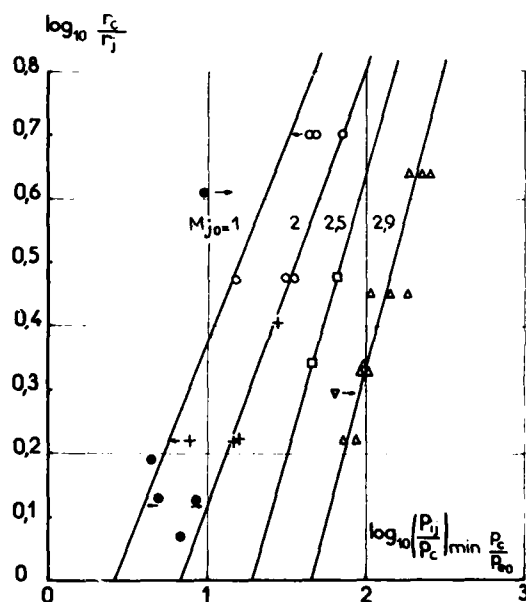


Fig. 39 CORRELATION POUR LA VALEUR MINIMALE DU RAPPORT  $P_c/P_{00}$  (d'après [30])

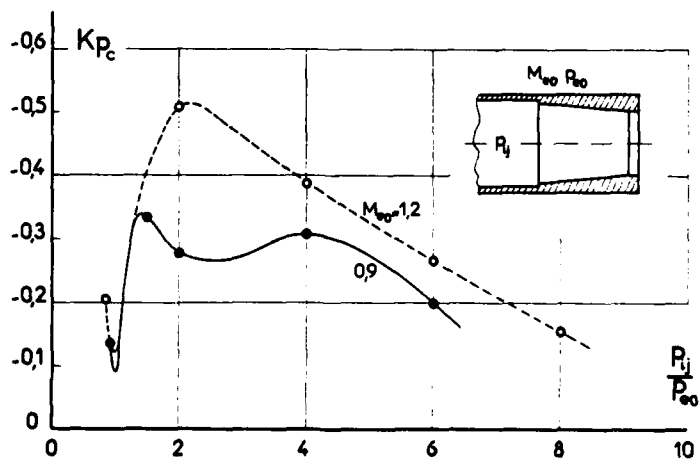


Fig. 40 PRESSION DE CULOT EN PRESENCE D'UNE TUYERE SONIQUE ECOULEMENT EXTERNE SUBSONIQUE ET SUPERSONIQUE (d'après [31])

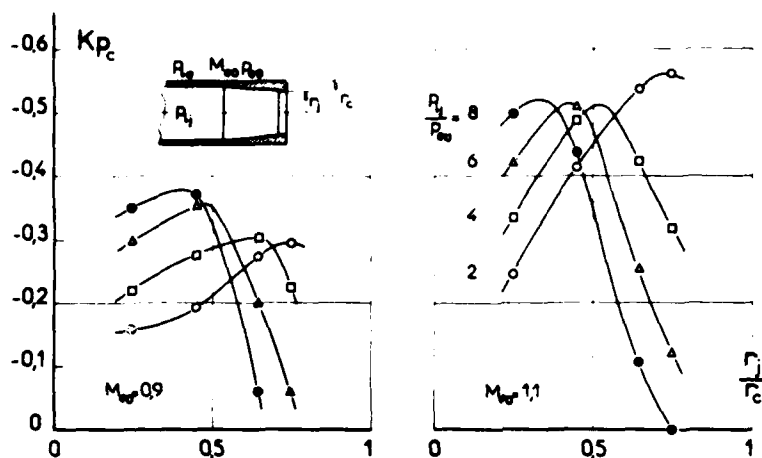


Fig. 41 EFFET DU RAYON DE LA TUYERE SUR LA PRESSION DE CULOT EN ECOULEMENT TRANSSONIQUE (d'après [31])

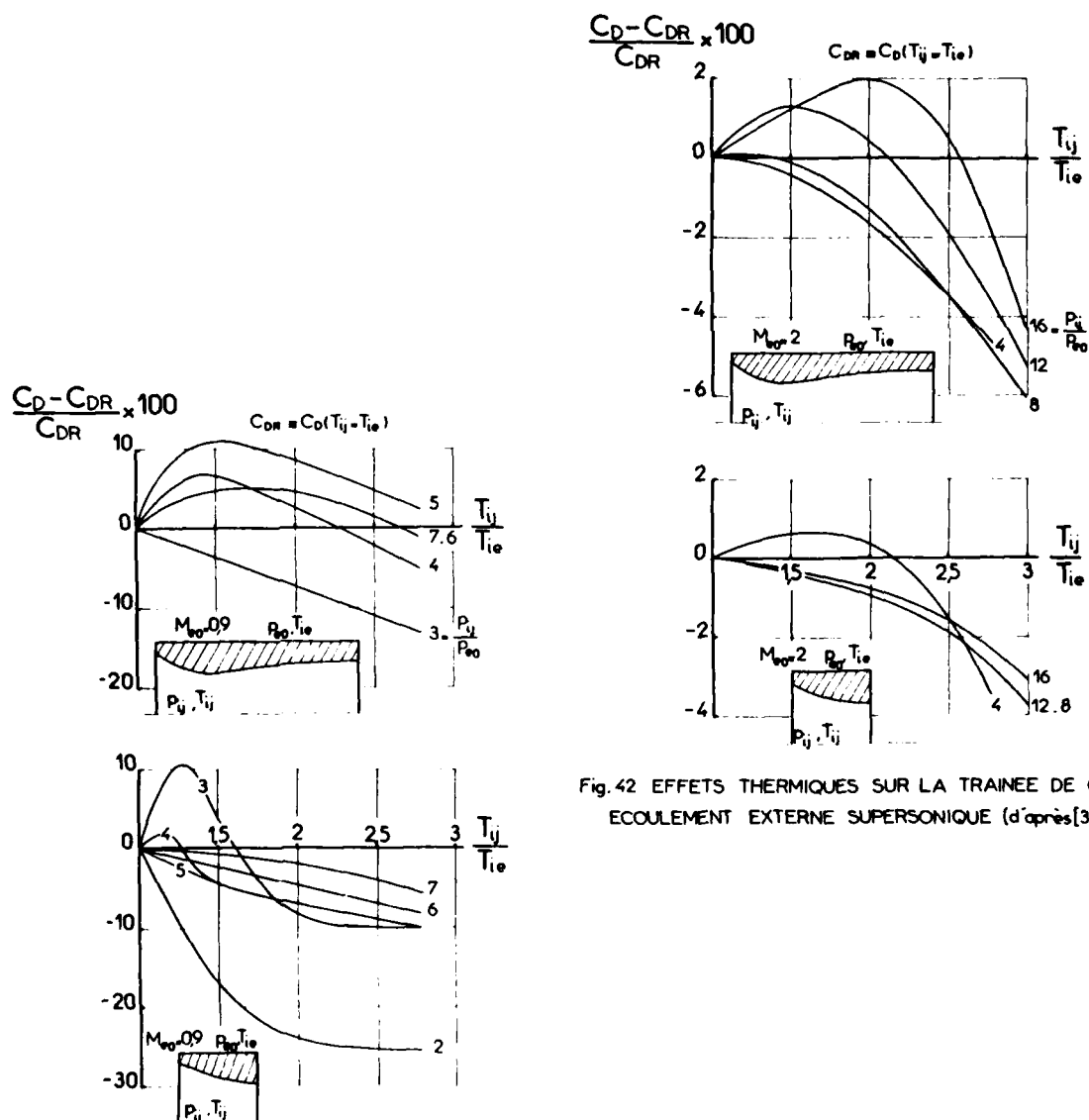


Fig. 42 EFFETS THERMIQUES SUR LA TRAINEE DE CULOT ECOULEMENT EXTERNE SUPERSONIQUE (d'après [32])

Fig. 43 EFFETS THERMIQUES SUR LA TRAINEE DE CULOT ECOULEMENT EXTERNE SUBSONIQUE (d'après [32])

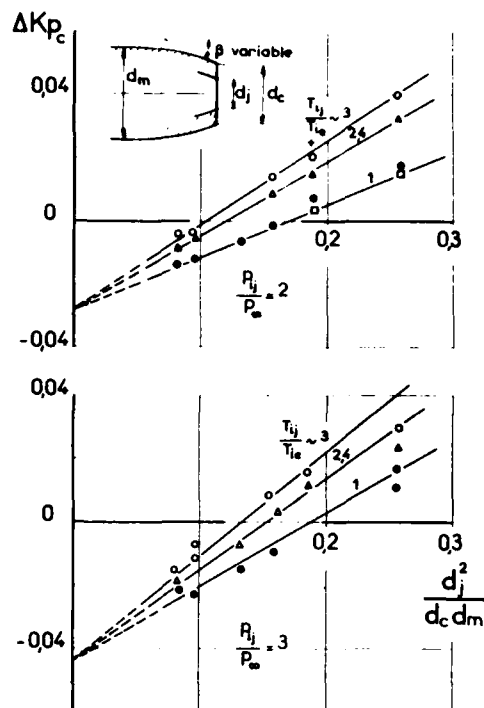


Fig. 44  
EFFET DE TEMPERATURE SUR LA PRESSION DE CULOT  
ECOULEMENT EXTERNE SUBSONIQUE ( d'après [21] )

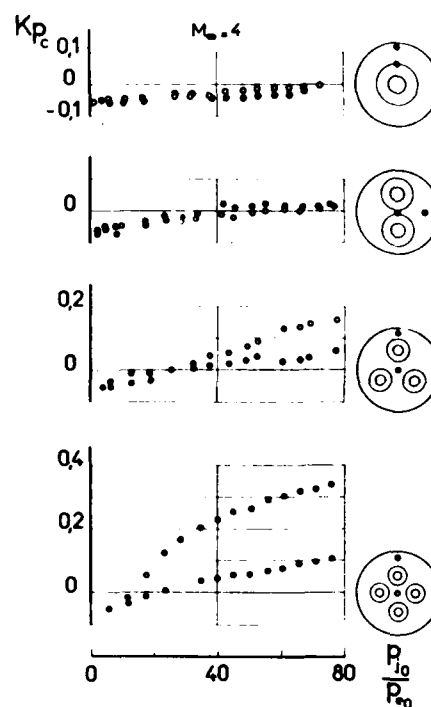


Fig. 45 CONFIGURATIONS MULTITUYERES  
COEFFICIENT DE PRESSION EN  
FONCTION DU RAPPORT DE DETENTE ( d'après [33] )

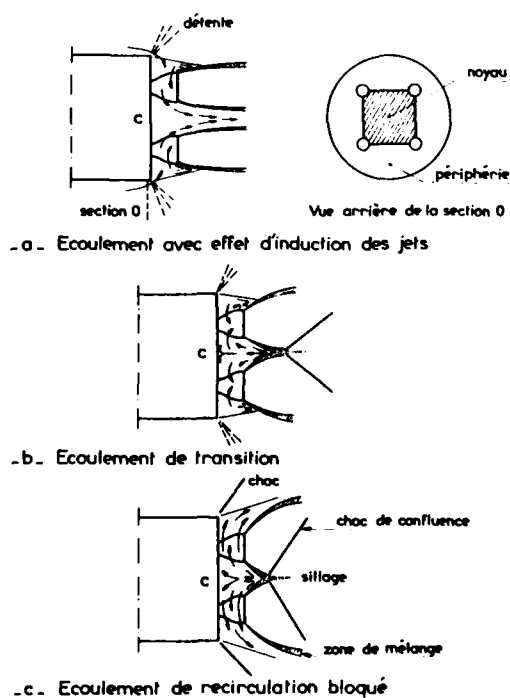


Fig. 46 STRUCTURE DE L'ECOULEMENT AU CULOT  
D'UN MISSILE QUADRTUYERES

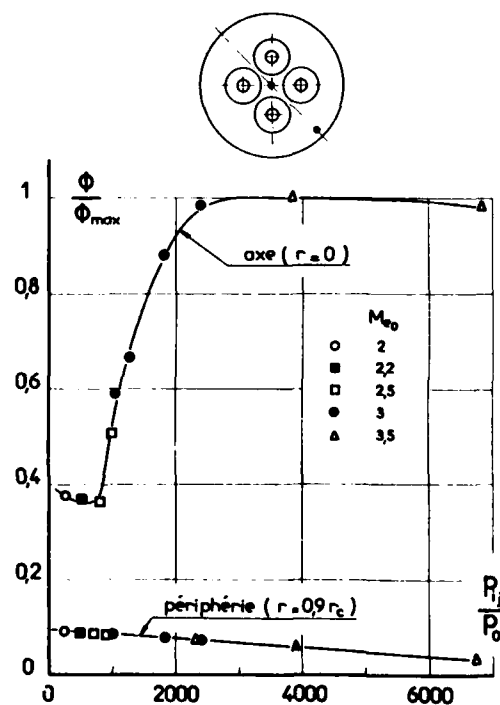


Fig. 47 EFFET DU RAPPORT DE DETENTE DES JETS  
SUR LE FLUX DE CHALEUR AU CULOT ( d'après [35] )

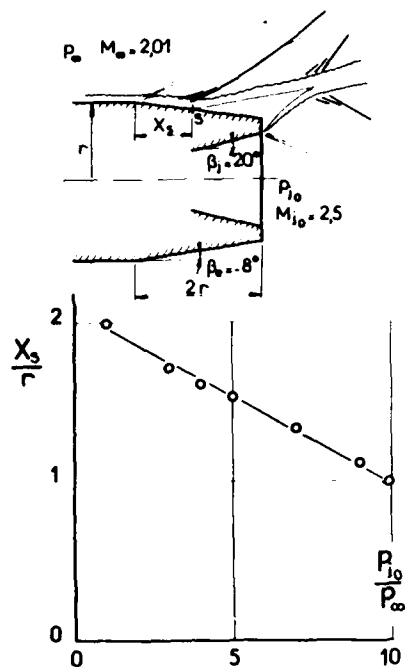
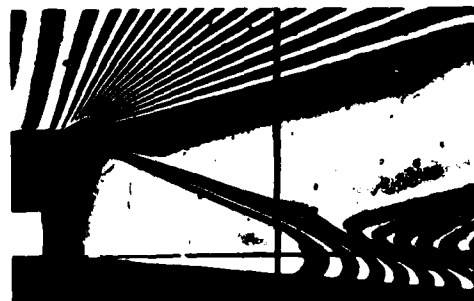


Fig. 48 DECOLLEMENT SUR UN ARRIERE-CORPS PAR EFFET D'ECLATEMENT DU JET INTERNE (d'après [36])



a - Interférogramme



b - Strioscopie continue ( $t = 0,02$  s)



c - Strioscopie "éclair" ( $t = 1 \mu s$ )  
(communiqué par I.S. DONALDSON)

Fig. 50 - VISUALISATIONS DU RECOLLEMENT TURBULENT EN AVAL D'UNE MARCHE

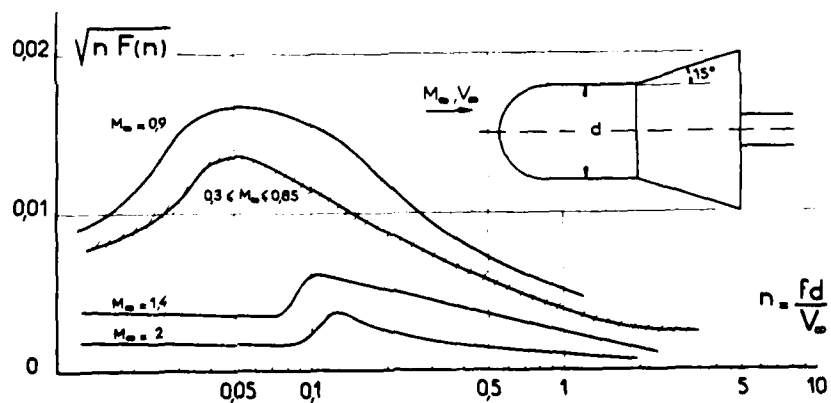


Fig. 49 SPECTRE DES FLUCTUATIONS DE LA PRESSION DE CULOT (d'après [38])



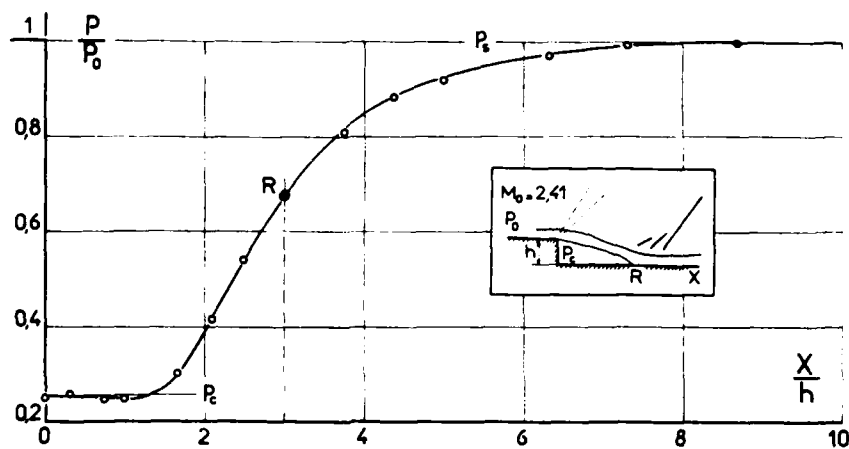


Fig. 51 - RECOLLEMENT TURBULENT EN AVAL D'UNE MARCHÉ  
DISTRIBUTION PARIETALE DES PRESSIONS

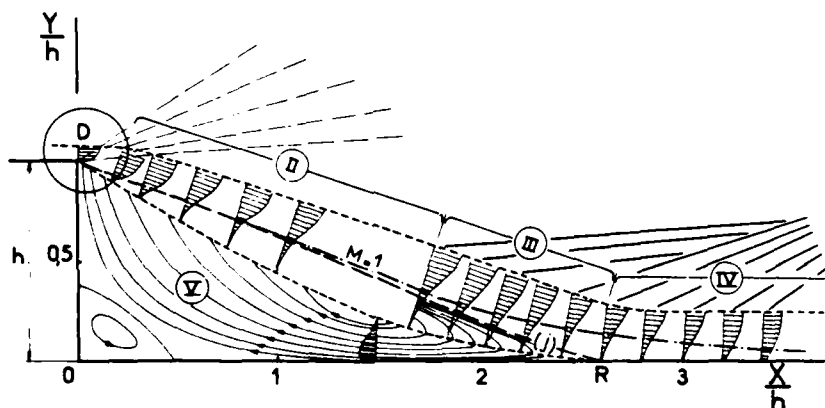


Fig. 52 - RECOLLEMENT TURBULENT SUPERSONIQUE EN AVAL D'UNE MARCHÉ

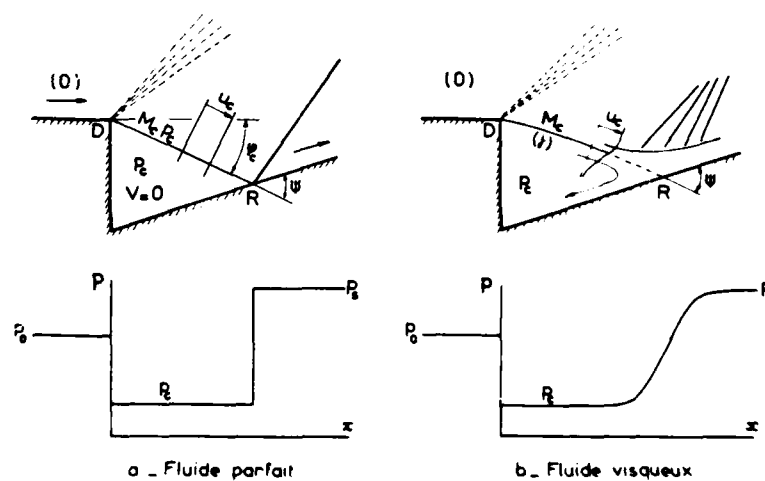


Fig. 53 - SCHEMATISATION DE L'ÉCOULEMENT EN AVAL D'UNE MARCHÉ

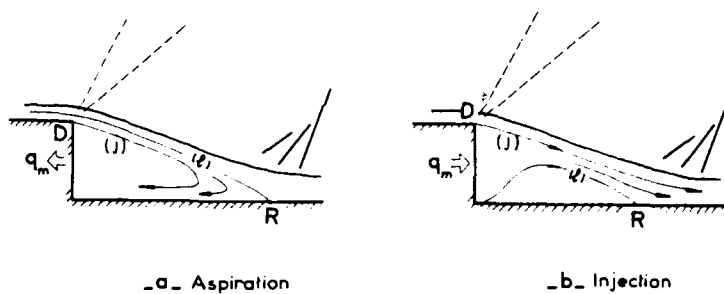


Fig. 54 - LIGNE DE COURANT LIMITE

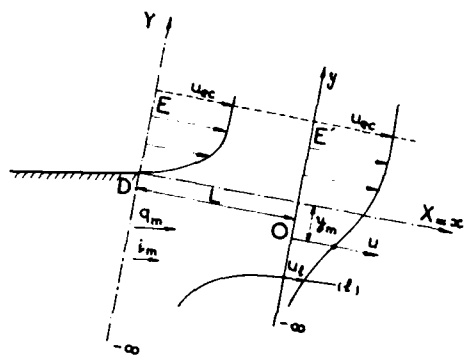
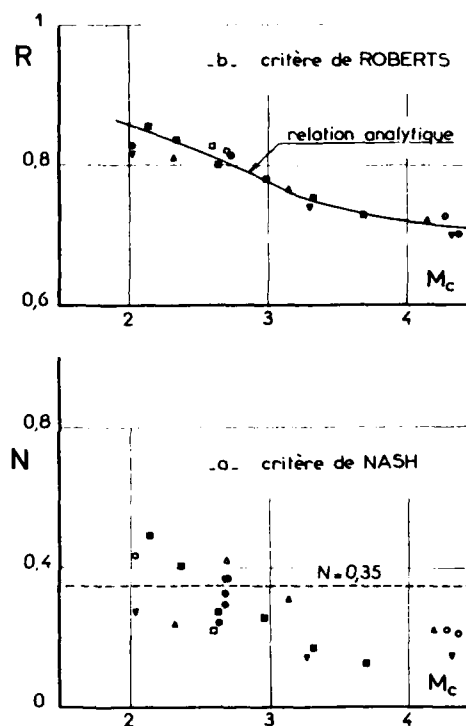
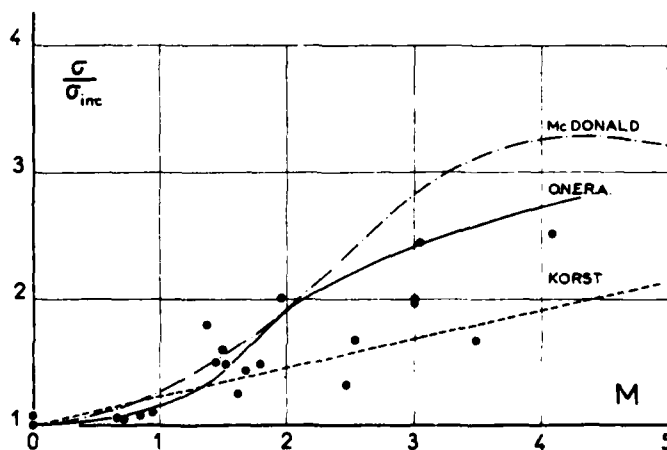
Fig. 55 - MISE EN PLACE DE LA LIGNE LIMITE  
DU MELANGE ISOBAREFig. 56 - CRITERES DE RECOLLEMENT DE NASH  
ET DE ROBERTS

Fig. 57 - EFFET DE COMPRESSIBILITE SUR LE PARAMETRE DE MELANGE TURBULENT

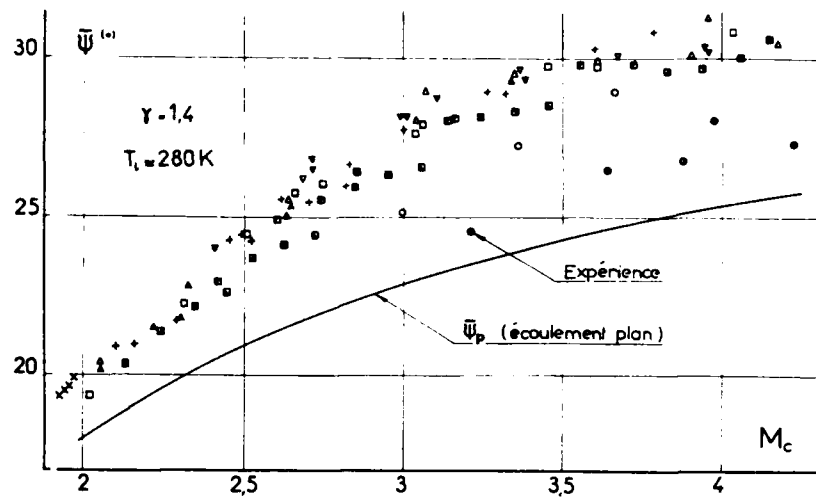
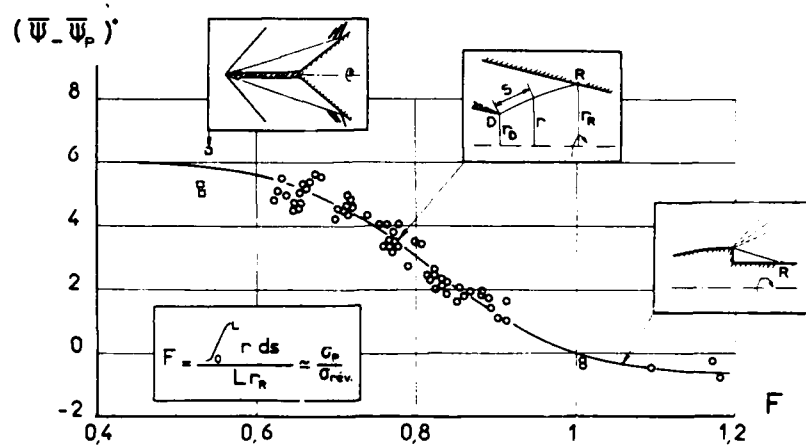
Fig. 58 - EFFET DE REVOLUTION SUR L'ANGLE DE RECOLLEMENT  $\Psi$ 

Fig 59 - LOI ANGULAIRE DE RECOLLEMENT GENERALISEE

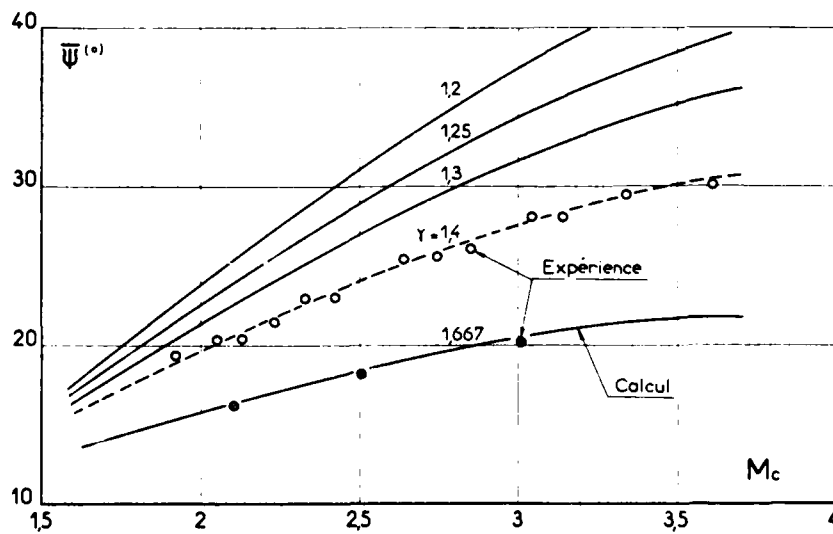
Fig 60 - EFFET DE  $\gamma$  SUR L'ANGLE DE RECOLLEMENT (écoulement de révolution)

Fig 61- GENERALISATION  
DE LA NOTION D'ANGLE DE RECOLLEMENT

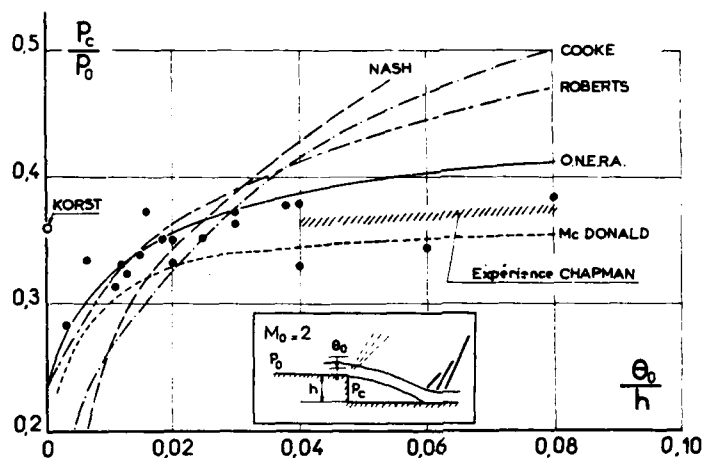
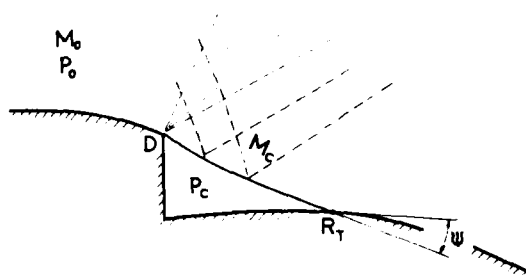


Fig. 62.-CALCUL DE LA PRESSION DE CULOT EN ECOULEMENT PLAN  $M_0=2$

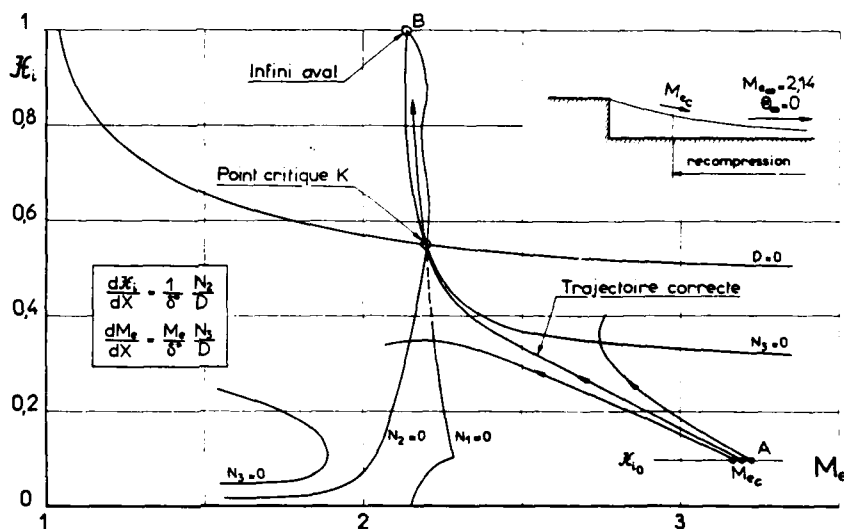


Fig. 63.-METHODE INTEGRALE  
TRAJECTOIRE DE LA SOLUTION DANS LE PLAN DE PHASE

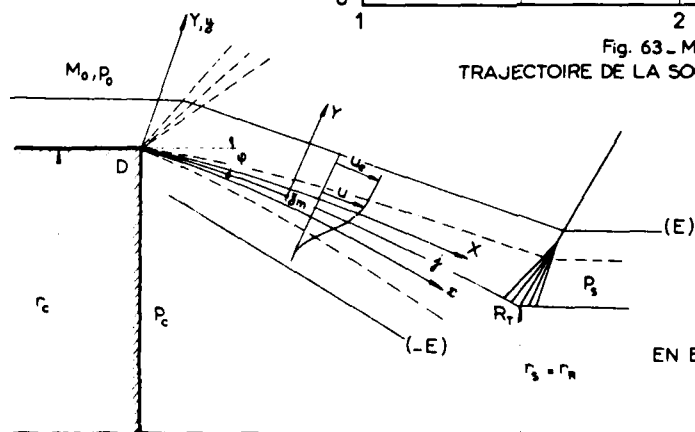


Fig. 64.-PRESSION DE CULOT  
EN ECOULEMENT SUPERSONIQUE DE REVOLUTION  
MODELE DE MUELLER

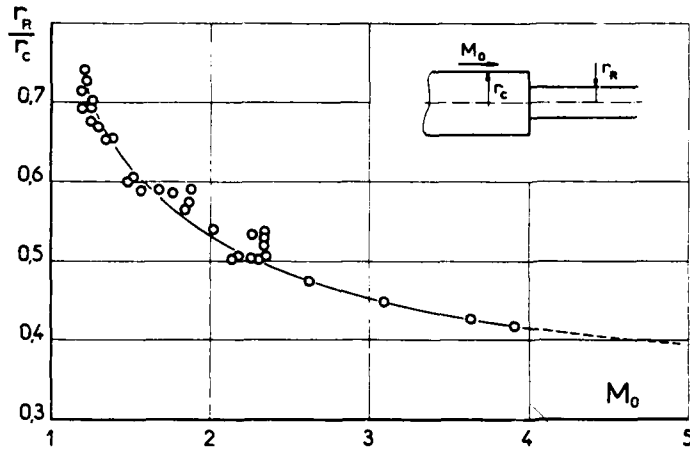


Fig. 65 - RAYON DU DARD FICTIF AU CULOT  
( d'après CHAPMAN [2] )

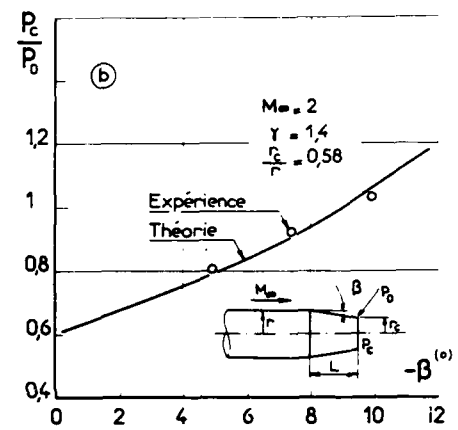
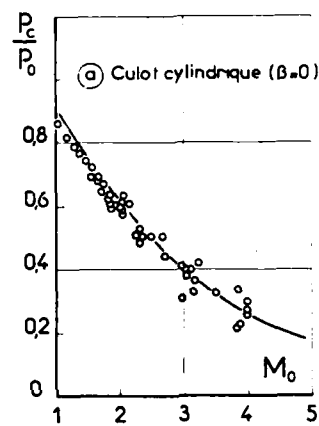


Fig. 66 - COMPARAISON CALCUL EXPERIENCE - THEORIE de MUELLER

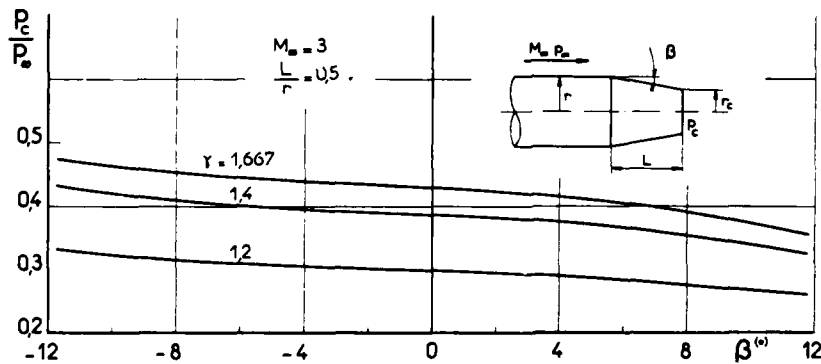


Fig. 67 - EFFET DE  $\gamma$  SUR LA PRESSION DE CULOT - THEORIE de MUELLER

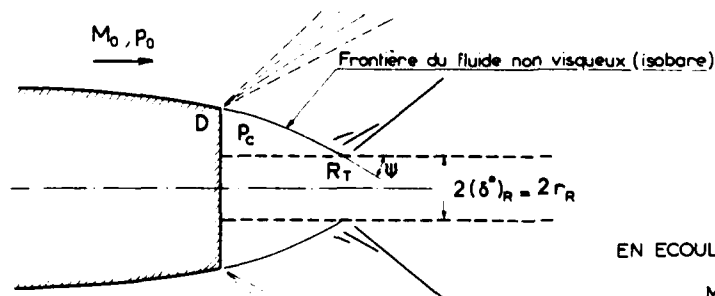


Fig. 68 - PRESSION DE CULOT  
EN ECOULEMENT SUPERSONIQUE DE REVOLUTION  
MODELE DE SIRIEIX ET DELERY

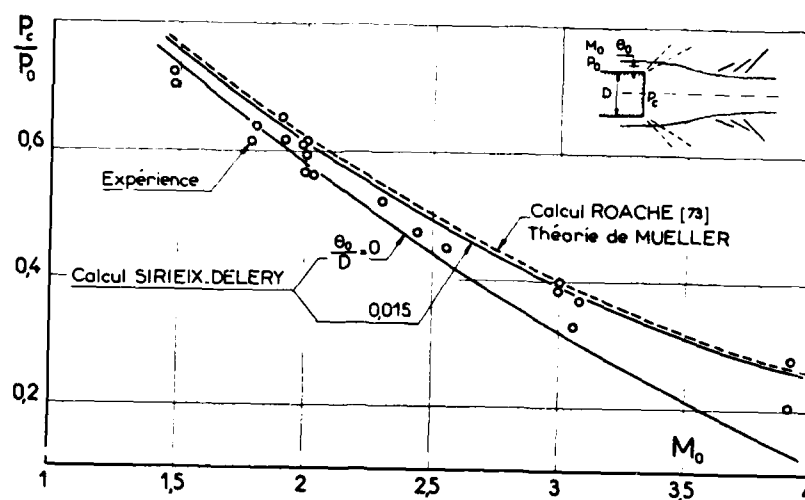


Fig. 69 - COMPARAISON CALCUL-EXPERIENCE  
THEORIES de SIRIEIX DELERY et de MUELLER

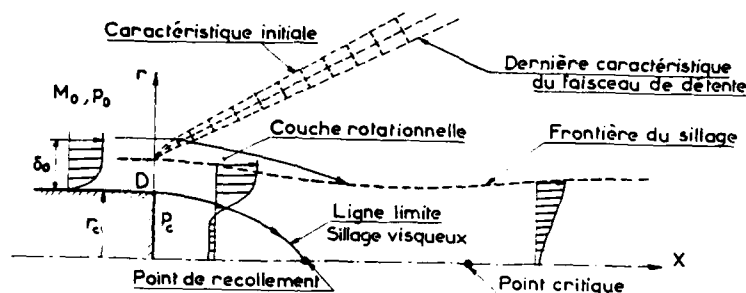


Fig. 70 - PRESSION DE CULOT EN ECOULEMENT SUPERSONIQUE DE REVOLUTION  
MODELE DE MEHTA

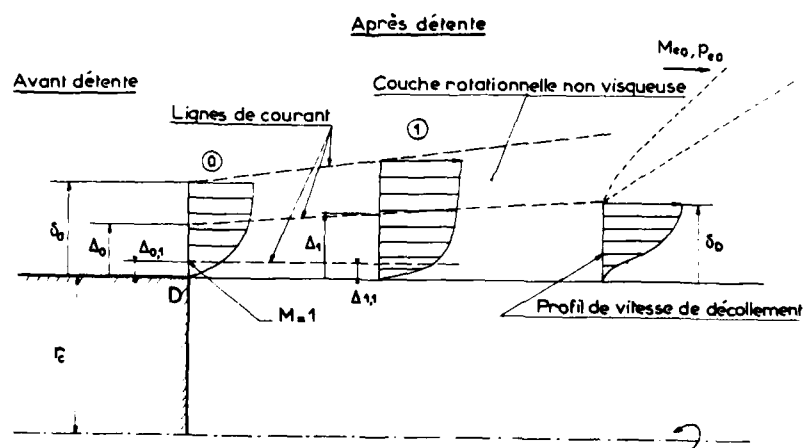


Fig. 71 - DETENTE DE LA COUCHE LIMITE INITIALE  
MODELE de MEHTA

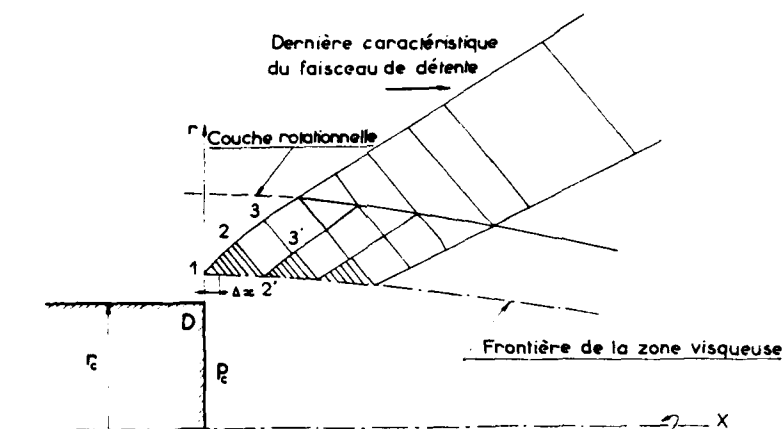
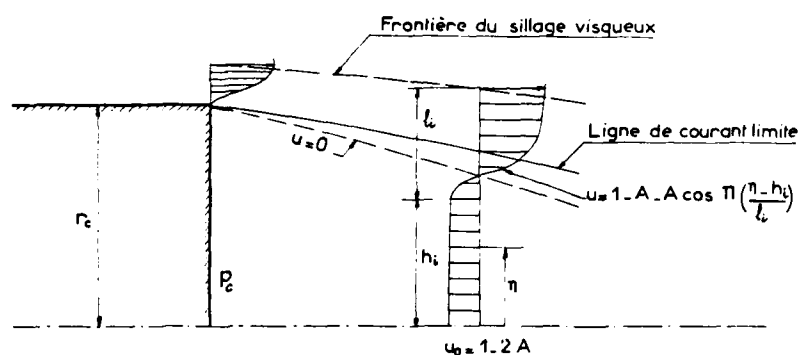
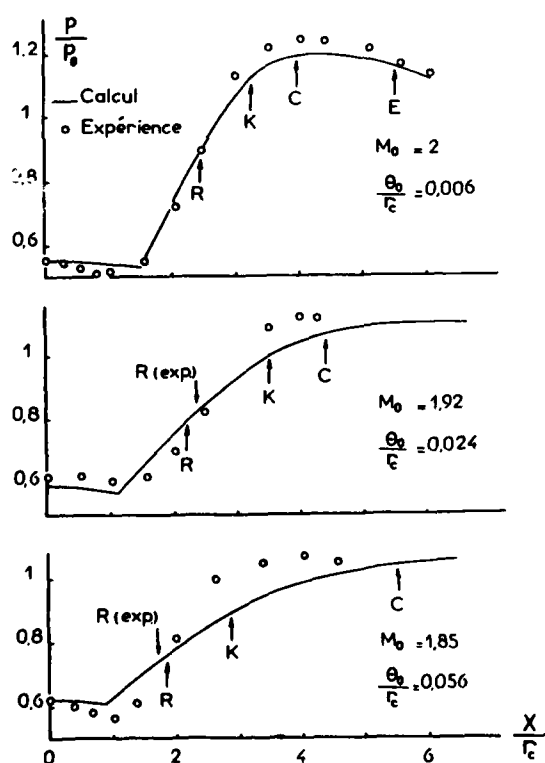
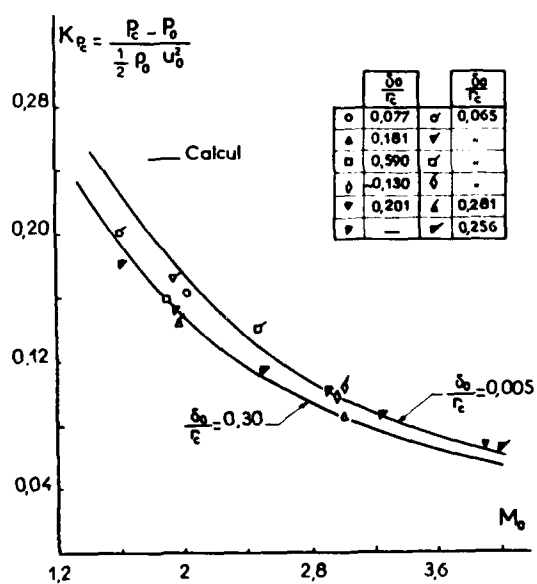


Fig. 72 - METHODE DES CARACTERISTIQUES APPROCHEE de MEHTA

Fig. 73 - PROFILS DE VITESSE PRES DU CULOT  
Famille à 2 paramètres de GREENFig. 74 - REPARTITION DE PRESSION SUR L'AXE DU SILLAGE  
(THEORIE de MEHTA)Fig. 75 - EFFET DU NOMBRE DE MACH AMONT  
SUR LA PRESSION DE CULOT  
(THEORIE de MEHTA)

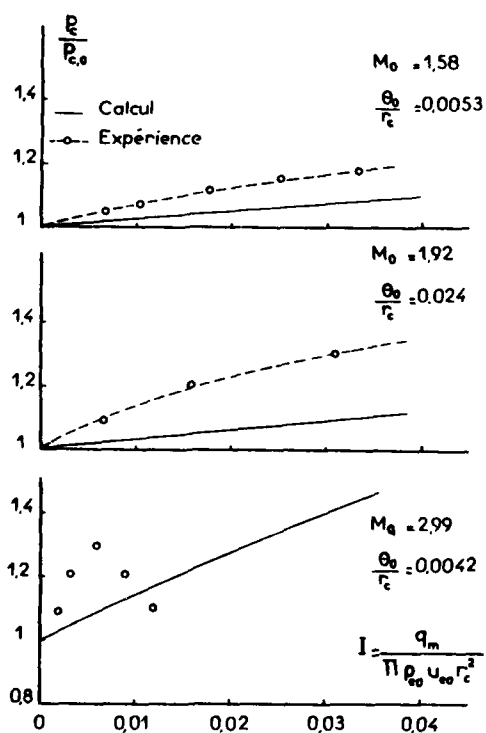


Fig. 76 - EFFET D'INJECTION DE MASSE AU CULOT  
(THEORIE de MEHTA)

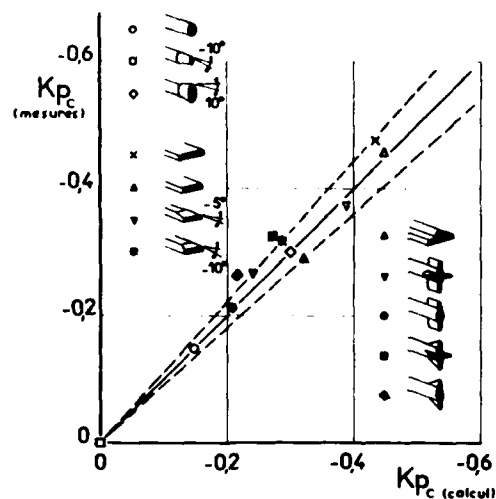


Fig. 77 - PRESSION DE CULOT EN ECOULEMENT SUBSONIQUE  
TRIDIMENSIONNEL - THEORIE de BUTSKO [86]

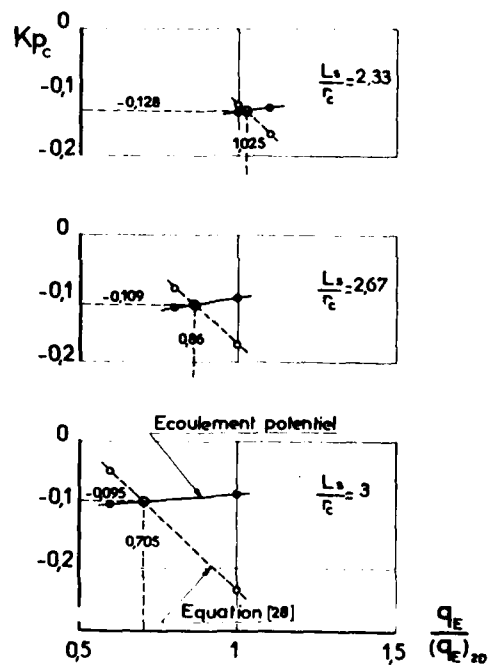


Fig. 79 - DETERMINATION DU DEBIT  $q_e$   
(THEORIE de VANWAGENEN)

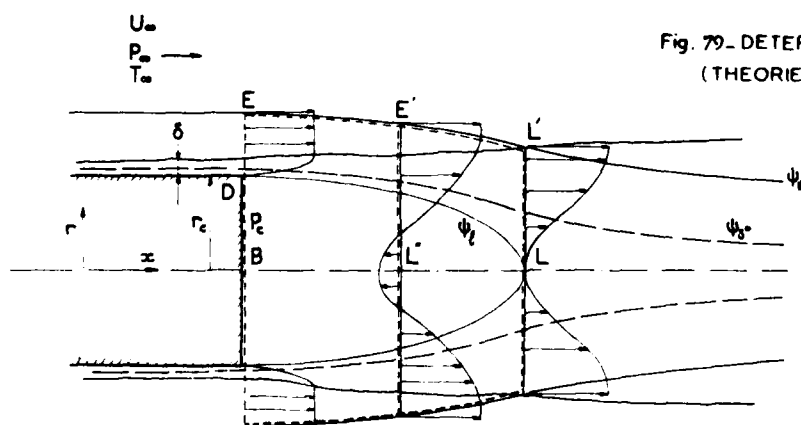


Fig. 78 - PRESSION DE CULOT EN ECOULEMENT SUBSONIQUE DE REVOLUTION  
MODELE de VANWAGENEN



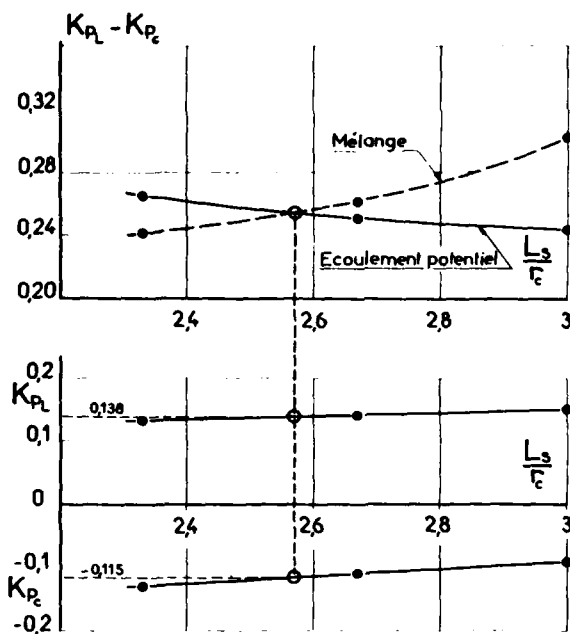


Fig. 80 DETERMINATION DE LA LONGUEUR DU DECOLLEMENT (THEORIE de VANWAGENEN)

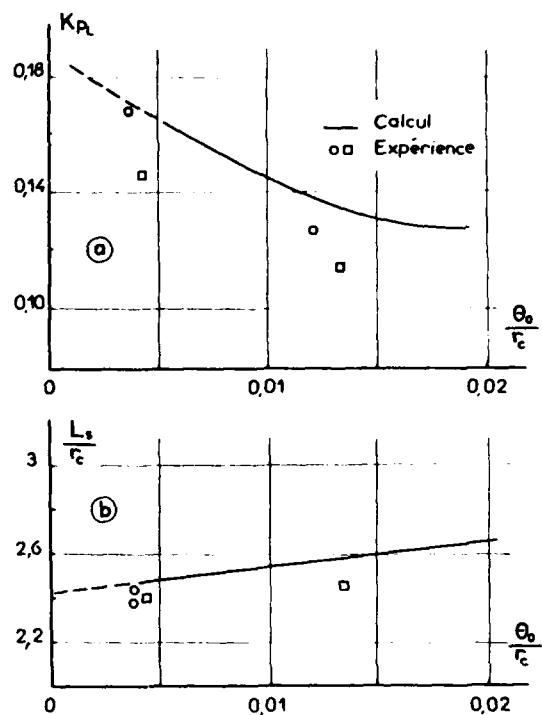


Fig. 82 COEFFICIENT DE PRESSION AU RECOLLEMENT ET LONGUEUR DE CAVITE (THEORIE de VANWAGENEN)

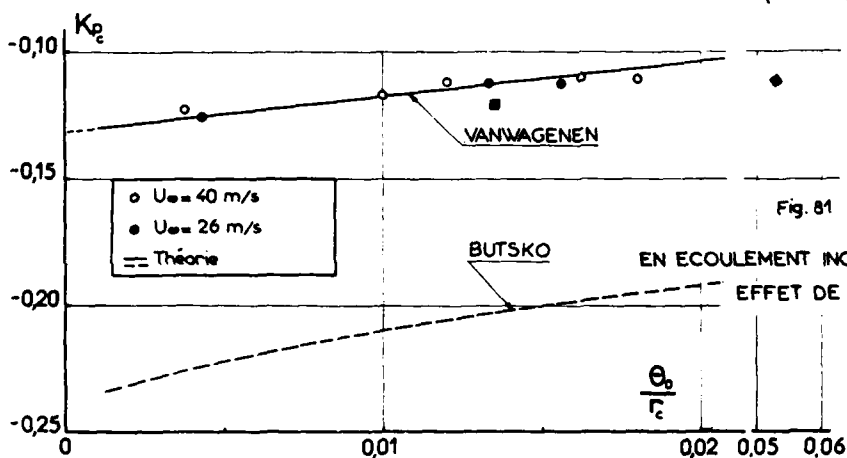


Fig. 81 PRESSION DE CULOT

EN ECOULEMENT INCOMPRESSIBLE DE REVOLUTION  
EFFET DE COUCHE LIMITE INITIALE

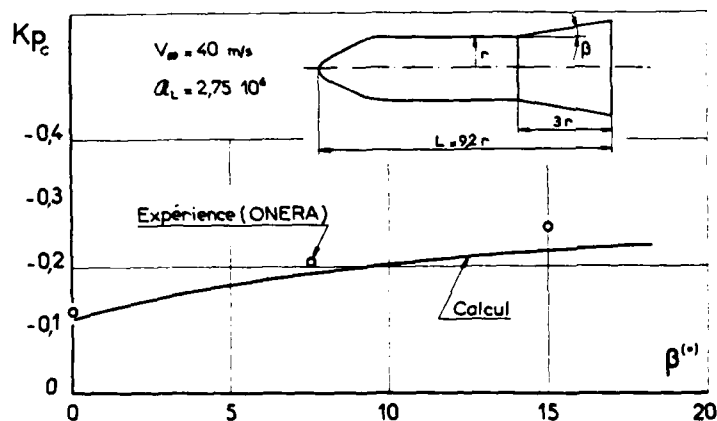


Fig. 83 PRESSION DE CULOT EN ECOULEMENT INCOMPRESSIBLE DE REVOLUTION  
EFFET D'UNE JUPE (THEORIE de VANWAGENEN ADAPTEE par CHAMPIGNY)

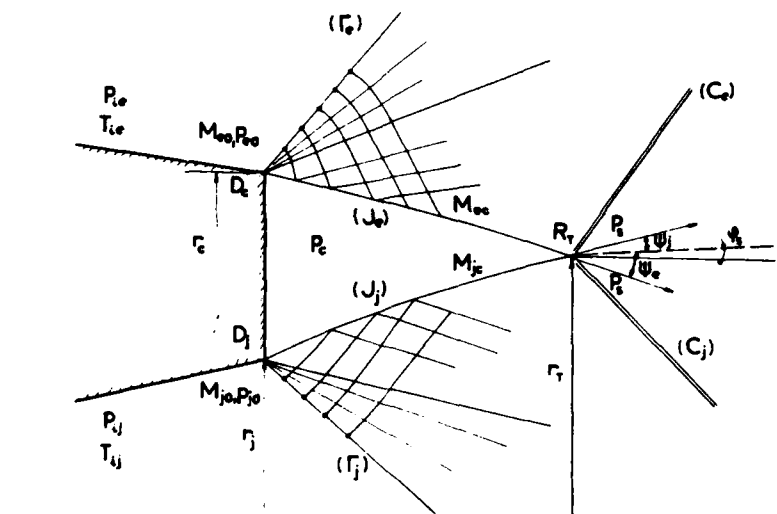
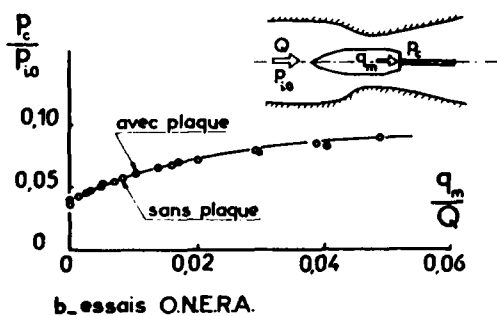
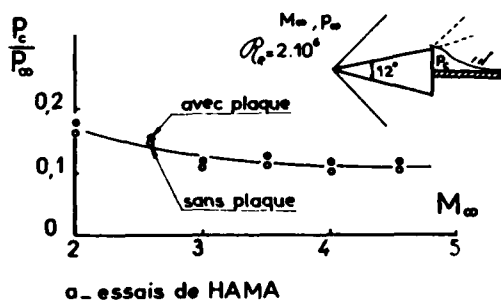
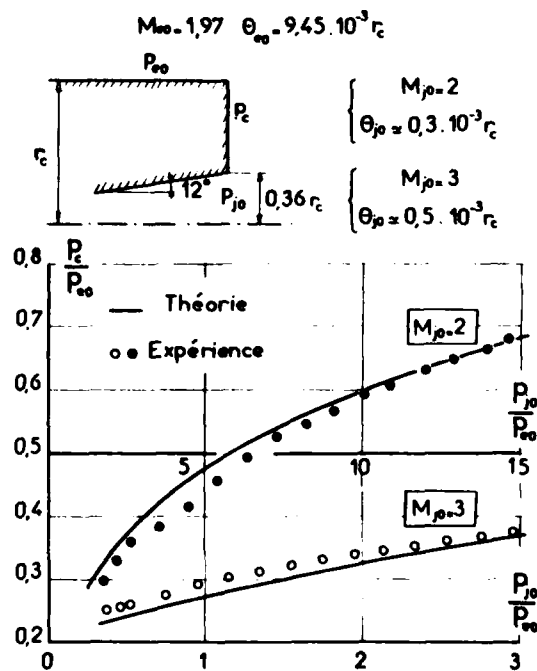
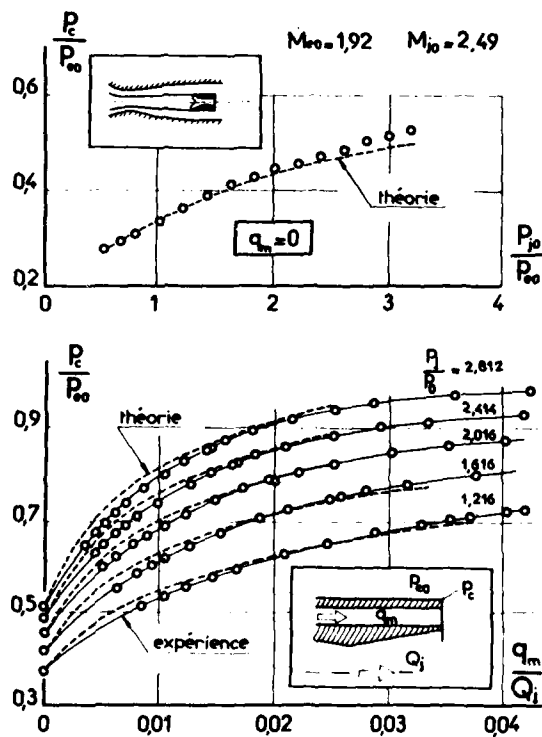
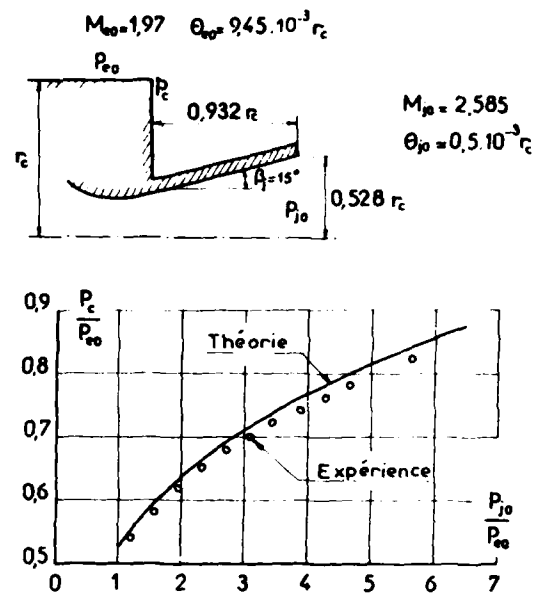
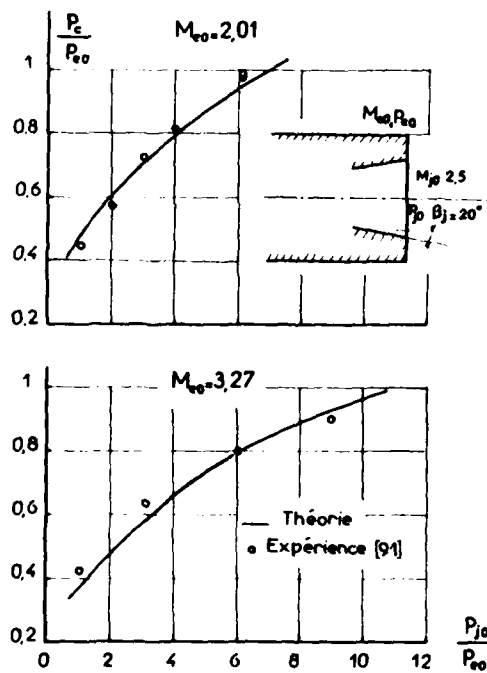


Fig. 84 CONFLUENCE EN AVAL D'UN CULOT - ECOULEMENTS DE FLUIDE PARFAIT

Fig. 85 RECOLLEMENT SUR PAROI  
ET RECOLLEMENT SUR UNE NAPPE FLUIDE



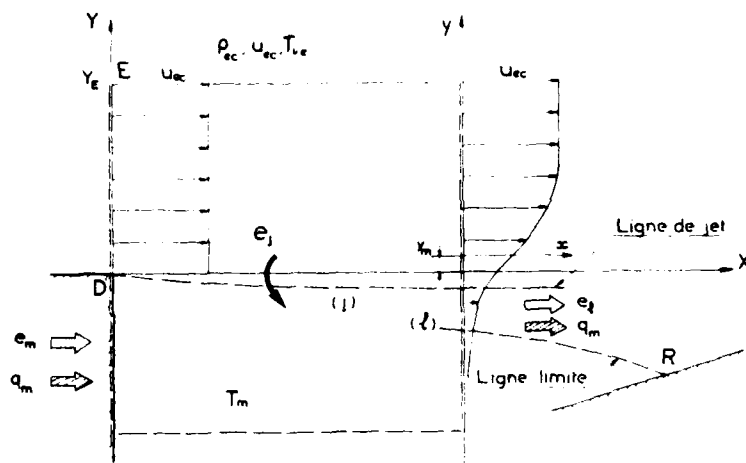


Fig. 90 MELANGE TURBULENT ISOBARE BIDIMENSIONNEL  
MODELE de KORST

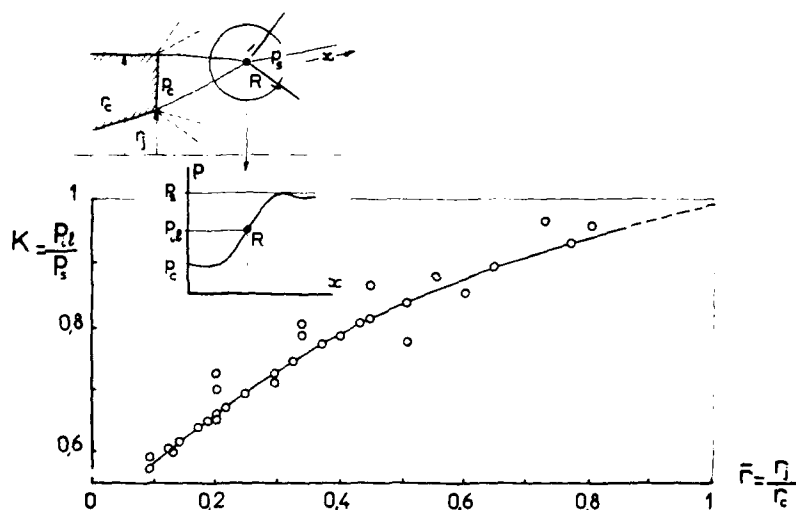


Fig. 91 MODIFICATION DU CRITERE DE KORST EN ECOULEMENT DE REVOLUTION  
(ADDY [92])

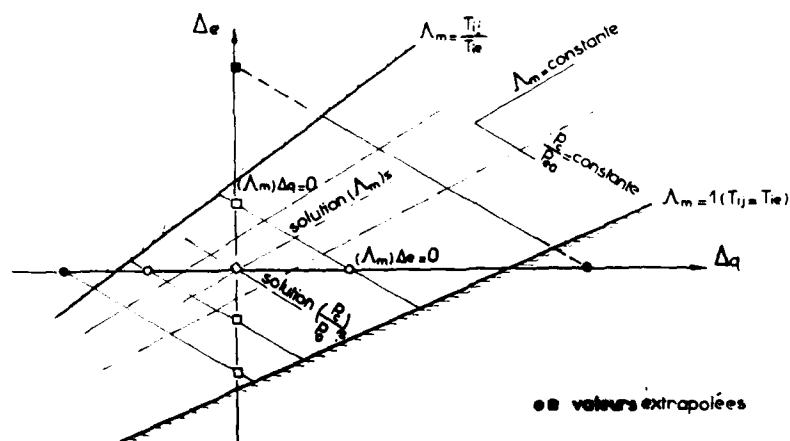


Fig. 92 RECHERCHE DE LA SOLUTION POUR LA PRESSION  
ET LA TEMPERATURE DE L'ECOULEMENT MIXE ISOENERGETIQUE  
(d'ADDY)

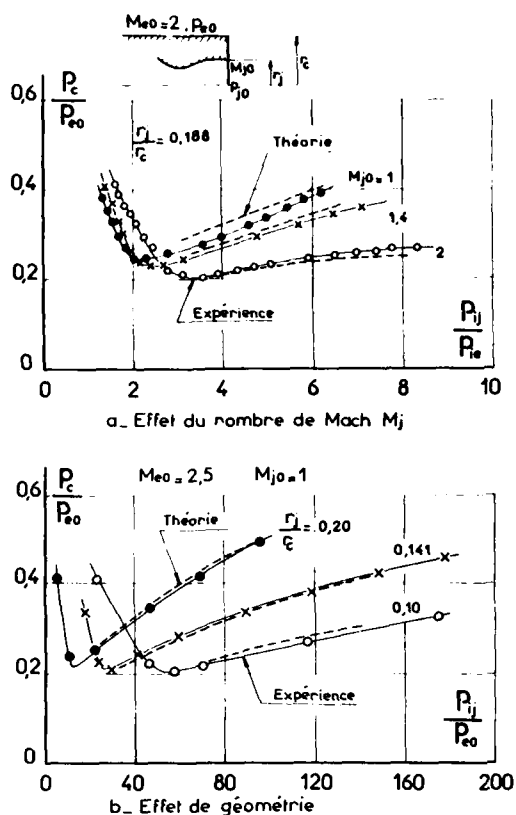
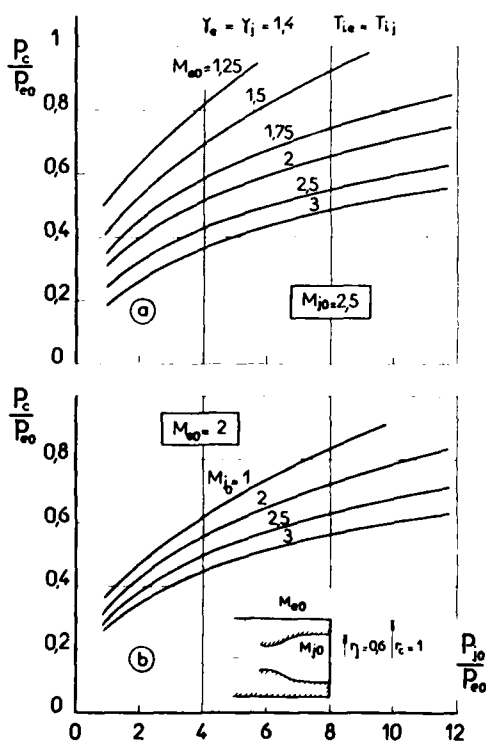
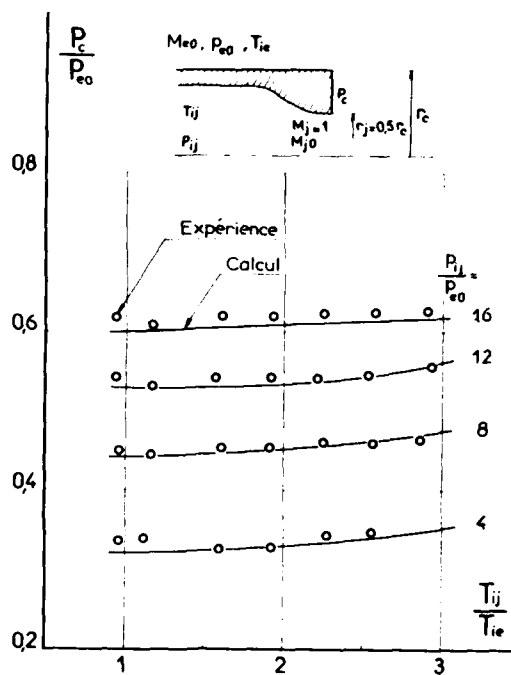
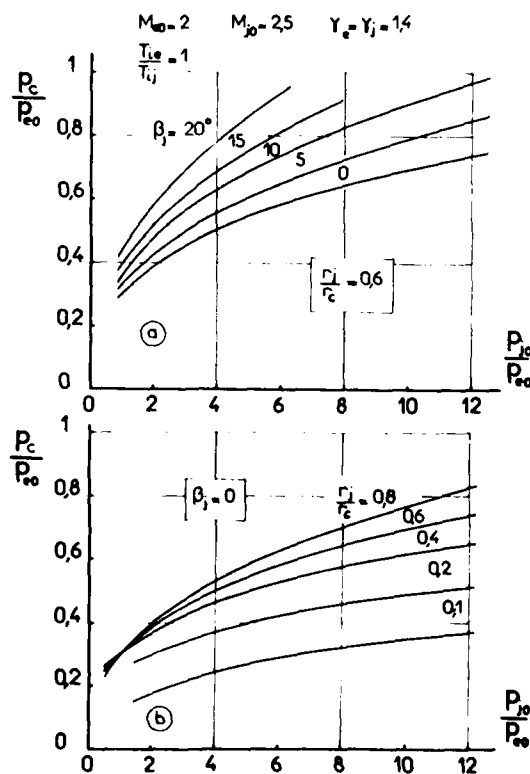
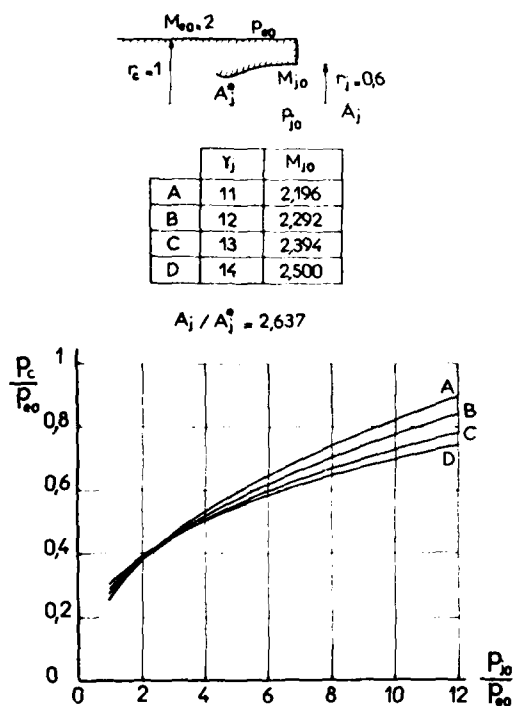
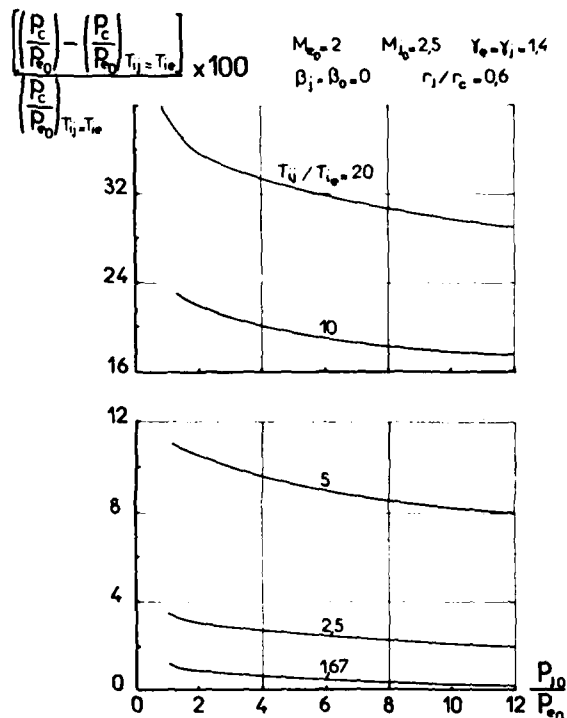
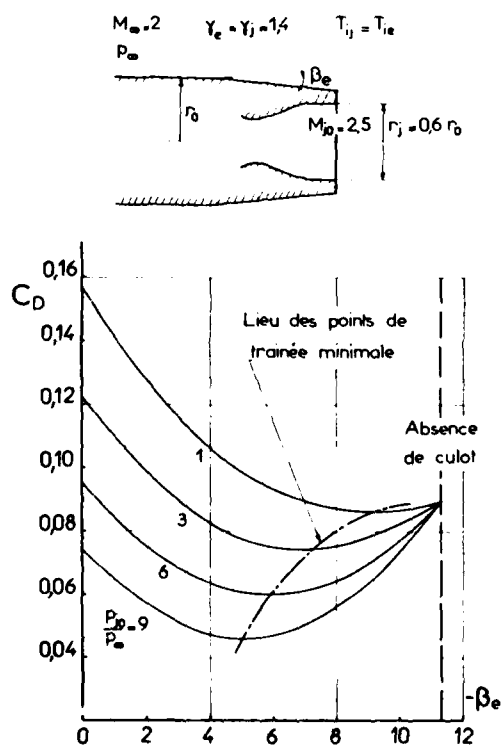
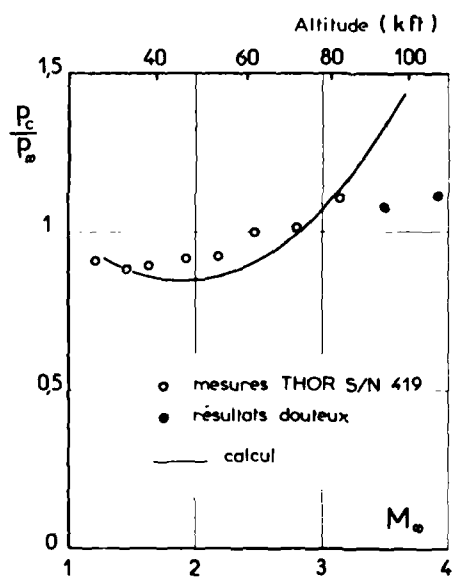


Fig. 93 - CONFLUENCE EN AVANT D'UN CULOT - THÉORIE D'ADDY

Fig. 95 VARIATION PARAMÉTRIQUE DE  $M_{00}$  (a)  
ET DE  $M_{j0}$  (b) (d'après ADDY [90])Fig. 96 VARIATION PARAMÉTRIQUE DES FACTEURS  
GÉOMÉTRIQUES: DEMI-ANGLE DE LA TUYÈRE (a)  
RAYON DE LA TUYÈRE (b) (d'après ADDY [90])

Fig. 97 VARIATION PARAMETRIQUE DE  $\gamma_j$  (d'après ADDY [90])Fig. 98 VARIATION PARAMETRIQUE DE  $\frac{T_{ij}}{T_\infty}$   
( d'après ADDY [90] )Fig. 99 OPTIMISATION DE LA TRAÎNÉE TOTALE (culot + rétréint)  
D'UN ARRIÈRE CORPS (d'après ADDY [90])Fig. 100 PRESSION DE CULOT D'UN ENGIN MONOTUYÈRE  
COMPARAISON A DES MESURES EN VOL (Théorie de HONG [93])

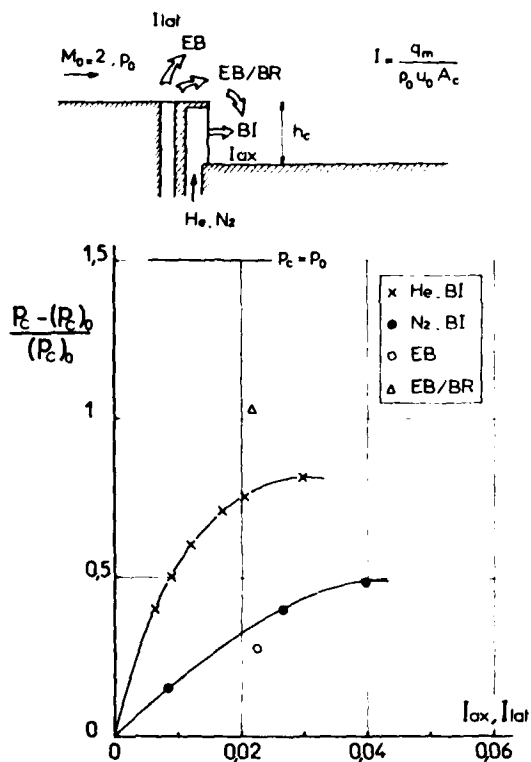


Fig.101 - EFFETS D'INJECTION ET DE COMBUSTION SUR LA PRESSION DE CULOT (d'après SCHADOW et CHIEZE [81])

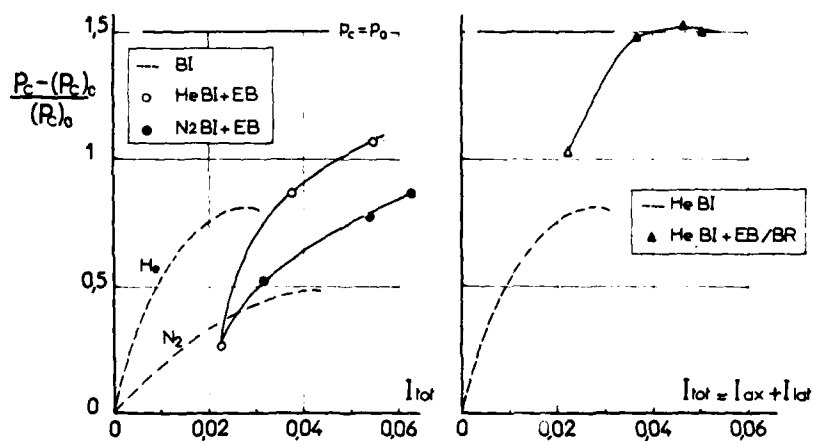


Fig.102-EFFETS CONJUGUES D'INJECTION ET DE COMBUSTION SUR LA PRESSION DE CULOT (d'après SCHADOW et CHIEZE [81])

THE CONTROL OF GUIDED WEAPONS  
by  
George G Erebner  
Aerodynamics Department  
Royal Aircraft Establishment  
Farnborough, Hants, England, GU14 6TD

SUMMARY

The controls are at the heart of a guided weapon because the instructions issued by the guidance system cannot be carried out unless the control system enables the manoeuvres to be achieved. The most common form of control is the deflected aerodynamic surface, which may be placed at the rear of the missile (tail control), at the nose (canard control) or near the centre of gravity (moving wing). The characteristics of these types are described, with examples of tail and canard controls and particular reference to interference effects.

The origins and effects of cross-coupling are briefly described. The possibility of constructing monoplane and cruciform tail control characteristics from single panel measurements, thereby saving wind tunnel test time, is illustrated by an example.

Other types of control considered are mechanical spoilers, jet reaction controls and thrust vector controls. Examples are given of typical characteristics of these three systems.

NOTATION

$b$	wing span
$c$	wing chord
$\bar{c}$	mean wing chord
$C_L$	lift coefficient
$C_\ell$	rolling moment coefficient
$C_m$	pitching moment coefficient
$C_y$	side force coefficient
$C_z$	normal force coefficient
$C_{zp}$	normal force coefficient on a single panel
$C_{bwc}$	coefficient of force or moment with controls undeflected
$C(\delta_1, \delta_2, \delta_3, \delta_4)$	value of $C_{bwc}$ with controls deflected
$d$	diameter
$d_b$	diameter of base
$D_1, D_2, D_3, D_4$	difference functions of coefficients
$h$	spoiler height
$K_W$ or $K_{W(B)}$	wing-body interference factors to normal force
$K_B$ or $K_{B(W)}$	
$k_W$ or $k_{W(B)}$	
$k_B$ or $k_{B(W)}$	
$K_\phi$	roll factor to normal force
$K_{C(W)}$	factor to account for the effect of a low velocity wake
$M$	Mach number
$p$	roll rate or pressure
$p_n$	components of increments in force and moment coefficients
$q_{mn}$	
$r_{lmn}$	
$s_{klmn}$	



$V$	velocity
$\alpha$	angle of incidence at zero roll angle
$\delta$	angle of trailing vortices below wing plane
$\delta_1, \delta_2, \delta_3, \delta_4$	deflections of control panels
$\bar{\epsilon}$	mean downwash angle
$\epsilon$	aileron deflection
$\eta$	elevator deflection, or general control deflection
$\zeta$	rudder deflection
$\theta$	thrust deflection angle
$\rho$	density
$\sigma$	total angle of incidence
$\varphi$	)
$\lambda$	) angle of roll

## 1. INTRODUCTION

This lecture is concerned with methods of controlling guided weapons. As I said in the first lecture of the Series, the controls are the essence of a guided weapon, because however clever the guidance equipment and autopilot may be in compensating for erratic characteristics in the static aerodynamics, they cannot function if the demanded manoeuvres cannot be realised by generating the appropriate control forces.

It is worth noting that during flight the controls of a guided weapon will probably never be at rest. Even when no change in control force is being demanded by the autopilot, the characteristics of the control loop, particularly non-linearities, give rise to a comparatively high frequency oscillatory signal which causes the control to vibrate or "jitter". This feature is not unwelcome to the designer as it avoids the limiting or "break-out" friction force in the mechanical system and thereby increases the speed of response when a demand is made. In addition, when hot gas actuators are used the "jitter" helps to prevent the accumulation of products of combustion in the pipes. In some control systems the control deflection is proportional to the manoeuvre demanded by the autopilot, with the "jitter" superimposed on top of it. In other control systems, known as "bang-bang" systems, the controls can take up only one or the other of two equal and opposite limiting positions. The control responds to a demand by deflecting to the limiting position in the appropriate direction. In a more refined application of the "bang-bang" principle the control is made to alternate continuously between the limiting positions and a resultant control force is obtained by varying the lengths of time spent on one side or the other.

The lecture is divided into two parts, the first being concerned with control by deflecting aerodynamic surfaces, the second with other forms of control. The first part includes all-moving surfaces at the tail and nose, moving wings, trailing edge and wing-tip controls. In general cruciform configurations will be studied, and the testing and representation of arbitrary combinations of control deflection are discussed. The second part deals with spoilers, jet reaction control and thrust vector control.

## 2. DEFLECTED AERODYNAMIC SURFACES

In the case of aircraft, most deflected surface controls are in the form of hinged panels at the trailing edge of a wing, stabiliser or vertical fin. On some high speed aircraft a complete stabiliser is hinged, and can provide both elevator and aileron control. This is the exception, however. In the case of guided weapons the use of all-moving surfaces is the rule, not the exception, since the requirements for trimmed incidence and lateral acceleration are more demanding than for aircraft, and because it is easier to minimise the hinge moments.

### 2.1 Tail Controls

The most common layout for aircraft and guided weapons is a combination of a body with a fixed wing placed close to the centre of gravity and another set of surfaces at the rear. On a guided weapon these rear surfaces not only act as stabilisers but may also act as all-moving controls for motion in pitch, yaw and roll. I put it in this way to emphasise that even though another method of control is chosen - say thrust vector control - the rear surfaces are still required to achieve the appropriate stability, unless a completely autostabilised system is chosen.

The control force developed on a horizontal pair of tail control panels in isolation can be estimated by putting the two panels together and treating them as an isolated wing, the "nett wing". At the rear of the body however this control force is modified by the following interference effects:

- a. Control-body interference due to the body incidence, in the same way as for fixed wing-body interference. This is represented by factors  $K_v$  and  $K_B$  to the normal force on the nett tail, where  $K_v$  takes account of the mean "body upwash" over the tail span, and  $K_B$  represents the carry-over lift on the body.

- b. Control-body interference due to control deflection. This is represented by factors  $k_W$  and  $k_B$  to the normal force on the nett tail arising from control deflection.
- c. The downwash/upwash field from parts of the body upstream of the control.
- d. The downwash/upwash field from the wing upstream of the control.
- e. The reduced dynamic pressure in the wake from the wing.
- f. Panel-panel interference at  $M < 1$  (for cruciform arrangements).
- g. Base effects.
- h. Gap effects.

The normal force on the nett tail is calculated in exactly the same way as for wings, so that the particular problems of tail controls are concerned with the values of the factors  $K_W$ ,  $K_B$ ,  $k_W$ , and  $k_B$ , the value of the induced velocity due to streamwise vortices, the reduced dynamic pressure, and the base and gap effects.

The body-tail interference factors commonly used may be obtained from slender-body theory, as described in references 1 and 2. By definition, therefore, they are independent of Mach number and strictly applicable to planforms such as delta wings of low aspect ratio rather than to rectangular planforms. Corresponding factors for non-slender shapes have been computed using linearised supersonic theory. These factors must be used intelligently and if there is any likelihood of the tail surfaces stalling, suitable plausible assumptions must be made about the manner of applying the factors, though strictly speaking the factors are not valid under these conditions. For example  $K_W$  represents the increase in incidence of the tail surface due to the upwash around the inclined body. It has the theoretical value 2 at the root section and decreases towards the tip. Thus the local incidence at the tail root may be twice the body incidence, even if the tail is undeflected, and this may bring the tail beyond its stalling incidence. Thus  $K_W$  should be applied to the incidence of the nett tail, not to the normal force, and a knowledge of the characteristics of the nett tail in a real viscous flow will indicate whether a loss of effectiveness is likely to occur. If tail controls are very close to the base, there is likely to be a loss of body carry-over lift (factors  $K_B$  and  $k_B$ ) at supersonic speeds, since the part of the body on which some of that lift would act is missing. This would be analogous to the situation with fixed surfaces.

At a roll angle other than zero the interference factor  $K_\phi$  also has to be included in the calculation of the panel loads.

The calculation of the downwash at tail surfaces is difficult, and the various attempts to do this have met with mixed success. Another lecturer has dealt in detail with this problem, along with the wing-body and body-tail interference mentioned above, so I will not deal with it in detail here. However some general remarks will be in order since it is impossible to treat control problems without considering the effect of downwash.

Behind a monoplane wing alone at incidence and at zero roll angle the trailing vortices lie at an angle below the stream direction, the downward velocity being the result of their mutual interference. As the vortex sheet moves downstream this mutual interaction causes the sheet from each half wing to roll up into a helix. Slender body theory predicts that the angle of the vortices below the stream direction,  $\delta$ , is given by:

$$\delta = \frac{8}{\pi^2} \alpha$$

In the case of a wing-body combination at incidence, the upwash around the body causes the vortices to lie above the direction given by the equation for the wing alone, more nearly in the free stream direction. In addition, in order to satisfy the boundary conditions at the surface of the body, image vortices of the trailing vortices must be included inside the body cross-section and their contribution to the downwash must be added to that of the wing trailing vortices. This system of vortices induces velocities in the whole region downstream of their point of origin, including the position of the tail surfaces, and the vertical component of these velocities - upwash or downwash - changes the effective incidence of the tail surfaces.

The downwash effect on the lift of downstream surfaces will probably be greatest when the surfaces are closest to the trailing vortices, and will therefore vary with incidence, particularly in the case of surfaces downstream of a wing-body combination, since the direction of the vortices will move away from the surfaces as the incidence angle increases. Also, this separation increases more rapidly as the longitudinal distance between wing and tail increases. In addition to the effect of the wing vortices, the tail surfaces are also influenced by any vortices shed from the body. The nett effect of the downwash on the tail depends on the relative span of the wing and the tail.

Methods for calculating downwash based on slender-body theory have been presented by Pitts, Nielson and Kaattari<sup>2</sup> and Owen and Maskell<sup>3</sup>. The main difference between them is that the former evaluates the interference load over the exposed tail span excluding the body, whereas the latter averages the downwash angle over the whole span including the body. At supersonic speeds it is also possible to apply linearised supersonic theory to estimate the downwash, using the relations for supersonic horseshoe vortices derived by Mirels and Haefeli<sup>4</sup>. Plascott<sup>5</sup> has presented a method for calculating downwash at supersonic speeds, based on a flow model consisting of a number of discrete trailing vortices lying in the free stream direction and applying the supersonic line vortex theory of Mirels and Haefeli. The method was applied to cruciform configurations at 45° roll angle as well as zero roll angle, and to configurations with the tail controls indexed at 45° to the wings.

Figure 1 shows a comparison between experimentally derived values of mean downwash and calculations by Plascott's method for two different cruciform configurations at speeds near Mach 2 and at zero roll angle. Methods of obtaining experimental values will be described later. In the upper diagram, the comparison is for a missile shape typical of the 1950s from tests by Bateman<sup>6</sup> at  $M = 1.9$ . The leading edge sweep of the wing is comparatively moderate (about  $60^\circ$ ) so that the free stream Mach number component perpendicular to the leading edge is about unity and therefore any leading edge vortex development is likely to be weak. The assumptions of Plascott's theory are therefore fairly plausible, and as can be seen from the diagram agreement with experiment is quite good, allowing for the usual scatter in deriving the experimental downwash.

In the lower diagram, the comparison is shown for a more recent configuration with a wing having a highly swept leading edge (about  $75^\circ$ ). The free stream Mach number component perpendicular to the leading edge is therefore about 0.5-0.6, and an appreciable leading edge vortex flow can be expected. The geometry of the trailing vortex system is therefore likely to be different from that of the first configuration and, in addition, the more highly swept wing will probably have a larger non-linear lift component. As a result the agreement between experiment and the calculation by Plascott's method is not good, and the discrepancy between them increases as the angle of incidence increases which indicates that the non-linear lift is playing a part. In both cases it is evident that the downwash decreases as the incidence increases, which is what one would expect as the trailing vortices move progressively away from the plane of the tail. In the case shown in Figure 1 the vortices were shed only from the horizontal wing panels and interacted (in terms of downwash) only with the horizontal tail panels. If the configurations are set at any other roll angle, the situation is much more complicated because vortices are shed from all four wing panels and interact with all four tail panels. In addition, as the incidence angle increases the vortices may pass across the tail surfaces from one side to the other. In general, a nett sidewash is induced as well as a nett downwash, except in the other symmetrical position at  $45^\circ$  roll angle. In Figure 2 we see the same configuration as in Figure 1 but at  $45^\circ$  roll. In the upper diagram the experimental mean downwash is smaller at low incidence angles, and decreases more slowly with increasing incidence, than at zero roll angle. The estimated curve shows the same trends, but the agreement with experiment is less good than at zero roll. In the lower diagram, the experimental downwash is very much the same as in Figure 1, and since the estimated values are greater than at zero roll, agreement between experiment and calculation is better - probably fortuitously. Various attempts have been made to improve this method by increasing the complexity - for example by increasing the number of horseshoe vortices and by forming an approximation for the effect of the singularities where the Mach cones from the origin intersect the tail surfaces - but no general improvement over a range of configurations was obtained.

Figure 3 shows a comparison between Plascott's method and the slender-body method of Pitts, Nielsen and Kaattari<sup>2</sup> for the two configurations of Figures 1 and 2 at zero roll angle. The slender-body method is clearly less accurate for the wing with lower leading edge sweep and is more accurate for the wing with higher leading edge sweep. In the latter case the reason is not too clear since the slender body theory, being a linear theory, does not allow for the presence and effect of leading edge vortices.

The problem of calculating the downwash on downstream surfaces is one of the most complex in weapon aerodynamics and as far as I know no generally applicable method, giving satisfactory accuracy over a wide range of geometry, incidence angle and roll angle, has yet been developed. In calculating the aerodynamics of a new weapon, reference to the downwash characteristics of a previous example of similar configuration is advisable to supplement theoretical estimates.

This raises the question of how to derive the experimental downwash from wind tunnel tests. The obvious method, of course, is to measure the flow directly at the tail plane position by means of suitable yawmeters. This kind of test programme is time-consuming. Though useful for purposes of research and analysis, such tests would not normally be done in the course of project testing, and so in practice the mean downwash on tail controls must be derived from measurements that would be done for general aerodynamic purposes, that is overall force and moment measurements, and possibly measurements of some of the forces and moments on an individual control panel. Even so, to derive the downwash it is necessary to test partial, or incomplete, models of the weapon, the body alone (B), the body plus controls (BC) and the body plus wings (WB) in addition to the complete model (WBC).

There are several methods of determining the mean downwash,  $\bar{\epsilon}$  depending on the nature of the data available:

$$K_{C(W)} \left(1 - \frac{\bar{\epsilon}}{a}\right) = \frac{C_{zWBC} - C_{zWB}}{C_{zBC} - C_{zB}} \quad (1)$$

where  $K_{C(W)}$  is a factor indicating the loss in tail effectiveness due to the low velocity wake from the wing.

$$K_{C(W)} \left(1 - \frac{\bar{\epsilon}}{a}\right) = \frac{C_{mWBC} - C_{mWB}}{C_{mBC} - C_{mB}} \quad (2)$$

$$K_{C(W)} \left(1 - \frac{\bar{\epsilon}}{a}\right) = \frac{C_{zp \text{ WBC}}}{C_{zp \text{ BC}}} \quad (3)$$

where  $C_{zp}$  is the normal force on an individual panel (assuming this to be at zero roll).

$$1 - \frac{\bar{\epsilon}}{a} = \frac{\eta_1 \text{ WBC}}{\eta_1 \text{ PC}} \quad (4)$$

where  $\eta_1$  is the control deflection at which the derived control normal force,  $(C_{zWBC} - C_{zWB})$  or  $(C_{zBC} - C_{zB})$  is zero.

$$1 - \frac{\bar{C}}{C} = \frac{\eta_2 WBC}{\eta_2 BC} \quad (5)$$

where  $\eta_2$  is the control deflection at which the control panel normal force is zero.

The first two equations, (1) and (2), are essentially the same, assuming that the centre of pressure of the control normal force is the same with and without the wing present. In practice the pitching moment due to the control can usually be measured with greater resolution than the normal force due to the control so Eq (2) may be preferable on that account.

Where the panel normal force on a control in the horizontal position has been measured, this can be used directly as in Eq (3) to measure the mean downwash. This differs from Eqs (1) and (2) in that these are based on forces including the "carry-over" lift on the body, whereas Eq (3) excludes this component. Finally, since the test will normally cover a range of control deflection, it is possible by interpolation to determine the control setting at which the control contribution to the total normal force is zero (as in Eq (4)) or at which the control panel normal force is zero (as in Eq (5)). As in the other equations, the downwash is determined by using the ratio of this force with wings present to the force with wings absent.

Let us turn now to measurements of the control power of various tail-control configurations to determine some of their characteristics. The purpose of tail controls is to apply a turning moment about the centre of gravity in order to change the incidence of the complete missile and hence change the total lift. It is clear, firstly, that the force on the tail control is in the opposite direction to that required on the complete missile and, secondly, that the effect of a given control force increases in proportion to the length of the moment arm between control and centre of gravity.

Figure 4 shows the effect of control deflection on the overall pitching moment of one of the configurations in Figures 1 to 3 at  $M = 1.4$ . The range of incidence is  $0^\circ$  to  $20^\circ$  and the control deflections range from  $-20^\circ$  to  $+20^\circ$ . It is clear that when  $\alpha = 20^\circ$  and  $\eta = +20^\circ$  the panel is at  $40^\circ$  to the free stream, and the upwash around the body will increase this on average by another  $5^\circ$  approximately. Though the wing downwash will reduce the total, it is not surprising that there are indications that the control is beginning to stall at this incidence. This combination of incidence and deflection is only likely to occur when a missile generating a large lateral acceleration in one direction is required to reverse rapidly and "pull" a large acceleration in the opposite direction. The same situation will apply of course with a combination of  $\alpha = -20^\circ$ ,  $\eta = -20^\circ$ .

It may be noted in passing that these characteristics illustrate a feature which I mentioned in my second lecture, that non-linear aerodynamic characteristics can enable a missile to trim at a non-zero incidence even when it is symmetrical. From Figure 4 we see that with the controls undeflected the missile will trim at  $8^\circ$  incidence.

The next two diagrams, Figures 5 and 6, show similar experimental results for a configuration with large delta wings and delta tail controls at zero roll. In these diagrams, the panel normal force,  $-C_{zp}$ , is plotted, and not the overall pitching moment. Another difference from Figure 4 is that the incidence  $\alpha$  covers the range  $-20^\circ$  to  $+20^\circ$  and the control deflection  $\eta$  covers only positive values up to  $20^\circ$ . In practice this coverage is equivalent to that of Figure 4. Figure 5 shows the results for  $M = 0.6$ . For constant values of  $\alpha$ , the variation of the panel normal force with control deflection is regular, but for constant values of  $\eta$  the variation of panel normal force with incidence contains an inflection at  $\eta = 0^\circ$  and  $10^\circ$  which increases to a more pronounced irregularity in the curve when  $\eta = 20^\circ$ . It is clear that a decrease in incidence from  $0^\circ$  to  $-10^\circ$  with  $\eta = 20^\circ$  can bring about an increase in panel normal force rather than a decrease. This is because the vortex interference at  $\alpha = -10^\circ$  causes an upwash rather than a downwash and hence increases the effective incidence of the control panel in the positive sense. This tends to be offset by the body upwash interference contribution to the effective incidence which is negative because the body is at  $\alpha = -10^\circ$ . The various components that contribute to the tail panel normal force are shown in Figure 7. It should be noted that  $k_{w(B)}$  does not arise because of the presence of a physical gap between the control panel and the body. This gap, which enables a flow of air around the root section from the higher pressure to the lower pressure decreases the net force on the panel in whichever direction it acts, and has to be allowed for by an empirical factor. According to inviscid slender-body theory, there should be a substantial loss of lift due to the gap between an all-moving control panel and the body. This does not appear to be found in practice, except when the gap is very large. Presumably with small gaps viscous effects or compressibility effects invalidate the theory. Figure 8 shows some of the results for a delta planform-body combination at  $M = 1.4$  presented by Dugan in Ref 9. The large percentage losses in lift due to the gap which are predicted by inviscid theory occurred only for small values of panel deflection and incidence angle and for large gaps. Further experimental results for the effect of gaps will be found in Refs 10 and 11.

In Figure 5, when  $\eta = 0^\circ$  and  $10^\circ$ , we see that the slope of the panel normal force against incidence is very small near  $\alpha = 0^\circ$ , indicating that the downwash is large. Then, as incidence increases, the value of the downwash decreases and the panel normal force increases more than linearly as a consequence.

Turning to Figure 6, and the results at  $M = 2.0$ , we see that the panel normal force slope near  $\alpha = 0^\circ$  when  $\eta = 0^\circ$  is greater than in Figure 5, indicating that the downwash was less than at subsonic speeds. The extreme irregularity in the curve between  $\alpha = 5^\circ$  and  $-5^\circ$  at  $\eta = 20^\circ$  has now disappeared, due to changes in the relative magnitudes of the components in Figure 7.

In Figure 9, we see similar illustrations of the panel normal force for the very slender wing-body control combination shown. Note the factor of 5 in the vertical scale between Figures 5 and 9 on one hand and Figure 9 on the other. In all these diagrams the coefficient  $-C_{zp}$  is based on the body cross-section area, but the control surface in Figure 9 is much smaller relative to this reference area than the control surface in Figures 5 and 6. Hence the magnitudes of the coefficients in Figure 9 are very much less. The

control deflections in these diagrams go as far as  $30^\circ$ , and we see that at  $M = 0.6$  the curve of normal force against control deflection has a maximum between  $\eta = 20^\circ$  and  $\eta = 30^\circ$  for all values of  $\alpha$ . This indicates that the panel, which has a sharp leading edge and a double wedge cross-section, is stalling in this region, and that increasing the deflection can cause a reduction in control power. The same thing clearly does not happen at  $M = 2.0$ . The curves for  $\eta = 20^\circ$  and  $\eta = 30^\circ$ , though somewhat irregular always show an increase in normal force with increasing deflection. Although the results in Figure 5 at  $M = 0.6$  only went as far as  $\eta = 20^\circ$ , it is quite likely that the stalling behaviour of that control would have been different from that in Figure 9, because the sharp-edged delta planform would be less prone to stall. One other difference may be noted between the results in Figures 5 and 9. With zero control deflection, the slope of panel normal force against incidence at  $M = 0.6$  is more linear in Figure 9 than in Figure 5, and, in particular, is greater near zero incidence. This suggests that the downwash at low incidence angles is greater behind the less slender wing of Figure 5 than behind the more slender wing of Figure 9.

In Figures 10 and 11, the panel normal force coefficient for the slender cruciform model of Figure 9 is plotted against roll angle at two angles of incidence, approximately  $6^\circ$  and  $20^\circ$ , for various control deflection angles and at  $M = 0.6$  and  $2.0$ . Perhaps the first thing to note is the shape of the curve for zero control deflection at  $M = 2.0$  and  $20^\circ$  incidence. Near  $-90^\circ$  roll angle, that is when the panel is almost vertical, the direction of the panel normal force is reversed over a range of about  $40^\circ$  in roll angle. It will be remembered that Figure 7 of my second lecture showed the panel normal force on this wing and the same characteristic reversal of load. In the present configuration the control panel may well act as an extension of the wing. At other values of control deflection up to  $30^\circ$ , the same dip is apparent. Although the effectiveness of the control is increasing, the panel normal force is never lost. The corresponding curves for  $M = 0.6$  show the same qualitative features without any unexpected loads or reversals. At  $6^\circ$  incidence the variation of panel normal force at both Mach numbers is much more regular.

The results of Figures 5, 6 and 9 to 11 are measured on a single control panel. In the tests of Figures 9 to 11, the "live" control panel and the one on the opposite side of the body were each deflected in the same direction, that is, as elevators. Thus the lift distribution induced on the body is correct, though not presented in these measurements. In Figures 5 and 6, only the "live" panel was deflected, and since the span of the panel is quite large compared with the body diameter it may be that the panel loads are not quite representative of those which would be measured if opposing controls were deflected in either an elevator or an aileron sense.

## 2.2 Canard Controls

Canard controls are movable surfaces mounted well ahead of the centre of gravity of the body, so that deflection of the controls applies a turning moment to the missile. The fixed surfaces are usually placed near the rear of the body. They are large enough to provide the required lateral acceleration in trimmed flight, with the appropriate level of stability. Canard controls therefore work on the same principle as tail controls, that is, to develop a lateral acceleration by turning the wing-body combination to an appropriate angle, and their location is generally chosen on the basis of convenience in installing the guidance and control system. The guidance equipment must almost certainly be placed in the nose, and if the autopilot, actuators and control surfaces can be located nearby a compact package is possible, avoiding the need for connections running the length of the body.

Aerodynamically, the first point to note is that canard controls are deflected so as to provide a force in the direction in which lateral motion is required, unlike tail controls which provide a force in the direction opposite to that of the required motion. The response from canard controls might therefore be more rapid. Secondly, canard controls are free from any downwash effects, but they themselves give rise to a downwash field at the fixed tail surfaces. They introduce a new independent variable into the problem of estimating downwash, namely the control deflection, which increases considerably the difficulty of a calculation which is already difficult enough. This downwash reduces the lift on the tail surfaces. The requirement for static stability usually means that the tail surfaces are considerably larger and of greater span than the control surfaces, and the lift due to control deflection is likely to be completely cancelled out by the loss of lift on the tail surfaces. This augments the turning moment effect which is the primary purpose of the control, but it means that there is no resultant force in the direction of the required motion. More seriously, however, it also means that any rolling moment generated by deflecting the canard controls as ailerons is likely to be completely cancelled out by the load induced on the tail fins. Canard controls are therefore regarded as unsuitable for missiles where roll position or roll rate have to be controlled. A way of overcoming this drawback will be mentioned later.

When canard controls are deflected and the body incidence changes in consequence, the angle of incidence of the control panels relative to the free stream increases and the panel loads are high. In extreme cases the control panels may stall. This is in contrast to tail controls for which the angle to the stream remains small as the body incidence increases, and control loads and body bending are kept low. The actuator power required for canard controls may therefore be greater than for tail controls.

In discussing tail controls it was said that the trailing vortices from fixed wings at incidence in the absence of a body would trail backwards approximately in the wing plane, whereas with a body present the upwash around the body moves the vortices upwards nearer to the free stream direction. In the case of canard controls, the trailing vortices due to deflection of the forward surfaces will not be affected by body incidence to the same extent. For example at zero body incidence there will be no upwash around the body and the trailing vortices will lie near the plane of the deflected control. Conversely, at zero deflection and non-zero body incidence, the direction of the vortices should be close to that arising from fixed surfaces. Clearly, then, care must be exercised in calculating the downwash behind deflected canard controls.

It is not customary for cruciform tail controls to be indexed with respect to cruciform wings, though Plascott<sup>5</sup> does use some results on such a configuration for comparison with his method of estimating downwash. It is more common, however, for fixed tail surfaces to be indexed with respect to canard controls. The reason for this is that, with in-line tail fins, the stability is low at small incidence angles because the horizontal tail fins are close to the trailing vortices. With increasing incidence the stability increases as the vortices move away above the tail. When the tail fins are indexed, the stability is greater

at low incidences and increases less rapidly as the incidence increases. These features are illustrated in Figure 12 where the normal force coefficient and pitching moment coefficient for the configuration shown are plotted at subsonic and supersonic speeds. At  $M = 0.5$ , the indexed fins clearly reduce the normal force, and although more stable at low incidence the indexed configuration is less stable above  $3^\circ$ . At  $M = 1.4$ , the loss of normal force due to indexing is less pronounced, and the pitching moment indicates reduced stability above about  $2^\circ$  incidence.

Further comparisons of the effect of indexing the tail fins have been obtained from the results of Spearman and Driver<sup>12</sup> and are shown in Figures 13 and 14. The roll angle is defined as zero when the canard surfaces are horizontal and vertical. The configuration is shown in Figure 13, in which is plotted the normal force coefficient due to adding canards to the body alone and to the body + rear wing combination, to illustrate the effect of the rear wing on this lift increment. Despite a certain amount of scatter it is clear that the normal force on the canard surface is effectively cancelled at low values of incidence. At higher incidence angles, as the trailing vortices move away from the wings, the incremental forces come closer together. The increments due to deflecting the canards by  $8^\circ$  in the elevator sense (all four controls at  $45^\circ$  roll angle) are plotted for the same four configurations in Figure 14. With in-line wings the control force on the canards is more than offset by the downwash effect at low incidence angles, so that the incremental force is negative. Similar results are obtained with indexed wings at zero roll angle, but are much less pronounced at  $45^\circ$  roll angle.

The fact that the control force may be more than offset by downwash effects has also been observed in other tests. In particular, the rolling moment due to canards deflected as ailerons may be reversed at low incidence angles by the downwash effect on the rear fins. As the incidence increases, the control rolling moment is not only restored but may be augmented due to changes in the effect of the downwash field.

It has already been mentioned that during a manoeuvre away from the symmetrical zero incidence attitude, the canard control deflection will be in the same direction as the change of incidence so that a high effective angle of incidence on the panel may be reached. If the control is required to be effective at high values of incidence and deflection it is likely that some care may be needed to ensure that the panels do not stall. Slender delta planforms with sharp leading edges are therefore preferable in such circumstances to essentially unswept planforms which may stall at comparatively low angles, depending on thickness-chord ratio and leading-edge shape.

The poor roll control characteristic of canard systems occurs because of the vortex interactions with the downstream surfaces, and if these surfaces can be decoupled in roll from the body then the rolling moment induced at the tail will not be transmitted to the body but will merely spin the tail in what is probably a harmless manner. For example the tail surfaces could be mounted on a cylinder which rotates on bearings around the main body. If the normal force on the cruciform tail panels depends strongly on roll angle, and the tail surfaces roll freely in a random manner, undesirable pitching oscillations may be set up, and if this is considered a possibility in any given case the tail panels may be deflected slightly in an aileron sense so as to spin them at a comparatively high rate. In this case, the average stability margin will lie between the  $0^\circ$  roll and  $45^\circ$  roll values.

Another way of aerodynamically decoupling canards from tail surfaces is to divide the body aft of the canard surfaces so that the two parts of the body can rotate relative to each other about their common axis. The front part contains the whole control system. When a rolling motion is demanded only the front part rolls. With no adverse interference from the tail fins and because of the very low inertia of the nose portion, a rapid response is obtained.

Although the main qualitative properties of canard controls are known, accurate estimation of the aerodynamic behaviour can still not be guaranteed because of the difficulties associated with the downwash calculations. Further analysis of accurate measurements is therefore still a highly desirable research objective.

### 2.3 Moving Wing Controls

In this system, the main lifting surfaces are placed near the centre of gravity and the stabilising surfaces are at the rear. In this case, however, it is the main lifting surfaces which are deflected for control purposes. Being near the centre of gravity, the control forces are not intended to change the body incidence but to generate the lateral acceleration directly and therefore with a fast response. The moving wings must therefore be of comparable size to fixed wings. If the body remains at approximately the same attitude as before wing deflection, the body contribution to the manoeuvre lift will be lost. This can be important at supersonic speeds since the adverse effect of increasing Mach number above  $M = 1$  is less for bodies than for wings. Apart from speed of response, the aim of limiting the range of body incidence is the main purpose of using a moving wing system, and there are two reasons why this limited range may be required:

- i Because the guidance equipment will not permit too large an angle of body incidence or too large a rate of change of incidence. This is because of the destabilising effects of aberration in the guidance system, and is particularly important at high altitude where large incidence or deflection angles are needed to generate the required lateral acceleration.
- ii Because the power unit is air-breathing and the inlets would be less effective at high incidence angles.

Aerodynamically, the moving wing system is qualitatively the same as a canard control system, with the moving surfaces upstream of the fixed surfaces. However, the proportions of the areas of the wing and tail surfaces will be different, and generally the wing will be of greater span than the tail. This means that the effect of the downwash from the deflected wing is not so extreme as with canard controls, and only a part of the wing lift is offset by the induced effects on the tail. This also means that a certain amount of roll control is likely to be available from a moving wing system. The downwash effect on the tail will tend to turn the missile body and increase the incidence to augment the control force. If such an incidence change is not acceptable, the moving wing must be placed with its centre of pressure slightly behind the centre of gravity.

Variations on this theme may be considered in practical cases. For example it may be impracticable to place canard controls as far forward as the aerodynamicist would like, because of the presence of guidance equipment, the fuze, the warhead, etc. In such a case the moving surfaces may have to be large enough to constitute a compromise between a canard and a moving wing system, and the precise aerodynamic requirement will depend on calculations of the performance including the effects of the guidance and control system.

The requirements for body incidence also inspire the study of systems where both wings and tail surfaces are deflected as controls. The tail controls can be used in several ways:

- i To damp body oscillations induced by wing movements. This can result in a body lift in the opposite direction to the wing lift.
- ii To align the body along the flight path. This ensures that body lift is zero but does not detract from the wing lift.
- iii To control body incidence to follow the wing deflection, so that high body pitch rates are avoided but the lift is not lost completely.

The criteria by which such control systems - indeed any control systems - are judged can only be those associated with overall missile performance and based on aerodynamic characteristics. However the aerodynamicist must ensure that adequate aerodynamic data are fed in to the studies, and this means consideration of practical features which may not be represented or accurately predicted by theoretical methods.

#### 2.4 Trailing Edge and Wing Tip Controls

The last form of deflected surface control that we will consider is that incorporated within a main lifting surface, such as a trailing edge flap or a movable wing tip. The former, of course, has been extensively studied for aircraft applications, but since aircraft wings are usually very different from missile wings the results are not necessarily directly applicable.

There are two obvious disadvantages of trailing edge controls compared with all-moving surfaces:

- i If the flap is hinged at the leading edge, the hinge moment is large, and therefore a large actuator is required. This can be overcome to some extent by using a mass balance, or an aerodynamic balance in the form of a small body projecting ahead of the tip of the control on which a compensating moment can be generated. Alternatively, the control, though placed adjacent to the main wing can be hinged about a line near its own centre of pressure. This means that the forward part of the control projects above or below the wing surface with possible loss of efficiency, particularly at supersonic Mach numbers where the trailing edge shock from the rear of the fixed wing may intersect the deflected control.
- ii The main lifting surface will generally have its centre of pressure near the centre of gravity of the missile, which means that the moment arm of the control about the centre of gravity will be comparatively small. For purposes of rotating the basic wing-body combination, therefore, it must be less effective than surfaces generating the same lift at the end of longer moment arms. However, on configurations which do not have a large lateral acceleration requirement, the only lifting surfaces may be at the rear, and in these circumstances trailing edge controls may be perfectly acceptable.

Figure 16 shows a comparison of the panel normal force coefficients due to deflecting the three controls<sup>7</sup> shown in Figure 15. For comparative purposes the areas of these controls were chosen so that the area multiplied by the distance from the centroid of the panel to the body axis was the same in all three cases, in order to establish a basis for comparing their effectiveness as roll controls.

The flagged symbols in Figure 16 represent the increment in panel normal force due to deflecting the controls  $20^\circ$  and the plain symbols the increment due to  $10^\circ$  deflection, over a range of incidence from  $-20^\circ$  to  $+20^\circ$ . At  $M = 0.6$ , the increment  $\Delta C_{Zp}$  with the tail control is quite constant with incidence at both  $10^\circ$  and  $20^\circ$  deflections. The trailing edge control is more effective at positive angles of incidence than at zero and negative values. At  $20^\circ$  deflection, the wing tip control seems to be most effective at zero incidence; at  $10^\circ$  deflection the experimental points are rather scattered but indicate roughly constant effectiveness with incidence. Relative to each other the tail control panel normal force coefficient is generally greater than that of the other two, and the trailing edge control is generally more effective than the tip control. It must be emphasised that these coefficients are based on the panel areas in each case, in order to compare the lift effectiveness in the three different positions. At  $M = 2.0$ , the effectiveness of the tail control is again fairly constant, though there is a systematic decrease as the modulus of the incidence increases. The trailing edge control increases in effectiveness as the incidence changes from  $-20^\circ$  to  $+20^\circ$ , whereas with the tip control there is a slight decrease in effectiveness on going from negative incidence to positive incidence. At negative incidence angles the relative effectiveness of the three controls at  $M = 2.0$  is much the same as at  $M = 0.6$ , but at zero and positive incidence angles the trailing edge control becomes clearly more effective than the tail control. This seems to be due to a loss of effectiveness of the tail control rather than increased effectiveness of the trailing edge control.

In Figures 17 and 18, the rolling moment coefficients due to deflecting each of the single control panels are plotted against incidence, again for two values of deflection,  $10^\circ$  and  $20^\circ$ . This time it should be noted that the rolling moment coefficient is based on the body cross-section area and body diameter, so that the comparison is valid for the condition initially chosen, that is, the product of the panel area and spanwise moment is constant. When  $M = 0.6$ , the trailing edge control at  $10^\circ$  deflection is roughly three times more effective as a roll control than the tail surface, and the tip control is roughly 1.5 to 2 times more effective. The two wing-mounted controls show greater variation with incidence, however. At  $20^\circ$  deflection, a similar relation exists as regards relative effectiveness, but in all three cases the variation with incidence becomes more erratic. In particular, the effectiveness of the tip control falls off rapidly as the incidence increases above  $0^\circ$ , and above  $9^\circ$  incidence the tip control is less effective than the tail control. When  $M = 2.0$ , the effectiveness of the tail surface as a roll control is about the same as at  $M = 0.6$  but the other two controls are much less effective than at the subsonic speed. For  $\eta = 20^\circ$ , the trailing edge control

becomes more effective at positive angles of incidence whereas the tip control becomes less effective as at  $M = 0.6$ .

The detailed behaviour of these various controls provides material for further study, but this is probably only worthwhile if the general characteristics are clearly acceptable for a given missile design.

## 2.5 Hinge Moments

For all the types and dispositions of control surfaces that we have considered, one of the most important characteristics is the moment of the panel normal force about the hinge line. The hinge moment is important because in almost all guided weapons it is desirable that the size and weight should be kept down and therefore that the control actuation mechanism should be as small and as light as possible. This is determined partly by the magnitude of the hinge moment and partly by the magnitude of the moment of inertia of the control panel about the hinge line.

If the centre of pressure of the control panel is behind the hinge line, then the hinge moment acts against the actuator when increasing the deflection away from the zero position, and acts with the actuator when the deflection is decreasing towards the zero position. The centre of pressure depends on missile incidence and roll angles, control deflection and Mach number, and in practice the hinge line must be positioned to be a good compromise between the different flight conditions. If the missile flight covers a small Mach number range, such as the high subsonic regime, say  $M = 0.7 - 0.8$ , then it should be possible to position the hinge line so that a small hinge moment is achieved at all times. On the other hand, if the controls are required to function over a wide range of Mach number, say, from 0.7 to 2.0, the hinge line must be chosen as the best compromise, based on studies of the behaviour of the control system as a whole, including the autopilot.

To obtain the hinge line position to the required accuracy, the centre of pressure may have to be located to within 1% or 2% of the length of the mean chord of the control. This is difficult to achieve by means of theoretical calculations only, since the estimation methods for typical missile surfaces in three dimensional viscous flow are not generally good enough. For canard controls and moving wings the task may be slightly easier since these surfaces are not in the downwash field of upstream surfaces, but in the case of tail controls the downwash field introduces difficulties. This field is non-uniform, but estimates and experimental derivations are only average values which are not sufficiently refined to enable the centre of pressure to be calculated. The centre of pressure, therefore, and the placement of the hinge line should be finally determined from wind tunnel tests covering the full speed and attitude range of the missile. These tests should be measurements of the control panel normal force and the pitching moment about whatever hinge line is chosen for the tunnel tests. It is usually possible and worthwhile to measure also the yawing moment and bending (roll) moment of the panel about the root section.

## 2.6 Control Cross-Coupling

So far we have considered only comparatively simple combinations of control deflection, such as the deflection of a single tail panel in a cruciform combination or deflections of two or four panels as elevators to generate a moment in a plane of symmetry. However on a missile with cruciform control surfaces, Cartesian control normally involves response to independent steering demands in pitch, yaw and roll, and so, in general, the four panels may all have different deflections. We must therefore consider how to obtain the resultant effect of deflecting four control panels in an arbitrary manner. This leads us to consider cross-coupling effects.

The force and moment components acting on a missile are functions of total incidence angle, roll angle and speed. They are also functions of the four control panel settings. Consider the view of a weapon from the rear, as in Figure 19, with incidence angle  $\sigma$  and roll angle zero. If the two vertical control panels are deflected equally as shown, to give a resultant side force to the left, the forces acting on the two panels will not be the same. This is because the upper panel is in a disturbed flow field on the lee side of the body. There may be a thick boundary layer of low dynamic pressure which would tend to reduce the panel force, and body vortices adjacent to the panel would induce local force increments. By comparison, the lower panel on the windward side is in quite a uniform flow with only a thin body boundary layer. If the two panel forces differ in magnitude as shown diagrammatically in Figure 19, there must clearly be a rolling moment generated as well as a side force, and this rolling moment is said to be a cross-coupling effect, that is, an unintentional by-product of a simple control movement due to the fact that the body is at incidence. In order to get a side force and only a side force the upper control in this case must be given a greater deflection than the lower so that the rolling moment is zero.

If we have a missile at an angle of incidence  $\sigma$ , and if, by experiment or theory, we know the load on a panel at any roll position from  $0^\circ$  to  $360^\circ$ , at any required deflection angle, can we then by simple addition obtain the control force generated by four cruciform panels in any combination of deflections? If we could, it would be easy to define the control characteristics of a guided weapon under any set of flight conditions. It would be unnecessary to spend a lot of money doing wind tunnel tests of a large number of different combinations of control deflection, and the mathematical representation of the aerodynamic control characteristic for performance calculations would be relatively easy. There is thus a strong incentive to study these possibilities.

In Ref 13, Forster and Southgate show the experimental results of deflecting four tail control panels as ailerons by  $10^\circ$ , in one case with no other deflection and in the other case with elevator and rudder deflections of  $20^\circ$ . The increment in rolling moment coefficient,  $\Delta C_{L\dot{\lambda}}$ , due to the aileron deflection at  $M = 1.6$  is plotted against roll angle  $\lambda$  in Figure 20. It is clear that when the elevator and rudder deflections are zero  $\Delta C_{L\dot{\lambda}}$  varies only slightly with roll angle. However with  $20^\circ$  elevator and rudder deflections the roll control moment varies greatly with roll angle and is usually very different from the first case. Indeed at a roll angle of  $285^\circ$  the increment in rolling moment is zero, so that the elevator and rudder deflections have completely destroyed the effect of the aileron deflection.



The same panel-to-panel interference can occur between elevator and rudder deflections ( $\eta$  and  $\zeta$  respectively), as shown by the experimental results shown in Figure 21. If, at zero roll angle, the rudders are deflected by  $-10^\circ$ , the incremental side force generated when the elevators are also deflected by  $-10^\circ$  is different from that generated when the elevators are undeflected. In Figure 21 the difference in incremental side force coefficient with and without elevator deflection is plotted against incidence angle at Mach numbers of 0.5 and 2.0. At  $M = 0.5$  the effect of elevator deflection is on average about 0.5 in  $C_y$ , that is, about 7% of the incremental side force (in a direction to reduce the negative increment resulting from  $-10^\circ$  control deflection). At  $M = 2.0$  the average change due to elevator deflection is negligible because, as will be noted later, at supersonic speeds panel-to-panel interference tends to decrease. As can be seen from the sketch of the body-control geometry in Figure 21, the panels are quite small relative to the body. If they had been relatively larger the panel-to-panel interference would probably have been greater.

## 2.7 The Representation of Arbitrary Deflections

These examples show another form of cross-coupling, due to mutual interference between control panels. The effect of deflecting any particular control panel may not be independent of the deflections of other panels, and the simple idea of constructing the total control characteristics by simple addition of single panel forces is not likely to be valid. However, the difficulties and cost of covering adequately the range of possible combined control deflections make it worth while to try to find a suitable simplified technique,<sup>13</sup> and a number of these have been attempted. One which will be briefly described is by Forster and Southgate. The starting point of their method is that the customary description of control deflections as aileron angle ( $\xi$ ), elevator angle ( $\eta$ ), and rudder angle ( $\zeta$ ) does not provide a proper understanding of aerodynamic cross-coupling, and that the force and moment resulting from arbitrary control deflections should be obtained as the sum of the contributions from the separate movements of each panel,  $\delta_1$ ,  $\delta_2$ ,  $\delta_3$ , and  $\delta_4$ . Let the coefficient of any component of force or moment on the complete missile with controls undeflected be  $C_{bwc}$ , and let the value of this component with the above control deflections be  $C(\delta_1 \delta_2 \delta_3 \delta_4)$ . Using the notation of Figure 19, if control panel 1 is deflected by an angle  $\delta_1$  the increment in the coefficient of force or moment is  $p_1$  so that

$$p_1 = C(\delta_1 0 0 0) - C(0 0 0 0) : \quad (6)$$

$p_2$ ,  $p_3$  and  $p_4$  are defined similarly.

Consider now control panels 1 and 2 given simultaneous deflections  $\delta_1$  and  $\delta_2$ . Then the resultant coefficient is  $C_{bwc} + p_1 + p_2 + q_{12}$ , where  $q_{12}$  is a mutual interference term.  $q_{23}$ ,  $q_{34}$ ,  $q_{41}$ ,  $q_{13}$  and  $q_{24}$  are defined similarly.

If three control panels are deflected together, corresponding triple interference terms  $r_{123}$ ,  $r_{234}$ ,  $r_{341}$  and  $r_{412}$  can be defined, and finally if all four are deflected together a quadruple interference term  $s_{1234}$  can be defined so that

$$\begin{aligned} C(\delta_1 \delta_2 \delta_3 \delta_4) = & C_{bwc} + p_1 + p_2 + p_3 + p_4 + q_{12} + q_{23} + q_{34} \\ & + q_{41} + q_{13} + q_{24} + r_{123} + r_{234} \\ & + r_{341} + r_{412} + s_{1234} \end{aligned} \quad (7)$$

The method is developed using difference functions on the assumption that triple and quadruple interferences and the mutual interference between opposite panels are negligible. That is

$$\begin{aligned} C(\delta_1 \delta_2 \delta_3 \delta_4) = & C_{bwc} + p_1 + p_2 + p_3 + p_4 + q_{12} + q_{23} \\ & + q_{34} + q_{41} \end{aligned} \quad (8)$$

In particular

$$C(\delta_1 \delta_2 0 0) = C_{bwc} + p_1 + p_2 + q_{12} \quad (9)$$

and

$$C(0 \delta_2 0 0) = C_{bwc} + p_2 \quad (10)$$

If we subtract these coefficients we get the difference function

$$\begin{aligned} D_1(\delta_1 \delta_2) &= C(\delta_1 \delta_2 0 0) - C(0 \delta_2 0 0) \\ &= p_1 + q_{12} \end{aligned} \quad (11)$$

which represents the change in the coefficient due to deflecting panel 1 with panel 2 already deflected. Similar difference functions  $D_2(\delta_2 \delta_3)$ ,  $D_3(\delta_3 \delta_4)$  and  $D_4(\delta_4 \delta_1)$  can be defined. These functions depend on incidence angle ( $\sigma$ ) and roll angle ( $\lambda$ ) as well as on the two control deflections, and there are five components, two of force along the y and z axes and three of moment about the x, y and z axes.

Equation (8) may then be written

$$\begin{aligned} C(\delta_1 \delta_2 \delta_3 \delta_4) = & C_{bwc} + D_1(\delta_1 \delta_2) + D_2(\delta_2 \delta_3) \\ & + D_3(\delta_3 \delta_4) + D_4(\delta_4 \delta_1) \end{aligned} \quad (12)$$

The practical application of this method therefore involves making wind tunnel measurements of the five components of overall force and moment for configurations with one control panel deflected (to give the  $p$  term) and with two adjacent control panels deflected (to give the  $q$  term). If the cruciform symmetry is sufficiently exact, the symmetry can be used to bring about a substantial reduction in the test programme. If we consider tests over a positive range of incidence angle,  $0^\circ \leq \sigma$ , and the complete range of roll angle  $0^\circ \leq \lambda \leq 360^\circ$ , then the diagrams of Figure 23 show us that, for example

$$\begin{aligned} -C_z(\sigma, \lambda, \delta_a, 0, 0, 0) &= -C_y(\sigma, \lambda + 90^\circ, 0, \delta_a, 0, 0) \\ &= C_z(\sigma, \lambda + 180^\circ, 0, 0, \delta_a, 0) \\ &= C_y(\sigma, \lambda + 270^\circ, 0, 0, 0, \delta_a) \end{aligned} \quad (13)$$

for one panel deflected, and

$$\begin{aligned} -C_z(\sigma, \lambda, \delta_a, \delta_b, 0, 0) &= -C_y(\sigma, \lambda + 90^\circ, 0, \delta_a, \delta_b, 0) \\ &= C_z(\sigma, \lambda + 180^\circ, 0, 0, \delta_a, \delta_b) \\ &= C_y(\sigma, \lambda + 270^\circ, \delta_b, 0, 0, \delta_a) \end{aligned} \quad (14)$$

for two adjacent panels deflected.

It is therefore necessary to deflect only one pair of panels if the roll coverage is complete. This is very convenient, for in many tunnels the roll angle can be controlled remotely from outside the tunnel whereas to change panel angles it is usually necessary to stop the tunnel, thereby wasting time. Indeed the argument can be carried further, in that, by testing both positive and negative incidence angles in the same run the effect of positive and negative control deflections can be obtained. In Ref 13, Forster and Southgate discuss the planning of a test programme and show how savings of 30% to 85% can be made in the number of tunnel runs. They also claim that the interpolation is more accurate using the D function technique, but to make use of the symmetry properties the accuracy of model manufacture and wind tunnel measurements must be high.

It is necessary to consider the validity of the basic assumption that the triple and quadruple interference terms,  $r$  and  $s$ , are negligible. Using simple theoretical concepts of supersonic flow, we can draw the limits of the Mach cone from the leading edge of a particular control panel root section and see where they intersect the other panels, as shown in Figure 22. The parts of the missile outside this Mach cone are unaffected by the deflection of this particular panel. For these typical proportions it can be seen that, in plan view, the panel opposite panel P lies outside the Mach cone for  $M \geq 1.56$  and the adjacent panel lies outside for  $M \geq 2.60$ . If the adjacent panel were deflected so that its trailing edge moved towards P, this limiting Mach number would be increased. In side view (Figure 22) the region of influence of the Mach cone is a function of the incidence angle.

At subsonic and transonic speeds, with the Mach cone absent or having a very large Mach angle, the likelihood of panel-to-panel interference is greater. The magnitude of such interference will depend on the detailed geometry, and suitable experimental results should be studied to determine this. Subsonic theory would help, of course, but viscous and non-linear effects would probably make the numerical results rather unreliable.

It should be recognised that, though the symbol  $p$  represents the increment in a particular force or moment coefficient when a single control panel is deflected, the changes in pressure which give rise to that force will not be confined to the panel itself but, in principle, will act over the whole body, including the other three control panels. Although the pressure changes on the deflected control panel will almost certainly be the main contributor to the total change in the force, in the present analysis we are concerned with the effect on the overall force and moment coefficients. Similarly the effect of mutual interference denoted by  $q$  is due to pressure changes which may occur over the whole configuration.

Forster and Southgate present comparisons between coefficients measured directly with all four panels deflected and the values synthesised from measurements with only one or two panels deflected, using the difference functions,  $D$ . These are shown in Figure 24. The configuration was a tail-controlled, winged missile and the results shown are for Mach number 1.55, incidence angle ( $\sigma$ ) =  $24.4^\circ$  ( $\pm 0.15^\circ$ ) and the panel deflections  $\eta = \zeta = 25^\circ$ ,  $\xi = 0^\circ$ . The comparison was therefore done at values of  $\sigma$ ,  $\eta$  and  $\zeta$  which makes it quite a severe test. The figure in brackets is the limit of repeatability of the incidence setting in the wind tunnel.

In an appendix to Ref 13, Forster and Southgate describe the formulation of a typical mathematical model, using the D function technique. The general problem of simplifying the representation of control effects is that of treating functions of several variables in a tractable manner. A method by Allen<sup>14</sup> is commonly used, whereby an empirically obtained function of many variables can be expressed in terms of functions of each variable singly. The number of functions required is minimised for a given accuracy.

### 3 OTHER TYPES OF CONTROL

The deflected aerodynamic surface is an efficient type of control and it meets the requirements of most guided missiles. However, in certain circumstances it is possible or necessary to use other methods of control, and the rest of this lecture considers three of these, namely mechanical spoilers, jet reaction controls and thrust vector controls. Since the control force available from deflected surfaces and spoilers is proportional to the dynamic pressure,  $\frac{1}{2}\rho V^2$ , these controls are least effective when the dynamic pressure is low, that is when the speed  $V$  is low or at high altitude where the air density,  $\rho$ , is low. In these conditions jet reaction controls or thrust vector controls may be needed to achieve the required manoeuvres.

### 3.1 Mechanical Spoilers

Controls of this type are not very common, but they are included for completeness. As the name implies, these controls act by "spoiling" the clean flow over some part of an aircraft or missile, thereby producing a change in the aerodynamic force. When they were introduced on aircraft, spoilers were of two main types. One type provides aileron control on wings by projecting narrow surfaces running spanwise along the wings' upper surfaces. They change the lift on the wing panels on which they are operating and hence apply a rolling moment to the aircraft. They are preferred to hinged trailing edge ailerons in some cases because a trailing edge control can cause an unacceptable amount of aeroelastic distortion on a sweptback wing, whereas a spoiler mounted further forward can apply the control force nearer the centre of the planform. Additionally, a trailing edge control can lose aerodynamic effectiveness at transonic speeds, and therefore considerable work was done on spoiler controls in the early days of transonic and supersonic aircraft. The other common type of spoiler on aircraft is the dive brake. Typically, this is mounted on the fuselage and consists of two or more flaps which fold outwards from the body to increase the drag considerably, and therefore slow the aircraft without upsetting the trim too much.

The subsonic and transonic flow about a spoiler is comparatively complex and will not be dealt with here. A theoretical treatment has been given by Woods<sup>15</sup>. Fig 25 shows a sketch by James of the two-dimensional supersonic flow over a spoiler on the upper surface of a flat plate<sup>16</sup>. The total force due to the increased pressure upstream is usually greater than that due to the decreased pressure downstream, so that the resultant force is towards the side opposite the spoiler. If the spoiler is placed near the front of the plate the region of increased pressure is reduced so that the resultant force may be reversed in direction. Conversely, if the spoiler is placed near the trailing edge the region of decreased pressure is reduced and the resultant force away from the spoiler is increased. Alternatively a gap may be made through the surface just behind the spoiler. The increased pressure on the front face of the spoiler and the decreased pressure on the rear face mean that there is a considerable drag increment when spoilers are used.

Fig 26, taken from Ref 17 by James, shows the rolling effectiveness of a spoiler at the trailing edge of a rectangular half-wing in the transonic speed range, compared with the effectiveness of a quarter-chord trailing edge flap deflected by  $4^\circ$ , and with a combination of the flap and spoiler. The measurements were made during free flight tests and expressed as the non-dimensional roll rate,  $pb/2V$ , since it is not possible to separate the rolling moment from the roll damping. It can be seen that the flap was generally more effective, except for speeds near  $M = 0.9$  where the spoiler was up to five times as effective as the flap. The effectiveness of a combination of the two methods is roughly equal to the sum of the flap and the spoiler separately.

Similarly, Fig 27, taken from Refs 18 and 19 by Lord and Czarnecki, compares the lift increment due to a full span spoiler and that due to a full span trailing edge flap on a tapered unswept wing at two supersonic speeds. The spoiler is on the upper surface, so that  $\Delta C_L$  is negative. With both types the control effectiveness increases at negative incidence angles, and the advantage of the flap over the spoiler is less at the higher Mach number.

Fig 28, taken from Ref 20 by Wiley, shows the increments in rolling moment produced by a spoiler at various positions on a delta wing at Mach numbers 0.6 and 0.9. The outside edges of the spoilers lie along a conical ray from the apex of the gross wing, and it is clear that at moderate angles of incidence the effectiveness of the spoiler is increased as it is moved back and extended spanwise. At the furthest forward position the control force is reversed, as I mentioned when describing the flow field. At incidence angles above about  $15^\circ$  the differences in effectiveness are considerably reduced. For the spoiler at position 3, Fig 29 shows the effect of spoiler height on the rolling moment increments at  $M = 0.6$ .

Some indication of the magnitude of the hinge moments of a flap-type spoiler, hinged about its leading edge, is given by the results from Ref 21 shown in Fig 30. The spoiler was at about 80% chord on the upper surface of a  $60^\circ$  delta wing. The hinge moment is plotted against spoiler height for Mach numbers 0.62 and 0.96, and incidence angles  $0^\circ$  and  $12^\circ$ . It is interesting to note that initially the hinge moment is negative which indicates that it helps the spoiler to open, but thereafter it becomes more positive and resists opening.

The effect of various spoiler type controls on a body can be illustrated from the results of tests at  $M = 4.3$  by Pecover<sup>22</sup>. These tests covered a range of ten possible control devices on a cone-cylinder-flare body, and three of the more effective of these have been chosen as examples. They are all at the rear of the body, and Figs 31 to 33 show the change in pitching moment due to moving the controls.

The first is a set of four control flaps on the flare, hinged at their leading edges and deflecting both outwards and inwards. The diagram shows the effect of deflecting a single control in each direction in the incidence plane, on both the windward and leeward sides of the body. As incidence angle increases, the flap on the windward side becomes more effective, on the leeward side it becomes less effective.

The second control is an eccentric disc at the back of the body, shown in Fig 32. This can be displaced from its central symmetrical position in any radial direction, and the diagram shows the effect of displacement in the incidence plane. At a given angle of incidence this control seems to be equally effective for displacements on the windward and leeward sides and for a given displacement the effectiveness increases with incidence angle. The disc causes a large increase in axial force which may be as significant in varying the pitching moment as the pressure changes induced on the body ahead of the disc.

The third control consists of four pairs of sweptback spoilers, arranged round the circumference of the base as shown in Fig 33. The experiment studied the effect of raising only one of the eight spoilers in the four positions on one side of the incidence plane. These positions on the port side were designated top port, port upper, port lower and bottom port as shown. Three spoiler heights were tested. It can be seen that the spoilers in the top and upper positions lose effectiveness as incidence is increased. There is little effect of incidence for the lower spoiler, but the bottom one is the most effective of all and becomes more effective as the incidence increases.

Of the ten forms of control tested by Pecover, the swept spoilers are the only ones which afford the possibility of roll control. Fig 34 shows the rolling moment induced by deflecting a single spoiler in the bottom port and top port positions, with two different spoiler heights. Spoilers on the starboard side would, of course, induce rolling moments in the opposite direction so that, for example, the bottom port could be combined with the top starboard.

The experimental results shown for spoilers on wings and a body are only a brief indication of their characteristics. Their main disadvantage compared with deflected surfaces is the comparatively large hinge moments which are likely to occur, so that their use will be limited to particular circumstances where this disadvantage and the appreciable drag increment are outweighed by the expected advantages.

There is a great deal of published information on spoilers, most of it dating from the 1950s. Generally the applications envisaged were to aircraft, but some of the material could be useful for weapon design. Ref 16 contains an extensive bibliography and Ref 28 is a bibliography of NACA work on wing controls of various kinds up to 1954.

### 3.2 Jet Reaction Controls

Let us now consider jet reaction controls. The principle of their operation at supersonic speeds is illustrated in Fig 35, taken from Ref 23 by Spaid and Cassel. This shows the type of flow pattern obtained in two dimensions when a sonic or supersonic jet is emitted from a slot into the airflow past the surface of a flat plate. It is a very complex flow field, and during the last 25 years many studies have attempted to define it and to determine the effect of the most important variables. In addition to the reaction force on the nozzle, the jet interacts with the external stream to cause changes of pressure upstream and downstream of the slot, very similar to those induced by a mechanical spoiler. For this reason controls of this type are sometimes referred to as "jet spoilers", but the primary control force is the jet reaction itself.

The ratio

$$\frac{\text{Interaction force} + \text{jet reaction thrust}}{\text{Jet reaction thrust in vacuo of a sonic jet with the same stagnation conditions and mass flow rate}}$$

is called the Jet Effectiveness Ratio or Amplification Factor, and it can be greater or less than 1, depending on the direction of the net interaction force. In general the jet reaction thrust in the numerator will depend on nozzle design and jet pressure ratio, so that the value of the mass flow in the denominator must be adjusted when the jet pressure ratio of the numerator is varied. In much of the experimental work, however, sonic jets were used in the models and consequently the mass flow was constant. It was therefore unnecessary to adjust the denominator for each pressure ratio.

The first step away from the two-dimensional case is to replace the two-dimensional slot on the plate by a slot of finite span or a circular hole. The external flow can now go round the side of the secondary jet and the force on the plate due to the interaction between the jet and the free stream is reduced. If the jet issues from a slot or hole in an axisymmetric body, the loss of interaction force is even greater.

The interaction force is increased if the jet is placed near the trailing edge of a surface or the base of a body, because the low pressure region downstream is behind the base. This emphasises the strong similarity to the mechanical spoiler. Conversely, if the jet is placed near the nose of a body, the interaction force is decreased. Fig 36, taken from Ref 24 by Watman and Meyer, shows the range of amplification factors measured in some of these cases, plotted against the ratio of the jet stagnation pressure to the free stream static pressure. Both sonic and supersonic nozzles were included and for the nose jets the boundary layer was laminar. The range of free stream Mach number was from 2.4 to 4.5. It can be seen that as the pressure ratio is increased the amplification factor for the flat plate decreases from about 3 to about 1.5. For a jet placed at the rear of an ogive-cylinder body, the expected reduction in amplification factor compared with a flat plate is evident, the factor varying from about 1.5 at low values of pressure ratio to about 1.0 at high values. With the jet near the nose, the interaction force reduces the total and is particularly marked at low pressure ratios but the factor approaches unity at high pressure ratios. Thus at high pressure ratios the interaction force is small for all the arrangements.

The use of jet reaction controls does not remove the need for aerodynamic stabilisation, unless a fully auto-stabilised system is used, and therefore tail surfaces may still be required. If so they can be used to increase the amplification factor as shown in Fig 37 taken from Ref 24. When the jet was emitted between a pair of cruciform delta surfaces the amplification factor was increased to the range of values typical of flat plates. The wings have had the effect of constraining the flow around the side of the orifice, and the amplification is a function of the wing span.

Fig 38 is an illustration of the comparative characteristics of a jet reaction control using a cold air jet and a deflected surface control, at high speeds and high altitudes. The choice of values for the various parameters is quite arbitrary. The jet is assumed to issue from a sonic nozzle on an axisymmetric body, the amplification factor varying from 1.35 at high pressure, high altitude, to 2.6 at the lowest pressure and altitude. The contrast between the control effectiveness of the two cases as altitude changes is quite marked.

So far I have presented the amplification factor as a function only of the jet pressure ratio and the shape of the nozzle-body combination. The factor can equally well be plotted against jet mass flow or momentum, and particularly for two-dimensional flow, this may be a more appropriate correlating parameter. The effectiveness also depends to some extent on the free stream Mach number and Reynolds number, boundary layer condition, angle of attack, jet exit diameter, nozzle design and jet inclination. With so many variables, it is unlikely that any set of universal design rules for practical applications will emerge.

The applications I have so far envisaged for jet reaction controls are at high supersonic or hypersonic Mach numbers at high altitude, and most research work has been aimed at these conditions. However there is

no reason why such controls should not equally well be considered for use at subsonic speeds, since the dynamic pressure may again be low. In a subsonic free stream the dynamic pressure will be generally less than the static pressure and the penetration of a sonic or supersonic secondary jet will be greater than through a supersonic external flow. Flow photographs indicate that the jet will not turn over until it has become subsonic. At very low free stream speeds much of the interference effect of the jet on the surface pressure is produced by entrainment, which tends to reduce the plate pressure both upstream and downstream. As the free stream speed increases the blockage effect becomes more apparent and the upstream pressure is increased. The values of amplification factor can be quite high. Schult in Ref 25 has quoted a value of about 10 for a jet issuing from a slit near the trailing edge of a wing, compared with 3 at supersonic speeds. In this case the jet was derived from a ram air supply. Much of the work on jets issuing from surfaces in a subsonic stream has been done in support of VTOL aircraft design, though in these cases the jets themselves may be subsonic. A description of entrainment effects has been given by Pradbury and Wood<sup>26</sup>.

Unless ram air is used, jet reaction controls require a source of energy additional to that available from the free stream and there may therefore be substantial penalties on missile size and weight. The secondary jet may be provided from a stored gas supply or a gas generator. Alternatively, part of the propulsive motor efflux may be used, but we shall see that if this is done it would be better applied to thrust vector control. Perhaps the most suitable application for a jet reaction system in comparatively small missiles would be for cases where a small control force is required for a short time, such as terminal guidance for a basically unguided weapon.

Jet reaction controls appear to offer an ideal application for a wholly fluidic control system. Among the advantages suggested are high reliability, insensitivity to electromagnetic and nuclear radiation, to shock and vibration and to high and low temperatures, and unlimited shelf life. A study at RAE, however, concluded that the problems of size, weight, power consumption and low speed of response outweighed the potential advantages.

There is a very extensive literature on the interaction of a secondary jet with an external stream, and Ref 23 contains a comprehensive bibliography. Ref 25 compares the roll control effectiveness of deflected surfaces, spoilers and jet reaction controls.

### 3.3 Thrust Vector Control (TVC)

Finally, we consider thrust vector control systems. These operate by interfering in some way with the efflux from a propulsive motor and thereby inducing a lateral control force. Naturally this control force is available only when the motor is operating. Although TVC systems function by causing an asymmetric flow condition in the propulsive nozzle, their effectiveness is usually described by using an equivalent deflection angle

$$\theta = \sin^{-1} \frac{\text{side force}}{\text{thrust force}}$$

Even when the nozzle itself is pivoted about a lateral axis the equivalent deflection is greater than the geometric deflection, indicating that an asymmetric nozzle flow exists.

Early examples of missiles using a form of thrust vector control are SS11 and Swingfire. Of course tilting nozzles have been used in the control of long range ballistic missiles, but these are outside the scope of our course, and in any case the motors are liquid fuelled which confers a degree of flexibility not possible with solid fuel rockets.

Ref 30 contains a review of TVC systems, but in general the open literature on the characteristics of various forms of TVC system is somewhat sparse, and much of the information which follows is unpublished. Fig 39 shows some of the devices which have been studied for application to missiles of higher power and higher performance than the two early applications mentioned above. Typical deflection angles are shown alongside. In two of the methods a fluid is injected into the nozzle just downstream of the throat<sup>29</sup>. An interference flow pattern is set up similar in principle to that obtained with a reaction jet in a free stream, and an asymmetric side force on the nozzle results. In one of the examples, liquid freon is injected into the nozzle, in the other example part of the hot jet efflux is tapped from the back of the motor chamber and reintroduced downstream of the throat. Between these two in effectiveness comes the axial sliding plate which can be moved out behind the nozzle exit plane to prevent continued jet expansion on one side and hence provide a side force. Next to it we have the semaphore spoiler which can pivot about a longitudinal axis and move progressively in and out of the efflux. The blade can be shaped to give a suitably graded variation of control force with deflection. Finally we have two systems which depend on rotation about a lateral axis, or, in the practical case, about two lateral axes at right angles using gimballed or universal bearings. In one case a "dome spoiler" can be deflected to provide control in any direction, in the other the nozzle itself is rotated as required. This can give rise to a sealing problem. One way of overcoming it is to connect the nozzle to the motor by a bellows. It is worth noting that with gimballed bearings it is not difficult to link the TVC control with deflected surfaces, so that a hybrid control system effective over a wide range of conditions is possible.

Fig 40 shows a tabulated comparison of some results obtained in a British TVC research programme. For a Cartesian control system four actuators are required with fluid injection systems, sliding plates and semaphore spoilers. With gimballed systems only two actuators are required. With semaphore and dome spoilers an appreciable thrust loss was found. The nozzle geometry was found to have only a second order effect on the equivalent thrust deflection obtained. This is not unexpected since missile nozzles are generally under-expanded to avoid excessive length. For the fluid injection systems motor duration was 2-3 seconds, for the sliding plate 10 seconds, for the semaphore spoiler 20 seconds and up to 1 minute for the swivelling nozzles.

The most expensive part of a TVC system is the actuation unit and the choice will therefore be dictated largely on grounds of relative cost. Electrical actuation is cheaper than cold gas pneumatic actuation, which in turn is cheaper than a hydraulic system. Hot gas and liquid injection systems fall somewhere between the first two, depending on the requirement. Tests with fluidic switching systems proved disappointing on grounds of attainable thrust deflection angle, size and weight.

Thrust vector controls show an advantage over deflected aerodynamic surfaces only when the latter are rendered comparatively ineffective due to low dynamic pressure. Under these conditions TVC enables very "agile" manoeuvres to be carried out, during which missiles may reach very high angles of incidence, and much of the recent interest in aerodynamic behaviour at these high angles is due to the power conferred by modern TVC systems. In particular the ability to make rapid changes in direction immediately after launch, while the forward speed is still low, has been demonstrated.

Apart from the effect of misalignments, no control in roll can be obtained by deflecting a single axisymmetric jet. However if multiple nozzles are used they can be deflected in combination to give a rolling moment as well as pitching and yawing moments.

The effect on the external aerodynamic characteristics of deflecting the thrust has not been widely studied. A recent paper by Fleeman and Nelson<sup>27</sup>, describes force and moment measurements on an ogive-cylinder body at angles of attack up to  $180^\circ$  with a cold air jet issuing from the base. The nozzle could be deflected by  $15^\circ$ , and the tests showed that at a Mach number of 2.5 this deflection affected the normal force and centre of pressure only at angles of attack greater than  $140^\circ$ . However if tail surfaces had been present on the body these would have generated a substantial part of the normal force. They are particularly susceptible to the effects of base flows, and hence the effect of jet deflection on the normal force and centre of pressure might have been more noticeable. At a subsonic Mach number of 0.85, the axisymmetric jet plume had a marked effect on body normal force at incidence angles above about  $40^\circ$ , so it is possible that at subsonic speeds the effects of thrust deflection on the external aerodynamics may be greater than those observed at  $M = 2.2$ .

It is interesting to compare the relative effectiveness of thrust vector control obtained by hot gas injection and jet reaction control using the same hot gas supply. For TVC the equivalent thrust deflection of  $12^\circ$  with a motor thrust of 3800 pounds (16900 Newtons) gives a side force of 790 pounds (3500 Newtons). If the same jet and sonic nozzle exhaust into a vacuum, the thrust would be about 190 pounds (850 Newtons), so that an amplification factor of about 4 is required from the jet reaction control to give the same side force as the TVC.

Thrust vector control is the only alternative system to challenge seriously the predominant position of deflected surfaces as a means of controlling guided weapons, and then only in a particular range of applications. However, nearly all missile designs are "special cases" in one way or another, and it is well to be aware of the characteristics of all the possible systems for achieving the required manoeuvres.

#### REFERENCES

- 1 J.N. Nielsen Missile Aerodynamics, McGraw-Hill, 1960.
- 2 W.C. Pitts Lift and centre of pressure of wing-body-tail combinations at subsonic, transonic and supersonic speeds.  
J.N. Nielsen  
G.E. Kaattari  
NACA Technical Report 1307, 1957.
- 3 P.R. Owen Interference between the wings and the tailplane of a slender wing-body-tailplane combination.  
E.C. Maskell  
RAE Report Aero 2441, 1951.
- 4 H. Mirels Line vortex theory for the calculation of supersonic downwash.  
R.C. Haefeli  
NACA Technical Note 1925, 1949.
- 5 R.H. Plascott The estimation of some of the effects of wing-control interference on guided missiles at supersonic speeds.  
RAE Technical Note Aero 2189, 1952.
- 6 P.J. Bateman Wind tunnel measurements of normal force and pitching moment on a scale model of Blue Jay missile at  $M = 1.41, 1.61$  and  $1.90$ .  
RAE Technical Note Aero 2265, 1954.
- 7 A.J. Sadler Preliminary analysis of the characteristics of wing tip, trailing edge and aft-mounted control surfaces on a monoplane delta wing-body combination of aspect ratio 0.83 at Mach numbers from 0.6 to 2.8.  
RAE Technical Memorandum Aero 962, 1966.
- 8 K.G. Winter Characteristics of aft-mounted, all-moving rectangular control surfaces on a slender cruciform missile at Mach numbers from 0.6 to 2.8.  
S.M. Mills  
RAE Technical Report 66326, 1966.
- 9 D.W. Dugan Experimental investigation of some aerodynamic effects of a gap between wing and body of a moderately slender wing-body combination at a Mach number of 1.4.  
NACA RM A55D08, 1955.
- 10 J.N. Nielsen Comparison between prediction and experiment for all-movable wing and body combinations at supersonic speeds - lift, pitching moment and hinge moment.  
G.E. Kaattari  
W.C. Drake  
NACA RM A52D29, 1952.
- 11 W.C. Drake Lift, drag and hinge moments at supersonic speeds of an all-movable triangular wing and body combination.  
NACA RM A53F22, 1953.

- 12 M.L. Spearman  
C. Driver Wind tunnel investigation at a Mach number of 2.01 of the aerodynamic characteristics in combined pitch and sideslip of some canard-type missiles having cruciform wings and canard surfaces with  $70^\circ$  delta planforms.  
NACA RM L54FO9, 1954.
- 13 C.A. Forster  
A.C. Southgate The difference function approach to the overall aerodynamics of guided weapons.  
Journal of the Royal Aeronautical Society, Vol 64, No 600, pp 783-803.  
December 1960.
- 14 C.D. Allen A method for the reduction of empirical multi-variable functions.  
Computer Journal, Vol 1, pp 196-200, January 1959.
- 15 L.C. Woods Theory of aerofoil spoilers.  
ARC 15,870, Aeronautical Research Council, Teddington, England.
- 16 K.W. James Some recent information on spoiler controls.  
RAE Technical Note Aero 2455, 1956.
- 17 K.W. James Control effectiveness tests on spoilers at transonic speeds in free flight.  
RAE Technical Note Aero 2286, 1954.
- 18 D.R. Lord  
K.R. Czarnecki Aerodynamic characteristics of several flap-type trailing-edge controls on a trapezoidal wing at Mach numbers of 1.61 and 2.01.  
NACA RM L54D19, 1954.
- 19 D.R. Lord  
K.R. Czarnecki Pressure distributions and aerodynamic characteristics of several spoiler-type controls on a trapezoidal wing at Mach numbers of 1.61 and 2.01.  
NACA RM L56E22, 1956.
- 20 H.G. Wiley A wind tunnel investigation at high subsonic speeds of the lateral control characteristics of various plain spoiler configurations on a 3-percent thick  $60^\circ$  delta wing.  
NACA RM L54D01, 1954.
- 21 H.G. Wiley  
R.I. Taylor Investigation at transonic speeds of the lateral-control and hinge-moment characteristics of a flap-type spoiler aileron on a  $60^\circ$  delta wing.  
NACA RM L53J05, 1954.
- 22 B.E. Pecover Wind tunnel force and moment investigation at  $M = 4.3$  into the application of various devices for the control of a cone-cylinder-flare configuration.  
RAE Report Aero 2673, 1963.
- 23 F.W. Spaid  
L.A. Cassel Aerodynamic interference induced by reaction controls.  
Agardograph No 173, 1973.
- 24 H. Watman  
R.C. Meyer A review of lateral jet-supersonic stream interactions with reference to reaction control applications.  
Grumman Aircraft Engineering Corporation, Report No ADR 01-07-63.2, 1963.
- 25 E.D. Schult Summary of roll controls applicable to fin-stabilised vehicles.  
NASA Technical Report R-197, 1964.
- 26 L.J.S. Bradbury  
M.N. Wood The static pressure distribution around a circular jet exhausting normally from a plane wall into an airstream.  
RAE Technical Note Aero 2978, 1964.
- 27 E.L. Fleeman  
R.C. Nelson Aerodynamic forces and moments on a slender body with a jet plume for angles of attack up to 180 degrees.  
AIAA Paper 74-110, 1974.
- 28 J.D. Brewer Description and bibliography of NACA research on wing controls, January 1946 - February 1955.  
NACA RM 54K24, 1955.
- 29 R.C. Parkinson Thrust vector control of rocket engines by secondary injection: design curves for gaseous and liquid injection.  
RPE Technical Report 71/6, 1971, Pocket Propulsion Establishment, Westcott, England.
- 30 B. Burgess Recent advances in thrust vector control for tactical missiles.  
The Aeronautical Journal of the Royal Aeronautical Society, Vol 77, No 774, August 1973.

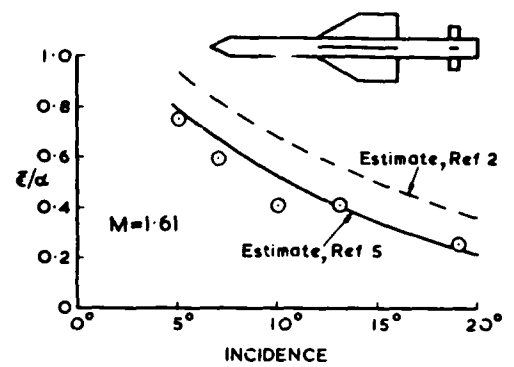
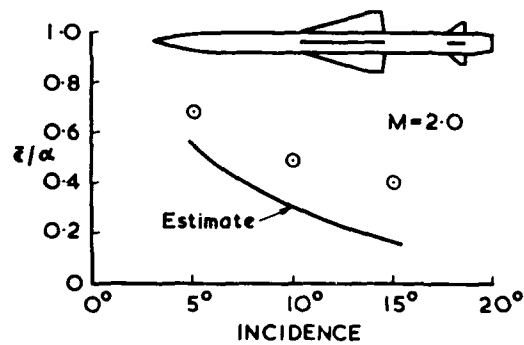
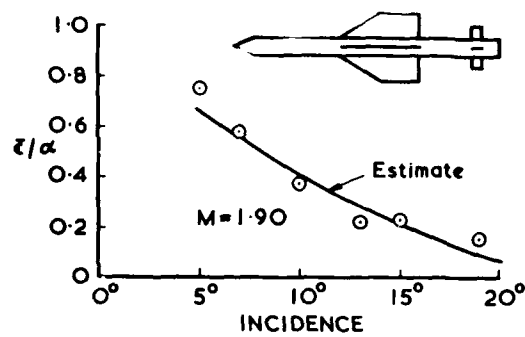


Fig 1 A comparison of experimental downwash and calculations by Plascott's method, at zero roll angle

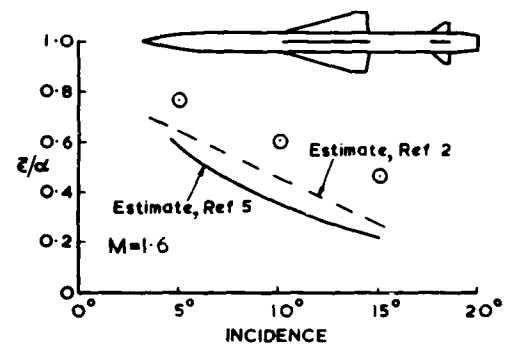
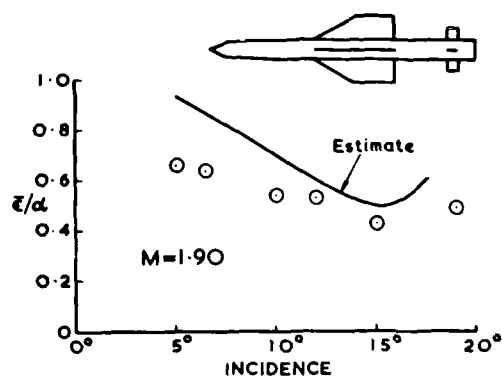


Fig 3 A comparison of two methods of estimating downwash

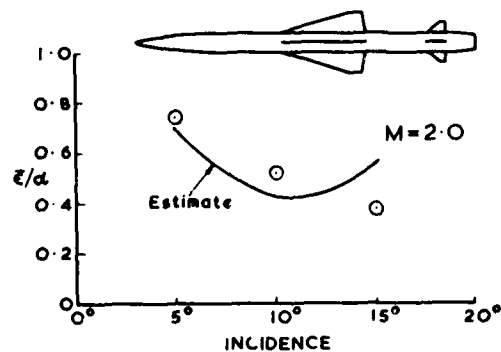


Fig 2 A comparison of experimental downwash and calculations by Plascott's method, at 450 roll angle



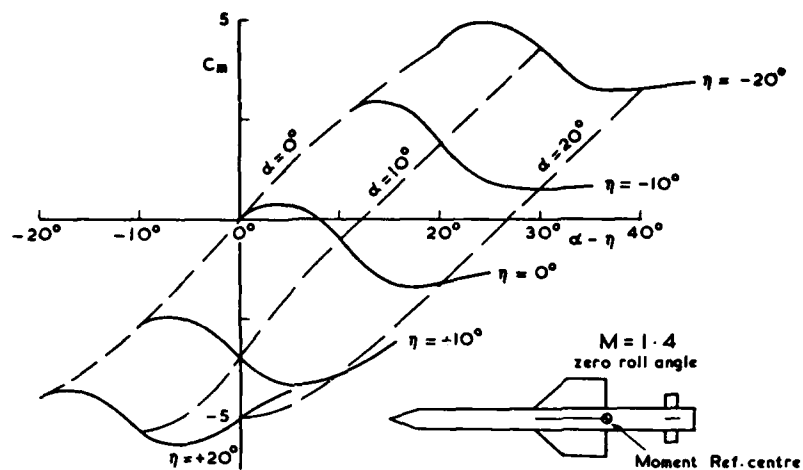
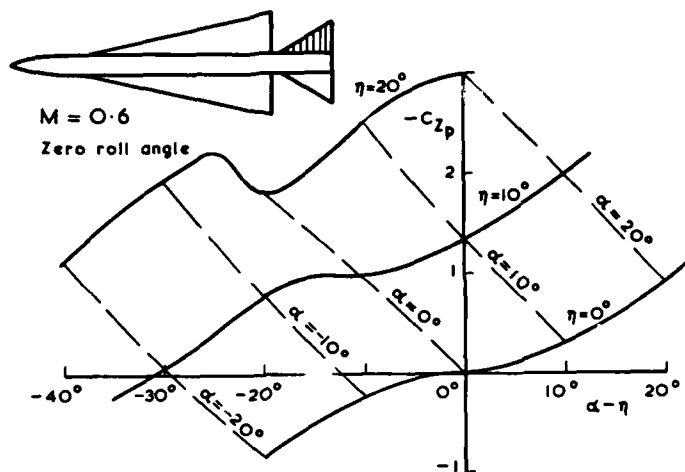
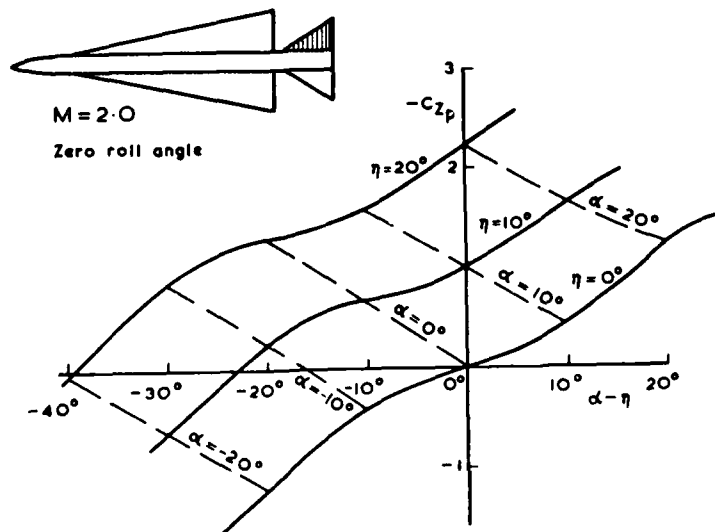


Fig 4 Effect of control deflection on overall pitching moment

Fig 5 Control panel normal force,  $M = 0.6$ Fig 6 Control panel normal force,  $M = 2.0$

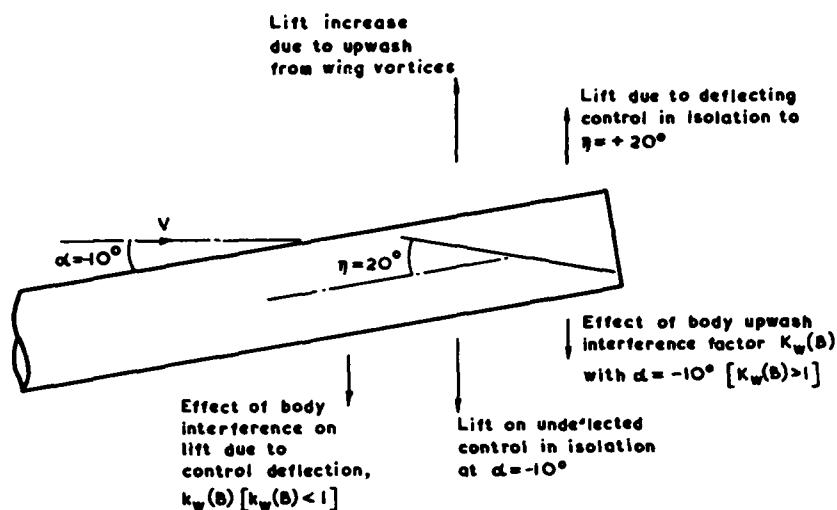


Fig 7 Contributions to lift on deflected tail control

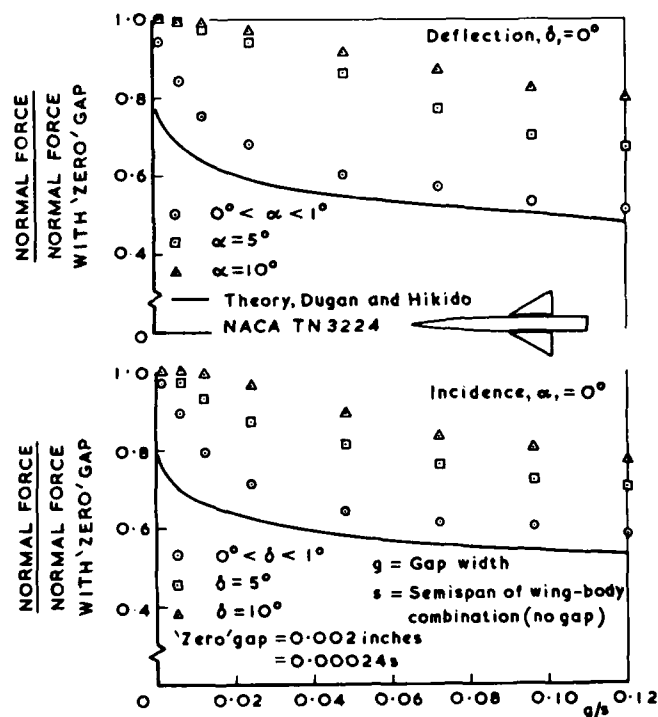


Fig 8 Effect of root gap on total wing-body normal force - taken from Ref 9

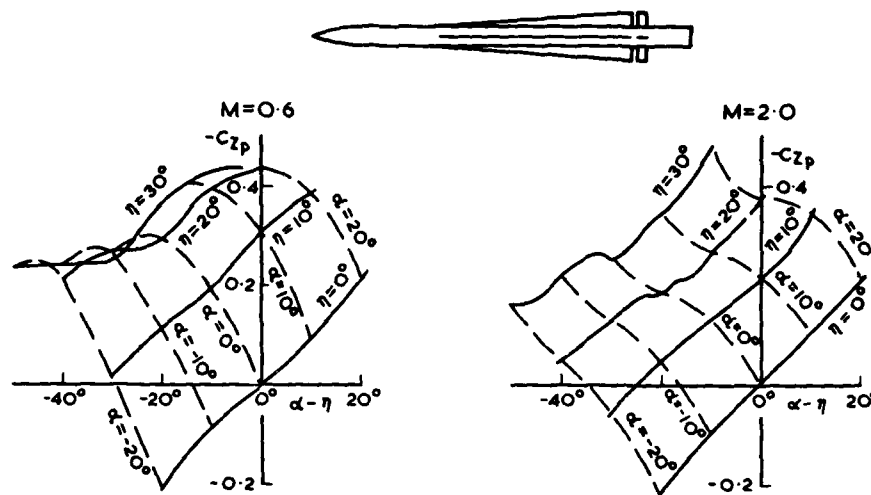


Fig 9 Control panel normal force: variation with incidence and deflection, zero roll angle

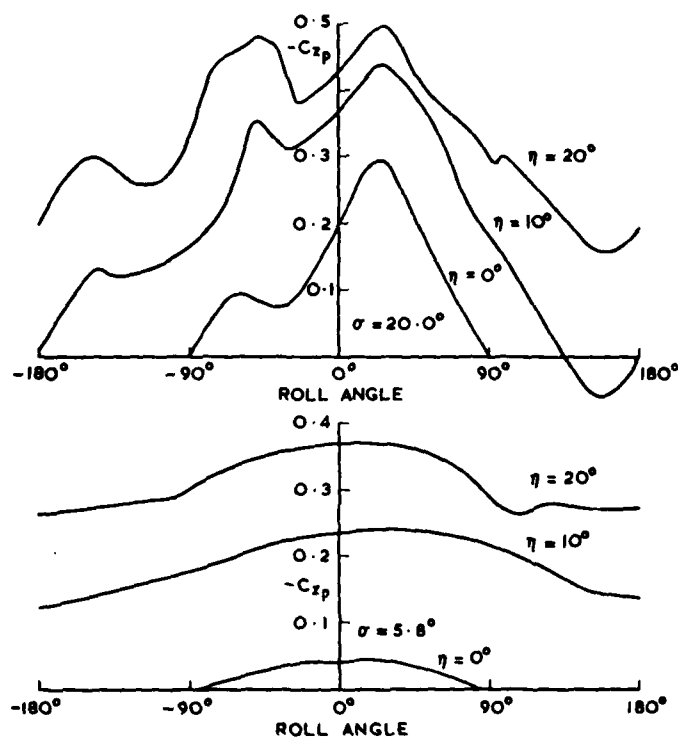


Fig 10 Control panel normal force: variation with roll angle,  $M = 0.6$

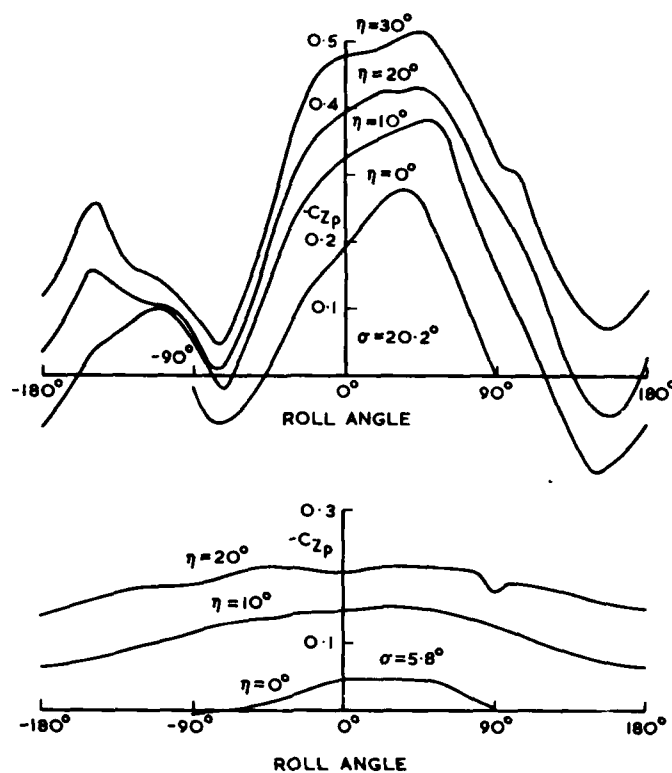


Fig 11 Control panel normal force: variation with roll angle,  $M = 2.0$

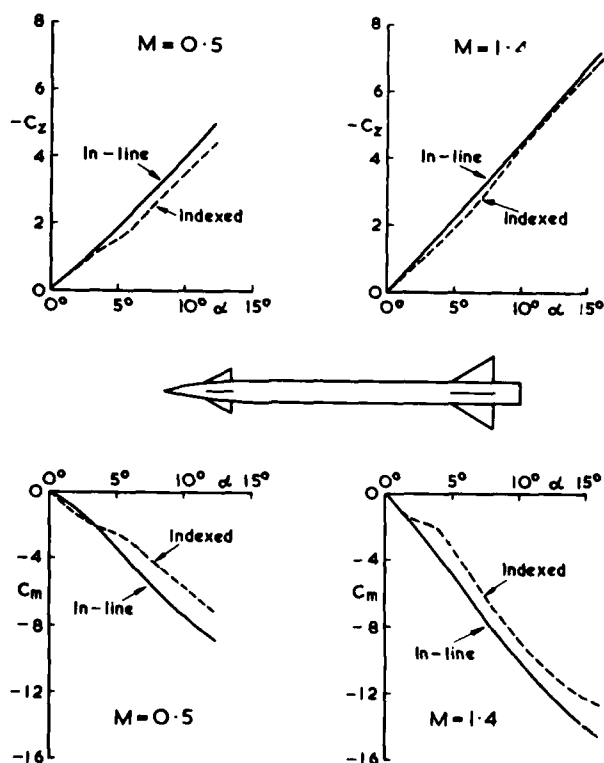


Fig 12 Comparison of normal force and pitching moment with in-line and indexed tail surfaces

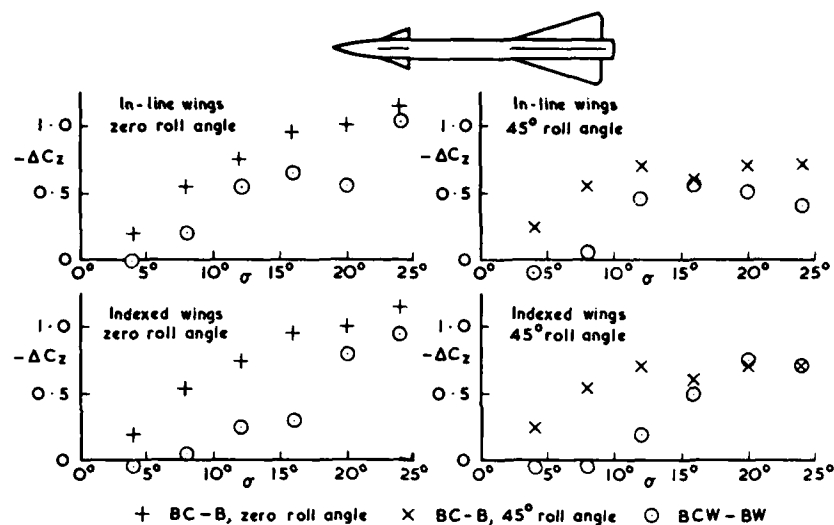


Fig 13 Derived normal force on canard controls, with and without rear wing: controls undeflected

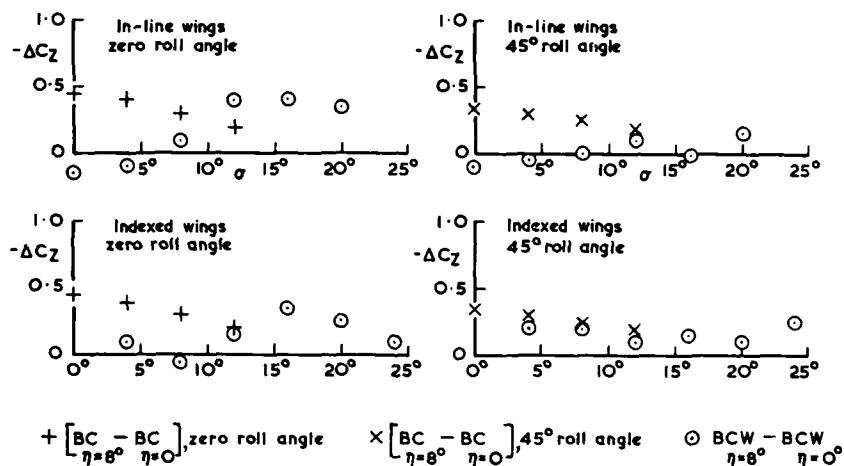
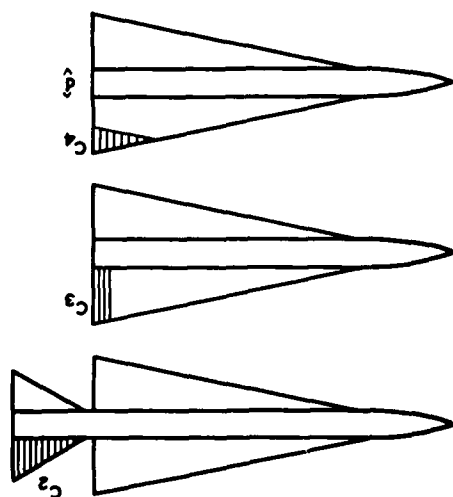


Fig 14 Derived normal force due to deflecting canard controls by 80°, with and without rear wing



$$(\text{Area of control}) \times (\text{distance from centroid to body centre line}) = 1.875 d^3$$

$$C_2 : \text{Panel area} = 1.875 d^2$$

$$C_3 : \text{Panel area} = 1.279 d^2$$

$$C_4 : \text{Panel area} = 0.908 d^2$$

Fig 15 Models with various control geometries

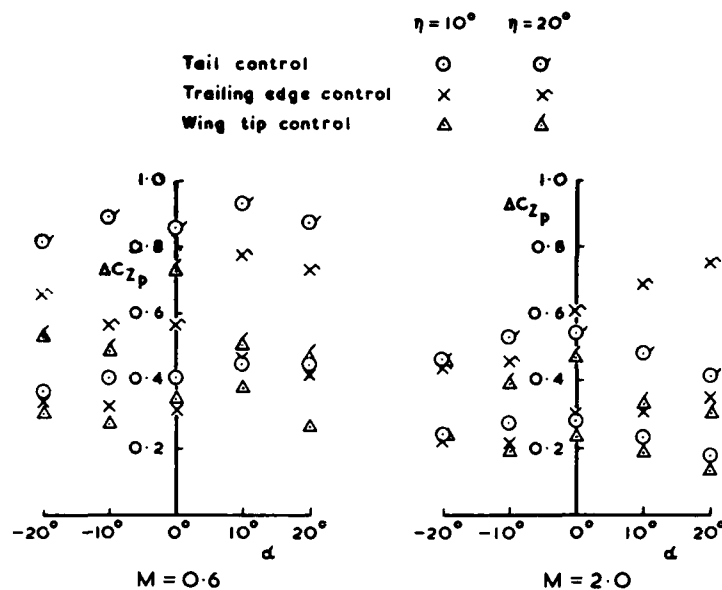


Fig 16 Control panel normal force coefficient based on panel area

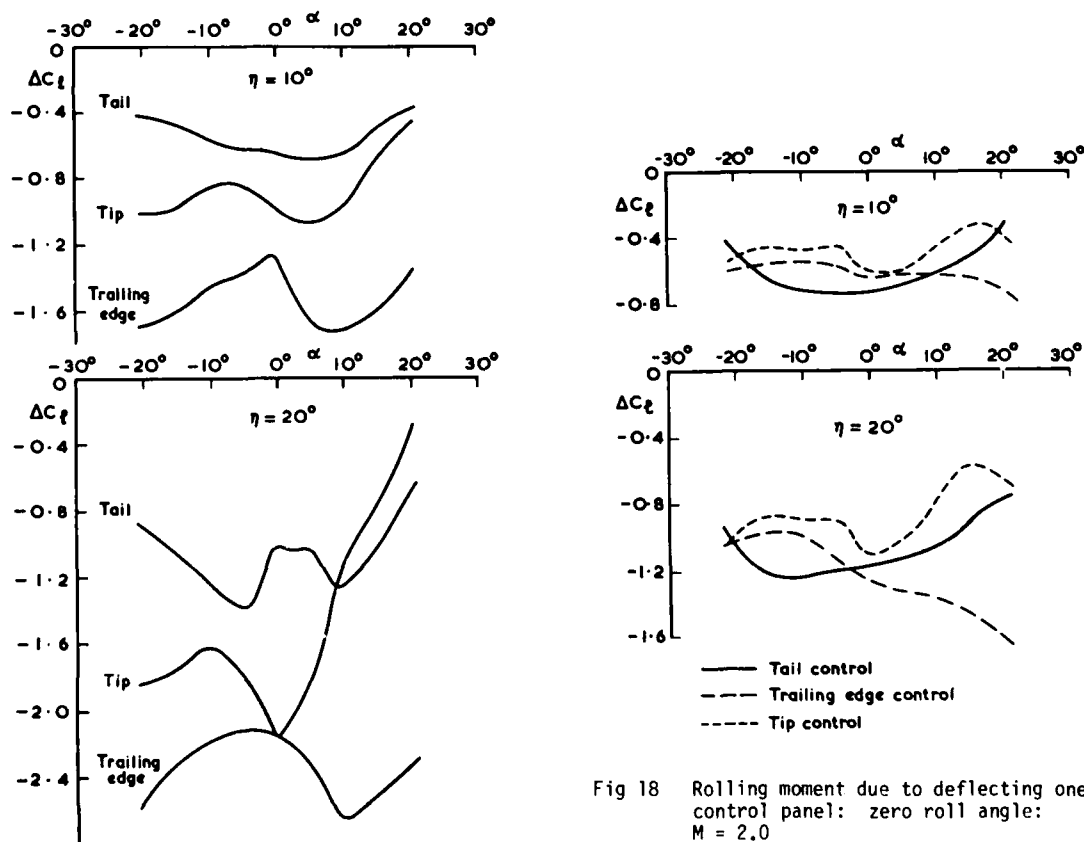


Fig 18 Rolling moment due to deflecting one control panel: zero roll angle:  $M = 2.0$

Fig 17 Rolling moment due to deflecting one control panel: zero roll angle:  $M = 0.6$

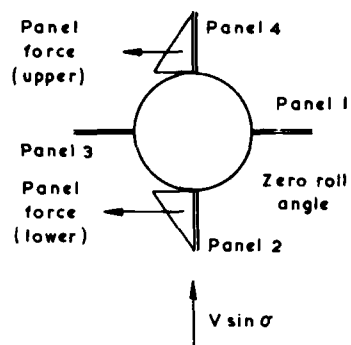


Fig 19 Differential force on upper and lower control panels

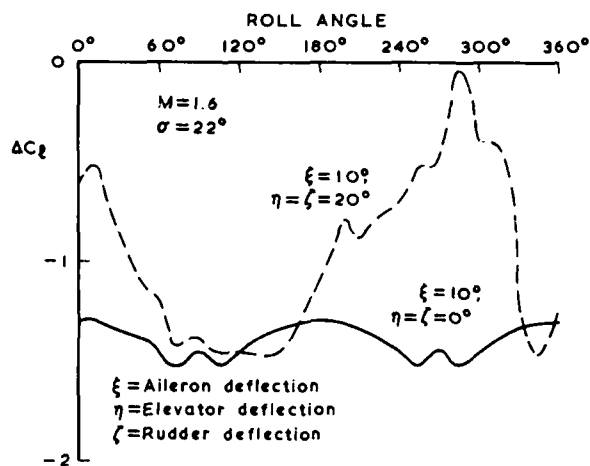


Fig 20 The effect of elevator and rudder deflection on roll control

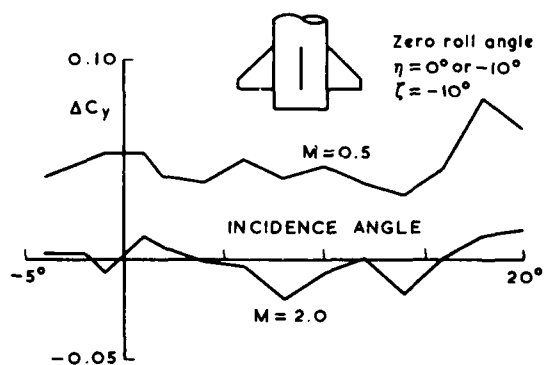


Fig 21 Change in yaw control force ( $\Delta C_Y$ ) due to  $10^\circ$  elevator deflection

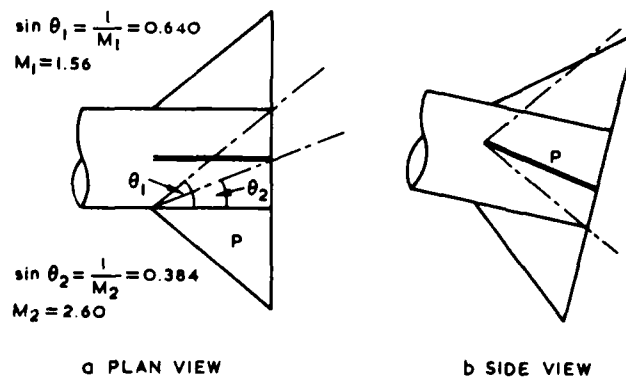


Fig 22 Geometry of panel-to-panel interference

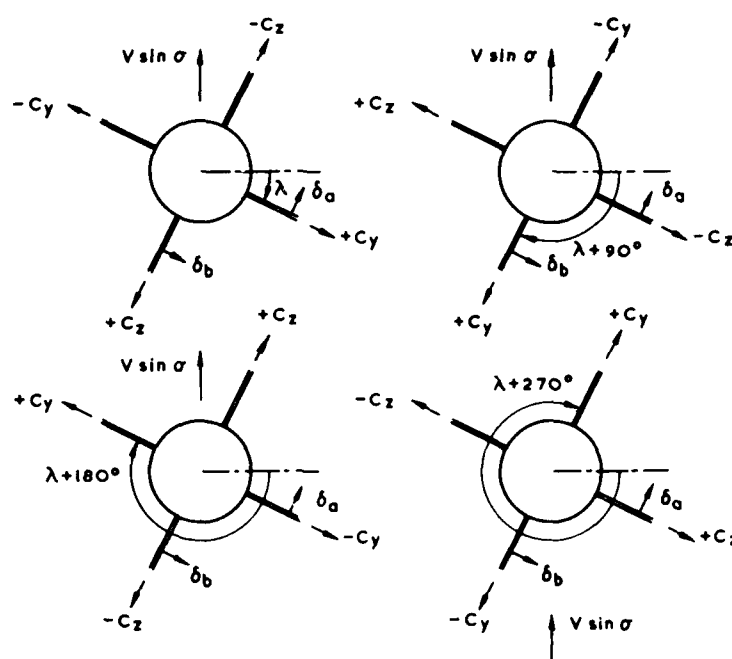


Fig 23 Symmetry relationships

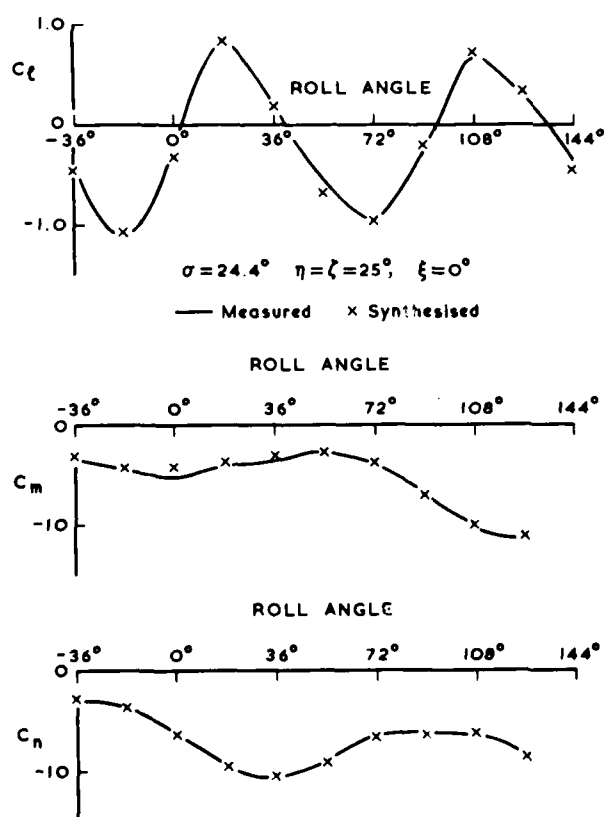
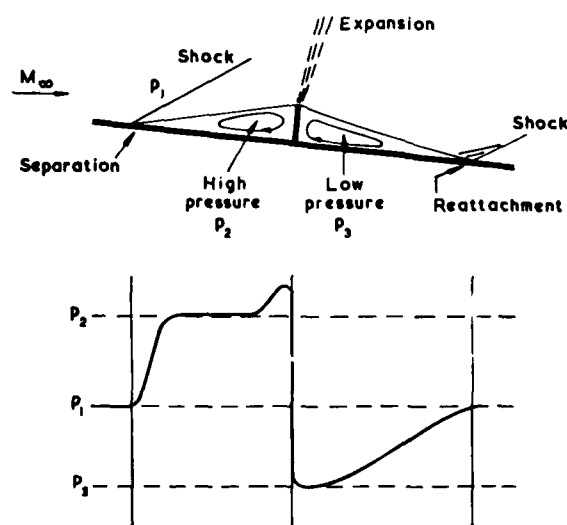
Fig 24 Comparison of measured and synthesised moments,  $M = 1.55$ 

Fig 25 Flow picture and static pressure near a spoiler on a flat plate (Ref 16)



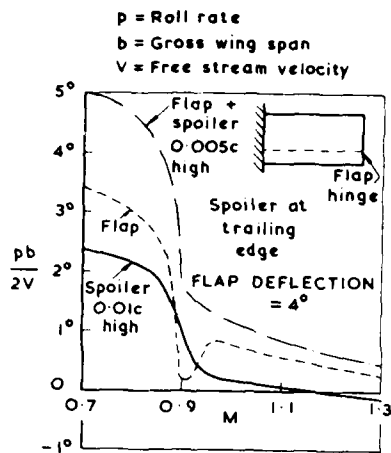


Fig 26 Roll effectiveness of a spoiler and flap at transonic speeds (Ref 17)

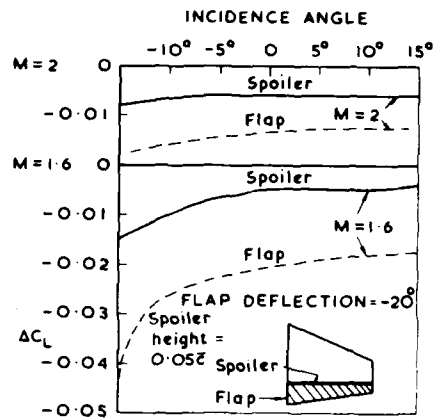


Fig 27 Lift increment due to a spoiler and flap at supersonic speeds (Refs 18 and 19)

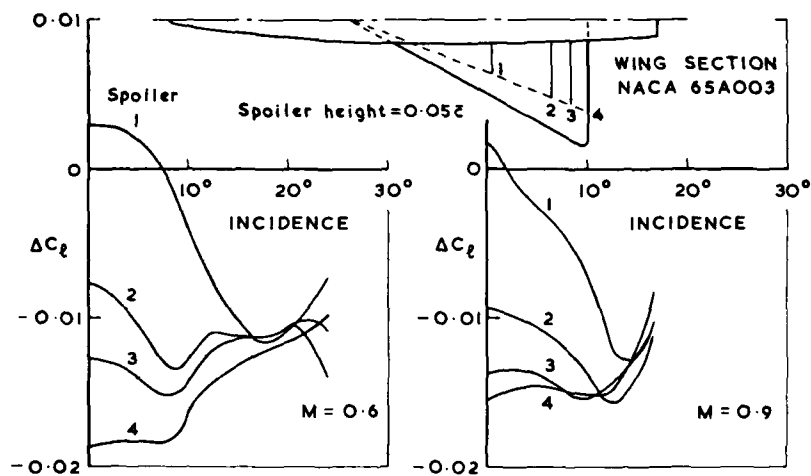


Fig 28 Change in rolling moment due to various spoilers on a delta wing (Ref 20)

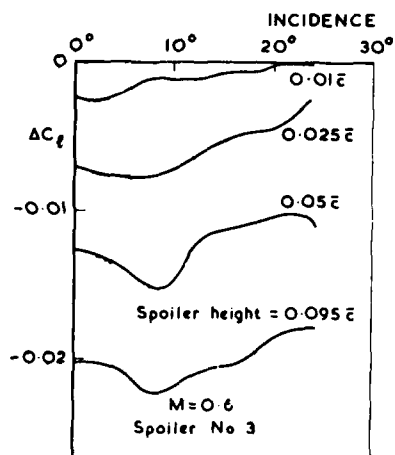


Fig 29 Effect of spoiler height on change in rolling moment (Ref 20)

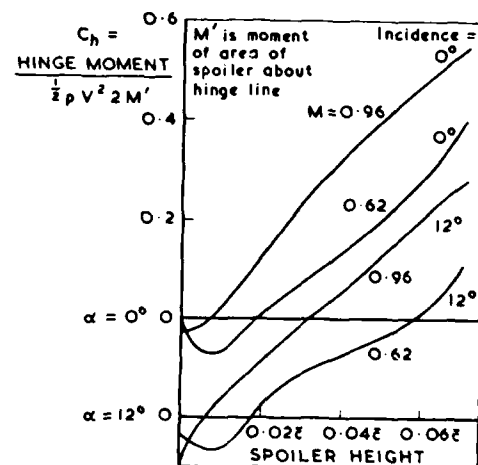


Fig 30 Hinge moments of flap-type spoiler on a delta wing (Ref 21)

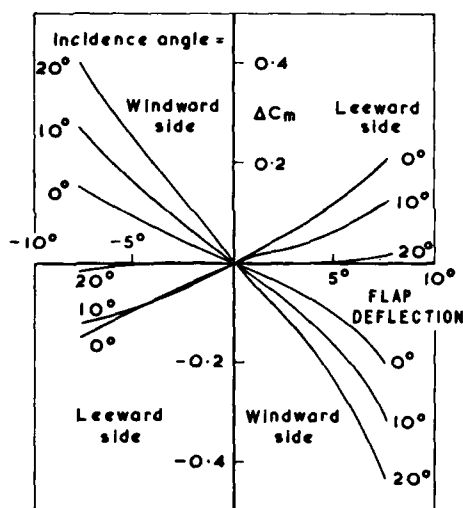
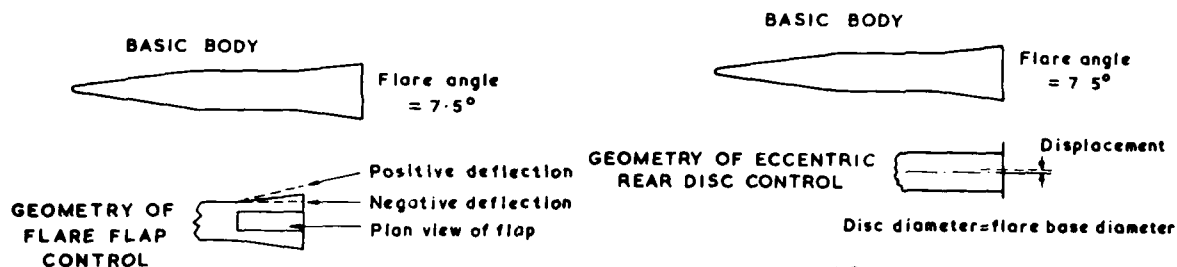


Fig 31 Change in pitching moment due to flap flare deflection,  $M = 4.3$  (Ref 22)

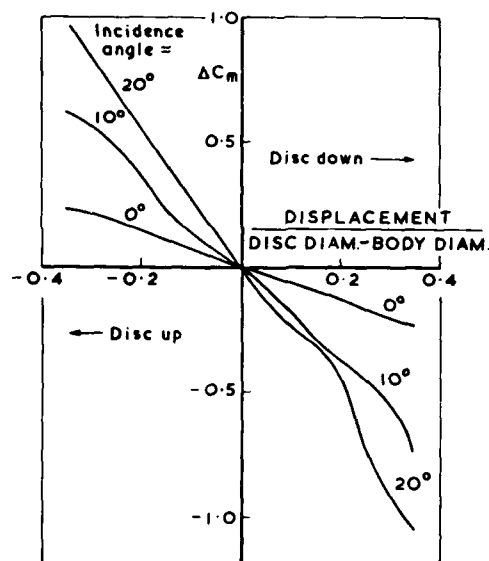


Fig 32 Change in pitching moment due to displacement of eccentric rear disc,  $M = 4.3$  (Ref 22)

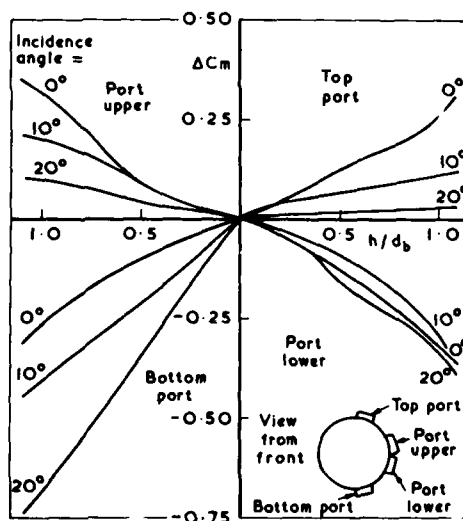
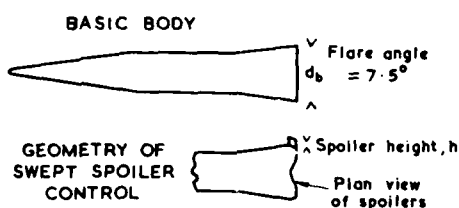


Fig 33 Change in pitching moment due to individual swept spoilers,  $M = 4.3$  (Ref 22)

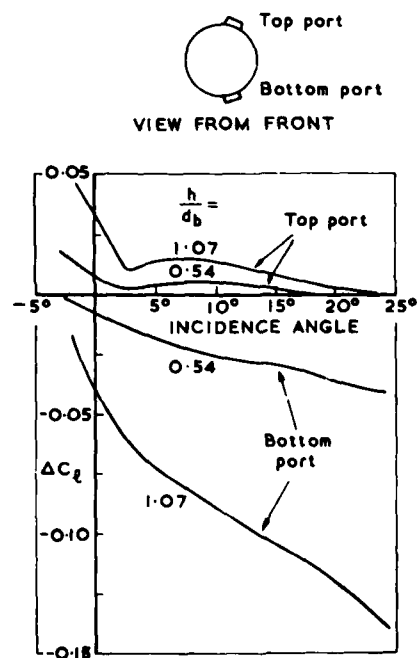


Fig 34 Change in rolling moment due to individual swept spoilers,  $M = 4.3$  (Ref 22)

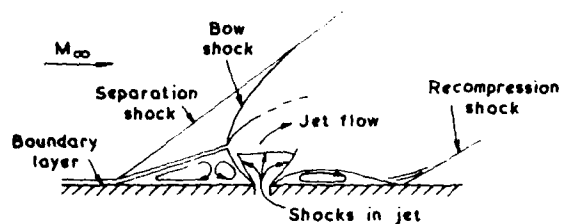


Fig 35 Typical flow pattern of two-dimensional sonic or supersonic jet in a supersonic stream (Ref 23)

#### AMPLIFICATION FACTOR

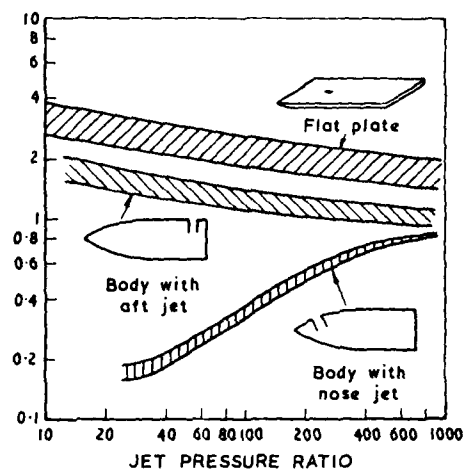


Fig 36 Amplification factors for sonic jets in a supersonic stream (Ref 24),  $2.4 \leq M_\infty \leq 4.5$

#### AMPLIFICATION FACTOR

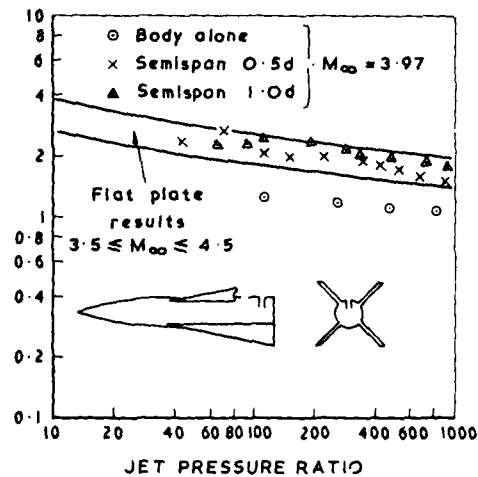


Fig 37 Effect of adjacent surfaces on amplification factor (Ref 24)

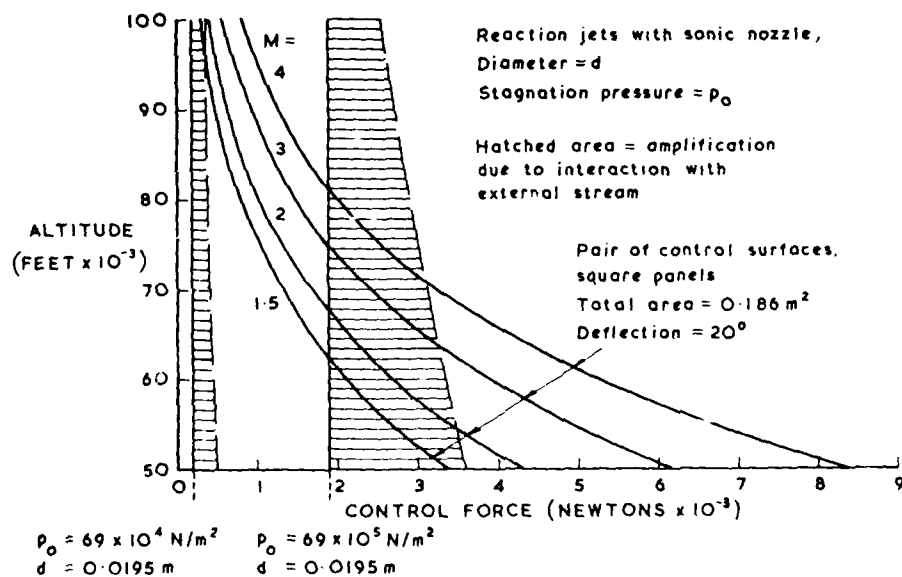


Fig 38 Comparison of deflected surface control and jet reaction control

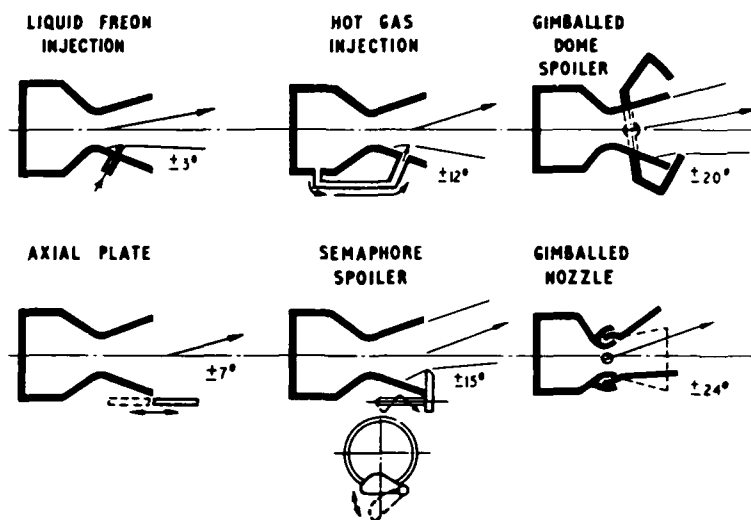


Fig 39 Some thrust vector control systems

Type	Maximum deflection	Motor thrust (pounds)	Motor temp	Notes
Liquid freon injection	$3.5^\circ$	7000	3800°K	4 valves, bang-bang
Sliding plate	$8^\circ$	8000	3800°K	4 actuators, bang-bang 100 pounds x 3 inches
Flexible nozzle	$8^\circ$	8000	3800°K	2 actuators, 2500 pound inches
Gimballed nozzle, bellows seal	$8^\circ$	6300	2880°K	2 actuators, 300 pound inches
Hot gas injection	$12^\circ$	3800	2750°K	4 valves, bang-bang
Semaphore spoiler	$15^\circ$	2200	2800°K	4 actuators, 40 pound inches each Thrust loss = 20-22%
Dome spoiler	$20^\circ$	2200	2800°K	2 actuators, 130 pound inches Thrust loss = 10-12%
Gimballed nozzle	$24^\circ$	2200	2800°K	2 actuators, 170 pound inches

Fig 40 Summary of some TVC systems

## STORE SEPARATION

Charles B. Mathews

AIRCRAFT COMPATIBILITY BRANCH

Air Force Armament Laboratory

Eglin AFB, Florida 32542

1 Introduction

Aircraft mission effectiveness and survivability are highly dependent upon the ability to carry and deliver air-delivered weapons with minimum penalty to speed and maneuvering performance. The consequences of high aerodynamic drag of external stores is quite obvious and has been aptly discussed in many publications; however, aerodynamic drag is not the only consideration. Perhaps more serious, and generally more common, is the necessity to place even more restrictive operating limitations on certain aircraft weapon combinations because of dangerous store release or jettison characteristics. These problems can be avoided, or significantly reduced, by proper aircraft and store design. During most of the past aircraft developments, aircraft design has usually been centered about roles other than air-to-ground weapon delivery. The F-101, F-4, and F-105 are classic examples. Consequently, this has often resulted in many compromises of air-to-ground weapon delivery capability. The ability to properly establish weapon system design criteria depends upon the development and use of accurate and reliable methods of predicting store trajectories. Experience has shown that the proper use of accurate predictive methods will not only result in increased delivery capability and enhance the safety of weapon delivery and jettison during flight testing or operational employment, but considerable savings of time and money can also be realized. Aircraft and store designs can be thoroughly investigated using analytical and wind tunnel models, and readily changed as necessary, prior to production or the fabrication of costly full scale prototypes. Store certification flight test programs can be considerably reduced by conducting a comprehensive wind tunnel test program and reducing the expensive full scale flight tests on the basis of wind tunnel and flight test correlation. Applying this philosophy to the USAF A-7D store certification program resulted in a documented savings of over \$16,000,000 (ref. 1). This chapter will comment on the significant parameters affecting store trajectories, describe some of the analytical and experimental techniques used to predict store separation trajectories, give examples of previous problems and their solutions, suggest methods for improving store separation and jettison characteristics, discuss the relationship of store separation perturbations to weapon delivery accuracy, and recommend attractive areas for additional research. To supplement this chapter the reader is referred to the excellent AGARD report on Store Separation by In Leon Gehring (ref. 2).

2 Factors in Store Separation2.1 Store Separation Categories

The store separation problem can be basically divided into three categories depending upon the type of store. The first category will be referred to as the Launch Problem. This involves the class of stores such as fuel tanks, gun pods, and racks complete with weapons, etc. which are released from an aircraft during normal operations, with the primary motive being safe separation. The second is the Delivery Problem which involves those stores such as unguided conventional dispenser munitions released in a package for the purpose of hitting a target. This problem not only requires that the item separate safely from the aircraft, but also requires a relatively unperturbed release for good delivery accuracy. The third is the Launch Transient Problem which is far more difficult to handle. It involves items such as direct attack electro-optical guided bombs which are released before launch. Typically these weapons have controls which are designed to avoid target breaklock due to release perturbations. Normal release is a danger to the launch aircraft, either in a jettison or a release situation, with active controls. The danger of these stores is separation due to abnormal control deflection soon after release which could result in a collision with the launch aircraft. As a result, flight control systems must be designed to handle these stores for this type of store.

The criteria for satisfactory store separation is that the store must clear the empty fuel tank causes no concern provided it is released within the desired jettison envelope. Obviously, this is not the case for a weapon designed for accurate delivery. The criteria for such solutions will be given in paragraph 2.2.

2.2 Store Separation Parameters

There are many parameters that affect store separation. These are depicted in Fig 1. Store separation is a highly coupled and repeat with each other.

out in the previous paragraph, different criteria exist for each category of the store separation problem, and the above parameters play roles of varying importance in each of these categories.

In general, stores having high density, high inertia, and high aerodynamic stability will exhibit the most desirable separation characteristics. It is not always practical to design stores with these characteristics as mission requirements can have a significant impact on external shape and mass properties. For example, a high density empty fuel tank would impose an impossible weight penalty on the aircraft with the fuel tank in the full configuration, or it would be extremely costly, and impractical, to design a rocket launcher (both full and empty) to the specifications of high density, high inertia, and high aerodynamic stability. Fortunately, when one or more parameters are compromised it may not be disastrous, for other parameters can often be adjusted to adequately compensate for those that were compromised. It is the often necessary compromise of these desirable characteristics that creates the problem and the requirement for fast and accurate store separation prediction techniques and facilities.

There has been much work done to study the effect of each parameter on the trajectory of a store. Reference 3 is an example of a comprehensive parametric study where the basic equations of motion were examined to study the significance of various parameters on both stable and unstable stores. The results were compared with trajectories generated in a wind tunnel and with full scale flight tests. Reference 4 is another example of a parametric study involving the F-14 and Phoenix missile. Again, it is emphasized that store separation parameters are highly coupled, and the variation of each plays a different role in each case. In general, however, these reports and other evidence support the following conclusions:

1. The most significant parameters are store stability, the bomb ejector rack induced moments, the aircraft flow field (function of Mach number and aircraft attitude) and the aircraft acceleration at release.
2. The effects of bomb rack ejection force, store weight and dynamic pressure are secondary and approximately the same for aerodynamically stable stores. These effects become more important as store stability decreases.
3. Store moments of inertia are relatively unimportant for aerodynamically stable stores but become more important as store stability decreases.
4. Flight path angle effects are normally small except for longitudinal store displacement; however, at the higher dive angles the store will remain in the disturbed aircraft flow field longer, thus flow field effects will be magnified.
5. Multiple, ripple releases are more critical than single releases because of mutual interference effects of the weapon immediately after release, reduction of ejection force due to multiple rack flexibility, and the increased probability of store to store collision.
6. Aerodynamic damping effects are relatively unimportant; however, in some rather special cases, for large or very heavy stores, the change in the store aerodynamic damping that can be induced by the motion (oscillation) of the parent aircraft may be large enough to cause significant effects on the flight behavior of the store (see refs. 5 and 6).

#### 2.2.1 Bomb Ejector Racks

No article on store separation is complete without at least a brief comment on bomb ejector racks. For the purposes of store separation, there are basically two types of bomb ejector racks in common use, those with single ejection pistons, and those with dual ejection pistons. Typical racks are shown in Figs. 2 and 3. The latter usually have orifices which are ground adjustable to meter the flow of ballistic gas from the ejection cartridges to the ejection pistons. This feature permits the force of each ejection piston to be independently varied from completely closed to full open. Thus, the ejection moment, and force, imparted to the store can be controlled throughout a considerably wide range. These ejector racks are referred to as "tunable" racks and are far superior to the single ejection piston rack, especially those with low ejection impulse. Figure 4 shows a comparison of the impulse performance between typical ejector racks of these two types.

The Triple Ejector Rack (TER) and Multiple Ejector Rack (MER) currently used in the United States are shown in Figs. 5 and 6. The US versions of these multiple carriers are presently equipped with bomb ejector racks having single ejector pistons (Fig. 2) and low impulse (Fig. 4). The United Kingdom version of the TER is similar but contains "tunable" dual ejector racks with high impulse. The stores carried on the bottom stations are ejected down, and the stores carried on the shoulder stations are ejected down and out at approximately 45 degrees. The problems associated with single piston racks and the advantages of the dual ejector will become highly evident in paragraph 5.4.1.2.

One of the big deficiencies in predicting accurate store trajectories is the lack of accurate bomb rack ejection data. Performance curves such as Fig. 4 are normally acquired at a ground based static ejection test stand and are used without

correction for temperature, store aerodynamic loading, and dynamic and elastic effects of the racks/pylons/wings. Adequate guidelines do not exist for correcting static bomb rack ejection data. The only known proposed procedure is outlined in ref. 7 which relates flight test and static end-of-stroke ejection velocity as shown in Fig. 7. The variation in bomb ejector rack impulse, and consequently store ejection velocity, due to MER flexibility can also be quite significant. Figure 8 from ref. 8 shows this variation as four 800-pound (363 kg) M-117 bombs are sequentially ejected from an F-4 centerline MER attached to a MER adapter and rigid test stand. The expected impulse is obtained during release of the first bomb, but diminishes to practically zero when the last bomb is released with no mass remaining on the MER to assist the reaction. Even though a fairly low impulse cartridge was used, the forward cantilevered section of the MER deflected away from the bomb being ejected by 3.5 inches (8.89 cm) laterally and 1.3 inches (3.3 cm) vertically. Reference 3 also reached the conclusion that "Present knowledge of the ejector forces produced by aircraft release systems in the actual flight environment is not sufficient to permit an accurate and detailed comparison of flight and wind-tunnel-generated trajectories using ground static calibration ejector data alone." References 9 thru 13 are excellent reports on bomb ejector racks and their contributions to store separation. The M. L. Aviation Company (UK) now has a contract to develop a bomb ejector rack test rig with a variable stiffness mounting to simulate torsional and flexural stiffness, damping frequency and so on.

### 2.2.2 Aircraft Flow Field

As concluded in ref. 3, the interference flow field about a store laden aircraft may be the most important parameter governing store trajectory. It is normally quite curvilinear in form and varies with aircraft, store, store position, adjacent stores, flight conditions, and aircraft attitude. Figure 9 shows the velocity components in various lateral planes measured about three M-117 bombs on a TER on the inboard wing station of an F-4 at 0.85 Mach (from ref. 14). Attention is directed to the large downwash at the nose of the weapon on the bottom station (approximately 200 ft/sec or 61 m/s) and the large upwash at the tail (approximately 100 ft/sec or 30 m/s). This typical flow characteristic produces an extremely large nose down aerodynamic pitching moment on large diameter 16 inch (41 cm) stores at higher Mach numbers and results in unsatisfactory trajectories for many weapons. This problem and possible solutions will be discussed in detail in paragraphs 5.3.4 and 5.4.1. Figure 10 shows the same results from a wind tunnel oil flow test conducted at the United States Air Force Academy.

The flow field about an F-4 does not always produce nose down moments. Figure 11 shows the variation in pitching moment coefficient as a large unstable store is translated vertically downward from its installed position on the inboard wing station of the F-4 aircraft. Also depicted in this figure are the highly significant and typical variations in the flow field (represented by variations in the pitching moment coefficient) with Mach number and aircraft angle of attack.

The use of the above type of experimental data to predict store trajectories will be discussed in detail in paragraph 3.2.2.

## 3 Store Separation Prediction Methods

There are basically two classes of methods commonly used to predict store separation trajectories. These are the purely theoretical techniques and various techniques based on the use of wind tunnel data. Each method has its own utility, and the decision as to which method, or methods, to use for a given problem must be made on the basis of the problem itself.

### 3.1 Theoretical Prediction Techniques

The theoretical techniques are difficult to apply and limited in application because of the lack of adequate transonic theory. They may, however, be used within their realm of applicability for studies of noncritical problems, to explain certain phenomena and in conjunction with wind tunnel test programs to reduce the scope of experimental effort. Reference 15 is an excellent report which compares theoretical techniques and experimental wind tunnel techniques to full scale flight test data. At this time, however, the wind tunnel is the only reliable store separation prediction technique that can be used with confidence throughout the flight regime of our present day tactical aircraft. This paper will address only the wind tunnel techniques.

### 3.2 Wind Tunnel Testing Techniques

There are essentially four major experimental techniques used today to predict store separation trajectories. They are the Captive Trajectory System (CTS), grid, flow angularity, and freedrop. Each has its advantages and disadvantages and the best method or combination of methods depends upon the individual problem. The first three of these techniques can best be employed by using the automated CTS rig, but off-line methods can be used if necessary. The CTS is generally considered the most versatile and accurate of the prediction methods and is often used as a base line for comparison of other techniques. The first two make use of the automation of the CTS rig for data acquisition; however, different types of data are acquired and in both cases the store trajectories are run at a later time rather than on-line as part of the wind tunnel test. The following paragraphs will briefly describe the four methods mentioned above, and discuss their advantages and disadvantages.

### 3.2.1 Captive Trajectory System (CTS)

The principle of the CTS is basically the same for all wind tunnels having this capability. The following extraction from ref. 16 describes a typical CTS.

The CTS is used primarily for the trajectory analysis of air-launched stores and is, in effect, a separation simulator which uses the wind tunnel as an analog function generator for the store's aerodynamic forces while the store is in the flow field of the parent aircraft. A typical installation is shown in Fig. 12. The CTS hardware consists of a six-degree-of-freedom store-model support system controlled by a closed-loop digital computer system which solves the equations of motion using the measured aerodynamic forces, mass, inertia, and other characteristics of store launch. The parent model is supported, inverted for convenience, from the tunnel's main support system at the desired angle of attack. The store, supported on the captive sting, instrumented with an internal six-component balance, and supported by the CTS, is removed a safe distance from the model until test conditions are established. The store is then moved to the launch position.

Initiation of the trajectory cycle causes the computer to read the tunnel conditions and store loads, convert the data to engineering units, and solve the equations of motion using the full scale (or other) mass, inertia, center of gravity, etc., applicable to the particular store being tested. The computer then commands the CTS to position the store to the computed location and orientation corresponding to post launch time and, in addition, predicts the store aerodynamic loads at that location. During the next data cycle, which is now initiated automatically, the computer compares the actual location with that requested and the measured loads with those predicted. If either the store position or measured loads are not within specified tolerances, appropriate adjustments are made automatically. The load prediction technique not only serves as a rejection mechanism for spurious data but also allows for an automatic adjustment of the trajectory step size. If the measured and predicted loads are not in agreement, the data are rejected and the step size is reduced by a factor of two. If the measured and predicted loads are in agreement for a number (typically six) of consecutive successful predictions, the interval is increased by a factor of two. The interval length is bounded by an arbitrary value which insures that sufficient points are taken to establish the trajectory. The total time for a complete data cycle is between three and six seconds. The time required for a complete trajectory encompassing one second actual flight time is less than 10 minutes.

Figure 13 shows a block-diagram of the CTS to be installed at the end of 1976 in the ONERA 1.76 x 1.75 m<sup>2</sup> transonic/supersonic wind tunnel S2 at Modane, France. The complete system is monitored by a digital computer and is typical of other CTS facilities.

#### 3.2.1.1 CTS Facilities

There are five known active CTS facilities in the United States. Two of these are located at the Arnold Engineering Development Center (AEDC) and are used with the four-foot (1.2 m) transonic wind tunnel (4T) and the AEDC Von Karman Facility (VKF) supersonic tunnels A, B, and C. Figure 12 shows the 4T CTS and ref. 17 provides more detail of the system. Figure 14 is a schlieren of a supersonic grid test of a MK-84 bomb released from the F-4 aircraft which shows the VKF CTS. The Schlieren was taken in the VKF Tunnel A which has a model injection system. This system allows the sting/model to be moved from the test section to a lower chamber for model configuration changes, etc., while the tunnel is in operation. Note the complicated flow field and shock wave patterns associated with the supersonic problem. More details of the VKF CTS can be obtained from ref. 18. The third active US government CTS system is located at the David Taylor Naval Ship Research and Development Center (DTNSRDC). The installation is in the 7 x 10 foot (2.1 x 3.0 m<sup>2</sup>) transonic wind tunnel and is depicted in Fig. 15. Additional details are to be found in ref. 19. The other two active systems located in the US are used in the Vought Aeronautics Company four-foot (1.2 m) high speed wind tunnel which is depicted in Fig. 16 and the Calspan Corporation eight-foot (2.4 m) transonic wind tunnel, Fig. 17. Additional details of these systems can be found in refs. 20 and 21.

The Aircraft Research Association, Ltd. (A.R.A.), Bedford, England, and the Office National d'Etudes et de Recherches Aérospatiales (ONERA), Paris, France, have both developed excellent facilities. Figure 18 depicts the A.R.A. system, referred to as a two-sting rig (T.S.R.), to be installed in their 9 x 8 foot (2.7 x 2.4 m<sup>2</sup>) transonic wind tunnel. The T.S.R. has been designed to be slender for transonic use and portable for installation in other tunnels of comparable size. The rig is suitable for use with complete parent aircraft models of about 1/8th full scale and with half models of about 1/4 scale; the relatively large size of store models considerably eases balance installation and model distortion difficulties. Further details are given in Refs. 22 and 23. The six-degrees-of-freedom are achieved by a double roll system for the vertical and lateral movements, with a third rotation/translation unit to provide roll re-orientation and longitudinal movement. The store pitch, roll and yaw angles are achieved by means



of a unit at the forward end of the translation sting. The position of the store relative to the parent aircraft model will be measured by a novel system using an upstream television camera.

Figure 19 shows schematically the mechanical system of the ONERA CTS rig to be installed in the ONERA 1.76 x 1.75 m<sup>2</sup> transonic/supersonic wind tunnel (S2). An arm with two hinges, each with two degrees of freedom, allows for vertical and horizontal motions along with missile angles of attack and yaw; then a dual roll rotation system ahead of the missile support, and a longitudinal motion at the rear part, achieve the required six-degrees-of-freedom. The rig is typical in that it can be used either for the captive trajectory method or for the grid method.

### 3.2.1.2 CTS Advantages

1. The CTS is generally considered quite accurate. Experience has shown excellent agreement with full scale flight test data. The AEDC CTS was used for the USAF A-7D store certification program mentioned in the Introduction. It is the primary technique used by the USAF for store separation programs and throughout the years has resulted in enormous savings of USAF resources through enhancing flight safety and reducing costly flight test time.
2. Store trajectories are conducted on-line as the wind tunnel operates. Data is obtained instantly, permitting immediate corrections or changes, if necessary.
3. CTS is relatively fast. The same number of equivalent trajectories require much less wind tunnel time than freedrop. This is especially true for continuous flow wind tunnels not equipped with model injection systems where much time is lost when the wind tunnel is stopped only for single store model replacement.
4. Only one CTS captive sting store model is required for testing of a given store. The store models are simple and do not have to be dynamically scaled as is the case for freedrop models.
5. Depending on computer software, the CTS can be used to simulate store trajectories where the aircraft released the store while in a dive/climb or accelerated flight.

### 3.2.1.3 CTS Disadvantages

Facilities operating captive trajectory systems are continuously conducting research and study programs directed toward improving the accuracy and expanding the capabilities of their system. Improved software and integration schemes are constantly being developed for new on-line computers which are faster and have increased storage capacity. References 23 thru 27 outline in detail some of the deficiencies in the system which have been noted throughout the years. Some of the general disadvantages are:

1. Weapon trajectories are often relatively short in duration because of the physical movement limitations of the CTS support structure and/or the balance limits of the captive model. Unstable stores that rotate rapidly and tumble are especially a problem. However, this has been significantly improved by the use of bent stings such as the one depicted in Fig. 12.
2. Once a trajectory is run for a given set of parameters, the trajectory data may become invalid if the mass, inertia, center of gravity, bomb rack ejection forces/moments, or any other physical properties are significantly changed. However, the interference coefficients may be extracted from the CTS data and used in a similar manner as grid data.
3. The captive sting or dual support method may require alteration to the store afterbody to accommodate the sting and also raises the question of sting effects on the store loads (Fig. 20). The results of extensive investigations to answer these questions are contained in refs. 23 thru 27. The investigations concluded that the effects of the support sting and store afterbody distortion are small. The investigations also concluded these effects were often insignificant, opposite in trend and tended to cancel each other. The case of neutrally stable stores was not investigated and these conclusions may not apply.
4. Only single releases can be investigated. Multiple, ripple, and salvo releases are not yet practical using CTS.
5. The feasibility of obtaining CTS trajectories of MER/TER jettison with attached stores has not been proven. Asymmetry in these configurations and the small size of the MER/TER beam make balance location and proper loading extremely difficult.
6. At this time on-line computing capability and/or the difficulty of modeling small scale control surfaces make some of the CTS facilities impractical for simulating trajectories for guided weapons having active autopilots and controls during release. However, in some cases the autopilot equations and the aerodynamic control effectiveness can be incorporated into the CTS computer program to provide a complete simulation.

7. Effective flow angles due to the release velocity of the store are not accounted for.

8. The present touchwire system used in the AEDC 4T facility (Fig. 21) has not always resulted in good alignment of the store in its proper carriage position. Touchwires are small electrical contacts that provide signal indication that the store is in the proper position. Vibration of the aircraft and/or store models contribute to this problem, and often the store must be displaced several inches full scale from the proper carriage position to start the trajectory. Figure 11 shows the dependence of the load gradients on the store vertical displacement. These gradients for the pitching moment are very severe near the carriage position. Touchwire gap and store alignment may be a major source of error as indicated in ref. 24.

One promising solution which is in development but has seen limited testing in the AEDC 4T tunnel is optical alignment. This method utilizes an infrared source and receiver in the aircraft model pylon as a doppler for precise measurement of store to pylon distances. This is an attractive area for additional research.

### 3.2.2 Grid

In this technique the grid data is normally obtained in the wind tunnel using a CTS rig. Ideally, the CTS is programmed to automatically traverse the store model through a given volume in the vicinity of the carriage station of interest and the aerodynamic loads on the store are measured at discrete points. The store may also be pitched, yawed, and rolled at these discrete points. The data is then incorporated in a six-degree-of-freedom trajectory program, and the aerodynamic forces and moments for the Euler equations of motion are retrieved according to the store's position and attitude relative to the aircraft. Figure 22 is a block diagram of a typical, modular six-degree-of-freedom computer program for trajectory analysis.

For a given configuration, the aerodynamic loads acting on the store in the vicinity of the aircraft are functions of Mach number and aircraft attitude as well as the store vertical, lateral, and longitudinal positions and pitch, yaw, and roll attitude. To acquire a comprehensive set of grid data accounting for all of these variables would result in an extremely lengthy wind tunnel test program as well as a computer program that requires a large amount of storage and run time. Reference 28 concluded that the interference coefficients varied considerably more with vertical displacement than with lateral or longitudinal displacement and that rotations in pitch, yaw, and roll at various points in the grid have a minimal effect on interference. Figure 23 shows plots of normal force and pitching moment coefficients versus store angle of attack at various yaw angles for an M-117 bomb in an aircraft interference flow field.  $C_N$  and  $C_M$  are rather insensitive to yaw angle, and the static stability derivatives ( $C_N$  and  $C_M$ ) are constant throughout the interference flow field. Thus the interference effects do not appear to be strong functions of store attitude. This suggests the use of a "limited grid" where data is taken only as a function of vertical displacement (and, of course, Mach number and aircraft attitude). The elimination of lateral and longitudinal data points at various store attitudes considerably reduces the required wind tunnel time and data handling requirements. Experience has proven this approach quite accurate for most store separation problems.

Figure 11 shows a strong dependence on Mach number and aircraft attitude. Reference 29 reports good correlation with freedrop using a "limited grid" of vertical displacement and store pitch at discrete points. It also supports the above argument; however, the variation in store incidence angle was limited to a range of  $+4^\circ$  and  $-4^\circ$ . Reference 30 reports on separation studies for three guided weapons where the interference coefficients were obtained only as functions of Mach number, aircraft attitude, and vertical translation. In all cases excellent correlation with CTS and full scale flight tests were obtained (see paragraph 5.7.1) indicating the importance of the initial (installed) aerodynamic loads and that good results can be obtained with "limited grid" data. Also, ref. 15 reports excellent results when "limited grid" is compared to full scale flight test, and ref. 19 reports on the use of the limited grid technique to investigate separation problems with a US Navy gun pod.

#### 3.2.2.1 Grid Advantages

1. Assuming data is obtained only for variations in Mach number, aircraft attitude and store vertical displacement, the "limited grid" technique requires less than half as much wind tunnel time as CTS to cover the same release conditions.

2. Grid is more general than CTS and freedrop but not as general as flow field. Once the data is obtained unlimited trajectories may be run for that store and aircraft configuration to study the effect of various store mass properties and bomb rack ejection characteristics. It is well suited for store design work provided the store external shape and aerodynamic characteristics do not change significantly. Although not as general as flow angularity, it is quite valuable for trouble shooting during a flight test program where time is usually critical.

3. There are no trajectory limitations due to sting travel, balance loads or tunnel boundaries.

4. Grid conveniently can be used to simulate trajectories for guided weapons having active autopilots and controls during release.

5. Grid can be used to simulate store trajectories where the aircraft released the store while in a dive/climb or accelerated flight.

### 3.2.2.2 Grid Disadvantages

1. Trajectories are not conducted on-line and problems cannot be detected early in the program.

2. Grid has the same store positioning problems as CTS (paragraph 3.2.1.3).

3. Grid is subject to the same sting interference and modified store afterbody effects as CTS (paragraph 3.2.1.3).

4. Multiple, ripple, or salvo releases cannot be investigated.

5. Errors can result because of the vast amount of data acquired when other than a "limited grid" is obtained.

### 3.2.3 Flow Angularity

In this technique flow angularity data is collected in the wind tunnel using a velocity probe often attached to a CTS rig (Fig. 24) rather than a store model for direct measurement of the aerodynamic forces and moments. The CTS is programmed to automatically traverse the probe through a given volume, or plane in the vicinity of the carriage station of interest and measure the change in local angle of attack and sideslip ( $\Delta\alpha$ ,  $\Delta\beta$ ) at selected points (Fig. 9). Once the flow angularity data is obtained it can be used to calculate the interference aerodynamics using free stream body build-up data for the weapon. Using the pitching moment as an example:

The free stream pitching moment coefficient slope for the total store can be represented by:

$$C_{m_{\alpha}} = C_{m_{\alpha B}} + C_{m_{\alpha F}}$$

Where  $C_{m_{\alpha B}}$  and  $C_{m_{\alpha F}}$  are the free stream pitching moment coefficient slopes of the body and fin respectively.

The interference pitching moment coefficient is calculated by:

$$C_{M \text{ INT}} = C_{m_{\alpha B}} \cdot \Delta\alpha_B + C_{m_{\alpha F}} \cdot \Delta\alpha_F$$

Where  $\Delta\alpha_B$  and  $\Delta\alpha_F$  are  $\Delta\alpha$  values at the center-of-pressure of the body and fins of the store. The other coefficients are calculated in the same manner.

The flow angularity data is used in a six-degree-of-freedom digital computer program for trajectory calculations. New interference coefficients are calculated due to changes in  $\Delta\alpha$  and  $\Delta\beta$  as the store translates and rotates within the volume containing the interference data. They are combined with the free stream coefficients to obtain the total aerodynamic forces and moments acting on the store at each point in the trajectory.

$$C_{M \text{ total}} = C_{M \text{ INT}} + C_{M \text{ free stream}}$$

The aerodynamic forces are then combined with the physical forces such as store mass, ejection force, etc., and the Euler equations of motion are integrated with respect to time to obtain a point by point trajectory. The block diagram of Fig. 22 is also applicable to this technique.

There are basically two approaches to the flow angularity technique. The first, by Korn, is described in detail in refs. 31 and 32. In this approach the flow angularities are obtained with the store, whose trajectory is to be calculated, installed in the carriage position. The flow field of Fig. 9 is the one which would be used for the bottom store of the TER. It essentially assumes that the store is ejected down into the flow field that is measured below and around the store, and that this flow field does not change due to the presence of the store as the store moves through its trajectory.

In the second approach by Blase and Barnes (ref. 33), the flow angularities are obtained without the store whose trajectory is to be calculated. The initial store loads are calculated using the flow angularities measured along a line where the centerline of the store would be located if it were installed. It assumes that the flow field is generated only by adjacent stores and structure, and the store whose trajectory is desired is immersed in this flow field. It also does not account for flow field changes due to the presence of the store as the store moves through its trajectory.

The first approach does not permit measurement of the true flow field around the store because of obvious probe/store physical interferences. The second does not

account for the change in flow field due to the installed store, that is, mutual interference effects are not considered.

The main point is that neither of the approaches described above is correct and there is no known practical method of accurately measuring the flow field about a store laden aircraft. To date, however, the two approaches have not been evaluated against each other and other techniques in a systematic manner. Additional research in this area is highly recommended.

In spite of the lack of technical rigor, correlation with other techniques such as CTS and full scale flight testing has generally been good in both cases. Figure 25 shows the comparison between the first (Korn) approach, and CTS. The trajectories are for a SUU-51/B bomb dispenser which is a high density, aerodynamically stable store (after fin deployment) approximately the size of an M-117 bomb. The simulated release was from the bottom station of the inboard wing station of the F-4 TER. The flow field of Fig. 9 was used for the trajectory calculations. Figure 26 shows the comparison between the second (Blöse, Barnes) approach, CTS, and full scale flight tests. These trajectories are for the guided weapon of paragraph 5.7.1. The flow field immediately below the clean aircraft pylon was used for the trajectory calculations.

#### 3.2.3.1 Flow Angularity Advantages

1. The trajectories generated by CTS, freedrop and other methods normally apply to a particular store only. Flow angularity data for a particular aircraft is taken at various Mach numbers and aircraft incidence angles and in principle can be applied to many representative store configurations. For example, the flow field data of Fig. 9 was taken for three M-117 bombs on a TER. This same data will also be used for any other three large diameter stores on a TER provided they are reasonably similar to the M-117. Data is taken for various sizes of single carriage stores and large and small stores on the MER/TER installed at various stations. Adjacent stores are also considered. Once the data bank is established, many stores and store configurations can be cleared with a minimum of expensive wind tunnel testing. Also, as new stores are developed, little or no additional wind tunnel testing may be required.

2. The data base provides a "quick look" capability and immediate response to operational requirements by eliminating the need to schedule wind tunnel time and fabricate store models. It is particularly valuable for trouble shooting during flight test program where time is usually critical.

3. The flow angularity data serves as an excellent data base for store design purposes. Many store designs can be iterated at minimum expense and changed without the need to conduct additional wind tunnel tests. Also, the data may be used to estimate the distributed carriage loads acting on the store for structural design purposes.

4. There are no trajectory limitations due to sting travel, balance loads, or tunnel boundaries.

5. Flow angularity can be used conveniently to simulate trajectories for guided weapons having active auto pilots and controls during release.

6. Flow angularity can be used to simulate store trajectories where the aircraft released the store while in a dive/climb or accelerated flight.

#### 3.2.3.2 Flow Angularity Disadvantages

1. The flow angularity technique is considered to be the least accurate of the wind tunnel testing techniques. There is considerable art involved in making certain assumptions such as the accurate location of the store center of pressure at various Mach numbers in an interference flow field, especially in the absence of good free stream store data. The method is not recommended for unfinned, unstable stores, or low density stores where the aerodynamics become much more important than the inertial factors. This is particularly true for clustered stores on MERs and TERs.

2. The technique requires a large initial investment in wind tunnel testing but is quite cost effective if a large number of stores and store configurations are to be cleared and/or if the aircraft becomes a prime weapon carrier and remains active for many years such as the F-4.

3. The previously discussed method of calculating the aerodynamic coefficients is subject to errors if the flow field gradients over the store are large.

4. Multiple, ripple, or salvo releases cannot be investigated.

5. Errors due to probe interference are unknown.

#### 3.2.4 Freedrop

Freedrop studies are made by releasing or ejecting dynamically scaled store models from a parent aircraft installed in the wind tunnel. The separation characteristics are determined from either high speed motion pictures or multiple exposure (strobe) still

photographs taken from two or three (ideally orthogonal) locations. The technique can be used to determine the separation characteristics of single, ripple, salvo, or jettison separations. The store motions are constrained only by collisions with the parent model or the tunnel boundaries. In some instances the stores may be recovered with little or no damage even when released at supersonic test conditions. The bomb rack ejection forces are generally simulated by small pistons driven by coil or leaf springs, pneumatic pistons or small solid propellant charges (e.g. in the UK).

The static forces and moments generated by a flow field will be scaled if the flow field and model geometry are similar to that of full scale. The aerodynamic accelerations of the scaled store will be similar if the static forces and moments, mass, center of gravity, and moment of inertia are scaled.

Three scaling laws, termed "heavy", "light", and "Froude", are commonly in use. Again, the best technique depends upon the problem, personal preferences, and wind tunnel facilities available. For example, the General Dynamics Corporation much prefers heavy model scaling, whereas the light model method is used almost exclusively at the Vought Corporation, and throughout the UK. The object is to preserve the proper ratios of mass, length, and time for the store models in order that the store model will transcribe the same linear and angular path with respect to the aircraft model as the full scale store would with the aircraft. Reference 16 and refs. 34 thru 40 discuss the scaling laws in detail and were used to develop the following discussion.

#### 3.2.4.1 Heavy Scaling

In this method the free stream Mach number is duplicated, and the proper aircraft flow field is preserved. It also preserves the ratio of the static aerodynamic forces to gravity forces (store weight) at the time of release. The dynamic derivatives ( $C_{mq}$ ,  $C_{m\dot{\alpha}}$ ) are not properly scaled, and the angular motions are underdamped; however, these are often less important than the gravitational forces. The requirement to maintain the proper ratio of static aerodynamic forces to gravity often make it difficult or impossible to obtain sufficiently dense materials. In this case "mass deficient" models as described in ref. 37 are used and the bomb rack ejection force is increased to assist the model in passing through the correct flow field as it separates the aircraft.

#### 3.2.4.2 Light Scaling

In this method the free stream Mach number is also duplicated; the aerodynamic forces are properly scaled; but the proper ratio of static aerodynamic forces to gravity forces is not preserved. The gravitational force is deficient by the ratio of the model to aircraft characteristic length. Angular motion is properly simulated; however, linear accelerations are incorrect; and the store model does not properly traverse the aircraft flow field. Unfortunately, there is no practical means available to scale the gravitational force; therefore, erroneous store separation characteristics can result from the freedrop technique. References 41 and 42 suggest the use of a ferromagnetic sphere to create a variable artificial gravity field about the wind tunnel test section. References 43 and 44 propose the development of a rig to accelerate the parent aircraft upward at the instant of store release for elimination of the gravity deficiency. An actuator and ejector synchronization system has been further developed from ref. 45 (see ref. 46) and this could offer improvements for "mass deficient" heavy model scaling as well as light scaling. This technique provides the required separation increment, but not the relative velocity increment between the separated store and free stream. In addition, it provides an unwanted component of vertical velocity to the aircraft model. Another technique is to vary the parent model incidence during the acceleration. This method maintains the correct local flow field around the aircraft model. However, the incidence of the flow field relative to the separated store is incorrect and the separated store is deficient of the vertical component of velocity. The merits of providing aircraft model incidence variation during acceleration are therefore questionable (ref. 46). Common corrective methods include increasing the bomb rack ejection force as above and later, with the use of a digital computer program, correcting the model trajectory by an increment depending on the square of the time scale and gravitational deficiency.

#### 3.2.4.3 Froude Scaling

In this method the Froude number is duplicated and all dynamic similarities are preserved. The free stream Mach number, however, cannot also be duplicated, and the technique is generally limited to the incompressible case.

#### 3.2.4.4 Freedrop/CTS Comparison

Reference 47 reports on a program where the CTS was used to study the effects of the various scaling laws and to evaluate the accuracy of the CTS. Freedrop tests were conducted with a variety of stable and unstable stores scaled according to the above methods. This provided a set of "flight" data to use as a base for comparison of CTS trajectories of these stores which were conducted using the mass and inertia of the full scale stores as well as those of the "heavy", "light", and "Froude" scaled freedrop models. The results of the test showed the CTS to correlate very well with freedrop. Typical agreement for a heavy model of an unstable store with very high pitch rates is shown in Fig. 27. Comparisons of the various scaling laws confirm the expectation that the heavy and Froude scaled linear motions, agree quite well with full scale,

whereas the linear motions of the light scaled models are much less than full scale. The angular motions, particularly in pitch, show the largest differences between the three scaling laws, with light model scaling showing the best correlation (ref. 47).

### 3.2.4.5 Propelled Missile Model

References 48 and 49 report on the freedrop tests of a dynamically scaled propelled missile in the Modane S3 intermittent transonic and supersonic wind tunnel. To this author's knowledge this is a unique test as the dynamically scaled missile model was fitted with a scaled microrocket engine which was actually fired in the wind tunnel after release of the missile model.

The heavy scaling laws as described above were used. The deviation between the theoretical value of the force of gravity and the actual weight was compensated for by adjusting the ejection device to impart a velocity which is homologous to that obtained in flight under the combined effect of the accelerations of ejection and gravity.

Small weight deviations are usually not important in the case of vertical ejection; however, the effect of gravity on the relative trajectory of a forward propelled missile becomes significant. Its effect was simulated by an aerodynamic force passing through the missile center of gravity. This force  $\Delta\alpha$  was obtained by setting the missile at a negative angle of incident  $\Delta\alpha$  relative to its normal position and rotating the fins by an angle  $\Delta\beta$  to satisfy the following relationships:

$$F_p \sin \Delta\alpha + C_z (\Delta\alpha, \Delta\beta) S q = \Delta Z$$

$$C_M (\Delta\alpha, \Delta\beta) S l q = 0$$

Where  $F_p$  is the engine thrust,  $C_M$  the pitching moment coefficient,  $S$  the reference area,  $l$  the reference length, and  $q$  the dynamic pressure.

It was necessary to study and make a set of solid-fuel microrockets to give the thrust required by test similarity conditions in each case for the tests on firing self-propelled missiles from a carrier aircraft. This thrust was set at as constant a value as possible throughout the duration necessary for observing the phenomenon in question. The tolerance of the deviation between the thrust direction and the geometric axis of the missile was the same order as that of actual missiles. Finally, the microrocket had to be made an integral part of the structure of the missile while maintaining the requirements for geometric and mass similarity.

Since the thrust scale generally varies with the Mach number and the firing altitude, it is indispensable to be able to adapt the thrust of the engine to the test configuration without changing the construction of the missile. This variation is achieved by changing the throat diameter.

Figure 28 shows the missile being launched in the S3 wind tunnel. Cross-checks of the flight and wind tunnel tests and comparisons with the calculated trajectories were made for missiles fired from a carrier aircraft. Certain of these comparisons had excellent results, the deviations obtained not being greater than the scattering of actual firings. Other comparisons dealing with the same type of missiles, but which were different from the first, were much less satisfactory: this can be attributed to the failure to correctly achieve the similarity of thrust for the microrocket engine in this case. A correction based on the difference between the actual and theoretical thrusts did not make it possible to obtain a true correspondence because it was not possible to account for the unknown interaction between the jet of the rocket and the aerodynamic field of the carrier.

### 3.2.4.6 Freedrop Advantages

In general most papers report good correlation between freedrop and full scale flight test. Freedrop can play an important role in any store separation program, especially where the jettison of multiple ejector racks and stores as a unit is involved. Some advantages are:

1. There are no physical limits due to sting travel. Trajectories are limited only by the camera field of view and the wind tunnel boundaries.
2. There are no sting effects and weapon afterbodies do not have to be altered to accommodate a captive sting.
3. A store can be installed in the proper carriage position on the aircraft pylon eliminating the CTS touchwire errors discussed in paragraph 3.2.1.3.
4. Multiple/ripple, and salvo releases can be conducted.
5. Freedrop is applicable to jettison problems involving MERs and TERs with attached stores.

6. Folding fins and retardation devices can be modeled and operated during the wind tunnel trajectory.

7. The effective flow angles due to the release velocity of the store are preserved.

#### 3.2.4.7 Freedrop Disadvantages

1. Stores must be dynamically scaled and are not always recoverable. Many models of the same store may be required to cover store inertia characteristics (i.e. full and empty fuel tanks) and the flight conditions desired. Models may be hard to work and/or expensive exotic materials may be required to meet certain mass requirements.

2. Freedrop is sometimes much slower than CTS for high speed continuous flow wind tunnels without injection systems. New drop models must be installed after each drop; therefore, the wind tunnel must be stopped. This is usually of no consequence for a blow-down or a low speed continuous flow wind tunnel, but freedrop proves to be slow and inefficient when conducted in high speed continuous flow wind tunnels not equipped with model injection systems. One run per hour is not uncommon.

3. Time-space data must be reduced if quantitative trajectory data is required.

4. Releases from accelerated and dive angle flight can only be simulated approximately.

5. Freedrop cannot be used to simulate trajectories for guided weapons having active autopilots and controls during release.

6. Freedrop is similar to CTS in that once a trajectory is run for a given set of parameters the trajectory data may become invalid if any of the store physical properties are significantly changed. However, the aerodynamic interference coefficients may be extracted from the data and used in a similar manner as grid data.

#### 4 Store Separation Flight Testing

Reference 50 contains an excellent description of store separation flight testing techniques and the methods used to reduce the data to quantitative form. The majority of the following discussion is extracted directly from this reference.

Much emphasis in the past few years has rightfully been placed on the preflight analysis efforts of aircraft/stores compatibility due to the high cost and risk factors that accompany actual flight testing. However, no analytical or wind tunnel prediction technique can be effectively used to reduce flight testing without some method of correlating the predicted store trajectory to its actual inflight trajectory. Without a quantitative inflight store separation trajectory definition system, it can never be determined if the prediction techniques used are accurate. The following describes the methods used by the US Air Force for the collection and reduction of store separation flight test data.

The aircraft used to release the stores is normally equipped with several high speed, 16mm motion picture cameras, normally operating at 200 frames/second and having time annotation on each frame. The cameras are mounted to view the store release from at least two angles, one of which should be as close as possible to a side view. So that camera data will be of the highest quality, the cameras should be equipped with automatic exposure control and wired such that when the pilot activates the stores release button, the cameras are immediately turned on but the stores release signal is delayed by approximately 0.5 seconds. This delay in release allows the cameras to reach full running speed prior to the photographing of the store release. The cameras then run for a preselected time (usually 3 - 5 seconds) and then automatically shut off. This relatively simple delay circuit installation has caused a significant increase of useable camera data since its initial use a few years ago. In addition to these data cameras, aircraft conditions at time of stores release are also recorded by means of a cockpit camera, an onboard data recording package tied into the aircraft instrument system, or (occasionally) by pilot, or flight crew readings of the cockpit instruments.

Once the store separation has been made, the quantitative photographic data must be reduced to a form similar to that of the predictions so that a direct comparison between predicted and inflight trajectories may be made. To do this, two techniques are currently employed by the US Air Force; one, called "photogrammetry" developed by the Air Force at Eglin AFB, and the other called "photo-imaging", developed by US Navy engineers at the Pacific Missile Test Center and Naval Weapons Center. Both are capable of providing excellent data, but the photo-imaging technique is superior in its usefulness and is considered to be state-of-the-art.

##### 4.1 Photogrammetric Data Reduction

In this method, both the store being released and the aircraft pylon must be painted with a background color and a contrasting-color pattern of dots whose positions are accurately known with reference to some specific point (see Fig. 29). Size and color of the spots is not fixed; they are optimized for accuracy and ease of film reading. However, at least a specified number of dots must be visible at all times in the film. Onboard camera lenses are selected so that both the store being released and the

part of the aircraft adjacent (pylon, for example) are visible on the film. After the release, each frame of the onboard-gathered movie film is processed through a film reader manually. These data, along with a series of geometric and physical constants, such as location of the reference dots with respect to a specific position, camera location and lens focal length, are input to a computer. The computer output is the store trajectory, printed out in terms of roll, pitch, and yaw angles and X, Y, and Z displacements of the store versus time. Although a two-camera solution would be preferable, a one-camera solution can be used most of the time and will provide accuracies of about  $\pm$  two inches (5 cm) for displacements and  $\pm$  two degrees for angular motions. The photogrammetric computer program requires starting estimates of store and camera orientation with respect to the aircraft. A final, iterated, solution is then obtained which achieves convergence for even poor starting values. After the first frame, the program employs previous frame results as the estimate for the succeeding frame. Because of this, wing flexure and vibration are automatically eliminated. The computer is programmed to print out the trajectories in both a tabular and plotted format, so that a direct comparison may be made between predicted and inflight trajectories.

#### 4.2 Photo-Imaging Data Reduction

This system utilizes an image matching technique to obtain spatial position and orientation of photographed objects with respect to recording cameras (see Fig. 30). The system begins by projecting each frame of the onboard flight-gathered data film through an optical system into a high resolution video camera and displaying the resulting image on a TV monitor located on an operator's console. Another high resolution video camera is positioned near the console to view an exact scale model of the store. This store model is mounted on a remotely-controlled six-degree-of-freedom model positioning mechanism. The video signal from this second TV camera is fed through a video mixer, and the resulting image is simultaneously displayed on the same TV monitor as that from the data film. The operator can adjust the position and orientation of the store model through the use of a set of levers on the console. He adjusts the store model until the image of the store on the positioner is exactly superimposed on the image of the store from the data film (a process similar to using a camera range finder). Once the two images are exactly aligned and superimposed, the operator can press a single button which transfers the encoded frame count and position data to an IBM card. Each frame of the film is similarly reduced until a card deck is generated. This deck is input to a computer program--just as in the photogrammetry process--to solve the spatial relationships. The output from the photo-imaging technique is a set of tabular data and selected plots which accurately define the store separation trajectory to compare directly with the predictions. This technique produces extremely accurate data ( $\pm$  0.1 ft [ $\pm$  3 cm] for displacements and  $\pm$  1.0° for angles) and has the added advantage of not requiring a complex painting scheme on the store and aircraft. Because of this, the cost of reducing the film data from a specific store separation is about one half that of the photogrammetric technique. A photo-imaging system now exists at three US Navy testing locations.

#### 4.3 CHASE

Reference 51 reports on a new photogrammetric technique called CHASE which was developed by the McDonnell Aircraft Company and used to support the F-15 program. CHASE is an analytical and software technique that yields six-degrees-of-freedom data with an accuracy equal to, or better than, any other existing system. The system is fast. A separation requires, on the average, only one hour on a film reader and two minutes on an average computer. Three important advantages are that the system requires little preparation since the stores need no marking; no special equipment is required; and the results are independent of the camera position. This last advantage is responsible for the system name, CHASE, as the ultimate objective for future development is the quantitative reduction of film taken from a "chase" aircraft.

The CHASE concept is shown in Fig. 31

- (1) In the field of view information of three targets on the airplane is read from the film. These three targets are referred to as Boresite Targets. Their positions are converted into included angles between the lines of sight from the camera. These lines form a tetrahedron, a rigid structure. The baseline dimensions of this tetrahedron are established using the aircraft stations of the boresight points. An iterative technique using the Laws-of-Cosines is used to locate the camera such that the projected radials make a best fit of the targets. When the coordinate sum of the successive radial errors is less than one inch, a solution has been established locating the camera. The orientation or look angle of the camera is computed using this camera location and the optical transfer functions. The camera location and orientation is computed for every frame that is processed. Each frame then is in itself a complete solution, and is not dependent upon another camera, nor is it time dependent. It adjusts for the conditions that exist at that very precise moment.

- (2) Using that same frame, three points are read on the store. Various features of the store having distinct outlines are used for these three points. Again the included angles to those points define another tetrahedron. Using the location of these points for the baseline of that



tetrahedron, the base is shifted around in the same manner until there is a best fit for the radials. When the sum of the differences is less than one tenth of an inch (2.5 mm), the location of the plane (the stores coordinate system in space) is established.

(3) At this point the store is numerically reconstructed. From this numerical representation the data, as requested by the user, is precisely furnished. Discrete points on, in or outside the store and attitudes of a preferred coordinate system are presented rather than the traditional nose, CG, tail. The analyst can now observe clearances of critical points. This is particularly beneficial for nonsymmetrical stores or those having protrusions.

The basis of the technique is that the Boresite Targets are precisely located on the aircraft. This makes it possible to accurately calculate the camera position relative to the aircraft at any one time. Accurate dimensional data on the store is contained in the software permitting accurate calculation of the store position relative to the camera at any one time. Therefore, the position of the store relative to the aircraft may be calculated as a function of time and independent of camera position.

The real success of the CHASE system is the result of innovative mathematics in the software and the use of extensive information files on boresight, optical calibrations, and aircraft instrumentation configuration. Vast improvements in optical calibration techniques for camera lenses were made during the development of CHASE. These improvements were probably the most significant single factor contributing to the success of CHASE.

#### 4.4 Summary of Flight Test Data Reduction Methods

All three of the methods described above provide accurate, useful quantitative data, both in a tabular and a plotted format. All of them are inherently accurate enough to provide good, usable data. The degree of mathematical accuracy obtained is not as important as how many of the error-causing factors are accounted for by the method, and (more importantly) whether the factors are compensated for or corrected. Data reduction accuracies of  $\pm 3$  inches (5.1 cm) and  $\pm 3$  degrees can be absolutely adequate, but not if the effect on store separation of wing flexibility, for instance, is not properly accounted for. Of all the error-causing factors, the ones which seem to be the most important (and most difficult to correct for) are connected with the camera optics. Errors caused by lens/camera alignment, calibration, internal manufacturing aberrations and uncertain optical centers are among the most important. Although great care must be exercised in developing a data reduction method which properly accounts for as many of the error-causing factors as is possible, equal care must be used in insuring that the method does not introduce other large errors through the human factor. A method which requires an inordinate amount of human input and manipulation of data prior to and during computer reduction is extremely liable to errors, particularly if no built-in test features are incorporated.

#### 5 Typical Store Separation Problems and Recommended Solutions

Much can be learned about store separation by examining past problems and successes. The desirable and undesirable parameters can be identified and this information, or design criteria, applied to new aircraft, bomb ejector rack, and store developments. This section will describe some of the store separation problems that have occurred in the past, discuss the parameters involved, and recommend corrective design criteria for future weapon system developments.

##### 5.1 Jettison Problems

##### 5.1.1 External Fuel Tanks

Figure 32 shows an external 600 gallon (2271 litre) empty fuel tank/pylon striking an FB-111A aircraft. This is a highly unusual case in that aerodynamic stability contributed to the incident, and the solution to the problem was to reduce the pitch plane stability. In the original design of the tank, the tail fins were arranged symmetrically in an "X" configuration (Fig. 33). The tank was slightly statically stable in the pitch plane but unstable in the yaw plane due to the presence of the pylon. The forward ejector of the tank/pylon release mechanism is forward of the tank center of gravity to impart a nose-down pitching moment, so the tank will develop a nose-down attitude and essentially "fly" down and away from the aircraft. When ejected, the tank/pylon pitched down and gave all indications of a satisfactory separation; however, as the stable tank pitched back up, the pylon caused the tank to roll approximately 90 degrees as the angle of attack changed from negative to positive. In this attitude there was no aerodynamic stability in the original pitch plane, and the pitching moment became more positive. The result is clearly shown. The low density of the tank was a contributing factor as the lift due to the nose-up attitude was sufficient to overcome the gravity force.

Reference 52 discusses the solution to the problem which was simply to reorientate the fins as shown in Fig. 33 to produce static instability in the pitch plane. This

causes the tank to continue to pitch down at an increasing pitch rate and reach large nose-down angles before it has time to yaw significantly, thus eliminating the possibility of pitch recovery.

Figure 34 shows an empty finned fuel tank being jettisoned from the A-37 aircraft. The fuel tank was constructed from a fire bomb shell and had a three fin configuration. The fin design was quite poor as the aerodynamics were unsymmetric and the area was too small to give the store positive static stability. In addition to an unsymmetrical unstable aerodynamic configuration, the item had very low density. Also, it was not ejected from the aircraft as the A-37 bomb racks are of the gravity release type that provide no ejection force to the store. This is a classic case where many of the undersirables, low density, static instability, and no ejection control coupled to cause a near catastrophe.

#### 5.1.2 Multiple Ejector Racks

Figure 35 shows a Multiple Ejector Rack with an empty munitions dispenser striking an F-4 aircraft. The MER, with a dispenser attached to the forward MER shoulder station, was ejected from the aircraft fuselage station. The package was low density, aerodynamically unstable and had a center-of-gravity forward of the bomb rack ejector which resulted in a nose-up pitching moment from the ejector.

This type of jettison problem is considered to be the most complex, difficult to accurately predict, and dangerous of all store separation problems, even when compared to the case of empty fuel tanks. (As a matter of interest, the aircraft was lost the day after this photograph was taken when additional jettison tests resulted in the MER striking the horizontal stabilizer). There are many different combinations of MER loadings, each of which changes the aerodynamics and mass properties of the package. In addition to the sheer numbers involved, the aerodynamics are unsymmetrical, impossible to predict analytically, and difficult to measure in the wind tunnel. The configurations are unsymmetrical, aerodynamically unstable, and of relative low density because of the large effective volume. The problem is too complex to model analytically, and the asymmetries and small size of the MER beam make it difficult to install strain-gage balances for CTS or grid studies. To date, the only known successful method for accurately predicting MER/TER jettison trajectories has been with the use of freedrop techniques.

#### 5.2 Jettison - Attractive Solutions

The most attractive solution to the jettison problem for aerodynamically unstable items is an aft pivot release system. This system restrains the aft end of a pylon, MER beam, or fuel tank so that the rotation is initially about the aft end rather than the center of gravity of the item. This causes the ejection forces to always produce a nose-down moment to the item although the ejector line-of-action may be aft of the center of gravity. A hook within the mechanism restrains the item in pitch until it reaches a predetermined nose-down pitch attitude and "flies" away from the aircraft.

The basic idea is not new. The B-58 external fuel tank, the F-111 pylons and fuel tank/pylons and all pylons of the F-15 employ this system. The F-111 system is limited, however, as the pivot points are not placed at the aft end of the item. Figure 36 shows the F-111 design which limits the combination of maximum restraint angle and pitch velocity to avoid collision of the aft end of the tank with the wing trailing edge.

##### 5.2.1 F-4 Aft Pivot Studies

Reference 53 reports on an analytical/wind tunnel program to expand the jettison envelope for the MER on the F-4 centerline station. The proposed aft pivot modification, which was not adopted, is shown in Fig. 37. The results of the investigation showed that:

1. Significant improvements in jettison characteristics would result.
2. An aft pivot release angle greater than 25 degrees would be required to achieve safe jettison of all MER configurations throughout the F-4 envelope.

##### 5.2.2 F-15 Aft Pivot Pylon

An aft pivot release system was incorporated at all F-15 major store stations for the pylons, MERs, and 600 gallon (2271 litre) fuel tanks. Reference 54 describes the design and testing of this system which is shown in Fig. 38. Aft pivots are installed at both the pylon/aircraft and the MER or fuel tank/pylon interfaces to provide for various jettison options that may be required by the pilot. Both CTS and freedrop wind tunnel testing were conducted to determine the jettison characteristics prior to flight test and establish an optimum aft pivot release angle for full/empty tanks throughout the desired jettison envelope.

Figure 39 shows the CTS tunnel installation which used a "bent sting". This allows longer and more informative trajectories to be obtained for items having high nose-down pitch rates. The aft pivot restraint was simulated by restricting the combination of pitch and vertical displacement within the CTS program until the store pitch reached the aft pivot release angle.

Figure 40 shows the freedrop model installed on the left wing pylon. The aft pivot mechanisms for both interfaces were modeled and can be seen in the photograph.

Figure 41 is an example of the correlation obtained between CTS, freedrop, and full scale flight tests. "Heavy scaling" laws were used for the freedrop models.

### 5.3 Delivery - Problems

#### 5.3.1 Unstable Stores

Figure 42 shows a finned firebomb released from a MER striking the horizontal stabilizer of an F-105 aircraft. Upon ejection, the store rotated to a slightly nose-up attitude due to the aerodynamic and bomb rack ejector moments. As was the case with the A-37 (para 5.1.1), the poor fin design did not provide sufficient stability for pitch plane recovery, and the nose-up attitude increased until sufficient lift was developed to cause the store to rise and strike the aircraft. This problem was corrected by redesign of the fin to provide positive static stability.

#### 5.3.2 Improper Mass Balance

Figure 43 shows a fast level flight ripple release of MK-82 bombs (inert) from the F-111 aircraft. All bombs pitched nose-up and seemed to float wildly under the aircraft. The bomb with the extreme nose-up pitch attitude struck the aircraft empennage causing severe damage, and one bomb went up over the top of the vertical stabilizer. Many factors contributed to this accident. To start with, improper filling and mass balance procedures had been used during the process of "building-up" the inert bombs for test purposes. The result was a lighter bomb with a forward center of gravity. The initial pitch-up was caused by the ejection force being applied aft of the weapon center of gravity. In addition, the tests were conducted at flight conditions of high dynamic pressure (.95 Mach at 1000 feet) which produced enough lift force at these nose-up attitudes for the bombs to "fly". Another contributing factor was the marginal static stability of the MK-82 bomb at this Mach number (and high angles of attack). Also, the stores were released from the very flexible MER having bomb ejector racks with low impulse single ejection pistons and no pitch control. This example shows the importance of proper center of gravity control and emphasizes the role of the bomb ejector rack as a primary parameter in store separation. Releases at high dynamic pressures must be carefully controlled, especially when the stores are statically unstable or marginally stable.

#### 5.3.3 Stores with Folding Fins

Figure 44 shows a "Rockeye" dispenser striking the fuselage of an A-7D aircraft. Note that only one of the stabilizing fins of the second store has fully opened. At the time of this photograph, the fins of the first store are in position; however, its fin opening was also delayed and erratic. The "Rockeye" dispenser has good static stability with the fins deployed, but is marginally stable with the fins in the stowed position. Also, the fins are not mechanically interconnected to insure simultaneous opening. The delayed and erratic fin opening resulted in the store being statically unstable and having highly unsymmetrical aerodynamics during the critical time period at release.

This example clearly illustrates the pitfalls of stores with folding fins, especially when the fins are not interconnected and the store is aerodynamically unstable at release.

#### 5.3.4 Pitch-Down - Bottom TER Station

Figure 45 shows the ripple release of SUU-30 dispensers from a MER carried on the centerline station of an F-105. Note the large nose-down pitch attitude of the store released from the forward bottom MER station. This characteristic is typical for any large diameter store released from the bottom TER station at high airspeeds. Figure 46 shows how the nose-down pitch attitude drastically increases for a SUU-51 dispenser for successive level flight F-4 releases at .6, .8, and Mach numbers, all at an altitude of 5000 feet.

This trajectory characteristic is a result of the large aerodynamic couple acting on the store as shown in Figs. 9 and 10 and discussed in para 2.2.2. Although the phenomenon is not completely understood, the characteristic pitch down is believed to be a strong function of the interference effects of the adjacent stores and the large over-pressure that develops in the cavity formed at the nose and in the center of the three stores. This is also evidenced by the fact that smaller diameter stores, which are spaced further apart and do not restrict or choke the flow, are much less affected.

Figure 47 shows a store having a hemispherical nose and similar in shape to the SUU-30 after release from the F-4 bottom inboard TER station at 1.15 Mach and 10,000 feet. The trajectory was clean and flat and the maximum pitch angle was less than ten degrees throughout the complete flight envelope. The primary differences between this store and the SUU-30 are that it is 12 inches (30.5 cm) in diameter with approximately 1.3 calibers of static stability as opposed to 16 inches (40.6 cm) in diameter and approximately .6 calibers of static stability for the SUU-30.

The top photograph of figure 48 shows the release of two stores from bottom F-4 TER stations at .9 Mach and 5000 feet altitude. The stores were released simultaneously from opposite wings to achieve, as close as possible, the same release conditions. The store in the bottom left photograph was 16 inches (40.6 cm) in diameter with the mass properties of a typical dispenser weapon. The fins were fixed and of maximum span to

provide as much static stability as possible. The store lengths were the same; but, the store in the bottom right photograph was 14 inches (35.6 cm) in diameter and had the mass properties of a typical dispenser weapon of that diameter (appropriately scaled down from 16 inch (40.6 cm diameter). The fins were similar in shape to the 16 inch (40.6 cm) diameter store; however, the smaller store diameter made it possible to increase the relative fin span (span to diameter ratio was higher) and provide slightly greater static stability. This flight test clearly shows the importance of aerodynamic interference and stability on store release characteristics.

The above flight tests and recent analytical studies indicate that store static stability is also a major factor. Figure 49 shows the results of varying aerodynamic stability on store pitch characteristics as other store parameters are held constant. The charts were constructed using wind tunnel grid data in a trajectory simulation computer program. Adequate store static stability is difficult to obtain with large payload cylindrical stores such as the SUU-30 and SUU-51 because physical constraints of TER geometry make it impossible to fit the store with large stabilizing fins unless they are folded and deployed after release. This approach was not successful in the case of the SUU-51 because the store rotates very rapidly; the tail does not translate; and the two remaining upper stores prevent the fins from opening when the store is released. The SUU-30 has fixed fins, but the store is only marginally stable at transonic Mach numbers. Another important factor not to be neglected is that most present US MERs and TERs are equipped with the low impulse single piston ejector rack as described in para 2.2.1

#### 5.4 Delivery - Attractive Solutions

##### 5.4.1 Pitch Down - Bottom TER Station

Since 1972 the USAF has been engaged in an aggressive program of analysis, wind tunnel test, and flight test in an attempt to better understand the phenomenon of the bottom TER station pitch-down problem and to correct or alleviate the problem for large diameter stores through store and bomb rack design changes. There is intense interest in obtaining a solution for the large diameter store, rather than limiting diameter to reduce aerodynamic interference and permit larger stabilizing fins, because of the large loss in weapon payload as store diameter is reduced. The investigations, which are reported on in detail in refs. 55 thru 59, included:

1. A parametric investigation of store nose shapes.
2. Oil flow and pressure distribution store models.
3. The effect of weapon ballast.
4. The addition of an aft stagnation plate to the TER in the vicinity of the store fins.
5. The effect of store staggering, that is the longitudinal movement of the bottom store with respect to the upper stores.
6. Various modifications to the forward aerodynamic fairing of the TER, which included total removal of the fairing.
7. The effect of a "tunable" dual piston ejector rack (para 2.2.1) to produce a mechanical nose-up moment to the store to assist in relieving the aerodynamic nose-down moment.

Of the above, only 6 and 7 were flight tested. Unfortunately, modifications to the forward TER fairing failed to show the improvements during the flight tests predicted during wind tunnel tests.

##### 5.4.1.1 Store Staggering

Figure 50 shows the significant reduction in installed aerodynamic pitching moment obtained for a SUU-51 dispenser caused by shifting the carriage position of the bottom station aft 16 inches or about 40.6 cm (full scale) with respect to the TER and upper stores. The data is based on wind tunnel tests. In addition to providing relief from adverse pitching moments, Chapter 2 shows that significant drag reductions can be realized with properly staggered multiple stores. Therefore, store staggering appears to offer considerable potential for both drag reduction and store separation improvements. Additional research in this area is highly recommended.

##### 5.4.1.2 Dual Ejector Rack

The dual ejector, high impulse, "tunable" bomb rack has shown very promising results. Figure 51 shows the release of SUU-30 dispensers from the F-4 inboard TER station using a TER equipped with high impulse "tunable" racks. The release was in level flight at .9 Mach and 5,000 feet altitude. In the left photographs, the rack orifices were set to deliver equal force to both ejection pistons; therefore, the aerodynamic pitching moment controlled the store motion, and excessive pitch-down still resulted.

In the right photographs the rack was "tuned" to deliver all of the available ejection force to the rear ejection piston such that sufficient nose-up mechanical moment

was developed to overcome the large nose-down aerodynamic moment. The resulting trajectory, again at .9 Mach and 5000 feet altitude, was relatively level, indicating the feasibility of using a bomb rack induced moment to correct the TER pitch-down problem.

#### 5.4.1.3 Self-Compensating Bomb Ejector Racks

Although it has been clearly demonstrated that "tuned" bomb racks have the potential of correcting release problems, the present racks must be set prior to take-off for particular flight conditions. If the rack is set to provide a nose-up moment to compensate for the large nose-down aerodynamic moments experienced at the higher airspeeds. Figure 52 shows computer simulation predictions (based on grid wind tunnel data) of SUU-30 releases from the F-4 with the "tunable" rack set to compensate for the pitch-down of the bottom TER station at higher airspeeds as described in paragraph 5.4.1.2 above. Full scale correlation is shown for these conditions that were flight tested. Note that excessive pitch-down is not predicted for the 1.2 Mach/200 feet release. This is because of the typical large reduction in the aerodynamic pitching moment coefficient above 1.0 Mach. Also, note that the pitch-up is becoming excessive at .5 Mach; however, a usable operational envelope still exists.

The aerodynamic loads acting on the stores vary considerably throughout the normal flight envelope of a modern tactical aircraft. Therefore, it would be highly desirable to have some method of changing the bomb ejector rack forces and moments in flight to compensate for these continuously changing aerodynamic loads.

References 60 and 61 discuss the concept of a self-compensating bomb ejector rack. Although the self-compensating bomb ejector rack is only conceptual, the idea has much merit and warrants further development. The in-flight loads acting on the stores would be sensed by instrumentation, and the orifices for each ejection piston would be continuously varied to compensate for these loads, thus minimizing the release perturbations. Reference 61 proposes the use of the aircraft fire control computer to provide intelligence to the rack for in-flight adjustment of the impulse to each ejection piston. The required data would be determined through wind tunnel and flight tests and pre-programmed for each store as a function of flight conditions. The latter approach is considered more practical. The self-compensating bomb ejector rack also offers much potential for solving other release problems in addition to the TER pitch-down

#### 5.4.2 Conformal Carriage

An attractive solution for improved weapon release characteristics is the concept of conformal carriage. Other chapters of this manual discuss the improvements that can be realized in reduced carriage drag and increased performance and handling qualities, through the use of this concept. The jointly sponsored US Navy/US Air Force F-4 Conformal Carriage program also included a comprehensive evaluation of the separation characteristics of general categories of conventional weapons such as a low drag general purpose bomb (MK-82), a dispenser munition (Rockeye), and two conceptual bluff weapon shapes. The program, reported on in ref. 62, included comprehensive wind tunnel testing and flight test demonstration in which approximately 200 weapons were safely released at speeds up to 1.6 Mach. The weapons were ejected from the Conformal Carriage pallet using the Lode 14A ejector racks (modified to use two ejection cartridges for higher impulse) which are "tunable" dual ejection piston racks with the capability of imparting an ejection velocity of about 15 feet per second (4.57 m/s) to a 500 pound (227 kg) store, which is comparable to the UK racks now in service with the Royal Air Force.

During the Conformal Carriage flight test program, 112 MK-82 bombs were released in single and ripple modes at Mach numbers from .6 to 1.6 and altitudes of 5,000 feet to 30,000 feet. Of these, thirty-five dive releases were made with release intervals of 60, 100, and 140 milliseconds. Also 20 Rockeye and 65 bluff stores were released. In general, excellent release characteristics were exhibited throughout the wide range of conditions demonstrated. The only exception was that the aft row of MK-82 bombs had a tendency to pitch-down 45 to 60 degrees at supersonic speeds. This trend was also noted during the wind tunnel test program as shown in Fig 53 which compares .95 Mach releases from the forward, middle, and aft rows. Figure 54 shows typical MK-82 releases at the higher Mach numbers and the excellent separation characteristics of a .95 Mach ripple release.

The excessive pitch-down of the aft row is attributed to upwash on the MK-82 tail fins due to the upslope of the aft closure of the Conformal Carriage pallet (see Fig. 53). This is considered to be a minor problem which can be corrected by future pallet designs and/or proper "tuning" of the bomb ejector racks. Self-compensating bomb ejector racks would offer additional improvements.

### 5.5 Delivery Accuracy

#### 5.5.1 Delivery Accuracy Parameters

There have been many studies dealing with the deviations, or inaccuracies, of unguided ballistic weapons, or the so-called "dumb bomb". These studies have included the effects of such factors as variation in release signal time interval, ejector cartridge ignition time/burning rate/impulse variation, bomb ejector rack hook opening time, weapon aerodynamic/mass properties, release conditions, atmospheric conditions, etc. The studies are normally conducted using six-degree-of-freedom (or less) trajectory

programs on high speed digital computers (Fig. 22). In ref. 63, Dr Arthur Maddox reports on a systematic parametric study to examine the sensitivity of weapon down range impact points to variations in the primary parameters affecting store separation. The studies were conducted in the pitch plane for three-degrees-of-freedom and included variations of:

- Aerodynamic Interference (Varied Parametrically)
- Release Velocity
- Dive Angle
- Release Altitude
- Bomb Ejector Rack Impulse
- Weapon Stability
- Weapon Mass/Inertia

The most significant conclusions were: (1) the end results are heavily dependent on weapon aerodynamics, mutual interference (flow field), and bomb ejector rack characteristics, and (2) the initial characteristics of the mutual interference play by far the largest role in determining the store separation motion. The latter is also a significant conclusion of para 5.6.

Reference 64 reports on a comprehensive five-degree-of-freedom trajectory study where the sensitivities of a high drag and low drag weapon were examined. The study did not include interference flow field effects. The sensitivity of weapon impact errors were presented in terms of down range and cross range miss-distances for uncertainties in the following parameters:

- Release Altitude
- Release Velocity
- Dive Angle
- Weapon Ejection Velocity/Force
- Weapon Weight
- Weapon Diameter
- Air Density
- Axial Force Coefficient

Conclusions were: (1) weapon miss-distance becomes more sensitive to errors in delivery altitude and dive angle as delivery speed increases; (2) level trajectories are more sensitive than dive trajectories; (3) weapon miss-distance becomes less sensitive to errors in release speed as the delivery speed is increased; (4) weapon miss-distance becomes more sensitive to errors in ejection velocity as airspeed increases, however, this trend reverses as dive is increased; (5) weapon miss-distance becomes more sensitive to errors in weapon parameters such as weight, axial force coefficient, maximum diameter and air density as the delivery speed is increased.

In addition to the above, ref. 64 also reported on the effects of uncertainties in:

- Heading
- Initial Angular Velocity (Pitch)
- Initial Pitch/Yaw Angle
- Inertia
- Aerodynamic Coefficients
  - Normal/Side Force
  - Pitch/Yaw Moment
  - Pitch/Yaw Damping

Trends from examination of the above parameters followed an irregular pattern due to the complex force and moment relationships present in trajectories where the bomb is both translating and oscillating simultaneously.

#### 5.5.2 Flow Field Induced Delivery Errors

While uncertainties in the parameters examined in the above reports can cause significant degradations in delivery accuracy, they are usually secondary when compared to the decrease in delivery accuracy that can result from aircraft/weapon aerodynamic mutual interference (flow field) effects, especially at the higher release speeds.

The large flow-field-induced weapon perturbations addressed in this section are of the type that are not hazardous to the aircraft. The primary concern is that the perturbations result in short rounds due to excessive weapon drag, increased dispersion, and decreased delivery accuracy. Ballistic tables for a given US aircraft are based on nominal values for weapons released from any station of the aircraft at a given set of flight conditions. However, the local flow about weapons on different stations of the same aircraft varies tremendously, even at the same flight conditions. This local variation in the flow field can result in extreme differences in the trajectories of weapons released from the same aircraft at the same flight conditions. Obviously, weapons released from those stations where interference effects, and perturbations, are the largest will have trajectories with the greatest deviation from the nominal value.

Reference 31 reports on a study where realistic flow field data were used to evaluate the effect of the local flow on the impact point of identical weapons released from different stations of the same aircraft. Table 1 shows the deviation in impact point of a stable weapon due to flow field effects. The flow field data was obtained from the wind

tunnel and utilized for the trajectory calculations as described in para 3.2.3. The data presented are for six 800-pound M-117 bombs (363 kg) released from the TER stations of the F-4 aircraft at 5000 feet and Mach numbers of 0.5, 0.7, and 0.9. The deviations shown are the distances between ground impact points for two trajectory runs on the computer which are identical, with the exception of flow field "off" and flow field "on". As can be seen, flow field effects can be quite significant, especially at the higher airspeeds. Of special note is the large deviation shown for the bottom TER station at .9 Mach even though this store pitched less than 35 degrees.

Figure 55 shows the ground impact pattern for the above case where the bombs are released in a "ripple pairs" mode at 40 millisecond intervals at .9 Mach and 5000 feet. Note in Table 1 that all down range deviations are short due to the induced drag of the perturbations from the flow field effects. In actual practice, this would be accounted for by a change in the bomb sight depression angle; consequently the pattern of this figure was appropriately centered by an adjustment of 250 feet (76 m). As before, the differences in the two impact patterns are due exclusively to flow field effects.

#### 5.5.3 Flow Field Induced Delivery Errors - Bottom TER Station

Table 2 shows the tremendous difference in the down range weapon impact point for a dispenser munition released from the F-4 bottom inboard TER station as release speed increases. The difference shown is due solely to flow field effects and was calculated using wind tunnel grid data in a three-degree-of-freedom trajectory program. The deviations of the first row were calculated using the characteristics of the standard US F-4 TER with its single piston ejector rack as described in para 2.2.1. Paragraphs 5.4.1.2 and 5.4.1.3 suggested the use of dual ejection and self-compensating bomb ejector racks as a possible solution, or improvement, for the bottom TER station pitch-down problem. The deviations of the second row were calculated using a hypothetical dual ejector self-compensating bomb rack where the ejection moments are "tuned" to compensate for the aerodynamic moments at the various airspeeds. As can be seen, this approach has the potential to significantly reduce but not eliminate the significant flow field effects. The main reason for this is that the ejection moments of current typical bomb ejector racks last only for about 100 milliseconds whereas the flow field effects are present for a much longer time.

#### 5.5.4 Potential Delivery Accuracy Improvement from Vertical Ejector Racks

The Vertical Ejector Rack (VER) is a multiple carrier similar to the MER and TER with the exception that the bomb ejector racks are arranged to eject all stores vertically down rather than ejecting some stores down and out at approximately 45 degrees (see para 2.2.1). There are two VER configurations presently being studied in the US. These are the VER-4 which carries four stores in two rows of two abreast, and the VER-2 which simply carries two stores side-by-side. The proposed US VER will have dual ejector, high impulse, "tunable" ejector racks utilizing standard ball lugs and self-adjusting sway braces. Although a systematic, comprehensive investigation has not been completed to quantitatively define the potential difference in delivery accuracy over present MERs and TERs it is expected that worthwhile improvements will be realized. This speculation is based on the following:

1. Adverse flow field effects and the pitch-down problem should be considerably reduced as the stores are no longer clustered in a group of three (see para 5.3.4).
2. Lateral dispersion should be reduced as the stores are now ejected downward rather than down and out at a 45° angle.
3. Increased bomb ejector rack impulse will provide greater store ejection velocity, and the store will transverse the aircraft interference flow field faster. This should reduce the perturbations caused by adverse flow field effects. In the case of the VER, the increased ejection velocity will not add to lateral dispersion as it would for the shoulder stations of the MER and TER.
4. The dual ejector "tunable" feature will allow adjustments to compensate for adverse aerodynamic moments and obtain improved trajectories.

This is an attractive area for additional research.

#### 5.5.5 Potential Delivery Accuracy Improvement from Conformal Carriage

The Conformal Carriage concept has considerable potential for improving weapon delivery accuracy. An important feature of this concept is structural rigidity. References 63 and 64 have shown that variation in store ejection velocity is a major parameter in decreased delivery accuracy. In the case of conformal carriage, the majority of the ejector rack impulse does work on the store. Little performance is lost due to carrier flexibility. Impulse characteristics/ejection velocities are much more consistent and do not exhibit the variations shown for the case of the MER as shown in Fig. 8 and discussed in para 2.2.1.

The most important feature, however, is that the flow field in proximity of the fuselage is very uniform, and the large undesirable weapon perturbations associated with underwing and clustered multiple carriage are minimized.

Figure 56 from ref. 62 shows the actual flight test ground impact pattern of 12 MK-82 bombs released at .95 Mach and 1900 feet AGL with a 100 millisecond ripple interval.

## 5.6 Launch Transient Analysis

During the past several years, the trend in nonnuclear weapon development has shifted from the more conventional types of unguided weapons to extremely accurate weapons with complex guidance and control systems. The majority of the new guided weapons have flight control systems that are active during the launch phase to rate stabilize the weapon and reduce adverse perturbations. At this time on-line computing capability and/or the difficulty of modeling small scale control surfaces make some of the CTS facilities impractical for simulating trajectories for guided weapons having active autopilots and controls during release. However, in some cases the autopilot equations and the aerodynamic control effectiveness can be incorporated into the CTS computer program to provide a complete simulation. The freedrop technique is totally impractical as it would require miniaturization of a complete weapon control system in a small dynamically scaled model. Two convenient techniques for this purpose are the flow field and grid as both are based on the type of wind tunnel data that may be used in a six-degree-of-freedom (SIXDOF) trajectory simulation program as shown in Fig. 22. The computer simulation includes mathematical models of the weapon seeker and flight control system. The simulation is modular in form and can readily be adapted to various weapons and aircraft simply by changing the applicable subroutines. For example, once the simulation is developed for a particular weapon, trajectories from various aircraft may be simulated by using the correct interference coefficients. The program has the option of using flow field angularity data (para 3.2.3) or grid data (para 3.2.2.) to calculate the interference coefficients. Normally, a sufficient number of control fixed CTS trajectories will be run for later correlation and program checkout.

The free stream aerodynamics for the weapon to be simulated are normally obtained from comprehensive wind tunnel tests of 0.20 (or larger) scale models of the weapon. The data, typically in block data form, is normally a total three-dimensional aerodynamic model in the aeroballistic axis system containing control effectiveness and damping terms.

The total aerodynamic coefficients acting on the weapon at any given time during the trajectory are obtained by summing the free stream, interference, and control contributions. For example, the total pitching moment coefficient (where  $\alpha$  is control surface deflection) may be obtained by:

$$C_{M_{total}} = C_{M_{FS}} + C_{M_{INT}} + C_{M_{\alpha}}$$

### 5.6.1 Procedure

The development of a complete trajectory simulation usually consists of building the applicable modules/subroutines of the SIXDOF program to include the aerodynamic interference coefficients, a complete aerodynamic model of the weapon with control effectiveness, and appropriate mathematical models of the weapon flight control system and seeker. Once this is accomplished, simulations may be made of the separation trajectories at various flight conditions throughout the desired envelopes. Uncontrolled, or jettison mode releases with fixed control surfaces, may be conducted by simply by-passing the seeker and flight control subroutines.

The first step in the procedure usually consists of conducting trajectory simulations for each flight condition where CTS trajectories were obtained. Good correlation between CTS and the SIXDOF simulations indicates a good aerodynamic model of the interference coefficients. Once this is obtained, the flight control system can be activated to investigate the controlled launch mode. In addition to normal launches, the simulation can also be used to study the results of failure of such components as the weapon's flight control system or the aircraft ejector rack.

Normally, the primary concern in a trajectory study is to ensure that the weapon separates safely throughout the flight envelope and that chances of weapon-to-aircraft collisions are extremely remote. This applies to the controls-fixed jettison mode as well as the controls-active launch mode. Another, but much less studied aspect, is whether the weapon's aerodynamics and flight control system are capable of handling the launch transients. In other words, will the seeker and gimbal platform of a guided weapon maintain lock on the target during the launch transient?

### 5.6.2 Launch Transient Study - Example

Reference 30 reports on an investigation to determine the cause of excessive break-lock for a guided weapon launched from the inboard wing station of the A-7 aircraft. During flight tests, 6 out of 11 weapons released from the inboard wing station failed to guide properly. The problem was not apparent for the outboard wing station where seven launches were made with only one failure.

Wind tunnel data for the SIXDOF simulations was obtained in the form of CTS and grid data. Six-degree-of-freedom launch simulations were conducted with the weapon autopilot off and compared with CTS trajectories obtained for the same flight conditions. When good correlation was obtained, leading to confidence in the aerodynamics, the autopilot and actuator math models in the SIXDOF simulation were then activated to simulate a normal controlled launch. The program adds the effect of the control deflections commanded by the autopilot which provides pitch and yaw rate and roll position stabilization to the weapon during the first two seconds of the launch phase.



Figure 57 shows the excellent correlation obtained between the computer and CTS prior to activation of the autopilot and controls. Figure 58 shows the correlation between flight test telemetry data and the active autopilot computer simulations. Flight test data for inboard launches were obtained for only two missions.

From the above, it was concluded that the model for A-7 inboard launch dynamics was fairly accurate, and a parametric investigation was conducted in an attempt to find some logical basis for the break-lock and to establish a launch envelope. A-7 inboard wing station launches were simulated for Mach numbers of 0.7, 0.75, 0.8, 0.85, 0.9, and 0.95 at altitudes of 5, 10, 15, and 20 thousand feet. A 45° dive angle and a zero degree gimbal offset angle were used in all cases. Time histories were obtained for the weapon angular positions, rates and accelerations and the seeker gimbal platform pitch, yaw, and roll positions, rates, and accelerations.

In conjunction with the computer simulations, a guidance unit was subjected to rate table tests to determine the maximum body rates/accelerations for the guidance units. The tests concluded that the guidance unit could withstand certain angular rates without breaking lock; however, no conclusions were made as to the effects of pitch/yaw/roll coupling or angular accelerations. Nevertheless, the investigation did prove the feasibility of this approach for defining the launch environment and the rates/accelerations the weapon seekers could expect to see during launch. Also, this type of study could assist in establishing seeker and guidance specifications.

The study also provided guidelines for recommending a launch envelope for the inboard wing station. The maximum absolute value of the body/gimbal rates and accelerations as functions of Mach number and altitude were obtained from the simulations. Figure 59 depicts the maximum absolute body pitch acceleration versus Mach number. In almost every case, a sharp break appears in the curve at about 0.9 Mach number indicating a large increase in the angular excursions at this point. At the lower altitudes, this break moves toward 0.85 Mach suggesting that something below 0.9 Mach would be a realistic launch limit to avoid excessive weapon perturbations.

#### 5.7 Store Design Problems

This section deals with the application of separation prediction methods to support store development programs. In each case serious design deficiencies which resulted in hazardous separation were discovered through wind tunnel testing and trajectory analysis. Proper design corrections were implemented prior to final design and fabrication of full scale test hardware. Early identification resulted in considerable money being saved by avoiding delays in the development and flight test programs and later redesign which would be much more costly.

##### 5.7.1 Large Guided Weapon - US

References 30 and 33 report on application of the flow angularity and grid techniques to investigate F-4 jettison and launch characteristics for a large guided weapon. The investigation was conducted during the early stages of the weapon development program and resulted in considerable changes in the initial design. Redesign was accomplished prior to fabrication of test hardware and considerable improvement of F-4 launch and jettison characteristics was realized.

The original weapon design (Fig. 60) had very large strakes and folding wing tips. The large 100 inch (254 cm) wing span increased glide range and terminal maneuverability. The large strakes were to decrease the "tips-out" static stability for better maneuverability and to reduce trim drag for better range. Because the wing tips were not mechanically interconnected to insure simultaneous opening and because wing tip opening reliability was less than 100 percent, it was decided that jettison and launch envelopes would be established on the basis of "tips-in" separation characteristics. Unfortunately, the weapon was approximately 28 inches (71 cm) statically unstable with the tips in, and the separation analysis revealed that the weapon would not safely separate from the inboard wing stations of the F-4 aircraft over a large portion of the desired jettison envelope (Fig. 61). The primary reason for the poor separation characteristics was the lack of basic aerodynamic static stability. Without resorting to a total redesign, the following three attractive solutions were first investigated:

1. Early wing tip deployment to increase stability.
2. Employing a preset nose-down pitch flap bias.
3. "Tuning" the bomb rack to effect a nose-down pitch at release.

The results of extensive analyses by both the US Air force and the weapon contractor showed that none of the above options, when considered singly or in combination, provided an acceptable solution. The increase in weapon stability provided by the wing tips occurred too late to appreciably change the early portion of the separation trajectory. Also, in some cases, tip deployment more than doubled the lift of the weapon, and the additional wing span compounded the aircraft/weapon clearance problem.

Load capabilities of the control actuators limited the available pitch flap bias to seven degrees, which was not sufficient to provide separation throughout the desired envelope. Figure 62 shows one frame of a computer generated movie of a grid

predicted trajectory of the weapon with seven degree nose-down pitch flap bias released from the F-4 at 0.9 Mach and 40,000 feet.

The best jettison results were obtained by "tuning" the bomb rack to the maximum allowable nose-down pitch. Although this option allowed jettison over most of the captive flight envelope, it was felt that excessive angular rates and accelerations generated by the bomb rack might result in weapon launch malfunctions.

Several weapon redesigns were investigated by the US Air Force and the contractor and are reported on in ref. 33. These investigations led to the revised design of Fig. 63. The folding wing tips were eliminated, and the strake size was reduced to provide approximately the same static stability as the original design with deployed wing tips and large strakes. Although reduction in the size of the aerodynamic surfaces was undesirable from the standpoint of glide range and maneuverability, it was judged to be necessary to obtain acceptable separation characteristics. Figure 64 shows the comparison of grid predicted trajectories and flight test results for the revised design with seven degrees of nose-down pitch flap bias at 0.9 Mach and 40,000 feet. Note the significant improvement in separation characteristics when compared to the original design at the same flight conditions (Fig. 62). Figure 65 shows the comparison of prediction and flight test at 0.8 Mach and 13,000 feet. Correlation between predictions and flight tests were considered to be excellent indicating that early redesign was indeed necessary to achieve satisfactory separation characteristics.

#### 5.7.2 Propelled Missile - France

Since 1962, the study of propelled missiles separation has been performed both at transonic and supersonic regimes inside the blow-down pressurized S3 Modane Wind Tunnel (section 0.76 x 0.80 m<sup>2</sup>). Figure 66 gives some typical results obtained with a propelled missile model fired from under the fuselage of a 1/15th scale MIRAGE III; the micro-rocket had 12 mm in diameter and a thrust of about 80 Newton with a combustion duration of 20 milli-seconds. During the initial tests, the pictures taken from a high speed movie show a very dangerous trajectory, and in fact, the missile hides the nose of the fuselage for these flight conditions; a correct trajectory was later obtained with a small deflection on the missile horizontal tail.

#### 6 Conclusions/Recommendations

The following conclusions and recommendations are based on specific discussions within the text. The paragraph of the text that relates to the conclusion/recommendation is noted at the end in parenthesis. The primary objective of this section is to highlight significant points and identify the most attractive areas for additional research.

- (1) The continued development, improvement, and use of store separation prediction techniques is cost effective, can result in increased mission capability and enhances flight safety (1).
- (2) Realistic bomb rack ejection data is required for accurate store trajectory simulations. This data is practically non-existent except for that obtained on rigid test stands which does not include the significant effects of rack/pylon/wing flexibility, temperature, and aerodynamic store loading (2.2.1).
- (3) The further development of optical alignment systems to precisely align the store models in the proper aircraft carriage position shows much promise for increasing CTS accuracy (3.2.1.3).
- (4) Additional research is required to determine the best method of employing the flow angularity technique. Also probe interference effects should be determined (3.2.3).
- (5) The "limited grid" technique assumes that the interference effects are primarily functions of vertical displacement rather than including lateral and longitudinal displacements or rotations as in the normal grid technique. A wind tunnel research program should be conducted to determine to what extent this assumption is valid (3.2.2).
- (6) A wind tunnel research program should be conducted to further investigate the effects of store staggering on reducing adverse installed forces and moments that cause poor separation trajectories. Multiple carrier configurations could possibly be optimized for separation as well as reduced drag (5.4.1.1).
- (7) The aft pivot release system for MER, pylon, and fuel tank jettison is an excellent approach to the very hazardous problem of unstable store jettison. However, the pivots must be located as far aft on the items as possible and restrain the items in pitch as long as possible to provide optimum results (5.2).
- (8) Additional research should be conducted to fully develop the concept of self-compensating dual ejector bomb racks (5.4.1.3).
- (9) The concept of "Conformal Carriage" offers the greatest potential for improvement of separation and delivery characteristics for unguided weapons. Additional wind tunnel testing is warranted to optimize the conformal carriage pallet for store separation and to eliminate the high speed pitch problems experienced with MK-82 bombs (5.4.2).

(10) Flow field effects can be extremely important in increasing dispersion and degrading delivery accuracy of unguided weapons. Pattern improvements for "dumb bombs" can be realized by adopting high impulse tunable bomb ejector racks and through new developments such as self-compensating racks and improved carriage concepts such as Vertical Ejector Racks and Conformal Carriage (5.5).

#### REFERENCES

1. A-7D Cost Reduction, letter from Commander, Naval Air Systems Command to Headquarters Aeronautical Systems Division, 30 Mar 1970.
2. Schindel, L. H., Store Separation, AGARD Report AGARD-AG-202, Jun 1975.
3. Marshall, J. C., and Summers, W. E., An Analysis of the Relative Importance of Parameters Required for the Simulation of Store Separation Trajectories, Aircraft/Stores Compatibility Symposium Proceedings, Vol 2, Dayton, Ohio, Dec 1971.
4. Dragowitz, C., Clark, J., and Johnson, R., Systematic Study of the Effects of Various Parameters on Store Separation, Aircraft/Stores Compatibility Symposium Proceedings, Vol 2, Dayton, Ohio, Dec 1971.
5. Orlik-Ruckemann, J. G., LaBeroe, J. G., and Hanff, E. S., Supersonic Dynamic Stability Experiments on the Space Shuttle, Journal of Spacecraft and Rockets, Vol 9 No. 9, Sep 1972.
6. Orlik-Ruckemann, J. G. and Iyengar, Example of Dynamic Interference Effects Between two Oscillating Vehicles, Journal of Spacecraft and Rockets, Vol II No. 9, Sep 1973.
7. Bottoms, W. C., Evaluation of the Captive Trajectory Technique of Wind Tunnel Testing for the Prediction of External Stores Flight Separation Trajectories, Aircraft/Stores Compatibility Symposium Proceedings, Vol 3, Dayton, Ohio, Dec 1971.
8. Proof Ejection Test of Douglas Aircraft Company Multiple Ejector Rack, and Triple Ejector Rack, Mounted to Aircraft Support Structure, McDonnell Aircraft Co. Report 053-024, Oct 1962.
9. Lockhart, J. W., Multiple Suspension Developments, Aircraft/Stores Compatibility Symposium Proceedings, Vol I, Eglin AFB FL, Nov 1969.
10. Kyle, R. L., Suspension System Considerations, Aircraft/Stores Compatibility Symposium Proceedings, Vol 1, Sacramento, Calif, Sep 1973.
11. Jendras, S. J., Ejection Release of Aerodynamically Unstable Stores, Aircraft/Stores Compatibility Symposium Proceedings, Vol 1, Arlington, VA, Sep 1975.
12. Hiscock, B., The Development of a Compact High Strength Ejector Release Unit for MRCA, Aircraft/Stores Compatibility Symposium Proceedings, Vol II, Arlington, VA, Sep 1975.
13. Hasquenoph, J. H., Advantages and Possible Developments of Release and Ejector Units Using the Saddle Suspension System, Aircraft/Stores Compatibility Symposium Proceedings, Vol II, Arlington, VA, Sep 1975.
14. Davis, R. E., Flow Field Characteristics Beneath the F-4C Aircraft at Mach Numbers 0.5 and 0.85, AEDC-TR-70-8, Feb 1970.
15. Spahr, H. R., Everett, R. N., Kryvoruka, J. K., A Multifaceted Store Separation Analysis, Proceedings of the Eighth AIAA Aerodynamic Testing Conference, Dallas, Texas, Jul 1976.
16. Binion, T. W., Jr., Special Wind Tunnel Test Techniques Used at the AEDC, AGARD Fluid Mechanics Panel Symposium, "Flight/Ground Testing Facilities Correlations," Valloire, France, Jun 1975.
17. Christopher, J. P. and Carleton, W. E., Captive Trajectory Store - Separation System of the AEDC - PWT 4-Foot Transonic Tunnel, AEDC-TR-68-200, Sep 1968.
18. Jones, J. H., Store Separation Testing Capabilities in the AEDC/VKF Supersonic and Hypersonic Wind Tunnels, Aircraft/Stores Compatibility Symposium Proceedings, Vol 1, Dayton, Ohio, Dec 1971.
19. Nichols, J. H. Jr. and Strachan, B. C., Effects of Fin and Ejector Rack Modifications on the Separation Characteristics of a Store When Jettisoned from an A-4 Airplane, DTNSRDC Report 2278, Sep 66.
20. Wolfe, J. A., A Computer Controlled Wind Tunnel Testing System for Investigation of Aircraft or Booster Separation Problems, Aircraft/Stores Compatibility Symposium Proceedings, Vol 3, Dayton, OH, Dec 1971.

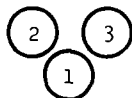
21. Captive Trajectory Testing 8-Foot Transonic Wind Tunnel, Calspan Corporation Report No. WTO-461, Aug 1967.
22. Haines, A. B., Techniques at A.R.A. for Store Trajectory Tests, A.R.A. Aero Memo No. 168, May 1975.
23. Marsden, P., Design Study for the Installation of a Two Sting Rig for Captive Store Trajectory in the A.R.A. 9 Ft x 8 Ft Transonic Wind Tunnel, A.R.A. Model Test Note M.76/1, Vol 1, 2, and 3, Jan - Feb 1975.
24. Dix, R. E., A Review of Methods of Measuring Aerodynamic Forces and Moments Acting on Captive Stores in Wind Tunnel Tests, AEDC-TR-72-108, Aug 1972.
25. Dix, R. E., Influences of Sting Support on Aerodynamic Loads Acting on Captive Stores, AEDC-TR-76-1, Mar 1976.
26. Arnold, R. J. and Epstein, C. S., The Uses and Limitations of the Captive Trajectory System in Store Separation Analyses, Aircraft/Stores Compatibility Symposium Proceedings, Vol 2, Dayton, Ohio, Dec 1971.
27. Arnold, R. J., Braud, S. C., and Hill, D. W. Jr., An Investigation of Factors Affecting the Accuracy of the Captive Trajectory Wind Tunnel Technique, Aircraft/Stores Compatibility Symposium Proceedings, Vol 4, Sacramento, Calif, Sep 1973.
28. Studwell, V. E., Experimental Aerodynamics of Multiple Weapon Carriage, AFATL-TR-71-5, Jan 1971.
29. Little, R. E., A Parametric Method of Aerodynamic Flow Field Investigation, Aircraft/Stores Compatibility Symposium, Vol 3, Sacramento, Calif, Sep 1973.
30. Mathews, C. B., Cason, R. D., McGirr, P. G., Carreras, E. M., A Technique for Investigating the Launch and Separation of Guided Weapons, Aircraft/Stores Compatibility Symposium, Vol 1, Arlington, VA, Sep 1975.
31. Korn, S. C., Use of the Flow Angularity Technique for Predicting Store Separation Trajectories, AFATL-TR-71-140, Oct 1971.
32. Korn, S. C., Validation and Expansion of the Flow Angularity Technique for Predicting Store Separation Trajectories, AFATL-TR-72-184, Sep 1972.
33. Blose, T. G., Barnes, R. M., Launch Transient Analysis: Essential Element of an Air Launched Weapon Configuration Development, Aircraft/Stores Compatibility Symposium Proceedings, Vol 1, Arlington, VA, Sep 1975.
34. Schlicher, J. H. Jr., F-111 Wind Tunnel Store Separation Testing Techniques, Aircraft/stores Compatibility Symposium Proceedings, Vol 6, Eglin AFB FL, Nov 1969.
35. Moore, S. B., Advanced Wind Tunnel Simulation System and Techniques for Aircraft Store Carriage and Delivery Studies, Aircraft/Stores Compatibility Symposium Proceedings, Vol 6, Eglin AFB FL, Nov 1969.
36. Reed, J. F. and Curry, W. H., Aircraft Separation Problems Associated with Nuclear Ordnance - A Survey, Aircraft/Stores Compatibility Symposium Proceedings, Vol 6, Eglin AFB FL, Nov 1969.
37. Brooks, D. L., Weapon Separation Clearance Procedures for the F-111 Aircraft, Aircraft/Stores Compatibility Symposium Proceedings, Vol 2, Dayton, Ohio, Dec 1971.
38. Garrone, A., Bucciantini, G., Barbantini, E., Comments on Wind Tunnel/Flight Correlations for External Stores Jettison Tests on the F-104S and G-91Y Aircraft, AERITALI Report, May 1975.
39. Barche, J., Letter to C. B. Mathews, USAF, on Heavy Model Separation Tests from 1:5 Alpha-Jet Model in the Modane S-2 Tunnel, Aug 1975.
40. Cox, G. A., Mathematical Modelling of External Store Jettison Trajectories Including Comparison with Flight Data, British Aircraft Corp LTD Report, Jun 1975.
41. Covert, E. E., Wind Tunnel Simulation of Store Jettison with the Aid of an Artificial Gravity Generated by Magnetic Fields, Journal of Aircraft, Vol 4, No. 1, Jan - Feb 1967.
42. Stephens, T., Wind Tunnel Simulation of Store Jettison with Magnetic Artificial Gravity, Aircraft/Stores Compatibility Symposium Proceedings, Vol 3, Dayton, Ohio, Dec 1971.
43. Hinson, W. F., Transonic and Supersonic Ejection Release of Six Dynamically Scaled External Store Shapes from a 0.086 Scale Model of a Current Fighter Plane, NASA TMX-128, Dec 1959.

44. Stores Release and Jettison - Improvement of "Light Model" Wind Tunnel Testing Techniques, Hawker - Siddeley Aviation LTD. Note No. Y.W.T. 2173, Apr 1973.
45. Newby, K. P., Status of Work on Accelerator for Improving the "Light Model" Free-drop Store Release Technique, Hawker-Siddeley Aviation, LTD. Note No. Y.W.T. Dev. 1588, Aug 1976.
46. Kewby, K. P., Light Model Store Separation, Hawker-Siddeley Aviation, LTD, Note 26.8.76, Aug 76.
47. Paulk, R. A., Experimental Investigation of the Effect of Various Scaling Laws on the Quality of the Freedrop Store Separation Simulation, AEDC-TR-76-24, 1976.
48. Coste, J., Firing and Release Tests on Models in the S3 Modane-Avrieux Wind Tunnel.
49. Coste, J. and Christophe, J., Wind Tunnel Studies of Aerodynamic Interactions Induced by Jettisonable Loads, report submitted at the AGARD/FMP Specialists Meeting, Silver Springs, MD, Sep 1970.
50. Epstein, C. S., Aircraft Stores Compatibility Analysis and Flight Testing, Aircraft/Stores Compatibility Symposium Proceedings, Vol 1, Arlington, VA, Sep 1975.
51. Aden, A., The Optimum Photo Analysis System, Aircraft/Stores Compatibility Symposium Proceedings, Arlington, VA, Sep 1975.
52. Watson, J. H., Batchelder, R. H., A Technique for Low Density Store Separation, Aircraft/Stores Compatibility Symposium Proceedings, Vol 2, Dayton, Ohio, Dec 1971.
53. Hollingsworth, W. B., Evaluation of a Pivot Release System for Jettison of MER/Conventional-Weapons Configurations from the Centerline Station of the F-4 Aircraft, Aircraft/Stores Compatibility Symposium Proceedings, Vol 3, Dayton, Ohio, Dec 1971.
54. Short, C. R. and Lanterman, B. J., A Pivot Mechanism to Provide an Extended Jettison Envelope for the F-15 Aircraft, Aircraft/Stores Compatibility Symposium, Vol 2, Sacramento, Calif, Sep 1973.
55. Summers, W. E., Separation Trajectories for the SUU-51B/B Store from the F-4C Aircraft, AEDC-TR-72-91, Jun 1972.
56. Summers, W. E., Effects of Variations in Triple-Ejection-Rack-Faring Geometry on Separation Characteristics of Two Stores from the F-4C Aircraft, AEDC-TR-72-197, Dec 1972.
57. Bright, D. J., Comparison Test of Standard and Modified TER-9A on the F-4, ADTC-TR-73-2, Jan 1973.
58. Holmberg, J. L., A Study of the SUU-51A/B Dispenser Munition High Speed Separation Problem and Proposed Solutions, AFATL-TR-73-114, May 1973.
59. Holmberg, J. L., Modifications of Triple Ejector Rack Geometry to Reduce Bottom Station Weapon Separation Perturbations at High Speeds, AFATL-TR-73-171, Aug 1973.
60. Kalivretenos, C. A., Schindel, L. H., and Maestri, R. R., Self-Compensating Store Ejection Technique, Aircraft/Stores Compatibility Symposium Proceedings, Vol 2, Dayton, Ohio, Dec 1971.
61. Maestri, R. R., Self-Compensating Store Ejection, Aircraft/Stores Compatibility Symposium Proceedings, Vol 2, Sacramento, Calif, Sep 1973.
62. Smith, R. E., Conformal Carriage Separation Program, Aircraft/Stores Compatibility Symposium, Vol 3, Sacramento, Calif, Sep 1973.
63. Maddox, A. R., A Parametric/Sensitivity Study of Store Separation, Aircraft/Stores Compatibility Symposium Proceedings, Vol 3, Sacramento, Calif, Sep 1973.
64. Gonzalez, J. M., Theoretical Sensitivity Analysis and System Delivery Accuracy Computations for High and Low Drag Weapons at Several Subsonic and Supersonic Delivery Conditions, AFATL-TR-70-110, Oct 1970.

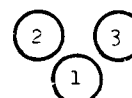
TABLE 1. EFFECT OF THE INTERFERENCE FLOW FIELD ON THE TERMINAL ACCURACY OF THE M-117 BOMB RELEASED FROM THE F-4 TER AT 5,000 FEET AND MACH NUMBERS OF 0.5, 0.7, AND 0.9

MISS DISTANCES - METERS

LEFT WING TER



RIGHT WING TER



MACH 0.5/0.7/0.9

STATION

RT WG

①	-46/-89/-140	+14/+23/+33	48/91/144
②	-9/-23/-45	+10/+31/+38	14/39/59
③	-7/-12/-12	+43/+63/+87	48/65/88

LT WG

①	-46/-89/-140	-14/-23/-33	48/91/144
②	-11/-18/-18	-44/-65/-88	46/67/96
③	-5/-18/-27	-11/-32/-38	12/37/47

Negative Downrange is Short  
Negative Crossrange is Right

TABLE 2. DIFFERENCE IN DOWNRAGE IMPACT POINT FOR A DISPENSER MUNITION RELEASED FROM THE F-4 BOTTOM INBOARD TER STATION AT VARIOUS MACH NUMBERS - SINGLE AND SELF-COMPENSATING DUAL EJECTOR RACKS

IMPACT DEVIATION COMPARISON

Release Conditions: 5,000 ft, straight and level

Standard TER  
1200 Lb (5338 N) Ejector Force

Mach	Ejector Moment		Deviation	
	(Ft. Lbs)	(N.M)	(Ft)	(M)
.5	350	475	565 (S)	172 (S)
.7	350	475	12 (S)	4 (S)
.9	350	475	499 (S)	152 (S)
1.05	350	475	484 (S)	148 (S)
1.2	350	475	1010 (S)	308 (S)

Dual Ejector TER  
5,000 lb (22,241 N) Ejector Force

Mach	Ejector Moment			
	(Ft. Lbs)	(N.M)	(Ft)	(M)
.5	407	552	72 (L)	22 (L)
.7	1087	1474	32 (L)	10 (L)
.9	3657	4958	32 (L)	10 (L)
1.05	4842	6565	74 (S)	23 (S)
1.2	5729	7767	250 (S)	76 (S)

(S) = W/INT lands short of no INT  
(L) = W/INT lands longer than no INT

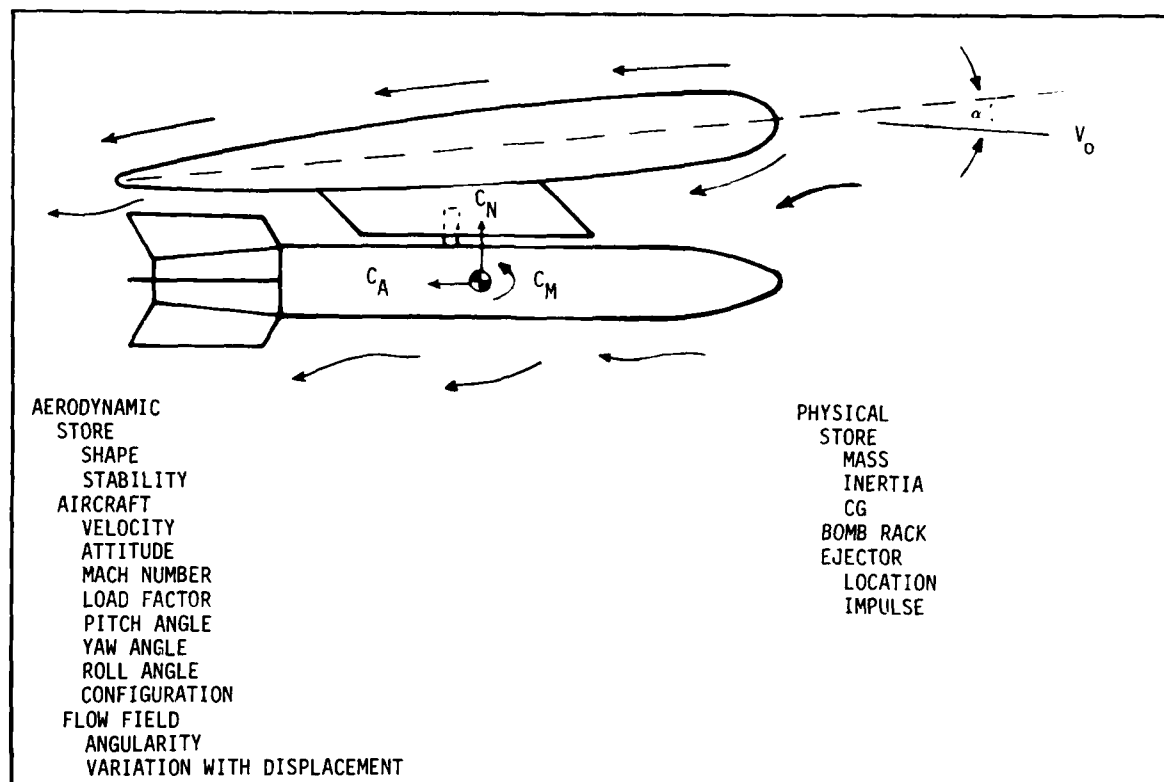


Figure 1 Store Separation Parameters

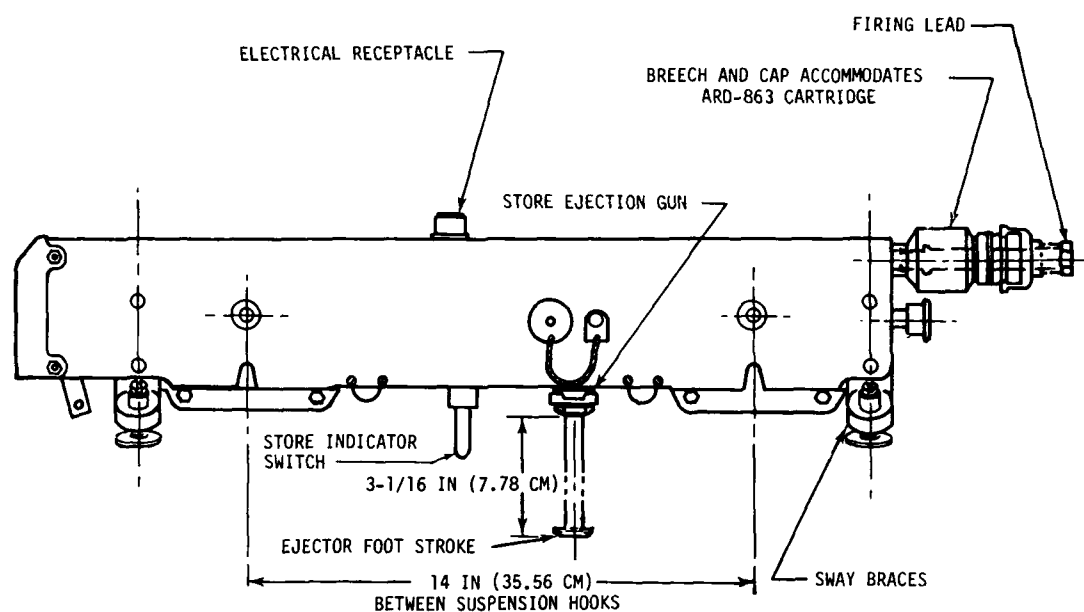


Figure 2 Bomb Ejector Rack - Single Ejection Piston

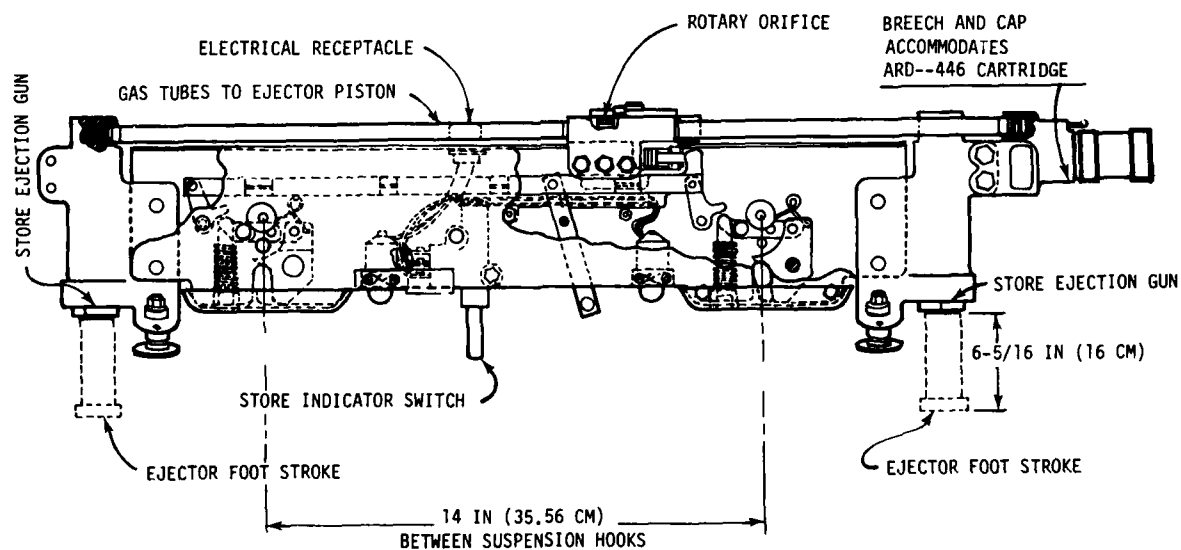


Figure 3 Bomb Ejector Rack - Dual Ejection Piston



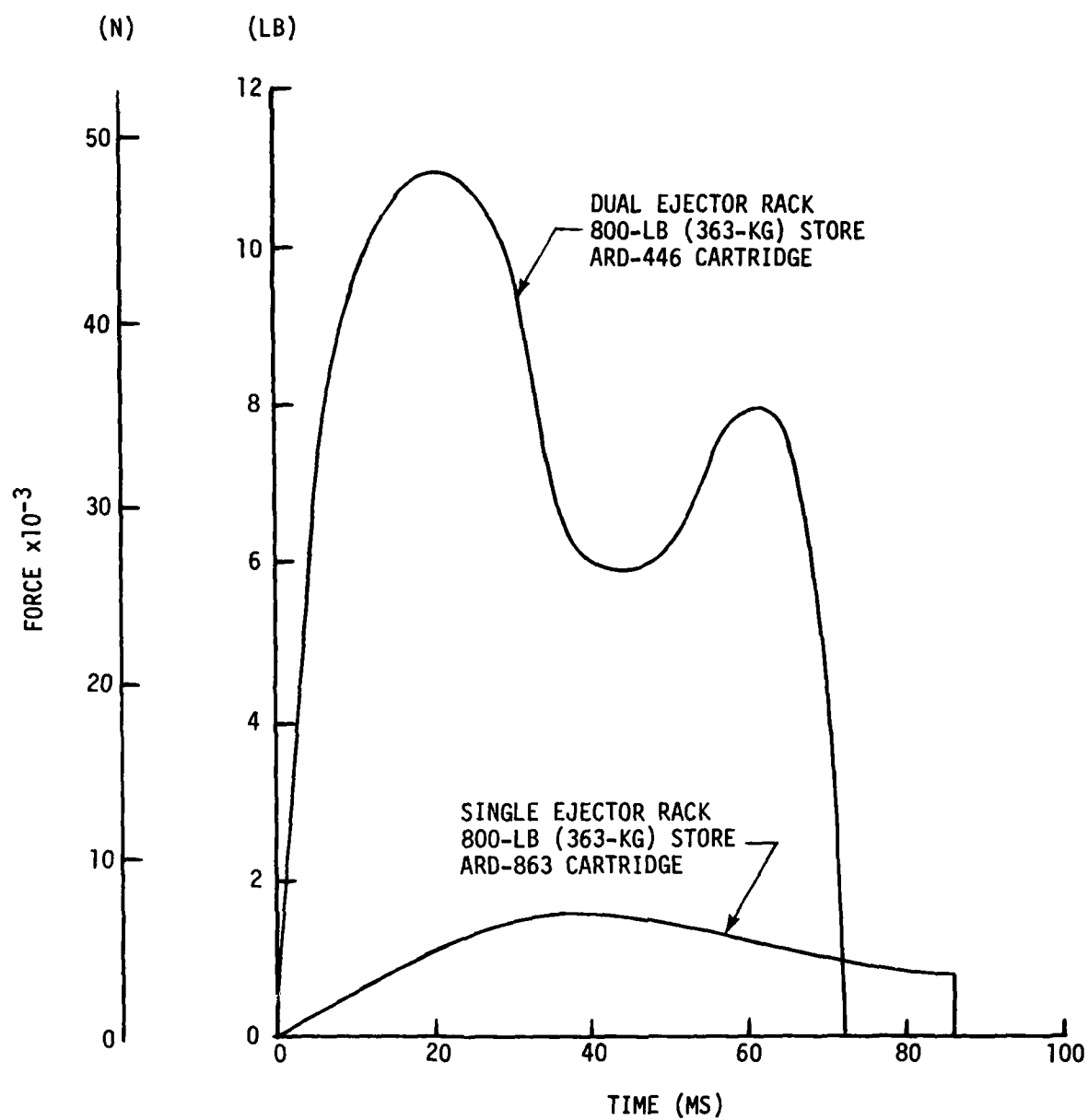


Figure 4 Impulse Performance of Typical Single and Dual Ejector Racks

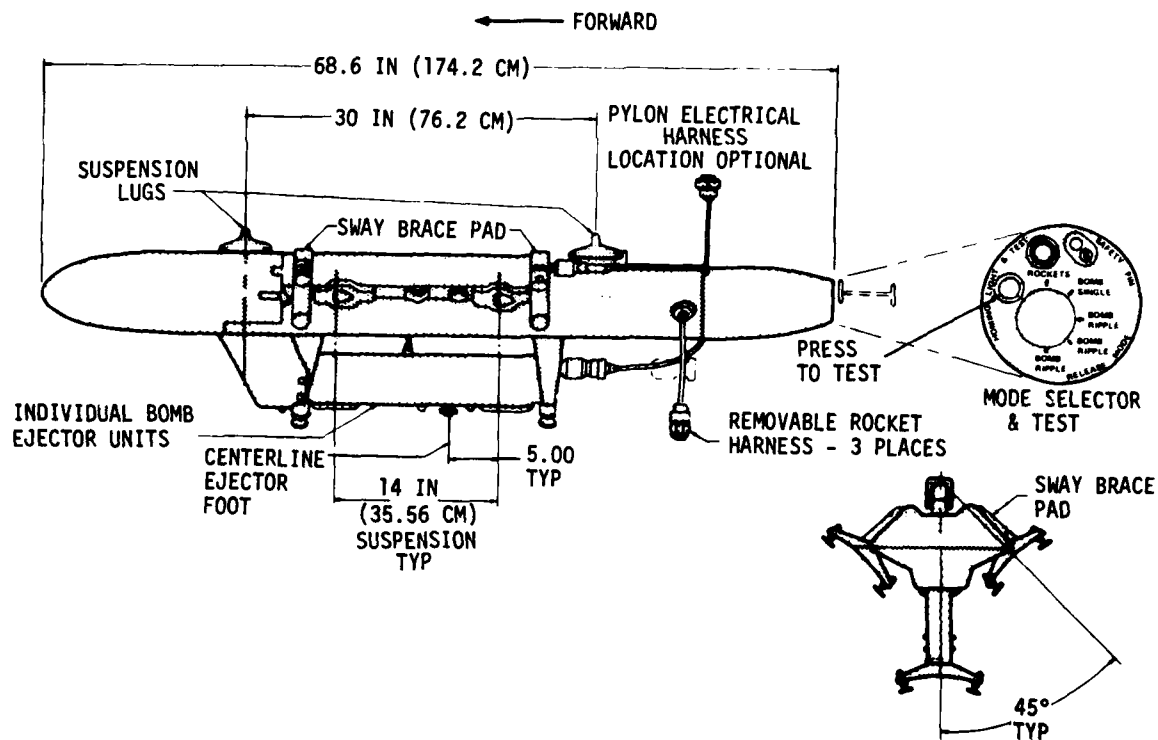


Figure 5 Triple Ejector Rack (TER)

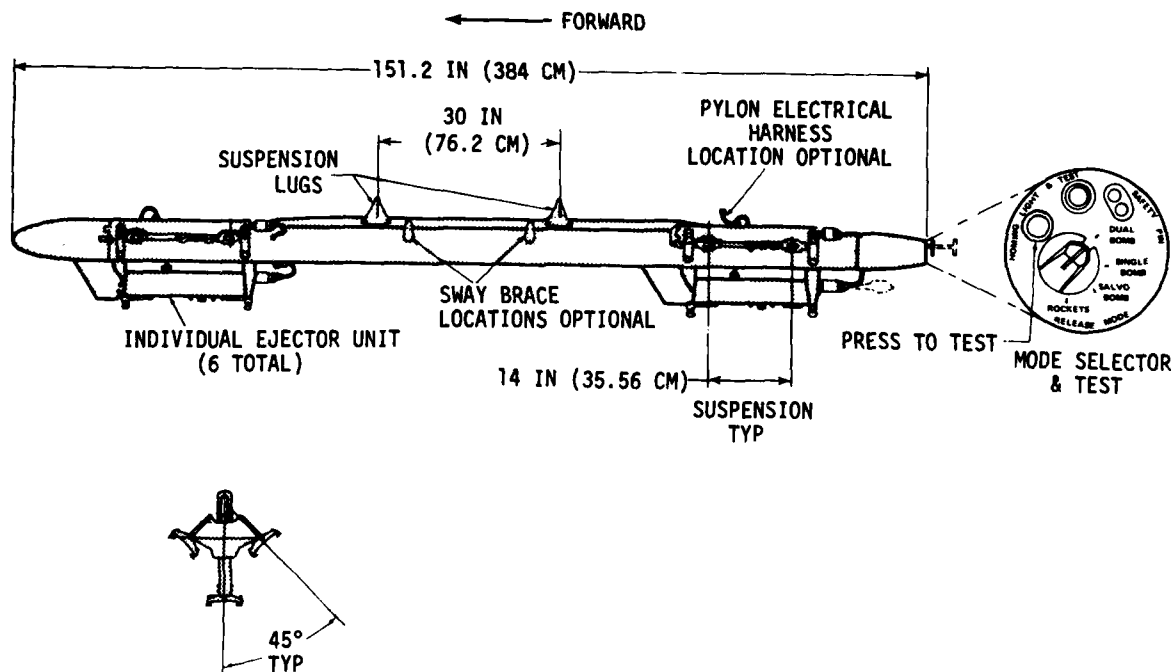


Figure 6 Multiple Ejector Rack (MER)

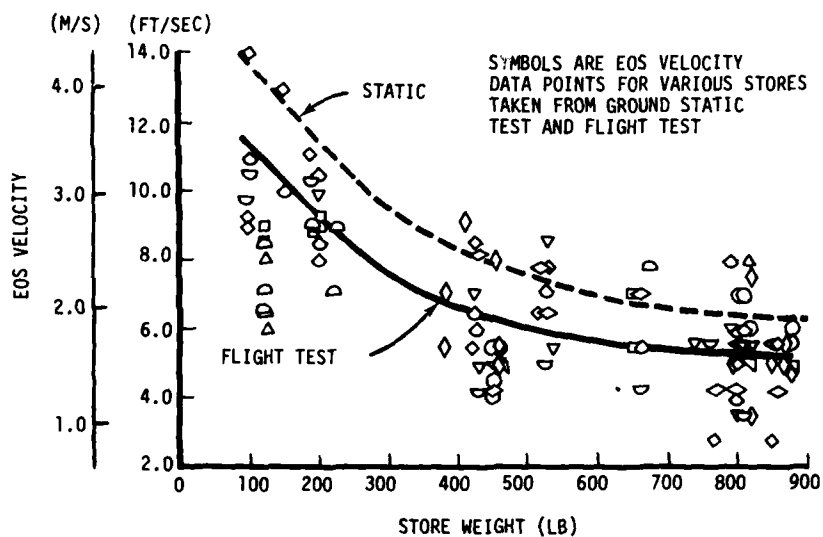


Figure 7 Flight Test Correction for Bomb Rack End-of-Stroke (EOS) Ejection Velocity

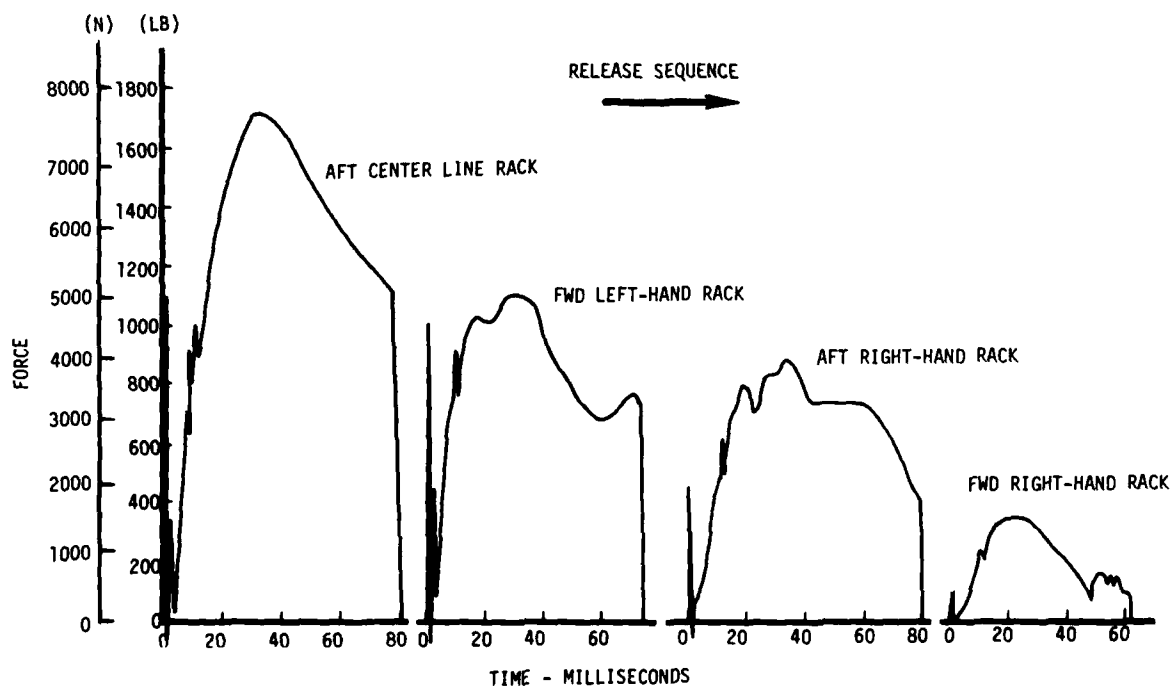


Figure 8 Impulse Variation for Ejection Tests of M-117 Bombs from the F-4 Centerline MER

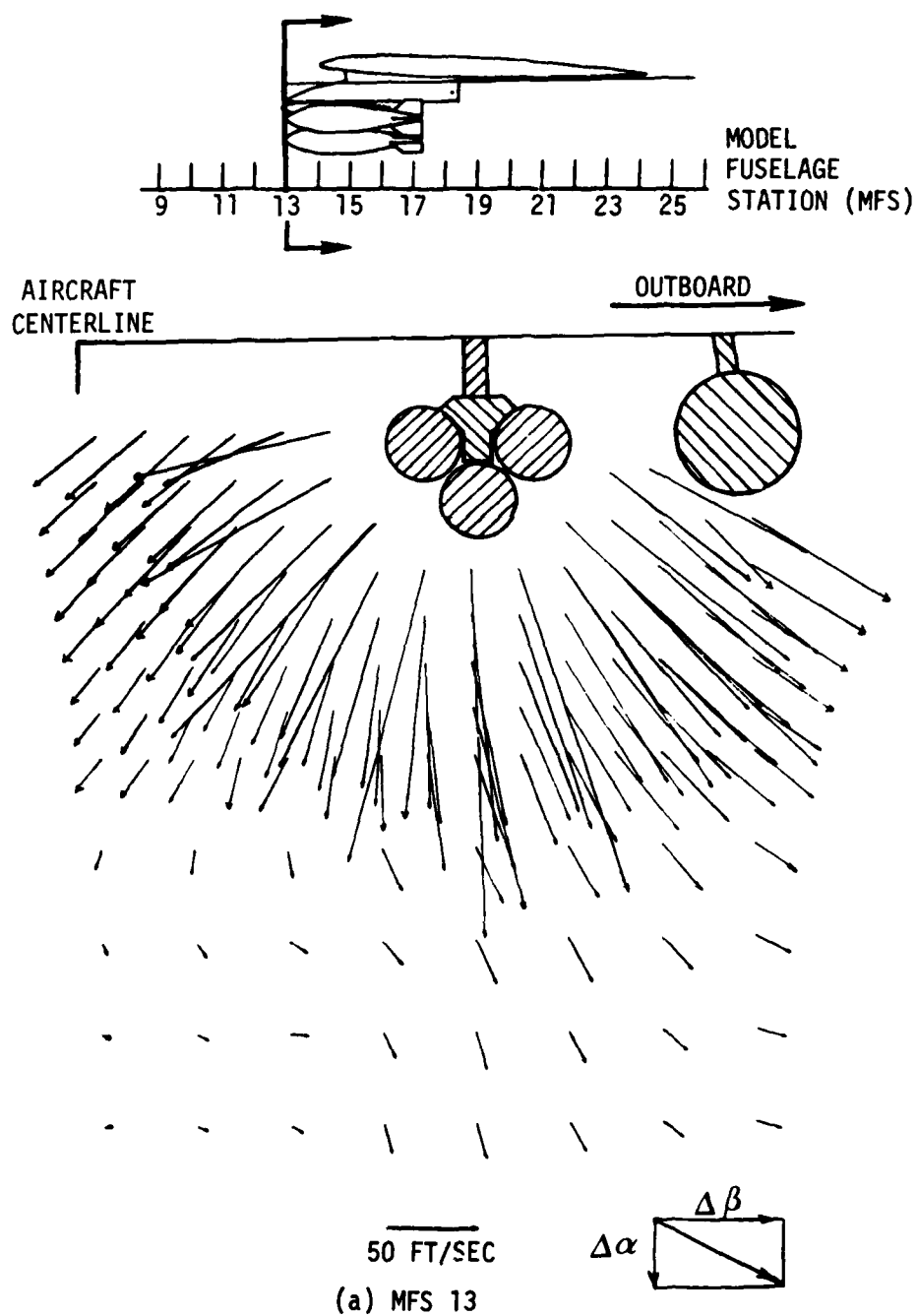


Figure 9 F-4 Interference Flow Field at 0.85 Mach (Asymmetric Configuration)

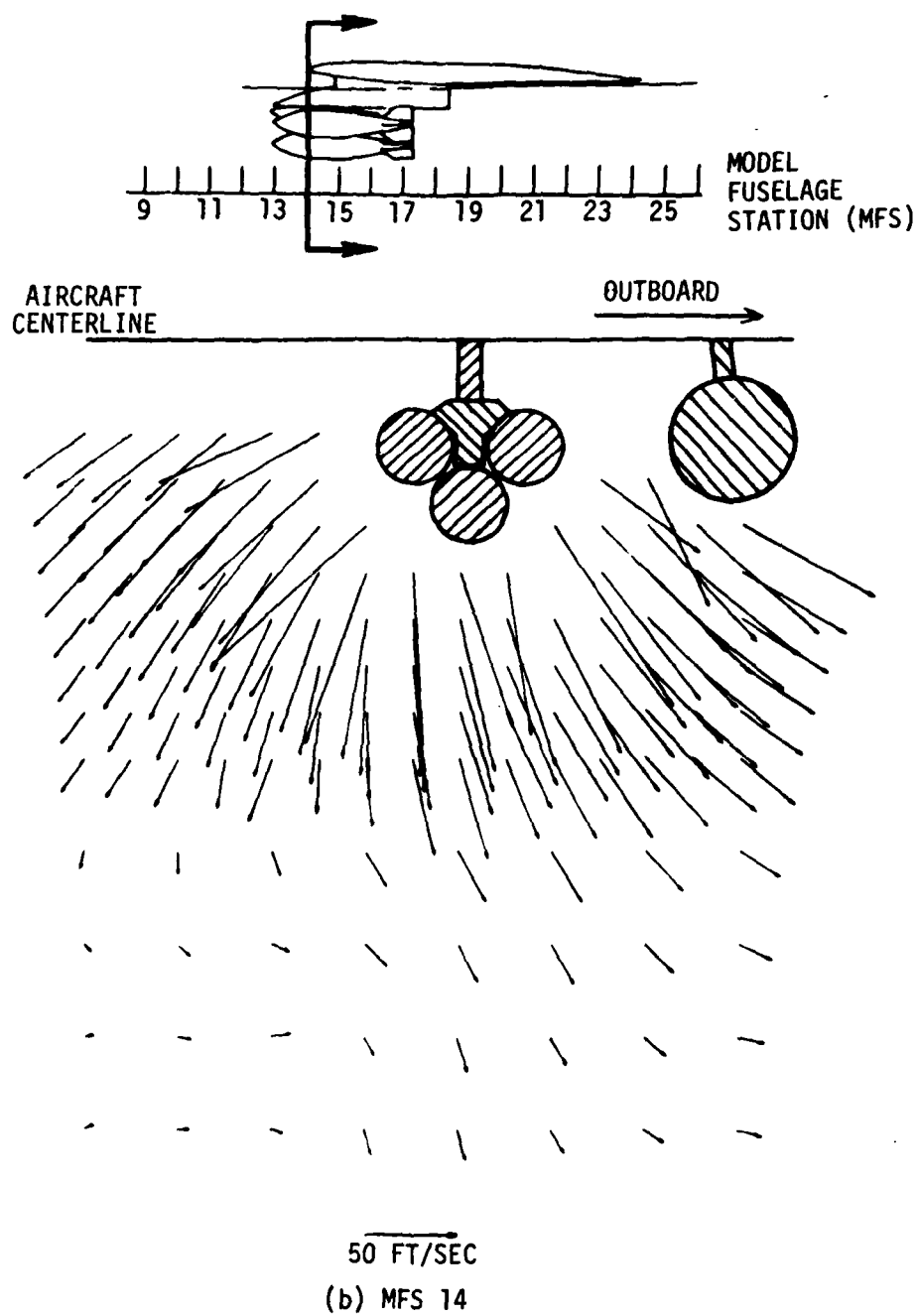


Figure 9 F-4 Interference Flow Field at 0.85 Mach (Asymmetric Configuration)  
(Continued)

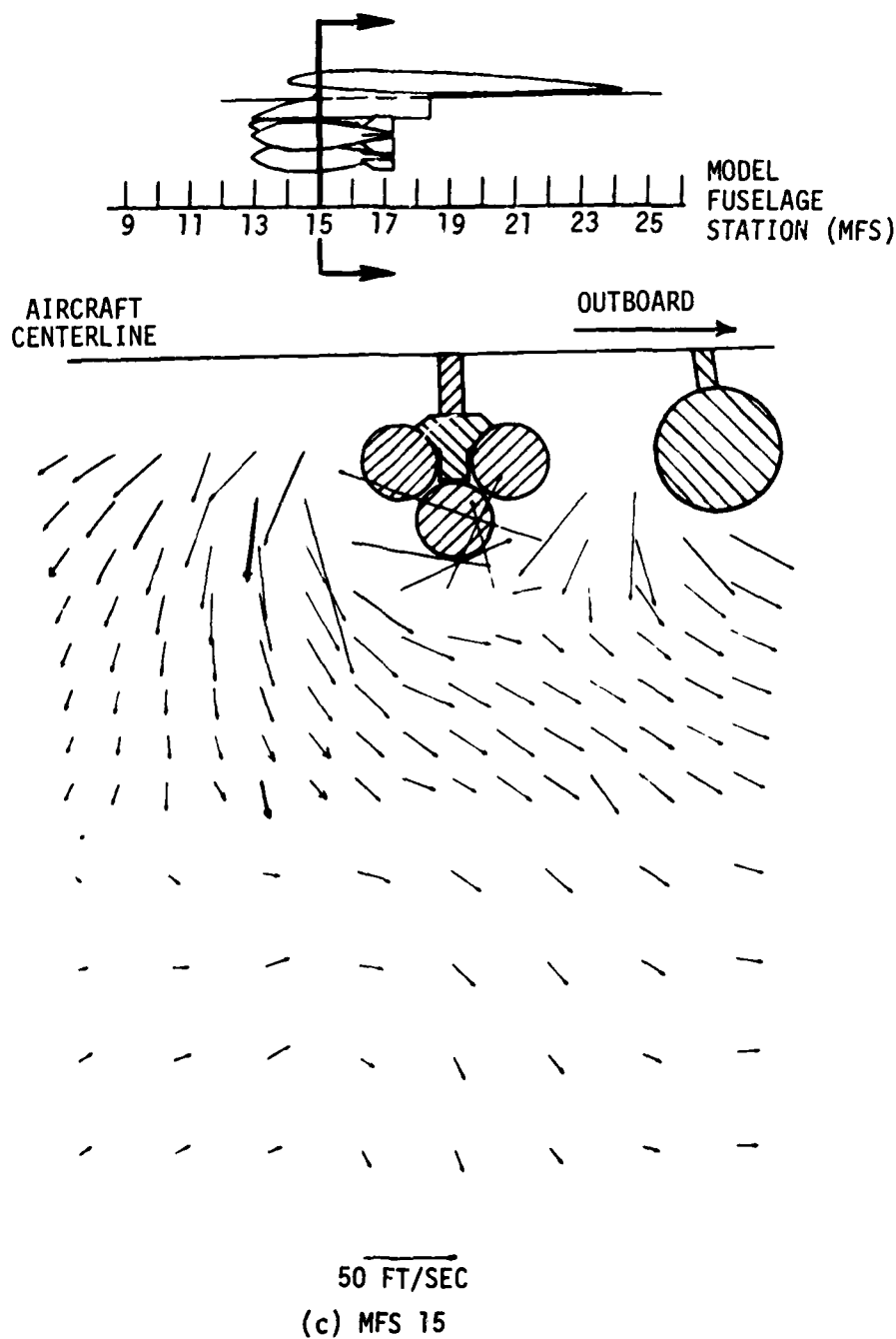
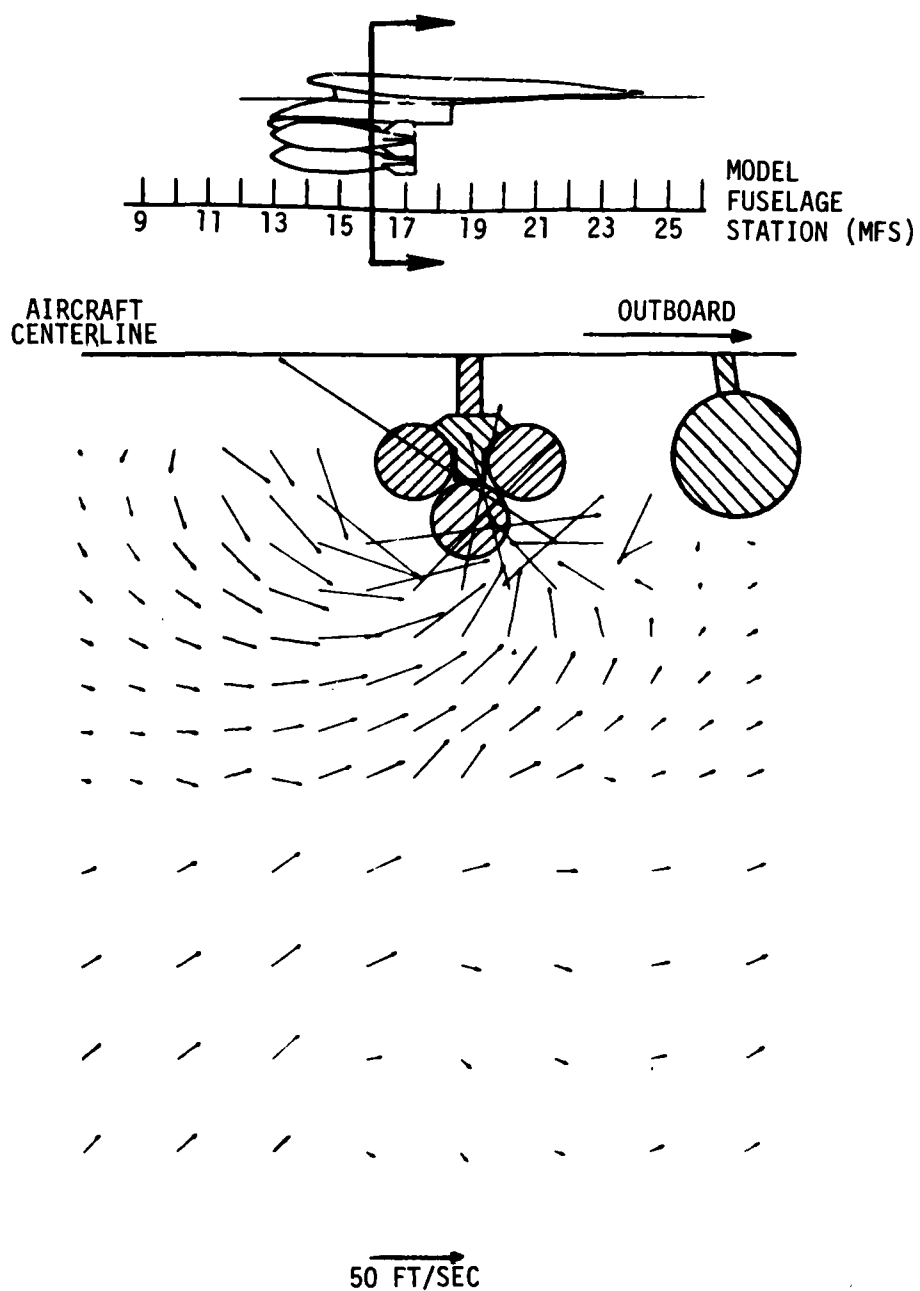


Figure 9 F-4 Interference Flow Field at 0.85 Mach (Asymmetric Configuration)  
(Continued)



(d) MFS 16

Figure 9 F-4 Interference Flow Field at 0.85 Mach (Asymmetric Configuration)  
(Continued)

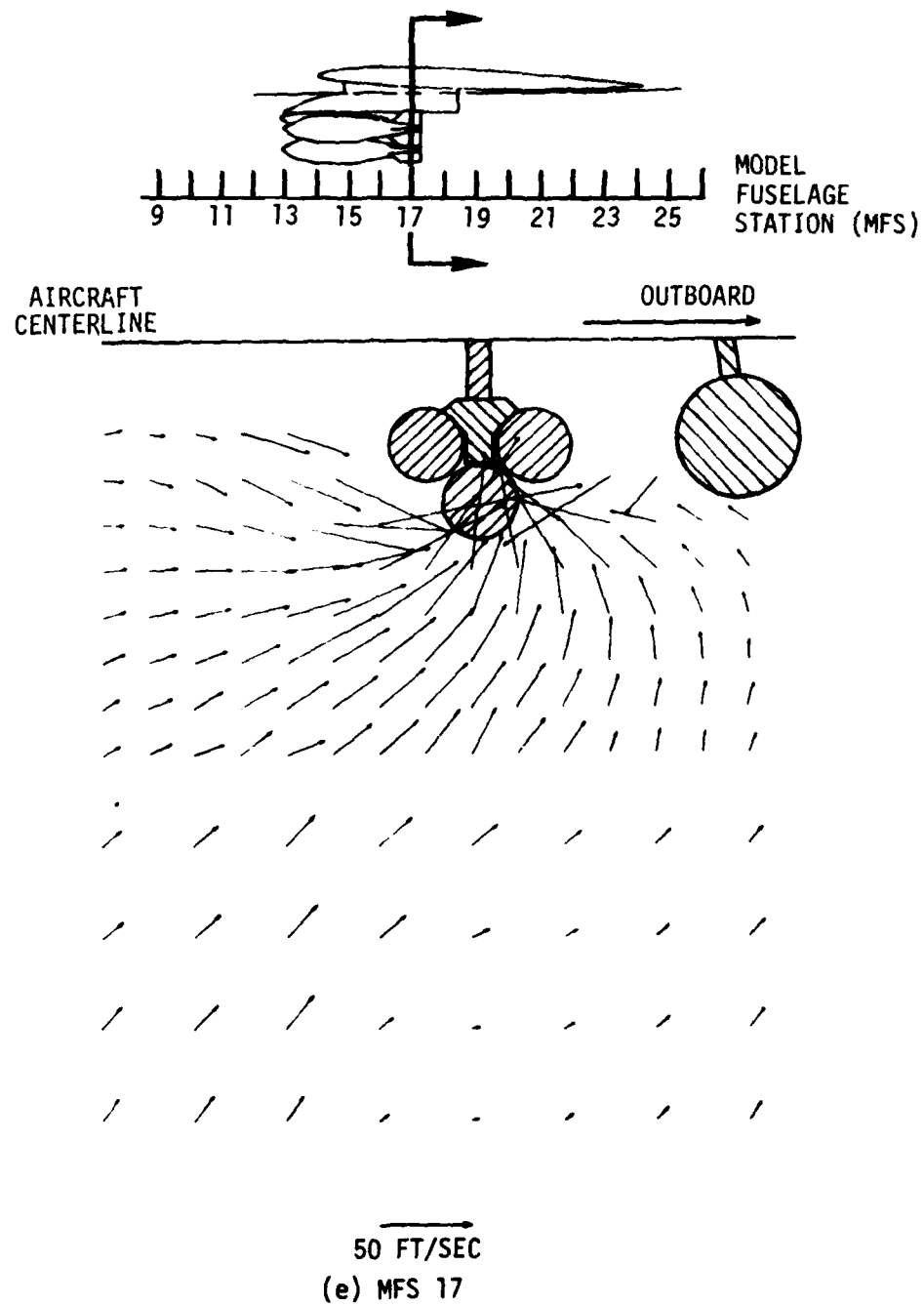


Figure 9 F-4 Interference Flow Field at 0.85 Mach (Asymmetric Configuration)  
(Continued)



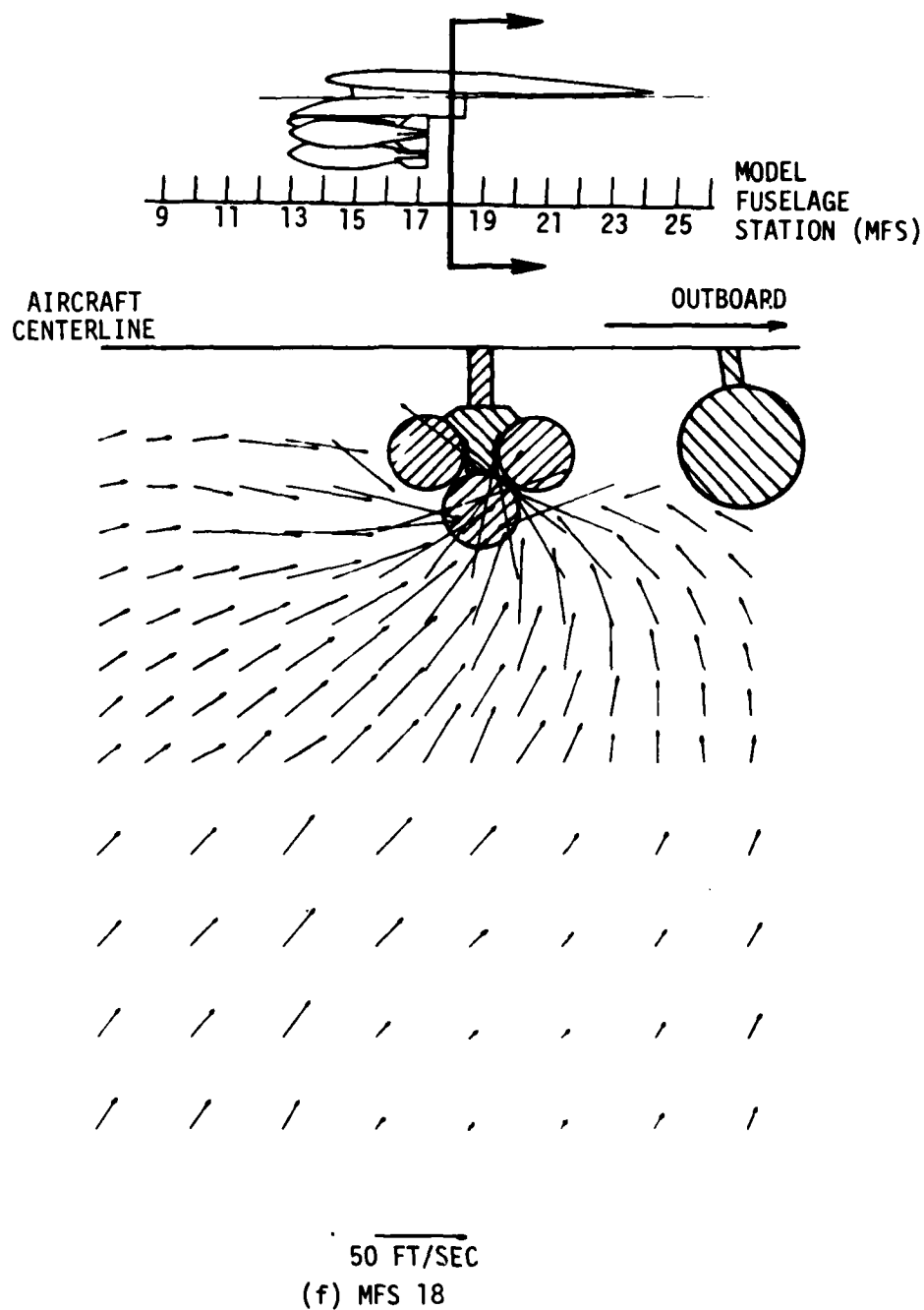


Figure 9 . F-4 Interference Flow Field at 0.85 Mach (Asymmetric Configuration)  
(Concluded)

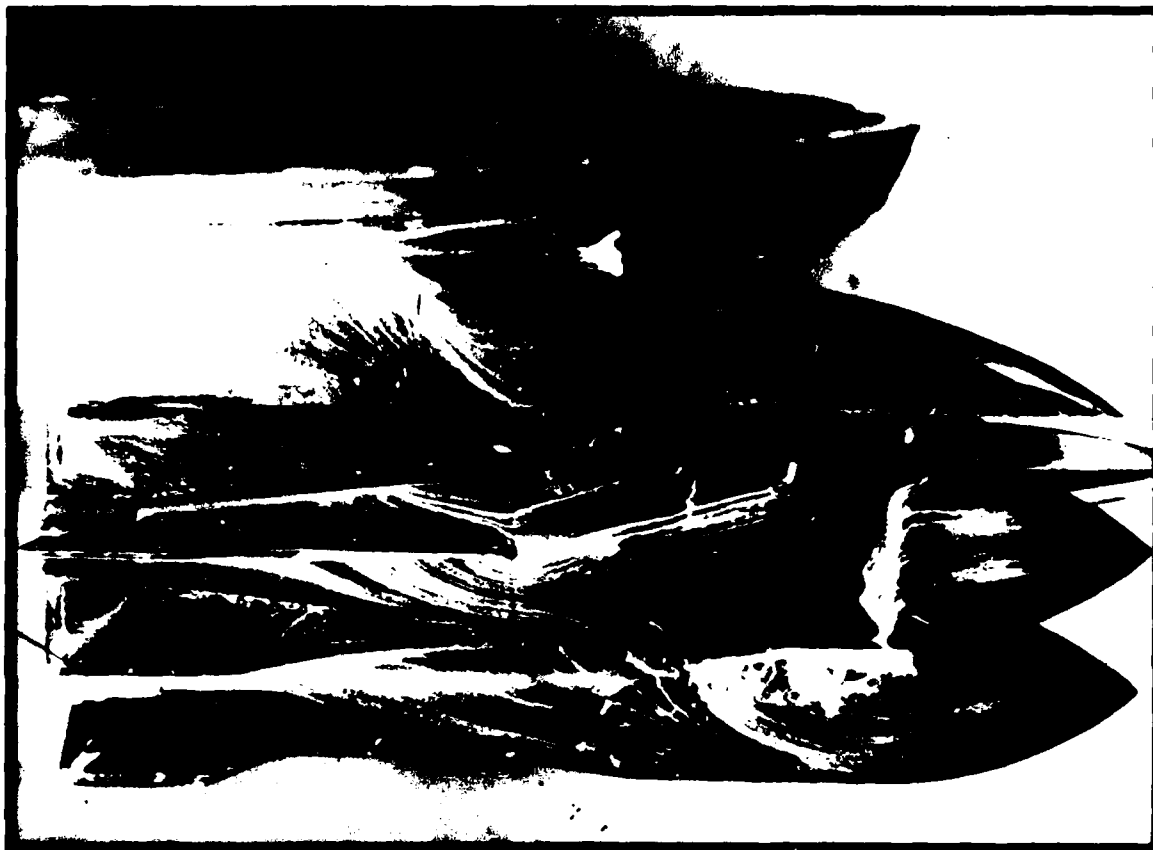


Figure 1 Oil Flow Test of Three X-117 Bombs on an F-4 Inboard Wing Station TER

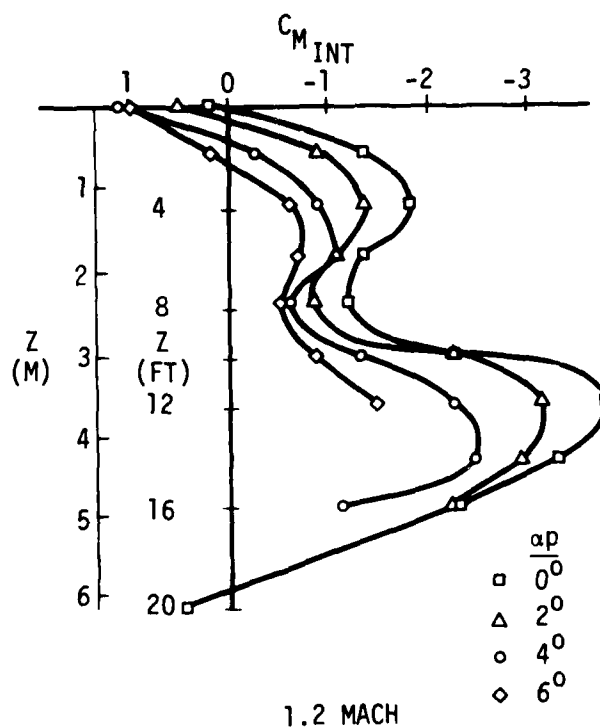
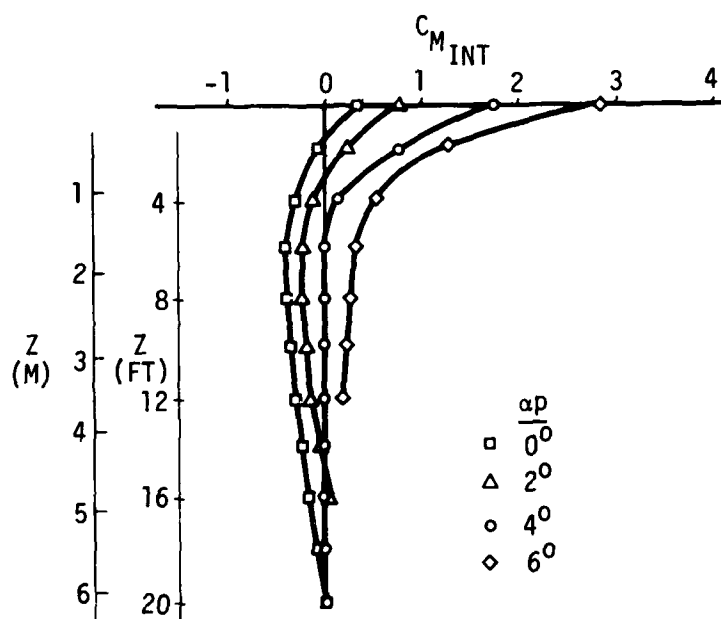


Figure 11 Variation in Interference Pitching Moment Coefficient with Store Vertical Displacement - F-4 Aircraft, 0.8 and 1.2 Mach

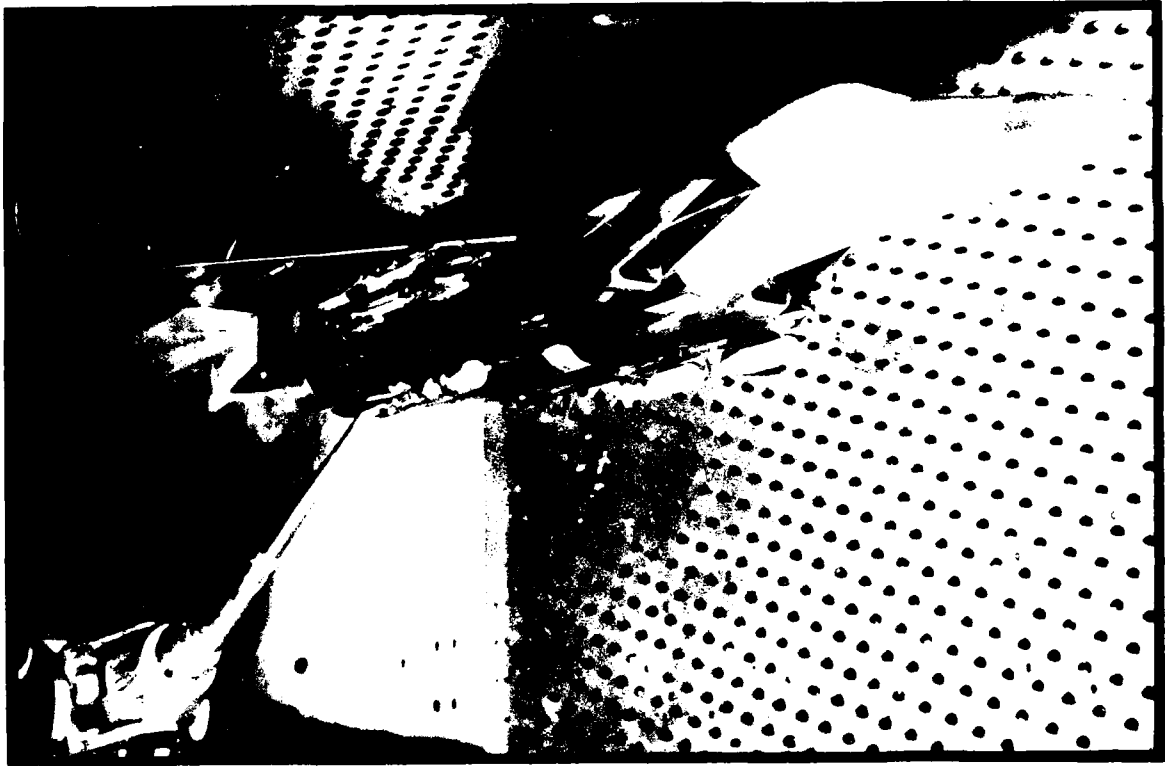


Figure 12 Typical TR Model Installation - 67

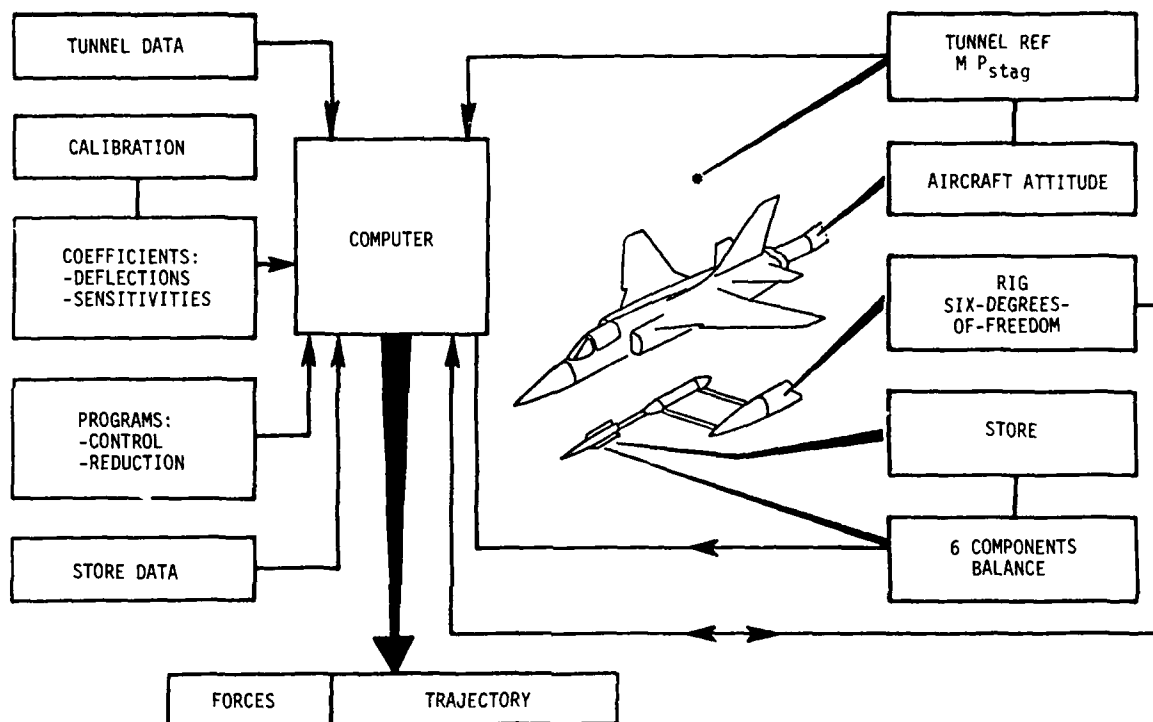


Figure 13 Block Diagram for the Six-Degrees-of-Freedom Rig for Captive Trajectory Study at the S2 Modane Wind Tunnel

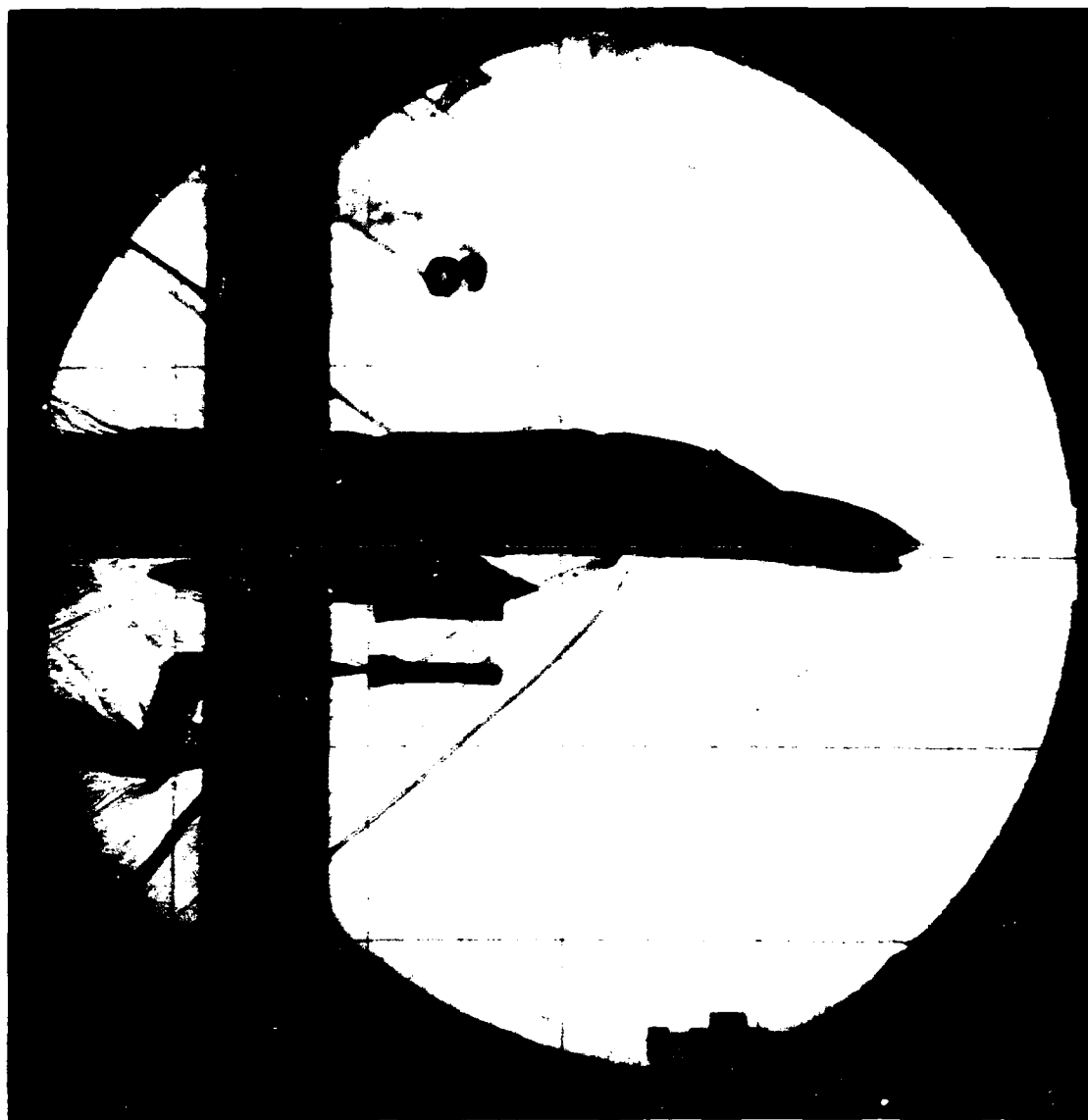


Figure 14 CTS - VKE Tunnel A





Figure 16 CTR - Wright Aeronautical Company 4-5 ft. (1.5 m) Transonic Wind Tunnel



THIS PHOTOGRAPH ORIGINATED AT  
CALSPAN CORPORATION, BUFFALO, N.Y.

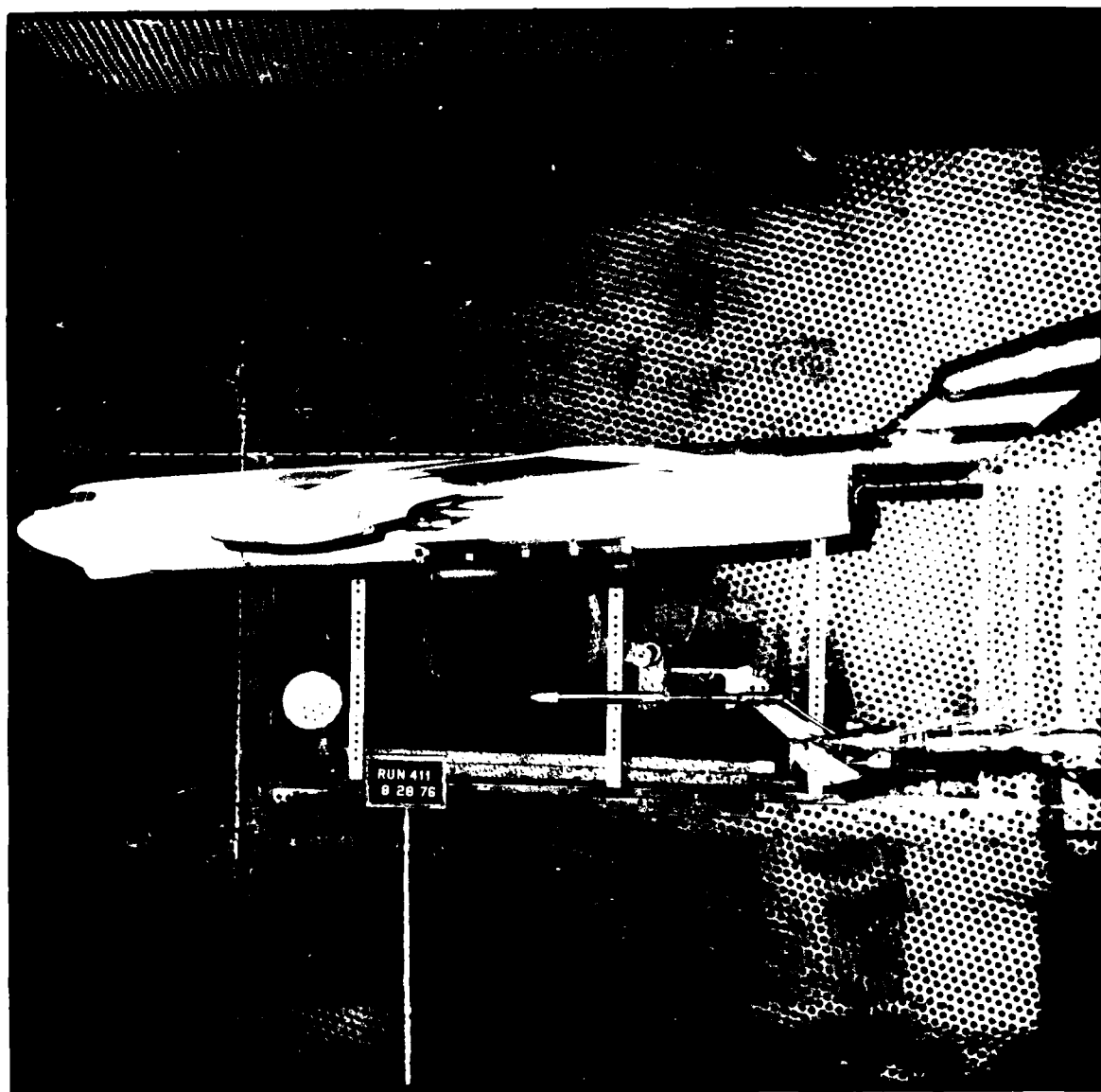


Figure 17 CTV - Calspan Corporation 8-Foot (2.4 M) Transonic Mini Tunnel

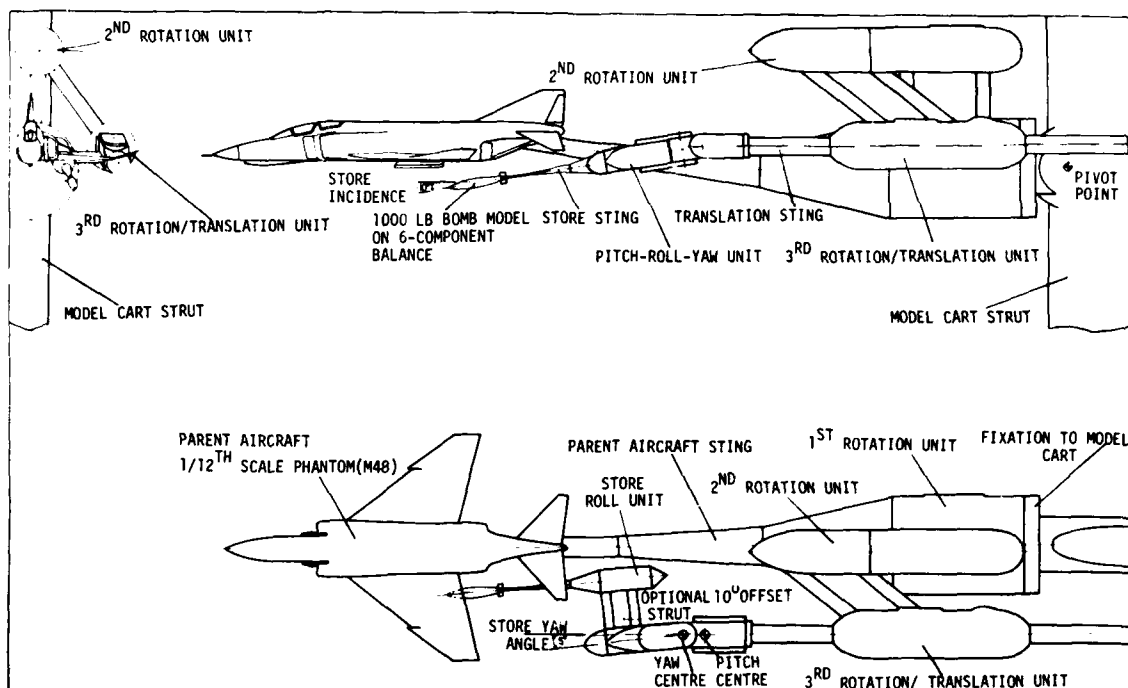


Figure 18 Two-Sting Rig - A.R.A. 9x8 Transonic Wind Tunnel

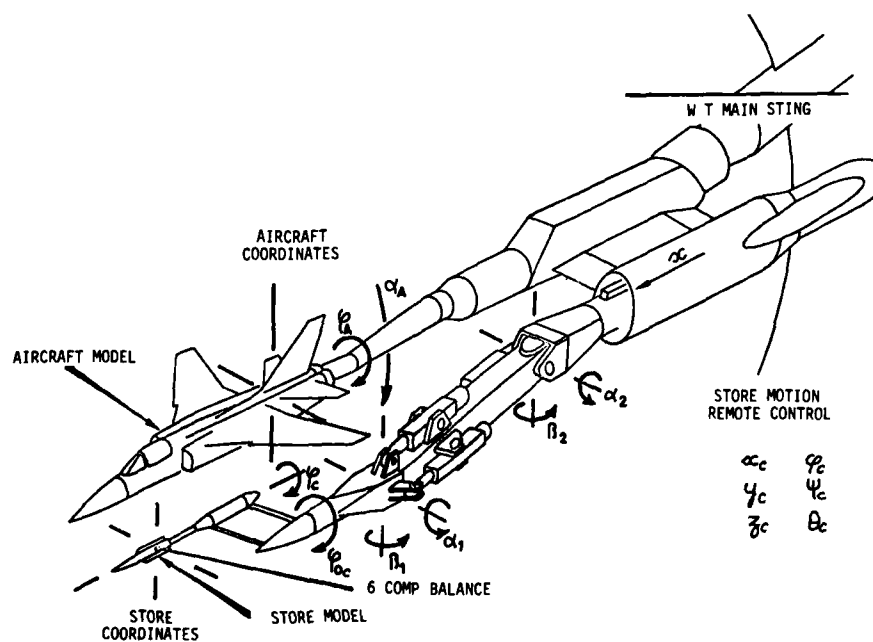
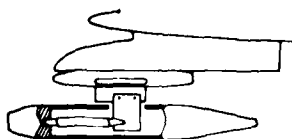


Figure 19 CTS - ONERA S2 Modane Wind Tunnel

MODE OF TESTINGINTERNAL BALANCE SUPPORT (IBS)

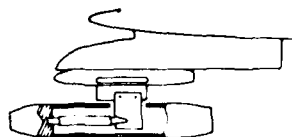
CORRECT CONFIGURATION OF STORE,  
SUPPORTED IN CORRECT CAPTIVE  
POSITION BY AN INTERNAL BALANCE  
ATTACHED TO THE RACK

BALANCE SENSES SIX COMPONENTS OF

FORCES AND MOMENTS ACTING ON THE  
CORRECT SHAPE IN THE CORRECT  
CAPTIVE POSITION

IBS, ALTERED AFTERBODY

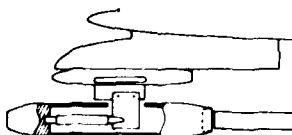
STORE WITH ALTERED AFTERBODY,  
SUPPORTED IN CORRECT CAPTIVE  
POSITION BY AN INTERNAL BALANCE  
ATTACHED TO THE RACK



FORCES AND MOMENTS ACTING ON THE  
ALTERED SHAPE IN THE CORRECT  
CAPTIVE POSITION

IBS, DUMMY STING

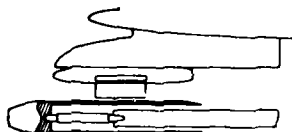
STORE WITH ALTERED AFTERBODY,  
SUPPORTED IN CORRECT CAPTIVE  
POSITION BY AN INTERNAL BALANCE  
ATTACHED TO THE RACK, WITH A  
DUMMY STING PROPERLY LOCATED  
TO SIMULATE STING-MOUNTING



FORCES AND MOMENTS ACTING ON THE  
ALTERED SHAPE IN THE CORRECT  
CAPTIVE POSITION, AND IN THE  
PRESENCE OF A STING

DUAL - SUPPORT (CBS TECHNIQUE)

STORE WITH ALTERED AFTERBODY  
SUPPORTED IN APPROXIMATELY  
THE CAPTIVE POSITION BY THE  
CAPTIVE TRAJECTORY SYSTEM  
(CTS) STING



FORCES AND MOMENTS ACTING ON THE  
ALTERED SHAPE IN APPROXIMATELY  
THE CAPTIVE POSITION, AND IN THE  
PRESENCE OF A STING

Figure 20 Four Modes to Investigate Store Afterbody Alteration and Sting Interference Effects

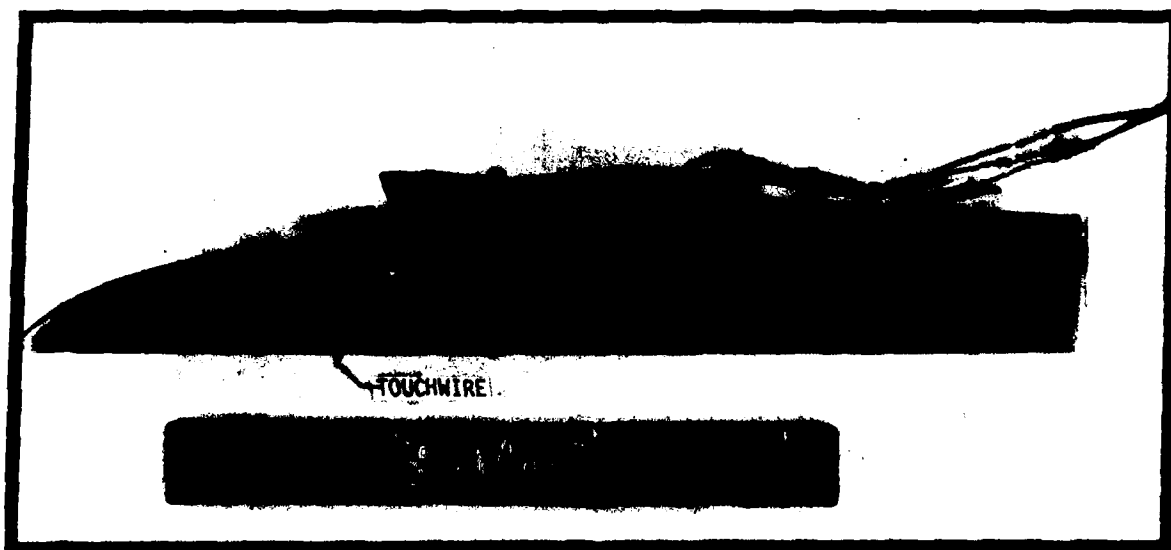


Figure 21 CTS Touchwire System

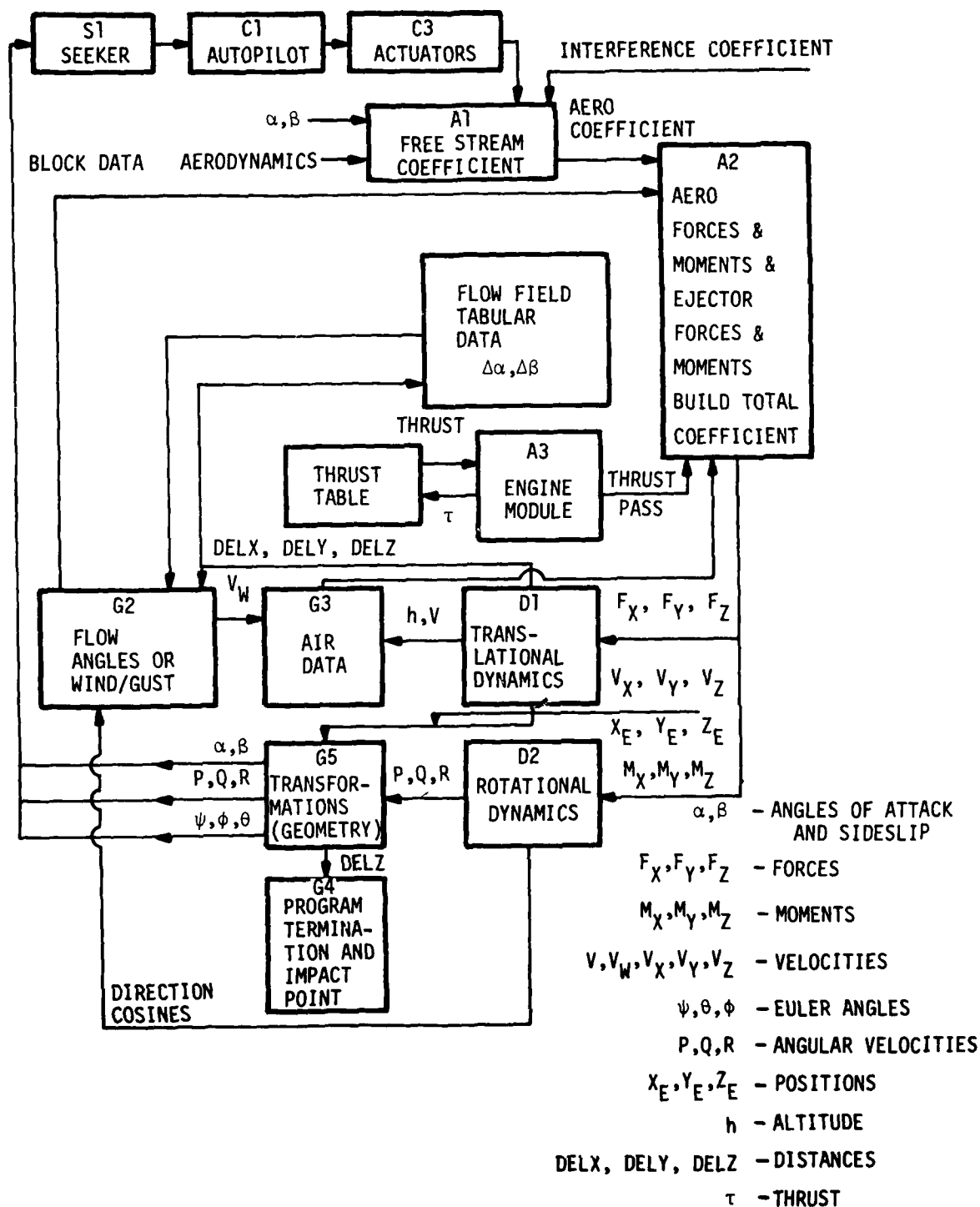


Figure 22

Block Diagram Showing Modules and Subroutines of a Typical Six-Degrees-of-Freedom Computer Simulation for Trajectory Analysis

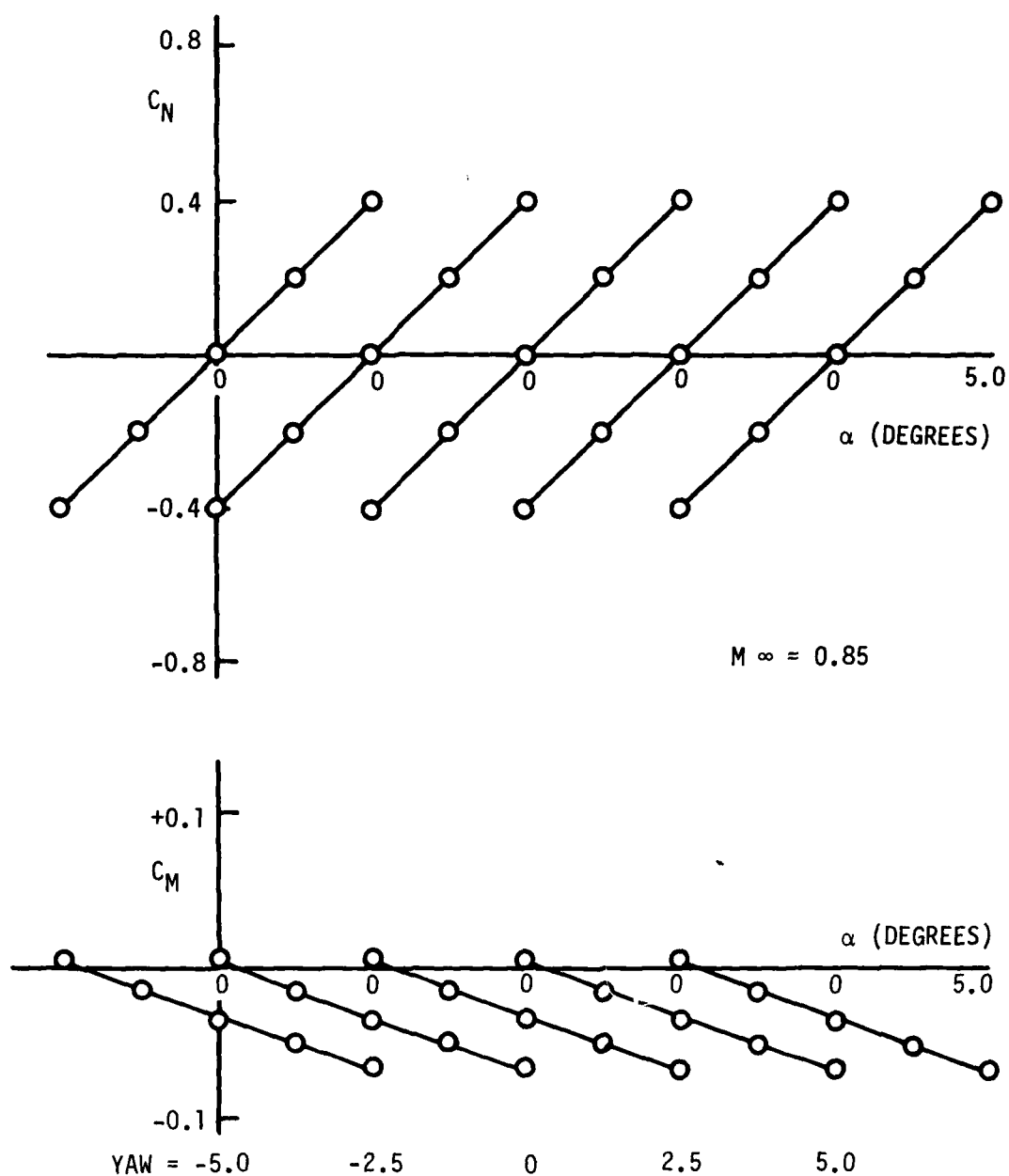


Figure 23 Normal Force ( $C_N$ ) and Pitching Moment ( $C_M$ ) Coefficients Versus Angle of Attack at Various Yaw Angles

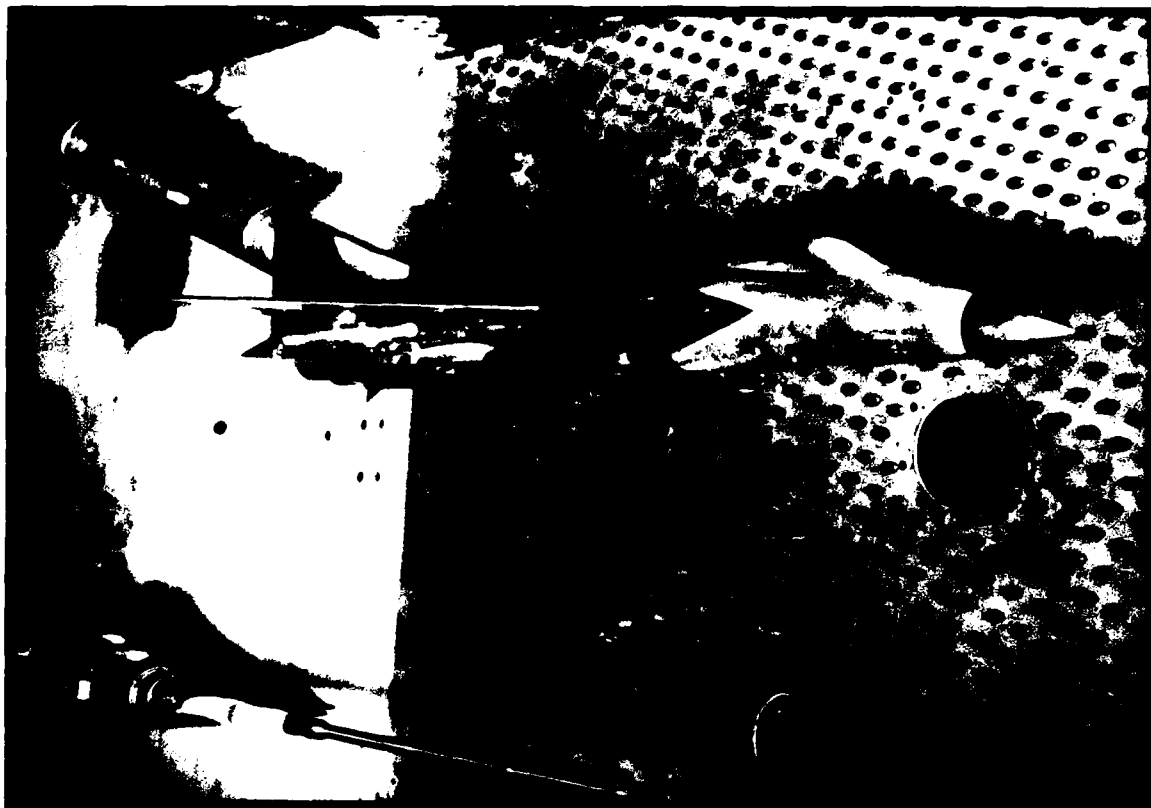


Figure 24 F-15 Flow Angularity Test

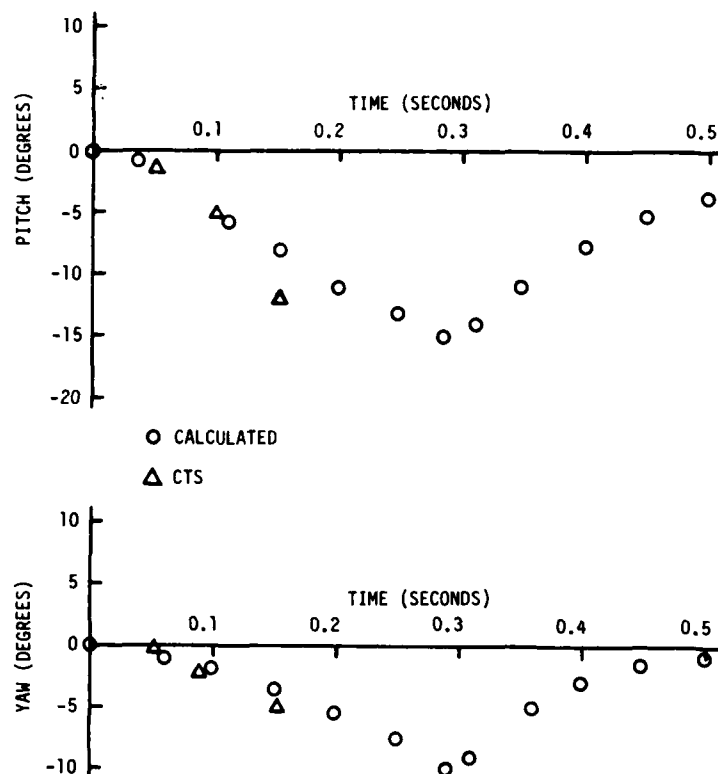


Figure 25 Pitch and Yaw Time Histories of a SUU-51/B Bomb Dispenser Ejected from the Bottom TER Station (Altitude 5,000 Feet and Mach 0.82)

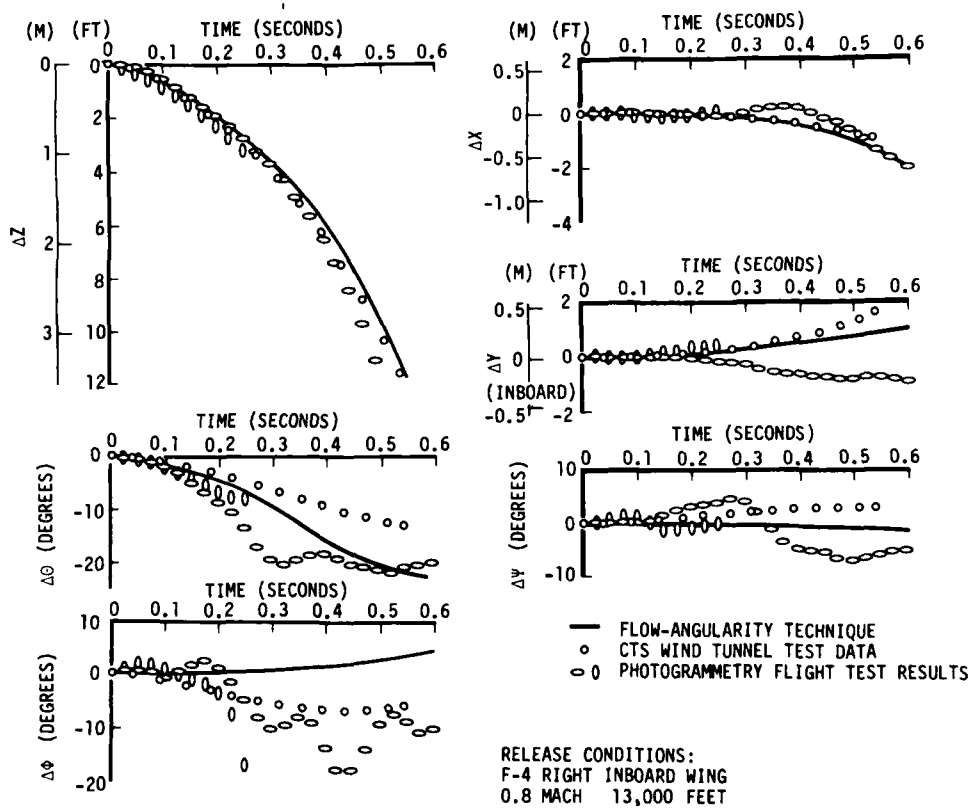


Figure 26 Correlation of Flow Angularity, CTS, and Flight Test

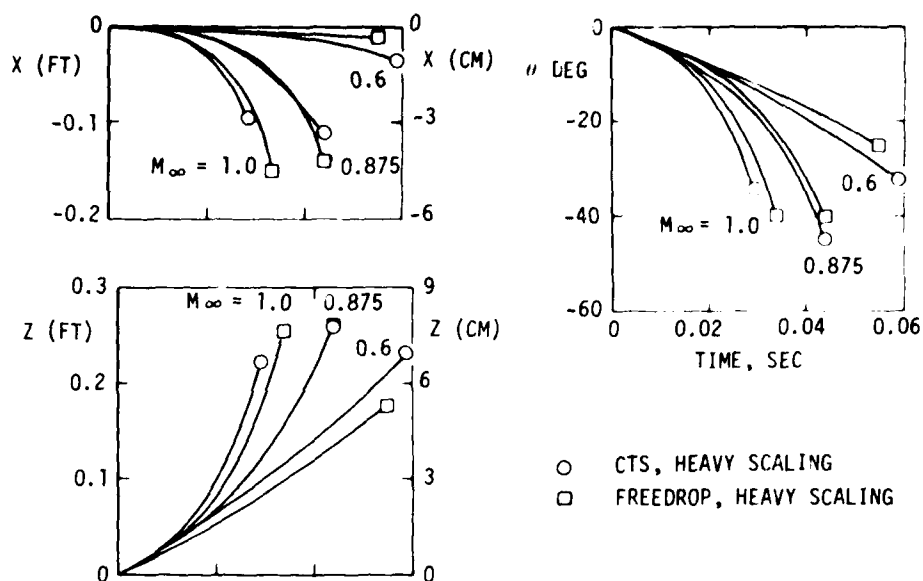


Figure 27 Comparison of Trajectories from CTS and Freedrop Test of a 600-Gallon Fuel Tank, Model Scale Dimensions

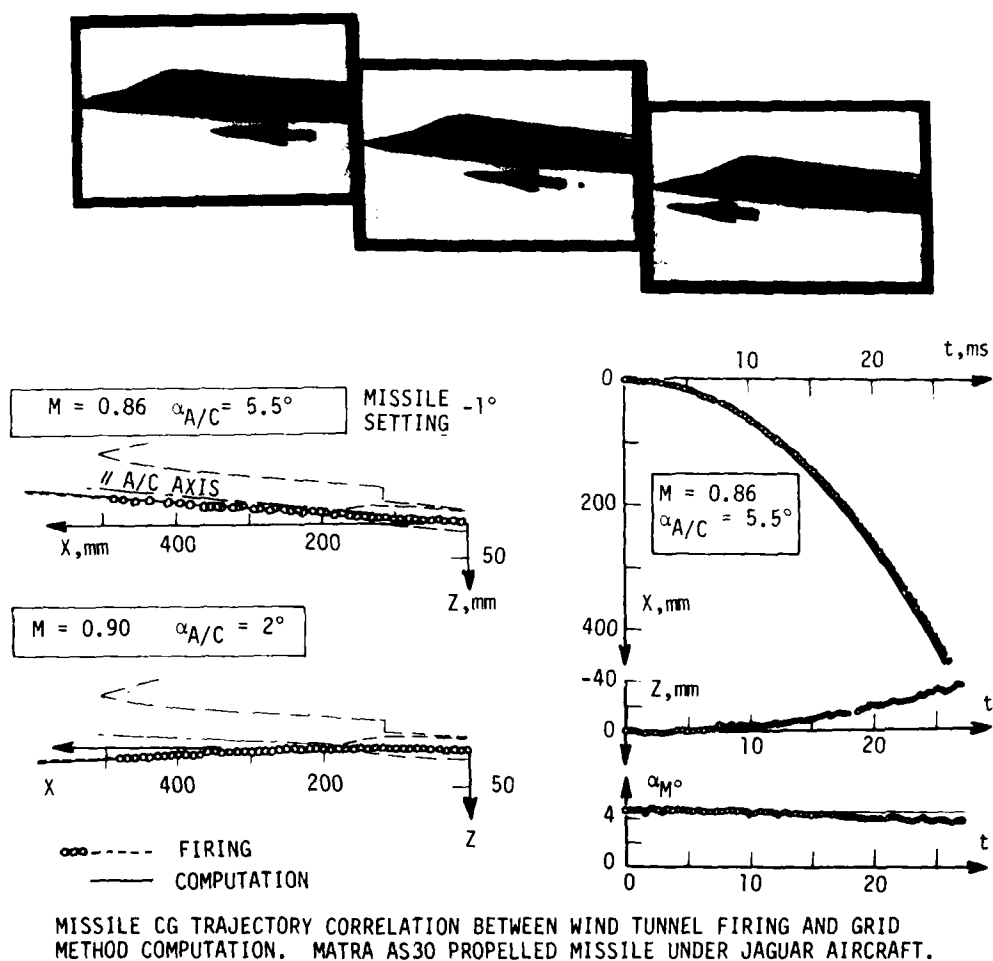


Figure 28 Launch of Dynamically Scaled Propelled Missile in the ONERA S3 Modane Blow Down Transonic Wind Tunnel



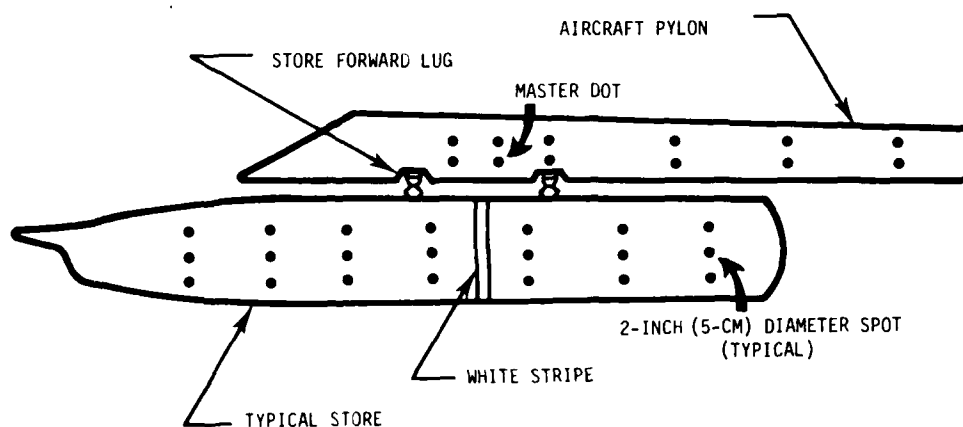


Figure 29 Typical Painting Pattern Used for Photogrammetric Data Reduction of Store Separation

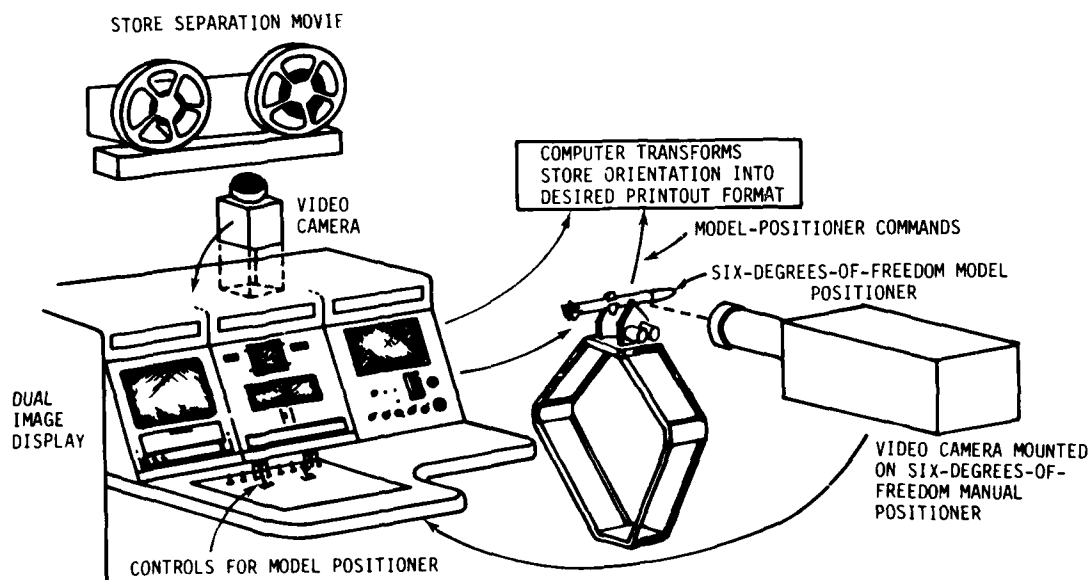


Figure 30 Photo-Imagine System Used for Flight Test Data Reduction of Store Separation

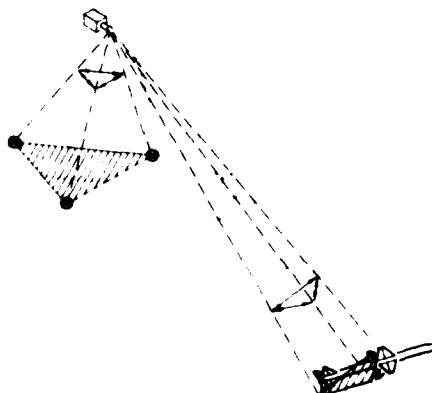


Figure 31 CHASE Concept

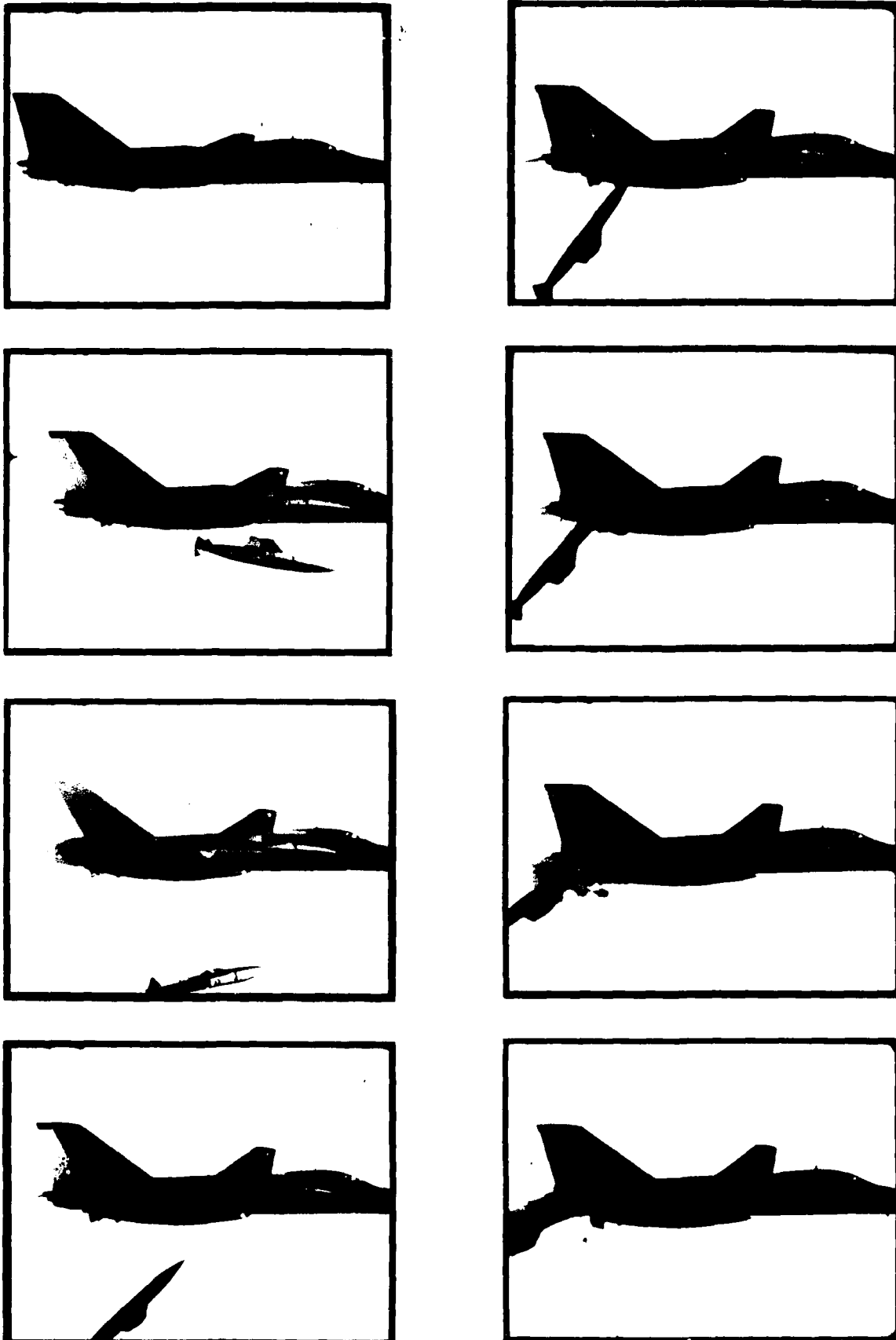
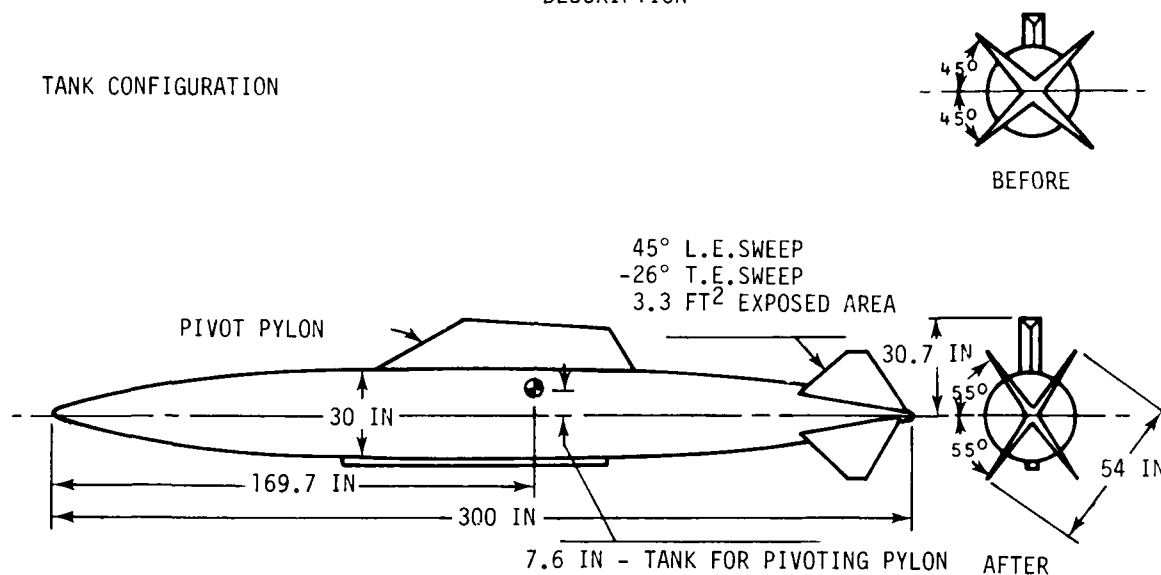


Figure 32 600-Gallon (271 Litre) Fuel Tank Striking FB-111A Aircraft

## DESCRIPTION

## TANK CONFIGURATION



MOUNTING ATTITUDE (STATIC)  
 PIVOTING PYLON STATIONS - CENTER LINE OF TANK INCLINED  
 2° DOWN FROM AIRCRAFT WATER LINE  
 WEIGHTS (EJECTABLE, RESIDUAL FUEL)  
 TANK WITH PIVOTING PYLON - 742 POUNDS

Figure 33 FB-111A 600-Gallon (2271 Litre) Tank/Pylon

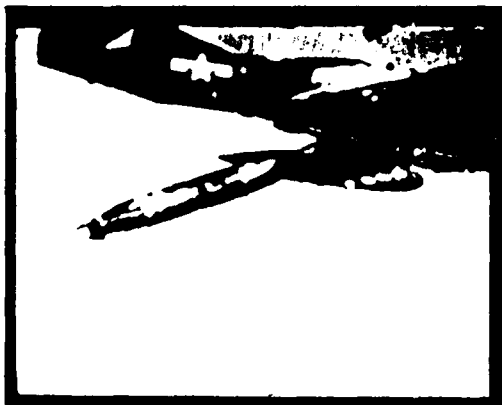
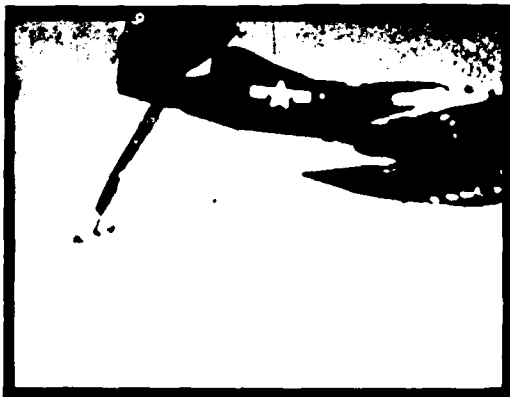
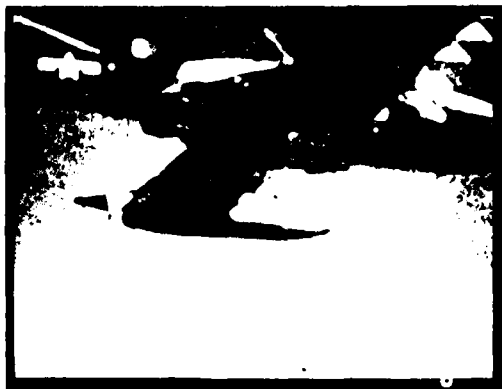


Figure 34 Fuel Tank Striking A-37 Aircraft

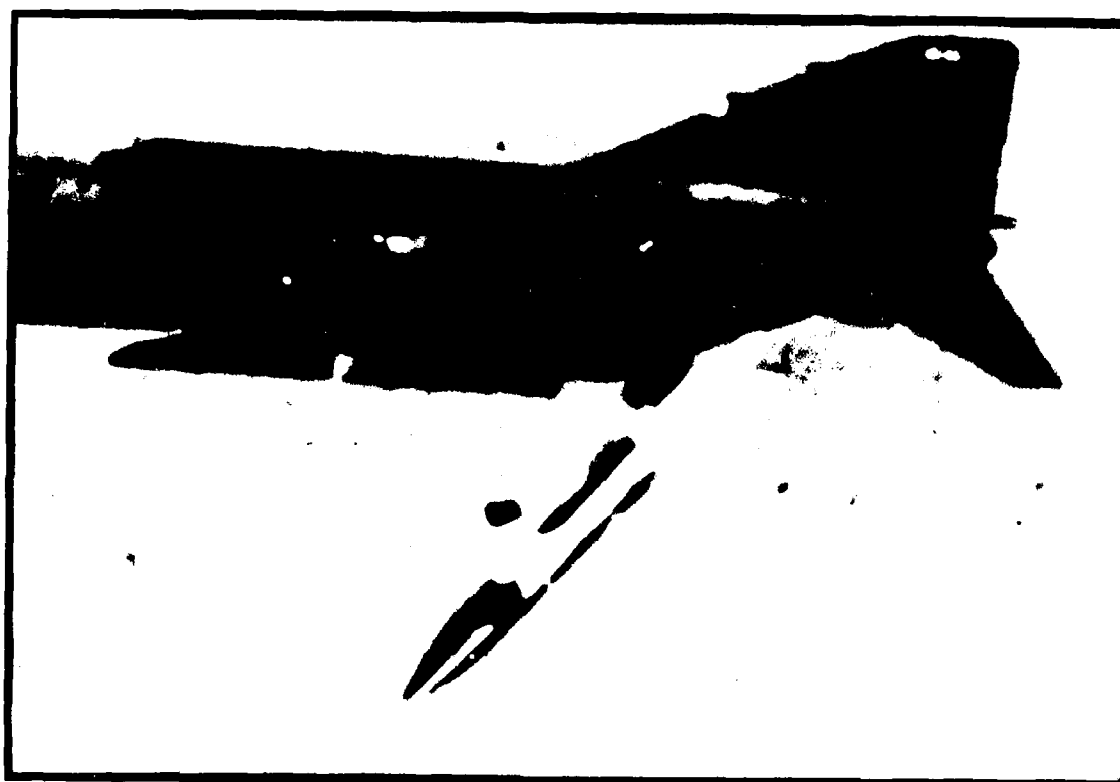


Figure 35 Multiple Ejector Rack Striking F-4 Aircraft

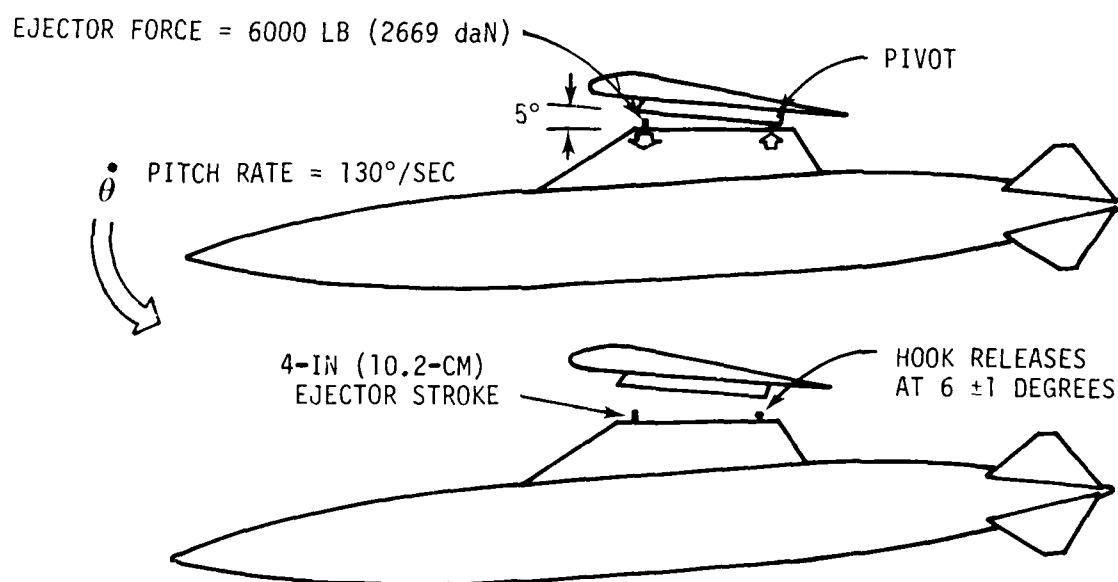


Figure 36 F-111 Tank/Pylon Aft Pivot System

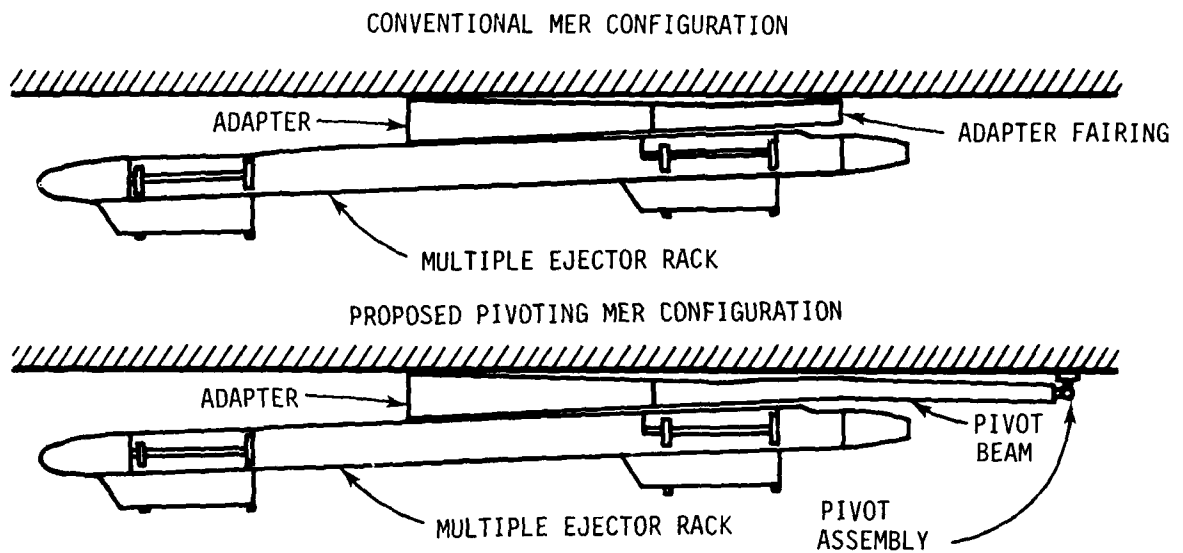


Figure 37 Conventional and Proposed Pivoting MER Configurations - F-4

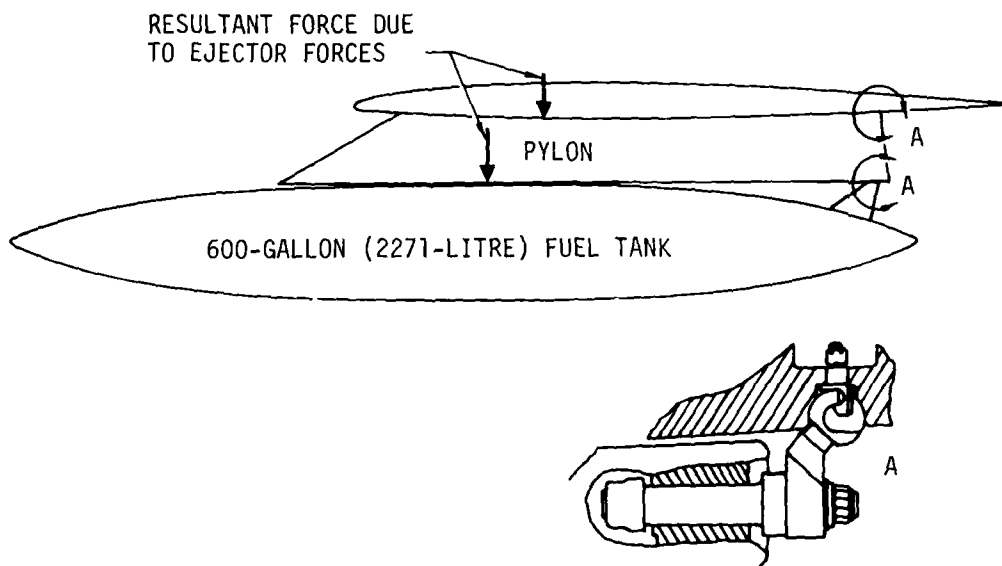


Figure 38 F-15 Aft Pivot Mechanism



Figure 39 CTS Test of F-15/600-Gallon (2271 Litre) Fuel Tank with Aft Fiver

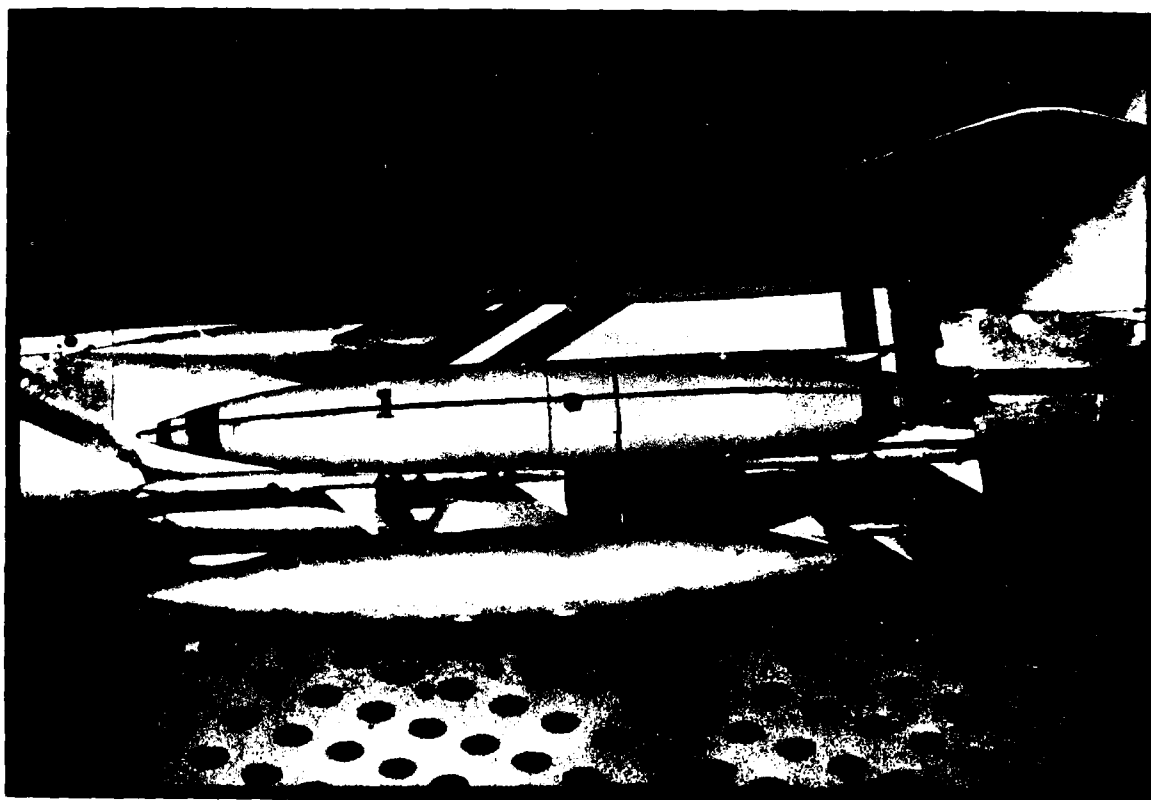


Figure 40 Freebody Test of F-15/600-Gallon (2271 Litre) Fuel Tank Aft Fiver

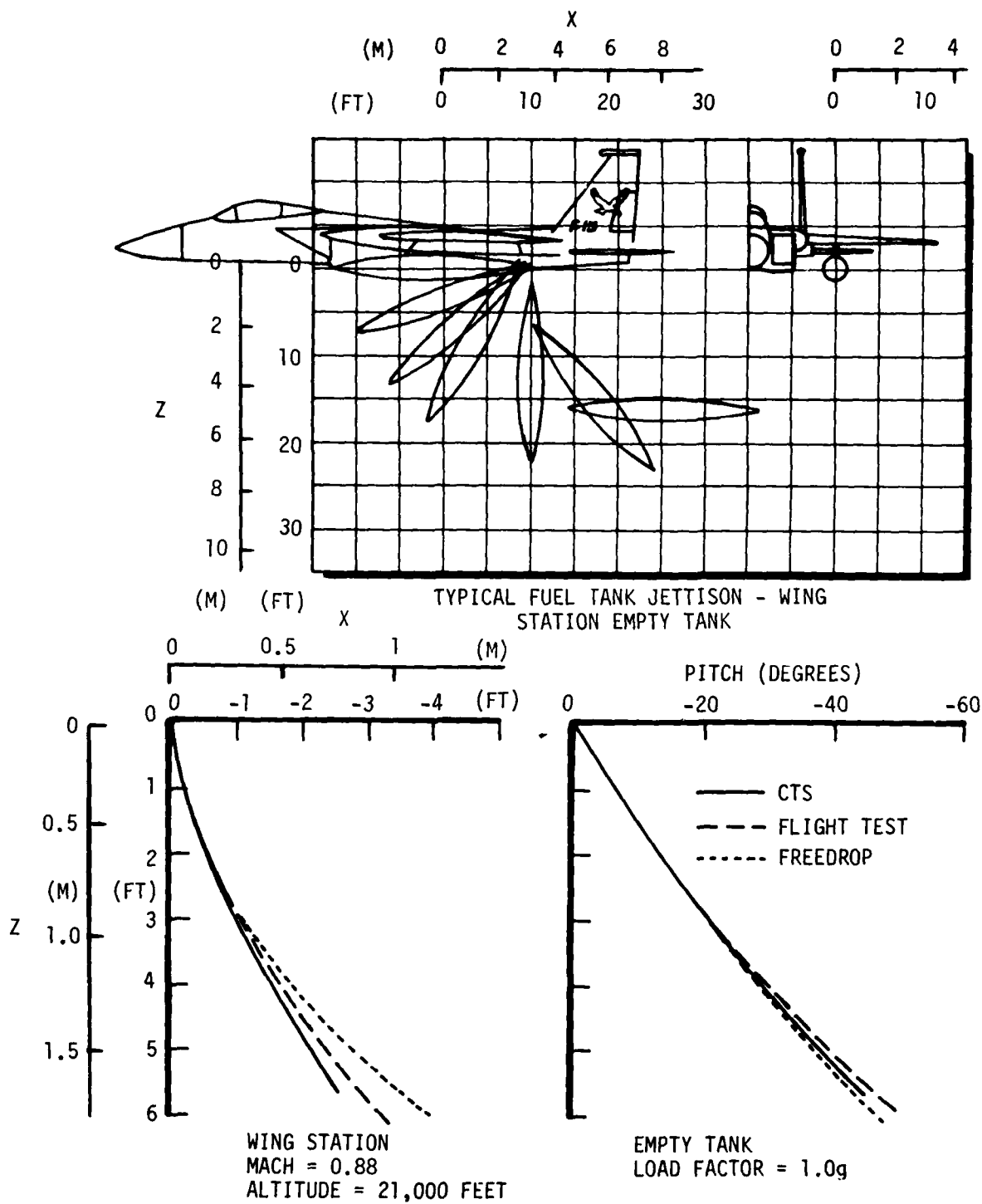


Figure 41 Comparison of F-15/600-Gallon (2271 Litre) Fuel Tank Captive Trajectory System, Freedrop, and Flight Test Data



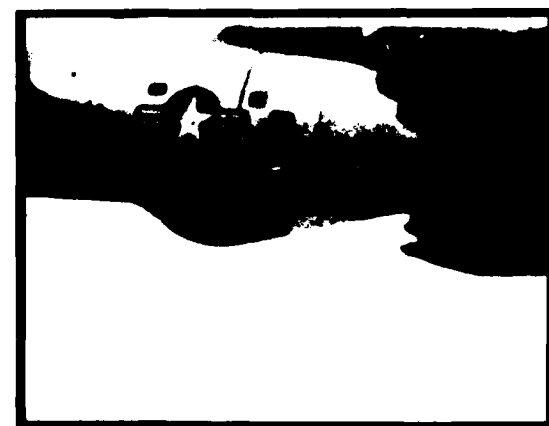
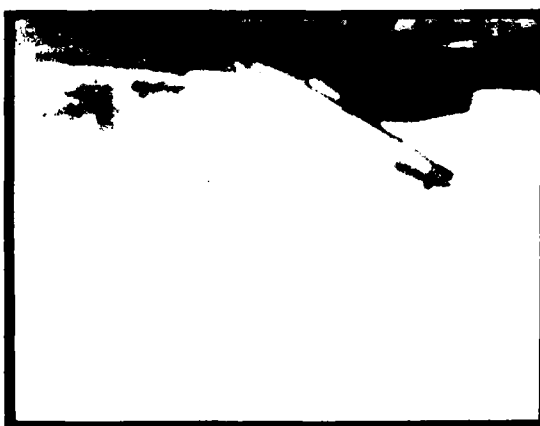
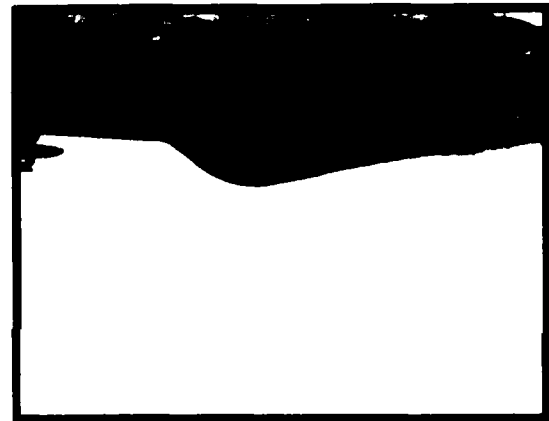
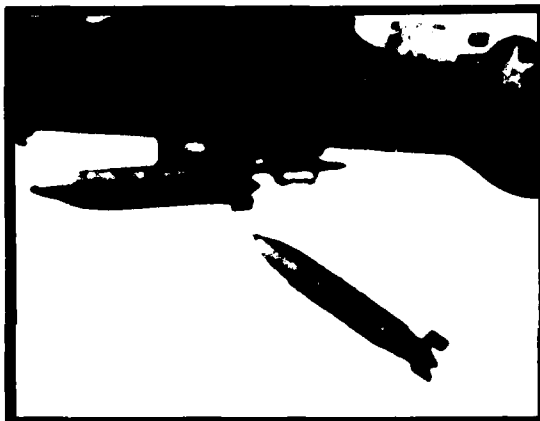
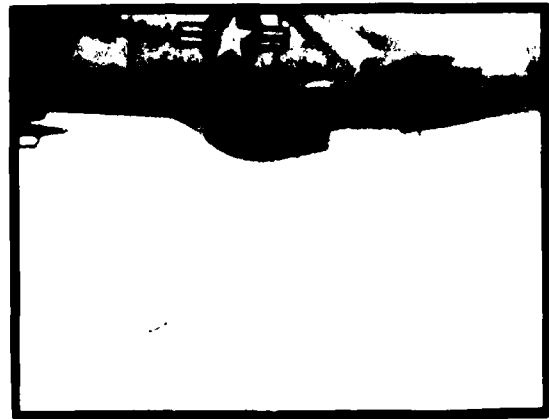


Figure 40 Finned Firebomb Striking F-105 Aircraft



Figure 43 Ripple Release of MK82 Bombs from F-111 Aircraft

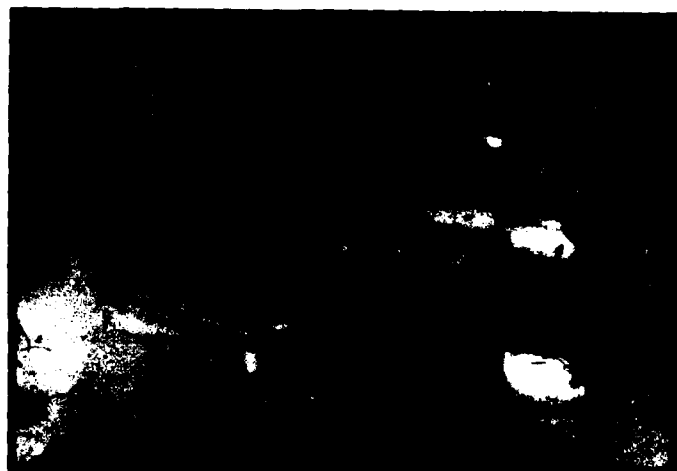


Figure 44 Rockeye Dispenser Striking A-7D Aircraft

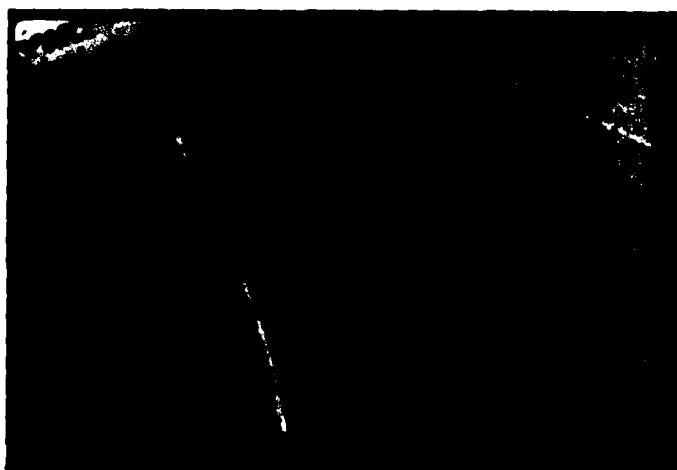


Figure 45 Ripple Release of SUU-30 Dispensers from F-105 Aircraft

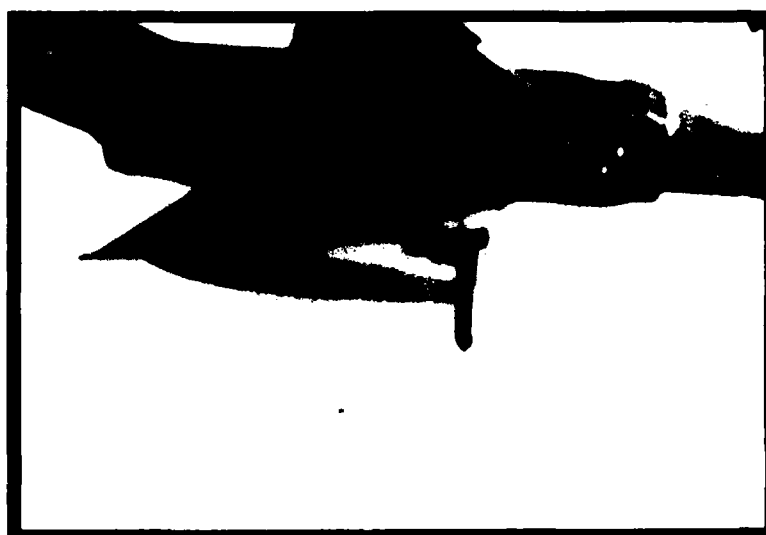
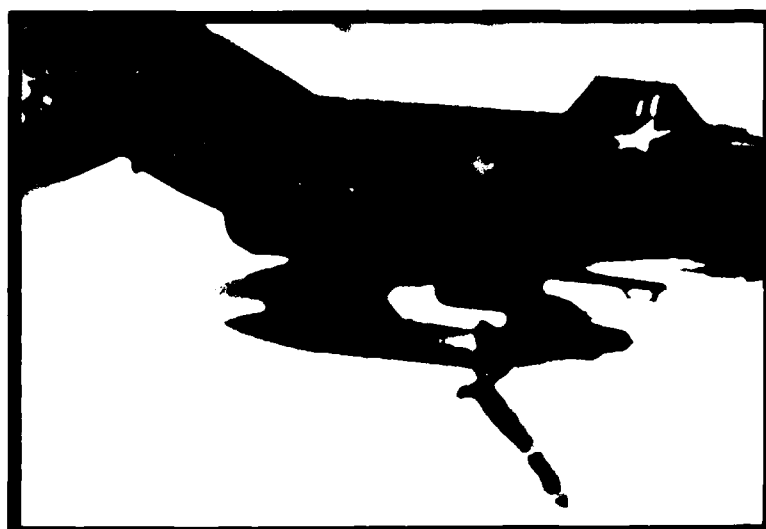
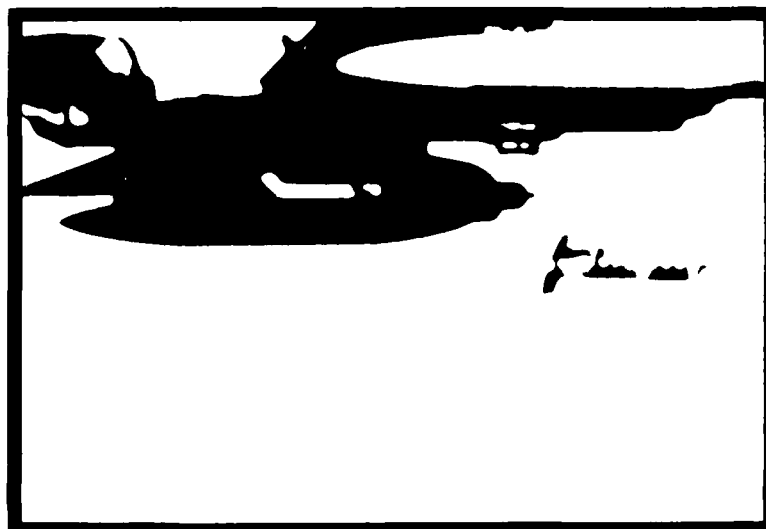


Figure 16 Successive Release of CUM-61 Dispensers from the F-4 Bottom TER Station at 0.6, 1.2, and 1.8 Mach and 1,000 Feet

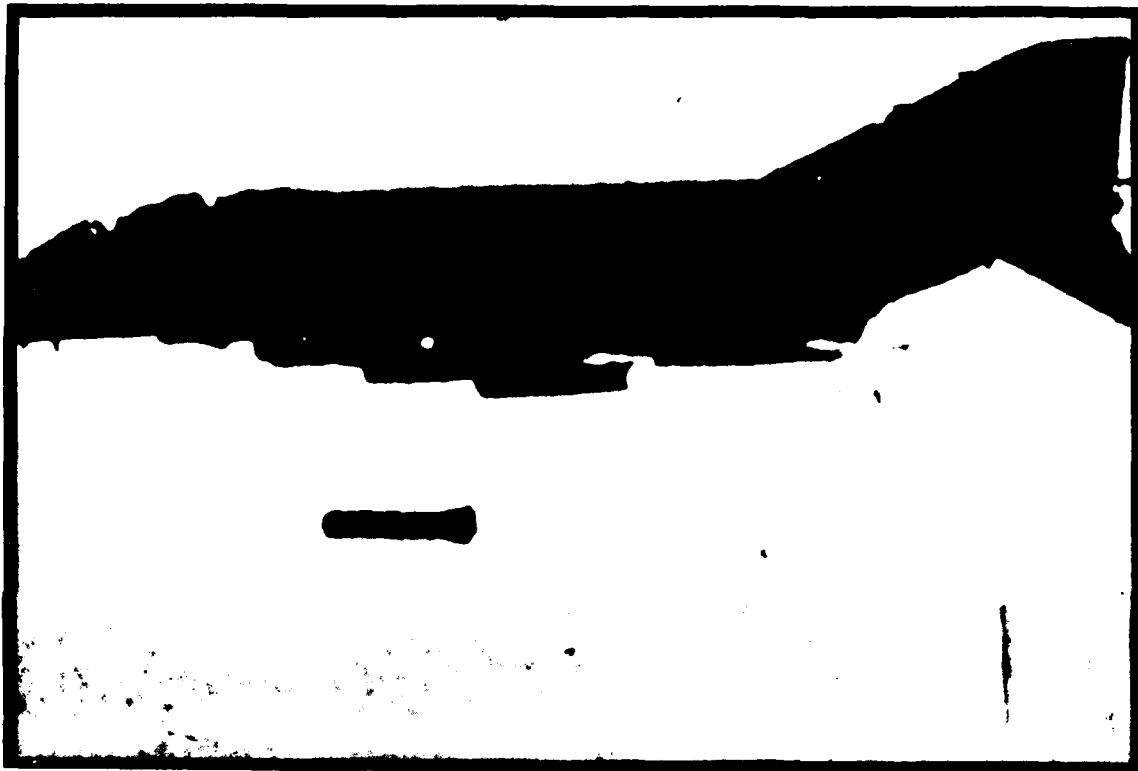


Figure 47 Release of 12-Inch (30.5 CM) Diameter Hemispherical Nose Store from the F-4 Bottom TER Station at 1.15 Mach and 10,000 Feet

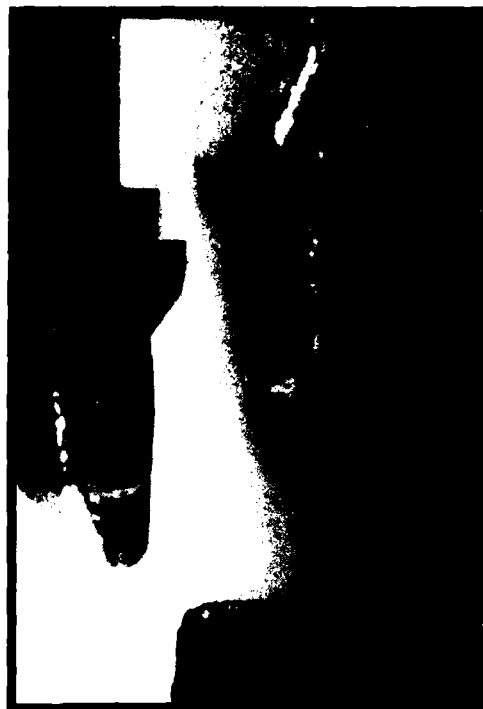


Figure 4a Simultaneous Releases of 14-Inch (35.6 CM) and 16-Inch (40.6 CM) Diameter Dispenser Weapons from the F-4 Bottom TER Station at 0.9 Mach and 5,000 Feet

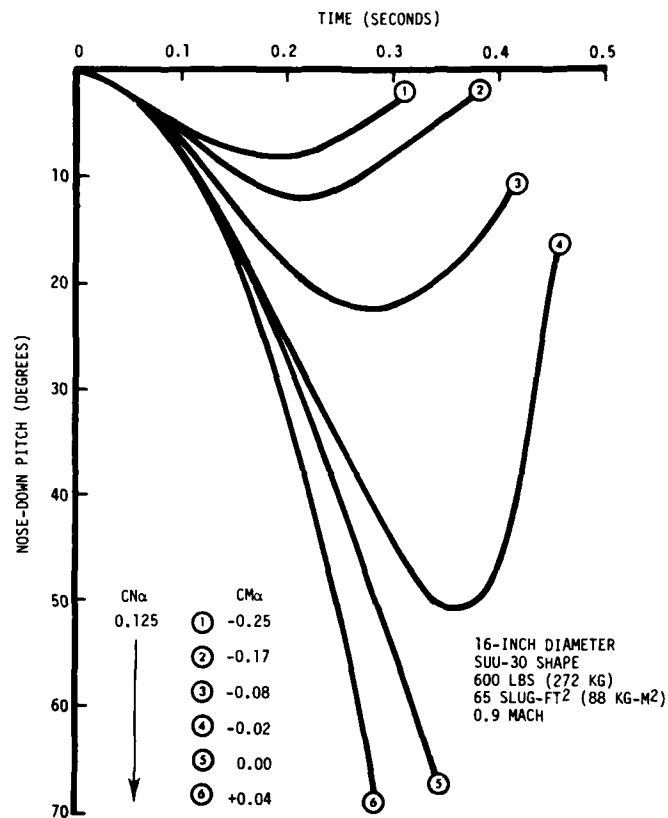


Figure 49 Effects of Varying Static Aerodynamic Stability on Store Pitch

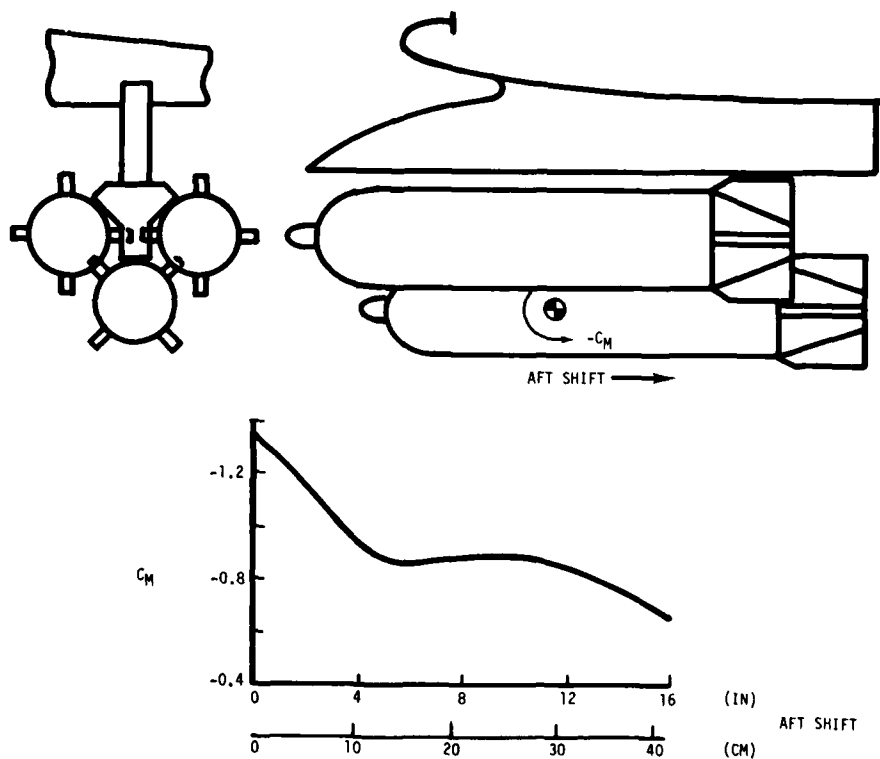


Figure 50 Change in Installed Aerodynamic Pitching Moment with Store Longitudinal Position at Transonic Speeds



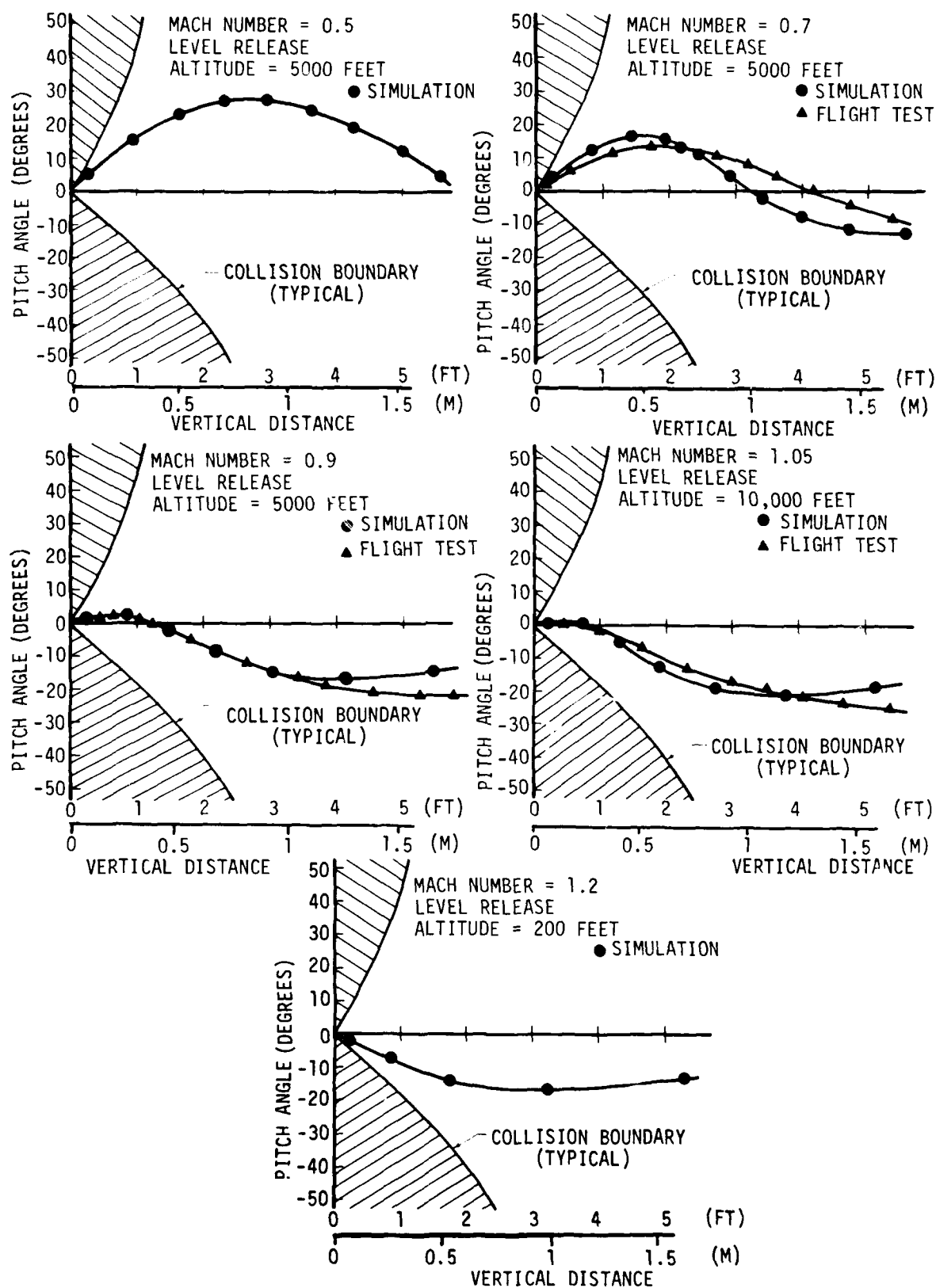


Figure 52 Predicted Releases of SUU-30 Dispensers from the Bottom Station of an F-4 Inboard TER at 0.5, 0.7, 0.9, 1.05, and 1.2 Mach Number



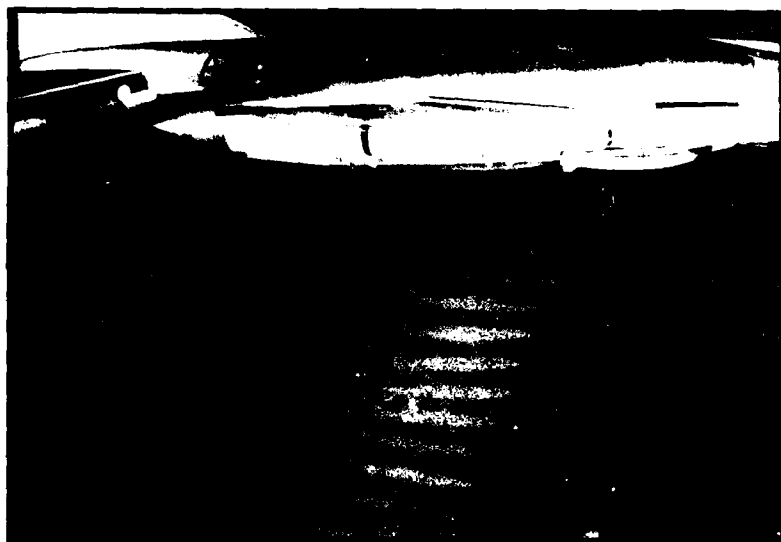
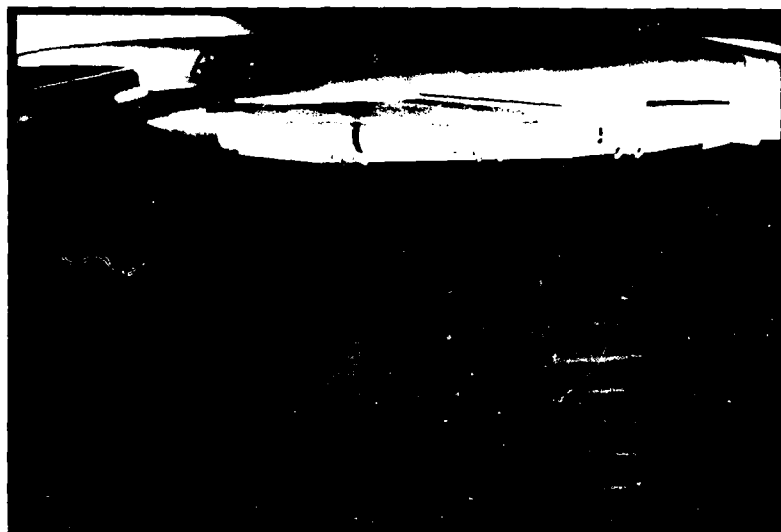


Figure 10. View of the propeller of the engine of the aircraft, showing the propeller blades and the propeller hub.

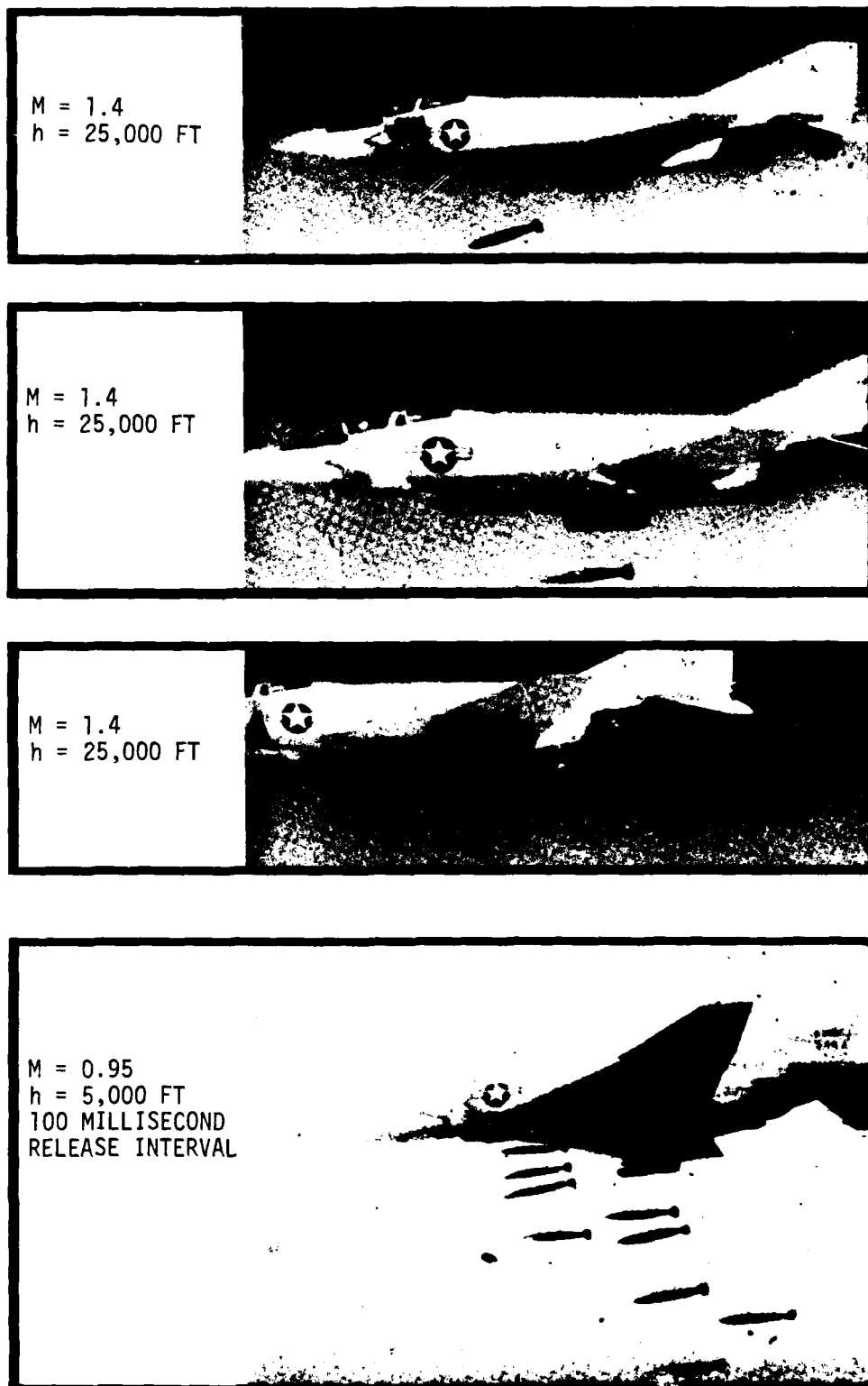


Figure 54 Flight Tests of MK82 Bombs Released from an F-4 Conformal Carriage Pallet



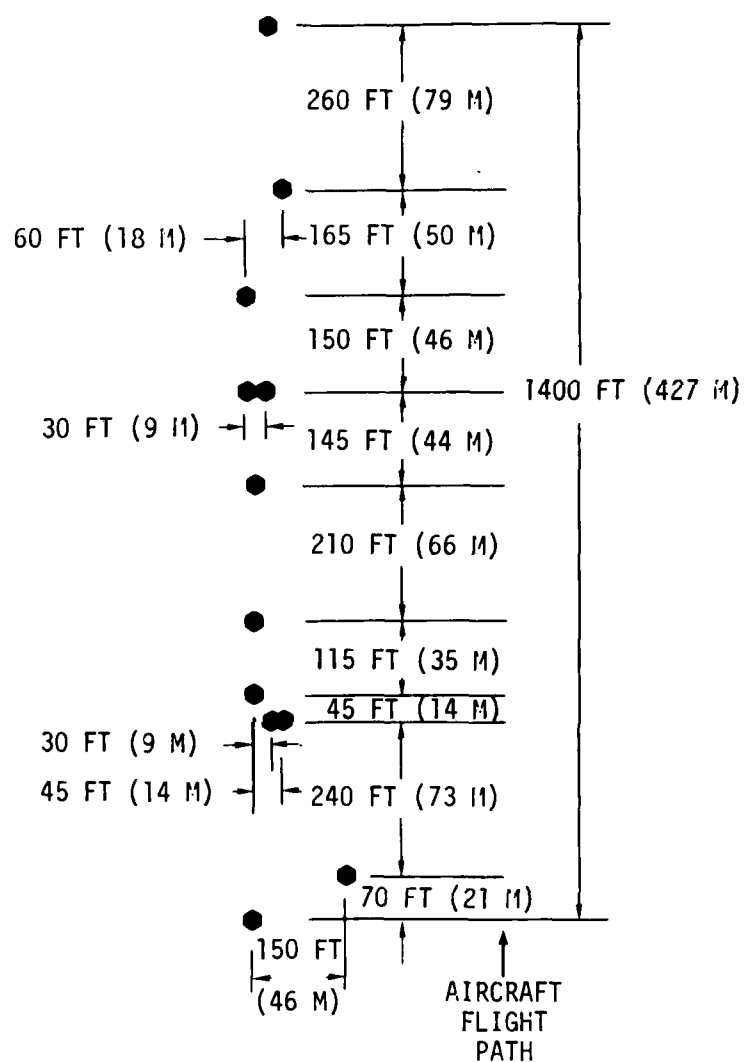


Figure 56 Ground Impact Pattern of 12 MK82 Bombs Released in a Ripple Mode at 100 Milliseconds from an F-4 Conformal Carriage Pallet at Mach 0.95 Mach and 1,900 Feet AGL

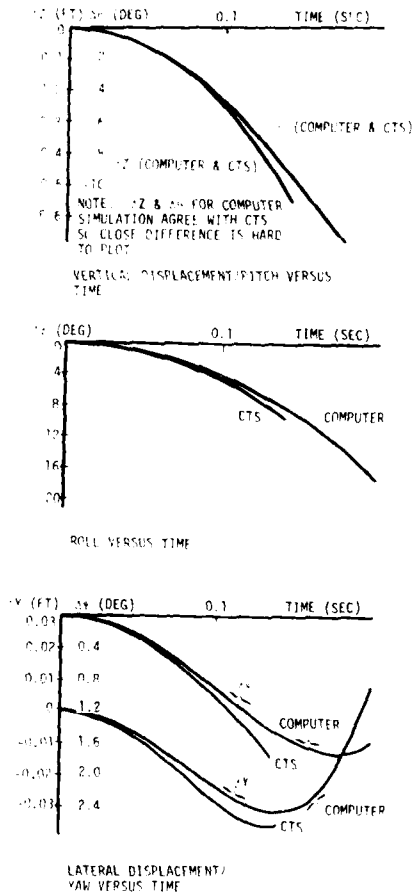


Figure 57 Comparison of CTS and Computer Simulation - Control System Off

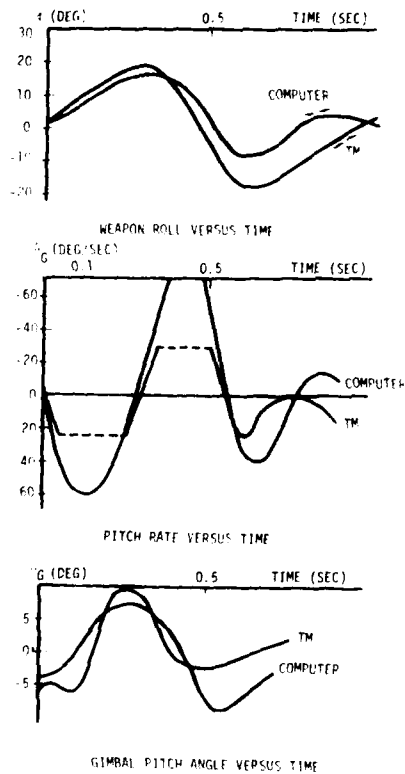


Figure 11.58 Comparison of Flight Test Telemetry Data and Computer Simulation - Control System On

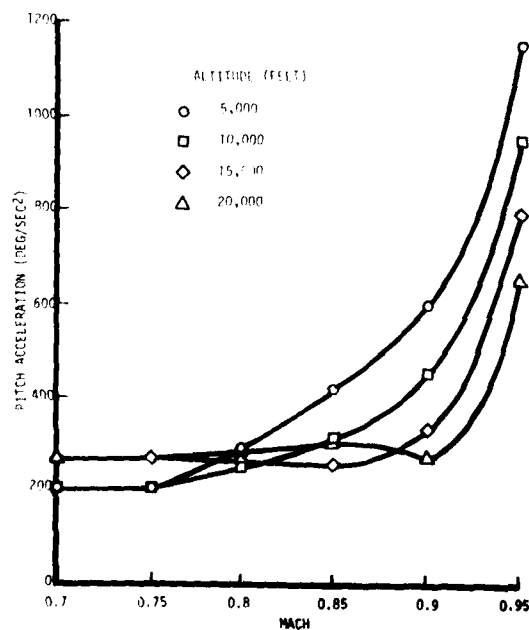


Figure 59 Maximum Body Pitch Acceleration vs Mach Number

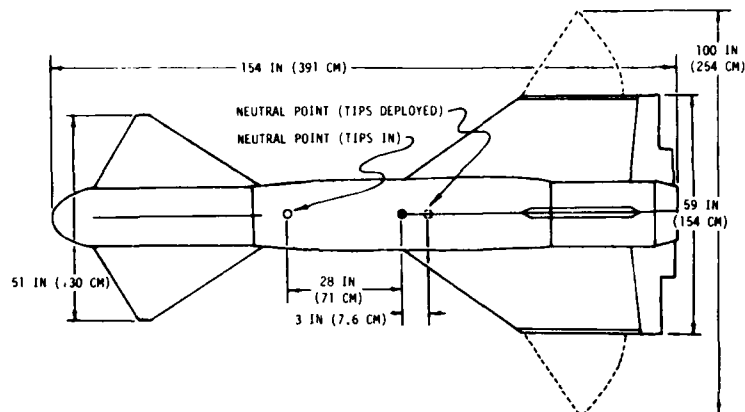


Figure 60 Original Guided Weapon Design

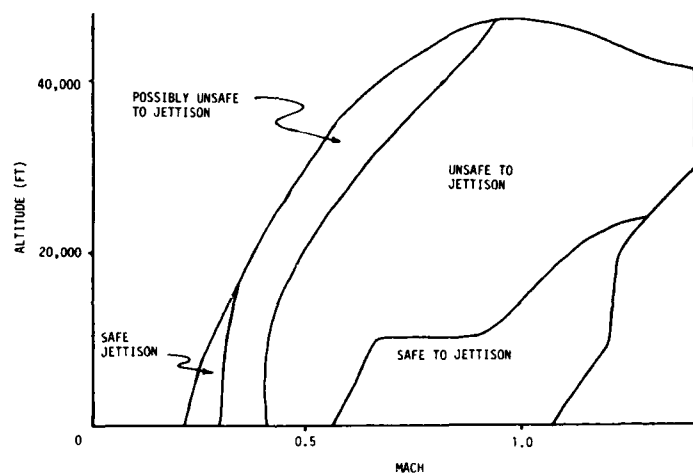


Figure 61 F-4 Jettison Envelope - Nominal Weight Aircraft



Figure 62 Frame of a Computer Generated Movie of a Grid Predicted Trajectory - F-4 Aircraft at 0.9 Mach and 40,000 Feet

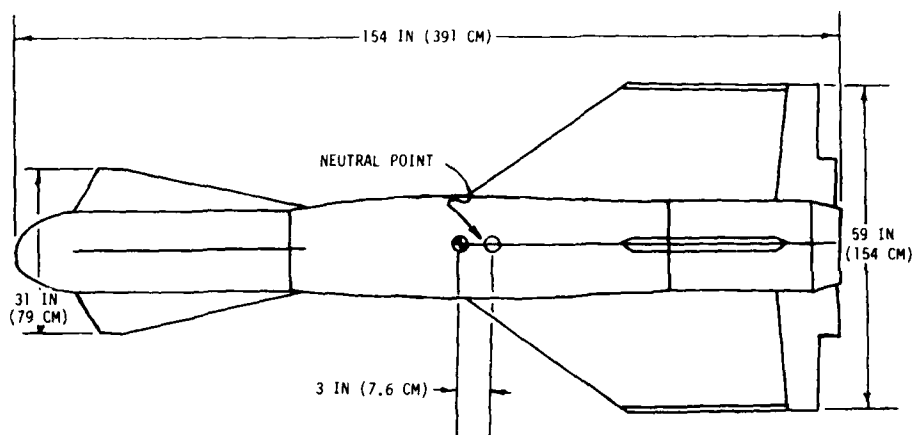


Figure 63 Revised Guided Weapon Design

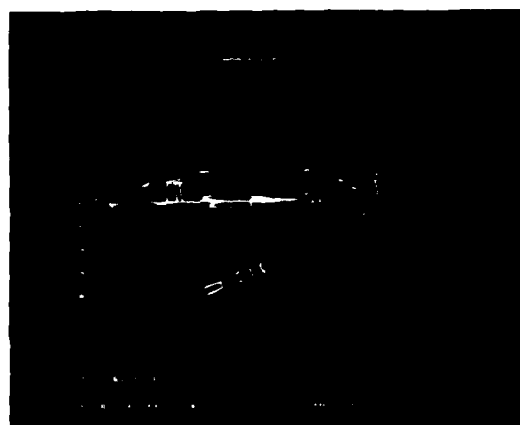
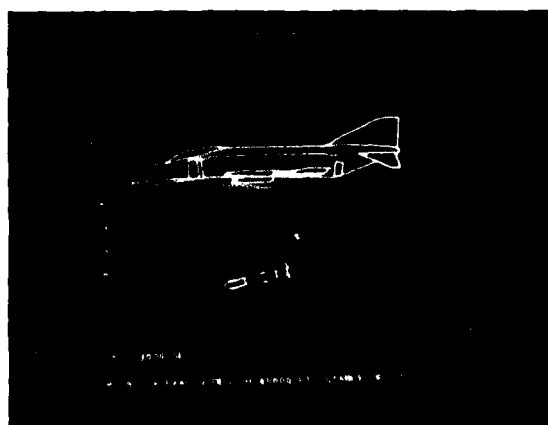
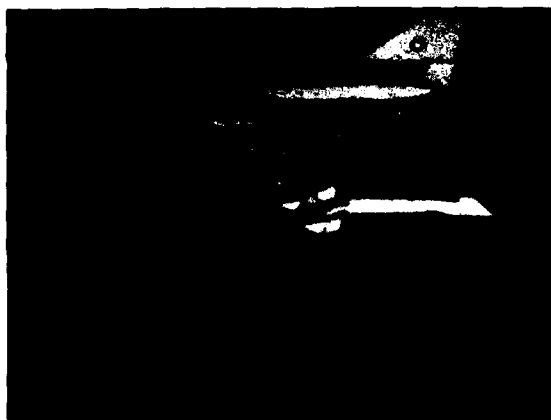
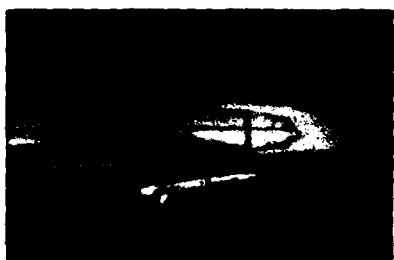


Figure 64 Comparison of Flight Test with Predicted Guided Weapon Trajectories - 0.9 Mach and 40,000 Feet

Figure 65 Comparison of Flight Test with Predicted Guided Weapon Trajectories - 0.8 Mach and 13,000 Feet

A INITIAL TEST  
TAIL DEFLECTION = 0  
THE MISSILE HITS THE A/C NOSE



B FINAL TEST  
TAIL DEFLECTION =  $-1^{\circ}$   
CORRECT TRAJECTORY

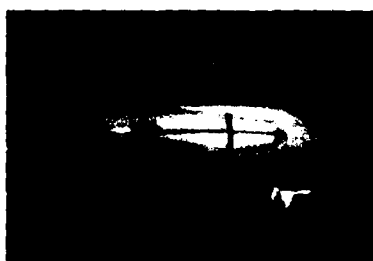
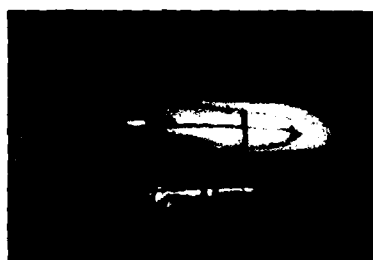
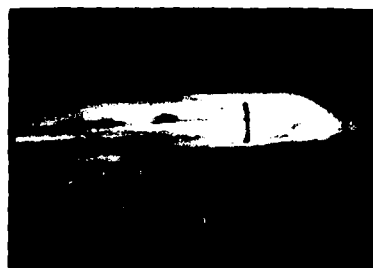


Figure 66 Propelled MATRA 511 Missile Model Fired in the ONERA S3 Modane Wind Tunnel Under a Mirage III, 1/15th Scale Model



## KINETIC HEATING OF HIGH SPEED MISSILES

by

Bryan E. RICHARDS

Professor in Department of Aeronautics/Aerospace  
 von Karman Institute for Fluid Dynamics  
 Chaussée de Waterloo, 72  
 B-1640 Rhode Saint Genèse, Belgium

SUMMARY

This paper provides a review of kinetic heating as related to high speed tactical missiles. The aspects considered are : the design problem; areas in which kinetic heating is important; the prediction of heating in attached and separated flows; measurements on configurations in flight and in wind tunnels; ground simulation of flows over models; and the measurement of kinetic heating. The experience is generally obtained from studies in related areas such as high speed aircraft, reentry vehicles, etc. rather than on tactical missiles since little information appears to be available on this application due to it being a fairly recently confronted problem area. Because of the wide coverage of the field, a generous list of references is provided to guide the reader to papers giving more refined details.

LIST OF SYMBOLS

$c_p$	specific heat at constant pressure	$\alpha$	thermal diffusivity
$g$	gravity constant	$\beta$	coefficient of volumetric expansion
$Gr$	Grashof number	$\gamma$	intermittency distribution
$h$	heat transfer coefficient, enthalpy	$\epsilon$	emissivity, eddy viscosity
$k$	thermal conductivity	$\kappa$	turbulent conductivity
$m$	pressure gradient parameter	$\mu$	viscosity
$n$	power related to pressure interaction theory	$\nu$	kinematic viscosity
$Nu$	Nusselt number	$\rho$	density
$P_{t2}$	pitot pressure	$\sigma$	Boltzmann constant
$Pr$	Prandtl number	$\theta$	momentum thickness
$Pr_t$	turbulent Prandtl number		
$q$	heat transfer rate		
$r$	recovery factor		
$R_N$	nose radius		
$Re$	Reynolds number		
$s$	distance along wall		
$St$	Stanton number		
$t$	time		
$T$	temperature		
$u$	streamwise velocity		
$x$	distance in streamwise direction		
$y$	distance at right angles to wall		
$z$	distance in a spanwise direction		

Subscripts

$e$	edge of boundary layer
$g$	gas
$n$	exponent
$o$	stagnation point
$r$	recovery, radiation
$tr$	beginning of transition
$tend$	end of transition
$w$	wall

Superscript

fluctuation quantity

## 1. INTRODUCTION

Kinetic heating of flight vehicles can be considered a relatively well studied problem at present. Experience already has been obtained with reentry ballistic missiles, manned space vehicles and high speed military and research vehicles. Heating due to attached flows over simple shapes can be reasonably well predicted, and it is well known that the most critical regions are at stagnation regions, on thin structures, such as wings and fins, and in the regions of reattaching shear layers caused by flow interactions. There have been, however, few publications on aerodynamic heating associated with tactical missiles since generally flight speeds and mission times have been small enough that no special design is required to combat it. For missiles with a speed range above Mach 2, when aerodynamic heating becomes significant in structural design ( $T_0 \sim 260^\circ\text{C}$  at sea level, see Fig. 1), some consideration should be given to verify whether production costs of thermally protected vehicles can be reduced and/or failures minimized by appropriate modification. It is thus to hypersonic flow studies that one must look for information useful to missile kinetic heating.

Compared with manned vehicles, which require to have a very low failure rate and a cabin environment in which humans can exist, the design of a missile to counter kinetic heating does not necessarily have to be so rigorous. However, it is desired to use inexpensive materials for the external skin whenever possible and delicate electronics, guidance systems or payload (for example most bombs and fuses have as their explosive charge some form of TNT, which melts at  $80^\circ\text{C}$ ) may be themselves affected by heat. Furthermore, the wider manoeuvre margins allowed by the absence of a pilot is likely to increase the likelihood of incurring highly localized heating rates due to shock-surface interactions.

In most cases the mission of a missile includes a short dash to its objective at a low drag incidence, with finally rapid manoeuvres at large incidences and control angles. The result of this is that steady state heat transfer and relatively isothermal wall conditions are unlikely to exist at the critical regions mentioned earlier. Hence one general problem that should be solved is a transient heat transfer situation with an arbitrary wall temperature variation. Another critical situation is that missiles carried by high speed aircraft to their launch point may be subjected to kinetic heating for extended periods such that the skin and perhaps most of the internal parts may achieve temperatures close to the flight recovery temperature. Indeed, the performance of the aircraft could be severely limited by temperature limits of the store (Ref. 1), as illustrated in figure 2. Active cooling systems are unlikely to be used because of their complexity and cost. Protection, if needed, will come from the use of heat sink cooling, use of appropriately high temperature resistant materials, low thermoconductivity materials such as silicon rubber and from the use of low temperature ablators.

A review of this kind is likely to appeal to four types of individuals: the missile designer, the missile user, the researcher and the educator. These individuals may require different information. The designer is likely to require information at all levels of sophistication. In the preliminary design phases only time and money for simple numerical predictions will be available. At later stages of design as more capital is risked by poor design then more sophisticated numerical calculations or wind tunnel tests are likely to be used. An organization specializing in missile design over an extended time is likely to expend much effort in adapting up-to-date numerical techniques and modern instrumentation and facility techniques to produce the most optimum design. The missile user has usually an interest in less sophisticated prediction methods to enable him to specify the vehicle he wants, and to assess the product in its design, trial and commissioning phases. The researcher to be effective and useful has to understand current problems in the area in order to keep ahead of the requirement of the designer or to be able to adapt his researches to the application. The educator is interested in providing a suitable training to the future workers in the field in fundamentals and experience. The article is written as far as possible keeping all these requirements in mind, but it must be emphasized that the subject is a broad one, and hence references for more deeper research are quoted generously in order to keep the review down to a reasonable size.

In the following chapter of this review, the elements of a design calculation are outlined. Chapter 3 outlines flow situations in which kinetic heating is most likely to be a problem. Chapter 4 deals with a review of prediction methods for attached flow situations. Heat transfer involved with flow interactions are discussed in Chapter 5. Some applications to configurations are presented in Chapter 6. Finally, some remarks on wind tunnel facilities for simulating aerodynamic heating are given in Chapter 7.

## 2. GENERAL DESIGN PROBLEM

A general but realistic design problem that may be considered is the heat transfer to a skin of finite thickness by forced convection, conduction through the skin and radiation from its surface to the exterior gas and the interior components as well as internal free convection. The problem is illustrated in figure 3. A few remarks on ablation protection will be made at the end of this chapter. The equations can be generalized as follows (Ref. 2).

### Forced convection

This is created by the viscous effects within the boundary layer through which the

fluid velocity decreases from the free stream velocity at the outer edge to zero adjacent to the wall. With this zero velocity condition, heat can be transferred between the fluid and the body only by conduction. This may be represented by Fourier's heat conduction law :

$$q = (k_g \frac{dT}{dy})_{y=0} \quad (1)$$

In practice, especially for turbulent boundary layers, to calculate the temperature gradient near the wall is complicated and hence the convection process is usually represented by :

$$q = h(T_r - T_w) \quad (2)$$

where  $h$  is a heat transfer coefficient (units watts/m<sup>2</sup>K) for  $q$  in watts/m<sup>2</sup> and temperature in K) to be calculated by appropriate solution of the boundary layer equations and  $T_w$  is the wall temperature.  $T_r$ , the recovery temperature (sometimes known as the adiabatic wall temperature) is calculated from :

$$T_r = T_\infty + r \frac{u_\infty^2}{2c_p} \quad (3)$$

$r$  is a recovery factor usually given a value of  $Pr^{0.5}$  (where  $Pr$  is the Prandtl number =  $\mu c_p / k$  and which has a value between 0.68-0.72 depending on temperature) for laminar flows and 0.89 or  $(Pr)^{1/3}$  for turbulent flows.

#### Radiation from wall

The surface will be losing heat by radiation to its surroundings at a rate given by the Stefan-Boltzmann law :

$$q_r = \sigma \epsilon T_w^4 \quad (4)$$

where  $\epsilon$  is the surface emissivity factor (tabulated for various materials in Ref. 2) and  $\sigma$  has a value of  $5.67 \times 10^{-8}$  W/m<sup>2</sup>K<sup>4</sup> to give  $q$  in W/m<sup>2</sup>.

#### Radiation to wall

The surface will be receiving back heat by radiation from the surrounding air of the amount :

$$q_r = \sigma \epsilon_g T^4 \quad (5)$$

where  $\epsilon_g$  is the gas emissivity and  $T$  is the temperature of the radiating gas. This source of heat transfer is usually small in comparison with the forced convection heat input.

#### Conduction through the skin

Here one must consider the transient condition that the heat transfer is time variant, and hence the energy storage in the material must be considered in addition to heat conduction. The general equation is known as the Fourier-Poisson heat conduction equation which in rectilinear coordinates is given by :

$$\frac{\partial T}{\partial t} = \alpha \left( \frac{\partial^2 T}{\partial x^2} + \frac{\partial^2 T}{\partial y^2} + \frac{\partial^2 T}{\partial z^2} \right) \quad (6)$$

where  $\alpha = k/\rho c_p$  is the thermal diffusivity of the material. This is a parabolic partial equation which requires an initial condition of the temperature distribution at time  $t=0$  and such boundary conditions as the heat transfer rate (or surface temperature) variation with time at the two bounding surfaces over the calculation period.

The solution is considerably simplified if equilibrium conditions hence steady or quasi-steady state conditions are achieved when the Fourier heat conduction equation is applicable, i.e. :

$$q = \frac{k(T_1 - T_2)}{y} \quad (7)$$

where  $T_1$  and  $T_2$  are the temperatures at the two bounding surfaces. A quasi-steady state situation occurs when the time for a significant change in average wall temperature is very large when compared to the characteristic time  $\ell^2/\alpha$ , where  $\ell$  is the mean thickness of the material. Reference 3 provides some standard solutions to equation 6.

### Radiation to interior

The equations for this contribution are similar to equations 4 and 5.

### Natural convection in interior

The fluid motion is caused by density differences. The heat transfer rate is usually determined from correlations involving the equation :

$$Nu = K (Gr \cdot Pr)^n \quad (8)$$

where  $N$  is the Nusselt number  $= \frac{hx}{k}$  ;

$$Gr \text{ is the Grashof number } = \frac{\Delta T x^3 \rho^2 g \beta}{u^2}$$

where  $\beta$  is a coefficient of volumetric expansion and  $\Delta T$  is a temperature difference.

All these equations should be solved simultaneously to arrive at the time history of skin or interior temperature during a mission. If quasi-steady state conditions are achieved, considerable simplification is achieved because of the change in conduction solution from equation 6 to equation 7. In many cases some of the contributions to heat transfer will be negligible and can be safely dropped from the calculation. The solution of the general heat transfer problem for typical aircraft or missile structures usually involves a finite element approach (Refs. 4, 5) involving the solution of a large number of simultaneous equations to be solved on a digital computer or analogue simulator. An approximate approach has been applied in reference 6. The transient conduction problem is out of the scope of this lecture, but the latter three references provide a preliminary guide to the subject. More sophisticated techniques and computer codes may arise from the present great interest in heat transfer in space vehicles.

This section serves to illustrate that the forced convection source of heating (in this application known as aerodynamic heating or kinetic heating) provides a primary role in determining a missile's capability of withstanding thermal effects. The normal input into a design program is the heat transfer coefficient,  $h$ , which is often given in its non-dimensional forms :

$$Nu = \frac{hx}{k} \quad (9)$$

or

$$St = \frac{h}{\rho u c_p} \quad (10)$$

where  $x$  is a distance from the stagnation point,  $k$  is the thermal conductivity of the gas,  $u$  the local gas velocity and  $c_p$  the specific heat of the gas.  $St$  is a statement of the proportion of energy/unit area of flow transferred to unit area of surface. Nusselt number is related to Stanton number through the Reynolds number (ratio of inertia forces to viscous forces) and the Prandtl number (ratio of "momentum diffusivity" or kinematic viscosity to thermal diffusivity,  $\nu/\alpha$  or  $\mu c_p/k$ ) by

$$Nu = St \cdot Re \cdot Pr \quad (11)$$

Such values can be predicted by various methods of differing complexity ranging from empirical relationships to full solution of the time-dependent three dimensional Navier-Stokes equations to be described in the following chapters.

Ablation protection will not be dealt with in this notes. Its use can be expected only for hypersonic speeds. For example, the X-15 (Ref. 7) flew at speeds up to Mach 6 without such protection. For an extension of its speed range to Mach 8, ablation materials to protect its nose and wing leading edges were examined (Ref. 8). A description of the development of the thermal protection system for the Apollo spacecraft is discussed in reference 9 and for the Space Shuttle in reference 10. An up-to-date review of ablation including 119 references is given in reference 11.

## 3. FLOW SITUATIONS CONTROLLING HEAT TRANSFER ON A MISSILE

A series of descriptive examples will be given in this chapter to provide the background for the review and to aid the location of possible areas of high heating.

### 3.1 Axisymmetric body at zero incidence

A typical body is given in figure 4. The vehicle should have a blunt nose if the vehicle speed is high enough such that kinetic heating is important. As will be illustrated later, stagnation heating is inversely proportional to the square root of nose radius, and furthermore it is desired to conduct heat away from this critical region. Along the cone surfaces an axisymmetric laminar boundary layer will develop. When a particular value of Reynolds number is achieved, the flow will undergo a transition to a turbulent boundary layer, when heat transfer rates will be typically tripled above the laminar values which would have existed at that point without transition. The transition region will be quite extensive, sometimes of the order of the length of the laminar region, and the heat transfer rate will rise monotonically from the laminar to the turbulent level.

The expansion around the corner will cause a gradual drop in heat transfer rate to its cylinder value. The flare on the body could cause a sufficiently high induced pressure gradient to separate the boundary layer which can initially lower or raise the heat transfer rate whether the boundary layer is laminar or turbulent, respectively. If separation exists on the flare, there will exist locally an intense increase in heat transfer rate just downstream of flow reattachment to a value many times that of the undisturbed flow and sometimes even greater than the stagnation point value. The flow will expand and develop in a similar way as past the shoulder, and finally expand around the base. Some interaction with the engine exhaust plume may cause locally high heat transfer rates on the base.

### 3.2 Body at angle of attack

In this case, the boundary layer is three dimensional providing more complication than axisymmetric flows. A stagnation line will occur along the windward generator and there exists a cross flow at the body side surfaces with an angle greater than the incidence of the body to the stream. A characteristic of the three dimensional boundary layer is that the direction of the shear stress at the surface is different from that of the flow at the edge of the boundary layer, with the result that the profile is skewed. Depending on the degree of skewness determines whether the profile in the outer flow streamwise direction can be considered quasi-two dimensional in the boundary layer solutions. With the change to an adverse pressure gradient, as the flow passes around the body, the flow is likely to separate, flow aligning shocks are formed and the flow reattaches giving a vortex flow behaviour. Lines of high heat transfer rate are formed in the region of flow reattachment lines. The level of heat transfer rate here does not usually exceed typical stagnation point values.

### 3.3 Component interactions (illustrated in figure 5)

Aerodynamic, flap and jet control and other protuberances will all have the effect of causing separation, hence high energy shear layer reattachment, the cause of localized regions of high heat transfer rates. Such flows may be subject to spanwise non-uniformities of the oncoming stream as well as finite span effects.

### 3.4 Wing-body interactions (figures 5, 6)

At zero incidences, corner boundary layer flows will cause minor localized high heat transfer rates near the corner. Much more severe problems occur with wings or tails at incidence in the presence of a body.

On the windward surface of such protuberances, a three dimensional separated region occurs and a region of very high heat transfer rate is found on the body near the wing body junction. On the leeward surface of the wing, if it is reasonably highly swept, leading edge vortex flow will occur with the reattaching shear layer likely to cause high heat transfer rates on the body along a line centered near the wing root at its leading edge. The surfaces within gaps between all moving control surfaces also are likely to encounter high heating rates.

### 3.5 Shock interactions (illustrated in figure 7)

Shocks caused by the nose on aerofoil leading edges or by accompanying bodies such as boosters engines or stores on a body, wing or pylon are also the cause of severe heating problems. If the shock is directed towards a stagnation region, many types of interaction can occur, some of which cause very high local heat transfer rates.

## 4. ATTACHED FLOW HEAT TRANSFER

In this section we assume that the flow can be dealt with by using the thin boundary layer approach with boundary conditions defined by inviscid flow solutions. Again, these latter solutions can be obtained at various degrees of complication and have been dealt with in other parts of the Lecture Series. Flows over simple configurations can be solved using the gasdynamic isentropic relations, flow across normal or oblique shocks, Prandtl-Meyer expansion, Newtonian and modified Newtonian theories, tangent cone and tangent wedge methods (see for example Refs. 12, 13). More complicated solutions of the inviscid supersonic flow relations involve the method of characteristics (Ref. 13), panel methods (Ref. 14) and the most up-to-date are the modern successive line over-relaxation techniques with fast solvers (NASA Ames Illiac Group) etc. Turning to the viscous part of the solution which involves the solution of the compressible laminar and turbulent boundary layer equations (in their differential or more simple integral forms), a good overall review (emphasizing turbulent flows, however) appears in a book by Cebeci and Smith (Ref. 15) of the McDonnell Douglas Aircraft Company suitable for application to aircraft and missiles. The full equations are presented and discussed in this book. Although the subject of heat transport is introduced, however, the contents of this book little discusses applications in heat transfer.

The solution of the boundary layer equations are usually approached in many ways involving different degrees of complication: firstly, "simple" methods involve correlation methods, integral methods and transformations to the inviscid equations, secondly, numerical solutions of the partial differential equations. Suitable available solutions will be briefly reviewed in the following subsections by using the state of the boundary layer as the primary classification. The simple correlation methods mentioned are presented in references 2 and 16. Many such simple methods are being used in the design of the space

shuttle orbiter showing that this approach should not be scorned (Ref. 17).

#### 4.1 Stagnation regions

A summary of early work on stagnation point heating on spherical and cylindrical shapes was made by Fay, Riddell and Kemp (Ref. 18). The most widely used predictions are those developed from the expressions of Fay and Riddell (Ref. 19) for these cases. Without flow dissociation, the following formula is used

$$q_0 = 0.763 \text{ Pr}^{-0.6} (\rho_e u_e)^{0.5} \left( \frac{\rho_w \mu_w}{\rho_e \mu_e} \right)^{0.1} \left( \frac{du_e}{ds} \right)_0^{1/2} [h_e - h_w] \quad (12)$$

where  $\rho$ ,  $u$ ,  $h$ ,  $\mu$  are density, velocity, enthalpy and viscosity and subscripts  $w$ ,  $e$ ,  $o$  mean at the wall, at the outer edge of the boundary layer and at the stagnation point and  $s$  is the distance from the stagnation point. Using modified Newtonian theory, the velocity gradient at the stagnation point of a sphere or cylinder with radius,  $R_N$ , is

$$\left( \frac{du_e}{ds} \right)_0 = \frac{1}{R_N} \sqrt{\frac{2pt_2}{\rho_e}} \quad (13)$$

where  $R_N$  is the sphere radius and  $pt_2$  is the stagnation pressure.

The heat transfer on the stagnation lines of yawed cylinders (representing leading edges of swept wings or bodies at high angles of attack) is discussed in reference 20. At large free stream Mach numbers, the effect of yaw is essentially to correct the unyawed value by  $(\cos \Lambda)^{1.1}$  where  $\Lambda$  is the sweep angle. At high enough Reynolds numbers and angles of sweep from  $40^\circ$  to  $60^\circ$ , it was found that the boundary layer on a swept cylinder was completely turbulent even at the stagnation line.

#### 4.2 Laminar boundary layer

A first order approximation concerns considering a surface as part of a flat plate. Eckert (Ref. 21) amongst others has shown that for a wide range of Mach numbers and temperatures, a close approximation is obtained for the skin friction coefficient on a flat plate in laminar (and turbulent) flow, by using the incompressible value evaluated at a temperature according to an intermediate (or reference) enthalpy (or temperature for a perfect gas). Application of a Reynolds analogy factor, relating the Stanton number to the skin friction is then used. A value of  $\text{Pr}^{-0.5}$ , equal to 1.18 for  $\text{Pr} = 0.72$  as ascribed to Colburn is usually used for this factor.

Heat transfer over more complicated axisymmetric shapes may be dealt with the similarity analysis of Lees (Ref. 22). More sophistication and probably adequate accuracy may be obtained by the relatively easy application of the Cohen and Reshotko (Ref. 23) method based on exact solutions for specified pressure gradients and heat transfer.

An efficient numerical scheme for both two dimensional and axisymmetric flows is presented by Cebeci and Smith (Ref. 15) based on the Keller-Box computational technique. In their book, however, they provide little evidence as to its accuracy in predicting heat transfer.

#### 4.3 Transition

Transition location usually provides the largest uncertainty in thermal protection design systems (see for example Ref. 10 concerning the Space Shuttle design). This may not be so critically important in high supersonic speed missiles since the chief problem areas are likely to be on stagnation regions and regions of impinging shear layers. There have been numerous correlations of transition location.

For a first order application, it can generally be assumed that transition will commence in the range of Reynolds numbers based on distance from the leading edge,  $Re_x$ , of around  $5 \times 10^5$ . A more convenient parameter to use is one based on a local boundary layer parameter such as  $Re_\theta$ . Use of such a parameter also reflects the reluctance of a boundary layer to undergo transition in a favourable pressure gradient. A value of  $Re_{\theta, tr} = 360$  is a universally used value (corresponding to an  $Re_x$  of  $3 \times 10^5$  on a flat plate,  $\theta_{tr} = 360$  is with zero pressure gradient).

References 15, 24, 25 give formulae which relate the transition momentum thickness Reynolds number,  $Re_{\theta, tr}$ , with the transition  $x$ -Reynolds number and which claim to take into account pressure gradient. For transition on airfoils, Crabtree (Ref. 26) correlated data with  $Re_{\theta, tr}$  against a pressure gradient parameter  $m = -\frac{\theta^2}{\nu} \frac{du}{dx}$  and found that appropriate data collapsed on this line. These methods relate, however, to incompressible flow. Hopkins et al. (Ref. 27) prepared some useful charts for estimating boundary layer transition in supersonic flows. This report reflects the number of parameters important in describing compressible boundary layer transition. Benek and High (Ref. 28) have developed a transition point prediction technique for compressible flows incorporating free stream disturbances and weak pressure gradients which has met with reasonable success for simple

configurations. All these reports provide simple criteria for a very complicated and truly unsolved problem area. The most recent review of the subject by Morkovin (Ref. 29) accentuates this point.

Transition does not occur instantaneously but usually over a considerable length, which for high speed flows can be of the same order as that over which the laminar boundary layer develops. Dhawan and Narashima (Ref. 30) demonstrate the particular behaviour of the mean velocity profiles within a transitional boundary layer and have provided an empirical correlation concerning the length of transition. Masaki and Yakura (Ref. 31) have shown that the length of transition over a large Mach number range of conditions can be reasonably approximated to the length of laminar flow. Chen and Tyson (Ref. 32) have developed a correlation for transition occurring on blunt bodies for both compressible and incompressible flow.

The heat transfer distribution in a transition region is often assumed to follow a linear variation joining the laminar value at the beginning of transition to the turbulent value at the end of transition. Slightly more sophistication is achieved by incorporating the physics of turbulent spot development in a simple fashion by "sharing" the laminar and heat transfer rates using an intermittency distribution similar to that of reference 30, i.e. :

$$\gamma(x) = 1 - \exp \{-0.412[(x-x_{tr})/\Delta x]^2\} \quad (14)$$

where  $\Delta x = (x_{tend} - x_{tr})/2.96$ ,  $x_{tr}$  and  $x_{tend}$  are the position of the beginning and end of transition.

For precise prediction of transition heating, note should be made of the so called "precursor effects" at high Mach numbers (Ref. 33).

Some more sophisticated methods have been used to calculate the boundary layer through transition. Harris (Ref. 34) developed a method for high Mach numbers cases. This requires, however, empirical information concerning transition location, transition length and an intermittency distribution to modify the eddy viscosity distribution through the transitional boundary layer. A similar approach has been developed by Adams (Ref. 35). The Cebeci-Smith (Ref. 15) method is in a more practical state for predicting missile flows, but requires similar empirical techniques.

Shamroth and McDonald (Ref. 36), however, have used a different approach in developing a practical method for computing the development of the boundary layer flow during transition which also takes into account boundary conditions such as free stream turbulence and wall roughness. The method also copes with relaminarization.

#### 4.4 Turbulent boundary layer

As in the case of laminar boundary layers, a first order approximation of calculating the heat transfer rate on a surface is in assuming that it is a flat plate with locally a zero pressure gradient. An appropriate reference enthalpy method to obtain skin friction is that of Eckert (Ref. 21) and Sommer and Short (Ref. 37). Spalding and Chi (Ref. 38) have presented a summary of early correlation methods for prediction of skin friction for compressible flow up to 1964 and developed an appropriate semi-empirical method. A more recent method is that of White and Cristophe (Ref. 39).

Care must be taken to apply an appropriate value of the Reynolds analogy factor to be used to assess heat transfer information (through the Stanton number) from the predicted skin friction coefficients. Hopkins and Inouye (Ref. 40), in providing the latest of many survey papers on correlation methods for predicting compressible boundary layers have indicated that the Van Driest method (Ref. 41) with a Reynolds analogy factor of 1.0, Spalding and Chi (Ref. 38) and Eckert (Ref. 20) with a von Karman Reynolds analogy factor (see Ref. 42) give the best predictions of heat transfer rate. The virtual origin of the turbulent boundary layer used to define the flow Reynolds number is normally taken near the end of transition.

Some scope for improvement over a wider range of wall to recovery temperature ratios may arise from application of Bradshaw's "Van Driest III" method (Ref. 43) of predicting skin friction which is based on a more generalized velocity profile law. However, at present no application of this to heat transfer prediction has yet been perceived in the literature. A value of Reynolds analogy factor near 1.1 appears to provide a suitable mean of values. Two examples of comparisons of Eckert's (Ref. 21) method with data from flight are shown in figures 8, 9 taken from the Bushnell et al article (Ref. 44). All of these preceding methods are developed for zero pressure gradient, but usually appear to give reasonable predictions of flows with modest pressure gradients.

Integral methods solve the von Karman integral momentum equation along with various auxiliary equations. These methods provide reasonably accurate predictions for a wide range of flow conditions except under severe pressure gradients, non equilibrium boundary layer conditions and to flows where the empirical correlations used within do not apply. The methods provide fast and inexpensive calculations, but have their limitations. A recent review of these is given in reference 44.

Significant advances are being made in solving the full boundary layer equations and are being incorporated in design codes (Refs. 44, 45, 46). Once this sophistication is considered for missile or aircraft applications, the full three dimensional equations should be taken into account. An optimistic review of current research programs given in

references 44 and 47 indicate that with increasing capabilities of digital computer systems and the maturing of three dimensional inviscid flow field codes, general purpose three dimensional boundary layer codes (i.e., attached flow cases) will become available in the next two or three year period. Designers should keep themselves up-to-date on this progress.

An example of such full solutions is the mean field closure methods. There are usually four closure assumptions which must be specified before a solution can be obtained. Three of them are those familiar in incompressible solutions to define the Reynolds stresses through the eddy viscosity or mixing length, i.e., the wall damping region, law of the wake region and wake or outer region. The fourth involves dealing with the Reynolds heating  $\overline{v'h'}$ , which is generally handled through the use of a "turbulent conductivity" :

$$\overline{v'h'} = \kappa \frac{\partial h}{\partial y} \quad (15)$$

which then allows the definition of a "turbulent Prandtl number" :

$$\text{Pr}_t \equiv \frac{\epsilon}{\kappa} \quad \text{or} \quad \kappa = \frac{\epsilon}{\text{Pr}_t} \quad (16)$$

Once  $\text{Pr}_t$  is known, the model for Reynolds stress can be used to determine  $\kappa$ . There are several codes available that are applicable to the kinetic heating problem and which are well documented. Examples are the method of Bradshaw, Ferris and Atwell (updated and put in Fortran IV language in Ref. 48), Stan5 (explained in detail in Ref. 49) based on the Spalding and Patankar numerical scheme.

## 5. VISCOUS INTERACTIONS

The most severe heating problems of high Mach number flight are associated with viscous-inviscid interactions. Complicated geometries expected in practical configurations can lead to regions of high compression causing the flow to separate. High values of heating are then obtained near the flow reattachment positions. Such "hot-spots" can lead to heat transfer rates sometimes considerably higher than the stagnation region values. Normally, for practical vehicles at cruise or design flight conditions, the interactions will occur in regions of turbulent flow. An excellent survey on such interactions is given by Korkegi (Ref. 50).

Prediction of even the simplest of these flows is extremely difficult. The type of flow field is categorized according to the order of magnitude of a characteristic Reynolds number. If the Reynolds number is large, the flow is made up of regions which, to a great extent, can be described by Euler's equations for inviscid flow, or by Prandtl's equations for boundary layer flow. However, the full Navier-Stokes equations usually are needed for the description of the flow in local zones where the above approximations fail; the existence of such zones tends to be the rule rather than the exception in practical missile flow fields. These regions in which the Navier-Stokes equations are needed, although small, often have an important influence over the complete flow and they are an essential feature of the flow field for the determination of the overall solution. Some classical examples are flow in the region of a wing trailing edge, shock-boundary layer interactions, boundary layer flow past a corner, base flow, separation over a compression corner, etc.

Large Reynolds number flows are likely to be turbulent and this is a feature of practical missile flows. The Navier-Stokes equations remain valid for turbulent flows, but numerical prediction of such flows with existing methods and computers cannot deal with the small scale three dimensional turbulent fluctuations. The result is that the time averaged Navier-Stokes equations are employed together with additional relations or differential equations for the various correlation terms in order to close the system of averaged equations. These additional equations, which constitute a turbulence model, are necessarily highly empirical. Hence, the usefulness of a calculation involving turbulent flow is linked strongly to the validity of the turbulence model used.

Solutions are being accomplished for simple flows at present, but full solutions of flow over configurations at realistic Reynolds numbers at a design level are not envisaged for at least 10 years (Ref. 47). The situation at present is that much reliance on prediction of kinetic heating in regions of flow interaction is based on empirical analysis of experimental information. Such methods are likely to persist for the far future, not only to provide information to designers but also to computer program developers. It is for this reason that later on in this review, importance is given to reviewing existing and future wind tunnel projects.

Each of the types of interaction mentioned in chapter 3 are discussed in the following subsections.

### 5.1 Compression corners and shock interactions

Extensive measurements of supersonic laminar, transitional and turbulent boundary layer separation over various configurations including a compression corner were made by Chapin, Kuehn and Larsen (Ref. 51). They clearly showed the strong influence of transition and the much larger pressure gradients associated with turbulent than with laminar separation. A review of heat transfer in separated and reattached flows was presented by Fletcher, Brundage and Page (Ref. 52) in 1970. A more recent and rather complete review on the overall problems of two dimensional laminar and turbulent shock wave-boundary layer interaction



in high speed flows has been made in 1975 by Hankey and Holden (Ref. 53). For a designer, the most important information of interest is the shock strength (impinging or induced by a wedge) required to achieve incipient separation, the length of the separated region and angle of the boundary shear layer for a particular shock strength and the heating level within the separated region and at or near the reattachment point for particular flow conditions. Correlations of some sort are available for each of these parameters, but however, only for simplified geometrical situations such as two dimensional flat plate flow or axisymmetric flow and generally only for fully laminar and fully turbulent conditions. Appropriate correlative graphs for most of the above parameters are presented in Hankey and Holden (Ref. 53).

One of the most important pieces of information concerns the maximum heating level in the separated region, generally occurring just downstream of flow reattachment. For both laminar and turbulent flows, experimentalists have related this parameter to the pressure distribution through a power law relation such as

$$\frac{q_{\max}}{q_0} = \left( \frac{p_{\max}}{p_0} \right)^n \quad (17)$$

where subscript 0 denotes undisturbed values. The mean value of  $n$  is 0.7 for laminar flows and 0.85 for turbulent flows. The peak pressure is an easier parameter to assess than heat transfer rate (Refs. 54, 55, 56).

For more complete solutions one must look to the development of numerical schemes for solving two dimensional or axisymmetric boundary layers. Some success has been achieved by the traditional technique of dealing with the viscous and inviscid flow fields separately and matching them appropriately, but as mentioned earlier some attention has to be given to the "elliptic" characteristics of the equations in the reverse flow separated regions within the "parabolic" boundary layer region. Hankey and Holden (Ref. 53) provide a review to developments in this area as well as in the solutions of the full Navier-Stokes solutions, which eventually must be solved for realistic flow conditions.

## 5.2 Wing-body and fin-body interactions

In supersonic flow, the interaction of the strong bow shock of a blunt fin or wing with laminar and turbulent boundary layers causes widespread upstream and lateral flow separation. This topic has been the object of concentrated research recently by groups at AFFDL, Princeton University, College of Aeronautics at Cranfield and VKI. The flow is characterized by a lambda shock structure in the plane of symmetry, which spreads out laterally downstream to form a broad three dimensional interaction region with strong vortical type flow. Local regions of high heating resulting from the fin interaction appear near the base and extend downstream at a fixed angle to the fin (Fig. 10)

These high heat transfer rates have been related to flow reattachment or impingement along a line associated with a vortex type flow (Ref. 50). Another explanation lies in the sweeping away laterally of the low energy flow in the lower boundary layer illustrated in figure 11 by the strong transverse pressure gradient thus thinning the shear layer near the fin (Ref. 57). Again the maximum heating has been related to the maximum pressure through a power law in the same way as for the two dimensional case (eq. 17) but the average value of  $n$  in this case seems to be closer to 0.8. This demonstrates that much higher heating rates are found in the three dimensional case than in the equivalent two dimensional case for the same pressure rise. Some experiments carried out at AFFDL (Ref. 58) indicated that the maximum heating was reduced by tripping the boundary layer with a row of roughness elements. This has been checked more thoroughly in some experiments at  $M=5.4$  at VKI in an as yet unpublished work, but not found in some later AFFDL work (Ref. 59). The mechanism for this phenomenon is yet unexplained. There abounds much more information on the three dimensional flow field and surface pressure field than on heat transfer measurements for this configuration.

## 5.3 Axial corner flow

Supersonic flow in axial corners formed by two intersecting flat surfaces has been the subject of experimental investigations for a decade and a half. A corner interaction occurs as a result of initial flow compression on one or both surfaces due either to boundary layer displacement effects or to the inclination of the surfaces with respect to the free stream or both. The flow field is quite complex as first found by Charwat and Redekopp (Ref. 60) as seen in figure 6.

The corner problem may be viewed as one involving a strongly disturbed inviscid flow field, and, in turn, the interaction of this flow field with surface boundary layers. Sharp peaks seen have been associated with the strong vortex or vortices attached to the corner. The corner heat transfer distribution has distinct features in common with two dimensional shock wave boundary layer interactions - a drop in heat transfer rates beyond separation (the trough) followed by a rise to high values (peaks) at reattachment. (See Fig. 12 taken from Ref. 61). Studies on corners with angles between surfaces different than  $90^\circ$  have also been made as reviewed in reference 50. Summarizing, regions of high heat transfer are obtained due to corner interaction, these are typically several times larger than undisturbed values, but not usually as high as stagnation point heating values.

#### 5.4 Base flows and vortex flows on expansion surfaces

Vortex flows as may arise on the lee -side of a fuselage or wing-body at angle of attack, causing possible regions of high heating and interference with control surfaces, have been well documented by Rainbird (Ref. 62) and Peake, Rainbird and Atraghji (Ref. 63). This problem of heating was brought into prominence with the space shuttle as reviewed in Ref. 17. Again heat transfer rates several times larger than undisturbed values are obtained around the centerline of wings alone, or on the body sides above the wing centered about the wing leading edge root. Furthermore, heat transfer rates do not usually achieve values typical of stagnation regions, but under certain circumstances may be considered important. A more recent review of the subject related to space shuttle is given in reference 64 with emphasis on the effects of surface temperature and Reynolds number on leeward shuttle heating.

Another review by Bertin (Ref. 65) focusses on the definition of the flow field in the base region and in the leeward separated flow behind a vehicle at high angle of attack (e.g., space shuttle) as an aid to determining the convective heat transfer distribution. Generally, the heat transfer due to the axisymmetric flow in the base region of a body at zero angle of attack are relatively small, however, there is a large change due to the onset of transition. Smaller effects due to Mach number, mass addition and wall temperature are also discussed. The free vortex layer type separation causes much higher heating, as noted above, which appears to be connected to the thinning of the viscous shear layer as a result of the outflow caused by the vortices. Again the effects of Reynolds number, Mach number, configuration and wall temperature on the flow field and heat transfer rate are discussed. The interesting feature in some of these latter references is in the approach in which the researcher is forced to make studies related to a specific project rather than with a fundamental objective in mind.

#### 5.5 Shock impingement

The most severe aerodynamic heating is undoubtedly due to shock impingement or the interaction of an externally generated shock with the bow wave at the leading edge of a blunt body (for example, that caused by an aircraft on its store). Examples of practical configurations in which shock impingement arises are shown in figure 7. This problem was identified by investigators at an early period, but it was not until the extensive study of Edney (Ref. 66) who obtained very detailed schlieren photographs of a remarkable quality, that understanding of the interference flow field was gained. Edney measured the shock impingement heating on a hemisphere, a blunted cone and a flat faced cylinder at Mach numbers of 4.6 and 7. Using the quasi steady techniques of laterally sweeping the models relatively slowly across a wedge generated shock in a test section, he obtained accurate local measurements of heat rates and pressures. Very localized heat transfer rates of the order of ten times stagnation heat transfer rates are achieved by such impinging flows. Peak pressures follow very nearly the same distribution of peak heating rates, with maximum values at essentially the same location away from the stagnation point of the hemisphere. This fact again suggests the validity of pressure-heat transfer correlations for this case. Edney found that peak heating rate increases with increasing impinging shock strength and Mach number.

A more recent study of shock interference heating directly following on Edney's work is that of Hains and Keys (Ref. 67). The study encompasses many shock impingement cases on hemispheres, wedges at high angle of attack and on swept fins as well as discussing the application of such results to the design of the space shuttle. Peak heating values of 17 times the stagnation value were recorded and it is predicted that up to 37 times it could occur on the space shuttle attached to the booster during the higher altitude part of the ascent ( $M = 10$ , 80,000 meters altitude). Further diagnosis of flows caused by impingement of a shock generated by a body on the leading edge of swept and unswept wings is presented by Bertin (Ref. 68).

### 6. MEASUREMENTS ON CONFIGURATIONS IN FLIGHT AND IN WIND TUNNELS

In this section, a series of brief statements on results of wind tunnel tests or flight tests and their comparison with engineering correlations are presented, in which surface heating on configurations is featured. There is a severe lack of information on tests on missile shapes at supersonic speeds (as opposed to reentry) and so the information has generally been gleaned from high speed research aircraft, and lifting reentry vehicle sources. It is believed, however, that these remarks are also relevant to missile heating.

Heat transfer measurements measured on the wing of the X-15 airplane at low and high angles of attack and on the fuselage at low angles of attack (Ref. 69) are overestimated by Eckert's reference enthalpy method (Ref. 21) and the theory of van Driest (Ref. 41). Adequate prediction by Eckert's method, however, can be obtained if the effect of wall temperature is neglected. This is further confirmed by reference 70. These results have been under some dispute but later results by Cary (Ref. 71) in ground facilities have substantiated the flight measurements.

Selected incompressible flat plate turbulent heating expressions used in an appropriate manner produce good correlation with flight test data over large ranges of Mach number, Reynolds number and wall temperature ratios for bodies with various cone angles and bluntness ratios (Zoby & Sullivan, Ref. 72). For  $Re = 10^7$  calculated heating rates based on Blasius or Schultz-Grunow friction factors were within +22 and -10% of measurements.

For  $10^7 < Re < 8 \times 10^7$  the Schultz-Grunow method gave better correlation.

A convenient correlation of local heat transfer rate with the local surface pressure for blunt cones at various angles of attack was derived by Widhopf (Ref. 73). A method is given by Wing (Ref. 74) for calculating the aerodynamic heating and shear stresses at the wall for tangent ogive noses that are slender enough to maintain an attached nose shock through that portion of flight during which heat transfer is significant. A method is developed by De Jarnette and Hamilton (Ref. 75) which calculates laminar, transitional and turbulent heating rates on space shuttle type configurations at angle of attack in hypersonic flow. Results for blunted circular cones and a typical delta wing space shuttle orbiter at angle of attack indicate that this method yields accurate laminar heat transfer rates and reasonably accurate transition and turbulent heat transfer rates. Improved heat protection of tail fin leading edges was sought by Overmier (Ref. 76) following a sounding rocket flight failure.

Heat transfer studies to an airfoil in oscillating flow reveal at large angle of attack, including those in which stall would occur in steady flow, a strong periodic starting vortex from the leading edge causing a dramatic reattachment of the flow and an increase in local Nusselt numbers by as much as a factor of 5 (Ref. 77). Experimental studies of vortex induced heating to a cone-cylinder body at Mach 6 by Hefner (Ref. 78) indicate that the most severe lee-surface heating need not occur as a result of the interaction of the primary vortices with the lee-surface. Vortex heating studies to cone flaps also at Mach 6 by Hefner and Whitehead (Ref. 79) indicate that locally high heating can occur on leeside flaps at vehicle angle of attack. This heating is generally less than the maximum heating at zero angle of attack (for the same flap deflection) but can be greater than the vortex induced heating on the configurational forebody at the same angle of attack.

In connection with space shuttle, the range of Mach number and Reynolds number has been expanded by Creel (Ref. 80) to assess their effect on orbiter/tank interference heating. The primary effect of interference in these tests is to cause transition to fully developed turbulent flow. As a result of extensive experimental studies, a technique has been developed for predicting shock shapes; pressures and turbulent heating rates on the leading edge of a fin, swept wing antenna or similar highly swept near its intersection with a high speed vehicle (Ref. 81).

There are significant increases in heat transfer rate over large regions of the Apollo command module due to the presence of protuberances and cavities (present in its reentry configuration) at  $M = 10$  and  $1.4 \times 10^6 < 2.6 \times 10^6$  (Ref. 82). For the evaluation of the thermal performance of RSI (reusable surface insulation) tiles for protection of space shuttle surfaces, results show that unfilled gaps between tiles seem hotter than comparable undisturbed areas and for transverse and axial gaps a trend of decreasing temperatures with decreasing gap width is evident (Brewer, Saydah, Nestler, Florence, Ref. 83). Dunavant and Throckmorton (Ref. 84) also show that heat transfer is significantly increased when one tile protrudes above another. Further information on gaps and many other topics has been discussed in relation to the ASSET reentry vehicle program by Neumann (Ref. 85).

A series of tests have been made to examine three dimensional shock wave/turbulent boundary layer interactions on a finned missile configuration by Hayes (Ref. 86) with aerodynamic heating providing the main focus of interest. The work is a continuation of fin/flat plate studies discussed earlier. The model was basically an ogive cylinder instrumented with 200 thin skin heat transfer sensors. During the test series several types of control surfaces (fins and canards) were mated to the body and test at different roll angles and an angle of attack ranges from 0 to  $12^\circ$ . The effect of gaps between the control surface and the bodies were examined. For the "sealed" control surfaces, the peak heating in the interaction region was correlated and found to be predicted by a pressure interaction theory with an exponent of 0.8 (Ref. 58).

Flight and wind tunnel measurements were conducted on a pylon-mounted store by Matthews and Keys (Ref. 1). The main objective of the tests was to substantiate the extrapolation of procedures used to assess the heating rates on a full scale store mounted on an F-111 in flight with those measured on a small scale model in a wind tunnel model. Some substantiating evidence was obtained; however, scatter in the flight test data prohibited any definite conclusion.

## 7. TESTING TECHNIQUES

### 7.1 Wind tunnels

The prediction of local heating over the whole surface of a missile (or aircraft) configuration can be stated as still a large way from possible, because of the complexity of the flow. Wind tunnel testing is hence likely to play a continuing important role for a period far enough in the future that new facilities are being considered. For flow Mach numbers below 5, there exist very few heated flow facilities available for studying kinetic heating. The fact that there are many tunnels with heated flows above Mach 5 is only for the reason of preventing flow condensation. For simulating flow over missiles at high supersonic Mach numbers, one could thus envisage replacing the hypersonic nozzles of these latter tunnels with lower Mach number versions. Because of the power levels needed to heat such flows, usually these hypersonic tunnels, thus also such converted tunnels, tend to have small test sections, so small that configurational testing is difficult to accomplish. Nevertheless, these facilities provide a useful service in testing simple models for single components of a configuration.

Two types of facilities could be of value in future development of high speed missiles in which heating plays a critical role. The first one would be used for testing a complete missile including its structure and systems. Such a tunnel should have a test section of large enough size to test a complete missile, a flow temperature range the same as the stagnation temperature range of future projected missiles and the correct Mach number and Reynolds number range. A call for such an "aerothermal wind tunnel" with a Mach number performance of 2 to 6 with actual flight time and temperature duplication and full scale Reynolds numbers for missiles is given in reference 87 (Fig. 13). A 6 ft (1.80 m) diameter test section would be sufficiently large to test most full scale tactical missiles. The operating envelope that would be required to provide flight duplication in a 6 ft diameter wind tunnel is given in figure 14. It can be seen that an air supply of 3000 lb/sec (1360 kg/sec) heated to 3000°R (1670°K) at a pressure of approximately 1500 lb/m<sup>2</sup> (100 atmospheres) would be required. This would constitute a major facility but reference 88 discusses that the technology for such a tunnel is available.

The other type of tunnel is one in which one wishes to test the aerodynamics and heating to the external surface of a configuration. In this case, both the flight time and true temperature do not have to be duplicated, hence one can fall back on economic short duration tunnels operating near the flow condensation temperature (although one should have sufficient flow temperature to create a heat transfer to models at ambient temperature for the lower Mach number cases). The important parameters to simulate are Mach number and Reynolds numbers. Provided the wall to recovery temperature ratio is more than a few percent higher than unity, the measured value of the heat transfer coefficient,  $h$ , (or  $St$  or  $Nu$ ) will be applicable for other wall temperatures. Higher accuracy can be achieved in  $h$  by using as high a  $T_w/T_r$  as possible. Although such facilities are on a scale which is modest compared to the "aerothermal tunnel" mentioned above (i.e., approximately 600 K, 2 m test section, 40 atm,  $2 < M < 6$ ), such tunnels do not exist at present, mainly because of a recognition of the requirement of such a facility only recently.

An interim "aerothermal" simulation technique for testing materials on simple flat plate or hemisphere shapes has been devised by Matthews and Stallings (Ref. 89). Conventional continuous hypersonic tunnels,  $M = 6$  and 10, were used to test materials mounted on a wedge at such an angle of attack and such supply conditions to get  $M$ ,  $Re$  and  $T_{stag}$  correct (see Fig. 15). Through such a technique it was possible to simulate the flow on the body surface and around a stabilizing fin of a missile at  $M = 4$ , altitude of 60,000 ft (18,000 m). A novel optical technique was described to measure the recession rate on tested materials.

For aerodynamic and heating simulation, to overcome the difficulties associated with the high power levels required and materials and instrumentation problems involved with continuously hypersonic operating tunnels, short duration tunnels were devised (for a review of such developments, see Lukasiewicz, Ref. 90) and have been found indispensable in the Apollo and space shuttle programs. For heat transfer studies, a further advantage is that fast response, sensitive and accurate transient methods of measurement can be used (Schultz and Jones, Ref. 91). The modest temperature requirement needed for aerodynamic heating studies of missile configurations suggest the application of a class of facility recently devised for the different application of heated turbine component testing (which also requires only a modest temperature) by Jones, Schultz and Hendley (Ref. 92) called the isentropic light piston tunnel. A large version of this turbine facility has been built at VKI (Refs. 93, 94). This VKI tunnel has been designed with a future possibility of using it for studies of heat transfer flows over vehicle configurations at high Mach numbers and its application to missile testing may be most appropriate. Its characteristics are for it to generate flow temperatures up to 600 K at pressures of 40 atmospheres for running times up to 1 second over which time it develops a power of 7 MW. It is driven economically from the Institute's 250 atm compressed air supply. With a Mach 4 nozzle, a test section size of 0.5 m diameter and a flow Reynolds number of  $1.8 \times 10^8$  per meter could be achieved.

## 7.2 Heat transfer measurements

In the case of testing in "aerothermal" test facilities, the main emphasis on measurement techniques will focus on temperature measurements of internal parts of the missile rather than heat transfer measurements to the exterior surface. The subject of temperature measurement is dealt with in detail in reference 95 and no further mention will be made on this except in relation to heat transfer measurements.

### 7.2.1 Steady state technique

Heat transfer measurements using steady state techniques are extremely difficult to carry out. The most complete and up-to-date review on this subject is given by Winter in reference 96 (which also, however, contains a review of transient techniques) based on work carried out at RAE in England. Another useful reference is that of Eckert and Goldstein (Ref. 97).

To make heat transfer measurements under steady state conditions it is necessary to supply power to a model equivalent to that transferred to the air stream or to extract power from the model accordingly as the model is maintained at a temperature higher or lower than the recovery temperature of the air stream. The latter technique is normally carried out by passing a cold liquid through the interior of the model. An example of the former is that carried out in the VKI 0.40 m continuous supersonic tunnel S-1 on a wedge (Ref. 98). The wedge was cast in an epoxy resin around thermocouples and then machined to produce a smooth surface and expose the thermocouple junctions. The heating element was provided by silver plating the whole surface using a mirror-silvering process resulting in a film of

fairly uniform thickness of about 1  $\mu\text{m}$ . The film was connected by silver paint to electrodes running along the sides of the model. If it is assumed that the film is of uniform thickness and resistivity and that the current is supplied uniformly, then the heat dissipated will be uniform over the whole surface. Thus measurements of the surface temperature,  $T_w$ , of the heated model and of the temperature,  $T_r$ , of the unheated model and a knowledge of the electrical power,  $q$ , dissipated per unit area enable a heat transfer coefficient,  $h$ , to be determined from

$$h = \frac{q}{T_w - T_r}$$

In any steady state technique, care is needed to ensure the equilibrium conditions have been obtained. For conditions of  $M = 2.2$  and Reynolds numbers of  $1.6$  and  $3.3 \times 10^6$  per m, a running time of 1 hour was required to reach equilibrium.

Although the method as described gives information at constant heat transfer, using multiple elements on a surface, constant model surface temperature can more easily be obtained and with appropriate automatic control the response time of the system could be as fast as the flow establishment or tunnel starting time, since no model temperature change is involved. This method would be much more complicated than the "semi-infinite slab" transient method to be described, but would be applicable in cases in which rapid tunnel start or rapid model injection was impractical (since the method is not dependent on the running time) and would prove useful in activating existing continuous or blowdown ambient temperature supersonic wind tunnels for kinetic heating studies (A further philosophy justifying this latter approach would be that less energy would be needed to heat the model than heat the flow). The heat transfer coefficients thus obtained would be applicable to the real situation as long as  $M$  and  $Re$  were simulated and the main conclusion would arise from the boundary layer characteristics (e.g., position of transition, boundary layer thickness, etc.) being not well simulated.

The more classic approach to steady state heat transfer measurement involved internally cooling a model fitted with a thin skin uniform skin and measuring the temperature gradient across the skin. The choice of material skin is a balance between a good conductor (high heat transfer rate, but low temperature difference) and a poor conductor (low heat transfer rate, but high temperature difference across the skin). Winter (Ref. 96) shows that for maximum sensitivity the temperature drop through the skin should be half the temperature drop in temperature from the aerodynamic recovery temperature to the coolant temperature. An extensive review is made by Winter on heat flow meters appropriate to these steady flow techniques, many developed at RAE - Bedford.

Another possible approach is through the use of the analogy of heat transfer with mass transfer. This has been applied in the form of measuring the sublimation rate of naphthalene (Eckert and Goldstein, Ref. 97).

### 7.2.2 Transient techniques

Measurements in aerodynamic heating facilities are more popularly carried out using transient techniques. These methods depend normally on a quick start tunnel flow (<0.1 secs) such as produced in such short duration facilities as shock tunnels, piston tunnels, etc., or on the rapid injection of the model into a blowdown or continuous tunnel. A typical range of techniques used is presented in reference 99.

The thin skin or calorimeter technique involves the measurement of the temperature of the thin skin made of a good conductor which has been thermally insulated on the back side (Refs. 91, 100). For a perfectly constructed gauge, the heat transfer rate is then given simply by the relation

$$q = \rho b c \frac{dT_w}{dt} \quad (18)$$

where  $\rho$ ,  $b$  and  $c$  are the density, thickness and specific heat of the skin material. In practice, imperfections in construction are such that the effective thickness,  $b$ , must be found by direct calibration. For the flows of interest, it is quite possible that the skin temperature rise is important with relation to the driving temperature,  $T_r - T_w$ , which must be taken into account in defining the heat transfer coefficient,  $h$ , i.e.

$$h = \frac{\rho b c \frac{dT_w}{dt}}{T_r - T_w} \quad (19)$$

Trimmer et al describe an analysis of the data to assess and eliminate errors due to heat conduction along the skin. Errors due to thermal radiation can normally be neglected. The temperature sensor can be a thermocouple, thin film resistance thermometer etc.. Response times of such heat sensors are of the order of 1-100 msec. and measurement can be made in a time of 10 msec - 1 second.

Another method was the measurement of the surface temperature of a thick layer of a poor conductor to assess the heat transfer rate. The technique is described in detail in reference 91. The measurement time is controlled by the thickness of the material, usually pyrex glass or quartz, required to cause the temperature change at the back surface to be small. Running times of up to 1 second have been achieved using this method (Ref. 101).

The response time is controlled by the characteristics of the temperature sensor which is usually selected to be a thin film platinum resistance gauge or thermocouple painted and baked on to the glass or ceramic backing material. This time can be as low as several microseconds. The heat transfer is then calculated using the following appropriate solution of the one dimensional heat conduction equation :

$$q = \frac{\sqrt{\omega C k}}{\sqrt{\pi}} \left[ \frac{I(t)}{\sqrt{t}} + \int_0^t \frac{I(t) - I(\tau)}{(t - \tau)^{3/2}} d\tau \right] \quad (20)$$

which can be carried out numerically or by the use of analogues. The analysis of numerical data from an on-line data acquisition system is reviewed in reference 102. A recent development is the use of MACOR<sup>R</sup> machinable ceramic available from Corning Glass from which complicated models can be machined and on which can be easily fired platinum film gauges (Ref. 103).

In the space shuttle program, considerable use was made of thermographic techniques for determining heat transfer patterns on these complicated configurations. Such techniques were the thermo-sensitive paints, phase change paints, liquid crystals and thermographic phosphors. These techniques are mentioned in references 91, 97 and 99 and their application to the space shuttle program in reference 17. Models were made of STYCAST, a moulding compound with low thermal conductivity which was selected to enhance the surface temperature variations on the model. For application to the above-mentioned short duration piston tunnel, most of the thermographic techniques will respond to the changes in surface temperature to a sufficient extent in the relatively long running time. This suggests an economic but effective way of generating experimental data of a developmental nature.

The most sophisticated technique available that has the attributes of the thermographic techniques with the accuracy of the transient techniques discussed earlier involves the use of an infra-red scanning camera (see paper 22 by D.L. Compton in Ref. 17). Combined with an on-line data acquisition system to deal with the vast amount of data collected, accurate overall surface measurements could be achieved on configurations. The method would require, however, some substantial development.

#### 8. CONCLUDING REMARKS

In this report, experimental and theoretical aspects of kinetic heating of missiles are reviewed. Simple correlation methods appear to be widely used and reasonably accurate for predicting heat transfer rates due to attached flow or near two dimensional or axis-symmetric surfaces. There is sufficient literature available to be aware that surface flow interactions can cause severe heating. Crude correlations have been devised to predict the level of the maximum heating rates achieved, provided the pressure field is known, but little information is available on the location of such regions of heating.

There have been recently dramatic advances in computational methods and computers to solve the full Navier-Stokes equations towards predicting the flow over complicated shapes, but even the most optimistic workers in this field expect one to wait another 10 or 15 years to achieve such solutions at a developmental level, even in well equipped establishments. There is thus a call for economic wind tunnel tests using easy-to-build models and heat visualization measuring techniques to provide rapid answers on complete configurations. Suitable measurement techniques are reviewed.

#### REFERENCES

1. MATTHEWS, R.K. & KEY, J.C.: Comparison of wind tunnel and flight test heat transfer measurements on a pylon mounted store.  
J. Aircraft, Vol. 14, No 6, June 1977, pp 565-568.
2. CRABTREE, L.F.; DOMMETT, R.L. & WOODLEY, J.G.: Estimation of heat transfer to flat plates, cones and blunt bodies.  
RAE TR 65137, July 1965.
3. CARSLAW, H.S. & JAEGER, J.C.: Conduction of heat in solids.  
Oxford University Press, 1947.
4. JOHNS, D.J.: Thermal stress analyses.  
Pergamon Press, September 1965.
5. SCHUH, H.: Heat transfer in structures.  
Pergamon Press, 1965.
6. JOHNS, D.J. & WOOLRIDGE, M.J.: Some approximate formulae for transient temperature prediction in aircraft type structures.  
J. Royal Aeron. Soc., Vol. 71, 1967, p. 223.
7. BEELER, D.E.: The X-15 research program.  
AGARD Report 289, October 1960.
8. CHAPMAN, A.J. & DOW, M.B.: Arc tunnel evaluation of some ablative heat shield materials for the X-15-2.  
NASA TN D 3753, February 1967.
9. ERB, R.B.; GREENSHIELDS, D.H.; CHAUVIN, L.T.; PAVLOVSKY, J.E.; STATHAM, C.L.: Apollo thermal protection system development.  
J. Spacecraft & Rockets, Vol. 7, No 6, June 1970, p. 727.

10. MASEK, R.V.; HENDER, D.; FORNEY, J.A.: Evolution of aerodynamic heating uncertainties for space shuttle.  
J. Spacecraft & Rockets, Vol. 11, No 6, June 1974, p. 368.
11. HURWICZ, H.; KRATSCH, K.M.; ROGAN, J.E.: Ablation.  
AGARDograph 161, March 1972.
12. LIEPMANN, H.W. & ROSHKO, A.: Elements of gasdynamics.  
Wiley 1957.
13. HAYES, W.D. & PROBSTEN, R.F.: Hypersonic flow theory. 2nd edition, Vol. I.  
Academic Press, 1966.
14. KRAUS, W.: Panel methods in aerodynamics; in  
"Computational Fluid Dynamics", VKI LS 87, March 1976; also  
"Numerical Methods in Fluid Dynamics", Hemisphere Publ. Corp., 1978, pp 237-297.
15. CEBECI, T. & SMITH, A.M.O.: Analysis of turbulent boundary layers.  
New York, Academic Press, 1974.
16. SAE Aerospace Applied Thermodynamics Manual. Part 1C - Engineering Fundamentals - Heat Transfer, and Part 4A - Boost Heat Transfer.
17. Space Shuttle Aerothermodynamics Technology Conference. Volume II - Heating.  
NASA TM X 2507, February 1972.
18. FAY, J.A.; RIDDELL, F.R.; KEMP, N.H.: Stagnation point heat transfer in dissociated air flow.  
Jet Propulsion, Vol. 27, No 6, June 1957, p. 672.
19. FAY, J.A. & RIDDELL, F.R.: Theory of stagnation point heat transfer in dissociated air.  
J. Aero. Sci., Vol. 25, No 2, February 1958, p. 73.
20. BECKWITH, I.E. & GALLAGHER, J.E.: Local heat transfer and recovery temperatures on a yawed cylinder at a Mach number of 4.15 and high Reynolds numbers.  
NASA TR R 104, 1961.
21. ECKERT, E.R.G.: Survey on heat transfer at high speeds.  
WADC TR 54-70, April 1954.
22. LEES, L.: Laminar heat transfer over blunt-nosed bodies at hypersonic flow speeds.  
Jet Propulsion, Vol. 26, No 4, April 1956, pp 259-269.
23. COHEN, C.B. & RESHOTKO, E.: The compressible laminar boundary layer with heat transfer and pressure gradient.  
NACA TR 1294, 1956.
24. MICHEL, R.: Etude de la transition sur les profils d'aile. Etablissement d'un point de transition et calcul de la traînée de profil en incompressible.  
ONERA Report 1/1578A, July 1951.
25. SMITH, A.M.O. & GAMBERONI, N.: Transition, pressure gradient and stability theory.  
Proc. 9th Int. Congr. Appl. Mech., Brussels, Belgium, 1956.
26. CRABTREE, L.F.: Prediction of transition in the boundary layer on an aerofoil.  
RAE TN Aero 2491, 1957.
27. HOPKINS, E.J.; JILLIE, D.W.; SORENSON, V.L.: Charts for estimating boundary layer transition on flat plates.  
NASA TN D 5846, 1970.
28. BENEK, J.A. & HIGH, M.D.: Transition prediction technique.  
AIAA J., Vol. 12, No 10, October 1974, pp 1425-1427.
29. MORIKOVIN, M.V.: Technical evaluation report of the Fluid Dynamics Panel Symposium on Laminar-Turbulent Transition.  
AGARD AR 22, June 1978.
30. DHAWAN, S. & NARASIMHA, R.: Some properties of boundary layer flow during transition from laminar to turbulent motion.  
J. Fluid Mechanics, Vol. 3, Part 4, January 1958, pp 418-436.
31. MASAKI, M. & YAKURA, J.: Transitional boundary layer considerations for the heating analyses of lifting re-entry vehicles.  
AIAA Paper 68-115, December 1968.
32. CHEN, K.K. & TYSON, N.A.: Extension of Emmons spot theory to flows on blunt bodies.  
AIAA J., Vol. 9, No 5, May 1971, p. 821.
33. STAINBACK, P.; WAGNER, R.D.; OWEN, F.K.; HORSTMAN, C.C.: Experimental studies of hypersonic boundary layer transition and effects of wind tunnel disturbances.  
NASA TN D 7453, March 1974.
34. HARRIS, J.E.: Numerical solution of the equations for laminar, transitional and turbulent boundary layers and comparison with experimental data.  
NASA TR R 368, 1971.
35. ADAMS, J.C. Jr: Eddy viscosity - intermittency factor approach to numerical calculations of transitional heating on sharp cones in hypersonic flow.  
AEDC TR 70-210, November 1970.
36. SHAMROTH, S.J. & McDONALD, H.: Assessment of a transitional boundary layer theory at low hypersonic Mach numbers.  
NASA CR 2131, November 1972.
37. SOMMER, S.C. & SHORT, B.J.: Free flight measurements of turbulent boundary layer skin friction in the presence of severe aerodynamic heating at Mach numbers from 2.8 to 7.0.  
NACA TN 3391, 1955.
38. SPALDING, D.B. & CHI, S.W.: The drag of a compressible turbulent boundary layer on a smooth flat plate with and without heat transfer.  
J. Fluid Mechanics, Vol. 18, Part 1, January 1964, pp 117-143.
39. WHITE, F.M. & CRISTOPH, G.H.: A simple new analysis of compressible turbulent two dimensional skin friction under arbitrary conditions.  
AFFDL TR 70-133, WPAFB, Ohio, February 1971.
40. HOPKINS, E.J. & INOUE, M.: An evaluation of theories for predicting turbulent skin friction and heat transfer on flat plates at supersonic and hypersonic Mach numbers.  
AIAA J., Vol. 9, No 6, June 1971, pp 993-1003.
41. VAN DRIEST, E.R.: Problem of aerodynamic heating.  
Aeron. Engrg. Rev., Vol. 15, No 10, October 1956, pp 26-41.

42. von KARMAN, Th.: The analogy between fluid friction and heat transfer. ASME Transact., Vol. 64, No 8, November 1939, pp 705-710.
43. BRADSHAW, P.: An improved Van Driest skin-friction formula for compressible turbulent boundary layers. AIAA J., Vol. 15, No 2, February 1977, pp 212-214.
44. BUSHNELL, D.M.; CARY, A.M.; HARRIS, J.E.: Calculation methods for compressible turbulent boundary layers. in "Compressible Turbulent Boundary Layers", VKI LS 86, March 1976.
45. REYNOLDS, W.C.: Computation of turbulent flows. Annual Review of Fluid Mechanics, Vol. 8, 1976, p. 183.
46. BRADSHAW, P.: The turbulent structure of compressible boundary layers. in "Compressible Turbulent Boundary Layers", VKI LS 86, March 1976.
47. CHAPMAN, D.R.: Status and prospects of computational fluid dynamics. in "Computational Fluid Dynamics", VKI LS 87, March 1976.
48. BRADSHAW, P.B. & UNSWORTH, K.: An improved FORTRAN program for the Bradshaw-Ferris-Ahwell method of calculating turbulent shear layers. Imperial College, Aero Report 74-02, February 1974.
49. CRAWFORD, M.E. & KAYS, W.M.: STAN5 - A program for numerical computation of two dimensional internal and external boundary layer flows. NASA CR 2742, December 1976.
50. KORKEGI, R.H.: Survey of viscous interactions associated with high Mach number flight. AIAA J., Vol. 9, No 5, May 1971, pp 771-784.
51. CHAPMAN, D.R.; KUEHN, D.M.; LARSON, H.K.: Investigation of separated flows in supersonic and subsonic streams with emphasis on the effect of transition. NACA TR 1356, 1958.
52. FLETCHER, M.S.; BRIGGS, D.G.; PAGE, R.H.: A review of heat transfer in separated and reattached flows. AIAA Paper 70-767, June 1970.
53. HANKEY, W.L. & HOLDEN, M.S.: Two dimensional shock wave/boundary layer interaction. AGARDograph 203, 1975.
54. BUSHNELL, D.M. & WEINSTEIN, L.M.: Correlation of peak heating for reattachment of separated flows. J. Spacecraft & Rockets, Vol. 5, No 9, September 1968, pp 1111-1112.
55. JOHNSON, C.B. & KAUFMAN, L.G. II: Interference heating from interactions of shock waves with turbulent boundary layers at Mach 6. NASA TN D 7649, September 1974.
56. NEUMANN, R.D. & BURKE, G.L.: The influence of shock wave boundary layer effects on the design of hypersonic aircraft. AFFDL TR 68-152, March 1969.
57. OSKAM, B.; VAS, I.E.; BOGDONOFF, S.M.: An experimental study of three dimensional flow fields in an axial corner at Mach 3. AIAA Paper 77-689, June 1977.
58. NEUMANN, R.D. & HAYES, J.R.: Prediction techniques for three dimensional shock wave/turbulent boundary layer interactions. AIAA J., Vol. 15, No 10, October 1977.
59. SPENCER, G.D.: AFFDL trip effects on interference heating. AEDC TR 77-61, 1977.
60. CHARWAT, A.F. & REDEKOPP, L.: Supersonic interference flow along the corner of intersecting wedges. AIAA J., Vol. 5, No 3, March 1967, pp 480-488.
61. BERTRAM, M.H. & HENDERSON, A. Jr: Some recent research with viscous interacting flows in hypersonic streams. Proc. Symp. Viscous Interaction Phenomena in Supers. & Hypers. Flow, USAF-ARL, May 1969, pp 1-30.
62. RAINBIRD, W.J.: Some problems of three dimensional separation about aircraft components. AIAA Paper 69-662, 1969.
63. PEAKE, D.J.; RAINBIRD, W.J.; ATRAGHI, E.G.: Three dimensional flow separations on aircraft and missiles. AIAA J., Vol. 10, No 5, May 1972, pp 567-580.
64. BERTIN, J.J. & GOODRICH, W.D.: Effects of surface temperature and Reynolds numbers on leeward shuttle heating. J. Spacecraft & Rockets, Vol. 13, No 8, August 1976, pp 473-480.
65. BERTIN, J.J.: A study of parameters which influence surface pressure and heat transfer in separated regions - a literature survey. U. Texas at Austin, Aerospace Engineering Report 74004, September 1974.
66. EDNEY, B.E.: Anomalous heat transfer and pressure distribution on blunt bodies at hypersonic speeds in the presence of an impinging shock. Aeron. Res. Inst. Sweden, Report 115, February 1968; also Effects of shock impingement on the heat transfer around blunt bodies. AIAA J., Vol. 6, No 1, January 1968, pp 15-21.
67. HAINS, F.D. & KEYES, J.W.: Shock interference in hypersonic flows. AIAA J., Vol. 10, No 11, November 1972, pp 1441-1447.
68. BERTIN, J.J.; GRAUMANN, B.W.; GOODRICH, W.D.: Aerothermodynamic aspects of shock interference patterns for shuttle configurations during entry. J. Spacecraft & Rockets, Vol. 10, No 9, September 1973, pp 545-546.
69. QUINN, R.D. & PALITZ, M.: Compression of measured and calculated turbulent heat transfer on the X-15 airplane at angles of attack up to 19°. NASA TM X 1291, September 1966.
70. GORD, P.R.: Measured and calculated structural temperature data from two X-15 airplane flights with extreme aerodynamic heating conditions. NASA TM X 1358, March 1967.



71. CARY, A.M. Jr: Turbulent boundary layer heat transfer and transition measurements for cold wall conditions at Mach 6.  
AIAA J., Vol. 6, 1968, p. 958.
72. ZOBY, E.V. & SULLIVAN, E.M.: Correlation of free flight turbulent heat transfer data from axisymmetric bodies with compressible flat plate relationship.  
NASA TN D 3802, 1967.
73. WIDHOPF, G.F.: Heat transfer correlation for blunt cones at angle of attack.  
J. Spacecraft & Rockets, Vol. 8, No 9, September 1971, pp1002-1004.
74. WING, L.D.: A method for calculating aerodynamic heating on sounding rocket tangent ogive noses.  
J. Spacecraft & Rockets, Vol. 11, No 6, June 1974, pp 357-362.
75. DE JARNETTE, F.R. & HAMILTON, H.H.: Inviscid surface streamline and heat transfer on shuttle type configurations.  
J. Spacecraft & Rockets, Vol. 10, No 5, May 1973, pp 314-321.
76. OVERMIER, D.K.: Development of airframe heat protection for a high performance sounding rocket.  
J. Spacecraft & Rockets, Vol. 4, No 11, November 1967, pp 1500-1504.
77. MILLER, J.A. & PUCCI, P.F.: Heat transfer to an airfoil in oscillating flow.  
ASME Transact., Series A : J. Engrg for Power, Vol. 93, No 4, October 1968, pp 461-468.
78. HEFNER, J.N.: Vortex induced heating to a cone-cylinder body at Mach 6.  
J. Spacecraft & Rockets, Vol. 11, No 2, February 1974, pp 127-128.
79. HEFNER, J.N. & WHITEHEAD, A.H. Jr: Vortex induced heating to cone flaps at Mach 6.  
J. Spacecraft & Rockets, Vol. 11, No 3, March 1974, pp 200-201.
80. CREEL, T.R. Jr: Mach number and Reynolds number effect on orbiter/tank.  
J. Spacecraft & Rockets, Vol. 10, No 8, August 1973, pp 535-537.
81. COLEMAN, H.W. & LEMMON, E.C.: Prediction of turbulent heat transfer and pressure on swept leading edges.  
J. Spacecraft & Rockets, Vol. 11, No 6, June 1974, pp 376-381.
82. BERTIN, J.J.: The effect pf protuberances, cavities and angle of attack on the wind tunnel pressure and heat transfer distribution for the Apollo commande module.  
NASA TM X 1243, 1966.
83. BREWER, R.A.; SAYDAH, A.R.; NESTLER, D.E.; FLORENCE, D.E.: Thermal performance evaluation of RSI panel gaps for space shuttle orbiter.  
J. Spacecraft & Rockets, Vol. 10, No 1, January 1973, pp 23-28.
84. DUNAVANT, J.C. & THROCKMORTON, D.A.: Aerodynamic heating to RSI tile surfaces and gap interactions.  
J. Spacecraft & Rockets, Vol. 11, No 6, June 1974, pp 437-440.
85. NEUMANN, R.D.: Special topics in hypersonic flow.  
AGARD LS 42, Vol. 1, 1972.
86. HAYES, J.R.: An overview of the test program and representative data taken on the modular missile configuration.  
AFFDL TM 77-90-FXG, October 1977.
87. Technical Staff, AEDC & ARO: Aerodynamic testing - a look at future requirements.  
AIAA Paper 78-765, AIAA 10th Aerodynamic Testing Conference, San Diego, April 1978.
88. TRIMMER, L.L. & MATTHEWS, R.K.: Supersonic aerothermal testing - a new requirement.  
AIAA Paper 78-733, AIAA 10th Aerodynamic Testing Conference, San Diego, April 1978.
89. MATTHEWS, R.K. & STALLINGS, D.W.: Materials testing in the VKF continuous flow wind tunnels.  
Paper presented at the AIAA 9th Aerodynamic Testing Conf., Arlington, Texas, June 1976.
90. LUKASIEWICZ, J.: Experimental methods of hypersonics.  
Marcel Dekker Inc., New York, 1973.
91. SCHULTZ, D.L. & JONES, T.V.: Heat transfer measurements in short duration hypersonic facilities.  
AGARDograph 165, 1973.
92. JONES, T.V.; SCHULTZ, D.L.; HENDLEY, A.D.: On the flow in an isentropic free piston tunnel.  
ARC R&M 3731, January 1973.
93. RICHARDS, B.E.: Isentropic light piston facilities for simulation of hot flows through turbines. in  
Advanced Testing in Turbomachines, VKI LS 78, April 1975.
94. CONSIGNY, H.; VILLE, J.P.; RICHARDS, B.E.: The VKI hot cascade tunnel CT2.  
VKI TN to be published.
95. HERZFELD, C.M. (ed.): Temperature, its measurement and control in science and industry. Volume 3.  
Rheinhold Publishing Company, 1962.
96. WINTER, K.G.: Notes on the measurement of aerodynamic heat transfer in model-testing facilities. in  
Compressible Turbulent Boundary Layers, VKI LS 86, March 1976.
97. ECKERT, E.R.G. & GOLDSTEIN, R.J.: Measurements in heat transfer. 2nd edition.  
McGraw Hill, 1976.
98. GINOUX, J.J.: A steady state technique for local heat transfer measurement and its application to the flat plate.  
J. Fluid Mechanics, Vol. 19, Part 1, 1964, pp 21-29.
99. TRIMMER, L.L.; MATTHEWS, R.K.; BUCHANAN, T.O.: Measurements of heat rates at the AEDC von Karman Facility.  
ICIASF'73 Record pp 35-44; published by IEEE.
100. NAYSMITH, A.: Measurement of aerodynamic heat transfer in intermittent wind tunnels.  
ARC CP 780, January 1964.
101. RICHARDS, B.E.: Developments in heat transfer measurements using transient techniques.  
ICIASF'77 Record; published by IEEE, September 1977.
102. OLDFIELD, M.L.G.; SCHULTZ, D.L.; JONES, T.V.: An on-line interactive minicomputer system for heat transfer measurements in a transient turbine cascade tunnel.  
ICIASF'77 Record; published by IEEE, September 1977.

103. SCHULTZ, D.L.; JONES, T.V.; OLDFIELD, M.L.G.; DANIELS, L.G.: A new transient cascade facility for the measurement of heat transfer rates.  
AGARD CP 229, Paper 31, February 1978.

#### Further references

- MICHEL, R.: Caractéristiques thermiques des couches limites et calcul pratique des transferts de chaleur en hypersonique.  
Progress in Aeronautical Sciences, Vol. 9, pp 123-214 ; Pergamon Press, 1968.  
DORRANCE, W.H.: Viscous hypersonic flow.  
New York, McGraw-Hill, 1962.  
POPE, A. & GOIN, K.L.: High speed wind tunnel testing.  
New York, Wiley, 1965.  
BRADSHAW, P.B.: Compressible turbulent boundary layers.  
Annual Review in Fluid Mechanics, Vol. 9, 1977.

#### ACKNOWLEDGEMENTS

The author would like to thank the following individuals who made suggestions after kindly reading the first draft of this paper prepared for an earlier von Karman Institute Lecture Series (VKI LS 86) in March 1976 : J.J. Bertin, G.G. Brebner, C. Mathews, R. Michel, R.D. Neumann, W. Oberkampf and K.G. Winter. Thanks are also due to Mme Toubeau who typed the manuscript.

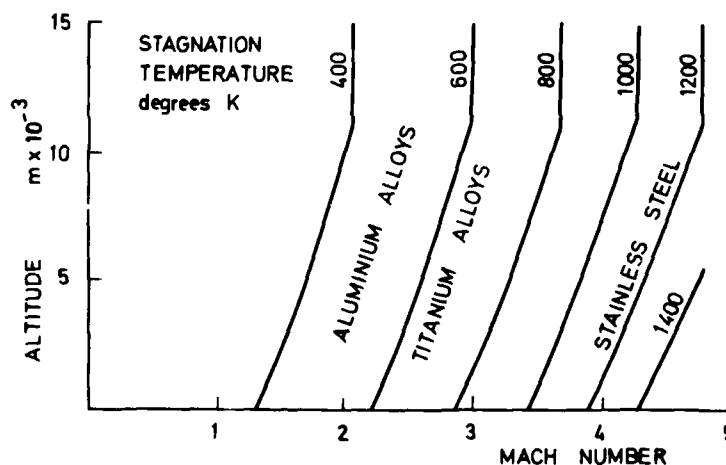


FIG. 1 FLOW STAGNATION TEMPERATURE IN HIGH SPEED FLIGHT

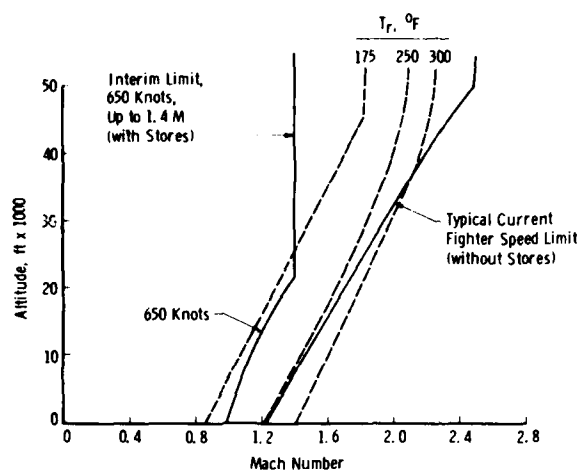


FIG. 2 PERFORMANCE ENVELOPE OF PRESENT-DAY AIRCRAFT (From Ref. 1)

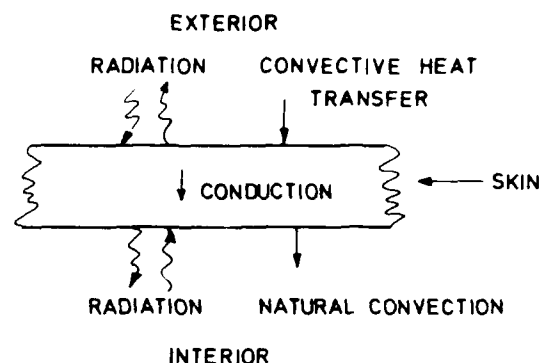


FIG. 3 THE GENERAL HEAT TRANSFER PROBLEM

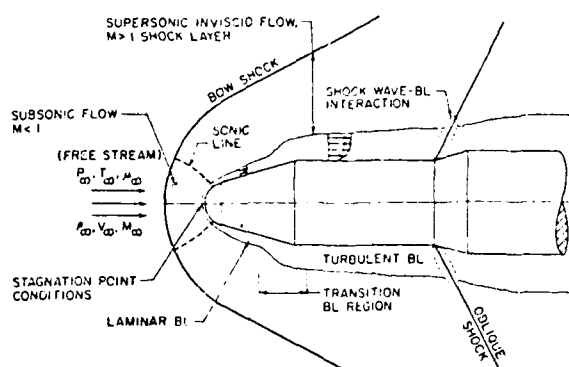


FIG. 4 TYPICAL MISSILE CONFIGURATION AND FLOW FIELD STRUCTURE

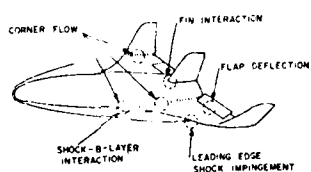


FIG. 5 REGIONS OF STRONG VISCOUS INTERACTION ON A HIGH MACH NUMBER VEHICLE

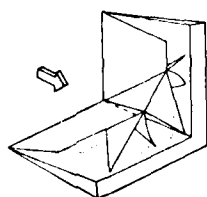


FIG. 6 CORNER FLOW STRUCTURE

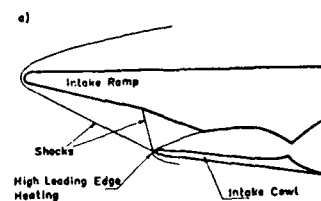


FIG. 7 PRACTICAL EXAMPLES OF SHOCK IMPINGEMENT HEATING

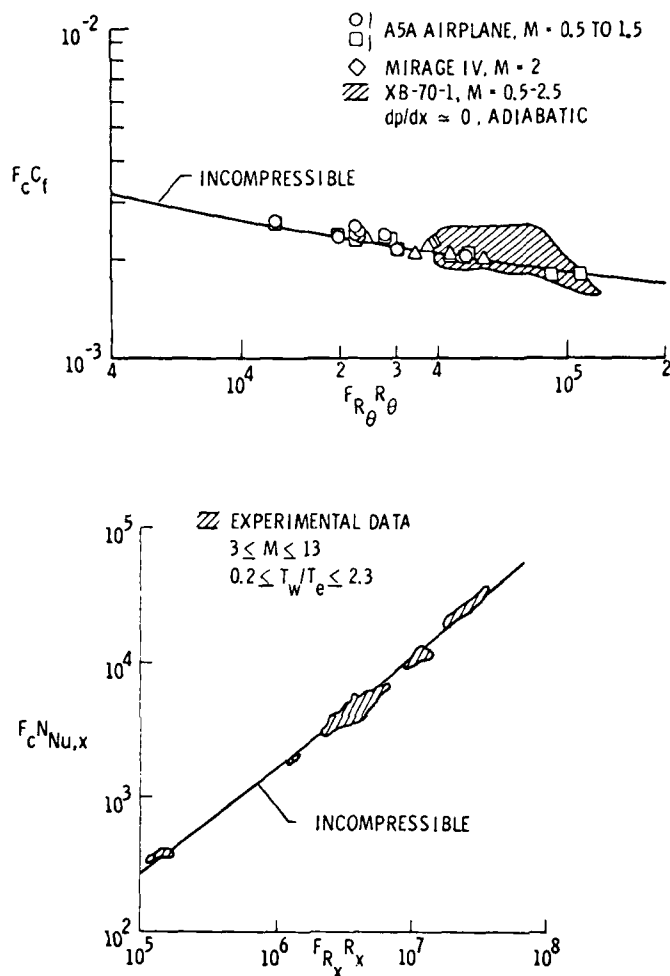


FIG. 9 PREDICTION OF TURBULENT HEATING TO SHARP AND BLUNT TIPPED AXISYMMETRIC BODIES IN FLIGHT BY ECKERT'S METHOD (From Ref. 44)

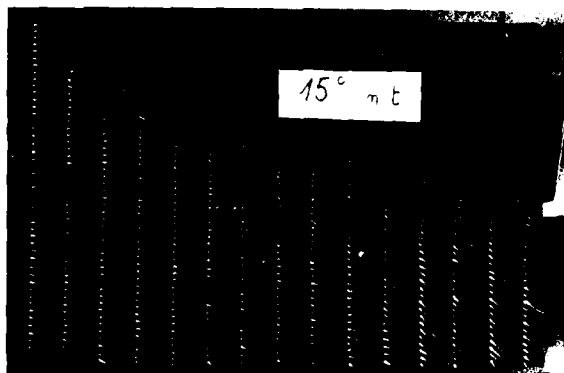


FIG. 11 FLOW VISUALIZATION OF FIN-TURBULENT BOUNDARY LAYER INTERACTION APPROPRIATE TO FIG. 10 (From VKI unpublished note)

FIG. 8 PREDICTION OF TURBULENT SKIN FRICTION ON CONVENTIONAL FLIGHT VEHICLES BY ECKERT'S METHOD (From Ref. 44)

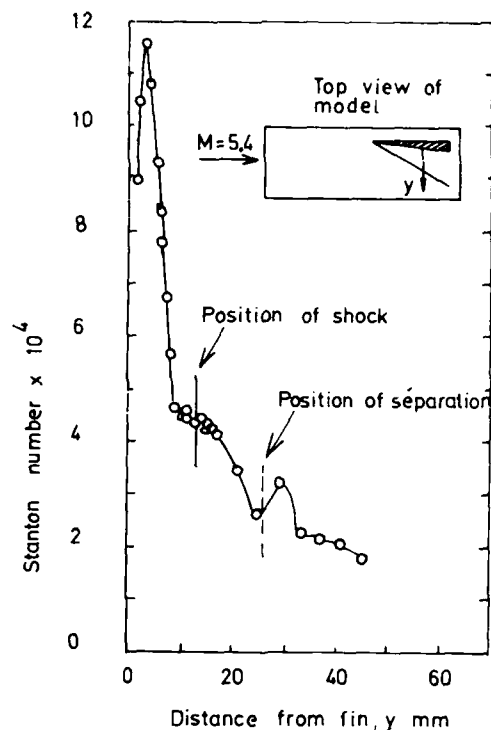


FIG. 10 HEAT TRANSFER DISTRIBUTION ON A SURFACE DUE TO A FIN AT  $15^\circ$ ,  $M = 5.4$ . (From VKI unpublished note)

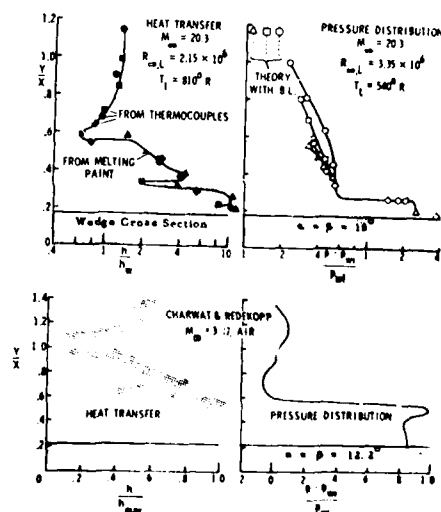


FIG. 12 SPANWISE HEAT TRANSFER AND PRESSURE DISTRIBUTION IN A CORNER FLOW FOR  $M = 3.17$  AND  $M = 20.3$  (From Ref. 61)

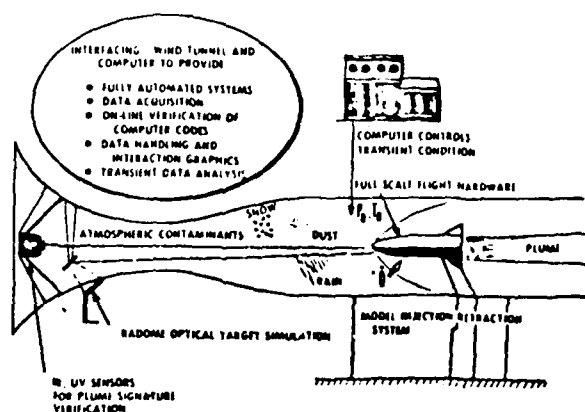


FIG.13 AEROTHERMAL WIND TUNNEL (M NUMBER 2 TO 6) (From Ref. 37)

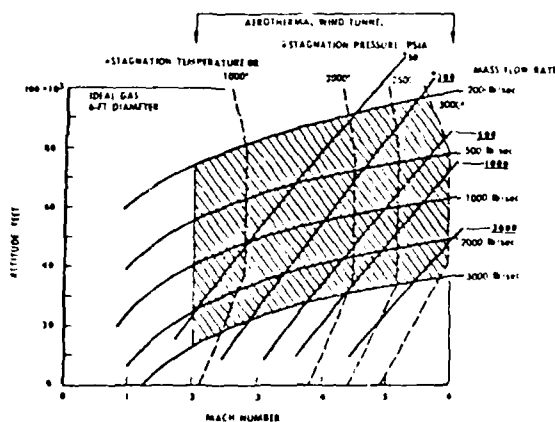
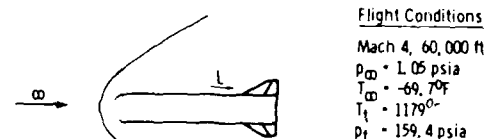
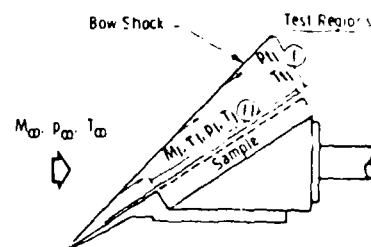
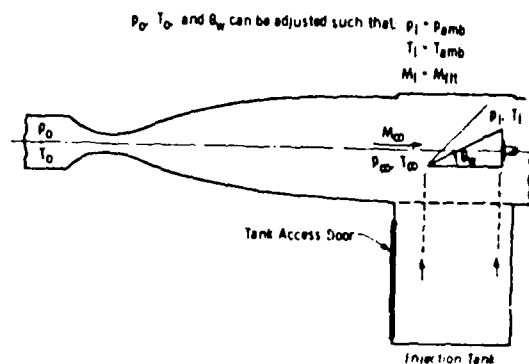


FIG.14 REQUIRED OPERATING ENVELOPE FOR AN ADVANCED AEROTHERMAL WIND TUNNEL - DUPLICATED FLIGHT (From Ref. 87)



#### Flight Conditions

Mach 4, 60,000 ft  
 $P_0 = 1.05$  psia  
 $T_0 = -69.7^\circ\text{F}$   
 $T_1 = 1179^\circ\text{F}$   
 $P_1 = 159.4$  psia

#### Local Conditions (Fin)

$p_1 \approx 0.914$  psia  
 $M_1 \approx 2.73$   
 $T_1 \approx 198^\circ\text{F}$

These conditions can be determined from analytical or experimental techniques.

#### a. Flight Environment

Utilizing AEDC-VKF Tunnel C,  $M_0 = 10$  (Real Gas Corrections  $< 4\%$ )

#### Nose

##### Test Region I

for  $\theta_w = 21$  deg

$P_0 = 2000$  psia &  $T_0 = 1179^\circ\text{F}$

The Flow Conditions Are:

$M_{1wt} = 4.0 = M_{0fht}$

$T_{1wt} = 1179^\circ\text{F} = T_{fht}$

$P_{1wt} = 159.4$  psia =  $P_{fht}$

#### Fin

##### Test Region II

for  $\theta_w = 29.7$  deg

$P_0 = 965$  psia &  $T_0 = 1265^\circ\text{F}$

The Flow Conditions Are:

$M_{1wt} = 2.73 = M_{fht}$

$P_{1wt} = 0.914$  psia =  $P_{fht}$

$T_{1wt} = 198^\circ\text{F} = T_{fht}$

#### b. Wind Tunnel Conditions Required to Duplicate Flight Environment

FIG.15 TECHNIQUE FOR MATERIALS TESTING IN THE AEDC CONTINUOUS FLOW WIND TUNNELS (From Ref. 89)

REPORT DOCUMENTATION PAGE											
1. Recipient's Reference	2. Originator's Reference	3. Further Reference	4. Security Classification of Document								
	AGARD-LS-98	ISBN 92-835-0234-5	UNCLASSIFIED								
5. Originator	Advisory Group for Aerospace Research and Development North Atlantic Treaty Organization 7 rue Ancelle, 92200 Neuilly sur Seine, France										
6. Title	MISSILE AERODYNAMICS										
7. Presented	on 5-6 March in Ankara, Turkey; 8-9 March in Rome, Italy and 12-16 March at the von Kármán Institute, Rhode-Saint-Genèse, Belgium.										
8. Author(s)/Editor(s)	Various		9. Date February 1979								
10. Author's/Editor's Address	Various		11. Pages 388								
12. Distribution Statement	This document is distributed in accordance with AGARD policies and regulations, which are outlined on the Outside Back Covers of all AGARD publications										
13. Keywords/Descriptors											
<table border="0"> <tr> <td>Missiles</td> <td>Flight control</td> </tr> <tr> <td>Aerodynamic characteristics</td> <td>Heat transfer</td> </tr> <tr> <td>Flow distribution</td> <td>External stores</td> </tr> <tr> <td>Aerodynamic configurations</td> <td></td> </tr> </table>				Missiles	Flight control	Aerodynamic characteristics	Heat transfer	Flow distribution	External stores	Aerodynamic configurations	
Missiles	Flight control										
Aerodynamic characteristics	Heat transfer										
Flow distribution	External stores										
Aerodynamic configurations											
14. Abstract											
<p>This course will treat all the chief aspects concerned with the aerodynamics of tactical missiles. It will be introduced with an extended overview of the more classical topics such as flow over wings and bodies, wing-body and wing-tail interference and aerodynamics of complete configurations. This course will contain more detailed communications on topics to which large advances are at present being made towards improvement of the effectiveness of missiles through external aerodynamic design. These topics are: control of missiles, high-angle of attack aerodynamics, base flow, kinetic heating and stores separation.</p> <p>The material in this publication was assembled to support a Lecture Series under the sponsorship of the Fluid Dynamics Panel and the Consultant and Exchange Programme of AGARD, and the von Kármán Institute for Fluid Dynamics.</p>											

<p>AGARD Lecture Series No.98 Advisory Group for Aerospace Research and Development, NATO MISSILE AERODYNAMICS Published February 1979 388 pages</p> <p>This course will treat all the chief aspects concerned with the aerodynamics of tactical missiles. It will be introduced with an extended overview of the more classical topics such as flow over wings and bodies, wing-body and wing-tail interference and aerodynamics of complete configurations. This course will contain more detailed communications on topics to which large advances are at present being made towards improvement of the effectiveness of missiles through external</p> <p>P.T.O.</p>	<p>AGARD-LS-98</p> <p>Missiles Aerodynamic characteristics Flow distribution Aerodynamic configurations Flight control Heat transfer External stores</p>	<p>AGARD Lecture Series No.98 Advisory Group for Aerospace Research and Development, NATO MISSILE AERODYNAMICS Published February 1979 388 pages</p> <p>This course will treat all the chief aspects concerned with the aerodynamics of tactical missiles. It will be introduced with an extended overview of the more classical topics such as flow over wings and bodies, wing-body and wing-tail interference and aerodynamics of complete configurations. This course will contain more detailed communications on topics to which large advances are at present being made towards improvement of the effectiveness of missiles through external</p> <p>P.T.O.</p>	<p>AGARD-LS-98</p> <p>Missiles Aerodynamic characteristics Flow distribution Aerodynamic configurations Flight control Heat transfer External stores</p>
<p>AGARD Lecture Series No.98 Advisory Group for Aerospace Research and Development, NATO MISSILE AERODYNAMICS Published February 1979 388 pages</p> <p>This course will treat all the chief aspects concerned with the aerodynamics of tactical missiles. It will be introduced with an extended overview of the more classical topics such as flow over wings and bodies, wing-body and wing-tail interference and aerodynamics of complete configurations. This course will contain more detailed communications on topics to which large advances are at present being made towards improvement of the effectiveness of missiles through external</p> <p>P.T.O.</p>	<p>AGARD-LS-98</p> <p>Missiles Aerodynamic characteristics Flow distribution Aerodynamic configurations Flight control Heat transfer External stores</p>	<p>AGARD Lecture Series No.98 Advisory Group for Aerospace Research and Development, NATO MISSILE AERODYNAMICS Published February 1979 388 pages</p> <p>This course will treat all the chief aspects concerned with the aerodynamics of tactical missiles. It will be introduced with an extended overview of the more classical topics such as flow over wings and bodies, wing-body and wing-tail interference and aerodynamics of complete configurations. This course will contain more detailed communications on topics to which large advances are at present being made towards improvement of the effectiveness of missiles through external</p> <p>P.T.O.</p>	<p>AGARD-LS-98</p> <p>Missiles Aerodynamic characteristics Flow distribution Aerodynamic configurations Flight control Heat transfer External stores</p>

<p>aerodynamic design. These topics are: control of missiles, high-angle of attack aerodynamics, base flow, kinetic heating and stores separation.</p> <p>The material in this publication was assembled to support a Lecture Series under the sponsorship of the Fluid Dynamics Panel, the Consultant and Exchange Programme of AGARD and the von Kármán Institute for Fluid Dynamics presented on: 5-6 March in Ankara, Turkey: 8-9 March in Rome, Italy and 12-16 March at the von Kármán Institute, Rhode-Saint-Genèse, Belgium.</p> <p>ISBN 92-835-0234-5</p>	<p>aerodynamic design. These topics are: control of missiles, high-angle of attack aerodynamics, base flow, kinetic heating and stores separation.</p> <p>The material in this publication was assembled to support a Lecture Series under the sponsorship of the Fluid Dynamics Panel, the Consultant and Exchange Programme of AGARD and the von Kármán Institute for Fluid Dynamics presented on: 5-6 March in Ankara, Turkey: 8-9 March in Rome, Italy and 12-16 March at the von Kármán Institute, Rhode-Saint-Genèse, Belgium.</p> <p>ISBN 92-835-0234-5</p>
<p>aerodynamic design. These topics are: control of missiles, high-angle of attack aerodynamics, base flow, kinetic heating and stores separation.</p> <p>The material in this publication was assembled to support a Lecture Series under the sponsorship of the Fluid Dynamics Panel, the Consultant and Exchange Programme of AGARD and the von Kármán Institute for Fluid Dynamics presented on: 5-6 March in Ankara, Turkey: 8-9 March in Rome, Italy and 12-16 March at the von Kármán Institute, Rhode-Saint-Genèse, Belgium.</p> <p>ISBN 92-835-0234-5</p>	<p>aerodynamic design. These topics are: control of missiles, high-angle of attack aerodynamics, base flow, kinetic heating and stores separation.</p> <p>The material in this publication was assembled to support a Lecture Series under the sponsorship of the Fluid Dynamics Panel, the Consultant and Exchange Programme of AGARD and the von Kármán Institute for Fluid Dynamics presented on: 5-6 March in Ankara, Turkey: 8-9 March in Rome, Italy and 12-16 March at the von Kármán Institute, Rhode-Saint-Genèse, Belgium.</p> <p>ISBN 92-835-0234-5</p>



B64a  
H

**AGARD**

NATO  OTAN

7 RUE ANCELLE · 92200 NEUILLY-SUR-SEINE  
FRANCE

Telephone 745.08.10 · Telex 610176

**DISTRIBUTION OF UNCLASSIFIED  
AGARD PUBLICATIONS**

AGARD does NOT hold stocks of AGARD publications at the above address for general distribution. Initial distribution of AGARD publications is made to AGARD Member Nations through the following National Distribution Centres. Further copies are sometimes available from these Centres; but if not may be purchased in Microfiche or Photocopy form from the Purchase Agencies listed below.

**NATIONAL DISTRIBUTION CENTRES**

**BELGIUM**

Coordonnateur AGARD - VSL  
Etat-Major de la Force Aérienne  
Quartier Reine Elisabeth  
Rue d'Evere, 1140 Bruxelles

**CANADA**

Defence Scientific Information Service  
Department of National Defence  
Ottawa, Ontario K1A 0Z2

**DENMARK**

Danish Defence Research Board  
Østerbrogades Kaserne  
Copenhagen Ø

**FRANCE**

O.N.E.R.A. (Direction)  
29 Avenue de la Division Leclerc  
92 Châtillon sous Bagneux

**GERMANY**

Zentralstelle für Luft- und Raumfahrt-  
dokumentation und -information  
c/o Fachinformationszentrum-Energie,  
Physik, Mathematik GmbH  
Kernforschungszentrum  
7514 Eggenstein-Leopoldshafen 2

**GREECE**

Hellenic Air Force General Staff  
Research and Development Directorate  
Hoflogos, Athens, Greece

**ICELAND**

Director of Aviation  
c/o Flugrad  
Reykjavik

**ITALY**

Aeronautica Militare  
Ufficio del Delegato Nazionale all'AGARD  
3, Piazzale Adenauer  
Roma/EUR

**LUXEMBOURG**

See Belgium

**NETHERLANDS**

Netherlands Delegation to AGARD  
National Aerospace Laboratory, NLR  
P.O. Box 126  
Delft

**NORWAY**

Norwegian Defence Research Establishment  
Main Library  
P.O. Box 25  
N-2007 Kjeller

**PORTUGAL**

Direcção do Serviço de Material  
da Força Aérea  
Rua da Escola Politécnica 42  
Lisboa  
Attn: AGARD National Delegate

**TURKEY**

Department of Research and Development (ARGE)  
Ministry of National Defence, Ankara

**UNITED KINGDOM**

Defence Research Information Centre  
Station Square House  
St. Mary Cray  
Orpington, Kent BR5 3RE

**UNITED STATES**

National Aeronautics and Space Administration (NASA)  
Langley Field, Virginia 23365  
Attn: Report Distribution and Storage Unit

THE UNITED STATES NATIONAL DISTRIBUTION CENTRE (NASA) DOES NOT HOLD STOCKS OF AGARD PUBLICATIONS, AND APPLICATIONS FOR COPIES SHOULD BE MADE DIRECT TO THE NATIONAL TECHNICAL INFORMATION SERVICE (NTIS) AT THE ADDRESS BELOW.

**PURCHASE AGENCIES**

*Microfiche or Photocopy*

National Technical  
Information Service (NTIS)  
5285 Port Royal Road  
Springfield  
Virginia 22161, USA

*Microfiche*

Space Documentation Service  
European Space Agency  
10, rue Mario Nikis  
75015 Paris, France

*Microfiche*

Technology Reports  
Centre (DTI)  
Station Square House  
St. Mary Cray  
Orpington, Kent BR5 3RE  
England

Requests for microfiche or photocopies of AGARD documents should include the AGARD serial number, title, author or editor, and publication date. Requests to NTIS should include the NASA accession report number. Full bibliographical references and abstracts of AGARD publications are given in the following journals:

**Scientific and Technical Aerospace Reports (STAR)**

published by NASA Scientific and Technical  
Information Facility  
Post Office Box 8757,  
Baltimore/Washington International Airport  
Maryland 21240, USA

**Government Reports Announcements (GRA)**

published by the National Technical  
Information Service, Springfield  
Virginia 22161, USA



Printed by Technical Editing and Reproduction Ltd  
Harford House, 7-9 Charlotte St, London W1P 1HD

REF ID: A64022